Transactions of the ASME®

Transactions of the ASME, Journal of Heat Transfer (ISSN 0022-1481) is published bi-monthly (Feb., Apr., June, Aug., Oct., Dec.) by The American Society of Mechanical Engineers, Three Park Avenue, New York, NY 10016. Periodicals postage paid at New York, NY and additional mailing offices. POSTMASTER: Send address changes to Transactions of the ASME, Journal of Heat Transfer, c/o THE AMERICAN SOCIETY OF MECHANICAL ENGINEERS, 22 Law Drive, Box 2300, Fairfield, NJ 07007-2300. **CHANGES OF ADDRESS** must be received at Society headquarters seven weeks before they are to be effective. Please send old label and new address. **STATEMENT from By-Laws.** The Society shall not be responsible for statements or opinions advanced in papers or ... printed in its publications (B7.1, Para. 3), **INDEXED** by Applied Mechanics Reviews and Engineering Information, Inc. Canadian Goods & Services Tax Registration #126148048.

Journal of Heat Transfer

Published Bimonthly by The American Society of Mechanical Engineers

VOLUME 124 • NUMBER 3 • JUNE 2002

TECHNICAL PAPERS

(Contents continued on inside back cover)

This journal is printed on acid-free paper, which exceeds the ANSI Z39.48-1992 specification for permanence of paper and library materials. ♾™
♻ 85% recycled content, including 10% post-consumer fibers.

Journal of Heat Transfer Volume 124, Number 3 JUNE 2002

Thermal Contact Conductance of Non-Flat, Rough, Metallic Coated Metals

M. A. Lambert
Mem. ASME,
Assistant Professor
Department of Mechanical Engineering,
San Diego State University,
San Diego, CA 92182-1323

L. S. Fletcher
Fellow ASME
Thomas A. Dietz Professor
Department of Mechanical Engineering,
Texas A&M University,
College Station, TX 77843-3123

Thermal contact conductance is an important consideration in such applications as nuclear reactor cooling, electronics packaging, spacecraft thermal control, and gas turbine and internal combustion engine cooling. In many instances, the highest possible thermal contact conductance is desired. For this reason, soft, high conductivity, metallic coatings are sometimes applied to contacting surfaces (often metallic) to increase thermal contact conductance. O'Callaghan et al. (1981) as well as Antonetti and Yovanovich (1985, 1988) developed theoretical models for thermal contact conductance of metallic coated metals, both of which have proven accurate for flat, rough surfaces. However, these theories often substantially overpredict the conductance of non-flat, rough, metallic coated metals. In the present investigation, a semi-empirical model for flat and non-flat, rough, uncoated metals, previously developed by Lambert and Fletcher (1996), is employed in predicting the conductance of flat and non-flat, rough, metallic coated metals. The models of Antonetti and Yovanovich (1985, 1988) and Lambert and Fletcher (1996) are compared to experimental data from a number of investigations in the literature. This entailed analyzing the results for a number of metallic coating/substrate combinations on surfaces with widely varying flatness and roughness. Both models agree well with experimental results for flat, rough, metallic coated metals. However, the semi-empirical model by Lambert and Fletcher (1996) is more conservative than the theoretical model by Antonetti and Yovanovich (1985, 1988) when compared to the majority of experimental results for non-flat, rough, metallic coated metals. [DOI: 10.1115/1.1464565]

Keywords: Thermal Contact Conductance, Electronic Equipment, Thermal Packaging

1 Introduction

Metallic coatings typically offer the greatest enhancement of thermal contact conductance in comparison to other classes of coatings and interstitial materials, as well as offering several other advantages. Metallic coatings do not evaporate or migrate as may greases and oils. Nor do metallic coatings leak from joints under high loading as may low melting point eutectic alloys. Thin metallic foils are tedious to insert into a joint and may wrinkle, thereby possibly even increasing contact resistance with respect to the bare junction. Elastomeric coatings, physically vapor deposited (PVD) ceramic coatings, and anodic coatings, because of their low thermal conductivity or high hardness (or both), seldom, if ever, provide the improvement in conductance attainable with metallic coatings. Hence, metallic coatings often afford the best solution.

There have been a number of experimental investigations of thermal contact conductance of metallic coated metals. Lambert and Fletcher [1] reviewed these in detail. O'Callaghan et al. [2] and Antonetti and Yovanovich [3,4] developed theoretical models, which yield nearly identical predictions and agree quite well with their experimental results.

Although these two theories accurately predict the slope of some of the experimental results in other investigations (listed as they are discussed in Section 5.0), the theories substantially overpredict the magnitude of most of those results. This disagreement is not because of any errors in the theories by O'Callaghan et al. [2] and Antonetti and Yovanovich [3,4]. Rather, it is because these theories invoke the assumption that the contacting surfaces are nearly optically flat with varying roughness. Optically flat surfaces are those with a flatness deviation, TIR (Total Included Reading), of less than 0.3 μm, or less than 0.6 μm combined for a pair of contacting surfaces. Nearly optically flat surfaces are herein defined as those with a TIR less than 1.0 μm, or less than 2.0 μm combined for both contacting surfaces. Most of the other experimental investigations reviewed by Lambert and Fletcher [1] utilized significantly non-flat specimens.

For most applications in which thermal contact conductance is a concern, the contacting surfaces, typically referred to as ''engineering'' surfaces, are not optically flat. Instead, they exhibit significant non-flatness, which causes macroscopic gaps and macroscopic contact resistance, just as microscopic surface features (roughness) give rise to microscopic contact resistance. The macroscopic contact resistance often predominates.

2 Model Development

2.1 Assumptions of the Model by Lambert and Fletcher [17].

1. Contacting surfaces are circular, macroscopically spherical (see Section 2.2 for underlying rationale), and microscopically rough with a Gaussian height distribution.
2. The contact micro-hardness, H_C, is determined from Vickers micro-hardness, H_V, and σ/m (Hegazy [5]). In practice, H_C is approximated as H_V or Knoop micro-hardness, H_K.
3. Heat flows only through solid contacts, i.e., fluid gap conductance and radiative heat transfer across gaps are negligible. Such conditions exist in vacuums and if the surfaces in contact do not differ too greatly in temperature.
4. Thermal rectification is not considered. This is the phenomenon in which conductance is greater in one direction than in the other, due to either dissimilar materials or roughness.

2.2 Selection of Spherical Macroscopic Surface Profile. A universal model capable of dealing with completely arbitrary sur-

Contributed by the Heat Transfer Division for publication in the JOURNAL OF HEAT TRANSFER. Manuscript received by the Heat Transfer Division May 19, 1997; revision received December 20, 2001. Associate Editor: T. Tong.

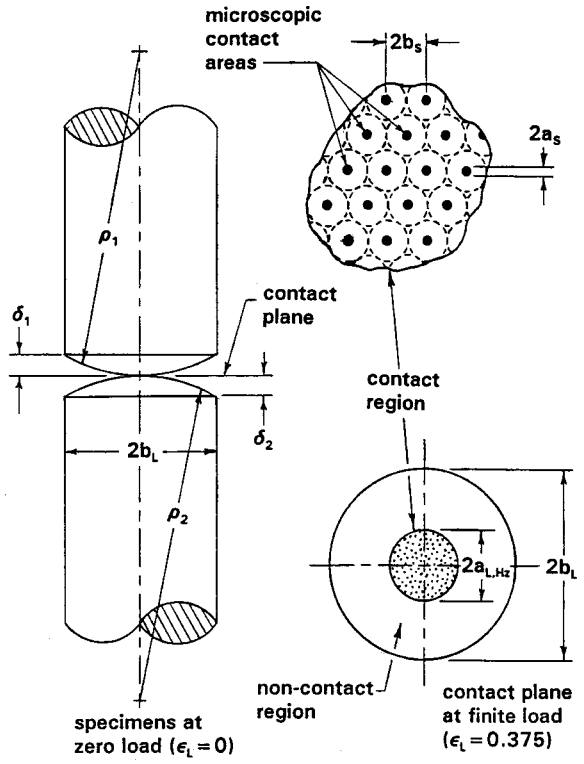

Fig. 1 Contacting spherical, rough surfaces showing the macroscopic contact radius, $a_{L,\mathrm{Hz}}$, predicted by Hertz [11], as incorporated in the models by Clausing and Chao [6] and Lambert and Fletcher [17]. Note that $a_{L,\mathrm{Hz}} \leq a_L$. Also shown is an idealized array of micro-contacts.

face profiles would probably be overly cumbersome at best, if not intractable. Wide applicability need not be sacrificed in the interest of simplifying the model. It is assumed herein that the macroscopic topography can be described by one or a few parameters, just as the microscopic topography is quite well described by combined root-mean-square roughness, σ, and combined mean absolute profile slope, m. A sphere is the simplest example, because its macroscopic profile is completely described by one parameter, its radius of curvature, ρ. This geometry is illustrated in Fig. 1.

Clausing and Chao [6], Mikic and Rohsenow [7], and Nishino et al. [8], among others, also used this simplification. This assumption is often justifiable, because nominally flat surfaces are often spherical, or at least are quite often crowned (convex) with a monotonic curvature in at least one direction.

2.3 Thermal Contact Resistance Model of Mikic [9]. Mikic [9] derived expressions for the total (microscopic, $R_{C,S}$, plus macroscopic, $R_{C,L}$) thermal contact resistance resulting from a non-uniform, axi-symmetric contact pressure distribution ($P = P(r)$), and these are given below. He did not address how to determine the pressure distribution, and this remains the crux of the problem.

$$R_{C,S} = 0.345 \frac{\sigma}{km} \left[\int_0^1 \frac{r}{b_L} \left(\frac{P}{H_C} \right)^{0.985} d\left(\frac{r}{b_L} \right) \right]^{-1} \tag{1}$$

$$R_{C,L} = 8 \frac{b_L}{k} \sum_{n=1}^{\infty} \frac{\left[\int_0^1 \frac{r}{b_L} \left(\frac{P}{P_{\mathrm{app}}} \right)^{0.985} J_0\left(\zeta_n \frac{r}{b_L} \right) d\left(\frac{r}{b_L} \right) \right]^2}{\zeta_n J_0^2(\zeta_n)} \tag{2}$$

In the present investigation, contact microhardness, H_C, and harmonic mean thermal conductivity, k, for uncoated metals are replaced by effective values, H' and k', for metallic coated metals, the latter parameters being developed by Antonetti and Yovanovich [3].

2.4 Pressure Distribution for Contact of Elastic, Rough Spheres. Greenwood and Tripp [10] developed a contact model for the elastic deformation of rough spheres. For applications where thermal contact conductance is relevant, contact loads are usually of such magnitude so as to cause only macroscopic elastic deformation. They introduced the following two dimensionless variables:

$$L^* = \frac{2L}{\sigma E' \sqrt{2\rho\sigma}} \tag{3}$$

$$P^* = \frac{P}{E' \sqrt{\sigma/8\rho}} \tag{4}$$

P^* and L^* are the dimensionless pressure and dimensionless load, respectively. The definition of P^* is not rigorously defined by Greenwood and Tripp [10] to be either the local, average, or apparent contact pressure. The definition of dimensionless load, L^*, however, is straight forward, because L is merely the contact load. The correlation developed herein employs L^*.

Hertz [11] developed a model for the pressure distribution and contact spot radius for two contacting, perfectly smooth, elastic spheres. For a given load, increasing the ratio of roughness to radius of curvature, σ/ρ, from zero (for a perfectly smooth sphere) causes an enlargement of the contact region and a reduction in the intensity of the contact pressure with respect to the Hertz [11] solution. Sasajima and Tsukada [12] defined two dimensionless ratios to characterize this behavior. $P_0/P_{0,\mathrm{Hz}}$ is the ratio of actual contact pressure (for rough spheres) to the contact pressure predicted by Hertz (for smooth spheres) at the center of contact (at $r=0$, where pressure is greatest). The ratio $a_L/a_{L,\mathrm{Hz}}$ is the actual macroscopic contact radius over the contact radius predicted by Hertz [11]. Tsukada and Anno [13] and Sasajima and Tsukada [12] give experimental and computed values of $P_0/P_{0,\mathrm{Hz}}$ for $L^* > 0.1$, that is, contacts for which sphericity is more pronounced. The model by Greenwood and Tripp [10] was used to extrapolate values of $P_0/P_{0,\mathrm{Hz}}$ for $L^* < 0.1$, as shown in Fig. 2. $P_0/P_{0,\mathrm{Hz}}$ is expressed by:

$$\frac{P_0}{P_{0,\mathrm{Hz}}} = \left(\frac{1}{1 + \frac{1}{(0.3585 \times (L^*)^{0.5840})^{1.11}}} \right)^{1/1.11} \tag{5}$$

Sasajima and Tsukada [12] developed an expression for contact pressure as a function of radial distance from the center of contact.

$$P(r) = P_0 \left[1 - \left(\frac{r}{a_L} \right)^2 \right]^{\alpha} \tag{6}$$

The exponent α is one for smooth spheres (large L^*) and is greater than one for rough spheres (small L^*) and asymptotically approaches 3. It is given by:

$$\alpha = 2 - \tanh[\log(L^*) - 1.8] \tag{7}$$

The ratio of the actual macroscopic contact radius (for rough spheres) to the Hertz [11] macroscopic contact radius (for smooth spheres), $a_L/a_{L,\mathrm{Hz}}$, is computed from $P_0/P_{0,\mathrm{Hz}}$ and α.

$$\frac{a_L}{a_{L,\mathrm{Hz}}} = \left[\frac{2(\alpha+1)}{3\left(\frac{P_0}{P_{0,\mathrm{Hz}}} \right)} \right]^{1/2} \tag{8}$$

The term b_L/a_L is the ratio of the surface radius to the actual macroscopic contact radius:

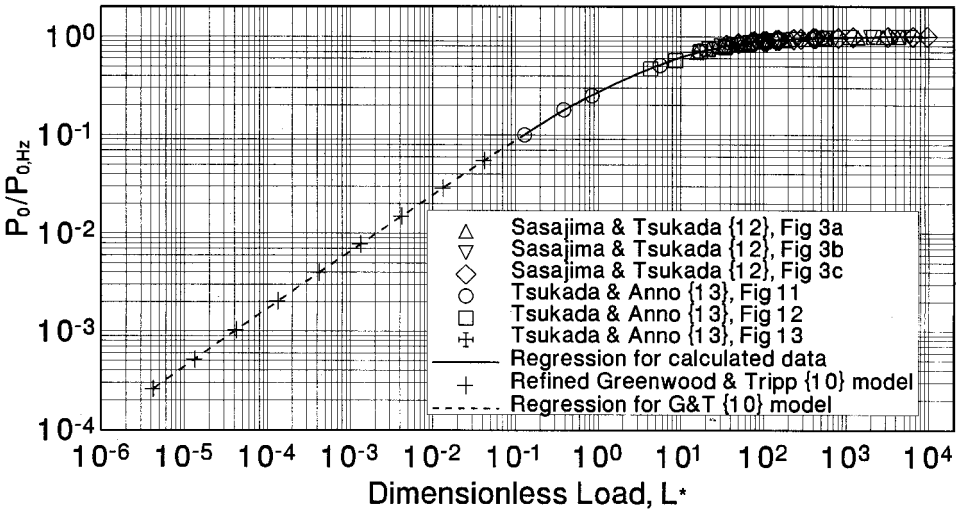

Fig. 2 Ratio of peak contact pressure $P_0/P_{0,Hz}$ (at $r=0$) for rough and smooth spheres

$$\frac{b_L}{a_L}=\frac{b_L}{\left(\frac{a_L}{a_{L,Hz}}\right)a_{L,Hz}}=\frac{b_L}{\left(\frac{a_L}{a_{L,Hz}}\right)\left(\frac{3L\rho}{4E'}\right)^{1/3}} \tag{9}$$

2.5 Model for Thermal Contact Conductance of Spherical, Rough Metals. The present model was obtained by using the contact model described above to define the pressure distribution, $P(r)$, in terms of load, mechanical properties, and surface geometry. $P(r)$ was then substituted into the expressions (Eqs. 1 and 2) by Mikic [9] for $R_{C,S}$ and $R_{C,L}$.

Buckingham Pi dimensional analysis was employed to determine the effect of each physical parameter on $R_{C,S}$ and $R_{C,L}$. This resulted in the following correlations.

$$R_{C,S}=\frac{6.15(L^*)^{0.484}\left(\frac{b_L}{a_L}\right)^2}{\left(\frac{km}{\sigma}\right)\left(\frac{L}{H_C\rho\sigma}\right)^{0.95}\left(\frac{P_0}{P_{0,Hz}}\right)^{0.67}} \tag{10}$$

$$R_{C,L}=\frac{1.44(L^*)^{0.954}\left(\frac{P_0}{P_{0,Hz}}\right)^{0.20}\left(\frac{b_L}{a_L}\right)^2}{\left(\frac{kL}{\rho\sigma^2E'}\right)} \tag{11}$$

Equations 10 and 11 contain $P_0/P_{0,Hz}$ raised to different powers. This was required in order to linearize both $R_{C,S}$ and $R_{C,L}$ in terms of L^*, so they could be expressed as power law regressions. Thermal contact conductance, $h_{C,S+L}$, is obtained from $R_{C,S}$ and $R_{C,L}$ by:

$$h_{C,S+L}=\frac{1}{R_{C,S}+R_{C,L}} \tag{12}$$

The predictive correlations for $R_{C,S}$ and $R_{C,L}$ are applicable for any conceivable range of conditions. The dimensionless load, L^*, was varied from 4.2×10^{-5} (i.e., essentially optically flat for any realistically sized component) up to 1.3×10^{4} (i.e., a smooth sphere for all practical purposes). The ratio b_L/a_L was varied from 10^{-4} up to 10^{3}. This covers the range of possibilities from an almost perfectly uniform pressure, where only the very center of the predicted $P(r)$ is actually brought to bear on the surface to a very small contact on a very large surface, say $a_L=1$ mm and $b_L=1.0$ m. However, for the wide range of surface measurements considered herein, which encompass nearly all likely practical situations, b_L/a_L varied between 1×10^{-1} and 2.53×10^{1}.

2.6 Estimation of Unspecified Parameters. Mean absolute profile slope, m, was rarely provided in experimental investigations performed in the 1960s and 1970s. To use data from those studies in the present analysis, m must be estimated. To this end Lambert [14] correlated m to σ for experiments in which both parameters were listed.

$$m_{1\ or\ 2}=0.076\sqrt{\sigma_{1\ or\ 2}\times10^6} \tag{13}$$

Uncertainty in this empirical correlation may, in extreme cases, be plus or minus a factor of two. However, profilometers capable of determining m are being used more and more in the electronics and spacecraft industries, so that estimation of m should no longer be necessary.

Also, experimental studies rarely list the radii of curvature, ρ_1 and ρ_2, of the specimen surfaces. To circumvent this difficulty, the combined radius of curvature, ρ, may be estimated from the combined non-flatness, TIR, of both surfaces. In the present study, the combined crown drop, δ, is assumed to equal TIR. See Fig. 1. Thus, ρ is:

$$\rho=b_L^2/2\delta \tag{14}$$

The concept of radius of curvature loses relevance if the surfaces are decidedly non-spherical. If this is so, the present model may substantially disagree (typically in an overly conservative fashion) with experimental data, but usually by no more than a factor of three.

For non-circular specimens, an effective macroscopic contact radius b_L' is defined as:

$$b_L'=\sqrt{A_{app}/\pi} \tag{15}$$

This expression is useful for commonly utilized square or rectangular surfaces (provided the length is not, say, more than twice the width for rectangular surfaces) or less frequently encountered triangular surfaces (approximately equilateral). This method of estimating b_L for non-circular contact surfaces is supported by the work of Yovanovich et al. [15].

3 Results and Discussion

Experimental results for thermal contact conductance of silver-coated nickel by Antonetti [16] are compared to the semi-empirical model of Lambert and Fletcher [17] and the theoretical model of Antonetti and Yovanovich [3,4] in Fig. 3. Antonetti and Yovanovich's [3,4] model very accurately predicts Antonetti's [16] results because he employed nearly optically flat specimens (TIR=1 μm). Lambert and Fletcher's [17] model reduces to An-

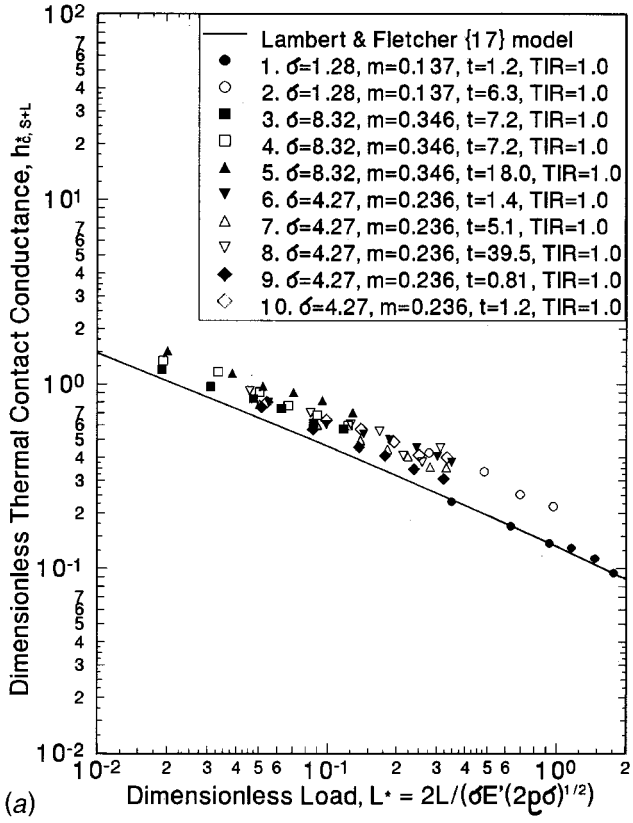

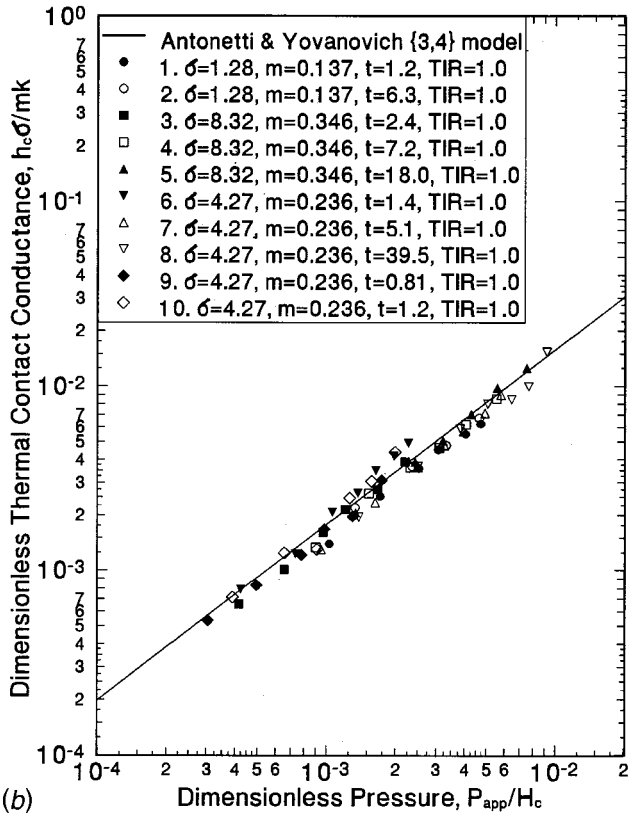

Fig. 3 Models by (*a*) Lambert and Fletcher [17] and (*b*) Antonetti and Yovanovich [3,4] compared to experimental thermal contact conductance results for physically vapor deposited (PVD) silver on nickel 200 by Antonetti [16]

tonetti and Yovanovich's [3,4] model for perfectly flat surfaces. Lambert and Fletcher's [17] model is slightly conservative (i.e., under-predictive) because it accounts for a minimal macroscopic contact resistance due to the slight non-flatness of Antonetti's [16] specimens.

Results from three investigations of metallic coated metals, Fried [18], Mal'kov and Dobashin [19] and O'Callaghan et al. [2] are plotted in Fig. 4. O'Callaghan et al.'s [2] experimental results agree well with both models, again because their data were obtained for nearly optically flat specimens for which both models are adequate. Antonetti and Yovanovich's [3,4] model over-predicts all of Fried's [18] and about half of Mal'kov and Dobashin's [19] experimental results. Lambert and Fletcher's [17] model under-predicts Mal'kov and Dobashin's [19] results and over-predicts Fried's [18] data. The significant scatter in Fried's [18] results suggests the presence of rather large uncertainties. Mal'kov and Dobashin [19] listed wide ranges of flatness deviation, TIR. Their experimental facility and data analysis are not well described, so it is not possible to estimate the accuracy of their work.

Figure 5 shows that Antonetti and Yovanovich's [3,4] model over-predicts all of Kang et al.'s [20] results, though their model accurately predicts the slope of the experiments. Lambert and Fletcher's [17] model roughly follows the mean of the data, though it does not reduce the scatter with respect to nor predict the slope as well as Antonetti and Yovanovich's [3,4] model. Kang et al. [20] employed aluminum alloy specimens with turned contact surfaces produced on a lathe. This preparation method yielded wavy surfaces that were not monotonically curved as is assumed in the model by Lambert and Fletcher [17]. Kang et al. [20] reported the typical trough to crest height of the wavy surfaces to be 10 μm, though they did not report the flatness deviation, TIR. In the present analysis TIR was assumed to equal the waviness height of 10 μm. The fact that the theory by Antonetti and Yovanovich [3,4] accurately predicts the slope of Kang et al.'s [20] experiments suggests that whatever non-flatness the surfaces exhibited was considerably smaller than the waviness. The fact that Lambert and Fletcher's [17] model predicts the mean magnitude of the data demonstrates that waviness was predominant over roughness in determining contact conductance. Kang et al. [20] noted that conductance decreased drastically as coating thickness, t, was increased from 0.25 μm to 5.0 μm, which they attributed to increased bulk resistance of the thicker coatings. However, it is much more likely that oxidation of the coating surfaces between steps during deposition of the multi-layer thicker coatings substantially increased the resistance.

As illustrated in Fig. 6, Antonetti and Yovanovich's [3,4] model substantially over-predicts Chung et al.'s [21] results by a factor of 5 to 100 and inaccurately predicts the slope, while Lambert and Fletcher's [17] model only moderately over-predicts the magnitude of the data and accurately predicts the slope. Chung et al. [21] did not report flatness deviation, TIR. The TIR value (10 μm) listed in Fig. 6 was assumed for the present study to facilitate analyzing the results by Chung et al. [21], because TIR$=10$ μm is typically achieved by grinding and polishing. However, it is quite possible that TIR for the specimens used by Chung et al. [21] was much greater than 10μm. They used specimens of the same aluminum alloy and size employed by Kang et al. [20], although Chung et al. [21] ground and polished their specimens instead of turning them. Grinding, lapping, and polishing operations often produce spherical surfaces. This may be why Lambert and Fletcher's [17] model accurately predicts the slope of Chung et al.'s [21] results, whereas Antonetti and Yovanovich's [3,4] theory does not.

Figure 7 shows that Antonetti and Yovanovich's [3,4] model over-predicts the experimental data reported by Sheffield et al. [22], while Lambert and Fletcher's [17] model predicts the mean and slope of the data quite well with relatively little scatter. Sheffield et al. [22] used specimens made of the same aluminum alloy and prepared in the same way as those used by Chung et al. [21].

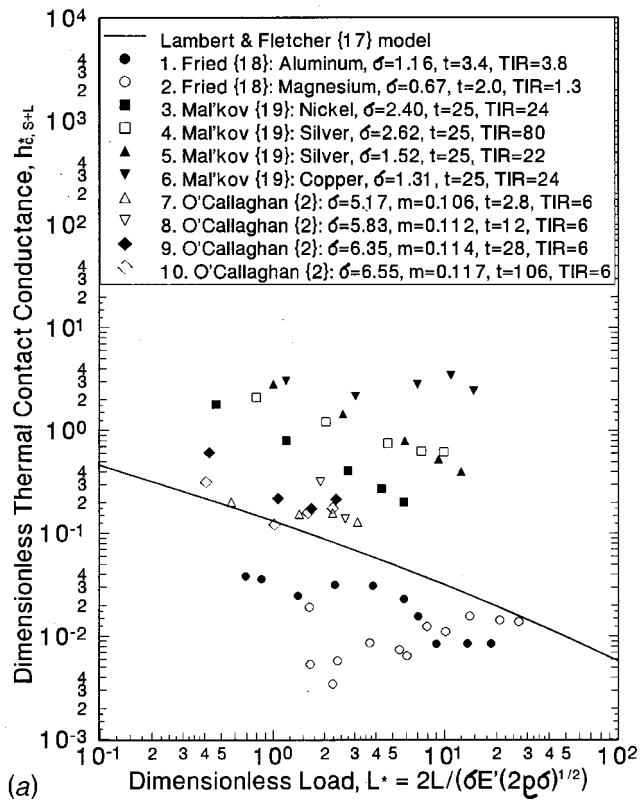

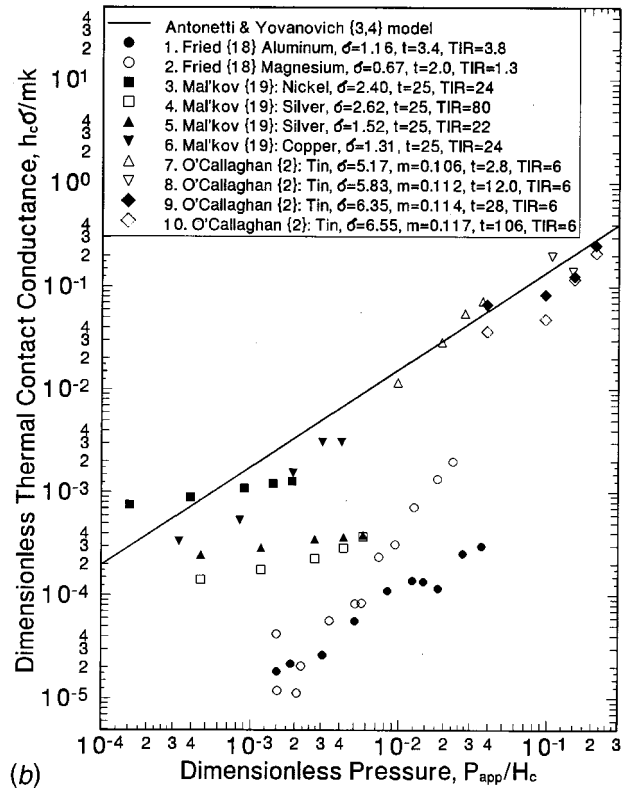

Fig. 4 Models by (*a*) Lambert and Fletcher [17] and (*b*) Antonetti and Yovanovich [3,4] compared to experimental thermal contact conductance results for PVD aluminum and magnesium on stainless steel 304 by Fried [18]; nickel, silver, and copper platings on stainless steel by Mal'kov and Dobashin [19]; and PVD tin on low alloy steel by O'Callaghan et al. [2]

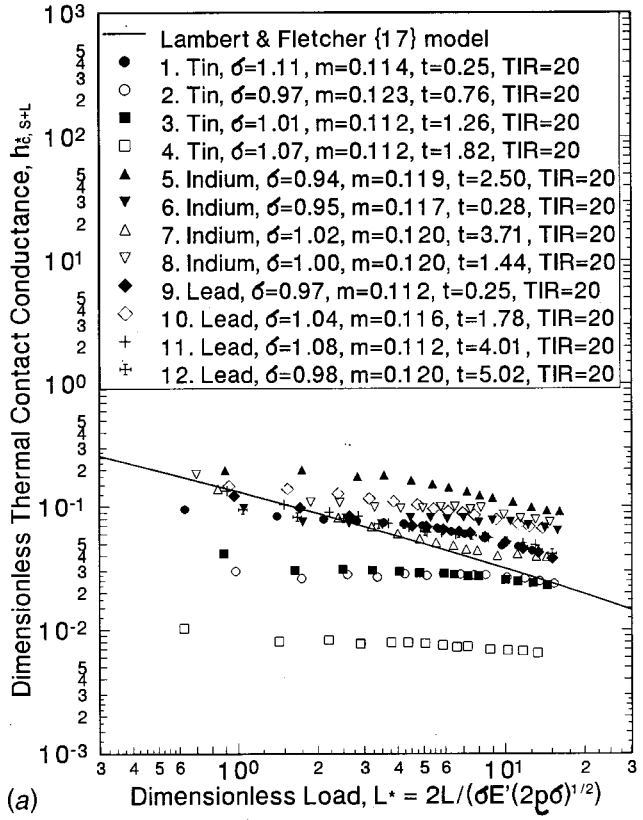

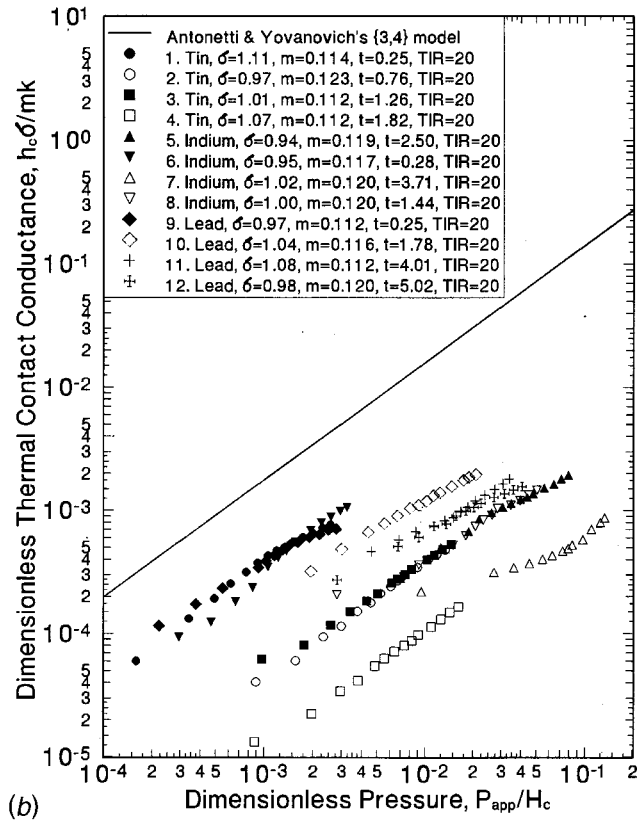

Fig. 5 Models by (*a*) Lambert and Fletcher [17] and (*b*) Antonetti and Yovanovich [3,4] compared to experimental thermal contact conductance results for physically vapor deposited (PVD) lead, tin, and indium on aluminum alloy 6061-T6 by Kang et al. [20]

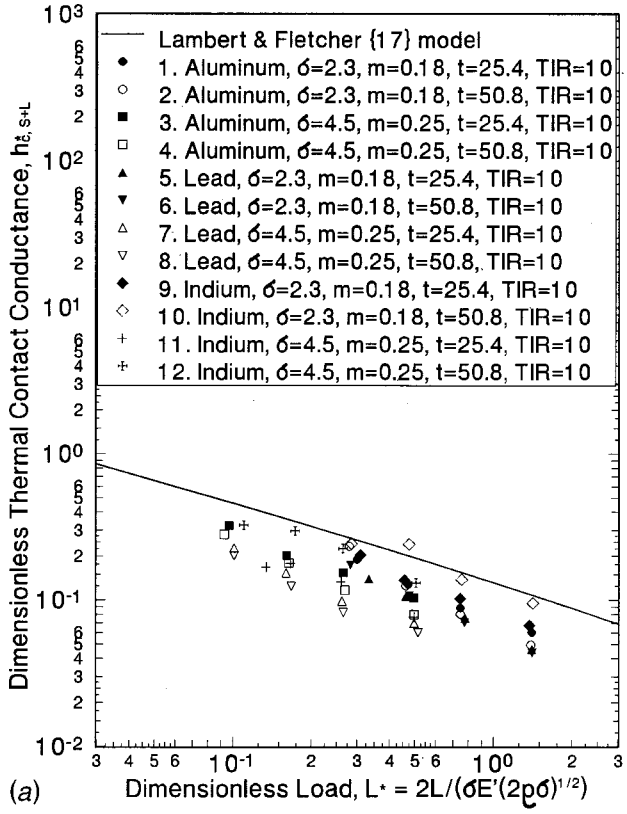

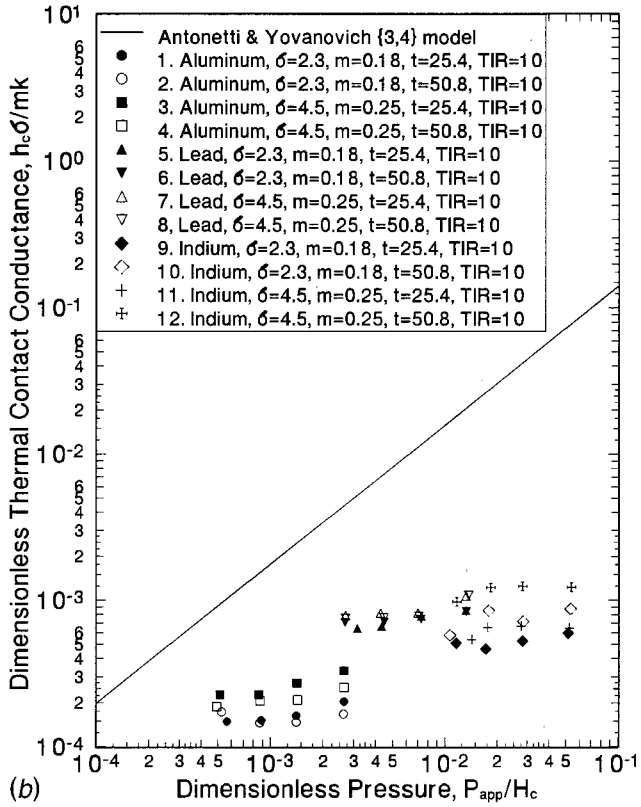

Fig. 6 Models by (*a*) Lambert and Fletcher [17] and (*b*) Antonetti and Yovanovich [3,4] compared to experimental thermal contact conductance results for physically vapor deposited (PVD) aluminum, lead, and indium on aluminum alloy 6061-T651 by Chung et al. [21]

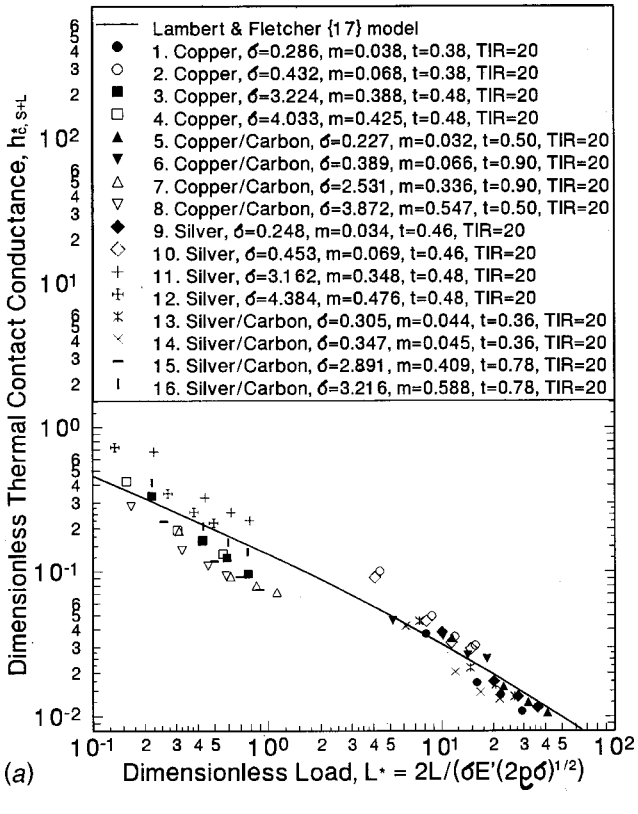

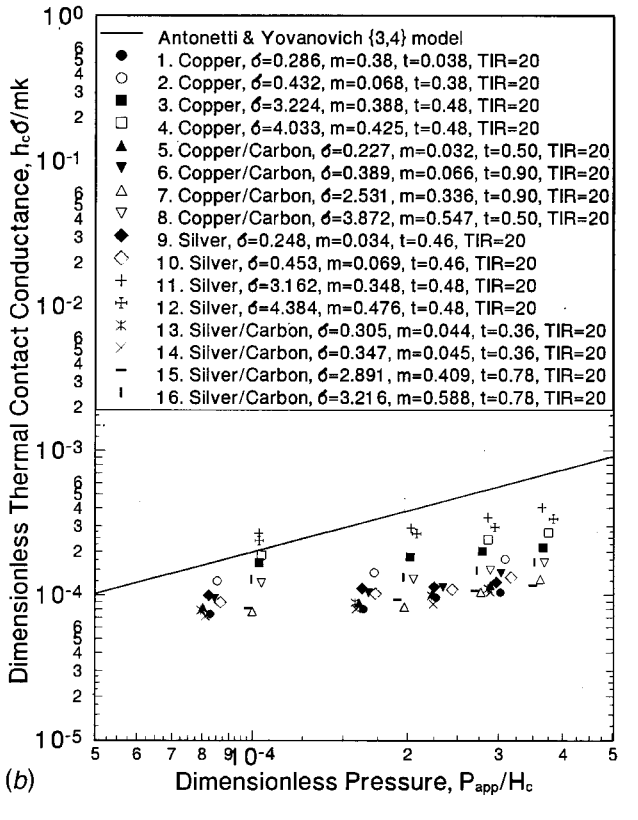

Fig. 7 Models by (*a*) Lambert and Fletcher [17] and (*b*) Antonetti and Yovanovich [3,4] compared to experimental thermal contact conductance results for (PVD) copper, copper/carbon, silver, and silver/carbon on aluminum alloy 6061-T651 by Sheffield et al. [22]

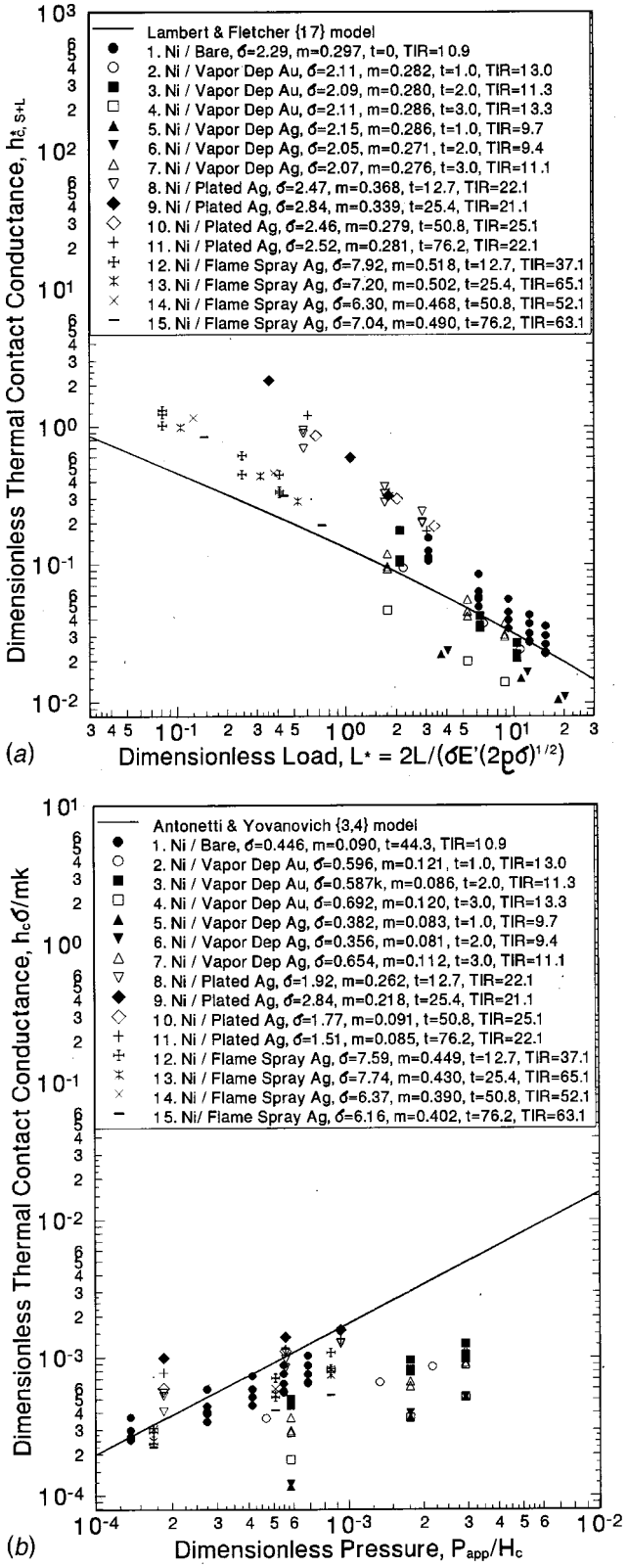

Fig. 8 Models by (*a*) Lambert and Fletcher [17] and (*b*) Antonetti and Yovanovich [3,4] compared to experimental thermal contact conductance results for electroless nickel plated copper to gold and silver coated (physically vapor deposited (PVD), electroplated, and flame sprayed) aluminum alloy A356-T61 by Lambert and Fletcher [23]

Thus, arguments similar to those made in conjunction with the results in Fig. 6 may be applied to the results in Fig. 7.

Figure 8 demonstrates that Lambert and Fletcher's [17] model is conservative (under-predictive) compared to most of the experimental results by Lambert and Fletcher [23], but their model predicts the slope of the results quite well. Antonetti and Yovanovich's [3,4] model is non-conservative (over-predictive) compared to most of the data and inaccurately predicts the slope. Lambert and Fletcher [23] prepared their aluminum alloy specimens using methods similar to those of Chung et al. [21] and Sheffield et al. [22]. Again, the arguments put forth to explain Fig. 6 also apply to Fig. 8.

Conclusions

Both the semi-empirical model by Lambert and Fletcher [17] and the theoretical model by Antonetti and Yovanovich [3,4] accurately predict thermal contact conductance of nearly optically flat (TIR$\leqslant 2\ \mu$m), rough, metallic coated metals. Additionally, through comparison with a large number of experimental results from the literature, the model by Lambert and Fletcher [17] is shown to provide usually conservative predictions of conductance for non-flat, rough, metallic coated metals.

Acknowledgments

This work was supported by the Naval Surface Warfare Center in Crane, Indiana (contract number N00164-94-C-0185). The authors would also like to thank Professor M. M. Yovanovich (emeritus) of the University of Waterloo, Ontario for graciously providing the much simpler, more elegant form of Eq. 5.

Nomenclature

a_L = macro-contact radius for rough spheres (m)
$a_{L,\mathrm{Hz}}$ = Hertz macro-contact radius for smooth spheres (m)
a_S = radius of micro-contact (m)
A_{app} = apparent contact area (m^2)
b_L = radius of surfaces in contact (m)
b_S = radius of heat flux channel for micro-contact (m)
E = modulus of elasticity (N/m^2)
E' = effective elastic modulus (N/m^2), $E'=[(1-\nu_1^2)/E_1+(1-\nu_2^2)/E_2]^{-1}$
$h_{c,s+L}$ = thermal contact conductance (W/m^2K), $h_{c,S+L}=1/(R_{c,S}+R_{c,L})$
H_C = contact micro-hardness (N/m^2)
H_K = Knoop micro-hardness (N/m^2)
H_V = Vickers micro-hardness (N/m^2)
J_0, J_1 = Bessel functions of the first kind
k = harmonic mean thermal conductivity (W/m-K), $k=2k_1k_2/(k_1+k_2)$
L = contact load (N)
L^* = dimensionless contact load, $L^*=2L/[\sigma E'(2\rho\sigma)^{1/2}]$
m = combined mean absolute profile slope (m/m), $m=(m_1^2+m_2^2)^{1/2}$
P = contact pressure (N/m^2)
P^* = dimensionless contact pressure, $P^*=P/[E'(\sigma/8\rho)^{1/2}]$
P_{app} = apparent contact pressure (N/m^2)
P_0 = maximum contact pressure (at $r=0$) for rough spheres (N/m^2)
$P_{0,\mathrm{Hz}}$ = Hertz' maximum contact pressure (at $r=0$) for smooth spheres (N/m^2)
r = distance from center of axi-symmetric contact (m)
$R_{C,L}$ = large scale thermal contact resistance (m^2K/W)
$R_{C,S}$ = small scale thermal contact resistance (m^2K/W)
TIR = non-flatness (Total Included Reading), (m), TIR $=\mathrm{TIR}_1+\mathrm{TIR}_2$
α = load redistribution parameter
δ = combined crown drop of surfaces (m), $\delta=\delta_1+\delta_2$

ε_L = ratio of macroscopic contact radius to surface radius, $a_{L,\mathrm{Hz}}/b_L$
ζ_n = nth root of Bessel function $J_1(\zeta_n)$
μ = micro$=10^{-6}$, combined with meters or inches
ν = Poisson ratio
ρ = combined radius of curvature (m), $\rho=(1/\rho_1+1/\rho_2)^{-1}$
σ = combined root-mean-square (rms) roughness (m), $\sigma=(\sigma_1{}^2+\sigma_2{}^2)^{1/2}$

Subscripts

Hz = Hertz' theory for contacting smooth spheres
L = large scale, macroscopic
n = index of summation
S = small scale, microscopic
0 = at axis or center of contact
1 = specimen or surface 1
2 = specimen or surface 2

References

[1] Lambert, M. A., and Fletcher, L. S., 1993, "A Review of the Thermal Contact Conductance of Junctions with Metallic Coatings and Films," AIAA Paper No. 92-0709, *AIAA Journal of Thermophysics and Heat Transfer*, **7**(4), pp. 547–554.

[2] O'Callaghan, P. W., Snaith, B., Probert, S. D., and Al-Astrabadi, F. R., 1981, "Prediction of Optimum Interfacial Filler Thickness for Minimum Thermal Contact Resistance," AIAA Paper 81–1166.

[3] Antonetti, V. W., and Yovanovich, M. M., 1985, "Enhancement of Thermal Contact Conductance by Metallic Coatings: Theory and Experiment," ASME Journal of Heat Transfer, **107**, pp. 513–519.

[4] Antonetti, V. W., and Yovanovich, M. M., 1988, "Using Metallic Coatings to Enhance Thermal Contact Conductance of Electronic Packages," Heat Transfer Eng., **9**(3), pp. 85–92.

[5] Hegazy, A. A., 1985, "Thermal Joint Conductance of Conforming Rough Surfaces," Ph.D. dissertation, University of Waterloo, Waterloo, Ontario, Canada.

[6] Clausing, A. M., and Chao, B. T., 1965, "Thermal Contact Resistance in a Vacuum Environment," ASME J. Heat Transfer , **87**(3), pp. 243–251.

[7] Mikic, B. B., and Rohsenow, W. M., 1966, "Thermal Contact Conductance," Technical Report No. 4542-41, Department of Mechanical Engineering, Massachusetts Institute of Technology, Cambridge, Mass., NASA Contract No. NGR 22-009-065.

[8] Nishino, K., Yamashita, S., and Torii, K., 1993, "Thermal Contact Conductance Under Low Applied Load in a Vacuum Environment," *Proceedings of the First International Conference of Aerospace Heat Exchanger Technology*, R. K. Shah and A. Hashemi, eds., Palo Alto, California, February 15–17, Elsevier, Amsterdam, pp. 763–788.

[9] Mikic, B. B., 1970, "Thermal Constriction Resistance Due to Non-Uniform Surface Conditions; Contact Resistance at Non-Uniform Interface Pressure," Int. J. Heat Mass Transf., **13**, pp. 1497–1500.

[10] Greenwood, J. A., and Tripp, J. H., 1967, "The Elastic Contact of Rough Spheres," ASME J. Appl. Mech., **89**(1), pp. 153–159.

[11] Hertz, H. R., 1896, *Miscellaneous Papers*, English Translation, MacMillan and Co., London.

[12] Sasajima, K., and Tsukada, T., 1981, "On the Approach Between a Sphere and a Rough Surface (2nd Report-Critical Condition to Yield Plastic Deformation in Contacting Bodies," (in Japanese), *Journal of the Japanese Society of Precision Engineering*, **47**(6), pp. 694–699.

[13] Tsukada, T., and Anno, Y., 1979, "On the Approach Between a Sphere and a Rough Surface (1st Report, Analysis of Contact Radius and Interface Pressure)," (in Japanese), *Journal of the Japanese Society of Precision Engineering*, **45**(4), pp. 473–479.

[14] Lambert, M. A., 1995, "Thermal Contact Conductance of Spherical, Rough Metals," Ph.D. dissertation, Texas A&M University, College Station, TX.

[15] Yovanovich, M. M., Burde, S. S., and Thompson, J. C., 1977, "Thermal Constriction Resistance of Arbitrary Planar Contacts with Constant Heat Flux," AIAA Paper No. 76–440.

[16] Antonetti, V. W., 1983, "On the Use of Metallic Coatings to Enhance Thermal Contact Conductance," Ph.D. dissertation, University of Waterloo, Waterloo, Ontario, Canada.

[17] Lambert, M. A., and Fletcher, L. S., 1996, "Thermal Contact Conductance of Spherical, Rough Metals," *AIChE National Heat Transfer Conference*, Houston, TX.

[18] Fried, E., 1966, "Study of Interface Thermal Contact Conductance, Summary Report," General Electric Company Document No. 66SD4471, Valley Forge, PA.

[19] Mal'kov, V. A., and Dobashin, P. A., 1969, "The Effect of Soft-Metal Coatings and Linings on Contact Thermal Resistance," Inzh.-Fiz. Zh., **17**(5), pp. 871–879.

[20] Kang, T. K., Peterson, G. P., and Fletcher, L. S., 1989, "Enhancing the Thermal Contact Conductance Through the Use of Thin Metallic Coatings," ASME Paper No. 89-HT-23.

[21] Chung, K. C., Sheffield, J. W., and Sauer, Jr., M. J., 1990, "Effect of Metallic Coated Surfaces on Thermal Contact Conductance: An Experimental Study," *6th Miami International Symposium on Heat and Mass Transfer*, Miami Beach, FL.

[22] Sheffield, J. W., Williams, A., Sauer, H. J., Jr., O'Keefe, T. J., and Chung, K. C., 1992, "Enhancement of Thermal Contact Conductance by Transitional Buffering Interfaces (TBI)," National Science Foundation Final Project Rep., NSF Grant No. CTS-8901871 (Thermal Systems Program), University of Missouri, Rolla, MO.

[23] Lambert, M. A., and Fletcher, L. S., 1995, "An Experimental Investigation of the Thermal Contact Conductance of Electroplated Silver Coatings," AIAA Paper No. 93-0846.

Measurements of Heat Transfer Coefficients From Supercritical Carbon Dioxide Flowing in Horizontal Mini/Micro Channels

S. M. Liao

T. S. Zhao
e-mail: metzhao@ust.hk
Assoc. Prof.,
Mem. ASME

Department of Mechanical Engineering,
The Hong Kong University of Science & Technology,
Clear Water Bay, Kowloon, Hong Kong, China

Heat transfer from supercritical carbon dioxide flowing in horizontal mini/micro circular tubes cooled at a constant temperature has been investigated experimentally. Six stainless steel circular tubes having inside-diameters of 0.50 mm, 0.70 mm, 1.10 mm, 1.40 mm, 1.55 mm, and 2.16 mm were tested. Measurements were carried out for the pressures ranging from 74 to 120 bar, the temperatures ranging from 20 to 110°C, and the mass flow rates ranging from 0.02 to 0.2 kg/min. It is found that the buoyancy effect was still significant, although supercritical CO_2 was in forced motion through the horizontal tubes at Reynolds numbers up to 10^5. The experimental results also indicate that the existing correlations developed in the previous studies for large tubes deviate significantly from the experimental data for the present mini/micro tubes. Based on the experimental data, a correlation was developed for the axially averaged Nusselt number in terms of appropriate dimensionless parameters for forced convection of supercritical carbon dioxide in horizontal mini/micro tubes cooled at a constant temperature. [DOI: 10.1115/1.1423906]

Keywords: Channel Flow, Convection, Heat Transfer, Microscale, Refrigeration, Supercritical Fluids

Introduction

As a non-flammable and non-toxic natural fluid, CO_2 has a zero ODP (ozone depleting potential) and a zero effective GWP (global warming potential). Thus, it will become a primary candidate for the next-generation environmental by benign refrigerant in automobile air-conditioning, railway air-conditioning, residential air-conditioning and heat pumps [1]. Since in some applications such as automobile air-conditioning and heat pump systems, the heat rejection temperatures are usually above the critical temperature of carbon dioxide (31.1°C), cycles using carbon dioxide as the refrigerant will have to operate in a transcritical cycle. As such, the heat rejection takes place above the critical pressure (about 74~120 bar) in a so-called gas cooler (corresponding to the condenser in the conventional subcritical systems), while the heat absorption remains below the subcritical region. The high working pressure and favorable heat transfer properties of CO_2 enable reduced tube diameters. A gas cooler made of extruded flat microchannel tubes of 0.79 mm in diameter has been reported [2]. The use of microchannels in the gas cooler will allow one to effectively handle high pressures without excessive wall thickness and material weight. In order to design a high efficiency gas cooler, a thorough understanding of convective heat transfer for supercritical carbon dioxide in cooled tubes is needed.

One of the most important characteristics of supercritical fluids near the critical point is that their physical properties exhibit extremely rapid variations with the change of temperature, especially near the pseudocritical point (the temperature at which the specific heat reaches a peak for a given pressure). This can be clearly seen from Fig. 1, where the specific heat c_p and density ρ of CO_2 at supercritical pressures of 80 and 100 bar (p_{cr} = 73.8 bar) are plotted based on the data from the NIST Refrigerants Database REFPROP [3]. The pseudocritical temperature T_{pc} of CO_2 as function of pressure can be best fitted by the following algebraic equation:

$$T_{pc} = -122.6 + 6.124p - 0.1657p^2 + 0.01773p^{2.5} - 0.0005608p^3, \quad (1)$$

where the pseudocritical temperature T_{pc} is in °C and the pressure p is in bar. It follows that $T_{pc} = 34.6$°C at $p = 80$ bar and $T_{pc} = 45.0$°C at $p = 100$ bar.

Forced convection of supercritical fluids such as water, carbon dioxide, nitrogen, hydrogen, and helium in channels have been extensively studied both experimentally [4–6] and numerically [7–9]. Many correlations, most of the Dittus-Boelter type $Nu = C\,Re^m Pr^n$, have been proposed for supercritical fluids with heating. The reference temperature method and the property ratio method have been employed to incorporate the variable-property effect [10]. Comprehensive reviews on previous work associated

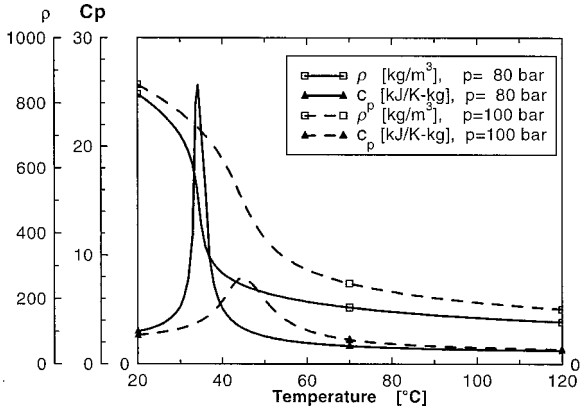

Fig. 1 Variations of the specific heat c_p and the density ρ of CO_2 at $p = 80$ and 100 bar

Contributed by the Heat Transfer Division for publication in the JOURNAL OF HEAT TRANSFER. Manuscript received by the Heat Transfer Division April 24, 2001; revision received September 24, 2001. Associate Editor: H. Bau.

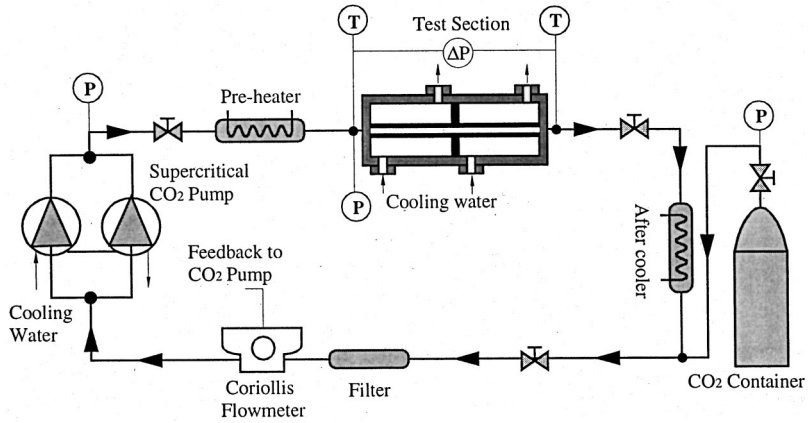

Fig. 2 Schematic diagram of the test loop

with variable property heat transfer and supercritical heat transfer are given by Kakac [10], Hall [11], and Polyakov [12]. It is generally agreed that the correlations do not show sufficient agreement with experiments to justify their use except in very limited conditions. The limitations imposed on a specific correlation should be carefully studied before its use in practical applications.

A literature survey indicates that only a few papers [4,5,8,13] have reported on the study of heat transfer of supercritical CO_2 under cooling conditions. In particular, experimental data on convective heat transfer of supercritical CO_2 in channels with a hydraulic diameter less than 2.0 mm are rather rare. Therefore, the purpose of this work was to study heat transfer from supercritical carbon dioxide flowing in mini/micro circular tubes in the temperature ranges relevant to the CO_2 gas coolers in the transcritical refrigeration systems. Six circular tubes having inside-diameters of 0.50 mm, 0.70 mm, 1.10 mm, 1.40 mm, 1.55 mm, and 2.16 mm were tested. Measurements were carried out at carbon dioxide pressures ranging from 74 to 120 bar and the temperature ranging from 20 to 110°C. In the following, we shall first describe our experimental apparatus and procedures. We shall then report the experimental results to show the effect of some important parameters including tube diameter, pressure, and mass flow rate and, the temperature difference between the bulk fluid and the wall on the heat transfer performance. Finally, the salient findings of the study will be summarized.

Experimental Apparatus and Procedures

The test loop constructed for the present investigation is schematically shown in Fig. 2. It consisted of a compressed CO_2 cylinder, a high-pressure CO_2 pump, a filter, a flow meter, a preheater, a test section, an after-cooler, and a couple of high-pressure fittings and valves. CO_2 with a purity of 99.5 percent was fed to the test loop from the compressed CO_2 cylinder and was circulated by the CO_2 pump (Model P-200, Thar Designs), which had an input pressure of 57 bar, a discharge pressure up to 680 bar, and a maximum mass flow rate of 0.2 kg/min. The pump is capable of control based on feedback from a pressure sensor or a flow meter. The mass flow rate was measured using a Coriolis-type Micro Motion mass flow meter (Model CFM-010M, with IFT9701 transmitter). The nominal range of the flow meter is 0–1.37 kg/min (0–22.8 g/s), with an accuracy of less than ±0.2 percent of reading. A pressure gage transducer (Model 3051CG5, Rosemount) was used to measure the static pressure at the inlet of the test section, while a differential pressure transducer (Model 3051CD3, Rosemount) was installed at both ends of the test section to measure the pressure drops. The pressure gage transducer and the differential pressure transducer were calibrated by using a pressure calibrator and the accuracy of the transducers was found to be ±0.2 percent of reading. The on-board microprocessor monitored the flow meter, calculated the flow rate and sent the feedback to the pump. In addition, a portable chiller was used to provide cooling for the CO_2 pump, the condenser and the test section.

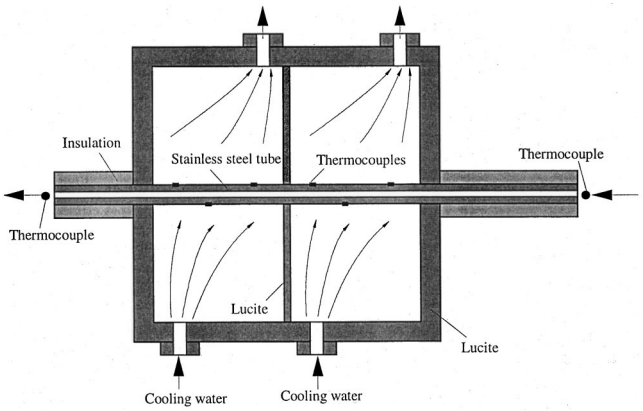

Fig. 3 Schematic diagram of the test section

Six circular tubes (stainless steel AISI 304) having inside-diameters/outside-diameters of 0.50 mm/0.80 mm, 0.70 mm/1.10 mm, 1.10 mm/1.47 mm, 1.40 mm/3.18 mm, 1.55 mm/2.05 mm, and 2.16 mm/3.18 mm were tested. Figure 3 shows the details of the test section. A horizontal circular tube to be tested was cooled by forced convection of cooling water. An insulated length of 110.0 mm preceded the cooled length of 110.0 mm, which was followed by an insulated exit length of 40.0 mm. The outer surface temperatures of the test tube were measured by six uniformly-spaced T-type thermocouples, while the temperatures of CO_2 at both the inlet (T_{in}) and the outlet (T_{out}) of the test tube were measured by two armored *T*-type thermocouples. All the thermocouples were calibrated in a constant temperature bath and the measurement error was found to be within ±0.2°C. The temperature of CO_2 at the inlet of the test tube was regulated by the pre-heater.

For all the experiments, the measured temperature difference between the outer surface of the insulated lengths at the both ends of the test section and the ambient indicated that the heat gain/loss from/to the ambient was negligibly small. Hence, the heat transfer rate $\dot{Q}$ from CO_2 to the tube wall can be obtained from the energy balance under a steady state:

$$\dot{Q} = \dot{m}(i_{in} - i_{out}), \tag{2}$$

Table 1 Measured wall temperatures along the test section

Test conditions	The outer wall temperatures of the test section measured by the six thermocouples (°C)					
	1	2	3	4	5	6
Case 1: d=2.16mm, p=79.53 bar, T_{in}=66.7°C, T_{out} =42.4°C	27.6	26.2	26.7	26.9	28.1	27.9
Case 2: d=1.40mm, p=100.44 bar, T_{in}=31.8°C, T_{out} =25.4°C	16.1	15.8	15.9	15.0	15.4	14.5
Case 3: d=0.70mm, p=79.29 bar, T_{in}=51.1°C, T_{out} =48.0°C	42.9	43.8	44.6	44.2	44.4	44.4

where $\dot{m}$ is the mass flow rate, while i_{in} and i_{out} denote the enthalpy of CO_2 at the inlet and the exit of the test section, respectively.

An outer wall mean temperature averaged over the entire cooled length can be obtained based on the readings of the six thermocouples under each test condition. In order to minimize errors in calculating mean wall temperatures, we attempted to keep the outer wall temperatures along the cooled length as uniform as possible. This was realized by adjusting separately the flow rates of the cooling water flowing through the two partitions of the test section (Fig. 3). The wall temperatures along the cooled length measured by the six thermocouples for three typical test conditions are listed in Table 1, which shows that the maximum temperature difference along the wall is within 2°C.

Based on the outer wall mean temperatures, the corresponding inner wall mean temperature of the test section T_w can then be calculated based on the wall thickness of the test tube, the outer wall mean temperature and the cooling power given by Eq. (2). Subsequently, a logarithmic mean temperature difference (LMTD) can be obtained for the test tube [14] as

$$\text{LMTD}=\frac{(T_{\text{in}}-T_w)-(T_{\text{out}}-T_w)}{\ln\left(\dfrac{T_{\text{in}}-T_w}{T_{\text{out}}-T_w}\right)}. \tag{3}$$

It should be mentioned that the derivation of the logarithmic mean temperature difference requires that the specific heat c_p be constant over the test tube. As shown in Fig. 1, although the specific heat c_p of supercritical CO_2 undergoes a rapid change with temperature near the pseudocritical point, the curve representing the variation of the specific heat with temperature becomes relatively flat at the temperature away from the pseudocritical point. In these experiments, for a given heat removal from the test section the temperature change of CO_2 near the pseudocritical point was rather small (less than 2°C) because the specific heat over this range is very high (see Fig. 1). Furthermore, in these experiments any large temperature change (above 10°C) of CO_2 took place far away from the pseudocritical point and the specific heat is nearly constant over this temperature range. Therefore, the use of the LMTD in this work is justified.

The average heat transfer coefficient h over the entire cooled length is determined from

$$h=\frac{\dot{Q}}{A^{*}\text{LMTD}}, \tag{4}$$

where A represents the inner surface of the test tube. The Nusselt number is defined as

$$\text{Nu}_w=\frac{hd}{k_w} \tag{5}$$

or

$$\text{Nu}_b=\frac{hd}{k_b}, \tag{6}$$

where d is the tube diameter, k is the thermal conductivity of the CO_2, and the subscripts w or b represent the case in which the properties are evaluated at the inner wall mean temperature T_w or at the bulk CO_2 mean temperature T_b defined as

$$T_b=\frac{T_{\text{in}}+T_{\text{out}}}{2} \tag{7}$$

with T_{in} and T_{out} being the CO_2 temperatures at the inlet and the exit of the test section.

The friction factor is defined as

$$f=\frac{\Delta p_f}{\dfrac{1}{2}\rho_b u_b^2}\cdot\frac{l}{d}, \tag{8}$$

where l is the length of the test section; ρ_b and u_b are the density and the bulk velocity of CO_2, evaluated at the bulk mean temperature T_b; Δp_f is the pressure drop across the test section due to the viscous friction and can be obtained from

$$\Delta p_f=\Delta p-\left(\frac{\rho_{\text{out}}u_{\text{out}}^2}{2}-\frac{\rho_{\text{in}}u_{\text{in}}^2}{2}\right), \tag{9}$$

where Δp is the total pressure drop across the test section measured by the differential pressure transducer; the subscripts *in* and *out* denote the quantities of CO_2 at the inlet and the outlet of the test section, respectively.

All the experimental data reported in this paper were processed based on the data for physical property of CO_2 provided by the NIST Refrigerants Database REFPROP [3].

Results and Discussion

Measurements were carried out at pressures of carbon dioxide ranging from 74 to 120 bar, temperatures ranging from 20 to 110°C, mass flow rates ranging from 0.02 to 0.2 kg/min, temperature differences (T_b-T_w) between the bulk CO_2 and the wall ranging from 2 to 30°C, and heat fluxes ranging from 10^4 to 2×10^5 W/m^2. The corresponding Reynolds numbers Re_b and Prandtl numbers Pr_b ranged from 10^4 to 2×10^5 and from 0.9 to 10, respectively. The inlet temperature of the cooling water was set to be 5°C, while the flow rates of the cooling water was varied from 0.1 to 0.5 kg/min. As such, the outlet temperature of the cooling water usually varied from 6 to 8°C.

Figure 4 shows the variation of the heat transfer coefficient h with the bulk mean temperature of CO_2 for the tube of $d=0.70$ mm at the mass flow rate of $\dot{m}=0.030$ kg/min with static pressures of $p=80$ and 100 bar. Note the horizontal bar at each data point in the figure representing the CO_2 temperature range over the test section. It is seen that at each pressure the heat transfer coefficient increased rapidly with the bulk temperature of the fluid, reached a peak value, and decreased gradually afterwards. Such a variation of the heat transfer coefficient suggests that the bulk mean temperature of the fluid has a substantial effect on the heat transfer performance near the critical point. Figure 4

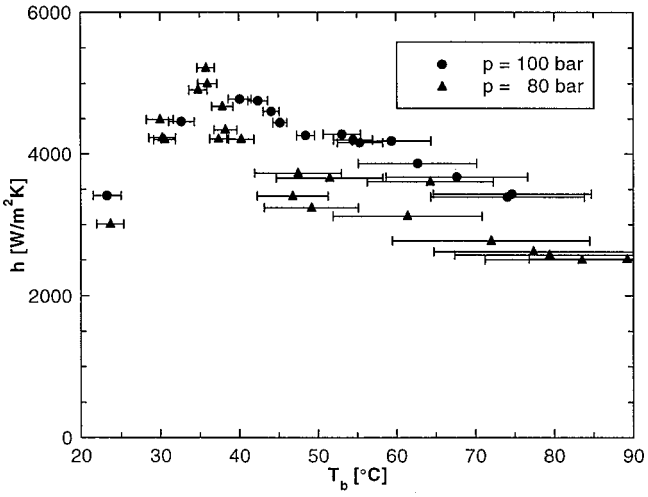

Fig. 4 Variations of the heat transfer coefficient h with the bulk mean temperature for the tube of $d=0.7$ mm at $\dot{m}=0.03$ kg/min for different static pressures of 80 and 100 bar (the horizontal bars represent the CO_2 temperature ranges over the test section)

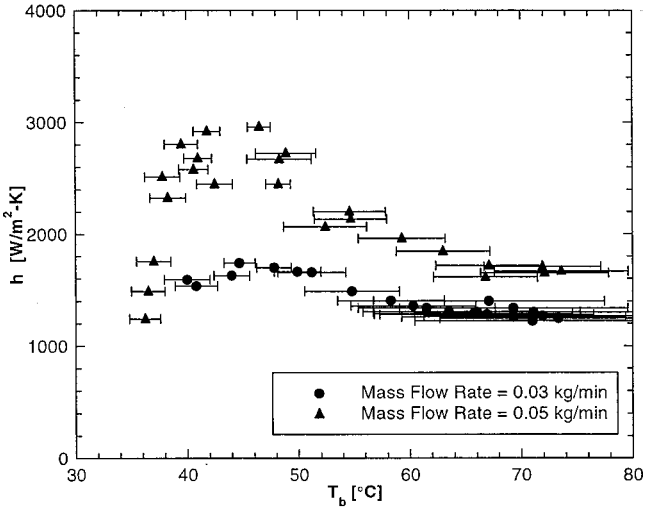

Fig. 5 The effect of the mass flow rates on the heat transfer coefficient h for the tube of $d=2.16$ mm and at $p=100$ bar (the horizontal bars represent the CO_2 temperature ranges over the test section)

also indicates that the peak value of the heat transfer coefficient decreased as the static pressure was increased from 80 bar to 100 bar. This is because the peak value of the specific heat c_p decreases with the decrease of pressure, as indicated in Fig. 1. It is also interesting to note from Fig. 4 that the heat transfer coefficient peak for each pressure occurred at a point near the corresponding pseudocritical temperature ($T_{pc}=34.6$°C at $p=80$ bar and $T_{pc}=45.0$°C at $p=100$ bar, as indicated in Fig. 1).

Figure 5 presents the effect of the mass flow rate on the heat transfer coefficient for $d=2.16$ mm and $p=100$ bar. As expected, the heat transfer coefficient increased as the mass flow rate was increased from $\dot{m}=0.03$ kg/min to $\dot{m}=0.05$ kg/min.

In order to investigate the effect of tube diameter on the heat transfer rate, we measured the variation of the Nusselt numbers Nu_b with the bulk mean temperature at $p=80$ bar for various tube diameters ($d=0.50$, 0.70, 1.10, 1.40, 1.55, and 2.16 mm). To have a meaningful comparison, both the Reynolds number Re_b and the Prandtl number Pr_b had to be kept constant for a given bulk mean temperature of the fluid. To this end, the experiments were conducted at a fixed ratio of the mass flow rate to the tube diameter at $\dot{m}/d=1.19$ kg/m-s. The variations of both the Reynolds number Re_b and the Prandtl number Pr_b with the dimensionless bulk mean temperature T_b/T_{pc} of the fluid under this condition are shown in Fig. 6, where T_{pc} represents the pseudocritical temperature of CO_2. Note that the unit of the temperature is K in calculating the ratio T_b/T_{pc}. The temperature difference between the bulk fluid and the wall was kept approximately the same by adjusting the flow rate of the cooling water for different tube diameters at the corresponding experimental conditions. The measured Nusselt numbers Nu_b under the above-described conditions are presented in Fig. 7, where the vertical error bars represent the uncertainties of the experimental data. For comparison, the Dittus-Boelter correlation for cooling constant property fluids

$$Nu_b = 0.023\, Re_b^{0.8} Pr_b^{0.3} \tag{10}$$

is also plotted in Fig. 7. It is clear from Fig. 7 that unlike heat transfer for constant-property fluids as represented by Eq. (10), for supercritical CO_2 the Nusselt numbers in the range of the

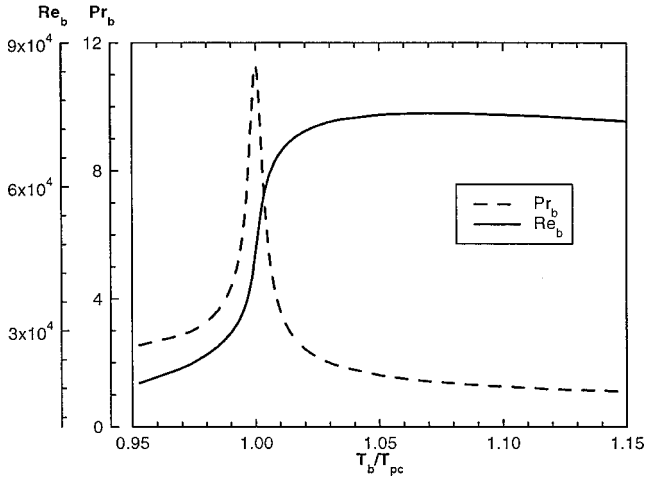

Fig. 6 Re_b and Pr_b Number versus T_b/T_{pc} at $\dot{m}/d=1.19$ kg/m-s

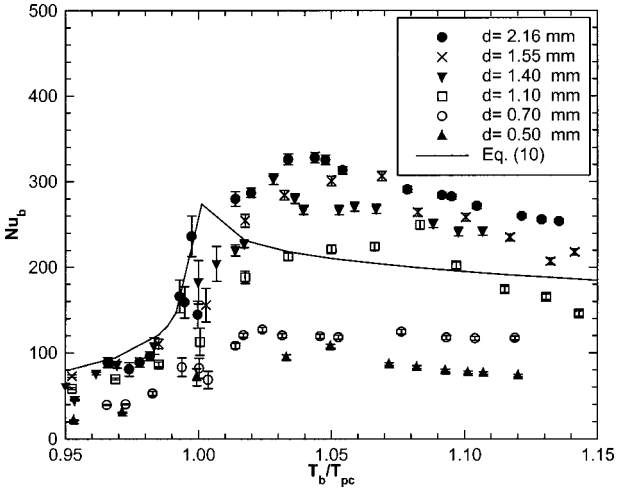

Fig. 7 The effect of the tube diameters on the Nusselt number Nu_b at $\dot{m}/d=1.19$ kg/m-s

measured temperatures ($0.95<T_b/T_{pc}<1.15$) were dependent very much upon the tube diameters, and they dropped substantially as the tube diameter was reduced from 2.16 mm to 0.50 mm. This fact suggests that for a given value of $\dot{m}/d$ the Nusselt numbers decrease as the tube size becomes smaller. Another observation that can be made from Fig. 7 is that the curve representing the variation of the Nusselt number with the dimensionless bulk mean temperatures became more flat as the tube diameter was reduced from 2.16 mm to 0.50 mm, implying that the effect of the fluid temperature (or the effect of its variable thermophysical properties) on the heat transfer rate is important for large-diameter tubes, but it becomes less significant as the tube size was reduced. It can also be seen from Fig. 7 that for the tubes having a diameter larger than 1.10 mm, the measured Nusselt numbers were higher than the values predicted by the Dittus-Boelter correlation given by Eq. (10). However, for the tubes having a diameter less than 1.10 mm, the measured Nusselt numbers became much lower than the values predicted by Eq. (10). One major reason for the above-described heat transfer behavior as a result of the change in tube sizes might be the buoyancy effect, even though the CO_2 was in forced motion in the horizontal tubes at very high Reynolds numbers (Re_b up to 10^5).

It is known that under certain conditions the buoyancy effect might still be significant even if a fluid is in forced motion through a horizontal channel. In such a case, the heat transfer performance depends not only on the Reynolds number Re_b, representing the strength of the primary flow due to the forced motion of the fluid, but also on the Grashof number Gr, representing the strength of the secondary flow induced by the buoyancy force. The Grashof number Gr is defined as

$$\mathrm{Gr}=\frac{(\rho_w-\rho_b)gd^3}{\rho_b\nu_b^2}=\frac{(\rho_w-\rho_b)\rho_b gd^3}{\mu_b^2} \tag{11}$$

with ρ_b and ρ_w denoting the density of CO_2 evaluated at the bulk mean temperature T_b and the wall mean temperature T_w, respectively; ν_b and μ_b represent the kinematic viscosity and dynamic viscosity of CO_2 evaluated at the bulk mean temperature T_b, respectively; and g is the acceleration of gravity. It has been shown theoretically that for horizontal channels, when

$$\frac{\mathrm{Gr}}{\mathrm{Re}_b^2}<10^{-3} \tag{12}$$

the buoyancy effect becomes negligible [6,10]. To access the accuracy of the criterion given by Eq. (12), Gr/Re_b^2 covered in this work for the tubes of $d=0.70$, 1.40, and 2.16 mm is compared with Eq. (12) in Fig. 8. It is interesting to note that the measuring points in terms of $\mathrm{Gr}/\mathrm{Re}_b^2$ for the tube of $d=2.16$ mm were higher than 10^{-3}, meaning that the buoyancy effect is important. However, the measuring points in terms of for the $\mathrm{Gr}/\mathrm{Re}_b^2$ for the tube of $d=0.70$ mm were lower than 10^{-3}, indicating that the buoyancy effect was less significant for this small tube. It is also seen from Fig. 8 that the measuring points for the tube of $d=1.40$ mm were mostly close to 10^{-3}. Considering that the buoyancy parameter $\mathrm{Gr}/\mathrm{Re}_b^2$ is proportional to the tube diameter d, it can be concluded that the impairment of heat transfer as a result of reduction in tube sizes was caused, partly at least, by the fact that the buoyancy effect became less important for small tubes.

The variation of the friction factor f with the Reynolds Number Re_b for $d=0.50$, 0.70, 1.40, and 2.16 mm at $\dot{m}/d=1.19$ kg/m-s and $p=80$ bar is shown in Fig. 9. The friction factor is seen to drop as the tube size was reduced.

The influence of the difference T_b-T_w between the bulk mean and wall mean temperature on the heat transfer rates is presented in Fig. 10 for $d=1.10$ mm and $p=80$ bar at $\dot{m}=0.1$ kg/min. The experimental results show that the Nusselt numbers changed significantly as the temperature difference T_b-T_w changed even if other conditions were kept the same, implying that the temperature difference T_b-T_w has an important influence on the heat transfer rates for supercritical fluids. This is because different bulk mean and wall mean temperature difference T_b-T_w will give different velocity and temperature profiles. In developing heat transfer correlations, the influence of the fluid bulk mean and wall mean temperature difference T_b-T_w is usually taken into account by using appropriate property parameter groups such as ρ_b/ρ_w, $\overline{c_p}/c_{pw}$, etc. The mean specific heat $\overline{c_p}$ is defined as:

$$\overline{c_p}=\frac{i_b-i_w}{T_b-T_w}, \tag{13}$$

where i_b and i_w denote the enthalpy of CO_2 evaluated at the bulk mean temperature T_b and the wall mean temperature T_w, respectively.

In developing heat transfer correlations for cooling supercritical fluids, it has been shown that a more accurate correlation can be obtained when the fluid properties are evaluated based on the wall temperature T_w rather than the bulk mean temperature T_b [4–5,8]. Petrov and Popov [8] proposed the following correlation for the local Nusselt number for cooling supercritical fluids:

$$\frac{\mathrm{Nu}_w}{\mathrm{Nu}_{0w}}=\left(1-m\frac{q_w}{\overline{\rho w}}\right)\left(\frac{\overline{c_p}}{c_{pw}}\right)^n, \tag{14}$$

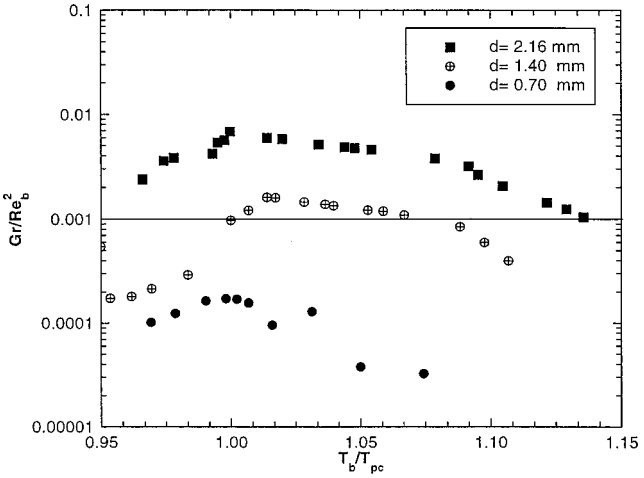

Fig. 8 $\mathrm{Gr}/\mathrm{Re}_b^2$ values versus T_b/T_{pc} at $\dot{m}/d=1.19$ kg/m-s

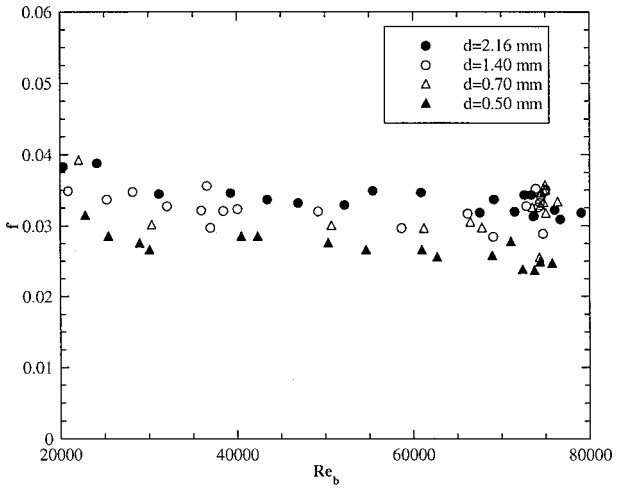

Fig. 9 The friction factor f versus Reynolds number Re_b at $\dot{m}/d=1.19$ kg/m-s and $p=80$ bar

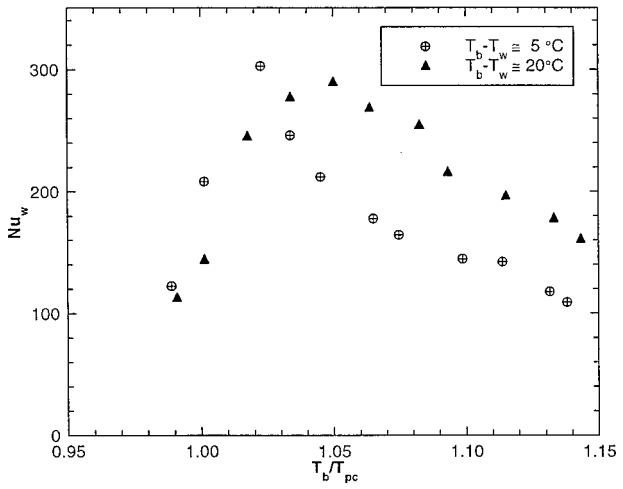

Fig. 10 The effect of the bulk mean and wall mean temperature difference $T_b - T_w$ on the Nusselt number Nu_b for $d = 1.1$ mm at $\dot{m} = 0.1$ kg/min

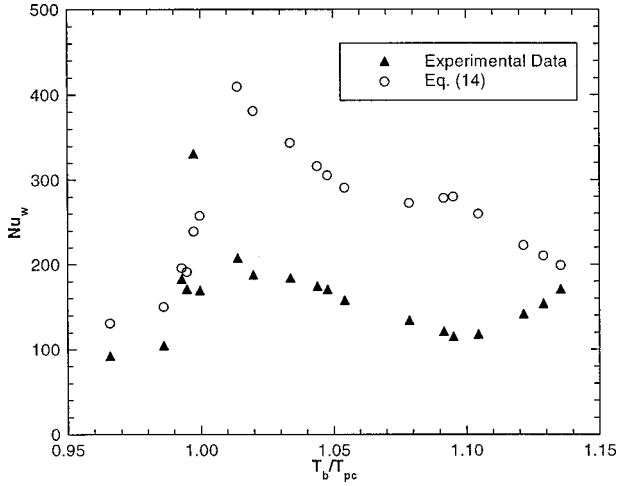

Fig. 11 Comparison of Eq. (14) and the experimental data for $d = 2.16$ mm, $\dot{m} = 0.15$ kg/min, and $p = 80$ bar

where

$$n = 0.66 - k(q_w/\overline{\rho w}) \quad \text{when} \quad \overline{c_p}/c_{pw} \leq 1,$$

$$n = 0.9 - k(q_w/\overline{\rho w}) \quad \text{when} \quad \overline{c_p}/c_{pw} > 1;$$

$$m = 0.001 \ \text{kg/J}; \quad k = 4 \times 10^{-4} \ \text{kg/J},$$

with q_w and $\overline{\rho w}$ representing the heat flux and the mass flux, respectively. In Eq. (14), Nu_{0w} is the Nusselt number for constant physical properties and is given by the Petukhov-Kirilov correlation [15]:

$$Nu_{0w} = \frac{\left(\frac{\xi}{8}\right) Re_w Pr_w}{12.7\left(\frac{\xi}{8}\right)^{1/2}(Pr_w^{2/3} - 1) + 1.07}, \tag{15}$$

where the friction coefficient ξ is obtained from

$$\xi = [0.79 \ln(Re_w) - 1.64]^{-2}. \tag{16}$$

Equation (14) is compared with the present experimental data for two different cases (Case 1: $d = 2.16$ mm, $\dot{m} = 0.15$ kg/min, and $p = 80$ bar; Case 2: $d = 0.70$ mm, $\dot{m} = 0.05$ kg/min, and $p = 80$ bar) in Figs. 11 and 12. It is seen from the both figures that Eq. (14) deviates significantly from the present experimental data. For the smaller tube $d = 0.70$ mm, the values predicted by the Petrov-Popov correlation, Eq. (14), are much higher than the experimental data, in particular in the region near the pseudocritical temperature. The Petov-Popov correlation was developed based on data for large-diameter tubes in which the buoyancy effect should be significant. However, the buoyancy effect was not explicitly included in the original Petov-Popov correlation. Therefore, the correlation fails when free convection becomes weak or absent (as in small-diameter tubes).

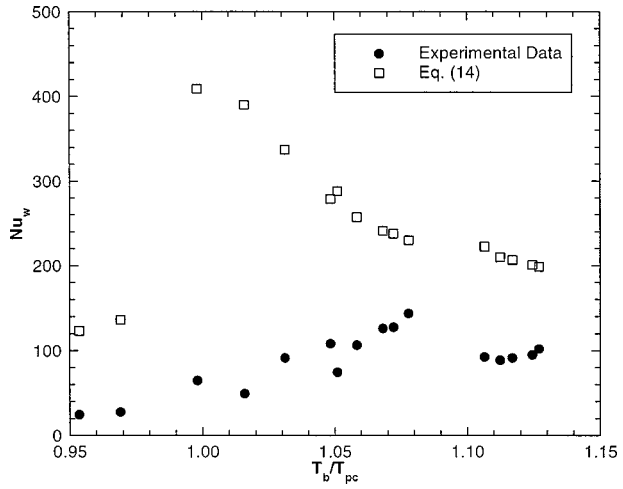

Fig. 12 Comparison of Eq. (14) and the experimental data for $d = 0.7$ mm, $\dot{m} = 0.05$ kg/min, and $p = 80$ bar

The above-presented experimental results suggest that the buoyancy effect, the temperature difference between the bulk fluid and the wall must be taken into account in developing heat transfer correlations for heat transfer from supercritical CO_2 flowing through horizontal tubes. Based on a least square fit of seventy-two experimental data for the circular tubes of $d = 0.50$ mm, 0.70 mm, 1.10 mm, 1.40 mm, 1.55 mm, and 2.16 mm, the following correlation was obtained for forced convection of supercritical CO_2 in mini/micro tubes cooled at a constant temperature:

$$\frac{Nu_w}{Nu_{dbw}} = 5.57\left(\frac{Gr}{Re_b^2}\right)^{0.205}\left(\frac{\rho_b}{\rho_w}\right)^{0.437}\left(\frac{\overline{c_p}}{c_{pw}}\right)^{0.411}, \tag{17}$$

where Nu_{dbw} is the Nusselt number for constant physical properties (evaluated at the wall mean temperature T_w) and is determined from the Dittus-Boelter correlation:

$$Nu_{dbw} = 0.023 \, Re_w^{0.8} Pr_w^{0.3}. \tag{18}$$

Substituting Eq. (18) into Eq. (17) yields

$$Nu_w = 0.128 \, Re_w^{0.8} Pr_w^{0.3}\left(\frac{Gr}{Re_b^2}\right)^{0.205}\left(\frac{\rho_b}{\rho_w}\right)^{0.437}\left(\frac{\overline{c_p}}{c_{pw}}\right)^{0.411}. \tag{19}$$

Equation (19) is compared with the experimental data in Fig. 13. The maximum relative error between Eq. (19) and the experimental data is about 18.9 percent, while the mean relative error between Eq. (19) and the experimental data is about 9.8 percent. Equation (19) is applicable in the range 74 bar $\leq p \leq$ 120 bar, 20°C $\leq T_b \leq$ 110°C, 2°C $\leq T_b - T_w \leq$ 30°C, 0.02 kg/min $\leq \dot{m} \leq$ 0.2 kg/min, $10^{-5} \leq Gr/Re_b^2 \leq 10^{-2}$ for the horizontal long tubes of 0.50 mm $\leq d \leq$ 2.16 mm.

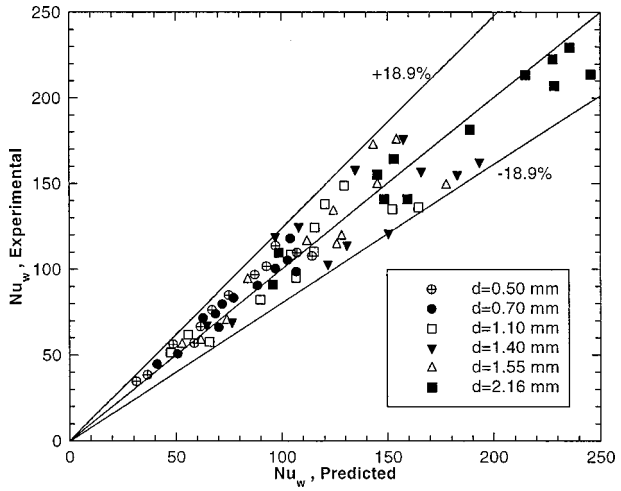

Fig. 13 Comparison of Eq. (19) and the experimental data

Uncertainty Analysis

The uncertainty in the experimental data was evaluated according to the methods introduced in NIST Technical Note 1297 [16]. Based on Eqs. (2)–(6), the relative standard uncertainty of the Nusselt number is given by

$$\frac{\delta \mathrm{Nu}}{\mathrm{Nu}} = \left(\left(\frac{\delta \dot{m}}{\dot{m}} \right)^2 + \left(\frac{\delta A}{A} \right)^2 + \left(\frac{\delta d}{d} \right)^2 + \left(\frac{\delta (\mathrm{LMTD})}{\mathrm{LMTD}} \right)^2 + \left(\frac{\delta (i_{\mathrm{in}} - i_{\mathrm{out}})}{(i_{\mathrm{in}} - i_{\mathrm{out}})} \right)^2 + \left(\frac{\delta k}{k} \right)^2 \right)^{1/2}, \tag{20}$$

where δ represents the absolute standard uncertainty of the corresponding quantity. From Eq. (20), it can be seen that the uncertainty in the Nusselt number was caused by uncertainties in the mass flow rate (0.2 percent), the logarithmic mean temperature difference (1 percent–2 percent), the heat transfer area (about 1 percent), the test tube diameter (about 1 percent, the diameter was measured in the micrograph of the mini/micro tube sections), the enthalpy difference and the conductivity. The uncertainties of the enthalpy difference and conductivity can be estimated based on the NIST Refrigerants Database REFPROP by taking into account the measurement uncertainties of the temperature (± 0.2°C) and pressure (0.2 percent). Since near the pseudocritical temperature T_{pc} the thermal properties become rather sensitive to any variation in temperatures (see Fig. 1), a small error in the temperature measurement will cause a large uncertainty in the Nusselt numbers. For this reason, the uncertainty of the Nusselt numbers Nu_b and Nu_w near the pseudocritical temperature ($T_{pc} \pm 3°C$) could be up to 30 percent. Except for the measuring points near the pseudocritical temperature, it is estimated that the relative standard uncertainty of the Nusselt numbers Nu_b and Nu_w was within 4 percent.

Concluding Remarks

Heat transfer from supercritical carbon dioxide flowing in horizontal mini/micro circular tubes cooled at a constant temperature was investigated experimentally. Six stainless steel circular tubes having inside-diameters of 0.50 mm, 0.70 mm, 1.10 mm, 1.40 mm, 1.55 mm, and 2.16 mm were tested under pressures of carbon dioxide ranging from 74 to 120 bar and the temperature ranging from 20 to 110°C. It has been shown that although supercritical CO_2 was in forced motion through the horizontal tubes at Reynolds numbers up to 10^5, the buoyancy effect was still significant, reflected by the fact that the Nusselt number decreased with the reduction in tube diameters. However, the influence of the buoyancy effect becomes weaker as the tube diameter is decreased due to the fact that the buoyancy parameter $\mathrm{Gr}/\mathrm{Re}_b^2$ is proportional to the tube diameter d. The experimental results also indicate that the existing correlations developed in the previous studies for large tubes deviate significantly from the experimental data for the present mini/micro tubes. Based on the experimental data, a correlation was developed for the axially-averaged Nusselt number in terms of appropriate dimensionless parameters for forced convection of supercritical carbon dioxide in mini/micro tubes cooled at a constant temperature. The results of this work are of significance for the design of the gas cooler of the transcritical carbon dioxide refrigeration system.

Acknowledgments

This work was supported by the Hong Kong RGC Earmarked Research Grant HKUST 6046/99E. The senior author (TSZ) gratefully acknowledges the Visiting Scholar Foundation of the State Key Laboratory of Multiphase Flow in Power Engineering at Xi'an Jiaotong University.

Nomenclature

A = inner surface of the test tube, m^2
c_p = specific heat, J/K-kg
d = inside-diameters of the test tube, m
g = acceleration of gravity, m/s^2
Gr = Grashof number, $Gr = (\rho_w - \rho_b)\rho_b g d^3/\mu_b^2$
H = average heat transfer coefficient, W/m^2-K
i = enthalpy, J/kg
k = thermal conductivity, W/m-K
l = length of the test section, m
LMTD = logarithmic mean temperature difference, °C
m = empirical constant
$\dot{m}$ = mass flow rate, kg/s
n = empirical constant
Nu = Nusselt number
P = pressure, bar
Pr = Prandtl number
$\dot{Q}$ = heat transfer rate, W
q = heat flux, W/m^2
Re = Reynolds number
T = temperature, °C or K
u = velocity, m/s

Greek symbols

δ = absolute standard uncertainty
Δp = pressure drop, Pa
μ = dynamic viscosity, kg/m-s
ν = kinematic viscosity, m^2/s
ρ = density, kg/m^3
$\overline{\rho w}$ = mass flux, kg/m^2-s
ξ = friction coefficient

Subscripts

0 = Petukhov-Kirilov correlation
b = bulk fluid
cr = critical
db = Dittus-Boelter correlation
f = viscous friction
in = CO_2 inlet of the test section
out = CO_2 exit of the test section
pc = pseudocritical
w = wall

References

[1] Lorentzen, G., and Pettersen, J., 1993, "A New Efficient and Environmentally Benign System for Car Air-Conditioning," Int. J. Refrig., **16**, No. 1, pp. 4–12.
[2] Pettersen, J., Hafner, A., and Skaugen, G., 1998, "Development of Compact Heat Exchangers for CO_2 Air-Conditioning Systems," Int. J. Refrig., **21**, No. 3, pp. 180–193.
[3] McLinden, M., Klein, S. A., Lemmon, E. W., and Peskin, A. P., 1998, NIST

Thermodynamic and Transport Properties of Refrigerants and Refrigerant Mixtures-REFPROP, Version 6.01, National Institute of Standards and Technology, USA.
[4] Krasnoshchekov, E. A., Kuraeva, I. V., and Protopopov, V. S., 1970, ''Local Heat Transfer of Carbon Dioxide at Supercritical Pressure under Cooling Conditions,'' Teplofiz. Vys. Temp., **7**, No. 5, pp. 922–930.
[5] Baskov, V. L., Kuraeva, I. V., and Protopopov, V. S., 1977, ''Heat Transfer With the Turbulent Flow of a Liquid at Supercritical Pressure in Tubes under Cooling Conditions,'' Teplofiz. Vys. Temp., **15**, No. 5, pp. 96–102.
[6] Jackson, J. D., Hall, W. B., Fewster, J., Watson, A., and Watts, M. J., 1975, ''Heat Transfer to Supercritical Pressure Fluids,'' U.K.A.E.A. A.E.R.E.-R 8158, Design Report 34.
[7] Lee, S. H., and Howell, J. R., 1998, ''Turbulent Developing Convective Heat Transfer in a Tube for Fluids Near the Critical Point,'' Int. J. Heat Mass Transf., **41**, No. 10, pp. 1205–1218.
[8] Petrov, N. E., and Popov, V. N., 1985, ''Heat Transfer and Resistance of Carbon Dioxide Cooled in the Supercritical Region,'' Thermal Engineering, **32**, No. 3, pp. 131–134.
[9] Zhou, N., and Krishnan, A., 1995, ''Laminar and Turbulent Heat Transfer in Flow of Supercritical CO_2,'' *Proceedings of the 30th National Heat Transfer Conference*, Vol. 5, ASME, Portland, OR, pp. 53–63.
[10] Kakac, S., 1987, ''The Effect of Temperature-Dependent Fluid Properties on Convective Heat Transfer,'' *Handbook of Single-phase Convective Heat Transfer*, S. Kakac et al., eds., John Wiley & Sons, New York, pp. 18.1–18.56.
[11] Hall, W. B., 1971, ''Heat Transfer Near the Critical Point,'' *Advances in Heat Transfer*, Vol. 7, J. P. Hartnett and T. F. Irvine, Jr., eds., Academic Press, San Diego, CA, pp. 1–86.
[12] Polyakov, A. F., 1991, ''Heat Transfer Under Supercritical Pressures,'' *Advances in Heat Transfer*, **21**, ed. J. P. Hartnett and T. F. Irvine, Jr., eds., Academic Press, San Diego, CA, pp. 1–53.
[13] Pettersen, J., Rieberer, R., and Leister, A., 2000, ''Heat Transfer and Pressure Drop Characteristics of Supercritical Carbon Dioxide in Microchannel Tubes Under Cooling,'' Proceedings, 4th IIR-Gustav Lorentzen Conference on Natural Working Fluids at Purdue, pp. 99–106.
[14] Adams, T. M., Abdel-Khalik, S. I., Jeter, S. M., and Qureshi, Z. H., 1998, ''An Experimental Investigation of Single-Phase Forced Convection in Microchannels,'' Int. J. Heat Mass Transf., **41**, Nos. 6-7, pp. 851–857.
[15] Petukhov, B. S., 1970, ''Heat Transfer and Friction in Turbulent Pipe Flow with Variable Physical Properties,'' *Advances in Heat Transfer*, Vol. 6, J. P. Hartnett and T. F. Irvine, eds., Academic, San Diego, CA, pp. 504–564.
[16] Taylor, B. N., and Kuyatt, C. E., 1994, ''Guidelines for Evaluating and Expressing the Uncertainty of NIST Measurement Results,'' NIST Technical Note 1297, National Institute of Standards and Technology, USA.

Heat Transfer and Pressure Drop Characteristics of Laminar Flow Through a Circular Tube With Longitudinal Strip Inserts Under Uniform Wall Heat Flux

S. K. Saha
Mechanical Engineering Department,
Bengal Engineering College,
Deemed University,
Howrah 711 103, West Bengal, India
e-mail: sujoy_k_saha@hotmail.com

P. Langille
Department of Mechanical Engineering,
Dalhousie University,
Halifax, Nova Scotia,
B3J 2X4, Canada
e-mail: ocean_wave_13@hotmail.com

Heat transfer and pressure drop characteristics in a circular tube fitted with full-length strip, short-length strip, and regularly spaced strip elements connected by thin circular rods have been investigated experimentally. The strips have been rectangular, square and crossed in cross-section with different aspect ratio. Laminar flow of water and other viscous liquids was considered. The rod diameter and length of the strip-rod assembly and the length of the strips were varied. Isothermal friction factor data has been generated. The heat transfer test section was heated electrically imposing axially and circumferentially constant wall heat flux (UWHF) boundary condition. Reynolds number, Prandtl number, strip length, strip ratio, space ratio, and rod-diameter govern the characteristics. Smaller rod-diameter in the strip-rod assembly or "pinching" of the strips in place rather than connecting the strip elements by rods performs better thermohydraulically. Short-length strips (upto a limited fraction of the test section tube length) perform better than the full-length strip. The friction factor correlation and the correlation for Nusselt number under UWHF condition for full-length strip have been modified to make them suitable for short-length strip as well as regularly-spaced strip elements. Thermal entrance length in the correlations is represented by Graetz number. Friction factor and Nusselt number correlations for short-length strips as well as regularly-spaced strip elements, in the limit, reduce to their full-length counterparts. [DOI: 10.1115/1.1423907]

Keywords: Augmentation, Enhancement, Experimental, Forced Convection, Heat Transfer, Laminar

Introduction

Heat exchangers are important engineering devices in many process industries since the efficiency and economy of the processes largely depend on the performance of the heat exchangers. High performance heat exchangers are, therefore, very much required. Improvement in the performance may result in the reduction in the size of the heat exchangers. Alternatively, a high performance heat exchanger of a fixed size can give an increased heat transfer rate; it might also give a decrease in temperature difference between the process fluids enabling efficient utilization of thermodynamic availability. This is particularly true for laminar flow since the heat transfer coefficients for laminar straight flow through a plain tube is very low.

A longitudinal rectangular plate insert in the tubes of heat exchangers is a good displaceable device and this enhances tubeside heat transfer rate. The buoyancy effect on laminar forced convection in a circular tube with longitudinal thin rectangular plate insert was studied by Chen and Hsieh [1].

Solanki et al. [2,3] conducted experimental and theoretical studies of laminar forced convection in tubes with polygon inner cores. Forced convection heat transfer in doubly connected ducts bounded externally by a circle and internally by a rectangular polygon of various shapes was analyzed using a finite element method. Hydrodynamically and thermally developed, steady, laminar flow of a constant property fluid was investigated. An insulated outer tube and constant heat flux at the inner core were considered. Temperature profiles as well as Nusselt numbers were presented.

Chen and Hsieh [4] numerically studied laminar mixed convection in a horizontal tube with a longitudinal square core. They assessed the performance of a number of longitudinal rectangular plate inserts used as tubeside heat transfer augmentative devices. The tube was subjected to axially uniform heat flux and peripherally constant wall temperature. The tube had an adiabatic rectangular plate insert. The flow was thermally developed and steady. The effects of the aspect ratio of the rectangular plate, the radius ratio of the circumscribed circle of the rectangular plate to the tube, and the eccentric installation on the net effect between heat transfer augmentation and pressure drop increase were determined.

A finite-difference based numerical study with a boundary-fitted coordinate system was made by Hsieh and Wen [5] to investigate the three-dimensional, steady-state, laminar entrance flow through an axially uniformly heated horizontal tube with different adiabatic longitudinal inserts. They performed parametric calculations to determine the nature and the effect of Reynolds number, Grashof number, aspect ratio and radius ratio of circumscribed circle of insert to outer tube on thermally driven secondary flows. They obtained typical streamline patterns, isotherms and axial velocity profile along the flow direction. They presented and discussed local friction factor, Nusselt number and entrance length in the hydrodynamically and thermally developing and fully developed regions. Flow visualization study was made and good agreement with corresponding numerical results was observed.

Heat transfer and pressure drop characteristics of laminar water

Contributed by the Heat Transfer Division for publication in the JOURNAL OF HEAT TRANSFER. Manuscript received by the Heat Transfer Division May 4, 2001; revision received October 1, 2001. Associate Editor: B. T. F. Chung.

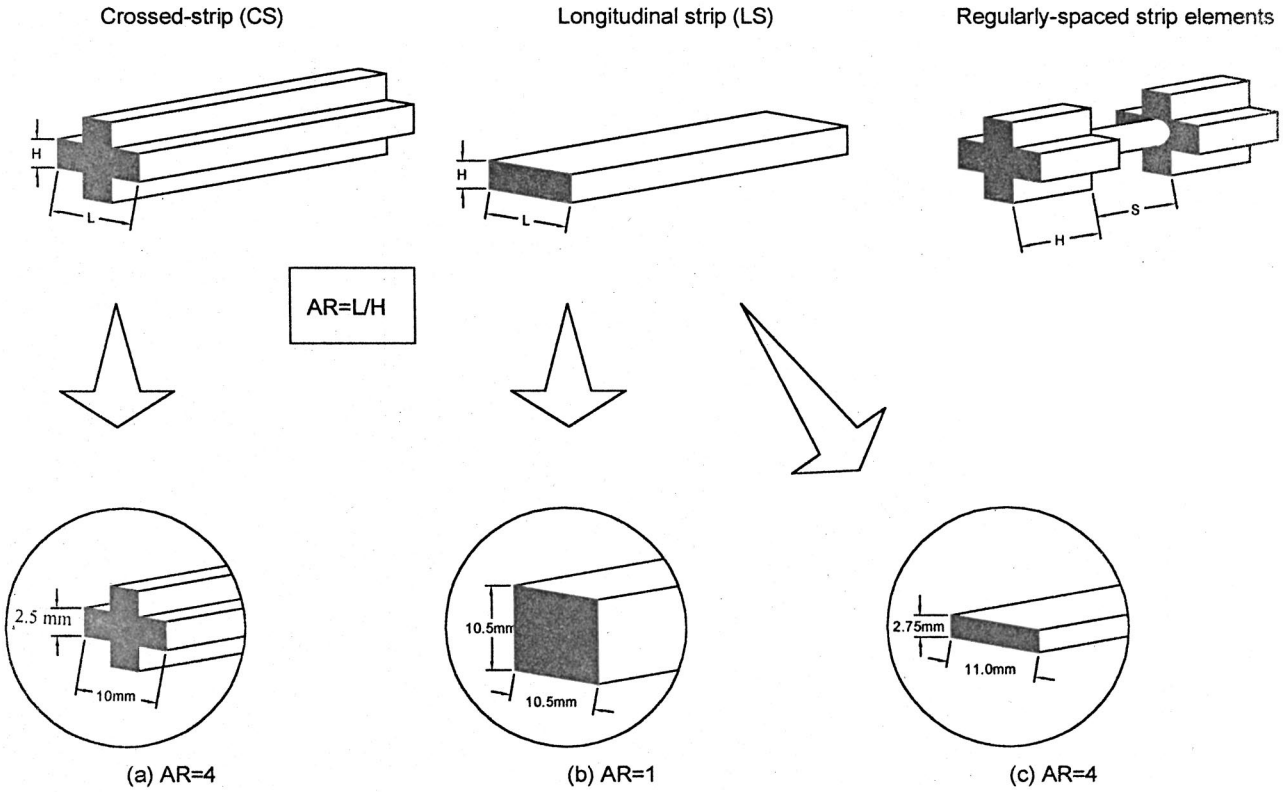

Fig. 1 The geometry and dimensions of the inserts used in this study

flow in horizontal tubes with longitudinal inserts were experimentally studied by Hsieh and Huang [6]. Testing was performed on tubes with square and rectangular as well as crossed longitudinal strip inserts with aspect ratios AR=1 and 4 and varied ratios of inlet mixed mean temperature to wall temperature. Flow visualization, using a dye-injection method, revealed a highly complex flow pattern including a secondary flow formed in the cross-section for crossed-strip inserts. The thermal entrance length was found and correlated in terms of Reynolds number. The enhancement of heat transfer as compared to a conventional bare tube at the same Reynolds number based on the hydraulic diameter was found by them to be about a factor of 16, while the friction factor rise was only about a factor of 4.5. This observation of Hsieh and Huang [6] encouraged the present investigators to try with short-length strips and short pieces of strips connected with small circular rods, making regularly-spaced strip elements (as shown in Fig. 1), instead of full-length strips extending from the upstream end to the downstream end of the tube. The whole purpose of the present experimental study was to examine whether further improvements in terms of thermohydraulic performance can be achieved or not. Saha and Dutta [7] and Saha et al. [8] achieved better thermohydraulic performance with short-length twisted tapes and regularly-spaced twisted-tape elements instead of full-length twisted tapes while working with twisted tapes.

In the present work, the strips are of longitudinal rectangular, square and crossed cross-section and full-length and short-length as well as regularly-spaced types. Small pieces of strips are connected (by welding) at the ends of thin circular rods to make the regularly-spaced strip elements. The lengths of the strip elements and the connecting rod elements in the regularly spaced strip elements are H and S, respectively. The strip ratio, y and the gap ratio, s are defined by H/D and S/D, respectively, where D is the internal diameter of the test-section tube. Figure 1 shows the geometry and dimensions of the inserts used in the study. The aspect ratio, AR of the strip is given by $AR=L/H$, where L and H are width and depth of the strips, respectively. The non-dimensional length, l of the short-length strips is given by $l=L_s/L$, where L_s and L are the length of the strip and the tube, respectively.

Four different working fluids, water (W), ethylene glycol (EG), servotherm medium oil (the trade name given by Indian Oil Corporation) (SMO) and polybutene 20 (PB20) were used to cover a wide laminar flow range of Reynolds number and Prandtl number. The ranges of independent parameters covered with different working fluids are shown in Table 1.

Ranges of additional parameters are as follows:

$$1{:}1,\quad 0.5,\quad 0.333,\quad 0.25$$

$$y{:}2.5 \leqslant y \leqslant 5$$

$$s{:}2.5 \leqslant s \leqslant 5$$

$$d(=d^*/D)=0.115-0.273,$$

Table 1 Ranges of independent parameters with different working fluids

Parameter	W	EG	SMO	PB20
Re	318-1280	170-738	25-517	25-215
Nu	5.5-6.5	88-192	255-647	1080-8731

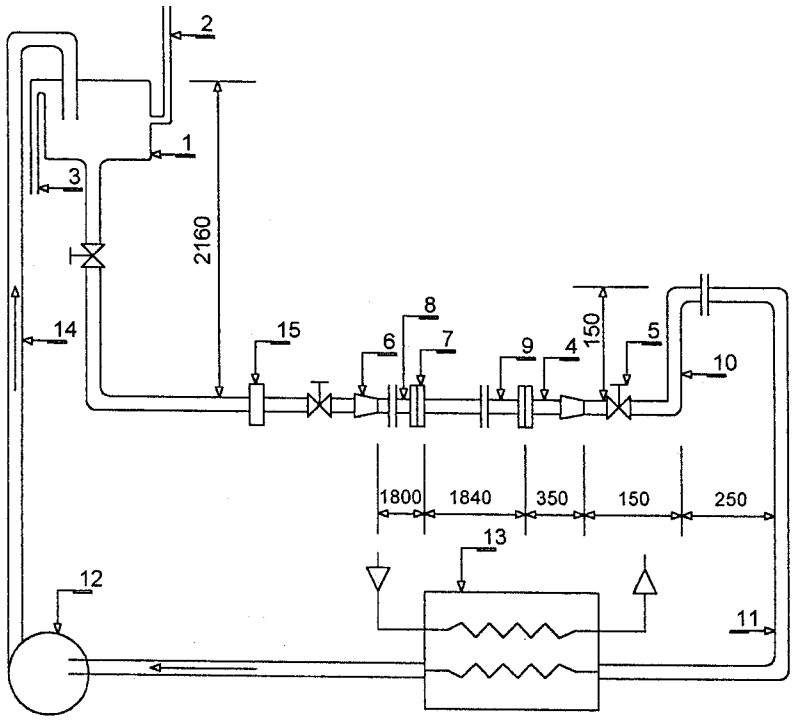

DIMENSIONS ARE IN MM

1. OVERHEAD TANK	8. CALMING SECTION
2. LEVEL INDICATOR	9. TEST SECTION
3. OVER FLOW TO SUMP	10. RISER
4. EXIT SECTION	11. FLOW OUTLET TO H.E.
5. NEEDLE VALVE	12. GEAR PUMP
6. REDUCER	13. HEAT EXCHANGER (H.E.)
7. FLANGES	14. SUPPLY TO TANK
	15. ROTAMETER

NOT TO SCALE

Fig. 2 The experimental setup

where d and d^* are the non-dimensional diameter and diameter of the rods, respectively.

The aspect ratio of the strips varied from 1 to 4. The correlations for friction factor and Nusselt number are also reported.

Experimental Setup

The investigations were carried out in a closed loop experimental facility shown in Fig. 2. The loop consisted of:

1 An overhead tank (0.25 m^3 capacity located at an elevation of 2.75 meters)
2 A calming section (1.8 m long, 13 mm i.d., 20 mm o.d., PVC tube)
3 The test section (details follow)
4 An insulated mixing section, i.e., exit section (13 mm i.d., 20 mm o.d., 350 mm long PVC tube)
5 A riser section with 150 mm high kink
6 A heat exchanger
7 A gear pump (1 HP)

The longitudinal strips were made of 0.5 mm thick stainless steel strips. The strips had hydrodynamically smooth surface finish and the roughness elements on the surface did not affect the performance of the inserts. The strips were made separately for pressure drop tests and heat transfer tests because of different diameters of the test sections. The strips were snugly fitted inside the tube. If the strips are fitted tightly inside the tube or the edges of the strips are not covered by insulating tape, the strip fin-effect may enhance the heat transfer rate. In the present investigation, the strips for heat transfer tests were covered with insulated tape to suppress the fin effect since the fin effect was not studied. Pieces of stainless steel rods of 3 mm, 2.5 mm, 2 mm, and 1.5 mm diameter (d^*) were used to make strip-rod assembly. Thus, for pressure drop tests, the non-dimensional rod diameter ($d = d^*/D$) were 0.231 (=3/13), 0.192 (=2.5/13), 0.154 (=2/13), 0.115 (=1.5/13) and those for heat transfer tests were 0.273 (=3/11) and 0.136 (=1.5/11). It should be noted here that the rod diameter for both the pressure drop test and the heat transfer test were physically equal. However, the non-dimensional rod diameter for the pressure drop test was different from that for the heat transfer test because of the small difference of the pressure drop test-section tube diameter from the heat transfer test-section tube diameter.

Strip elements were welded to the ends of the rods to make the regularly-spaced strip elements.

A PVC tube of 1.85 m long, 13 mm i.d. and 20 mm o.d. was used as test section for the pressure drop tests. The pressure taps were made of 30 mm long, 3 mm i.d., 4.5 mm o.d. acrylic tube. Threads were cut on one end of the taps and drilled holes on the

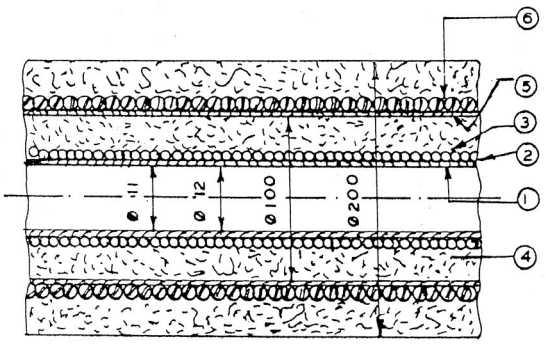

DIMENSIONS ARE IN MM

1- TEST TUBE
2-FIBERGLASS TAPE INSULATION
3-FIBERGLASS INSULATED NICHROME HEATER WIRE
4- GLASSWOOL BLANKET INSULATION
5-THIN G.I. CYLINDER
6-ASBESTOS ROPE

Fig. 3 Heat transfer test section

test section were threaded internally. The threaded portion of the taps was covered with Teflon tape before inserting them into the tapped hole to prevent leakage. Additionally, using Araldite ensured the rigidity of the taps. Flexible PVC tubing to a manometer connected the pressure taps at either end of the test section. Pressure drop was measured by means of vertical U-tube manometer with dibutyl phthalate (specific gravity 1.047) and mercury as the manometric fluid for lower Re and higher Re, respectively. This ensured reasonably good accuracy by producing large-scale reading with dibutyl phthalate for lower Re.

The heat transfer test section is shown in Fig. 3. It consisted of a 1.84 m long, 11 mm i.d., 12 mm o.d. stainless steel (304 SS) tube. The tube was uniformly heated by passing alternating current from a stabilized three-phase source through 30 SWG fibre glass insulated nichrome wire having 16 Ω/m resistance wound around the tube. The electrical winding (any two consecutive turns) of each heater in a given segment of the test section was made in opposite directions so that current passed in both directions to cancel the electro-magnetic field effects. Electrical resistance was measured in several sections to ensure uniform heat flux. The heater was made in three sections, each section having four parallel heaters. Autotransformers were used to regulate the heat flux supplied to the test section. To measure the outside wall temperature of the tube, 30 SWG copper-constantan thermocouples were used. The thermocouples were silver soldered and were first taken through the circumferential grooves and then radially through the heater wire turns and the insulation put on the test section. Eleven thermocouples were installed on the outside wall of the tube to measure the wall temperature. The first five were placed at 15 mm, 115 mm, 225 mm, 350 mm, and 430 mm from the point where the heating started and the remaining six were placed at 525 mm, 565 mm, 627 mm, 688 mm, 738 mm, and 788 mm from the downstream end. Using polytetrafluoroethylene spacers positioned between flanges minimized axial conduction losses. Winding asbestos rope and putting a glasswool blanket of 50 mm thickness around the asbestos rope minimized the radial

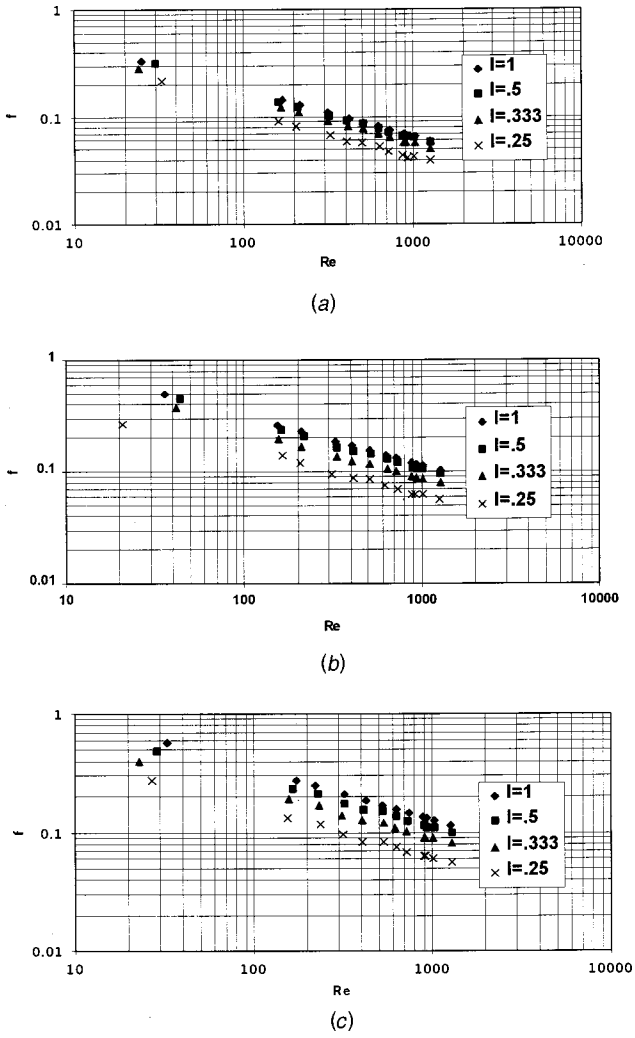

Fig. 4 Variation of friction factor with Reynolds number for short-length strips: (*a*) cross strip; Aspect ratio 4; (*b*) longitudinal strip (aspect ratio 4); and (*c*) longitudinal strip (aspect ratio 1)

heat losses. The asbestos rope was wound on a GI (Galvanized Iron) cylinder (split in two halves) to protect the electrical connections. The space between the heater wire and the GI cylinder was also filled with glasswool. A precision digital multimeter measured the thermocouple output. The power input was calculated from the measured voltage and the resistance of the nichrome wire heater. The current was also measured to provide a crosscheck. Fluid bulk temperature measurements were made at the inlet and the exit of the test section. Wire meshes were used in the exit (mixing) section at the downstream end of the test-section tube. Wire meshes provided thorough mixing of the fluid to give the accurate outlet bulk mean temperature of the fluid. Saha et al. [8] and Hong and Bergles [9] have observed that the circumfer-

Table 2 Percent reduction in friction factor for $l<1$ compared to that for $l=1$

AR	Length =0.5	Length =0.333	Length=0.25
CS4	8-12	18-20	38-44
LS4	15-18	28-35	45-50
LS1	20-25	33-35	55-58

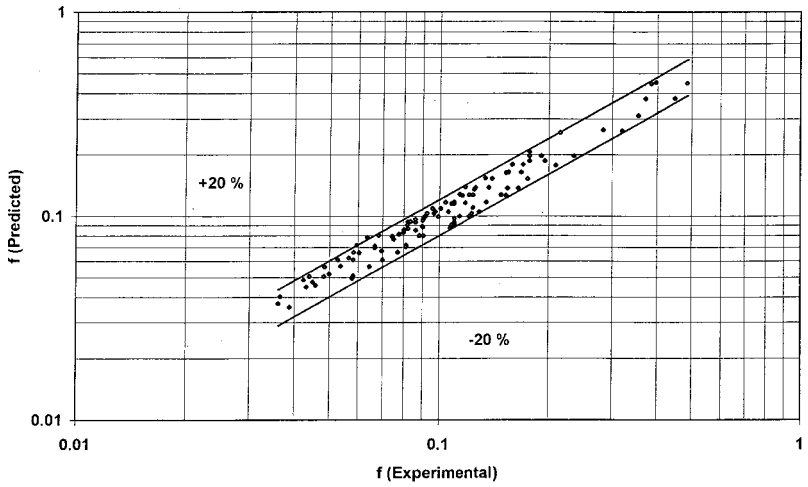

Fig. 5 Comparison of experimental friction factor with that predicted from Eq. (7) for short-length strips

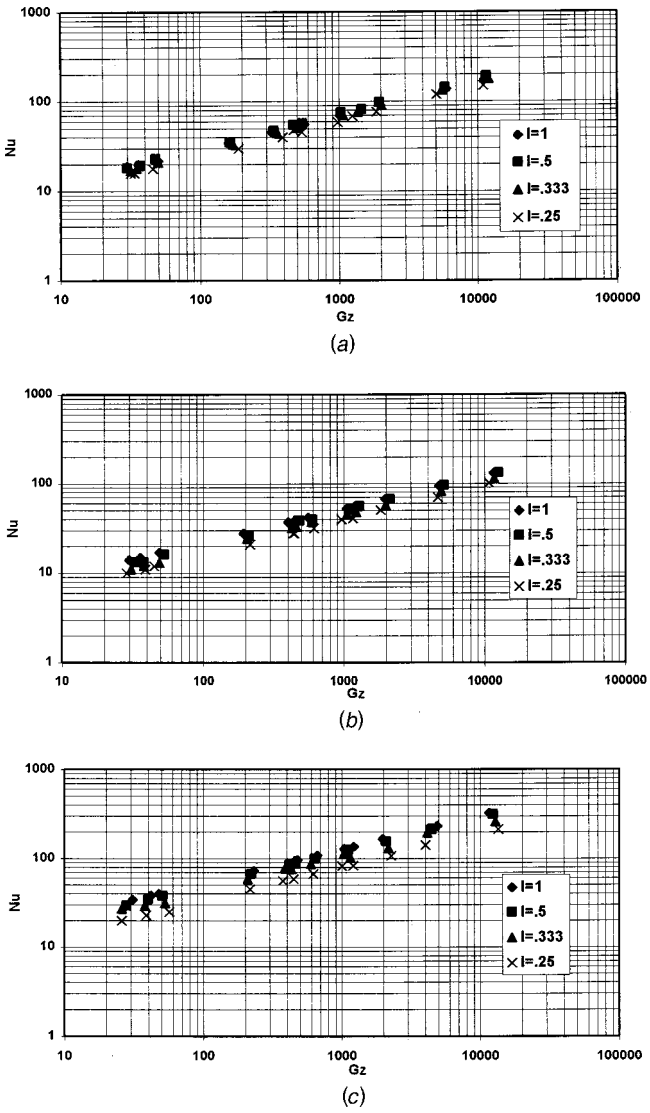

Fig. 6 Variation of Nusselt number with Graetz number for short-length strips: (*a*) cross strip (aspect ratio 4); (*b*) longitudinal strip (aspect ratio 4) and (*c*) longitudinal strip (aspect ratio 1)

ential temperature variation for flow through the tube having this type of insert is very small. For the present investigation, measurement of circumferential temperatures (at six equidistant locations along the periphery) at a typical axial location confirmed that. Accordingly, no further circumferential variation of temperature was measured in the present investigation.

Operating Procedure and Data Reduction

(a) Pressure Drop Tests. The pressure drop tests were carried out in the PVC tube. The friction factor was defined as

$$f = \tfrac{1}{2}[(\Delta P_z)/(\rho V_0^2)](D/z), \tag{1}$$

where

$$V_0 = \dot{m}/(\rho A_0) \tag{2}$$

and ΔP_z is the pressure drop over a length z.

Before the pressure drop measurements were taken, the test section was freed of air bubbles by venting them through the riser section at the end of the test section. The fluid flow was taken from the overhead tank where a constant level was maintained. Typically 15 minutes were required for settling of flow after each change of mass flow rate. In addition to controlling the mass flow rate, the fluid was heated as necessary to obtain a reasonable range of laminar Reynolds number. The manometer was used to measure pressure drop. The mass flow rate was measured by three rotameters which covered the entire range of mass flow rates.

(b) Heat Transfer Tests. The heat transfer tests were performed in the stainless steel tube. Ethylene glycol, servotherm medium oil and polybutene 20 provided substantial variation in Pr. The length averaged Nu was defined as

$$\mathrm{Nu} = \frac{hD}{k} = \frac{Q}{\pi DL}\left[\int_0^L \frac{dz}{T_{wz} - T_{bz}}\right]\left(\frac{D}{k}\right), \tag{3}$$

where

$$Q = V^2/R = \dot{m} C_p (T_{bo} - T_{bi}). \tag{4}$$

Q was measured by two methods (i.e., measuring electrical power input and the heat gained by the working fluid) as shown in Eq. (4). The arithmetic mean of two values was taken. Data with variation by more than 5 percent in two methods were discarded since, in the steady state, the values obtained by two methods should be equal if there is no significant heat loss from the test section. The wall temperature T_{wz} at any z in Eq. (3) was measured directly, whereas T_{bz} was calculated by interpolation assum-

Table 3 Percent reduction in Nusselt number for $l<1$ compared to that for $l=1$

AR	Length=0.5	Length=0.333	Length=0.25
CS4	2-4	7-10	15-20
LS4	8-11	17-21	27-30
LS1	15-18	25-28	35-40

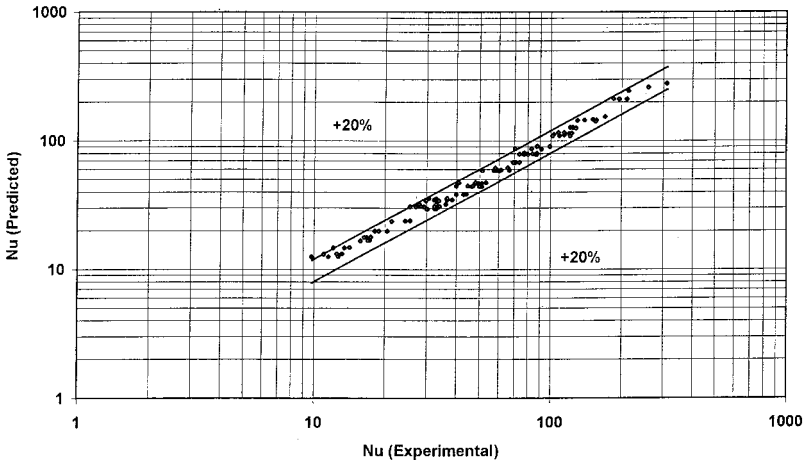

Fig. 7 Comparison of experimental Nusselt number with that predicted from Eq. (8) for short-length strips

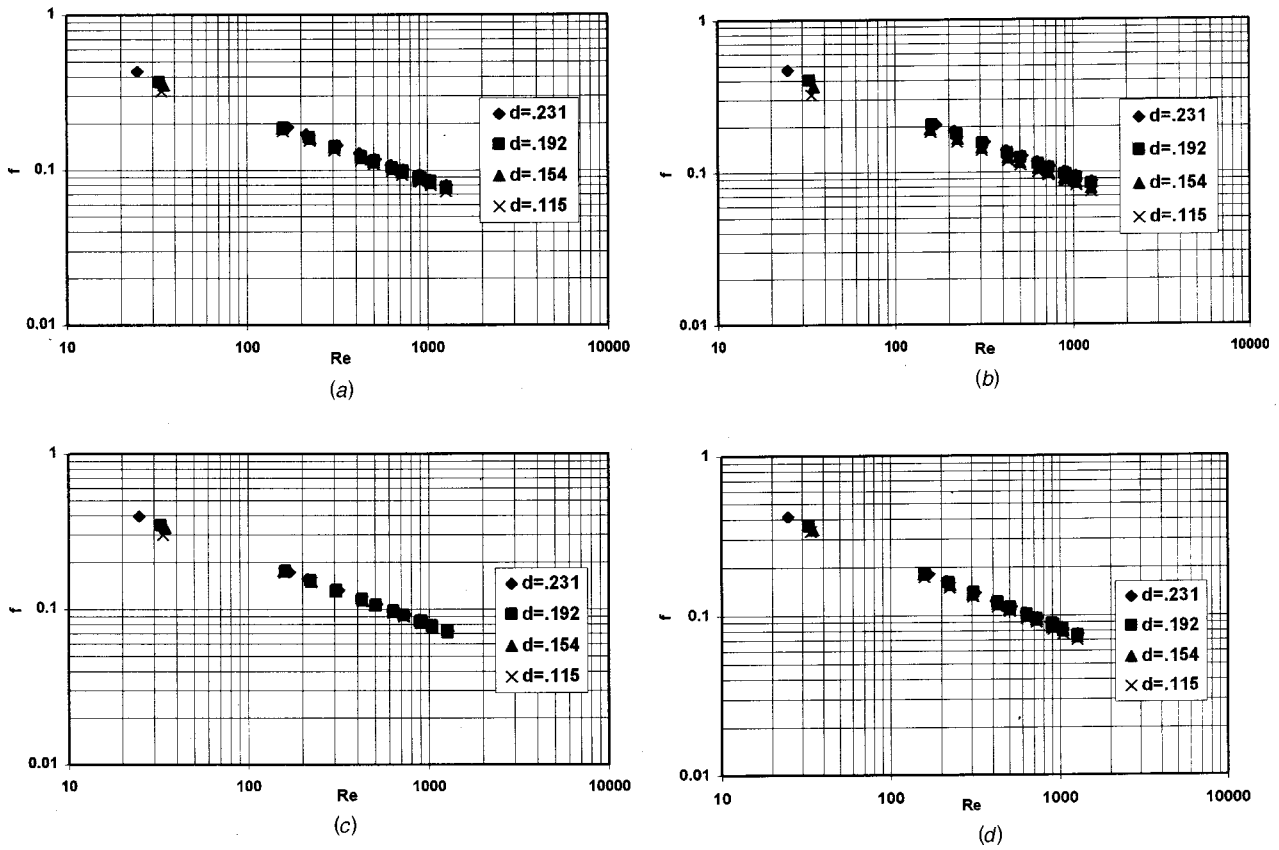

Fig. 8 Variation of friction factor with Reynolds number for regularly-spaced strip elements—cross strip (aspect ratio 4): (*a*) $y=2.5$, $s=5$; (*b*) $y=2.5$, $s=2.5$; (*c*) $y=5$, $s=5$; and (*d*) $y=5$, $s=2.5$

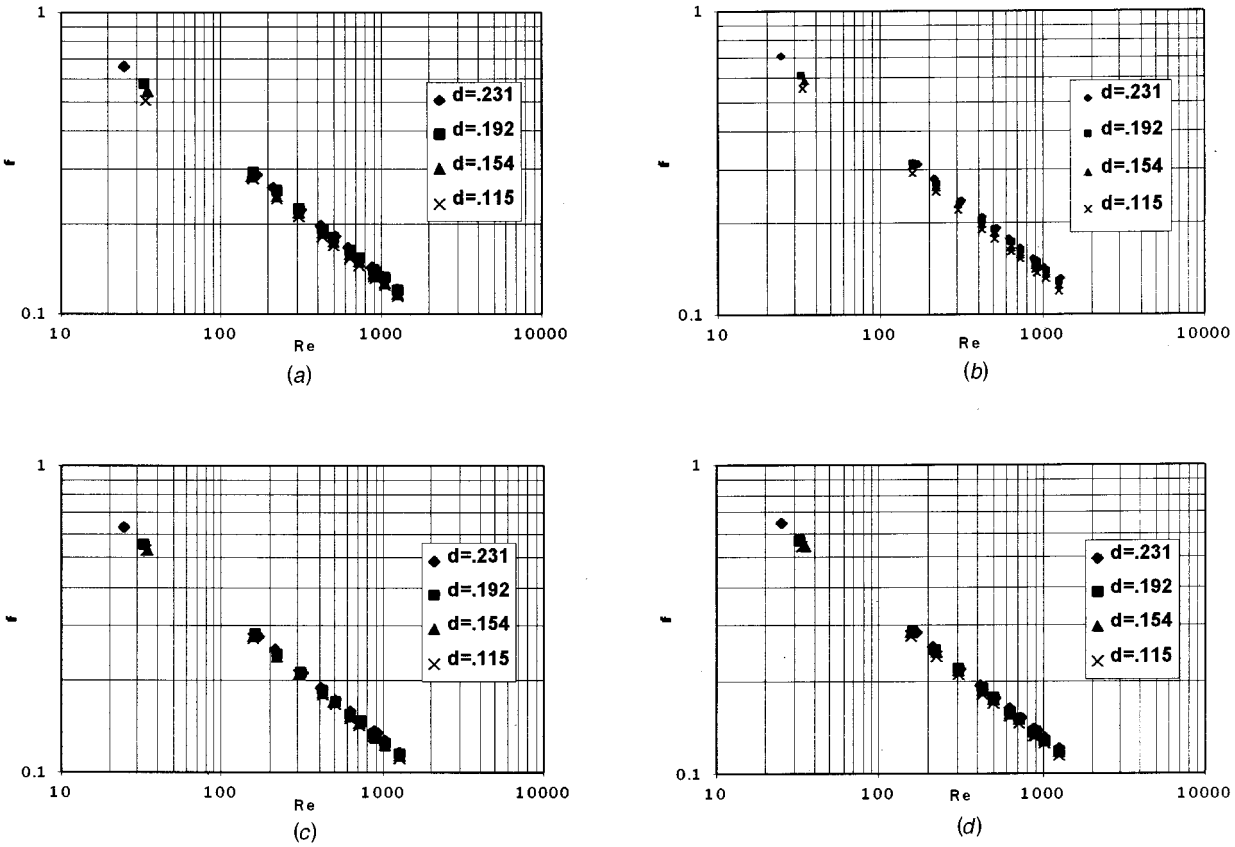

Fig. 9 Variation of friction factor with Reynolds number for regularly-spaced strip elements—longitudinal strip (aspect ratio 4): (*a*) $y=2.5$, $s=5$; (*b*) $y=2.5$, $s=2.5$; (*c*) $y=5$, $s=5$; and (*d*) $y=5$, $s=2.5$

ing linear variation of fluid bulk temperature along the length of the tube. A thermal steady state was generally reached in 60–120 minutes. Data acquisition began after steady state operation was achieved. The minimum and the maximum changes in the fluid viscosity from the inlet to the outlet section were 4 percent and 20 percent of the value at the inlet, respectively. Hence all fluid properties were calculated at $(T_{bi}+T_{bo})/2$ and functional relationships of properties with temperature given by the suppliers of fluids were used for this purpose. No significant improvement is expected, Hong and Bergles [9], by using the film temperature. The tube wall temperature drop was calculated by considering the steady state, one-dimensional radial heat conduction equation and this drop was applied uniformly along the length of the tube. The wall temperature and the bulk temperature were combined with the heat flux to give the axially local heat transfer coefficient and the Nusselt number. The axially averaged Nusselt number was obtained by Simpson's rule of numerical integration. The flow was hydrodynamically fully developed and the fluid had uniform temperature profile at the entrance of the test section. The inside tube diameter rather than the hydraulic diameter was used in defining Nu and Re for performance analysis and easy comparison. Marner et al. [10] proposed this envelope diameter approach for reporting enhanced tube data. Buoyancy effect was considered negligible since the Richardson number was less than unity even for the worst case.

An uncertainty analysis conducted along the lines suggested by Kline and McClintock [11] showed that the uncertainties involved in the friction factors were within ± 5 percent whereas those involved in the estimation of Nusselt number and Reynolds number were within ± 6 percent and ± 2 percent, respectively.

Results and Discussion

The results obtained in this study are presented and discussed in this section. But before that, the correlations [Eqs. (5) and (6)] for the isothermal friction factor and Nusselt number for full-length strips developed by Hsieh and Huang [6] are presented below for ease of discussion:

$$f = 49.96\,\mathrm{Re}^{-0.44}(D_h/D)^{1.18}(\mathrm{AR})^{-1.53} \tag{5}$$

$$\mathrm{Nu} = 1.233(\mathrm{Gz})^{0.38}(\mu_b/\mu_w)^{0.14}(D_h/D)^{-0.74}(\mathrm{AR}+1)^{0.41}. \tag{6}$$

Part A: Data for Short-Length Strips

Data for Friction Factor. Figure 4 shows the variation of experimental friction factor with Reynolds number for short-length strips ($l=0.5$, 0.333, 0.25). Also the data for full-length strip ($l=1$) are presented in the figure as a baseline data. Figures 4(*a*), 4(*b*), and 4(*c*) show, respectively, the cases of cross strip (aspect ratio 4 (CS4)); longitudinal strip (aspect ratio 4 (LS4)), and longitudinal strip (aspect ratio 1 (LS1)). Friction factor for $l=1$ in all the cases are in agreement with Eq. (5) within ± 12 percent. This validated the present experimental setup. Friction factor for $1<1$ reduces, as expected, for all cases compared to $l=1$ case. The reduction in percentage friction factor for $l<1$ compared to $l=1$ is given below in Table 2.

For $l<1$, the mixing stops and the secondary flow ceases downstream of the strip and perhaps the straight flow akin to flow through a bare tube ensues. In general, the smaller the strip length and thus the smaller the additional frictional surface, the larger the reduction in friction factor compared to the full-length strip. The reduction in f increases with the increase in Re. For all $l<1$, the

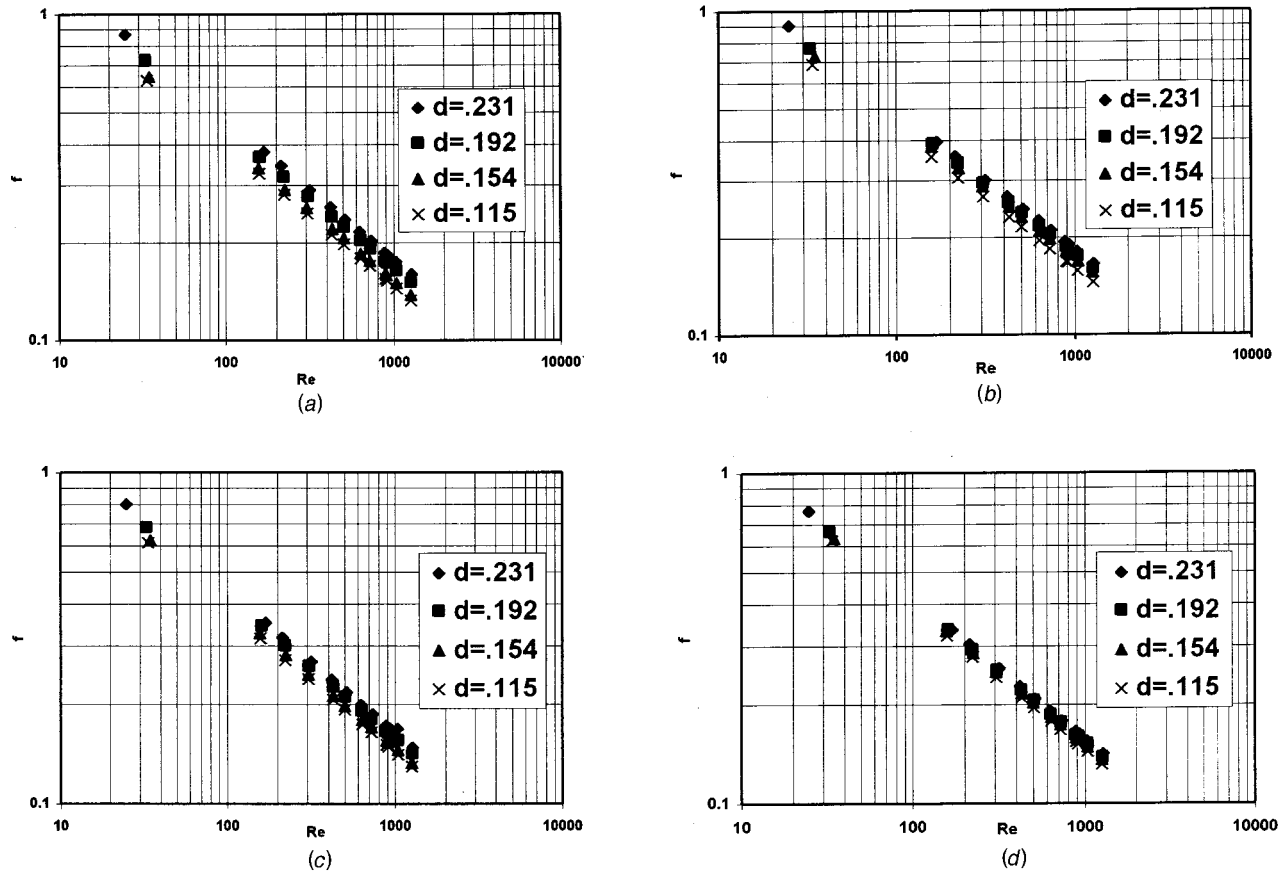

Fig. 10 Variation of friction factor with Reynolds number for regularly-spaced strip elements—longitudinal strip (aspect ratio 1): (*a*) $y=2.5$, $s=5$; (*b*) $y=2.5$, $s=2.5$; (*c*) $y=5$, $s=5$; and (*d*) $y=5$, $s=2.5$

reduction in friction factor is maximum for the case of LS1 and it is minimum for CS4; the case of LS4 falls in between. This is because of the availability of minimum surface area for frictional drag for LS1 when $l<1$ compared to the case when $l=1$. The reduction in friction factor in the case of CS4 is less than that in the case of LS4 because, in the former case, the mixing due to secondary cross flow causing momentum loss is more important than the additional surface available for frictional drag with CS4.

Correlation. Since the short-length strips and (it will be observed later that) the regularly-spaced strip elements (for the values of y and s considered here) perform better than the full-length strips, the correlations for f and Nu have been developed to predict the friction and the heat transfer characteristics. The need for such correlations can never be overemphasized. The thermal-hydraulic performance depends upon the fluid and the geometrical characteristics of the duct and a variety of mechanisms that influence the flow field. Consequently, empirically derived correlations require a very large database (generated in the present investigation) that covers a wide range of variation of the independent parameters. In the present work, all the correlations have been developed by least squares log-regression fit. The correlation for friction factor for short-length strip is given by Eq. (7) below:

$$f=49.96\,\mathrm{Re}^{-0.44}(D_h/D)^{1.18}(\mathrm{AR})^{-1.53}(1+aX+bX^2+cX^3), \tag{7}$$

where $X=(l-1)^{0.2}(D_h/D)^{0.075}\,\mathrm{Re}^{0.44}$; $a=-8.21\mathrm{E}-02$; $b=7.53\mathrm{E}-0.3$; $c=-2.10\mathrm{E}-04$. Equation (7) predicts 99 percent of 108 experimental data within ± 20 percent as shown in Fig. 5. It can be seen from Eq. (7) that $l=1$ gives the correlation (Eq. (5)) for full-length strips.

Data for Nusselt Number. Figure 6 shows the variation of Nusselt number with Graetz number for short-length strips: (*a*) CS4; (*b*) LS4; and (*c*) LS1. Here also the figure shows the values of Nu for $l=1$. The present experimental data for $l=1$ for all cases agree with Eq. (6) within ± 14 percent. It is seen in Fig. 6 that Nu for $1<1$, for all the cases, is less than that for $l=1$. However, as can be seen from the table below, the reduction percentage in Nu is not as large as is observed in case of f even though the trends for both Nu and f are qualitatively the same. The reduction percentage in Nu for $1<1$ compared to that for $l=1$ is given in Table 3.

Thus it can be seen that the reduction in Nusselt number in all cases is less than that in case of friction factor, i.e. the temperature profiles are much more flatter than the velocity profiles. This observation is very useful from the thermohydraulic point of view since it can be concluded that short-length strips (upto $l=0.3$) perform better than the full-length strips. The performance evaluation according to Bergles et al. [12] confirms this conclusion.

Correlation. Equation (8) below is the correlation for Nusselt number for short-length strips under UWHF condition:

$$\mathrm{Nu}=1.233(\mathrm{Gz})^{0.38}(\mu_b/\mu_w)^{0.14}(D_h/D)^{-0.74}(\mathrm{AR}+1)^{0.41}(1+aX+bX^2+cX^3), \tag{8}$$

where $X=(l-1)^{0.2}(D_h/D)^{0.068}\mathrm{Gz}^{0.38}$; $a=-3.85\mathrm{E}-02$; $b=2.67\mathrm{E}-03$; $c=-5.04\mathrm{E}-05$. It is evident from Eq. (8) that $l=1$ gives the correlation for full-length strips (i.e., Eq. (6)). Figure 7 shows the comparison of Nusselt number predictions of Eq. (8) with the present experimental data. 98 percent of 108 data are predicted within ± 20 percent.

Table 4 The average percent increase in friction factor for regularly-spaced strip elements compared to full-length strips

CS4				
d	Y=2.5, s=5	Y=2.5, s=2.5	Y=5, s=5	Y=5, s=2.5
0.231	15	25	5	10
0.192	10	20	3	8
0.154	8	12	2	5
0.115	5	8	1	2
LS4				
d	Y=2.5, s=5	Y=2.5, s=2.5	Y=5, s=5	Y=5, s=2.5
0.231	10	18	5	8
0.192	8	15	3	6
0.154	5	12	2	5
0.115	3	8	1	3
LS1				
d	Y=2.5, s=5	Y=2.5, s=2.5	Y=5, s=5	Y=5, s=2.5
0.231	30	35	20	15
0.192	22	30	15	12
0.154	12	26	8	10
0.115	8	18	5	7

Part B: Data for Regularly-Spaced Strip Elements

Friction Factor Data. Figures 8–10 show the variation of friction factor with Reynolds number for regularly spaced strip elements for CS4, LS4, and LS1, respectively; in each case (*a*) $y=2.5$, $s=5$; (*b*) $y=2.5$, $s=2.5$; (*c*) $y=5$, $s=5$, and (*d*) $y=5$, $s=2.5$. All the figures also show the dependence of friction factor on the rod-diameter in the strip-rod assembly. It can be seen from the figures that friction factor decreases with the decrease in the rod-diameter. For all the cases, it has been observed that the flow is both hydrodynamically and thermally (heat transfer results follow) periodically fully developed after few (2–4) cycles in the strip-rod assembly; one cycle being the combination of one strip module and one rod module. The friction factor for all cases of the regularly spaced strip elements increases compared to the case of full-length strips. The average percentage increase in friction factor for regularly-spaced strip elements compared to full-length strips is presented in Table 4. Table 4 shows that, for each aspect ratio, the lower the values of y and s, the more the percent

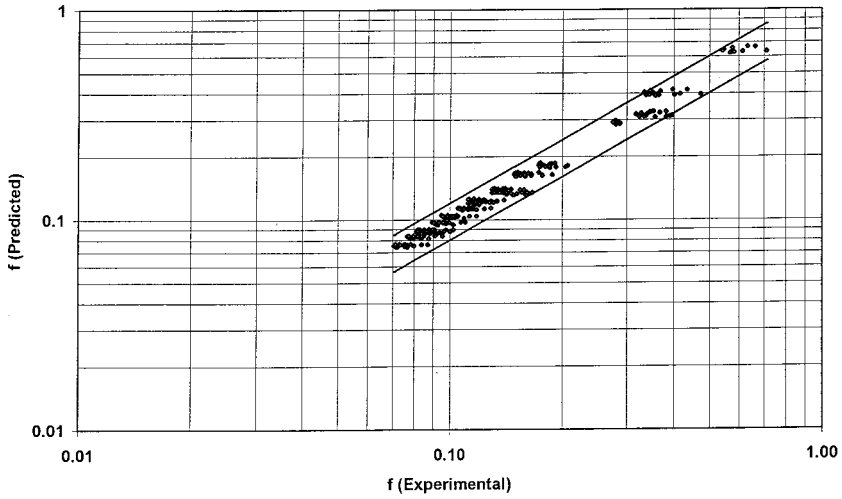

Fig. 11 Comparison of experimental friction factor with that predicted from Eq. (9) for regularly-spaced strip elements

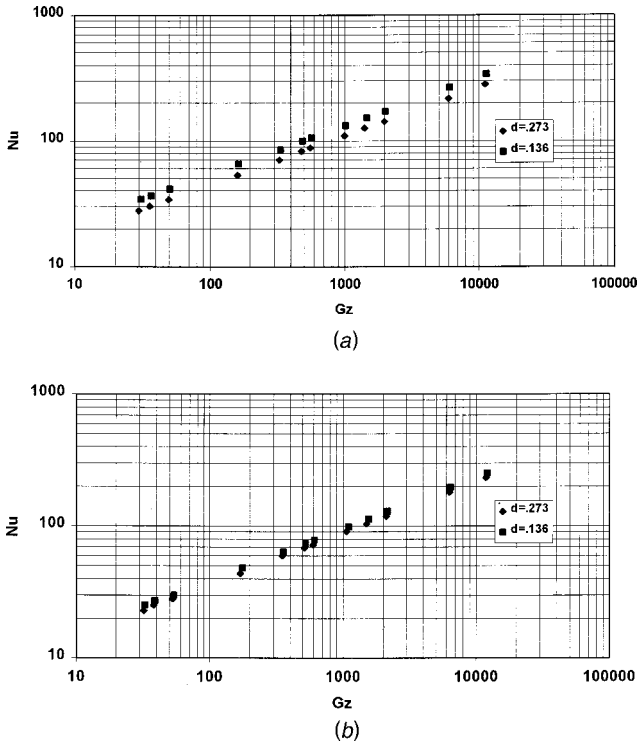

Fig. 12 Variation of Nusselt number with Graetz number for regularly-spaced strip elements—cross strip (aspect ratio 4): (*a*) $y=2.5$, $s=2.5$; and (*b*) $y=5$, $s=5$

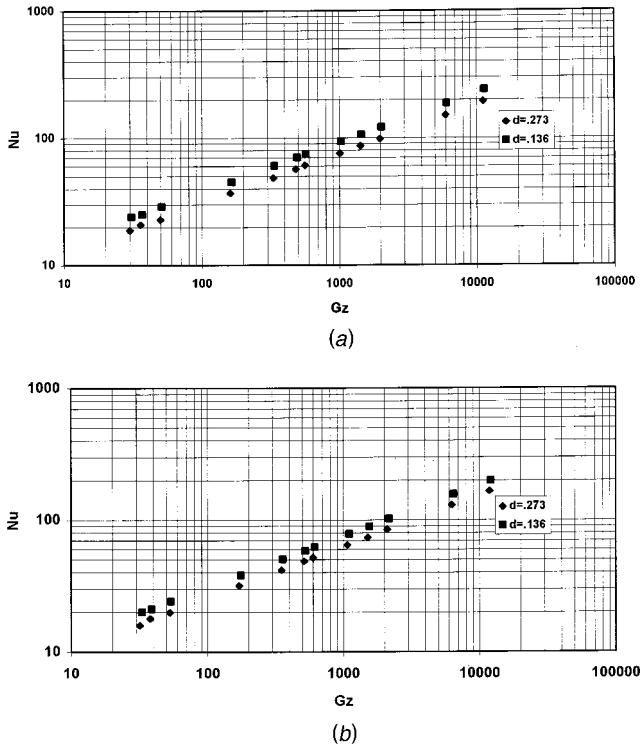

Fig. 13 Variation of Nusselt number with Graetz number for regularly-spaced strip elements—longitudinal strip (aspect ratio 4): (*a*) $y=2.5$, $s=2.5$; and (*b*) $y=5$, $s=5$

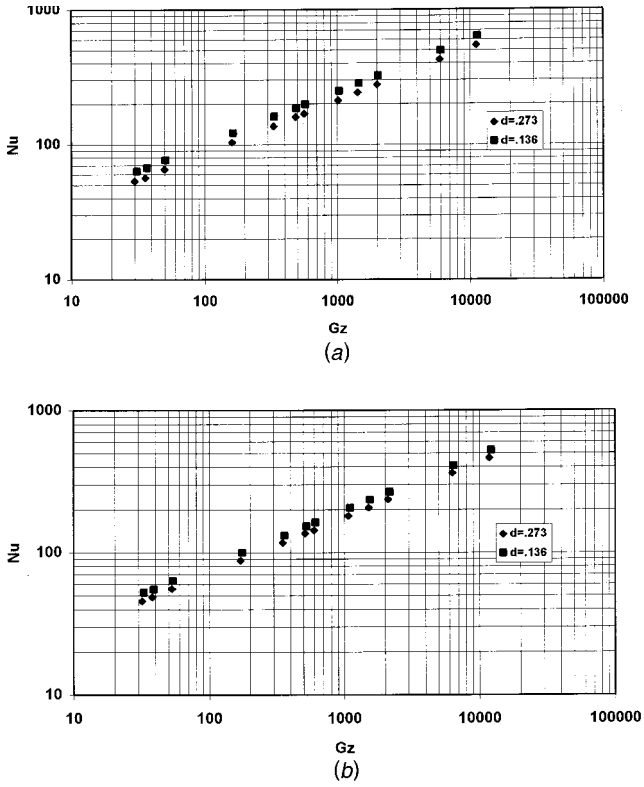

Fig. 14 Variation of Nusselt number with Graetz number for regularly-spaced strip elements—longitudinal strip (aspect ratio 1): (*a*) $y=2.5$, $s=2.5$; and (*b*) $y=5$, $s=5$

increase in friction factor compared to that in the case of full-length strips. This is due to the fact that frictional surface increases with more number of strip elements in case of smaller y and there is more fluid mixing and associated momentum loss with more number of gaps in case of smaller s. For a given y and s, the percent increase in friction factor is maximum for LS1 and minimum for LS4 and the case of CS4 falls between the two since the available surface for frictional drag is maximum for LS1 and minimum for LS4 and that for CS4 is between the two. It is also observed from Table 4 that the percent increase in friction factor decreases with the decrease in rod diameter for each combination of y and s. This can be explained from the fact that, as the rod diameter decreases, there is less secondary flow and the fluid has less chance to mix resulting in smaller momentum loss and pressure drop. It can be concluded that smaller rod diameter in the strip-rod assembly is good from the hydraulic and pumping power point of view because of decreased pressure drop.

Correlation. Equation (9) below is the correlation for friction factor for regularly spaced strip elements:

$$f=49.96\,\mathrm{Re}^{-0.44}(D_h/D)^{1.18}(\mathrm{AR})^{-1.53}(1+aX+bX^2+cX^3), \tag{9}$$

where $X=\mathrm{Re}^{0.44}(ys)^{0.1}e^{ds}(D_h/D)^{0.17}$; $a=1.31\mathrm{E}-02$; $b=-2.96\mathrm{E}-04$; $c=1.99\mathrm{E}-06$. It can be seen that $s=0$ makes Eq. (9) identical to Eq. (5), the correlation for full-length strips and $d=0$ in Eq. (9) makes it suitable for the case when the strip elements are ''pinched'' in place rather than these being connected by thin rods. Figure 11 shows the comparison of present experimental data with that predicted from Eq. (9). 98 percent of 576 data are predicted within ± 20 percent.

Nusselt Number Data. Figures 12–14 show the variation of Nusselt number with Graetz number for regularly spaced strip elements for CS4, LS4, and LS1, respectively. The figures are for

Table 5 Average percent increase in Nusselt number for regularly-spaced strip elements compared to that for full-length strips

CS4			LS4			LS1		
d	Y=2.5, s=2.5	Y=5, s=5	d	Y=2.5, s=2.5	Y=5, s=5	d	Y=2.5, s=2.5	Y=5, s=5
0.273	45	20	0.273	35	15	0.273	55	32
0.136	75	30	0.136	65	38	0.136	80	48

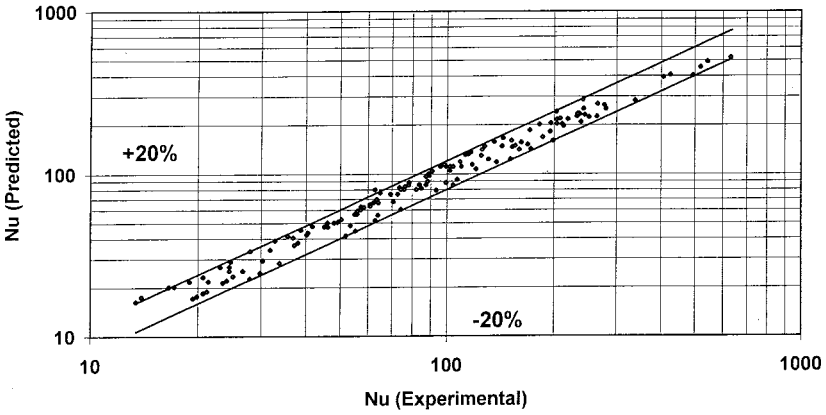

Fig. 15 Comparison of experimental Nusselt number with that predicted from Eq. (10) for regularly-spaced strip elements

(*a*) $y=2.5$, $s=2.5$; and (*b*) $y=5$, $s=5$. In each figure, the dependence of Nusselt number on the rod-diameter in the strip-rod assembly is also shown; in contrast with *f*, with decreasing rod-diameter Nu increases. Table 5 below shows the average percent increase in Nusselt number for regularly spaced strip elements compared to that for full-length strips.

Table 4 and Table 5 show that the Nusselt number for regularly spaced strip elements for all cases is higher than that for the full-length strips; the increase in Nusselt number is much more than the increase in friction factor. This is an overall good observation from the thermohydraulic point of view and this has been confirmed by the performance analysis suggested by Bergles et al. [12].

It may be noted here that the heat transfer measurements were taken for less number of cases than that for the pressure drop measurements. This is so, because it took long time for the system to reach thermal steady state for a single run, especially for SMO and PB20 and it was practically impossible to accommodate all possible combinations of *y*, *s*, and *d*. However, the data generated was sufficient for the development of a correlation suitable for the design purpose. For small rod diameter cases, the heat transfer increases more. The reason is that the local values of Nusselt numbers in the inlet region of the strip section do not show sharp decline, Date and Saha [13]. In fact the local Nusselt numbers remain almost constant in both the strip and the annular sections. Also, for the small diameter cases, negative axial velocities are not expected [13] even at the first axial step in the strip section, and thus the secondary flow is not suppressed. A small rod diameter thus has a favorable overall effect. Hence doing away with the connecting rod and locating the strip elements in place-probably by ''pinching'' the tube is desirable, if it is practically feasible.

Correlation. Equation (10) below is the correlation for Nusselt number for regularly-spaced strip elements with UWHF condition:

$$\mathrm{Nu}=1.233\mathrm{Gz}^{0.38}(\mu_b/\mu_w)^{0.14}(D_h/D)^{-0.74}(\mathrm{AR}+1)^{0.41}(1+aX+bX^2+cX^3); \quad (10)$$

where $X=\mathrm{Gz}^{0.38}(ys)^{0.1}e^{ds}(D_h/D)^{0.12}$; $a=3.32\mathrm{E}-02$; $b=-5.18\mathrm{E}-04$; $c=1.96\mathrm{E}-06$.

Figure 15 shows the comparison of Nusselt number predictions of Eq. (10) with experimental data for regularly-spaced strip elements with UWHF condition. 96.5 percent of 144 data are predicted within ± 20 percent. $s=0$ reduces Eq. (10) to Eq. (6). $d=0$ makes Eq. (10) applicable for the strip elements being ''pinched.''

Conclusions

Experimental data for friction factor and Nusselt number (for UWHF condition) for longitudinal full-length strip, short-length strip and regularly-spaced strip elements in a circular tube have been presented and discussed in the present report. The strips have been crossed-type, rectangular and square in cross-section. The aspect ratio of the strips varied. Four different fluids, viz., water, ethylene glycol, servotherm medium oil and polybutene 20 have been considered. This has enabled generating a large database covering a wide range of independent parameters like Re and Pr. The short-length strip upto a limited value (0.3) of 1 and regularly spaced strip elements for $2.5<y<5$ and $2.5<s<5$ have been found to perform better than the full-length strips. Friction factor reduces by 8–58 percent and Nusselt number reduces by 2–40 percent for short-length strips. For regularly-spaced strips elements, friction factor increases by 1–35 percent and Nusselt number increases by 15–75 percent. For these cases, correlations for friction factor and Nusselt number have been developed. The effect of inserts length and spacing have been lumped into polynomial functions for correlations. The thermal entrance length has

been represented by Graetz number in the correlations for Nusselt number. The correlations have predicted the experimental data satisfactorily.

Nomenclature

A_c = axial flow cross-sectional area, m^2
A_0 = plain tube flow cross-sectional area, $\pi D^2/4$, m^2
AR = L/H, aspect ratio, dimensionless
C_p = constant pressure specific heat, J/(kgK)
D = internal diameter of the test tube, m
D_h = hydraulic diameter of the test tube $[=(4A_c)/P]$, m
d^* = rod diameter, m
d = non-dimensional rod diameter (d^*/D), dimensionless
f = fully developed Fanning friction factor based on internal diameter of the tube, Eq. (1), dimensionless
Gz = Graetz number, RePr d/L, dimensionless
H = length/depth (in the cross-section) of the strip elements, m
h = heat transfer coefficient, $W/(m^2K)$
k = fluid thermal conductivity, W/(mK)
L = length of the test section, width of the strip, m
$\dot{m}$ = mass flow rate of fluid, kg/s
Nu = axially averaged Nusselt number based on internal diameter of the tube $[(hD)/k]$, dimensionless
P = wetted perimeter in the particular cross-section of the duct, m
ΔP_z = pressure drop over a length z, N/m^2
Pr = fluid Prandtl number $[(\mu C_p)/k]$, dimensionless
Q = heat input to the test section, W
R = resistance of the heater element, Ω
Re = Reynolds number based on internal diameter of the tube $[(\rho V_0 D)/\mu]$, dimensionless
S = gap length between two consecutive twisted-tape elements, m
s = space ratio $(=S/D)$, dimensionless
T_{bi} = inlet bulk mean temperature of the fluid, °C
T_{bo} = outlet bulk mean temperature of the fluid, °C
T_{bz} = local bulk mean temperature of the fluid, °C
T_{wz} = local tube wall temperature, °C
ΔT_w = wall-to-bulk fluid temperature difference, K
V_0 = mean velocity based on plain tube diameter, $m/\rho A_0$, m/s
y = twist ratio $(=H/D)$, dimensionless
V = voltage output from the autostat, V
Z = axial length, m

Greek Symbols

δ = tape thickness, m
μ = fluid dynamic viscosity, kg/ms
ρ = density of the fluid, kg/m^3

Subscripts

b = at bulk fluid temperature
h = based on hydraulic diameter, D_h
w = at tube wall temperature

References

[1] Chen, J. D., and Hsieh, S. S., 1992, "Buoyancy Effect on the Laminar Forced Convection in a Horizontal Tube With a Longitudinal Plate Insert," Int. J. Heat Mass Transf., **35**, pp. 263–267.
[2] Solanki, S. C., Saini, J. S., and Gupta, C. P., 1985, "An Experimental Investigation of Fully Developed Laminar Flow in a Non-Circular Annulus," *Proc., 8th Nat. Conf. on Heat Mass Transfer*, HMTA 34-85, Vishakhapatnam, IN.
[3] Solanki, S. C., Prakash, S., Saini, J. S., and Gupta, C. P., 1987, "Forced Convection Heat Transfer in Doubly Connected Ducts," Int. J. Heat Fluid Flow, **8**, pp. 107–110.
[4] Chen, J. D., and Hsieh, S. S., 1991, "Assessment Study of Longitudinal Rectangular Plate Inserts as Tubeside Heat Transfer Augmentative Device," Int. J. Heat Mass Transf., **34**, pp. 2545–2553.
[5] Hsieh, S. S., and Wen, M. Y., 1996, "Developing Three-Dimensional Laminar Mixed Convection in a Circular Tube Inserted With Longitudinal Strips," Int. J. Heat Mass Transf., **39**, pp. 299–310.
[6] Hsieh, S. S., and Huang, I. W., 2000, "Heat Transfer and Pressure Drop on Laminar Flow in Horizontal Tubes With/Without Longitudinal Inserts," ASME J. Heat Transfer, **122**, pp. 465–475.
[7] Saha, S. K., and Dutta, A., 2001, "Thermohydraulic Study of Laminar Swirl Flow Through a Circular Tube Fitted With Twisted Tapes," ASME J. Heat Transfer, **123**, No. 3, pp. 417–427.
[8] Saha, S. K., Gaitonde, U. N., and Date, A. W., 1989, "Heat Transfer and Pressure Drop Characteristics of Laminar Flow in a Circular Tube Fitted With Regularly-Spaced Twisted-Tape Elements," Exp. Therm. Fluid Sci., **2**, pp. 310–322.
[9] Hong, S. W., and Bergles, A. E., 1976, "Augmentation of Laminar Flow Heat Transfer in Tubes by Means of Twisted-Tape Inserts," ASME J. Heat Transfer, **98**, pp. 251–256.
[10] Marner, W. J., Bergles, A. E., and Chenoweth, J. M., 1983, "On the Presentation of Performance Data for Enhanced Tubes Used in Shell-and-Tube Heat Exchangers," ASME J. Heat Transfer, **105**, pp. 358–365.
[11] Kline, S. J., and McClintock, F. A., 1953, "Describing Uncertainties in Single Sample Experiments," Mech. Eng. (Am. Soc. Mech. Eng.), **75**, pp. 3–8.
[12] Bergles, A. E., Blumenkrantz, A. R., and Taborek, J., 1974, "Performance Evaluation Criteria for Enhanced Heat Transfer Surfaces," Paper FC 6.3, *Proc. 5th Int. Heat Transfer Conf.*, Tokyo, Vol. 2, pp. 239–243.
[13] Date, A. W., and Saha, S. K., 1990, "Numerical Prediction of Laminar Flow and Heat Transfer Characteristics in a Tube Fitted With Regularly-Spaced Twisted-Tape Elements," Int. J. Heat Fluid Flow, **11**, pp. 346–354.

H. Chattopadhyay
PEHT Group,
Central Mechanical Engg. Research Instt.,
Durgapur 713 209, India

G. Biswas
e-mail: gtm@iitk.ac.in
Mem. ASME
Dept. of Mechanical Engineering,
Indian Institute of Technology Kanpur,
Kanpur 208016, India

N. K. Mitra[1]
Mem. ASME
Institut für Thermo- und Fluiddynamik,
Ruhr-Universität Bochum, Germany,
44780 Bochum, Germany

Heat Transfer From a Moving Surface Due to Impinging Slot Jets

Turbulent flow field and heat transfer in an array of slot jets impinging on a moving surface have been numerically investigated by Large-eddy Simulation (LES) technique in the range of Reynolds numbers between 500 and 3000. The surface velocity, directed perpendicular to the jet, is varied up to two times the jet velocity at the nozzle exit. The Nusselt number distributions for various surface velocities are presented. It has been observed that on one hand increasing velocity of the impingement plate reduces heat transfer, while on the other hand distribution of Nusselt number over the impingement surface becomes more uniform with the increased surface velocity.
[DOI: 10.1115/1.1470489]

Keywords: Forced Convection, Heat Transfer, Impingement, Jets, Turbulence

Introduction

Heat transfer in impinging jets has drawn the attention of researchers because of its extensive application to various industrial and practical situations. Impinging jets are often used for heating, cooling or drying of surfaces. Examples include drying of textiles, film and paper, annealing of glass; processing of some metals, cooling of gas turbine components and electronic equipment; freezing of tissues etc. The transport phenomena due to jet impingement have been discussed widely in available literature, e.g., Viskanta [1] and Downs and James [2].

In most *manufacturing* applications, the impingement surface is in motion on which an array of impinging jets is directed. While numerous articles exist on jet impingement, relatively few studies have dealt with the effect of surface motion. It has been pointed out by Chen et al. [3] that many manufacturing systems rely on available correlations for stationary surface, while the manufacturing processes require correlations that include the effect of surface motion. It must be borne in mind that very often the quality of the processed product is directly linked to the amount of heat transfer. Thus, a thorough analysis of impingement heat transfer on a moving surface is desirable in simulation of processes like metal manufacturing [4].

Subba Raju and Schlünder [5] have measured spatially averaged heat transfer coefficients due to a single impinging jet on a moving, constant temperature metal belt. They found that the area averaged heat transfer coefficients increase with the surface speed by factors of 1.5–2.0 and then attain constant values. Numerical modeling of turbulent, planar air jet on a rectangular duct was performed by Huang et al. [6]. They have found that at higher plate speeds, Nusselt numbers are smaller at the locations where the surface motion is opposed to the dividing jet flow, and higher where the surface motion and the dividing jet flow are in the same direction.

Zumbrunnen et al. [7] have estimated the effect of plate motion on heat transfer in the film boiling regime. They have considered forced convection cooling by impinging jets. The governing equations for mass momentum and energy are solved by the integral method for film boiling in forced convection boundary layer flow on a flat isothermal plate in motion parallel to the flow direction. The conclusion of this study is that the plate motion plays an extremely important role when the plate speed exceeds the liquid velocity.

A similarity solution of the Navier-Stokes equations was utilized to obtain the flow velocity on a moving plate under the condition of negligible interference between the adjacent jets (Zumbrunnen [8]). The velocity components derived from the similarity solution were used to determine heat and mass transfer. The stagnation region heat transfer for a single incident jet decreased only where surface temperature decreased in the direction of surface motion. Results demonstrated the importance of accounting for thermal interactions between the jet and moving surface, where the moving surface temperature is not spatially uniform. In the case of spatially uniform surface temperature, there was no change in stagnation region heat transfer. This result is in excellent agreement with the more general model of Zumbrunnen et al. [9]. Zumbrunnen et al. [9] have developed a boundary-layer type analytical model of a single planar jet impinging on a constant heat flux and constant temperature, moving surface in the laminar regime. It is observed that with increasing surface velocity, heat transfer distributions away from the impingement point (in the direction of plate movement) becomes more uniform.

Polat and Douglas [10] conducted experiment on heat transfer from multiple impinging jets on a permeable moving surface. Their study showed a decrease in heat transfer with increasing surface motion while the amount of through flow increased heat transfer.

Chen et al. [3] have developed a numerical model, taking into account the effect of neighboring jets. Their model determines the distribution of convective heat transfer in the laminar range, for an array of submerged planar jets impinging on a moving surface with uniform heat flux or constant temperature condition. The surface motion is directed perpendicular to the jet. Unlike the earlier investigations, they simulate the moving surface without imposing cross flow. With increasing plate speed, flow separation did not occur near the flow-merging plane. The heat transfer distribution became more uniform but the total heat transfer reduced. Thus the results suggest that neglecting the effects of surface motion can lead to overestimation of heat transfer. In the present work, an attempt has been made to investigate numerically convective heat transfer in the range of Reynolds numbers between 500 and 3000 with the surface velocity of the impingement plate varying up to two times the jet velocity at the nozzle exit. In industrial applications, the use of rectangular axial jets in rows is very common. We have considered a periodic element of such a

[1]Deceased on 14th October, 1999.

Contributed by the Heat Transfer Division for publication in the JOURNAL OF HEAT TRANSFER. Manuscript received by the Heat Transfer Division July 24, 2001; revision received January 24, 2002. Associate Editor: H. S. Lee.

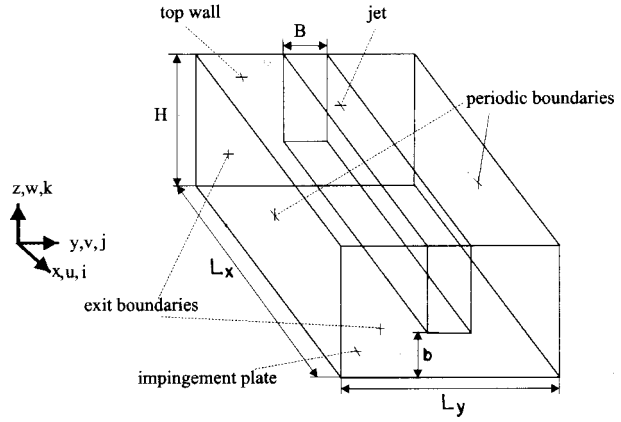

Fig. 1 Computational domain

configuration as the computational domain (Fig. 1). Attention has been focused on the case of nozzle height to jet width ratio of two. It may be mentioned here that the characteristic length for defining Re is twice the jet width, which is the hydraulic diameter for such a configuration (Martin [11]). Large-eddy Simulation (LES) has been used as the tool for predicting the turbulent flow field.

A flow field with multiple jet impingement is quite complex. Laschefski et al. [12,13] presented systematic numerical studies of arrays of impinging laminar jets from slot nozzles (rectangular jets) and found that the flow remains laminar for $Re_{2B}<400$. Depending on the Reynolds number and nozzle height, the flow below the nozzle is laminar (stagnation zone) and changes its state to turbulent during the wall jet development.

Cziesla et al. [14] have computed flow and heat transfer in slot jets, impinging on a stationary surface in the range of Reynolds numbers between 2000 and 10000 for three-dimensional configuration using a locally dynamic model due to Piomelli and Liu [15]. The results obtained using the code compared well with experimental results and direct numerical solution.

A few comments on LES in flow modeling, particularly with respect to jet impingement studies will be appropriate here. Detailed discussion of turbulence modeling for convective heat transfer is given by Benocci [16] who noted the geometry dependence of the model and the necessity of spatial tuning of the model coefficients for the variation in flow geometry. Recently Tzeng et al. [17] have concluded that the accuracy of prediction concerning heat transfer in impinging jets strongly depends on the grid distribution, the choice of turbulence model and the numerical scheme used in spatial discretization. Lakshminarayana [18] gave a classification and review of turbulence models with special emphasis on engineering applications where the restrictions of eddy viscosity models were pointed out. Eddy viscosity based models fail in the case of three-dimensional flows with curvature, rotation, blowing and suction. In such situations, the use of Reynolds Stress Equations model or solutions using Large-eddy Simulation (LES) is advocated.

Basic Equations and Subgrid Closure

The method of LES involves the application of a filter operation to the three-dimensional, time-dependent Navier-Stokes equations. The larger scale motion is solved directly, whereas the subgrid scale motion is modeled. Equations (1), (2), and (3) are the conservative and nondimensional form of continuity, momentum, and energy equations for incompressible flows, written for the large scales which are denoted by an overbar

$$\frac{\partial \overline{u_i}}{\partial x_i}=0 \tag{1}$$

$$\frac{\partial \overline{u_i}}{\partial t}+\frac{\partial \overline{u_i u_j}}{\partial x_j}=-\frac{\partial \overline{p}}{\partial x_i}+\frac{1}{\mathrm{Re}}\frac{\partial^2 \overline{u_i}}{\partial x_j^2}-\frac{\partial \tau_{ij}}{\partial x_j} \tag{2}$$

$$\frac{\partial \overline{T}}{\partial t}+\frac{\partial \overline{u_j}\,\overline{T}}{\partial x_j}=\frac{1}{\mathrm{RePr}}\frac{\partial^2 \overline{T}}{\partial x_j^2}-\frac{\partial q}{\partial x_j} \tag{3}$$

with

$$\tau_{ij}=\overline{u_i u_j}-\overline{u_i}\,\overline{u_j} \tag{4}$$

and

$$q=\overline{u_j T}-\overline{u_j}\,\overline{T}. \tag{5}$$

For nondimensionalization, the following transformation has been used

$$x_i=\frac{x_i^*}{2B},\quad u_i=\frac{u_i^*}{w_{\mathrm{in}}},\quad p=\frac{p^*}{\rho w_{\mathrm{in}}^2},\quad T=\frac{T^*-T_\infty^*}{T_w^*-T_\infty^*}$$

and

$$t=\frac{t^* w_{\mathrm{in}}}{2B}.$$

In the above expressions, w_{in} is the nozzle exit velocity, T_∞ is the temperature of the incoming stream and all starred quantities are dimensional variables. The Reynolds number Re in Eqs. (2) and (3) is based on the nozzle inlet velocity, w_{in} and the hydraulic diameter of the geometry, $2B$. The Prandtl number is $\mathrm{Pr}=\mu c_p/k$.

The terms τ_{ij} and q in Eqs. (4) and (5) are the contributions of the small scales to the large scale transport equations, which are to be modeled. The most commonly used subgrid scale model is based on the gradient transport hypothesis which correlates τ_{ij} to the large scale strain-rate tensor

$$\tau_{ij}=-2\nu_T \overline{S}_{ij}+\frac{\delta_{ij}}{3}\tau_{kk} \tag{6}$$

and analogously

$$q=\frac{\nu_T}{\mathrm{Pr}_t}\frac{\partial \overline{T}}{\partial x_j}. \tag{7}$$

Here, ν_T is eddy viscosity and Pr_t is the turbulent Prandtl number and is assumed unity. The term δ_{ij} is Kronecker delta, $\tau_{kk}=\overline{u_k' u_k'}$ and $\overline{S}_{ij}$ is given by

$$\overline{S}_{ij}=\frac{1}{2}\left(\frac{\partial \overline{u_i}}{\partial x_j}+\frac{\partial \overline{u_j}}{\partial xi}\right). \tag{8}$$

Lilly [19] proposed an eddy viscosity proportional to local large-scale deformation

$$\nu_T=(C_S\Delta)^2|\overline{S}|. \tag{9}$$

Here, C_s is a constant, Δ is the grid filter scale, and $|\overline{S}|=(2\overline{S}_{ij}\overline{S}_{ij})^{1/2}$. Invoking Eq. (9) in (7) yields

$$\tau_{ij}-\frac{\delta_{ij}}{3}\tau_{kk}=-2C\Delta^2|\overline{S}|\overline{S}_{ij}. \tag{10}$$

The quantity C is the Smargorinsky coefficient (basically this is square of C_s), which depends on the type of flow under consideration. Lilly [19] and Germano et al. [20] suggested a method to calculate C for each time step and grid point dynamically from the flow field data. In addition to the grid filter which signifies the resolved and subgrid scales, a test filter is introduced for computation of C. The width of the test filter is larger than the grid filter width. Our computations were carried out using the model suggested by Piomelli and Liu [15]. To avoid ill conditioning of C, a local averaging over adjacent grid cells, following Zang et al. [21], was carried out.

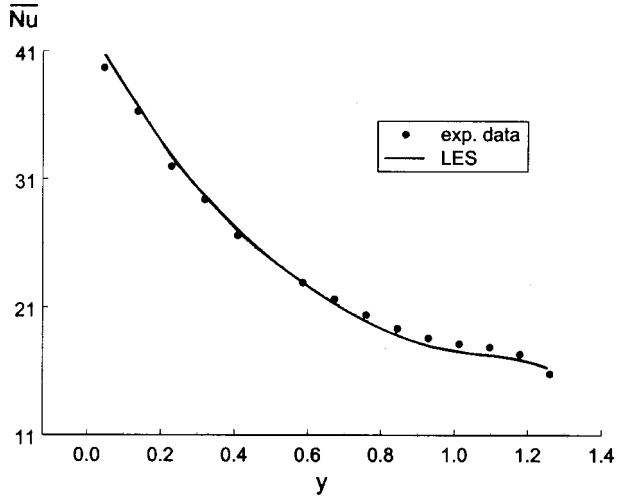

Fig. 2 Comparison of numerical results with the experiment of Schlünder et al. [26]

Method of Solution

The basic equations have been solved by a fractional step finite difference technique due to Kim and Moin [22]. For the convective terms, the Adams-Bashforth scheme is used to get second order accuracy in time discretization. A central discretization of the temporal term in Eq. (2) and (3) to get an accuracy of second order is highly unstable and would lead to so called *leap frogs*, i.e., an unsteady course in velocity, temperature and pressure field (see Tran and Morchoisne [23]). Crank-Nicholson scheme is used to discretize the diffusive terms. The program is based on the finite difference technique, and a staggered-grid arrangement is chosen for implementing the discretization schemes. The time discretization of the Navier-Stokes equations can be written as

$$\frac{\overline{u_i}^{n+1}-\overline{u_i}^{n}}{\Delta t}+\nabla\overline{p}^{n+1}=-\frac{3}{2}conv^{n}+\frac{1}{2}conv^{n-1}+\frac{1}{2\mathrm{Re}}(diff^{n}+diff^{n+1}) \tag{11}$$

where, the convective and diffusive terms are denoted by *conv* and *diff*. The index n symbolizes the current time step, $n-1$ being the previous and $n+1$ is the next time step. Replacement of the velocity of the following time step $\overline{u_i}^{n+1}$ by an intermediate velocity $\overline{u_i}^{*}$ can be written as

$$\overline{u_i}^{*}=\overline{u_i}^{n+1}+\Delta t\nabla\overline{p}^{n+1} \tag{12}$$

which, does not fulfill the continuity equation and yields the following term

$$\frac{\overline{u_i}^{*}-\overline{u_i}^{n}}{\Delta t}=-\frac{3}{2}conv^{n}+\frac{1}{2}conv^{n-1}+\frac{1}{2\mathrm{Re}}(diff^{n}+diff^{n+1}). \tag{13}$$

Application of Eq. (1) to Eq. (12) gives finally the Poisson equation for the pressure field

$$\nabla^2\overline{p}^{n+1}=\frac{1}{\Delta t}\nabla\cdot\overline{u_i}^{*}. \tag{14}$$

Once the pressure field is solved, Equation (12) yields the final velocity field

$$\overline{u_i}^{n+1}=\overline{u_i}^{*}-\Delta t\nabla\overline{p}^{n+1}. \tag{15}$$

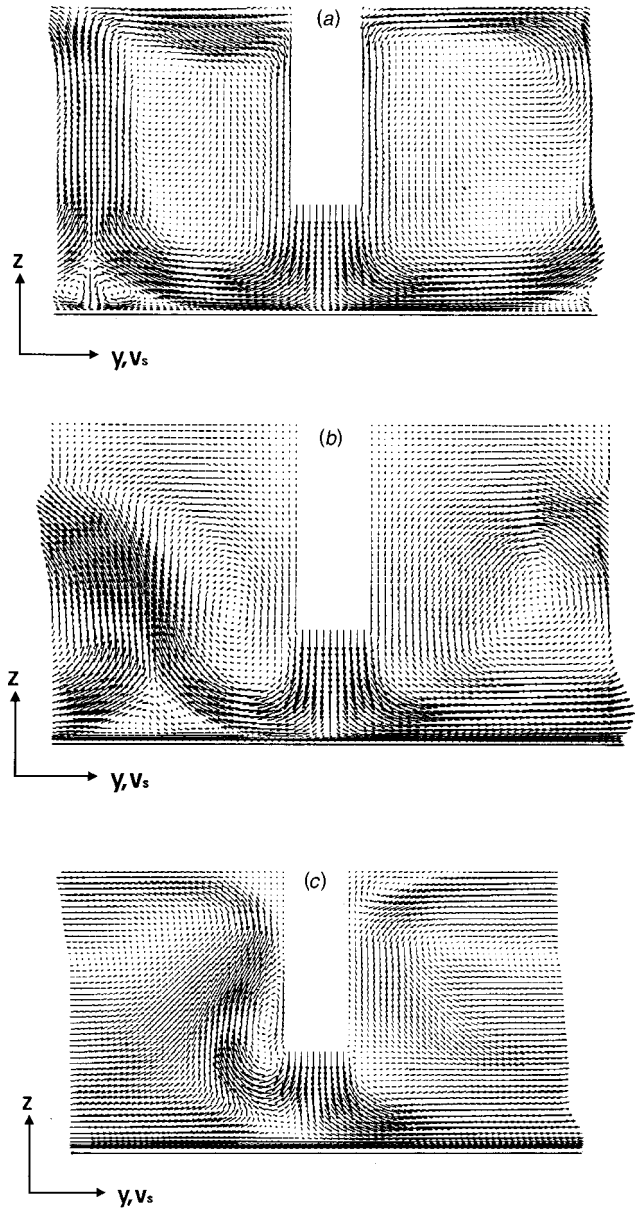

Fig. 3 Instantaneous velocity vectors for different surface velocity (*a*) $v_s=0.1$, (*b*) $v_s=0.5$, and (*c*) $v_s=1.0$

Boundary Conditions

At the jet exit, a constant velocity profile (w_{in}) is used. No-slip conditions are assumed on the fixed walls (Dirichlet type of boundary condition), on the impingement plate v_s is directly prescribed. The near wall area over the impingement plate is computed directly using refined grid. A characteristic feature of the present geometry is the inflow from the ambient into the computational domain due to the entrainment effect by jet flows. The amount of backflow at the exit planes is unknown. Consequently, the exit boundary condition has to fulfil the condition of mass conservation. Integration of the pressure Poisson equation (14) yields

$$\int_G\int\int(\nabla^2\overline{p}^{n+1})dV=\frac{1}{\Delta t}\int_G\int\int(\nabla\cdot\overline{u_i}^{*})dV. \tag{16}$$

Application of the Gauss divergence theorem gives

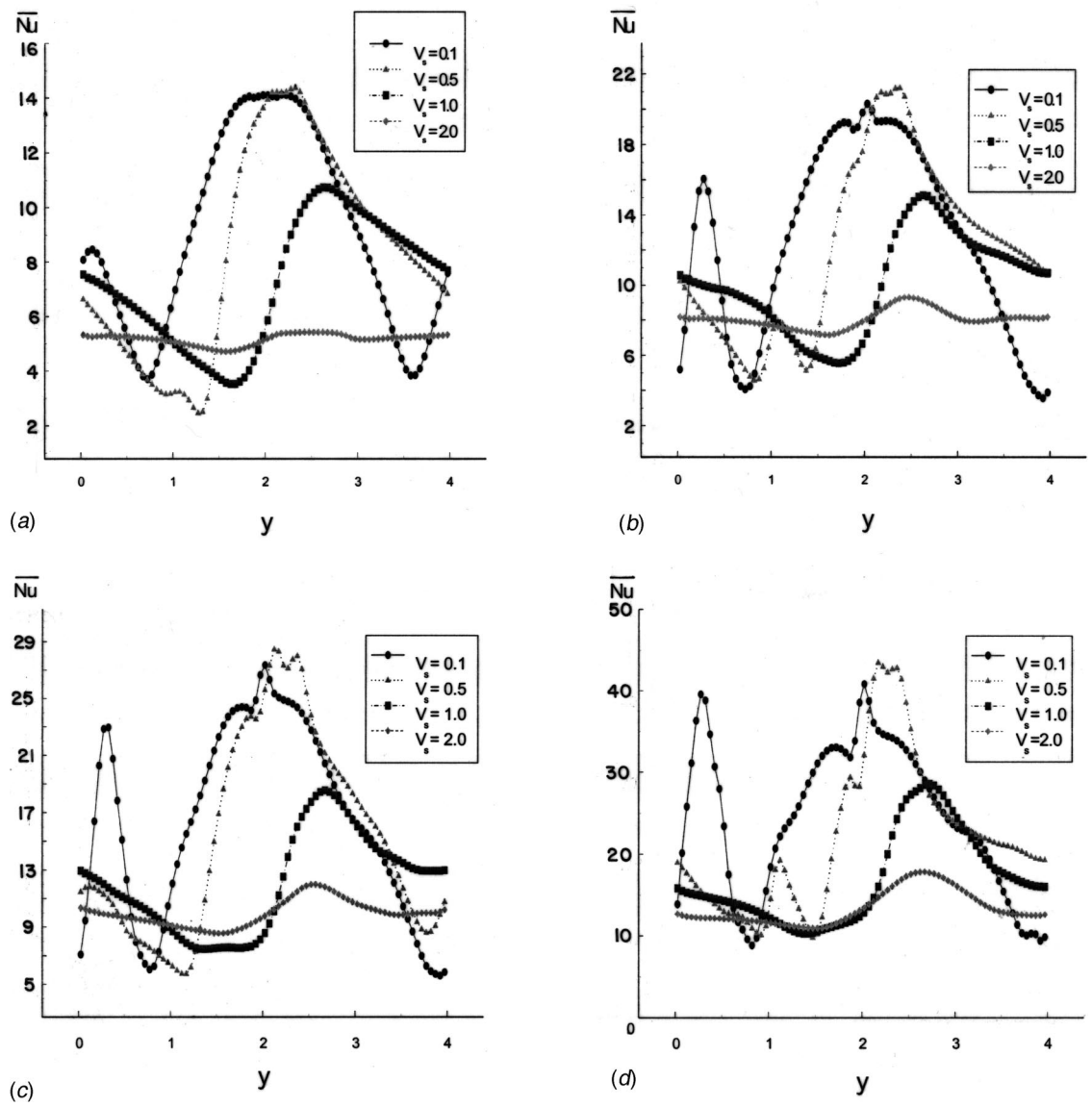

Fig. 4 Distribution of span-averaged Nusselt number at different surface velocities for Re=(*a*) 500, (*b*) 1000, (*c*) 1500, and (*d*) 3000

$$\int\int_{\partial G}\left(\frac{\partial \overline{p}^{n+1}}{\partial n}\right)dS=\frac{1}{\Delta t}\int\int\int_{G}(\nabla\cdot\overline{u}_i^*)dV. \tag{17}$$

It can be shown that the pressure boundary condition, ''zero first derivative'' cannot be used for jet flows. Since the intermediate velocity field u_i^* is the solution of the momentum equation and do not fulfil the global continuity in contrast to flows without backflow across the exit plane (e.g., channel flows), the term on the left hand side in Eq. (17) also does not need to be zero. A pressure boundary condition is implemented according to Childs and Nixon [24] and Grinstein et al. [25]

$$\overline{p}_e=0.7\overline{p}_i+0.3\overline{p}_\infty. \tag{18}$$

The pressure at the exit plane $\overline{p}_e$ is an interpolated value between the pressure of the last interior cell of the domain, $\overline{p}_i$ and the ambient pressure, which is known a priori. Accordingly the turbulent pressure fluctuations across the exit planes are possible. The temperature on the impinging plate was assumed to be uniform and was set to unity. The incoming jet is at ambient condition, i.e., $T=0.0$. The zero gradient temperature boundary conditions was used at the exit planes. The computational domain is a periodic element of a jet bank. Thus the spacewise periodic boundary condition has been imposed at $y=0$ and $y=Ly$ (see Fig. 1).

Definition of Nusselt Number

The heat transfer characteristic of the jet is characterized by the Nusselt number distribution over the impingement plate. The Nusselt number is defined as

$$\mathrm{Nu}=\frac{h(2B)}{k} \tag{19}$$

with the convective heat transfer coefficient h, the thermal conductivity k of the fluid and the hydraulic diameter of the configuration, $2B$. The heat transfer coefficient is defined as

$$h=\frac{q''}{T_w-T_\infty} \tag{20}$$

which, gives

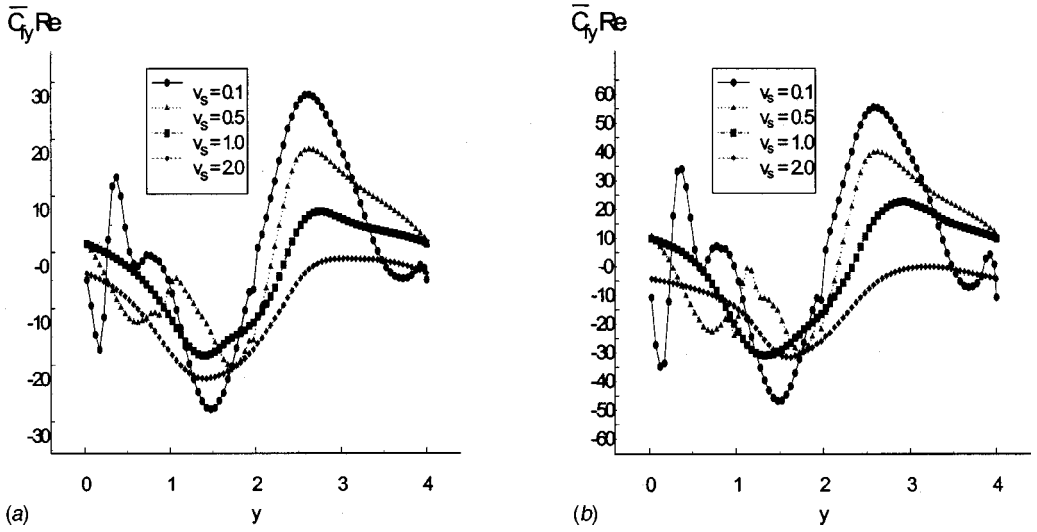

Fig. 5 Distribution of span-averaged friction coefficient at Re=(*a*) 1000 and (*b*) 3000

$$\mathrm{Nu}=\frac{-\left.\frac{\partial T}{\partial z}\right|_S 2B}{T_w-T_\infty}. \tag{21}$$

Here is q'' the local heat flux, T_w is the temperature of the impingement plate and T_∞ the temperature of the ambience, which is the same temperature at the nozzle exit. The Nusselt number distribution can be averaged on the surface area A to obtain a global Nusselt number

$$\mathrm{Nu}_{av}=\left(\frac{1}{A}\right)\int\int\frac{-\left.\frac{\partial T}{\partial z}\right|_S 2B}{T_w-T_\infty}dxdy. \tag{22}$$

Results and Discussions

The spread of the domain (see Fig. 1), L_y in the y direction is 4. The span-length of the domain, L_x in the x direction is 5. The height of the computational domain, H has been 3. The nozzle height to jet width ratio is 2, which means the nondimensional height, b is 1. Chen et al. [3] have also consider a situation for the nozzle height to jet width ratio of 2.

Computations have been performed on an IBM RISC workstation. We have used $82\times82\times54$ stretched grids with finest grid of $\Delta z=0.005$ on the impingement plate and then Δz has been increased in the normal direction continuously by a factor of 1.25 till $b=0.27$. Beyond $b=0.27$, uniform Δz of 0.0625 was employed. We have compared the Nusselt number distribution due to the above-mentioned grid-mesh with that due a mesh of size $102\times102\times68$ to assert the grid independence of the present computation. In absence of experimental data on a moving surface, the code has been validated by comparing the distribution of span-averaged Nusselt number due to LES computations with experimental data of Schlünder et al. [26] at Re=6500, as shown in Fig. 2 (here $y=0$ refers to the impingement point). In the present work, span-averaged Nusselt number distribution in y-direction entails spatial averaging of local Nusselt numbers in the x-direction and obtaining its distribution along y coordinate. For time averaging, 250 instantaneous fields over 40,000 time steps have been used. The adequacy of the sample size has been asserted by comparing several quantities with the ensemble average of 350 samples. Time-averaged quantities are indicative of averaged quantities over a long duration, with 20 periodic cycles.

Velocity vectors on the vertical $(y-z)$ midplane, i.e., at $x=2.5$ for the nondimensional surface velocities of 0.1, 0.5, and 1.0 and Re=1500 are presented in Fig. 3, which clearly demonstrates the influence of plate speed on the flow structure. When the surface velocity is one tenth of the jet velocity at the nozzle exit, the flow structure does not differ much from that for the stationary surface, except for the appearance of additional vortical structure at the left corner of the impingement plate (Fig. 3(a)). This is a consequence of the opposed-condition between the flow issuing from the nozzle and that moving with the plate. With the increased plate speed, the flow underneath the nozzle opening gets more deflected in the direction opposite to the surface motion (Fig. 3(*b*)). At higher plate speeds, the surface motion mostly influences the flow adjacent to the impingement surface. It may be pointed out that with surface motion, the stagnation line spanning the plate, no longer appears in the flow domain. Flow patterns obtained due to LES computations agree qualitatively with the results of Chen et al. [3].

Figure 4 shows the variation of time and span-averaged Nusselt number for Re=500, 1000, 1500, and 3000 for the surface velocities of 0.1, 0.5, 1.0, and 2.0. The distribution for a particular surface velocity follows a self-similar pattern. We observe that the distribution curve flattens with increasing v_s. If we refer back to the plot of velocity vectors, we can relate this distribution pattern with the flow field. At lower values of Re, vortical structure and zones of weak and strong mixing on the plate surface, cause the nonuniform distribution. A local peak and trough in Nusselt number distribution for all Re can be observed for $v_s=0.1$, in the regions where the vortical structure appears. We notice a shifting in the location of peak value of $\overline{\mathrm{Nu}}$ in the downstream direction of plate velocity. In Fig. 5, distribution of y-component of skin friction coefficient (averaged over x-direction) is plotted for Re =1000 and 3000. At higher plate speeds, it can be seen that $\overline{c}_{fy}$ is always negative indicating that the plate motion is no longer aided by the flow and flow separation does not take place. Thus flow in the immediate vicinity of the plate is mostly influenced by the surface velocity and less affected by jet structure, thereby producing a more uniform heat transfer coefficient.

Figure 6 shows the effect of Re on the Nusselt number distribution at particular surface velocities of 0.1 and 1.0. As expected, $\overline{\mathrm{Nu}}$ increases with increasing Re but the distribution profile remains self-similar at a particular plate speed. The shift in peak value of $\overline{\mathrm{Nu}}$ in the direction of surface motion is more at higher Re for a particular plate speed. For instance, at $v_s=0.1$, the location of the peak value of $\overline{\mathrm{Nu}}$ for Re=3000 shifts 0.2 units downstream from the location of the peak at Re=500. For a surface

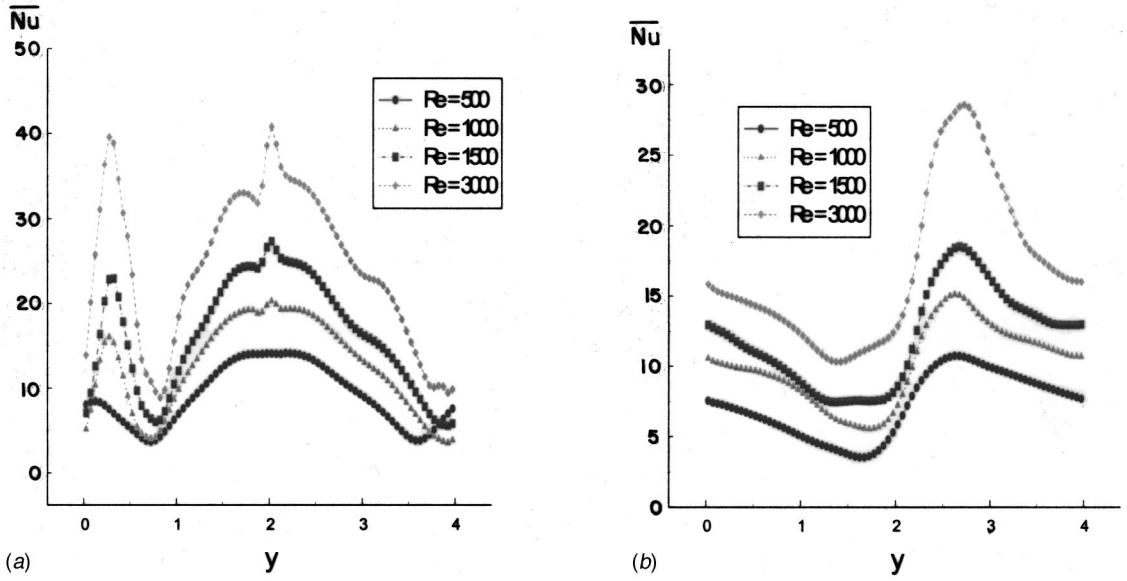

Fig. 6 Effect of Reynolds number on Nusselt number distribution for two surface velocities (*a*) $v_s=0.1$ and (*b*) 1.0

velocity equal the jet velocity at nozzle exit, the corresponding shift is almost one half of the nondimensional length or the jet width.

Figure 7 shows two-dimensional distribution of time-averaged Nusselt number on the impingement surface at different surface velocities for Re=3000. The distribution of the Nusselt number flattens out with increasing surface velocity. When the surface velocity is two times the jet velocity at the nozzle exit, the distribution becomes almost uniform.

Table 1 summarizes the results of the time-averaged global Nusselt numbers over the range of surface velocities and Reynolds numbers of interest. Global Nusselt number (average value

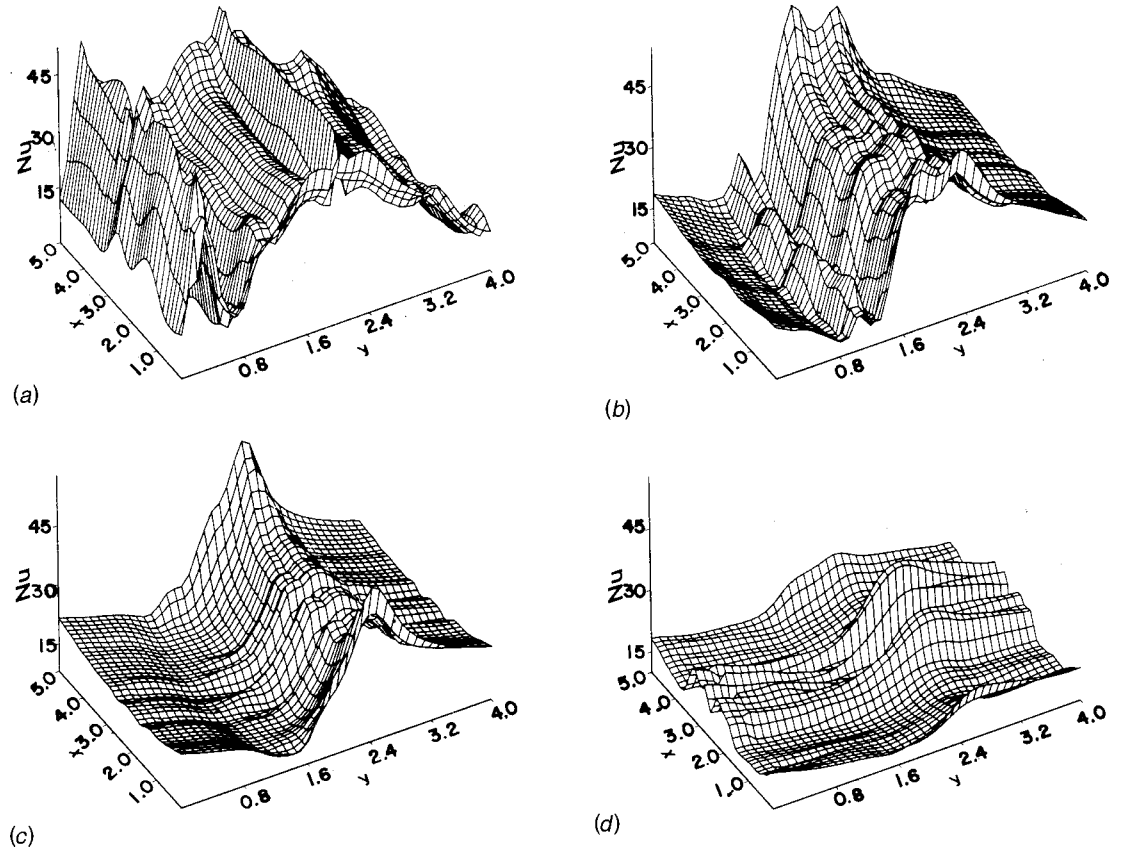

Fig. 7 Distribution of local Nusselt number over the impinging surface for Re=3000 at different surface velocities (*a*) $v_s=0.1$, (*b*) 0.5, (*c*) 1.0, and (*d*) 2.0

Table 1 Time-averaged global Nusselt number

Re	Nu_{av}				
	$v_s = 0.0$	$v_s = 0.1$	$v_s = 0.5$	$v_s = 1.0$	$v_s = 2.0$
500	9.08	9.02 (1)	8.71 (4.1)	7.41 (18.4)	5.82 (36)
1000	13.34	13.16 (1.3)	12.66 (5)	10.67 (20)	8.48 (36.4)
1500	17.29	17.12 (1.3)	16.03 (7.2)	12.77 (26.1)	10.55 (38.9)
3000	25.90	25.53 (1.4)	23.07 (10.9)	17.8 (31.2)	14.67 (43.4)

(bracketed terms indicate percentage reduction in value compared with value for the stationary surface, i.e. $v_s = 0.0$)

over the impingement surface) in the Reynolds number range of 500 to 3000 for surface velocities of 0.1, 0.5, 1.0, and 2.0 are presented here. The bracketed figure indicates percentage reduction in Nu_{av} due to various surface velocities as compared with the case of the stationary surface. Consider the case of Re=1000, for the stationary plate, the computed value of average Nusselt number is 13.34. The value reduces monotonically to 8.48 for v_s of 2.0. For $v_s=0.1$, the value of global Nu_{av} is 13.16, about 1 percent less than that for the stationary surface. Thus for a low value of surface velocity, the change in heat transfer is negligible. This is possibly due to the fact that loss in heat transfer due to plate motion is balanced by the augmentation due to mixing of flow by newly formed vortical structures. When the plate speed is half the jet speed, heat transfer reduces by 5 percent, when the plate speed is equal to the jet speed this reduction is 20 percent and when the plate speed is double the jet speed, the reduction in heat transfer is 36 percent. Similarly at a Reynolds number of 3000, values of Nu_{av} at plate speeds of 0, 0.1, 0.5, 1.0, and 2.0 are respectively 25.9, 25.53, 23.07, 17.80, and 14.67. The corresponding reduction in heat transfer in the cases of nonzero plate velocity is 1.4 percent, 10.9 percent, 31.2 percent, and 43.8 percent, respectively. We observe that for the same value of surface velocity, the reduction in heat transfer is more at higher Re. It is to be noted that our results for three-dimensional turbulent jets agree qualitatively with those of Chen et al. [3] for laminar two-dimensional jets.

Concluding Remarks

Heat transfer due to jet impingement on a moving surface has been studied in the turbulent regime using LES. The capability of LES in predicting complex flow field and associated heat transfer is clearly demonstrated. The heat transfer and flow results can be summarized in the following way. With increasing plate velocity, the magnitude of maximum Nusselt number decreases underneath the nozzle and the span-averaged Nusselt number distribution over the spread of the plate becomes more uniform. The total heat transfer reduces with increasing plate speed. While the reduction in heat transfer is not much pronounced in the lower range of surface velocities, the reduction in heat transfer can be up to 40 percent at higher plate speeds (i.e., for $v_s>0.5$). The flow structure in the immediate vicinity of the plate is dictated by the surface velocity. For the same surface velocity, the reduction in heat transfer is more at higher Reynolds numbers.

Proper experimentation on heat transfer in impinging jets on moving surfaces is required for more rigorous comparison. Future work should include the constant heat flux surface condition. As such, the surface condition can be best simulated if the conduction of the plate is taken into account. This issue can be addressed through solution of a conjugate problem. Effects of nozzle height and spacing are to be determined.

Nomenclature

B = slot nozzle width
b = nozzle-to-plate spacing
conv = convective terms of Navier-Stokes equations
diff = diffusive terms of Navier-Stokes equations
H = height of the computational domain
h = heat transfer coeficient, $q''/(T_w-T_\infty)$
k = thermal conductivity
L = dimension of the computational domain
Nu = Nusselt number
$\overline{\text{Nu}}$ = span-averaged Nusselt number
p = pressure
Pr = Prandtl number
q'' = heat flux between impingement plate and fluid
Re = Reynolds number, $W_{\text{in}}(2B)/\upsilon$
t = temperature
t = time
u = velocity component in x-direction
w_{in} = nozzle exit velocity
V = velocity component in y-direction
w = velocity component in z-direction
x,y,z = spatial coordinates

Greek Symbols

α = thermal diffusivity
ν = kinematic viscosity
τ = turbulent shear stress

Subscripts

∞ = ambience
av = average
max = maximum
s = surface velocity
w = wall

Superscripts

$'$ = small scale motion
$*$ = intermediate (e.g., intermediate velocity u^*)
n = current time step
$n-1$ = previous time step
$n+1$ = following time step

References

[1] Viskanta, R., 1993, "Heat Transfer to Impinging Isothermal Gas and Flame Jets," Exp. Therm. Fluid Sci., **6**, pp. 111–134.
[2] Downs, S. J., James, E. H., 1987, "Jet Impingement Heat Transfer—A Literature Survey," ASME Paper No. 87-H-35.
[3] Chen, J., Wang, T., and Zumbrunnen, D. A., 1994, "Numerical Analysis of Convective Heat Transfer From a Moving Plate Cooled by an Array of Submerged Planar Jets," Numer. Heat Transfer, Part A, **26**, pp. 141–160.
[4] Kohring, F. C., 1985, "Waterwall Water-Cooling System," *Iron Steel Engg*., pp. 30–36.
[5] Subba Raju, K., and Schlunder, E. U., 1977, "Heat Transfer Between an Impinging Jet and a Continuously Moving Surface," Waerme- Stoffuebertrag., **10**, pp. 131–136.
[6] Huang, P. G., Mujumdar, A. S., and Douglas, W. J. M., 1984, "Numerical Prediction of Fluid Flow and Heat Transfer Under a Turbulent Impinging Slot Jet with Surface Motion and Crossflow," ASME Paper No. 84-WA/HT-33.
[7] Zumbrunnen, D. A., Viskanta, R., and Incropera, F. P., 1989, "The Effect of Surface Motion on Forced Convection Film Boiling Heat Transfer," ASME J. Heat Transfer, **111**, pp. 760–766.
[8] Zumbrunnen, D. A., 1991, "Convective Heat and Mass Transfer in the Stagnation Region of a Laminar Planar Jet Impinging on a Moving Surface," ASME J. Heat Transfer, **113**, pp. 563–570.
[9] Zumbrunnen, D. A., Incropera, F. P., and Viskanta, R., 1992, "A Laminar Boundary Layer Model of Heat Transfer Due to a Nonuniform Planar Jet Impinging on a Moving Plate," Waerme- Stoffuebertrag., **27**, p. 311–319.
[10] Polat, S., and Douglas, W. J. M., 1990, "Heat Transfer Under Multiple Slot Jets Impinging on a Permeable Moving Surface," AIChE J., **36**, pp. 1370–1378.
[11] Martin, H., 1977, "Heat and Mass Transfer Between Impinging Gas Jets and Solid Surfaces," Adv. Heat Transfer, **13**, pp. 1–60.
[12] Laschefski, H., Cziesla, T., Biswas, G., and Mitra, N. K., 1996, "Numerical Investigation of Heat Transfer by Rows of Rectangular Impinging Jets," Numer. Heat Transfer, Part A, **30**, pp. 87–101.
[13] Laschefski, H., Cziesla, T., and Mitra, N. K., 1997, "Evolution of Flow Structure in Impinging Three-Dimensional Axial and Radio Jets," Int. J. Numer. Methods Fluids, **25**, pp. 1083–1103.
[14] Cziesla, T., Biswas, G., Chattopadhyay, H., and Mitra, N. K., 2001, "Large-

Eddy Simulation of Flow and Heat Transfer in an Impinging Slot Jet,'' Int. J. Heat Fluid Flow, **22**, pp. 500–508.
[15] Piomelli, U., and Liu, J., 1995, ''Large-Eddy Simulation of Rotating Channel Flows Using a Localized Dynamic Model,'' Phys. Fluids, **7**, pp. 839–848.
[16] Benocci, C., 1991, ''Modeling of Turbulent Heat Transport—A State-of-the-Art,'' von Karman Institute for Fluid Dynamics, Technical Memorandum 47.
[17] Tzeng, P. Y., Soong, C. Y., and Hsieh, C. D., 1998, ''Numerical Investigation of Heat Transfer Under Confined Impinging Turbulent Slot Jets,'' Numer. Heat Transfer, Part A, **35**, pp. 903–924.
[18] Lakshminarayana, B., 1985, ''Turbulence Modeling for Complex Shear Flows,'' AIAA J., **24**(12), pp. 1900–1917.
[19] Lilly, D. K., 1992, ''A Proposed Modification of the German Subgrid-Scale Closure Method,'' Phys. Fluids A, **4**(3), pp. 633–635.
[20] Germano, M., Piomelli, U., Molin, P., and Cabot, W. H., 1991, ''A Dynamic Subgrid-Scale Eddy Viscosity Model,'' Phys. Fluids A, **3**(7), pp. 1760–1765.
[21] Zang, Y., Street, R. L., and Koseff, J. R., 1993, ''A Dynamic Subgrid-Scale Model and its Application to Turbulent Recirculating Flows,'' Phys. Fluids A, **5**(12), pp. 3186–3196.
[22] Kim, J., and Moin, P., 1985, ''Application of a Fractional-Step Method to Incompressible Navier-Stokes Equations,'' J. Comput. Phys., **59**, pp. 308–323.
[23] Tran, K. D., and Morchoisne, Y., 1989, ''Numerical Methods for Direct Simulation of Turbulent Shear Flows,'' von Karman Institute for Fluid Dynamics, Lecture Series 1989–90.
[24] Childs, R. E., and Nixon, D., 1986, ''Unsteady Three-Dimensional Simulations of a VTOL Upwash Fountain,'' AIAA Paper No. 86-0212.
[25] Grinstein, F. F., Oran, E. S., and Boris, J. P., 1987, ''Direct Numerical Simulation of Axisymmetric Jets,'' AIAA J., **25**, pp. 92–98.
[26] Schlünder, E. U., Krötzsch, P., and Hennecke, F. W., 1970, ''Gesetzmäßigkeiten der Wärme- und Stoffübertragung bei Prallströmung aus Rund- und Schlitzdüsen,'' Chemie-Ing.-Techn., **42**, pp. 333–338.

Effect on Natural Convection of the Distance Between an Inclined Discretely Heated Plate and a Parallel Shroud Below

Oronzio Manca
Dipartimento di Ingegneria Aerospaziale e Meccanica, Seconda Università degli studi di Napoli, Aversa (CE), Italy
e-mail: manca@unina.it

Sergio Nardini
Dipartimento di Ingegneria Aerospaziale e Meccanica, Seconda Università degli studi di Napoli, Aversa (CE), Italy
e-mail: nardini@unina.it

Vincenzo Naso
Dipartimento di Energetica, Termofluidodinamica, applicata e Condizionamenti ambientali, Università degli studi di Napoli Federico II, Napoli, Italy
e-mail: vinaso@unina.it

An experimental study on air natural convection on an inclined discretely heated plate with a parallel shroud below was carried out. Three heated strips were located in different positions on the upper wall. The distance between the walls, b, was changed in the range 7.0–40.0 mm and two values of the heat flux dissipated by the heaters were taken into account. Several inclination angles between the vertical and the horizontal were tested. The wall temperature distribution as a function of the channel spacing and the inclination angle, the source heat flux, the number and the arrangement of the heat sources are presented. The analysis shows that, for angles not greater than 85 deg, increasing the distance between walls does not reduce the wall temperatures, whereas at greater tilting angles (>85 deg) there is an opposite tendency. This is confirmed by flow visualization at angles equal to 85 deg and 90 deg and b =20.0 and 32.3 mm. Dimensionless maximum wall temperatures are correlated to the process parameters in the ranges $1.2 \cdot 10^4 \leqslant Ra_l \cos\theta \leqslant 8.6 \cdot 10^5$; $0\ \text{deg} \leqslant \theta \leqslant 88\ \text{deg}$; $0.48 \leqslant l/b \leqslant 1.6$ *and* $10 \leqslant L/b \leqslant 32.6$ *with* $1.0 \leqslant d/l \leqslant 3.0$; *the agreement with experimental data is good. The spacing which yields the best thermal performance of the channel is given. Local Nusselt numbers are evaluated and correlated to the local Rayleigh numbers and the tilting angles in the ranges* $20 \leqslant Ra_{x'} \leqslant 8.0 \cdot 10^5$ *and* $0\ \text{deg} \leqslant \theta \leqslant 88\ \text{deg}$. *The exponent of monomial correlations between local Nusselt and Rayleigh numbers are in the 0.23–0.26 range. Comparisons with data from the literature, in terms of Nusselt number, exhibited minor discrepancies, mainly because of some difference in test conditions and of heat conduction in the channel walls.*
[DOI: 10.1115/1.1470488]

Keywords: Cavities, Experimental, Heat Transfer, Natural Convection

Introduction

Natural convection is widely used in the thermal control of many systems because of its cheapness, easy maintenance and reliability. For this reason several configurations with different boundary conditions are investigated. An extensive survey was presented by Raithby and Hollands [1] and by Gebhart et al. [2]. The removal of heat from electronic components by means of natural convection was studied out by Peterson and Ortega [3] and, more recently, by Yeh [4]. In many passive cooling situations the heat sources are mounted on arrays of boards, which can be modeled as heated flat plates forming a part of a channel. In modern electronic systems the heating of the plate is not uniform, since heat-dissipating components are discretely spaced. In order to improve the thermal approach to these systems, reference to discrete heat sources on walls has been made by Choi and Ortega [5].

As far as air natural convection from a vertical plate with a step discontinuity in the wall temperature is concerned, Schetz and Eichorn [6] conducted an experiment with a Mach-Zender interferometer. Kelleher [7] derived velocity and temperature profiles in the region immediately above the discontinuity by using asymptotic series. The wall heat flux was obtained in terms of a simple polynomial. The natural convection flow due to multiple isolated heated elements on a vertical plate was studied analytically by Jaluria [8]. The dependence of temperature and velocity fields on the heat input and on the distance between the heated elements was pointed out. The heat transfer coefficient for an element located in the wake of another turned out to be affected by energy input and location. Ravine and Richards [9] presented results of an experimental study of natural convection heat transfer from a discrete thermal source located on a vertical plate. Lee and Yovanovich [10] approximated the nonsimilar natural convection phenomena using an integral and pseudo-transient technique. A simple technique for nonsimilar convection heat transfer problems with step discontinuities was presented by Park and Tien [11]. The predicted temperature and velocity fields were compared with existing similarity solutions and experimental results validated the use of the proposed method in many practical situations. Tewari and Jaluria [12] carried out an experimental study on the natural and mixed convection heat transfer from two finite width heat sources, at uniform heat flux, located on a vertical or horizontal plate. The orientation of the surface had a strong effect on the interaction of the wakes from the heat sources. Kramtsov et al. [13] carried out an experimental and numerical investigation of the initial stage of free convective flow and heat transfer development near a vertical heated plate with a stepwise change in heat flux for a smooth surface and a surface with periodic steps. The two-dimensional natural convection flow arising from a long, finite size, heat source located on a vertical or inclined (in the 0 deg–70 deg range of the angle from the vertical) plate was investigated experimentally by Goel and Jaluria [14]. The dependence of nonboundary layer effects and of the conjugate transport effects on the heat input and the size of the source was studied. Flow separation was observed at large inclination angles.

As far as vertical channels with flush-mounted discrete heat sources are concerned, Ravine and Richards [15] carried out an

Contributed by the Heat Transfer Division for publication in the JOURNAL OF HEAT TRANSFER. Manuscript received by the Heat Transfer Division July 24, 2000; revision received January 7, 2002. Associate Editor: R. L. Mahajan.

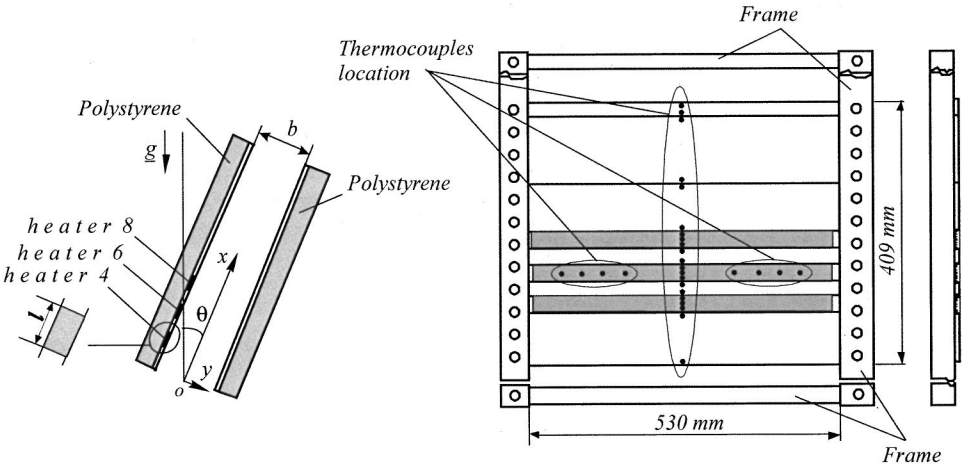

Fig. 1 Side view of the channel and sketch of the experimental arrangement

xperimental study on natural convection heat transfer from a discrete strip source located on the wall of a vertical channel. Natural convection in a vertical channel asymmetrically heated by equal length and equally spaced discrete strips was numerically studied by Yan and Lin [16]. Results for an open ended channel as a limiting case were presented by Chadwick et al. [17] in an experimental study on air natural convection in a vertically vented cavity with two flush-mounted strip heat sources. Elpidorou et al. [18] carried out a numerical study on the same problem investigated experimentally in [15], whose data agreed well with their numerical predictions.

The effect of radiation on the heat removal in a vertical channel with discrete heat sources was investigated numerically by Nickell et al. [19], for symmetric heating, and experimentally by Manca et al. [20], for asymmetric heating. The maximum wall temperature was unaffected by the emissivity when only one heat source was on, whereas in the configurations with more than one strip heated the radiative contribution to the heat transfer due to a greater emissivity lowered the maximum wall temperature. The liquid cooling of ten flush-mounted discrete heat sources by means of mixed convection in vertical channels was experimentally investigated by Joshi and Rahall [21]. A very similar configuration, with a single column of eight flush heated sources mounted on one wall of a vertical channel was studied by Joshi and Knight [22]. In a numerical study on mixed convection heat transfer in inclined channels, one wall heated and the other unheated, with isothermal periodic discrete heating Yucel et al. [23] analyzed extensively the influence of the angle and of the imposed flow rate on Nusselt numbers. A single isoflux flush-mounted strip cooled by mixed convection was investigated numerically by Choi and Ortega [5]. A reversed flow was observed at low Reynolds number and high Grashof numbers, which noticeably affected the heat transfer coefficient, although the entrainment of air from the exit section changed the flow and temperature fields significantly. Manca et al. [24] investigated experimentally air natural convection on a heated inclined plate with a parallel shroud below for $b=20.0$ mm. Uniform heat flux discrete sources were flush-mounted on the heated plate. The dependence of wall temperatures on the inclination angle, on the heat flux and on the location of the heaters was pointed out. Correlations between local Nusselt numbers and local Grashof numbers were derived, for the prediction of the thermal performance of the system.

The aim of the present experimental study is to increase knowledge in the field of natural convection in channels with discrete heat sources, with particular reference to inclined channels, for which no data are available in the literature. Reference is made to an inclined discretely heated plate with a parallel shroud below. The wall temperature distribution as a function of the channel spacing and of the tilting angle, the source heat flux, the number and the arrangement of the heat sources is presented. Dimensionless maximum wall temperatures are correlated to the process parameters. Local Nusselt numbers are evaluated and correlated to the significant process parameters. Flow visualized patterns of the air are also reported.

Experimental Apparatus

Test Section and Apparatus. The experimental arrangement and the centerline section of the two parallel plates are sketched in Fig. 1. The channel is 409 mm long and 450 mm wide; the distance between the plates varies in the 7.0–40.0 mm range. The upper heated wall is a combination of flush-mounted isoflux heated and unheated strips arranged in the guise of a plate by a Plexiglas frame. In this way, a large number of configurations could be easily achieved. Strips are cut from a 3.2 mm thick and 530 mm wide phenolic fiberboard plate (typical thermal conductivity: 0.17 $\mathrm{W\,m^{-1}\,K^{-1}}$); their surfaces facing the channel are coated with a 16 μm thick copper layer. Strips of different length are employed along the direction of the flow: each heated strip is 25.4 mm long whereas one of the unheated strips is 101.6 mm long, two are 76.2 mm long and three are 25.4 mm long. When assembling the plate, care was taken to achieve a nearly 0.2 mm gap between each heated strip and the adjacent unheated strip, in order to avoid any electric contact and to obtain a uniform thermal resistance of the air gap. Three 25.4 mm strips could be heated by passing a direct electrical current through the copper layer facing the channel. It is cut into a serpentine shape, the overall length of the track being 2.20 m; the expected electric resistance is 0.55 Ω. A thick copper bar, bolted to the electric supply wire, is soldered to the ends of each heater. No electric resistance between the heater and the bars could be measured during preliminary tests. The dissipated heat flux per strip is evaluated with an accuracy of ± 2 percent by measuring the voltage drop across the heater and the current passing through it. The shroud is a 3.2 mm thick and 530 mm wide phenolic fiberboard plate.

The low emissivity value of the walls is obtained by laying a 25 μm thick self-adhesive aluminum foil on their copper surface. The radiometric direct measurement of the total normal emissivity, carried out with an accuracy of ± 5 percent by comparison with a black body source, gave a 0.1 value for the aluminum foil. Electric insulation between the copper surface and the aluminum on the heated plate is assured by uniformly spraying an electrically insulating varnish onto it before coating. Side walls of the channel are made of Plexiglas rectangular rods placed between the principal walls at their lateral edges. The rods were precisely machined within an accuracy of ± 0.03 mm. The spacing of the channel is

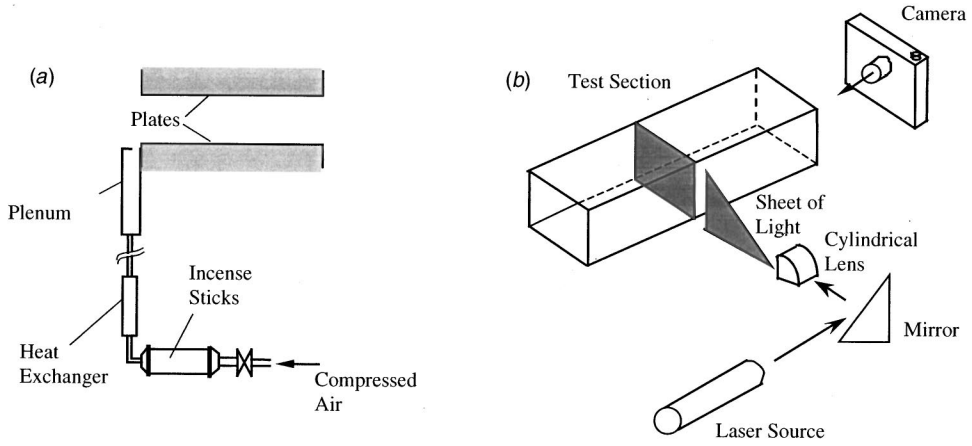

Fig. 2 Sketch of the visualization apparatus

measured with an accuracy of ±0.25 mm by a dial-gauge equipped caliper, which can resolve 0.025 mm. The channel is open to the ambient along the top and the bottom edges. The walls are fastened together by the above mentioned Plexiglas frame, which is designed in such a way as to avoid interactions with the fluid flow in the proximity of the channel bottom. The clearance of the bottom edges of the plates above the supporting table is 250 mm. Back side heat losses are reduced by sticking a 150 mm polystyrene block on the rear surface of the walls. The test section is secured to a tilting support frame. Discrete inclination angles of the channel in the range 0 deg–90 deg are obtained by a worm screw and cog wheel device, with an accuracy of ± 0.5 deg. A finer adjustment (± 0.05 deg) is obtained in the range 85 deg–90 deg from the vertical by a micrometric screw system. The entire apparatus is located within an enclosed room which is accurately sealed to eliminate extraneous air currents.

Wall temperatures are measured by 0.50 mm OD ungrounded iron-constantan thermocouples, embedded in the fiberboard very close to the back side of the copper layer and bonded with a 3M epoxy glue. They are run horizontally, parallel to the surfaces, thereby lying along isotherms, to minimize conduction heat losses in the leads. All thermocouples are placed in the centerline of the channel. Three thermocouples are located in each heated strip: one is at mid-length and the others are 2.5 mm from the edges, as it is shown in Fig. 1. Eight additional thermocouples are located ±75.0, ±100.0, ±125.0, and ±150.0 mm horizontally outward from the channel centerline at mid-length of one of the heaters, to provide indications of the horizontal variations of the wall temperature. Two thermocouples are placed in each unheated strip 2.5 mm from the upper and lower edges. Six thermocouples are distributed along the centerline of the unheated wall. Ambient air temperature is measured by similar thermocouples. Twenty-four thermocouples are affixed to the rear surface of the heated plate and embedded in the polystyrene to allow the evaluation of conductive heat losses. Thermocouples voltage is recorded to 1 μV. Each thermocouple is calibrated by means of a reference standard thermometer (Pt 100). The calibration of the temperature measuring system showed an estimated precision of the thermocouple-readout system of ±0.2 K. A HP 3054A automatic data acquisition system and a HP 85F personal computer are used for data collection.

Flow Visualization. Flow visualization is carried out by burning incense sticks in a steel tube, connected to a compressor (Fig. 2). In order to reduce the temperature of the smoke, it is first passed through a glass heat exchanger and then it is sent to a plenum below the inlet section of the channel, far enough so that it does not disturb the air flow at the inlet. The visualization is made possible by means of a laser sheet, generated by a He-Ne laser source. More details about the visualization technique are reported in Manca et al. [25].

Test Configurations. For the sake of generality, every configuration is designated by a set of numbers. The first denotes how many of the heaters are on (I: one heater on; II: two heaters on; III: three heaters on); the second denotes the location of the heaters on the walls, by subdividing them into sixteen equal length (25.4 mm) strips, starting from the bottom end of the channel. Thus,

I-n means: one heater is on—the strip n is heated

II-n_1,n_2 means: two heaters on—the strips n_1 and n_2 are heated

III-n_1,n_2,n_3 means: three heaters on—the strips n_1, n_2, n_3 are heated

In the present work experiments were run with heaters in the positions 4, 6, and 8.

Preliminary tests showed the temperature distribution to be symmetric with reference to the x-y plane within ±0.3°C. Moreover, since a 1.5°C maximum deviation from the centerline temperature was measured when the latter was 68.9°C, wall temperatures were assumed as being independent of z within $z = \pm 50$ mm.

Data Reduction

Significant Parameters. Heat transfer results are presented in terms of a local Rayleigh number

$$\mathrm{Ra}_{x'} = \mathrm{Gr}_{x'}\mathrm{Pr} = \frac{g\beta q_{c,1} x'^4}{\nu^2 k}\mathrm{Pr} \tag{1}$$

and of a strip Rayleigh number

$$\mathrm{Ra}_l = \mathrm{Gr}_l\mathrm{Pr} = \frac{g\beta q_{c,1} l^4}{\nu^2 k}\mathrm{Pr} \tag{2}$$

where $q_{c,l}$ is the spatially-averaged convective heat flux on a heated strip

$$q_{c,l} = \frac{1}{l}\int_0^l q_c(x')dx \tag{3}$$

The Nusselt number is based on the difference between the wall and the inlet fluid temperatures, rather than on that between the wall and the bulk fluid temperatures, since the last can not easily be measured in practical applications. The local Nusselt number is defined as following

Table 1 Percentage uncertainty values (U_{Xi}/X_i 100)

Variable	T_o	$T_w - T_o$	q_c	q_r	$q_c + q_r$	q_Ω	q_k	b
Uncertainty	0.068	4.0	5.7	5.0	2.5	2.0	4.2	1.3

$$\mathrm{Nu}_{x'} = \frac{q_{c,1}}{T_w - T_o}\frac{x'}{k} \tag{4}$$

A dimensionless maximum wall temperature can be defined as

$$T^+_{w,\max} = \frac{T_{w,\max} - T_o}{\dfrac{q_{c,l}b}{k}} \tag{5}$$

The thermophysical properties of the air are evaluated at the reference temperature $(T_w + T_o)/2$, with T_w being the local wall temperature.

Estimate of the Convective Heat Flux. Local convective heat flux, $q_c(x)$, is not uniform because of radiation and conduction. Experimental data were reduced by first introducing the convective local heat flux in the equations presented above

$$q_c(x) = q_\Omega(x) - q_k(x) - q_r(x) \tag{6}$$

where $q_\Omega(x)$ is the local heat flux due to Ohmic dissipation, which is assumed to be uniform, $q_k(x)$ denotes the local conduction heat losses from the plate and $q_r(x)$ is the local radiative heat flux from the plate. For each run, the terms $q_k(x)$ were calculated by a three-dimensional finite difference numerical procedure, which evaluated the temperature distribution in the polystyrene from the measured temperatures at the rear face of the plates. The predicted temperatures in significant configurations of the system had been previously compared with those measured by thermocouples embedded in the polystyrene insulation and the agreement was very good, the maximum deviation being 3 percent. The $q_r(x)$ terms were calculated for each temperature distribution in the wall, ambient temperature and channel spacing, according to the procedure described by Webb and Hill [26]. In all runs of the present work the unheated region of the plates was divided into 1 inch strips along the channel length and each heater was divided into 1/3 inch strips. A two-dimensional temperature distribution at the surfaces of the principal walls was assumed, according to the aforementioned indications from preliminary tests. The maximum and minimum values of the ratio $q_{c,l}/q_\Omega$ were 0.98 for Case I-4, $b = 12.3$ mm, $q_\Omega = 340\ \mathrm{W\,m^{-2}}$ $\theta = 0$ deg and 0.87 for Case III-4,6,8 $b = 20.0$ mm, $q_\Omega = 660\ \mathrm{W\,m^{-2}}$, $\theta = 90$ deg, respectively.

Uncertainty Analysis. The uncertainty of the values of Ra_l, Ra_x, and $\mathrm{Nu}_{x'}$, was evaluated following the procedure suggested in [27,28]. Accordingly, the uncertainty of the dependent variable R as a function of the uncertainties of the independent variables X_i is given by the relation

$$U_R^2 = \left(\frac{\partial R}{\partial X_1}U_{X_1}\right)^2 + \left(\frac{\partial R}{\partial X_2}U_{X_2}\right)^2 + \cdots + \left(\frac{\partial R}{\partial X_j}U_{X_j}\right)^2 \tag{7}$$

Therefore, on the basis of Eqs. (1), (2), (4) and of the not negligible uncertainties of the values of the independent variables reported in Table 1, the uncertainty of Ra_x, ranged from 17 percent at the smallest value of x' to 4 percent at the largest. The uncertainties of Ra_l, and Nu_x, turned out to be 4 and 7 percent, respectively.

Results and Discussion

Experiments were run with five spacing values: 7.0, 12.3, 20.0, 32.3, and 40.0 mm. The Ohmic heat fluxes were: 340 and 660 $\mathrm{W\,m^{-2}}$. The cooling medium was air, the inlet temperature of which was nearly 21.5 °C in all tests; its fluctuations were within ±0.5 °C during each test.

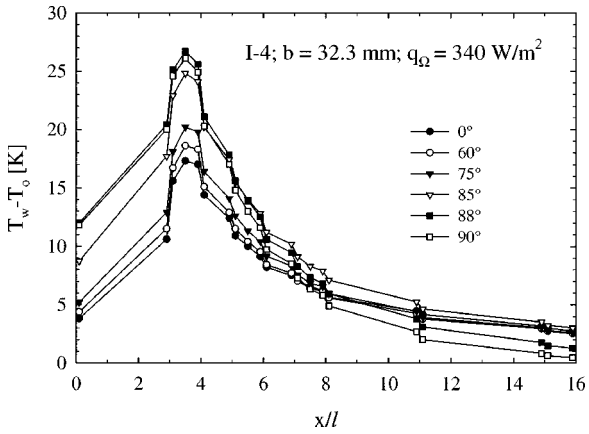

Fig. 3 Wall temperature rise above the ambient temperature as a function of the coordinate along the channel length and of the angle, for the Case I-4, $b = 32.3$ mm and $q_\Omega = 340\ \mathrm{W\,m^{-2}}$.

Wall Temperatures. The wall temperature rise above the ambient temperature as a function of the coordinate along the channel and of the tilting angle is presented in Fig. 3, for the Case I-4, $b = 32.3$ mm and $q_\Omega = 340\ \mathrm{W\,m^{-2}}$. If reference is made to the heated part of the wall, we can notice only a slight dependence of the maximum wall temperature on the inclination angle in the 0 deg–60 deg range, its variations being 1.3 °C at 340 $\mathrm{W\,m^{-2}}$, whereas this variation is 2.2 °C at 660 $\mathrm{W\,m^{-2}}$. From 60 deg to 88 deg, the greater the tilting angle the greater the temperature variations. Finally, the maximum wall temperature decreases when the angle changes from 88 deg to 90 deg. As far as the unheated region of the wall is concerned the figure shows temperature profiles upstream of the heated strip very similar to the ones described above, contrary to those in the downstream region, which depend on the distance from the heater. Very inclined channels ($\theta = 88$ deg and 90 deg) exhibit a greater decrease in wall temperatures, which, downstream of $x/l = 8$, turn out to be the minimum ones. On the contrary, at $\theta = 85$ deg higher wall temperatures are noticed, which can be interpreted as shown in Fig. 4. The increase in the wall temperatures of the channel is caused by the choking of the flow in its exit section. The buoyancy forces raise the fluid and separate it from the lower wall, thus reducing the pressure near it and allowing the inflow of cooler ambient fluid along the lower wall in the proximity of the exit section. This phenomenon occurs also at $\theta = 0$ deg (Fig. 4(*a*)). The inflow effect increases as far as $\theta = 88$ deg, as sketched in Figs. 4(*b*) and 4(*c*) and, consequently, the temperature of the heated strip increases. On the contrary, in the horizontal channel (Fig. 4(*d*)) the wall temperature never increases, or rather it decreases, because the ambient fluid entering the channel from both ends along the lower wall first reverses its direction in the proximity of the heated strip and then flows along the upper wall. In the following the above described flow path will be referred to as "C-loop". Temperature profiles can be divided into three groups, respectively for $\theta = 0$ deg–60 deg, $\theta = 75$ deg–80 deg and $\theta = 85$ deg–90 deg.

The wall temperature rise above the ambient temperature as a function of the coordinate along the channel length and of the tilting angle is presented in Fig. 5, for $q_\Omega = 340\ \mathrm{W\,m^{-2}}$ and for different channel gaps. Figure 5(*a*) shows that in Case I-4 and for $\theta \leqslant 75$ deg the lower the channel spacing the smaller the wall temperature upstream of the heater whereas the greater the downstream wall temperatures. This depends on the effect of the fluid inflow in the exit section of the inclined channel and on some outflow effect in its inlet section, which is more marked at $\theta = 85$ deg and $\theta = 88$ deg. Both effects are weaker at the lower spacing values, particularly at $b = 12.3$ mm. As a matter of fact, the inflow of cool ambient fluid along the lower wall and its mixing within the hot flow coming from the inner part of the

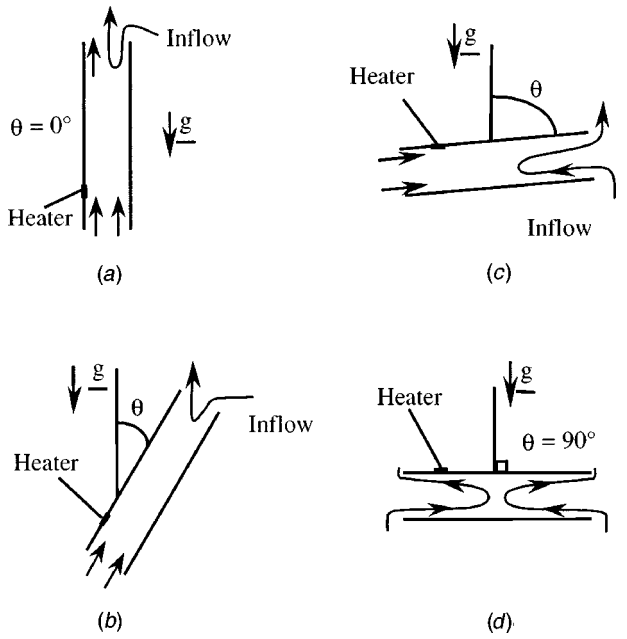

Fig. 4 Sketch of the air inflow near the exit section of the channel

channel enhances the heat transfer near the exit section whereas the outflow along the upper wall, coming from the hotter inner regions of the channel, warms up the upper part of the inlet section. The effect of the channel spacing turns out to be poor, the wall temperature variations being smaller than 1 °C. In Case I-8 in the heated region the spacing affects the wall temperature as it is shown in Fig. 5(*b*). The differences between the temperature values of the profiles for $\theta=60$ deg and $\theta=88$ deg decrease when the gap b increases since the larger the gap the stronger the recirculation of the flow. In fact, at $b=12.3$ mm, the differences between the maximum temperature values at $\theta=88$ deg and at $\theta=60$ deg are nearly 8.5 °C for Case I-4 and nearly 10.3 °C for Case I-8.

The wall temperature rise above the ambient temperature as a function of the coordinate along the channel length and of the angle, for $q_\Omega=340$ W m^{-2}, Case II-4, 6 and $b=20.0$, 32.3, 40.0 mm, is presented in Fig. 6. We can still notice, as in Cases I, marked differences between three groups of wall temperature profiles, for $\theta=0$ deg–60 deg, $\theta=75$ deg–80 deg, $\theta=85$ deg–90 deg. When the inclination angle is smaller than 88 deg, the downstream heated strip is always hotter than the upstream one, whereas at $\theta=88$ deg and $\theta=90$ deg the upstream heater is the hotter. In fact, the heat from the downstream heater is removed by the air flow the temperature of which has already been raised by the upstream heater. Figures 6(*a*), 6(*b*), and 6(*c*) show that this occurs at all channel spacing values. It is noticeable

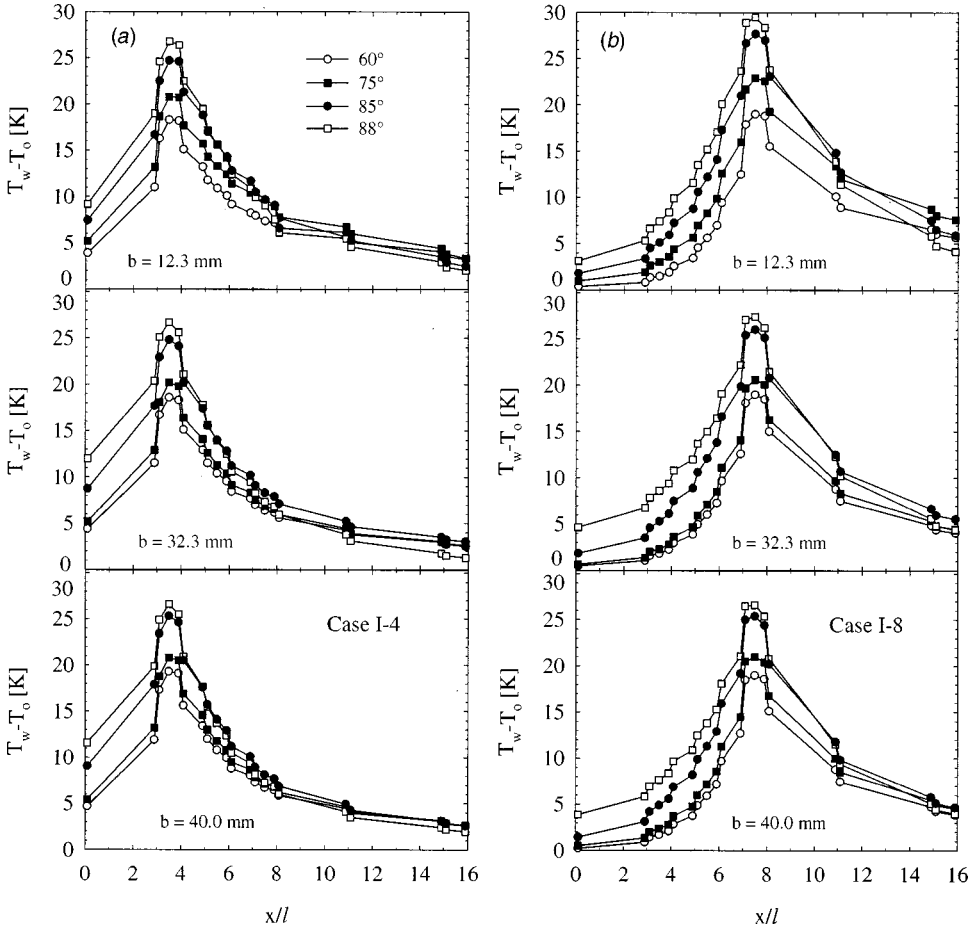

Fig. 5 Wall temperature rise above the ambient temperature as a function of the coordinate along the channel length and of the angle, for $q_\Omega=340$ W m^{-2}: (*a*) Case I-4; (*b*) Case I-8

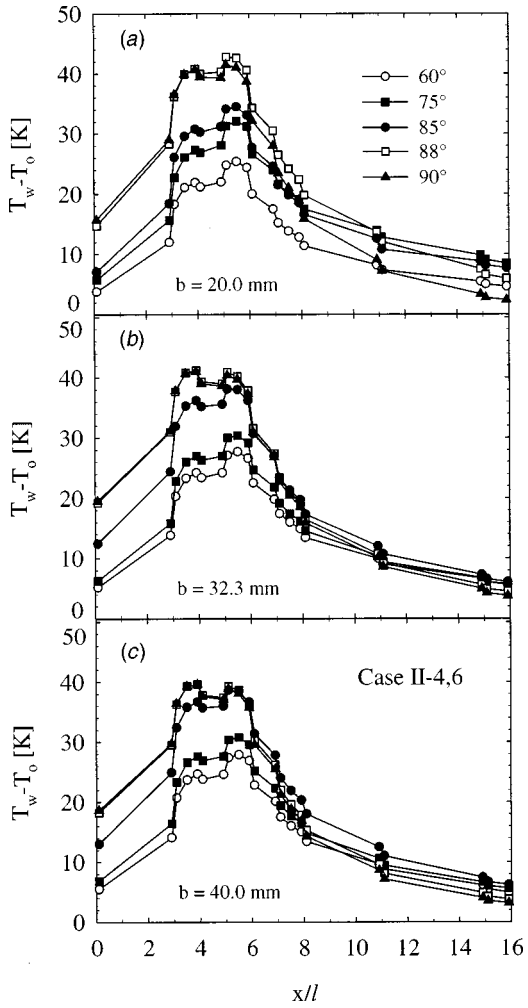

Fig. 6 Wall temperature rise above the ambient temperature as a function of the coordinate along the channel length and of the angle, for the Case II-4, 6 and $q_\Omega = 340\ \mathrm{W\,m^{-2}}$: (*a*) $b = 20.0$ mm; (*b*) $b = 32.3$ mm; (*c*) $b = 40.0$ mm

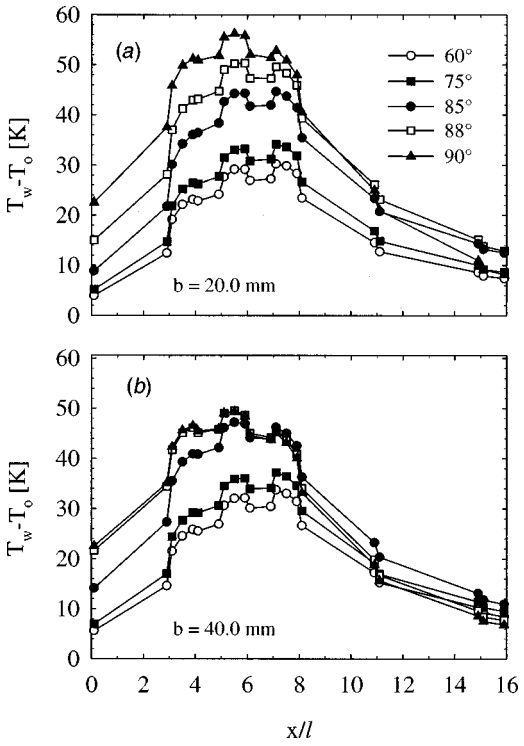

Fig. 7 Wall temperature rise above the ambient temperature as a function of the coordinate along the channel length and of the angle, for the Case III-4, 6, 8 and $q_\Omega = 340\ \mathrm{W\,m^{-2}}$: (*a*) $b = 20.0$ mm; (*b*) $b = 40.0$ mm

that at $\theta = 88$ deg and at $\theta = 90$ deg no variation occurs in the wall temperatures of the heated strip #4 passing from $b = 20.0$ mm to $b = 32.3$ mm, whereas for $b = 40.0$ mm temperatures of both heaters are lower than those for $b = 32.3$ mm. This is caused by the ambient air inflow, which is enhanced for large tilting angles and large spacing values that allow the entering air to flow as far as to the heater #6. Nevertheless, as it was observed but not presented here, the temperature of the downstream heater is unaffected by the upstream heated strip when the distance between the two heaters is larger than a limiting value, which depends on the thermal conductivity of the wall, the heat flux and the emissivity of the walls.

The wall temperature rise above the ambient temperature as a function of the coordinate along the channel length and of the angle, for Case III-4,6,8, $q_\Omega = 340\ \mathrm{W\,m^{-2}}$ and $b = 20.0$ and 40.0 mm is reported in Figs. 7. In this Case too, temperature profiles can be grouped in the same way as in the previous Cases. At increasing inclination angles the maximum wall temperature displaces from strip #8 to strip #6 and, for $\theta = 90$ deg, the temperature profile is nearly symmetrical. As in Cases II, the larger the spacing the higher the wall temperature in the $\theta = 0$ deg–85 deg range.

Figure 8, where the maximum temperatures referred to the ambient temperature as a function of the channel gap for $\theta = 0$ deg, 75 deg, 85 deg, for the Case I-4 and $q_\Omega = 340\ \mathrm{W\,m^{-2}}$ are presented, shows that the 20.0 mm gap yields a nearly optimum thermal performance of the channel which, anyway, is practically unaffected by slightly different values of the spacing. One should notice that the greater the number of the heaters in a given length of the wall the more similar is the thermal performance to that of an utterly heated plate. The evaluation of the optimal channel spacing in inclined channels with utterly heated walls was carried on in [29]. Furthermore, passing from $\theta = 75$ deg to 85 deg determines a larger increase of the maximum wall temperature than passing from $\theta = 0$ deg to 75 deg.

Dimensionless maximum wall temperature rise as a function of the inclination angle, for different spacing, heat flux values and configurations, is presented in Figs. 9 and 10. Figure 9 shows that in Cases I maximum wall temperatures are nearly equal, and are dependent on the spacing but almost independent of the heat flux and the tilting angle as it is expected looking at wall temperature profiles for θ values less than 60 deg. For larger angles up to 88

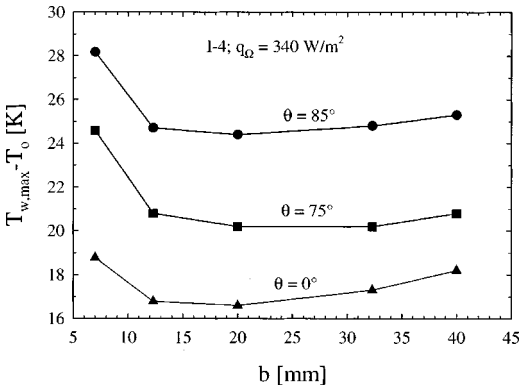

Fig. 8 Maximum wall temperature rise above the ambient temperature as a function of the channel gap and of the inclination angle, for the Case I-4 and $q_\Omega = 340\ \mathrm{W\,m^{-2}}$

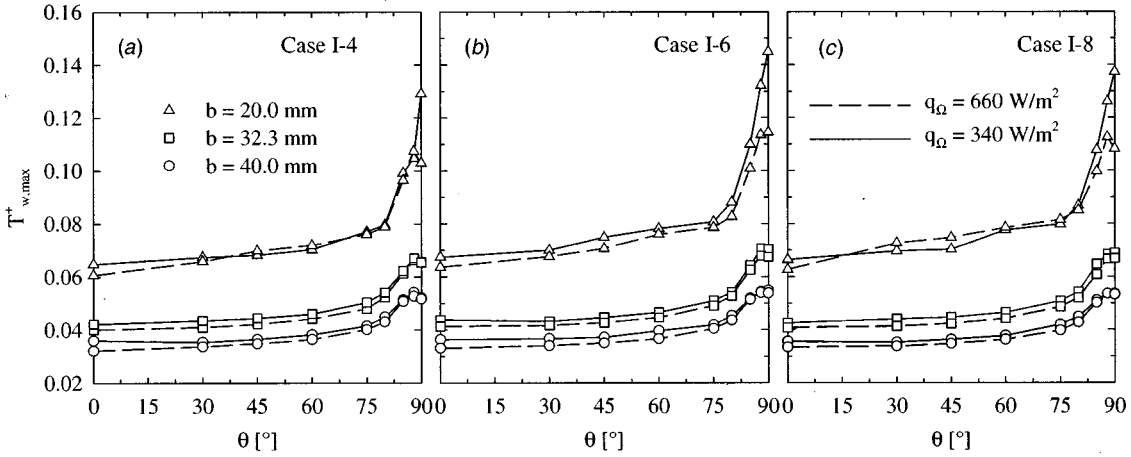

Fig. 9 Dimensionless maximum wall temperature rise as a function of the inclination angle, for $q_\Omega = 340\ \mathrm{W\,m^{-2}}$ and $q_\Omega = 660\ \mathrm{W\,m^{-2}}$, $b = 20.0$, 32.3, and 40.0 mm: (*a*) Case I-4; (*b*) Case I-6; (*c*) Case I-8

deg, the maximum temperature values increase. For $b = 20$ mm and $q_\Omega = 340\ \mathrm{W\,m^{-2}}$ maximum temperature increases sharply at $\theta = 90$ deg whereas in the others investigated configurations it weakly decreases. This is due to the C-loop which at $\theta = 90$ deg penetrates more deeply into the channel for larger values of heat flux and of the channel spacing. Furthermore, for the Case I-6 and $\theta > 75$ deg the dimensionless maximum temperature values are slightly larger than those for the Cases I-4 and I-8. Figure 10 shows that in the Case III-4,6,8 maximum wall temperature profiles are very similar. It is worth remembering that at large inclination angles in Cases II and III the first and the second strips, respectively, are the hotter one, whereas at small angles they are the cooler ones.

In the design and the thermal control of electronic systems it is very useful to know the maximum temperature of the component, all other parameters and the heat flux being known. To this end, correlations have been derived between the significant process parameters. In order to obtain a better regression coefficient, three different correlations have been proposed for the heater in Cases I and for the second and the third heated strip, in Cases II and Case III, respectively. They are presented, together with experimental results, in Figs. 11, for different values of the heat flux and of the channel spacing. Data for Cases II have been better correlated by

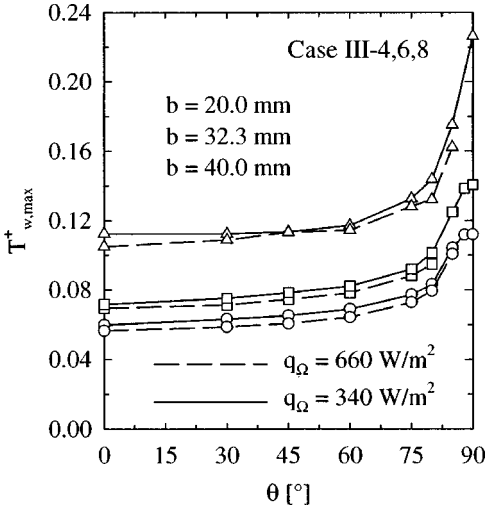

Fig. 10 Dimensionless maximum wall temperature rise as a function of the inclination angle, for Case III, $q_\Omega = 340\ \mathrm{W\,m^{-2}}$ and $q_\Omega = 660\ \mathrm{W\,m^{-2}}$, $b = 20.0$, 32.3, and 40.0 mm

introducing the d/l ratio, where the distance between the heaters is $d = 50.8$ mm in Cases II-4,6 and II-6,8 and $d = 101.6$ mm in Case II-4,8. The parameter ranges are: $1.2 \cdot 10^4 \leqslant \mathrm{Ra}_l \cos\theta \leqslant 8.6 \cdot 10^5$; $0\ \mathrm{deg} \leqslant \theta \leqslant 88\ \mathrm{deg}$; $0.48 \leqslant l/b \leqslant 1.6$ and $10 \leqslant L/b \leqslant 32.6$ with $1.0 \leqslant d/l \leqslant 3.0$.

Flow Visualization. Some pictures of the flow patterns in Cases when only one heater was on (Cases I) are reported in the following. The visualization of the flow patterns in the exit region of the channel for all Cases I, different Ohmic heat fluxes and tilting angles is presented in Figs. 12. Figure 12(*a*) shows that the air, after flowing along the lower wall, separates from it at about $x = 280$ mm, thus determining a pressure drop which allows the inflow of ambient air through the exit section of the channel. It can be seen that the rising air chokes the flow and that the flow is laminar. Mass flow rate entering into the channel from the leading edge and flowing over the upper wall decreases and, as a consequence, it reduces the heat transfer rate from the heated strip. Besides, the air flowing over the upper wall does not allow the direct heat transfer from the hot upper plate to the inflow air from the outlet section. This is in agreement with the observations on the Figs. 3 and 9 and the description given in Fig. 4. Similar considerations are suggested by Fig. 12(*b*), which shows the penetration of the air inflow as far as nearly 130 mm from the exit section of the channel. Some differences can be observed in the slope, which is more marked in Case I-8 than in Case I-4, probably because, in the former case, the air entrainment is less effective. Patterns in the horizontal channel are shown in Figs. 12(*c*), 12(*d*), and 12(*e*). They point out a common ''C-loop'' shape of the air, which, after flowing along the lower wall, inverts its direction and flows along the upper wall. In this Case the air coming from the ambient flows directly over the warmer upper plate, thus increasing the heat transfer rate. In Case I-4, at both heat fluxes (Fig. 12(*c*) and (*d*)), the flow reverses in the section which is about 110 mm from the exit end of the channel. In Case I-6, Fig. 12(*e*), the flow pattern is quite similar, apart from a deeper penetration of the inflow into the channel.

Nusselt Numbers. In the following reference is made to local Rayleigh and Nusselt numbers evaluated at $x' = 2.5$, 12.7, 22.9 mm from the leading edge of each strip, according to Eqs. (1) and (4).

Local Nusselt and Rayleigh numbers were first correlated by means of the equation

$$\mathrm{Nu}_{x'} = a\,\mathrm{Ra}_{x'}^{b} \tag{8}$$

the coefficients of which, for each heated strip in all cases and for

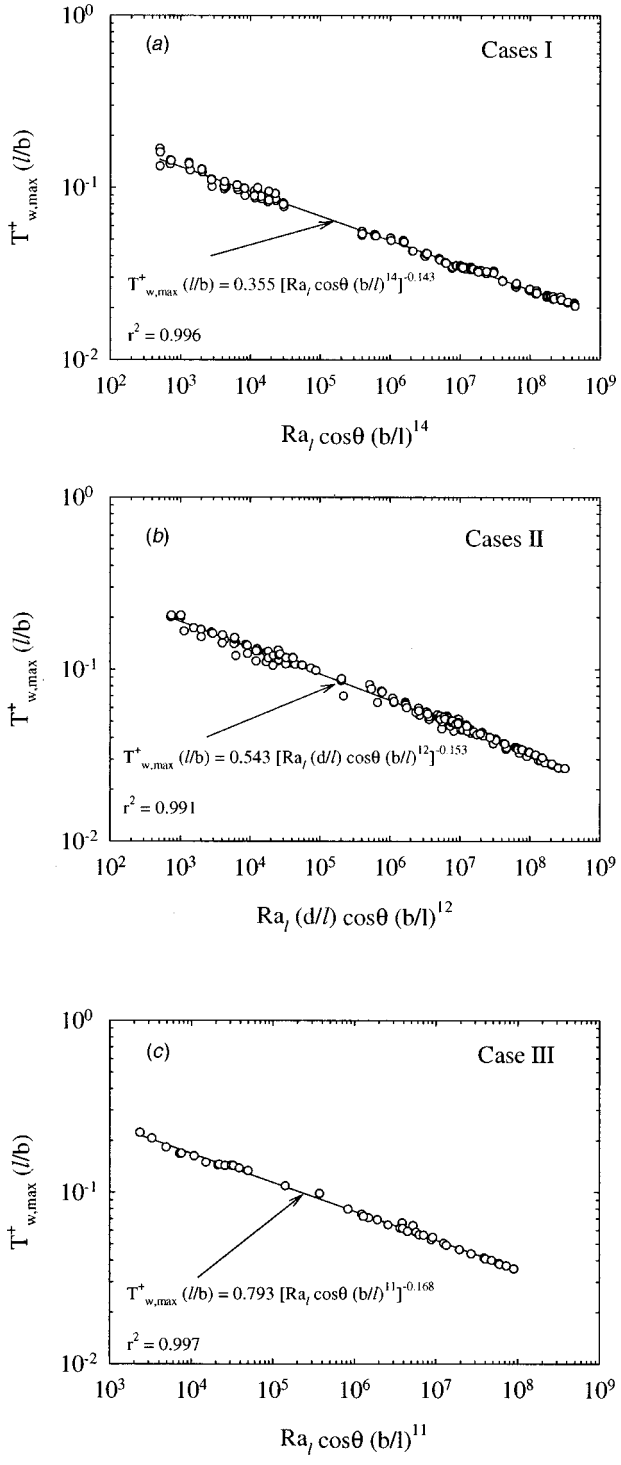

Fig. 11 Dimensionless maximum wall temperature rise as a function of the strip Rayleigh number, the cosine of the inclination angle, the ratio of the channel spacing to the strip length (*a*) Cases I; (*b*) Cases II; (*c*) Case III

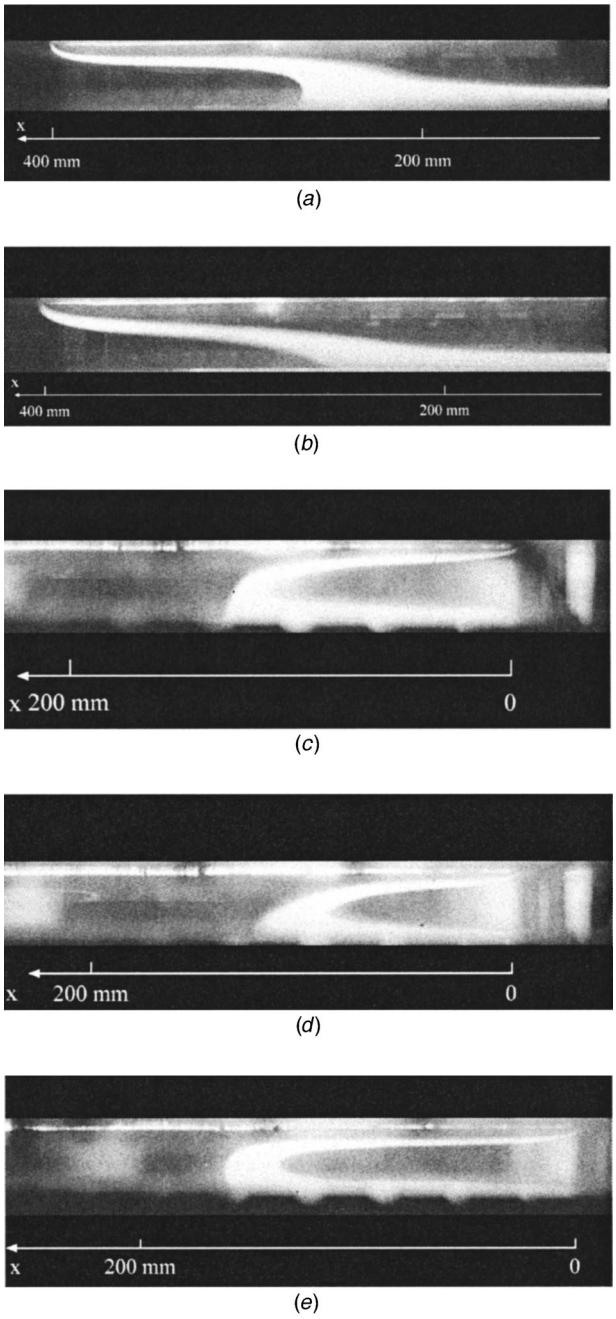

Fig. 12 Visualization of the flow patterns in the exit region of the channel for $b=32.25$ mm: (*a*) Case I-4, $q_\Omega=660$ W m^{-2}, $\theta=85$ deg; (*b*) Case I-8, $q_\Omega=660$ W m^{-2}, $\theta=85$ deg, (*c*) Case I-4, $q_\Omega=340$ W m^{-2}, $\theta=90$ deg; (*d*) Case I-4, $q_\Omega=660$ W m^{-2}, $\theta=90$ deg; (*e*) Case I-6, $q_\Omega=660$ W m^{-2}, $\theta=90$ deg

each investigated inclination angle, are reported in Table 2. The parameter ranges are: $20 \leqslant \mathrm{Ra}_{x'} 8.0 \cdot 10^5$; $0 \text{ deg} \leqslant \theta \leqslant 90$ deg; $0.48 \leqslant l/b \leqslant 1.6$ and $10 \leqslant L/b \leqslant 32.6$. At any angle the maximum value of the coefficient "*a*" is that of the strip #4, whereas the minimum value is that of the strip #8, their difference diminishing at increasingly tilting angles. For all strips, we can also remark that the larger the inclination angle the greater the coefficient "*b*," the value of which varies in the narrow 0.23–0.26 range. The regression coefficients are low, apart from that for the strip #4, which is always the first to release heat to the air flowing in the channel.

Data in the whole range of the inclination angles was correlated by means of the equation

$$\mathrm{Nu}_{x'} = a(\mathrm{Ra}_{x'} \cos\theta)^b \tag{9}$$

The coefficients, for each heater in all Cases, are presented in Table 3. The parameter ranges are: $20 \leqslant \mathrm{Ra}_{x'} \leqslant 8.0 \cdot 10^5$; $0 \text{ deg} \leqslant \theta \leqslant 88$ deg; $0.48 \leqslant l/b \leqslant 1.6$ and $10 \leqslant L/b \leqslant 32.6$.

Table 2 Coefficients in Eq. (8) for each strip in all Cases and for each investigated inclination angle in the range $20 \leq Ra_{x'} \leq 8.0 \cdot 10^5$

Strip	Coefficient	Inclination angle (deg)								
		0	30	45	60	75	80	85	88	90
4	a	0.745	0.727	0.704	0.671	0.596	0.548	0.439	0.363	0.360
	b	0.233	0.233	0.233	0.233	0.234	0.235	0.238	0.242	0.244
	r^2	0.986	0.983	0.983	0.980	0.976	0.971	0.960	0.963	0.950
6	a	0.573	0.563	0.545	0.517	0.453	0.421	0.347	0.306	0.310
	b	0.241	0.242	0.242	0.242	0.253	0.244	0.248	0.250	0.252
	r^2	0.957	0.957	0.957	0.957	0.949	0.949	0.949	0.952	0.951
8	a	0.523	0.500	0.488	0.468	0.423	0.391	0.338	0.312	0.320
	b	0.250	0.252	0.252	0.253	0.253	0.254	0.255	0.257	0.257
	r^2	0.959	0.959	0.959	0.958	0.954	0.956	0.956	0.965	0.968

The coefficients in Eq. (9) for the single heated strip in Cases I and for the upstream strip for Cases II, for Case III and for all Cases are reported in Table 4, in the same ranges of the process parameters as those for Table 3. The best regression coefficient is that of Case III, likely because the data refer only to the first strip. Local Nusselt number as a function of the local Rayleigh number and of the tilting angle, for the upstream strip in all Cases, is presented in Fig. 13.

It is worth noticing that the proposed correlations do not involve explicitly the process parameters "*d*" and "*b*." However, the distance between two consecutive heaters, *d*, affects the local Nusselt number, in terms of the measured wall temperatures. As to the channel gap, *b*, correlations taking explicit account of it exhibited regression coefficients negligibly larger than those of Eqs. (8) and (9), without the channel gap.

Comparisons Among Nusselt Numbers. Comparisons among Nusselt numbers for a vertical channel are reported in the following. The values of Nusselt numbers derived in this work are first compared in Table 5 with those from the correlations by Wirtz and Haag [30], at the same value of the Rayleigh number, Ra, referred to the channel gap. For the sake of comparison, reference is made to the mean value of Nusselt number on the heater, Nu. As far as Case III is concerned, Nusselt number by the present work is evaluated with reference to the average convective heat flux from the three heaters and the unheated regions between them. The agreement is good for the larger values of the Rayleigh number whereas at its lower values Nusselt numbers by Wirtz and Haag [30] are lower. As a matter of fact, the adiabatic region of the wall downstream of the strip enhances the entrainment of the air in the channel and the heat transfer rate. Moreover, the heat conduction in the wall decreases the temperature of the upstream heaters, thus increasing the Nusselt number.

Present values of the ratio of the Nusselt number of the upper (downstream) heater, Nu_u, to that of the lower (upstream) heater, Nu_l, are then compared to those given by Jaluria [8], at the same value of the d/l ratio for Cases II-4,6 and Cases II-4,8, in Table 6. A good agreement is pointed out, the differences being about -13 percent. They are probably due to the heat transferred by the heated strip to the unheated region of the wall, which, on turn, releases some heat to the air. The heat transfer from the downstream strip to the warmer air as well as the Nusselt number are, therefore, reduced.

Table 3 Coefficients in Eq. (9) for each strip in all Cases in the ranges $20 \leq Ra_{x'} \leq 8.0 \cdot 10^5$ and 0 deg $\leq \theta \leq$ 88 deg

Strip	Coefficient		
	a	b	r^2
4	0.806	0.231	0.974
6	0.650	0.238	0.953
8	0.622	0.244	0.946

Table 4 Coefficients in Eq. (9) for the single heated strip in Cases I and for the upstream strip in Cases II, Case III, all Cases, in the ranges $20 \leq Ra_{x'} \leq 8.0 \cdot 10^5$ and 0 deg $\leq \theta \leq$ 88 deg

Coefficient		Upstream strip		
	Cases I	Cases II	Case III	All Cases
a	0.885	0.765	0.710	0.806
b	0.235	0.232	0.230	0.233
r^2	0.986	0.983	0.992	0.974

Conclusions

The effect of the distance between an inclined plate, partially heated and downward-facing, and a parallel shroud on natural convection was experimentally investigated. The partial heating was obtained by discrete sources at uniform heat flux. Local wall temperatures of the heated surface were measured and local Nusselt and Rayleigh numbers were evaluated. Some photographs related to the flow visualization at two inclination angles from the vertical (85 deg and 90 deg) were achieved for two Cases.

Increasing the distance between the shroud and the discretely heated plate affects the phenomenon in two different ways. At angles not larger than 85 deg the larger the channel gap the weaker the chimney effect and, as a consequence, the higher the maximum wall temperature. At larger angles the effect is the opposite, because of the air flow between the two plates, with inflow and outflow motions at the open ended sections, which are more marked at increasing distances between the plates. The latter phenomenon is confirmed by the flow visualization.

A 20.0 mm gap yields a nearly optimum thermal performance of the channel which, anyway, is practically unaffected by slightly different values of the spacing.

Correlations between the maximum dimensionless temperature and the strip Rayleigh numbers multiplied by $(b/l)^5$ were evaluated for each heating case (one, two or three heaters on) in the parameter ranges: $1.2 \cdot 10^4 \leq Ra_l \cos\theta \leq 8.6 \cdot 10^5$; 0 deg $\leq \theta \leq$ 88 deg; $0.48 \leq l/b \leq 1.6$ and $10 \leq L/b \leq 32.6$ with $1.0 \leq d/l \leq 3.0$.

Correlations between local Nusselt and Rayleigh numbers were also obtained in the ranges: $20 \leq Ra_{x'} \leq 8.0 \cdot 10^5$; 0 deg $\leq \theta \leq$ 88 deg; $0.48 \leq l/b \leq 1.6$ and $10 \leq L/b \leq 32.6$.

Comparisons with data from the literature, in terms of Nusselt number, exhibited minor discrepancies, mainly because of some difference in test conditions and of heat conduction in the channel

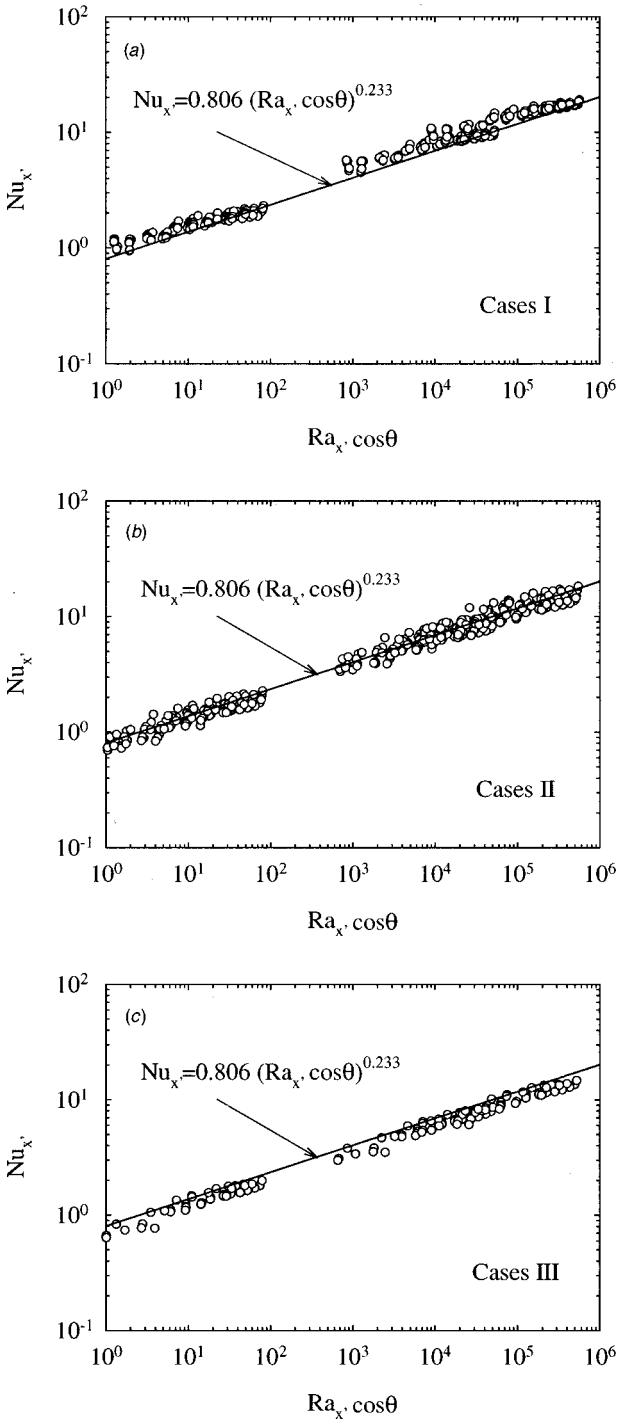

Fig. 13 Local Nusselt number as a function of the local Rayleigh number and of the tilting angle, for the upstream strip in all Cases

walls. They recommend that a deeper insight be given into the heat flux dissipated by each heater, the distance between the strips and the heat conduction in the walls.

Acknowledgment

The MURST, the Seconda Università degli studi di Napoli and Università degli studi di Napoli Federico II funded this work with a 1999 grant. A special acknowledgement is given to the reviewers, whose suggestions improved the paper.

Table 5 Comparison between Nusselt numbers from present experimental data and Nusselt numbers from the correlation given by Wirtz and Haag [30]

Run	Ra	Nu (1)	Nu (2)	Δ (%)
Case I-4 b=20.0 mm	$1.24\cdot10^5$	15.9	11.9	34
Case III b=20.0 mm	$1.14\cdot10^4$	9.1	6.6	38
Case III b=40.0 mm	$4.16\cdot10^5$	16.1	16.1	0

(1) Present experimental data.
(2) Wirtz and Haag [30].

Table 6 Comparison between the ratio Nu_u/Nu_l from present data and those from Fig. 6 in Jaluria [8], for Case II-4,6 and Case II-4,8, $q_\Omega = 340$ W m^{-2} and $q_\Omega = 660$ W m^{-2}

d/l	Nu_u/Nu_l (1)	Nu_u/Nu_l (2)	Δ (%)
1	0.84	0.94	- 11
3	0.87	1.0	- 13

(1) Present experimental data.
(2) Jaluria [8].

Nomenclature

a, b = coefficients in Eqs. (8) and (9)
b = channel spacing, m
d = distance between two consecutive heaters, m
Gr_l = strip Grashof number, Eq. (2)
$Gr_{x'}$ = local Grashof number, Eq. (1)
g = acceleration of gravity, m s^{-2}
k = thermal conductivity, W m^{-1} K^{-1}
L = channel length, m
l = strip length, m
$Nu_{x'}$ = local Nusselt number, Eq. (4)
Pr = Prandtl number
q = heat flux, Wm^{-2}
R = dependent variable, Eq. (7)
Ra_l = strip Rayleigh number, Eq. (2)
$Ra_{x'}$ = local Rayleigh number, Eq. (1)
r^2 = regression coefficient
T = temperature, °C
T^+ = dimensionless temperature
U = uncertainty, Eq. (7)
X_i = independent variable, Eq. (7)
x = coordinate along the channel length, m
x' = coordinate along the strip length, m
y = coordinate along the channel spacing, m
z = coordinate along the channel width, m

Greek Symbols

β = volumetric coefficient of expansion, K^{-1}
ν = kinematic viscosity, m^2 s^{-1}
θ = inclination angle, deg

Subscripts

c = convective
k = conductive
l = refers to an average value along the strip length
max = maximum
o = ambient

R = refers to the dependent variable
r = radiative
w = wall
X_i = refers to the independent variable
Ω = Ohmic dissipation

References

[1] Raithby, G. D., and Hollands, K. G. T., 1985, *Handbook of Heat Transfer*, W. M. Roshenow, J. P. Hartnett, and E. N. Ganic, eds., McGraw-Hill, New York, pp. 6.1–6.93.

[2] Gebhart, B., Jaluria, Y., Mahajan, R., and Sammakia, B., 1988, *Buoyancy-Induced Flows and Transport*, Hemisphere, Washington D.C.

[3] Peterson, G. P., and Ortega, A., 1990, *Thermal Control of Electronic Equipment and Devices in Heat Transfer*, **20**, Academic Press, pp. 181–314.

[4] Yeh, L. T., 1995, ''Review of Heat Transfer in Electronic Equipment,'' ASME J. Electron. Packag., **117**, pp. 333–339.

[5] Choi, C. Y., and Ortega, A., 1993, ''Mixed Convection in an Inclined Channel with a Discrete Heat Source,'' Int. J. Heat Mass Transf., **16**, pp. 3119–3134.

[6] Schetz, J. A., and Eichorn, R., 1964, ''Natural Convection with Discontinuous Wall-Temperature Variations,'' J. Fluid Mech., **18**, pp. 167–176.

[7] Kelleher, M., 1971, ''Free Convection from a Vertical Plate with a Discontinuous Wall Temperature,'' ASME J. Heat Transfer, **93**, pp. 349–356.

[8] Jaluria, Y., 1982, ''Buoyancy-Induced Flow Due to Isolated Thermal Sources on a Vertical Surface,'' ASME J. Heat Transfer, **104**, pp. 223–227.

[9] Ravine, T. L., and Richards, D. E., 1988, ''Natural Convection Heat Transfer from a Discrete Thermal Source on a Vertical Surface,'' ASME J. Heat Transfer, **110**, pp. 1007–1009.

[10] Lee, S., and Yovanovich, M. M., 1989, ''Natural Convection from a Vertical Plate With Step Changes in Surface Heat Flux,'' *Heat Transfer in Convective Flows*, ASME HTD-Vol. 107, pp. 239–247.

[11] Park, S. H., and Tien, C. L., 1990, ''An Approximate Analysis for Convective Heat Transfer on Thermally Nonuniform Surfaces,'' ASME J. Heat Transfer, **112**, pp. 952–958.

[12] Tewari, S. S., and Jaluria, Y., 1991, ''Convective Heat Transfer with Buoyancy Effects from Thermal Sources Mounted on a Flat Plate,'' AIAA Journal of Thermophysics and Heat Transfer **5**(2), pp. 199–207.

[13] Kramtsov, P. P., Martynenko, O. G., Burak, V. S., Shikh, I. A., and Vollsov, S. V., 1995, ''Nonstationary Convection Near a Vertical Surface with Periodic Change in Heat Flux,'' Exp. Heat Transfer, **8**, pp. 229–239.

[14] Goel, S., and Jaluria, Y., 1986, ''Thermal Transport from an Isolated Heat Source on a Vertical or Inclined Surface,'' Proc. of 8th IHCT, **3**, San Francisco, Hemisphere, New York, pp. 1341–1346.

[15] Ravine, T. L., and Richards, D. E., 1988, ''Natural Convection Heat Transfer from a Discrete Thermal Source on a Channel Wall,'' ASME J. Heat Transfer, **110**, pp. 1004–1007.

[16] Yan, W. M., and Lin, T. F., 1987, ''Natural Convection Heat Transfer in Vertical Open Channel Flows with Discrete Heating,'' Int. Commun. Heat Mass Transfer, **14**, pp. 187–200.

[17] Chadwick, M. L., Webb, B. W., and Heaton, H. S., 1991, ''Natural Convection from Discrete Heat Sources in a Vertically Vented Rectangular Enclosure,'' Exp. Heat Transfer, **4**, pp. 199–216.

[18] Elpidorou, D., Prasad, V., and Modi, V., 1991, ''Convection in a Vertical Channel with a Finite Wall Heat Source,'' Int. J. Heat Mass Transf., **34**, pp. 573–578.

[19] Nickell, T. W., Ulrich, R. D., and Webb, B. W., 1987, ''Combined Natural Convection and Radiation Heat Transfer from Parallel Plates with Discrete Heat Sources,'' *ASME Paper 87-WA/EPP-1*.

[20] Manca, O, Nardini, S., Naso, V., and Ruocco, G., 1995, ''Experiments on Natural Convection and Radiation in Asymmetrically Heated Vertical Channel with Discrete Heat Sources,'' ASME HTD-Vol. 317, pp. 309–319.

[21] Joshi, Y., and Rahall, R. G., 1993, ''Mixed Convection Liquid Cooling of Discrete Heat Sources in a Vertical Channel,'' *6th Int. Symp. on Transport Phenomena in Thermal Engineering*, Seoul, Korea, pp. 297–303.

[22] Joshi, Y., and Knight, D. L., 1990, ''Natural Convection From a Column of Flush Heat Sources in a Vertical Channel in Water,'' ASME J. Electron. Packag., **112**, pp. 367–374.

[23] Yucel, C., Hasanaoui, M., Robillard, L., and Bilgen, E., 1993, ''Mixed Convection Heat Transfer in Open Ended Inclined Channels with Discrete Isothermal Heating,'' Numer. Heat Transfer, Part A, **24**, pp. 109–126.

[24] Manca, O., Nardini, S., and Naso, V., 2000, ''Experimental Analysis of Air Natural Convection on Inclined Discretely Heated Plates with a Parallel Shroud Below,'' Int. J. Heat Technology, **18**(1), pp. 19–26.

[25] Manca, O., Morrone, B., and Nardini, S., 1997, ''Visualization of Natural Convection in Inclined Heated Parallel Plates,'' *Proc. of Eurotherm Seminar No. 45 on Thermal Management of Electronic Systems*, Vol. II, pp. 283– 292.

[26] Webb, B. W., and Hill, D. P., 1989, ''High Rayleigh Number Laminar Natural Convection in an Asymmetrical Heated Vertical Channel,'' ASME J. Heat Transfer, **111**, pp. 501–507.

[27] Kline, S. J., and McClintock, F. A., 1953, ''Describing Uncertainty in Single Sample Experiments,'' Mech. Eng. (Am. Soc. Mech. Eng.), **75**, pp. 3–12.

[28] Moffat, R. J., 1988, ''Describing the Uncertainties in Experimental Results,'' Exp. Therm. Fluid Sci., **1**, pp. 3–17.

[29] Manca, O., and Nardini, S., 2001, ''Thermal Design of Uniformly Heated Inclined Channels in Natural Convection with and without Radiative Effects,'' Heat Transfer Eng., **22**(1), pp. 13–28.

[30] Wirtz, R. A., and Haag, T, 1985, ''Effect of an Unheated Entry on Natural Convection Between Vertical Parallel Plates,'' *ASME Paper No. 85-WA/HT-14*.

Gm Salam Azad
Research Assistant
e-mail: salam.azad@swpc.siemens.com

Je-Chin Han
Marcus Easterling Chair Professor
e-mail: jchan@mengr.tamu.edu

Department of Mechanical Engineering,
Turbine Heat Transfer Lab,
Texas A&M University,
College Station, TX 77843-3123

Ronald S. Bunker
GE R&D Center,
Schenectady, NY 12301

C. Pang Lee
GE Aircraft Engines,
Cincinnati, OH 45215

Effect of Squealer Geometry Arrangement on a Gas Turbine Blade Tip Heat Transfer

This study investigates the effect of a squealer tip geometry arrangement on heat transfer coefficient and static pressure distributions on a gas turbine blade tip in a five-bladed stationary linear cascade. A transient liquid crystal technique is used to obtain detailed heat transfer coefficient distribution. The test blade is a linear model of a tip section of the GE E^3 high-pressure turbine first stage rotor blade. Six tip geometry cases are studied: (1) squealer on pressure side, (2) squealer on mid camber line, (3) squealer on suction side, (4) squealer on pressure and suction sides, (5) squealer on pressure side plus mid camber line, and (6) squealer on suction side plus mid camber line. The flow condition during the blowdown tests corresponds to an overall pressure ratio of 1.32 and exit Reynolds number based on axial chord of 1.1×10^6. Results show that squealer geometry arrangement can change the leakage flow and results in different heat transfer coefficients to the blade tip. A squealer on suction side provides a better benefit compared to that on pressure side or mid camber line. A squealer on mid camber line performs better than that on a pressure side. [DOI: 10.1115/1.1471523]

Keywords: Cooling, Experimental, Flow, Heat Transfer, Turbines

Introduction

Gas turbine blades usually have a gap between the blade tip and the stationary shroud surface known as a tip gap. This tip gap results in a reduction in the blade force, the work done, and therefore, the efficiency. This occurs because the leakage-flow (flow through the tip gap) passes over the blade tip without being turned and producing work. The subsequent mixing of the leakage flow with the main passage flow also reduces the momentum of the main flow, thus, reducing the efficiency. This hot leakage flow also increases the thermal loading on the blade tip, leading to a high local temperature and thus, is considered as a primary cause of blade distress. A conceptual view of blade tip leakage flow is shown in Fig. 1. Designers desire to improve efficiency by reducing the tip gap, or by implementing a more effective tip leakage sealing mechanism. However, it is difficult to completely seal the hot leakage flow through the tip gap. It is also difficult to cool the blade tip. Thus, it is considered to be a critical and susceptible region to blade distress. A common technique to reduce the tip leakage flow is to use a recessed tip, which is known as a squealer tip. A squealer tip allows a smaller tip clearance, but reduces the risk of a catastrophic failure, should the tip rub against the shroud. A smaller tip gap reduces the flow rate through the tip gap, resulting in smaller losses and lower heat transfer to the tip. The squealer tip also acts as a labyrinth seal for increasing flow resistance. Thus, it is important to get maximum benefit from the squealer tip geometry. A squealer rim could be limited to both sides (pressure and suction sides) of the blade, one or the other side, only at the mid-camber line, or combinations of these. Variations in squealer geometries would have strong effects on tip leakage flow and heat transfer. Thus for an efficient airfoil design, it is important to know both the flow field and heat transfer behavior for various squealer geometry arrangements for gas turbine blades.

Despite its importance, no major experimental or numerical study has been done to investigate this issue. The difficulty of undertaking such a study may be the cause of having fewer data available in the existing literature. However, few studies are done in a limited fashion to understand this issue. Bunker and Bailey [1,2] experimentally investigated the heat transfer coefficient and leakage flow for various chordwise sealing strips in a cascade. The wooden strips, glued to the tip surface did not participate in the surface thermal response, but served to set up a desired flow resistance to affect the main tip surface heat transfer. They placed two strips, one along the mean camber line of the tip section and the other close to the airfoil pressure side. Heyes et al. [3] studied

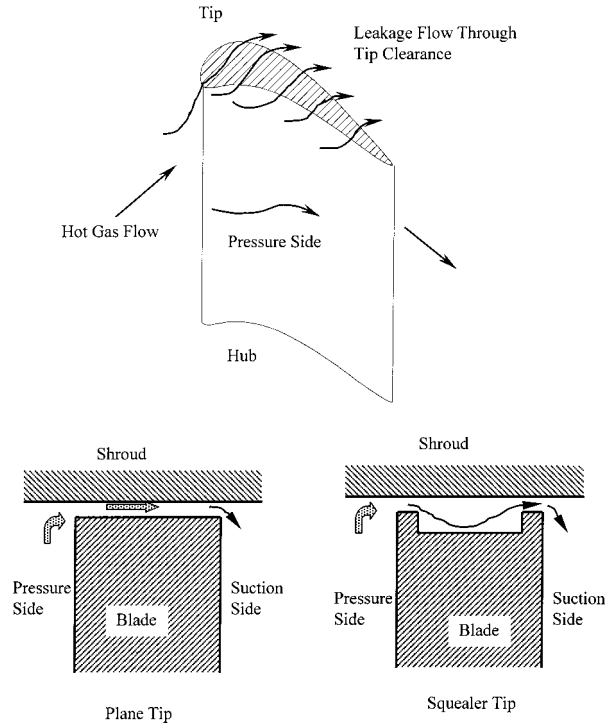

Fig. 1 A conceptual view of blade tip leakage flow

Contributed by the Heat Transfer Division for publication in the JOURNAL OF HEAT TRANSFER. Manuscript received by the Heat Transfer Division April 19, 2001; revision received January 29, 2002. Associate Editor: H. S. Lee.

the tip leakage flow field for two different squealer tip geometries, a single suction side squealer and a single pressure side squealer. No heat transfer data were reported. In an earlier study, Azad et al. [4] reported detailed heat transfer and leakage flow only for a two-sided (suction and pressure sides) squealer tip for various tip gaps. However, the effects of various geometry arrangements were not studied. Dunn and Haldeman [5] reported time-averaged heat flux data for a recessed tip, a lip, and a platform of a transonic turbine blade. Ameri et al. [6] numerically investigated the flow and heat transfer on the squealer tip for 2 and 3 percent cavity recess. Ameri et al. [7] also numerically investigated the effect of tip clearance and casing (shroud) recess on heat transfer and stage efficiency for different recess depths. In a recent study, Ameri [8] numerically investigated the heat transfer on a gas turbine blade tip with a mean-camberline strip. Yang and Diller [9] reported local heat transfer coefficient on a squealer tip model based on a single point measurement on the cavity bottom. Metzger et al. [10] and Chyu et al. [11] studied heat transfer on rectangular, grooved tip models. This covers the available literature on experimental and numerical squealer tip flow and heat transfer.

However, many experimental and numerical investigations on only the flow field in and around turbine blade tip models have been reported. Studies by Bindon and Morphus [12], Bindon [13] and Moore et al. [14] contribute to the understanding of the flow field in tip gaps. Yaras and Sjolander [15] studied the effect of simulated rotation on tip leakage and found a significant reduction in the gap mass flow. Sjolander and Cao [16] studied the flow field in an idealized turbine tip gap. Kaiser and Bindon [17] investigated the effects of tip clearance, tip geometry and multiple stages on turbine stage efficiency in a rotating turbine rig environment. Lakshminarayana [18] developed a predictive model for stage efficiency and compared it to existing data. Booth et al. [19] and Wadia and Booth [20] comprehensively studied tip losses and measured overall and local blade tip losses for many tip geometry configurations.

Several heat transfer studies report on plane tips. Mayle and Metzger [21] did the earliest study on plane blade tip heat transfer. Metzger et al. [22] used several heat flux sensors on flat tips for two different tip gaps in a rotating turbine rig. Bunker et al. [23] studied blade tip heat transfer and leakage flow for the first stage blade flat tip of a typical large power generation turbine. Ameri and Steinthorsson [24,25] predicted rotor blade tip and shroud heat transfer for the Space Shuttle Main Engine turbine. Ameri and Bunker [26] performed a computational study for blade tip heat transfer distributions of a large power generation turbine. Azad et al. [27] studied detailed heat transfer and leakage flow for the smooth tip of a GE E^3 blade. Teng et al. [28] studied blade tip heat transfer on a large-scale linear model in a low speed wind tunnel.

The present study will fulfill the need for additional heat transfer and leakage flow data for various squealer tip geometry arrangements. The transient liquid crystal technique is used for heat transfer measurements. The test section is a five-bladed linear cascade, the three middle blades have a tip gap of 1.5 percent of blade span. The tip profile is a first stage rotor blade tip of a GE-E^3 engine. Experiments are done at an inlet free-stream turbulence intensity of 6.1 percent. The effects of unsteady wakes, shock waves, Mach numbers, and blade rotation, which may be important at real operating conditions are not considered in this study. The cascade inlet total pressure is 143 kPa, and the exit average static pressure is 108.3 kPa, which gives an overall blade pressure ratio of 1.32. The cascade mass flow rate for the first 60 sec of test time is about 5.9 kg/s. During the blowdown test, the inlet air velocity is about 85 m/s; the exit air velocity is 199 m/s and the corresponding Reynolds number based on axial chord length and exit flow velocity is 1.1×10^6. The corresponding Mach numbers at the inlet and exit are 0.25 and 0.59, respectively.

Experimental setup

The test section of an experimental blow down facility with a five bladed linear cascade is shown in Fig. 2. A detailed description of this facility is given in Azad et al. [27]. The facility maintains a steady downstream velocity within 3 percent for one minute. Hot-film anemometry measurements, using a TSI IFA-100 unit show the free-stream turbulence intensity level of 6.1 percent at 6 cm upstream from the test-blade leading edge.

The two end blades of the five bladed cascade serve as guide vanes and the outside wall, while the center blade is the test blade. The cascade inlet dimensions are 31.1 cm wide and 12.2 cm high (span). Each blade has a constant cross section, a 12.2 cm span, and a 8.61 cm axial chord length. This test blade tip profile dimension is three times the size of a GE-E^3 blade tip profile. The aluminum blades are EDM machine finished. The test section's top, bottom and sides are made of 1.27 cm clear polycarbonate (Lexan); however, a 1.2 cm thick clear acrylic plate replaces the top cover plate (shroud) for heat transfer tests for the best optical access to the test blade.

The blade leading edge pitch is 9.15 cm. The throat width is 4.01 cm, which, with a span of 12.2 cm, gives a throat aspect ratio of about 3. The inlet flow angle to the test blade is 32.01 deg and the exit angle is 65.7 deg, giving a total turning of 97.71 deg. A tip gap of 1.97 mm (1.5 percent of blade span) is maintained between the tip and shroud surface for the test blade and the two adjacent blades. Hard rubber gaskets of desired thickness are placed on top of the sidewalls, the trailing edge tailboards and the two outer guide blades to create this tip gap.

Figures 3 and 4 show the various arrangements of the squealer rim on the blade tip surface. Figure 3(*a*) shows a tip with a squealer rim on the pressure side, while Figs. 3(*b*) and 3(*c*) show tips with a squealer rim on the suction side and mid camber line, respectively. Figures 4(*a*), 4(*b*), and 4(*c*) show tips with squealers on the pressure side and suction side, squealers on the pressure side and the mid camber line and squealers on the suction side and on the mid camber line, respectively. A total of 52 static pressure taps (inner diameter 1.35 mm) are used to measure the shroud surface pressure distribution. Pressure taps are located around the tip edge, along the mean camber line and surrounding the tip edge at a distance of 12.52 mm from the edge perimeter as shown in

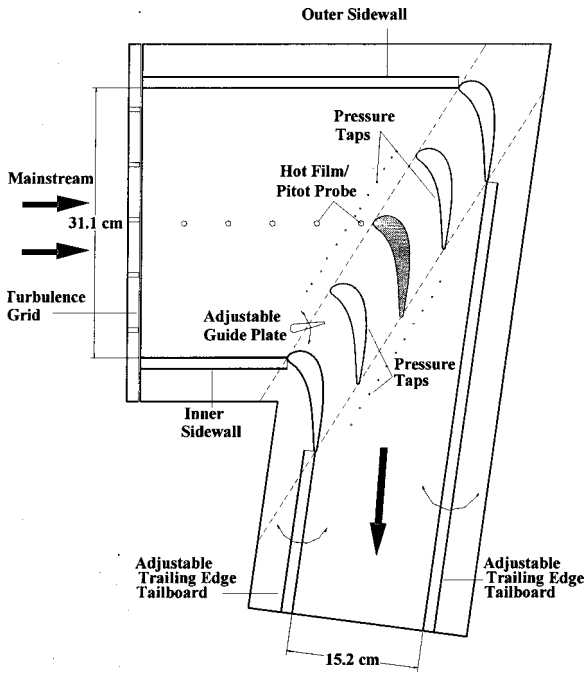

Fig. 2 Test section with 5-bladed cascade

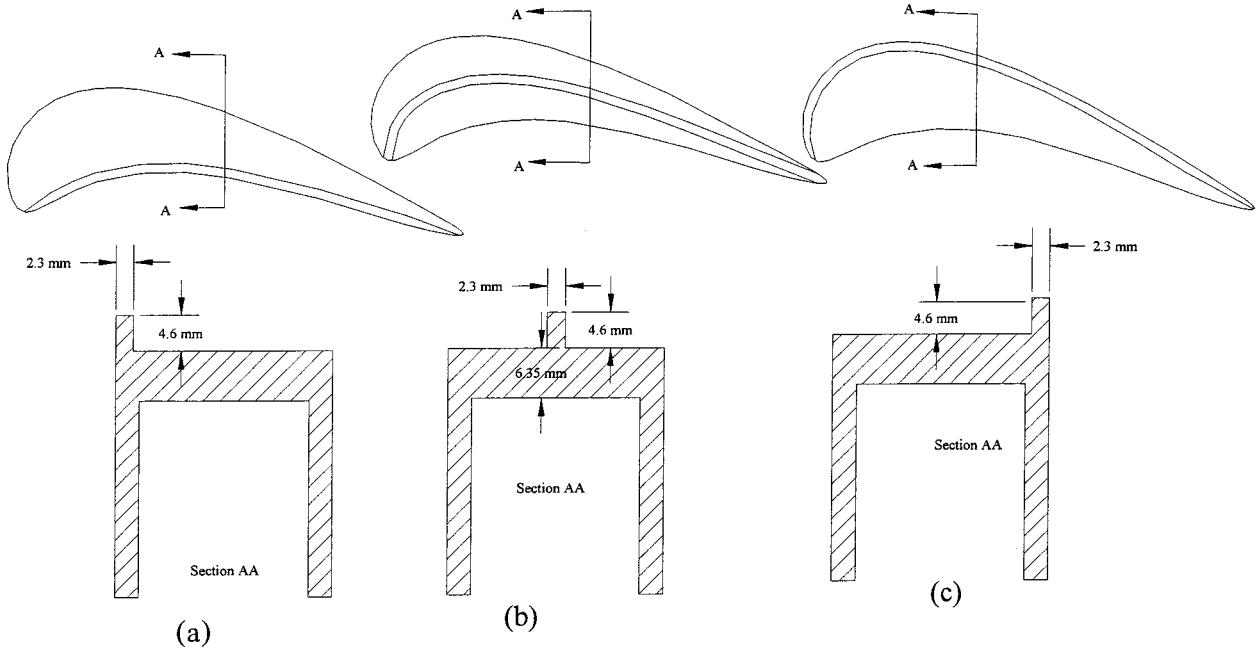

Fig. 3 Removable squealer tip-various one-sided squealer geometry

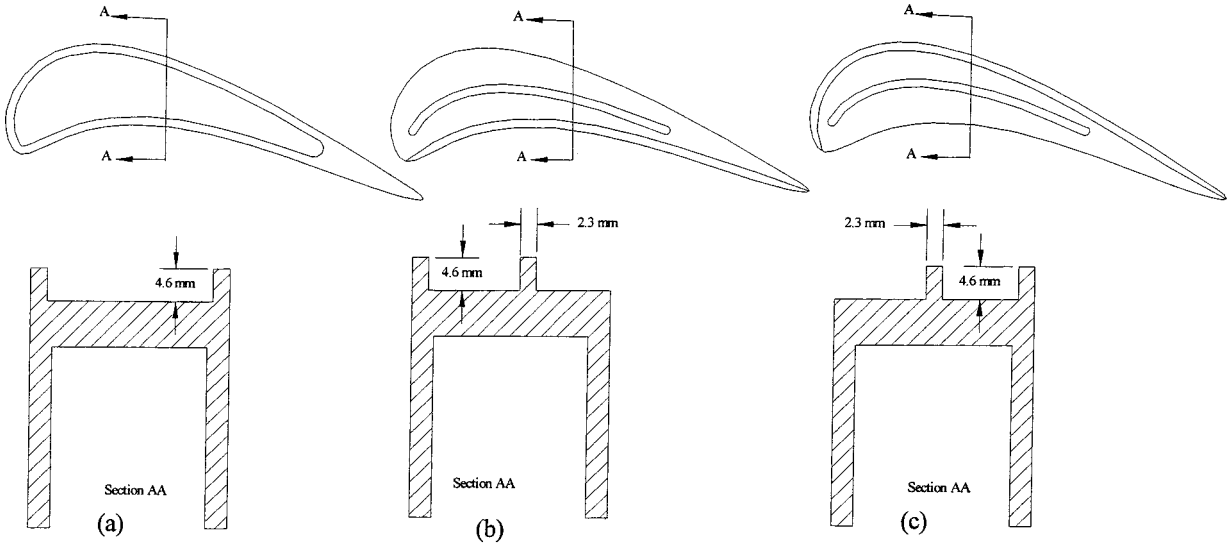

Fig. 4 Removable squealer tip-various two-sided squealer geometry

Fig. 5. The static pressures on the shroud surface may slightly differ from the tip surface pressure. The trend is usually the same; however, the magnitude differs from PS to SS, as noted by Bunker et al. [23]. The heater arrangement and the heating method are the same for each of the blades, as shown in Fig. 6. The lower portion of the blade is made of aluminum for structural rigidity. The upper portion of the blade has an inner aluminum core and an outer shell (cap) made of black polycarbonate with a low value of thermal conductivity suitable for transient liquid crystal test. The base thickness of the polycarbonate shell is 6.35 mm and the wall thickness is 3.175 mm. It is closely fitted and glued with the inner aluminum core for better rigidity. Three cartridge heaters are embedded into the inner core and provide heat to the aluminum core which in turn heats the outer polycarbonate shell. The blade is fastened to the bottom endwall with screws. The shroud pressure and blade tip heat transfer measurements are done for each blade tip configuration.

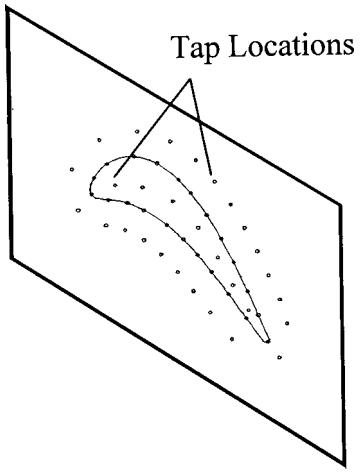

Fig. 5 Pressure tap locations on shroud surface

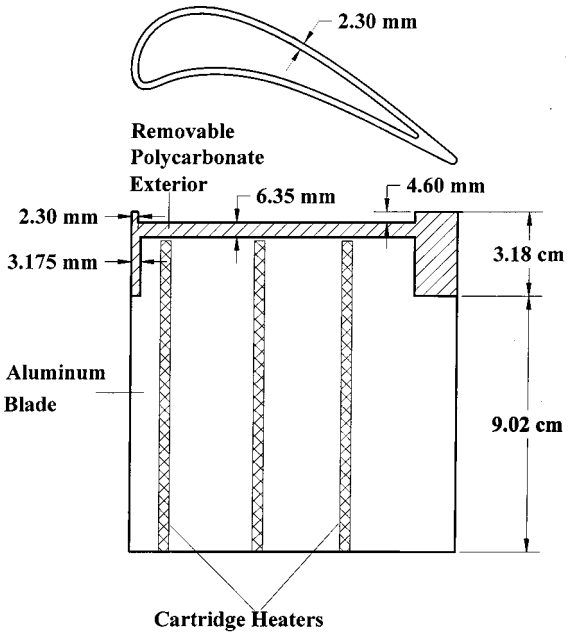

Fig. 6 Heater arrangements on a sample heat transfer blade

Theory and Procedure

In using the transient liquid crystal technique the tip is assumed as a one-dimensional semi-infinite solid surface with a convective boundary condition. The solution for the one-dimensional equation at the surface ($x=0$) is:

$$\frac{T_w - T_i}{T_m - T_i} = 1 - \exp\left(\frac{h^2 \alpha t}{k^2}\right) erfc\left(\frac{h\sqrt{\alpha t}}{k}\right) \tag{1}$$

The local heat transfer coefficient (h) can be calculated from the above equation once the initial surface temperature (T_i), the mainstream temperature (T_m), the liquid crystal color change temperature (T_w) and the time of color change (t) are known.

Heat transfer measurements are made at the preset flow conditions for which the pressure measurements were taken. A threshold intensity method of transient liquid crystal technique is used. Liquid crystals of wide band 30 to 35°C (R30C5W) made by Hallcrest are used. With the polycarbonate shell attached to the inner core, the blade tip surface is initially coated with a thin layer of thermochromic liquid crystals, and the blade is then fastened in the test cascade. Next, the cartridge heaters are turned on for three hours. The cartridge heaters heat the inner aluminum blade core and the polycarbonate shell to a steady and uniform initial temperature of about 60°C. The initial tip surface (including the rim surface) temperature distribution is measured using thermocouples placed on the blade tip surface at different locations. Two thermocouples are also placed on the suction and pressure sides in the near-tip region toward the trailing edge. These two thermocouples serve as a reference to check the initial tip surface temperature during the heat transfer test. This process of heating the blade and measuring the initial temperature is repeated several times before the final heat transfer test is conducted to ensure repeatability of the recorded initial temperature. The initial temperature is quite uniform (within 2°C) throughout the tip surface, except for the rim and near the trailing edge region. These surface temperatures are then used to generate an initial temperature map on the whole tip surface including the squealers. For the actual heat transfer tests, the thermocouples from the tip surface are removed, the blade is then washed and re- sprayed with liquid crystals. The blade is put back into the cascade and the cartridge heaters are turned on for three hours. A region of interest (ROI) for data collection is selected and a background light intensity is corrected based upon the lighting conditions on the ROI. Once the lighting, threshold and initial temperature distribution are set, the system is ready for the blow down test. The heater power is turned off immediately before the flow starts. Only one test is done per day in a controlled environment (test cell doors are closed and the room temperature is controlled). The reference thermocouples check the initial surface temperature during a heat transfer test. Thermocouples placed at the cascade inlet provide the free-stream temperature, which is about 24°C. The blade surface color change is monitored using an image processing system consisting of a RGB video camera, a computer, a RGB color monitor and a color frame grabber board. The frame grabber board is controlled using commercially available software OPTIMAS. The RGB camera is used to view the liquid crystal surface. The camera is focused using the RGB color monitor as a reference. The camera captures real time images and the captured image is translated into a data file. Thus, quantifiable color change time data are obtained, which is used to obtain heat transfer distributions. The test duration is short enough (~10–30 sec) to use the semi-infinite solid assumption.

The experimental uncertainty is determined using the method of Kline and McClintock [29]. The uncertainty of the local heat transfer coefficient measured by this method is estimated to be ±7.9 percent or less. The uncertainty estimation does not include the effect of two-dimensionality on the squealer rim and near the edges, where a two-dimensional conduction effect is present. Due to this one-dimensional assumption, the results at the tip edges and on the rim are less reliable, and may suffer more uncertainty than the reported value because of the two-dimensional conduction effect. However, so far there has been no data reported for this region, and thus this will at least provide a baseline for further study. It is noteworthy that the acrylic blade material (polycarbonate) has a very low thermal conductivity of 0.18 W/m K. The liquid crystal color change transition occurs at the surface, which is kept at nearly a uniform initial temperature. Test duration is also smaller (~10–30 sec) than the time required for the temperature to penetrate the full thickness of the insulating acrylic material. Thus, a one-dimensional transient, semi-infinite solid assumption is valid throughout the surface, except near the tip edges and on the squealer rims.

Results and Discussion

The effects of squealer geometry arrangements on shroud pressure distribution and tip heat transfer coefficient distribution are presented and discussed in this section. The squealer rim height for each case is 3.77 percent of blade span. Shroud static pressure and tip heat transfer coefficients are measured for 1.5 percent tip clearance.

Figure 7 shows the ratio of total pressure at inlet to local static pressure (P_t/P) contours on the shroud surface for three different tip geometries with 1.5 percent tip clearance. Figure 7(a) shows contours for pressure side squealer, while Figs. 7(b) and 7(c) show cases for mid camber line and suction side squealers, respectively. These contour plots help explain the heat transfer results on the tip surface. The small circles on the contour plots represent the pressure tap locations in reference to the tip. The pressure taps along the tip perimeter are connected by a line to indicate the tip profile. A smaller P_t/P value means higher static pressure, while a larger value means a lower static pressure. The lower P_t/P value on the PS indicates that the leakage flow enters the tip gap at this location, while the higher P_t/P value on the SS indicates that the leakage flow exits the tip through this location. In reality, the leakage flow path is three dimensional in nature with multiple sources and sinks. These pressure plots cannot give a firm understanding of the three-dimensional leakage flow; however, they definitely give a general indication of the leakage flow field. The pressure side squealer case in Fig. 7(a) shows a larger value of P_t/P near the mid-suction side, which indicates a very low static

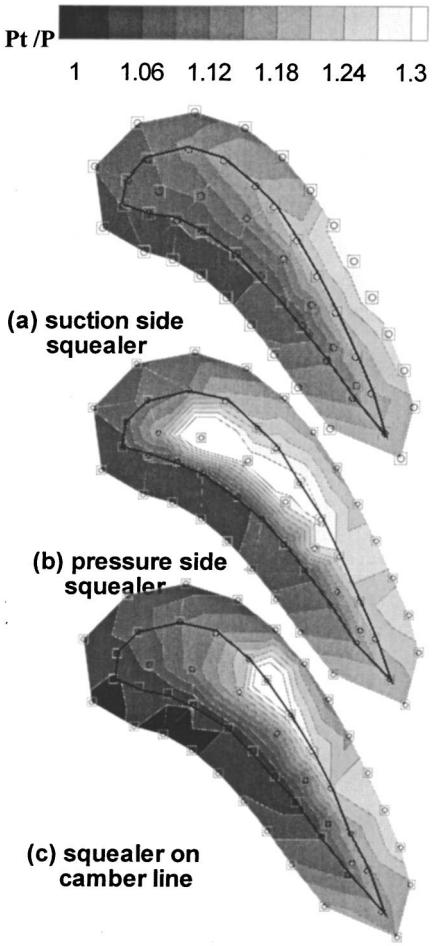

Fig. 7 Shroud pressure distributions—one-sided squealer

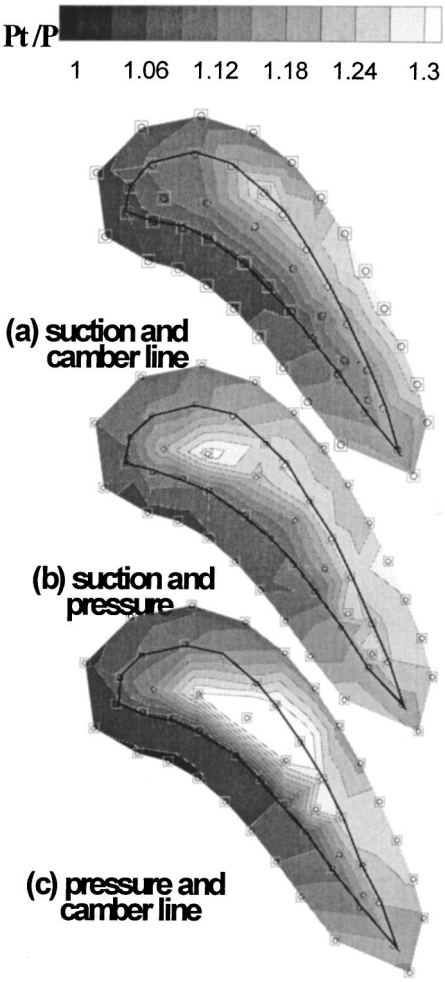

Fig. 8 Shroud pressure distributions—two-sided squealer

pressure in this region. The mid camber line squealer case in Fig. 7(*b*) shows a smaller pressure ratio than the pressure side squealer case, and the suction side squealer case shows the smallest pressure ratio among the three cases. A feature that is noteworthy is a low pressure region is present just downstream (in the flow direction sense) of each squealer position. It is the chordwise extent of this region, which determines the integrated leakage flow. This pressure ratio distribution clearly shows that PS has a longer extent than camber line, which is itself longer than the SS extent. While we may infer the leakage reduction from this result, moving the low pressure region outside of the tip profile may actually cause the interactions of the aero losses with the mainstream flow to increase. Since the apparent tip leakage flow is smallest for suction side squealer case, the heat transfer coefficient should also be smaller for this case. This will be seen in the heat transfer results. Heyes et al. [3] also concluded that the suction side squealer provides less leakage over pressure side squealer. Bunker and Bailey [1], on the other hand, mentioned that pressure side sealing strip (squealer) reduces the tip leakage flow when compared with mid chord sealing strip. However, the pressure side sealing strip enhanced the tip heat transfer coefficients compared with mid chord sealing strip or without a sealing strip. They did not study the suction side sealing strip case. Their result was based on a different airfoil and hence, their result cannot be compared directly with our findings.

Figure 8 shows pressure ratio distribution for the double squealer cases. Figure 8(*a*) shows a typical squealer tip case, while Figs. 8(*b*) and 8(*c*) show cases for squealer on pressure side plus mid camber line, and suction side plus mid camber line, respectively. Among these three cases, the suction side plus mid camber line squealer case provides better leakage protection, resulting in a lower heat transfer coefficient as will be seen later. The pressure side plus mid camber line squealer case shows the highest pressure ratio between the SS and PS. Thus, the leakage flow may be higher when compared with a typical squealer case of Fig. 8(*a*). However, for the typical squealer case (suction plus pressure side squealer), the leakage flow may be higher towards the trailing edge, as indicated by a higher pressure ratio in this region. This effect will also be reflected in the heat transfer results.

Figure 9 shows the tip local heat transfer coefficients for single squealer geometry, while Fig. 10 shows the tip local heat transfer coefficients for double squealer geometry. Figure 10(*a*) represents a typical squealer geometry with a cavity depth of 3.77 percent of blade span. The distribution clearly shows various regions of low and high heat transfer coefficients on the tip and (squealer) rim surface. The magnitude of the heat transfer coefficient varies from 350 to 1150 W/m^2K on the tip surface and on the trailing edge portion. However, the heat transfer coefficient on the squealer rim is much higher at about 800 to 1700 (not plotted) W/m^2K. The plots are presented in the range of 400–1100 W/m^2K to clearly distinguish different lower and higher heat transfer zones on the tip surface and to compare with other cases. The average heat transfer coefficient values on the rim are presented separately in a line plot to show the magnitude of the heat transfer coefficient on the rim. The pressure side squealer case in Fig. 9(*a*) shows the highest heat transfer coefficients when compared with case 9(*b*), the mid camber line squealer and case 9(*c*), the suction side

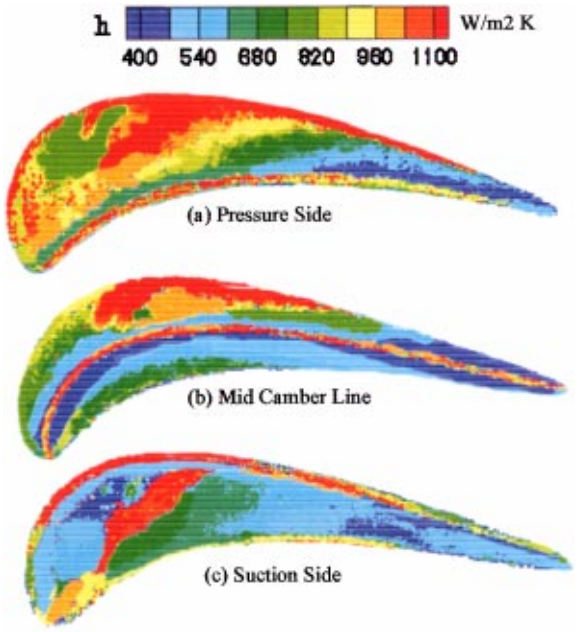

Fig. 9 Local heat transfer coefficient distributions—one-sided squealer (Full color in on-line version of the journal)

squealer. It shows a higher heat transfer coefficient on the rim and from the leading edge toward the mid chord suction side. This location actually corresponds to the leakage flow path. In this case, the flow separates at the pressure side rim and after passing over the rim, reattaches on the tip surface. Flow reattachment causes high heat transfer coefficients on the tip surface. The suction side squealer case provides a low level of heat transfer coefficient almost all over the surface except on the squealer rim and along a line from leading edge to the suction side as seen in Fig. 9(*c*). This location of high heat transfer corresponds to the tip

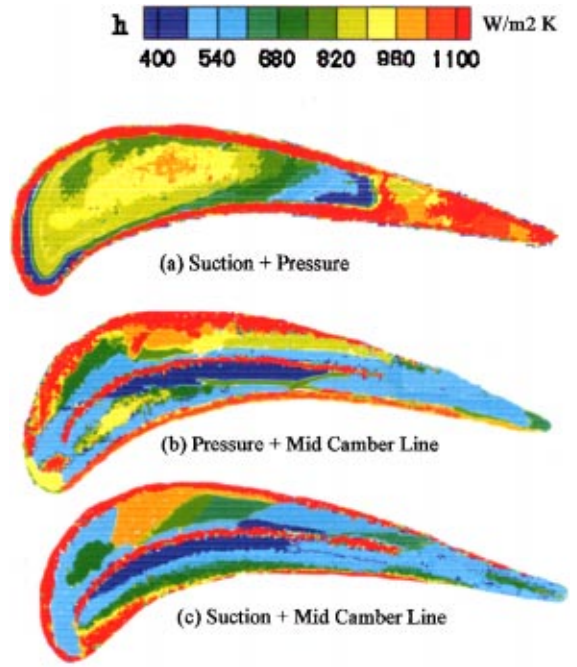

Fig. 10 Local heat transfer coefficient distributions—two-sided squealer (Full color in on-line version of the journal)

leakage flow path. The suction side squealer restricts the leakage flow to a minimum through the tip gap, resulting in a lower heat transfer coefficient over the tip surface.

Figure 9(*b*) shows heat transfer coefficients for a tip that has a squealer on the mid camber line. It shows that the highest heat transfer coefficient occurs in the suction side around mid chord region and on the squealer rim. The pressure side shows a lower heat transfer coefficient than the suction side. The trailing edge region shows a very low heat transfer coefficient. The central portion of the tip (near the squealer) also shows a low heat transfer coefficient. In this case, the location of the squealer rim is such that a flow separation zone may occur on the pressure side of the squealer rim, and another separation zone may occur on the suction side prior to flow reattachment. These separation areas have lower heat transfer coefficients and the reattachment zones on the suction side have higher heat transfer coefficients. Ameri [8] also predicted somewhat similar results for a different blade tip with a mean-camberline strip.

Figure 10(*a*) shows the heat transfer coefficient for a typical squealer tip, while Figs. 10(*b*) and 10(*c*) show the heat transfer coefficient for a squealer on the pressure side plus mid camber line, and suction side plus mid camber line, respectively. One important geometric aspect needs to be clarified before discussing the results. The typical squealer tip has an enclosed cavity surrounded by the suction and pressure side squealers, while the other two cases have no enclosed cavities; the squealers are separated from each other and the trailing edge is level with the tip surface. However, for the typical squealer case, the trailing edge is level with the squealer rim surface. Results for the typical squealer case show that on the cavity bottom, the heat transfer coefficient is higher in the upstream-central region; however, it is much lower in the mid-chord region toward the pressure side and downstream-end of the cavity toward the trailing edge. A recirculating dead-flow zone is observed far downstream at the end of the cavity surface. Leakage flow may be entrapped in this narrow region, which causes the heat transfer coefficient to be the lowest in this region. On the other hand, the leakage flow may have an impingement effect on the cavity surface. It separates on the pressure side rim and may reattach inside the cavity surface. Thus, a higher heat transfer coefficient is observed on the central upstream region of the cavity bottom. The high heat transfer on the rim may be due to the flow entrance and exit effect and due to our one-dimensional assumption. The leakage spills out of the cavity and exits through the suction side rim and the trailing edge. This may cause more mixing, resulting in a higher heat transfer coefficient in the suction side rim and the trailing edge. However, for the open squealers (cases 10(*b*) and 10(*c*)), the trailing edge region shows a low level of heat transfer coefficient. The pressure side shows a lower heat transfer coefficient compared to the suction sides. The location of the mid squealer rim in both cases creates flow separation zone on the pressure side resulting in a lower heat transfer coefficient. The suction side for case 10(*b*) shows higher heat transfer coefficients when compared with case 10(*c*). This may be due to a flow reattachment on the suction side. For case 10(*c*), the suction side has low heat transfer coefficients except toward the leading edge mid chord region. This may be a flow separation zone. The flow reattaches on the suction side near the mid chord region resulting in a high heat transfer coefficient. No experimental or numerical heat transfer data are available in the literature to compare with this result.

The averaged heat transfer coefficients are presented in Figs. 11 and 12. The averaged heat transfer coefficient is calculated along a line perpendicular to the axial chord and plotted as a function of normalized axial distance from the leading edge. The result shows that the heat transfer coefficient on the tip bottom surface is smaller when compared with the rim surface. For single squealer case of Fig. 11, the tip bottom surface for pressure side squealer shows the highest averaged heat transfer coefficient, while the suction side squealer case shows the lowest. However, the pattern

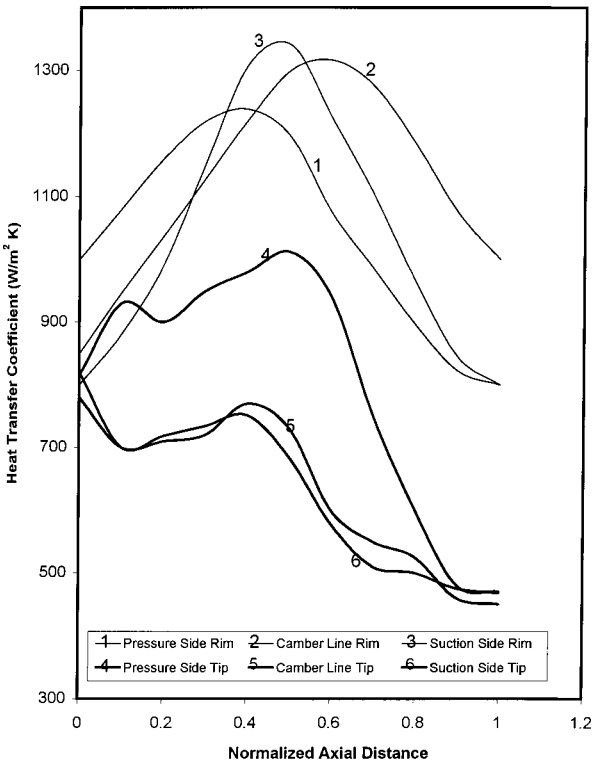

Fig. 11 Averaged heat transfer coefficient—one-sided squealer

on the squealer rim surface differs from the bottom surface. Heat transfer coefficient on the rim surface for pressure side squealer is highest among the single squealer arrangements for the region from the leading edge to 25 percent axial chord. From midchord to the trailing edge, the heat transfer coefficient is the lowest for the pressure side squealer case, while it is highest for camber line squealer case. Thus, for the single squealer, a pressure side squealer case provides the highest total averaged heat transfer coefficient, while suction side and mid chord squealer cases provide somewhat equal but lower heat transfer coefficient than a pressure side squealer case. For the double squealer cases in Fig. 12, the rim surfaces show higher heat transfer coefficient than the cavity or tip bottom surface. On the cavity or tip bottom surface, the heat transfer coefficient is smaller for suction side plus mid camber line squealers when compared to pressure side plus mid camber line squealers. A typical suction side plus pressure side squealers case shows higher averaged heat transfer coefficient from 10 to 40 percent axial chord. For axial chord larger than 50 percent it is the lowest. The results for the squealer rim surface do not follow any particular pattern.

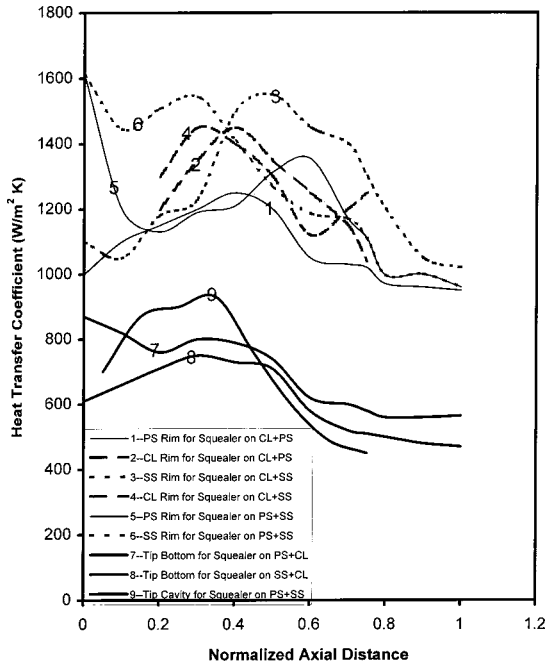

Fig. 12 Averaged heat transfer coefficient—two-sided squealer

Conclusion

The effect of tip squealer geometry arrangement on heat transfer coefficient on the tip surface of a gas turbine blade is investigated. Six different tip geometries are studied. The blade tip model is a linear tip section of a GE E^3 blade mounted in a non rotating linear cascade. A transient liquid crystal technique is used to measure detailed heat transfer coefficients. Static pressure distributions on the stationary shroud surface provide complementary information helping to explain the local heat transfer behavior on the tip surface. A typical Reynolds number based on airfoil axial chord and an exit velocity is 1.1×10^6 and an overall pressure ratio of 1.32 is used. The major findings are:

1 Detailed measurements provide a better understanding of the local heat transfer behavior on the blade tip surface.

2 The pressure measurements on the shroud surface provide complementary information of the tip leakage flow pattern. These pressure data provide a basis for determining the tip leakage flow, which also helps to explain the heat transfer results.

3 A single squealer geometry on the tip surface acts as a sealing to the tip leakage flow and reduces tip leakage.

4 The location of the squealer can change the leakage flow and result in very different heat loads to the blade tip. A squealer on the suction side provides reduced leakage compared to that on the pressure side or the mid camber line. A squealer on the mid camber line performs better than that on a pressure side.

5 In general, a single squealer performs better than a double squealer in reducing overall heat transfer to the tip.

6 A single or a double open squealer provides lower heat transfer coefficient on the trailing edge than a typical enclosed squealer.

7 A higher heat transfer coefficient exists on the rim surface because of the entrance and exit effect. A one-dimensional assumption may also contribute for this higher heat transfer coefficient.

8 A single squealer on the suction side provides the best sealing to leakage flow among all the cases studied here.

Acknowledgment

This study was sponsored by NASA-Lewis Research Center under grant number NAG3-2002. The NASA technical team is Mr. Robert Boyle and Dr. Raymond Gaugler. Their support is greatly appreciated. Experiment related technical discussion with Dr. Srinath Ekkad of Louisiana State University was helpful and is acknowledged.

Nomenclature

C = tip clearance gap
C_p = coefficient of pressure
C_x = axial chord length of the blade (8.61 cm)
h = local convective heat transfer coefficient (W/m^{2}K)
k = thermal conductivity of blade tip material (0.18 W/m K)
LE = leading edge of the blade

P = local static pressure
P_{avg} = averaged static pressure
P_t = total pressure at the inlet
PS = pressure side of the blade
SS = suction side of the blade
t = transition time for liquid crystal color change
TE = trailing edge of the blade
T_i = initial temperature of the blade tip surface
T_m = mainstream temperature of the flow
T_w = color change temperature of the liquid crystal, green-to-red
Tu = free stream turbulence intensity level at the inlet
X = axial distance (cm)
α = thermal diffusivity of blade tip material (1.25×10^{-7} m^2/s)

References

[1] Bunker, R. S., and Bailey, J. C., 2000, "Blade Tip Heat Transfer and Flow With Chordwise Sealing Strips," International Symposium on Transport Phenomena and Dynamics of Rotating Machinery (ISROMAC), Honolulu, Hawaii, pp. 548–555.

[2] Bunker, R. S., and Bailey, J. C., 2000, "An Experimental Study of Heat Transfer and Flow on a Gas Turbine Blade Tip with Various Tip Leakage Sealing Methods," 4^{th} ISHMT / ASME Heat and Mass Transfer Conference, India.

[3] Heyes, F. J. G., Hodson, H. P., and Dailey, G. M., 1991, "The Effect of Blade Tip Geometry on the Tip Leakage Flow in Axial Turbine Cascades," ASME Paper No. 91-GT-135.

[4] Azad, G. S., Han, J. C., and Boyle, R. J., 2000, "Heat Transfer and Flow on the Squealer Tip of a Gas Turbine Blade," ASME Paper No. 2000-GT-195.

[5] Dunn, M. G., and Haldeman, C. W., 2000, "Time-Averaged Heat Flux for a Recessed Tip, Lip, and Platform of a Transonic Turbine Blade," ASME Paper No. GT-0197.

[6] Ameri, A. A., Steinthorsson, E., and Rigby, L. D., 1997, "Effect of Squealer Tip on Rotor Heat Transfer and Efficiency," ASME Paper No. 97-GT-128.

[7] Ameri, A. A., Steinthorsson, E., and Rigby, L. D., 1998, "Effects of Tip Clearance and Casing Recess on Heat Transfer and Stage Efficiency in Axial Turbines," ASME Paper No. 98-GT-369.

[8] Ameri, A. A., 2001, "Heat Transfer and Flow on the Blade Tip of a Gas Turbine Equipped with a Mean-Camberline Strip," ASME Paper No. 2001-GT-0156.

[9] Yang, T. T., and Diller, T. E., 1995, "Heat Transfer and Flow for a Grooved Turbine Blade Tip in a Transonic Cascade," ASME Paper No. 95-WA/HT-29.

[10] Metzger, D. E., Bunker, R. S., and Chyu, M. K., 1989, "Cavity Heat Transfer on a Transverse Grooved Wall in a Narrow Flow Channel," ASME J. Heat Transfer, **111**, pp. 73–79.

[11] Chyu, M. K., Moon, H. K., and Metzger, D. E., 1989, "Heat Transfer in the Tip Region of Grooved Turbine Blades," ASME J. Turbomach., **111**, pp. 131–138.

[12] Bindon, J. P., and Morphus, G., 1988, "The Effect of Relative Motion, Blade Edge Radius and Gap Size on the Blade Tip Pressure Distribution in an Annular Turbine Cascade with Clearance," ASME Paper No. 88-GT-256.

[13] Bindon, J. P., 1989, "The Measurement and Formation of Tip Clearance Loss," ASME J. Turbomach., **111**, pp. 258–263.

[14] Moore, J., Moore, J. G., Henry, G. S., and Chaudhury, U., 1989, "Flow and Heat Transfer in Turbine Tip Gaps," ASME J. Turbomach., **111**, pp. 301–309.

[15] Yaras, M. I., and Sjolander, S. A., 1991, "Effects of Simulated Rotation on Tip Leakage in a Planar Cascade of Turbine Blades, Part I-Tip Gap Flow," ASME Paper No. 91-GT-127.

[16] Sjolander, S. A., and Cao, D., 1995, "Measurements of the Flow in an Idealized Turbine Tip Gap," ASME J. Turbomach., **117**, pp. 578–584.

[17] Kaiser, I., and Bindon, J. P., 1997, "The Effect of Tip Clearance on the Development of Loss Behind a Rotor and a Subsequent Nozzle," ASME Paper No. 97-GT-53.

[18] Lakshminarayana, B., 1970, "Methods of Predicting the Tip Clearance Effects in Axial Flow Turbomachinery," ASME J. Basic Eng., **92**, pp. 467–482.

[19] Booth, T. C., Dodge, P. R., and Hepworth, H. K., 1982, "Rotor Tip Leakage: Part I—Basic Methodology," ASME J. Eng. Power, **104**, pp. 154–161.

[20] Wadia, A. R., and Booth, T. C., 1982, "Rotor Tip Leakage: Part II—Design Optimization Through Viscous Analysis and Experiment," ASME J. Eng. Power, **104**, pp. 162–169.

[21] Mayle, R. E., and Metzger D. E., 1982, "Heat Transfer at the Tip of an Unshrouded Turbine Blade" *Proc. Seventh Int. Heat Transfer Conf.*, Hemisphere Pub., New York, pp. 87–92.

[22] Metzger, D. E., Dunn, M. G., and Hah, C., 1991, "Turbine Tip and Shroud Heat Transfer," ASME J. Turbomach., **113**, pp. 502–507.

[23] Bunker, R. S., Bailey, J. C., and Ameri, A. A., 1999, "Heat Transfer and Flow on the First Stage Blade Tip of a Power Generation Gas Turbine: Part 1: Experimental Results," ASME Paper No. 99-GT-169.

[24] Ameri, A. A., and Steinthorsson, E., 1995, "Prediction of Unshrouded Rotor Blade Tip Heat Transfer," ASME Paper No. 95-GT-142.

[25] Ameri, A. A., and Steinthorsson, E., 1996, "Analysis of Gas Turbine Rotor Blade Tip and Shroud Heat Transfer," ASME Paper No. 96-GT-189.

[26] Ameri, A. A., and Bunker, R. S., 1999, "Heat Transfer and Flow on the First Stage Blade Tip of a Power Generation Gas Turbine: Part 2: Simulation Results," ASME Paper No. 99-GT-283.

[27] Azad, G. S., Han, J. C., Teng, S., and Boyle, R., 2000, "Heat Transfer and Pressure Distribution on a Gas Turbine Blade Tip," ASME Paper No. 2000-GT-194.

[28] Teng, S., Han, J. C., and Azad, G. S., 2001, "Detailed Heat Transfer Coefficient Distributions on a Large-Scale Gas Turbine Blade Tip," ASME J. Heat Transfer, **123**, pp. 803–809.

[29] Kline, S. J., and McClintock, F. A., 1953, "Describing Uncertainties in Single Sample Experiments," Mech. Eng. (Am. Soc. Mech. Eng.), **75**, pp. 3–8.

Self-Preserving Properties of Unsteady Round Nonbuoyant Turbulent Starting Jets and Puffs in Still Fluids

R. Sangras[1]

O. C. Kwon[2]

G. M. Faeth

e-mail: gmfaeth@umich.edu

Department of Aerospace Engineering,
The University of Michigan,
Ann Arbor, MI 48109-2140

The self-preserving properties of round nonbuoyant turbulent starting jets, puffs, and interrupted jets were investigated both experimentally and theoretically for flows in still and unstratified environments. The experiments involved dye-containing fresh water sources injected into still fresh water within a large windowed tank. Time-resolved video images of the flows were obtained using a CCD camera. Experimental conditions were as follows: jet exit diameters of 3.2 and 6.4 mm, jet exit Reynolds numbers of 3000–12,000, jet passage lengths in excess of 50 injector passage diameters, volume of injected fluid for puffs and interrupted jets up to 191 source diameters, and streamwise penetration lengths up to 140 source diameters. Near-source behavior varied significantly with source properties but the flows generally became turbulent within 5 source diameters from the source and self-preserving behavior was generally observed at distances greater than 20–30 source diameters from the source. Within the self-preserving region, both the normalized streamwise penetration distance and the normalized maximum flow radius varied as functions of time in agreement with estimates for self-preserving turbulent flows to the following powers: 1/2 for starting nonbuoyant jets and 1/4 for nonbuoyant puffs and interrupted jets. Effects of injected fluid quantity for self-preserving puffs and interrupted jets could be handled by correlating the location of the virtual origin as a function of the volume of the injected fluid represented by the number of passage lengths of injected fluid. In particular, the virtual origin for puffs was independent of injected fluid volume for injected passage lengths less than 120 but became proportional to the injected fluid volume thereafter, defining a boundary between puff and interrupted-jet behavior.
[DOI: 10.1115/1.1421047]

Keywords: Jets, Scaling, Turbulence, Unsteady, Vortex

Introduction

A theoretical and experimental investigation of the temporal development of round turbulent nonbuoyant starting jets, puffs (due to a brief release of source fluid), and interrupted jets (due to extended but finite releases of source fluid) in still environments is described. Study of these flows is motivated by practical applications to the unconfined and unsteady turbulent flows resulting from the initiation of steady and interrupted gas and liquid releases caused by process upsets, explosions and unwanted fires, among others. Due to their simplicity, these flows also are of interest as classical fundamental flows that illustrate the development of unsteady turbulent flows. As a result, observations of these flows are useful in order to provide data needed to evaluate methods of predicting their properties. The present experiments emphasized the mixing properties of these flows far from the source, where effects of source disturbances are lost, where flow structure is largely controlled by the conserved properties of the flow, and where the flow approximates self-preserving turbulent flow behavior (and appropriately-scaled properties of the flow became independent of streamwise distance, see Kouros et al. [1], Witze [2], Kato et al. [3], Hyun et al. [4] and references cited therein). Particular advantages of self-preserving turbulent flows are that this region significantly simplifies both the presentation of experimental data and numerical simulations needed to evaluate models of the flows because potential effects of poorly calibrated source disturbances have been lost. In addition, the scaling rules quantify valuable fundamental interactions between the turbulent mixing properties and the conserved properties of the flows.

Past experimental, theoretical and computational studies of round nonbuoyant turbulent starting jets, puffs, and interrupted jets have been reported by a number of workers [1–8]. For example, starting jet studies have been reported by Kouros et al. [1], Witze [2], Kato et al. [3], Hyun et al. [4], Adriani et al. [5], and Hill and Ouelette [6]. Apart from these studies, under-expanded high-speed, starting jets have been studied by Hill and Ouelette [6], Rubas et al. [7], and Birch et al. [8], finding that high pressure jets and sprays scale similar to turbulent starting jets if use is made of an equivalent diameter. Turbulent puffs have been studied by Grigg and Stewart [9], Richards [10], and Kovasznay et al. [11]. Turbulent vortex rings, which have similarities to puffs, have been investigated by Glezer and Coles [12], Maxworthy [13,14], Johnson [15], and Shariff and Leonard [16]. These studies have provided self-preserving scaling rules that describe the main features of these flows but corresponding measurements of self-preserving flow properties are surprisingly limited. In addition, recent studies of the self-preserving properties of steady buoyant turbulent plumes due to Dai et al. [17,18] and Sangras et al. [19–22] show that self-preserving behavior generally is only observed at distances farther from the source than previously thought (e.g., streamwise distances greater than roughly 100 source diameters). On the other hand, Sangras and Faeth [23] recently observed self-preserving behavior of a variety of round turbulent flows at dis-

[1]Currently with the Department of Mechanical Engineering, Worcester Polytechnic Institute, Worcester, Massachusetts.

[2]Currently with the Mechanical and Aerospace Engineering Department, Princeton University, Princeton, New Jersey.

Contributed by the Heat Transfer Division for publication in the JOURNAL OF HEAT TRANSFER. Manuscript received by the Heat Transfer Division February 2, 2001; revision received August 3, 2001. Associate Editor: H. S. Lee.

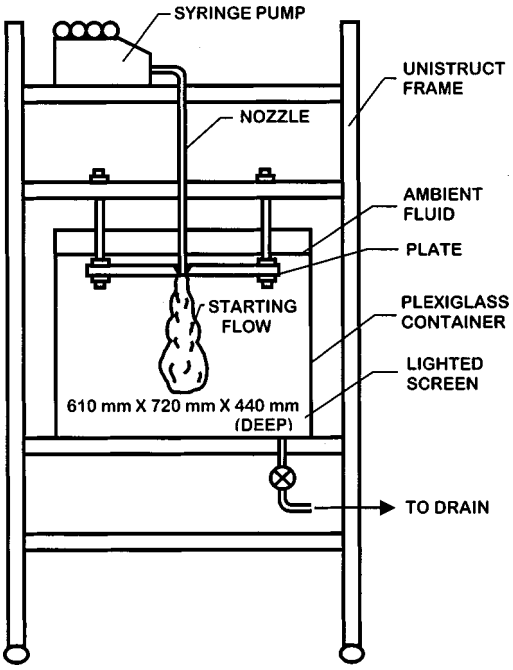

Fig. 1 Sketch of the test apparatus for round nonbuoyant starting jets, puffs, and interrupted jets in still environments

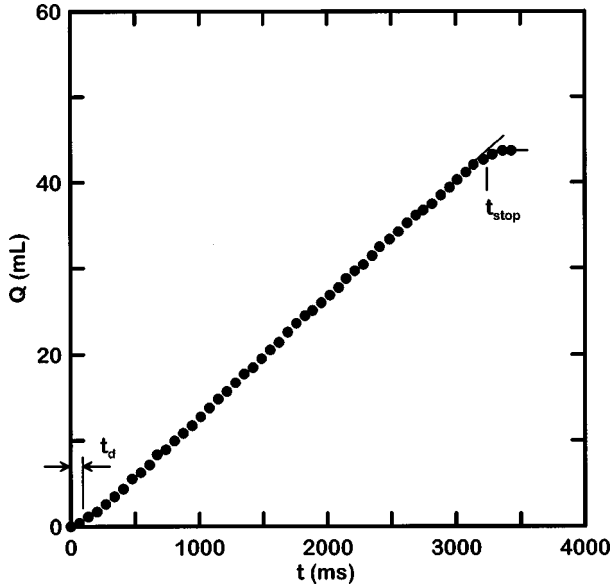

Fig. 2 Flow rate transients due to starting and stopping of the source syringe pump

tances as small as 20–30 source diameters from the source. Notwithstanding these discrepancies, however, these observations raise concerns about whether existing measurements of the self-preserving behavior of round turbulent nonbuoyant and buoyant unsteady flows were carried out far enough from the source to properly observe self-preserving behavior.

In view of the previous discussion, the present investigation considered the self-preserving properties of round nonbuoyant turbulent starting jets, puffs, and interrupted jets in still environments. The specific objectives of the study were as follows:

1. Measure the streamwise and cross stream penetration properties of these flows as a function of time for various source diameters, source Reynolds numbers and amounts of injected source fluid (for puffs and interrupted jets).
2. Use the measured penetration properties to evaluate self-preserving scaling and to determine empirical factors needed to correlate streamwise and radial penetration properties for these flows.
3. Examine the relationships between nonbuoyant turbulent starting jets and puffs, and between nonbuoyant turbulent puffs and vortex rings.

The experiments involved fresh water sources injected into a still fresh water bath. Penetration properties were measured from flow visualizations consisting of time-resolved video records of dye-containing injected source liquids. Present observations extended to streamwise penetration distances on the order of 140 source diameters.

Experimental Methods

Apparatus. The experiments adopted methods of using fresh water modeling of turbulent flows suggested by Steckler et al. [24]. A sketch of the test apparatus appears in Fig. 1. The test apparatus consisted of a plexiglass (18 mm thick) tank open at the top. The water bath within the tank was rectangular and had inside plan dimensions of 610×720 mm and an inside depth of 440 mm. The bath was filled with fresh water to a depth of roughly 400 mm, using water from the laboratory water supply. The bath water was allowed to stand until heated to room temperature so that bubbles caused by the presence of dissolved air in the water could be removed. The test bath was fitted with a valved drain, flush with the tank bottom, so that the water could be removed from time-to-time.

The jet injectors were smooth round glass tubes having inside diameters of 3.2 and 6.4 mm. Injector passage length/diameter ratios were 50 and 100 respectively, for diameters of 6.4 and 3.2 mm, to help ensure fully-developed turbulent pipe flow at the jet exit for sufficiently large jet Reynolds numbers [25]. The injectors were mounted vertically and discharged roughly 5 mm below the liquid surface. The injectors passed through a horizontal plexiglass plate (280×432 mm plan dimensions×12 mm thick) with a tight fit. The injector exits were mounted flush with the lower surface of the plate in order to provide well-defined entrainment conditions near the jet exit. The source liquid was supplied to the injector using up to two syringe pumps (Harvard Apparatus, PHD 2000, Model 70-2000 Syringe Pump, each with four 150 cc syringes mounted in parallel). These pumps were computer controlled to start, stop and deliver liquid at preselected times and rates. Pump flow rates were calibrated by collecting liquid for timed intervals. In addition, the start and stop times of the syringe pumps were monitored using the video records.

The start-up behavior of the pumps was investigated by measuring the volume of fluid the pumps discharged as a function of time during a transient pumping process where the pumps were started and then stopped after pumping for a timed interval. Typical measured quantities of water injected by the pumps as a function of time for this process are illustrated in Fig. 2 for a pump operation time of 3200 ms. The time delay, t_d, required for the pumps to discharge at a steady flow was computed by extending the steady flow straight line to the time axis. This time was then subtracted from the original time records to correct for start-up conditions. A typical time delay was roughly 100 ms, however, the time delay varied with the flow rate and was measured for all test conditions. A corresponding stop time could also be defined, as shown in Fig. 2, and was calibrated in the same manner. Red dyes were added to the source liquid in order to facilitate flow visualization.

Instrumentation. Measurements of source flow dimensions as a function of time were obtained from video records. The bath was illuminated for these observations using two 650 W quartz lamps (Color Tran, quartz king dual 650, Model 116-011). The

Table 1 Summary of test conditions for round nonbuoyant turbulent starting jets, puffs, and interrupted jets

Parameter	Value
Source and ambient fluid	Water
Fluid density, ρ	998 kg/m^3
Fluid kinematic viscosity, ν	1.0 mm^2/s
Source diameter, d	3.2 and 6.4 mm
Source flow rate, $\dot{Q}_0$	7-30 cc/s
Souce passage length/diameter ratio, L/d	50 and 100
Source Reynolds number, $u_0 d/\nu_0$	3,000-12,000
Source fluid discharged for puffs, $Q_0/(A_0 d)$	30-191
Streamwise penetration distance, $(x_p\text{-}x_0)/d$	0-140
Characteristic flow time, $(t\text{-}t_d)u_0/d$	0-17,300

[a]Fresh water jets injected from a round tube into a still water bath having dimensions 610×720×440 (deep) mm at an ambient pressure and temperature of 99.0 ± 0.5 kPa and 297 ± 0.5 K.

appearance of the dye-containing injected source liquid was recorded as a function of time using a color video CCD camera (Panasonic Model No. WV-CL 352). This camera has a 682×492 pixel array (yielding a resolution of 0.5 mm per pixel) with an 8-bit dynamic range, and a 12 mm focal length×f1.8 lens (WV aspherical-LA/208). Color still photographs of the flows were also obtained with a Nikon FM2 camera having an 85 mm focal length ×f1.4 lens and using conventional Fuji-color film.

The video records were analyzed to provide the maximum mean streamwise penetration distance (taken as the average of the largest streamwise distance of injected source liquid from the jet exit), the mean maximum radial penetration distance as a function of time from the start of injection, and the mean radial penetration distance of the jet-like portion of these flows as a function of distance from the jet exit. These mean values were obtained by averaging the results of ten separate tests at a particular jet exit condition. Experimental uncertainties (95 percent confidence) of the various measurements of the video records were as follows: less than 7 percent for times from the start of injection, less than 8 percent for mean maximum streamwise penetration distances and less than 15 percent for mean maximum radial penetration distances. The experimental uncertainties of the streamwise and radial penetration distances were largely governed by sampling errors due to the irregular turbulent boundaries of the present turbulent source liquid flows.

Test Conditions. The test conditions for the present round nonbuoyant turbulent starting jets, puffs, and interrupted jets are summarized in Table 1. The test conditions involved jet exit diameters of 3.2 and 6.4 mm, jet exit Reynolds numbers of 3000–12,000, various amounts of injected liquids for puffs and interrupted jets comprising liquid columns having the same diameter as the jet exit and lengths in the range 30–191 source diameters, dimensionless streamwise penetration distances, $(x_p-x_0)/d$, of 0–140, and characteristic flow times, tu_0/d, in the range 0–17,300.

Theoretical Methods

A parameter that is useful for estimating when nonbuoyant turbulent flows from steady and interrupted sources become self-preserving is the distance from the virtual origin normalized by the source diameter, $(x-x_0)/d$ [17]. This parameter measures the distance needed to modify distributions of mean and fluctuating properties from conditions within a passage to conditions in an unbounded flow (e.g., to eliminate source disturbances). Past work with steady round turbulent buoyant plumes suggests $(x-x_0)/d$ >80 for self-preserving conditions, see [17] and references cited therein. On the other hand, Sangras and Faeth [23] observed self-preserving behavior for turbulent round nonbuoyant starting jets and puffs and buoyant starting plumes and thermals at distances greater than 20–30 source diameters from the source. It is known that the properties observed (e.g., distributions of mean quantities, distributions of fluctuating quantities, power spectral densities, etc.) can have a considerable influence on conditions where self-preserving behavior is observed [17,18]; nevertheless, the differences between the observations of Dai et al. [17,18] and Sangras and Faeth [23] concerning conditions where self-preserving behavior is observed for round nonbuoyant and buoyant turbulent flows should be resolved.

Assuming that the flow is within the self-preserving region, expressions for the streamwise penetration distance of the present round turbulent flows from steady and interrupted sources are either available from past work or are readily found using past methods, see [1–3,5,6,9–12,16,26,27] and references cited therein. The configurations of the present nonbuoyant flows for these analyses are similar, as sketched in Fig. 3. Both steady and interrupted sources are illustrated in Fig. 3, with the latter leading to the formation of a puff or an interrupted jet. For present purposes, lengthy source flows of puffs, initially yielding a starting jet approaching self-preserving behavior, will be termed interrupted jets.

Major assumptions for present considerations are similar to earlier analyses to find self-preserving flow scaling: physical property variations in the flows are assumed to be small, steady sources start instantly and subsequently maintain constant source properties, interrupted sources start and stop instantly and maintain constant source properties during the period of flow, and virtual origins in both distance, x_0, and time, t_d, are used to maximize conditions where self-preserving behavior is observed. Finally, for convenience, source properties are assumed to be uniform. This last approximation is not a critical assumption, however, because the details of the sources are not important within the self-preserving region of the present flows; instead, conserved properties of the flows are adequately prescribed by mean source properties.

Under these assumptions, the temporal variation of the maximum streamwise penetration distance can be expressed as follows within the self-preserving regions of the present unsteady turbulent flows:

$$(x_p-x_0)/d=C_x((t-t_d)/t^*)^n, \tag{1}$$

where

$$t^*=d/u_0. \tag{2}$$

The corresponding temporal variation of the maximum radial penetration distance can be expressed most conveniently in terms of the streamwise penetration distance, (x_p-x_0), as follows:

$$r_p/(x_p-x_0)=C_r. \tag{3}$$

The values of C_x, C_r, and n vary depending upon the particular starting flow that is being considered. The values of C_x and C_r are best-fit empirical parameters of the self-preserving analyses and will be considered later when the measurements are discussed. The values of n, however, follow from the requirements for self-preserving flows and can be expressed as follows for the present unsteady flows:

$$\begin{aligned} n&=1/2,\ \text{nonbuoyant starting jets;}\\ n&=1/4,\ \text{nonbuoyant puffs or interrupted jets} \end{aligned} \tag{4}$$

Naturally, flows for puffs are identical to those for starting jets until the source flow of the puff has been interrupted or stopped. Thus, present consideration of puffs is mainly limited to times of source-flow operation that are small compared to the minimum times required to develop self-preserving starting jet behavior.

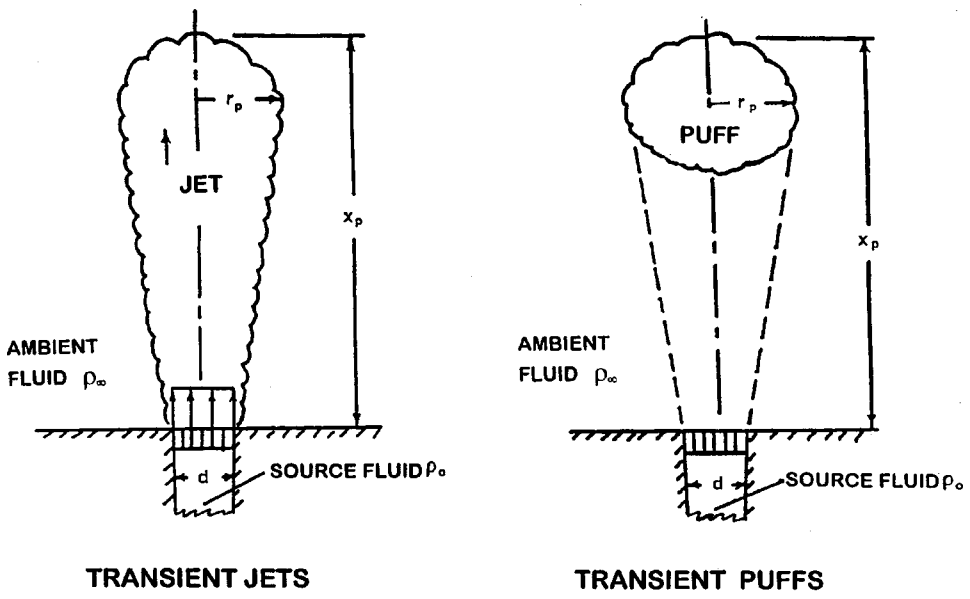

Fig. 3 Sketches of round turbulent flows from starting jets and puffs

Consideration of longer source operation times for puffs, or the corresponding behavior of steady nonbuoyant turbulent jets after termination of the source flow, was also undertaken, however, in order to better understand the transition of a starting jet into a puff, for conditions where the time of operation of the starting jet was sufficiently long to achieve self-preserving starting jet behavior. Such flows will be considered to be interrupted jets in the following, as noted earlier.

Results and Discussion

Results for nonbuoyant starting jets, puffs and interrupted jets (long puffs) are discussed in the following. Findings for starting jets and puffs include visualization of the flow, correlation of measured streamwise penetration distances as a function of time with the appropriate self-preserving scaling law from Eq. (1), and correlation of measured maximum radial penetration distances as a function of time with the appropriate self-preserving scaling law from Eq. (3). Findings for interrupted jets, however, are limited to correlation of measured streamwise penetration distances as a function of time with the appropriate self-preserving scaling law from Eq. (1). The ranges of test conditions, e.g., $(x_p-x_0)/d$, and values of n, C_x, and C_r of present and past studies of round nonbuoyant turbulent starting jets are summarized in Table 2. Similar information for round nonbuoyant turbulent puffs and interrupted jets is summarized in Table 3.

Starting Nonbuoyant Jets. Video images of a typical round nonbuoyant starting turbulent jet at various times after initiation of the flow are illustrated in Fig. 4. It can be seen that the flow boundary is relatively smooth near the jet exit but becomes roughened and turbulent-like a few diameters from the jet exit at small times after the start of injection. With increasing time, however, the transition to a roughened surface shifts toward the jet exit, a trend that has been observed by others for starting flows, see [3]. The turbulent region of the flow extends from the transition condition to the farthest streamwise penetration location of the nonbuoyant starting jet, which includes the vortex at the tip of the flow that has been observed during most previous studies of this flow, see Witze et al. [2], Kato et al. [3], Glezer et al. [12], Maxworthy [13,14], and references cited therein. The flow radius is seen to vary smoothly from the jet exit to the maximum radius condition near the tip of the flow, in the jet-like region of the flow, with no tendency to form a cap-like (or mushroom-cloud-like) structure associated with the leading vortex (the image at 4530 ms is somewhat untypical in this respect). This behavior of the flow radius is also similar to other observations of starting jets [3,4].

Normalized streamwise penetration distances of starting jets are plotted according to the self-preserving scaling of Eqs. (1) and (2) in Fig. 5. Near-source penetration properties exhibit a variety of behaviors depending on source properties, however, all the measurements follow the self-preserving correlation reasonably well at large dimensionless times, e.g., $(t-t_d)u_0/d>100$. These conditions correspond to normalized streamwise penetration distances, $(x_p-x_0)/d>30$, which is much nearer to the source than values of $(x-x_0)/d>100$ needed to reach self-preserving behavior for steady round buoyant turbulent plumes based on measured mean concentration and velocity distributions [17,18]. A possible explanation for these differences is the different fundamental stabilities of starting and steady turbulent flows; another explanation is that self-preserving behavior frequently is established at different distances from the source depending on the property that is observed [17,18].

Normalized maximum radial penetration distances (near the jet tip) of starting jets are plotted according to the self-preserving scaling of Eq. (3) in Fig. 6. Note that more near-source points are plotted for the radial penetration results appearing in Figs. 6–8

Table 2 Summary of properties of starting round nonbuoyant turbulent jets[a]

Source	Medium	Re_0	$(x_p-x_0)/d^b$	n	C_x	C_r
Present	Liquid	3,000-12,000	140	1/2	2.6	0.16
Adriani et al. [5]	Gas	5,200-53,000	20	---	---	---
Hyun et al. [4]	Gas	2,500	63	---	---	---
Kuoros et al. [1]	Liquid	53,000	21	---	---	0.09-0.10
Lahbabi et al. [29]	Liquid	2,600	---	1/2	2.9	---
Rizk [30]	Liquid	---	15	---	---	0.13
Witze [2]	Gas	2,400-9,200	70	1/2	2.5-3.2	---

[a]Injection of nonbuoyant turbulent round jets into still environments with parameters n, C_x and C_r based on Eqs. (1)-(3).
[b]Maximum streamwise penetration distance observed.

Table 3 Summary of properties of round nonbuoyant turbulent puffs, interrupted jets, and vortex rings[a]

Source	Medium	Re_0	$(x_p-x_0)/d^b$	n	C_x	C_r	$Q_0/(A_0/d)$
Puffs and Interrupted Jets:							
Present	Liquid	3,000-12,000	100	1/4	8.0	0.18	30-191
Kovasznay et al. [11]	Gas	---	18	---	---	0.29	---
Richards [10]	Liquid	---	---	1/4	---	0.25	---
Grigg & Stewart [9]	Liquid	500	15	1/4	4.0	---	6.5
Vortex Rings:							
Glezer & Coles	Liquid	24,000	100	1/4	3.2	---	3.4
Johnson [15]	Gas	---	70	2/3	---	---	0.8-3.1

[a]Injection of nonbuoyant turbulent round jets into still environments with parameters n, C_x and C_r based on Eqs. (1)-(3).
[b]Maximum streamwise penetration distance observed.

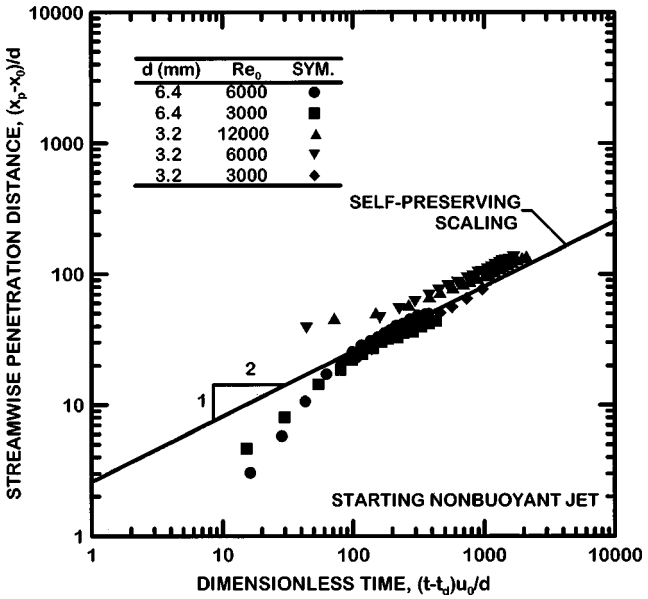

Fig. 5 Streamwise penetration distances of jets as a function of time for round nonbuoyant turbulent starting jets in still environments

than are shown in Fig. 5; these points are omitted from Fig. 5 to reduce overlap and improve clarity. The normalized radial penetration distance has relatively large values in the region nearest the source where the measurements were made; such behavior is expected, however, because this property becomes infinitely large at the virtual origin. The normalized maximum radial penetration distance decreases at first with increasing streamwise distance and after reaching a minimum at $(x_p-x_0)/d$ of 15–30, becomes relatively constant in the self-preserving region where $(x_p-x_0)/d>30$. For self-preserving conditions, $r_p/(x_p-x_0)=C_r=0.16$ from Table 2 which is shown on the plot for reference purposes. This value is comparable to the outer boundary of steady round turbulent jets based on measured distributions of mean velocities and mixture fractions, see [28]. It is also evident from the jet images illustrated in Fig. 4 that this value of $r_p/(x-x_0)$ is maintained along the sides of the jet within the self-preserving region.

A summary of existing measurements of the self-preserving properties of nonbuoyant starting jets appears in Table 2. The measurements of the streamwise penetration coefficient, C_x, by Witze et al. [2], Lahbabi et al. [29], and the present study agree within 23 percent of each other. The only measurements of the radial penetration coefficient, C_r, have been performed by Kouros et al. [1], Rizk [30], and the present study. Present values of C_r are significantly larger than those of Kouros et al. [1] and Rizk [30], which is readily explained by noting that the range of these measurements, $(x_p-x_0)/d$ of 15–21, generally corresponds to the region where flow radii are smaller than the present fully self-preserving region for $(x_p-x_0)/d>20-30$, see Fig. 6. Another possible reason for the differences between the present study and the results of Kouros et al. [1] is the existence of non-uniform source exit velocities in the study by Kouros et al. [1]. They also observe separation of the starting vortex from the rest of the jet which was not observed during the present study.

In addition to the streamwise and radial penetration coefficients, C_x and C_r, two additional parameters were measured to help describe the structure of nonbuoyant starting jets. The first, called the trailing jet radius, is plotted in Fig. 7 as a function of the streamwise distance. The starting nonbuoyant jet consists of a starting vortex and a trailing jet. The starting vortex was assumed to be circular with a radius given by the maximum radial penetration of the jet head. The portion of the jet behind this starting

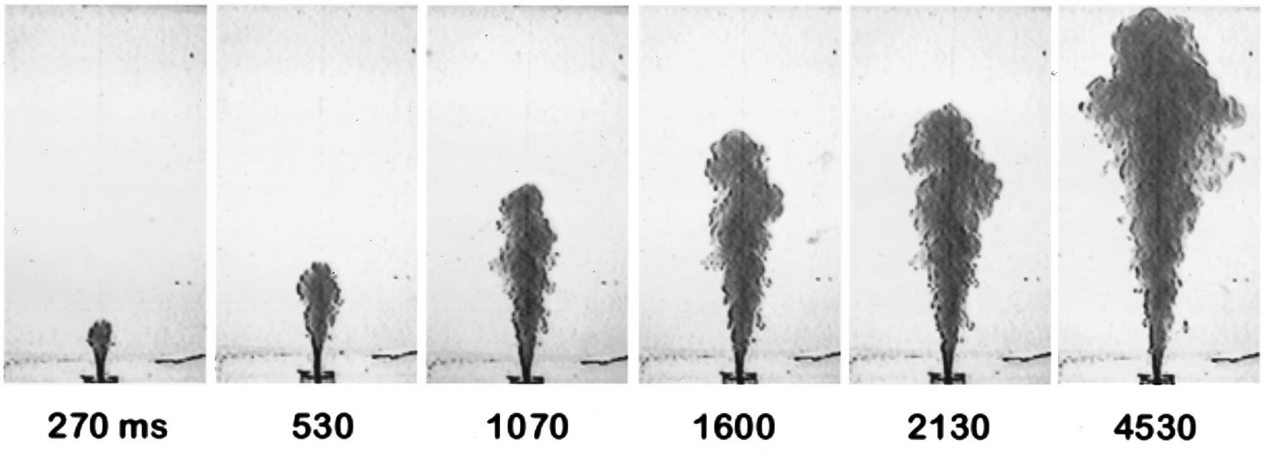

Fig. 4 Visualization of a round turbulent nonbuoyant starting jet in a still environment ($d=6.4$ mm, $u_0=460$ mm/s, and $Re_0=3000$)

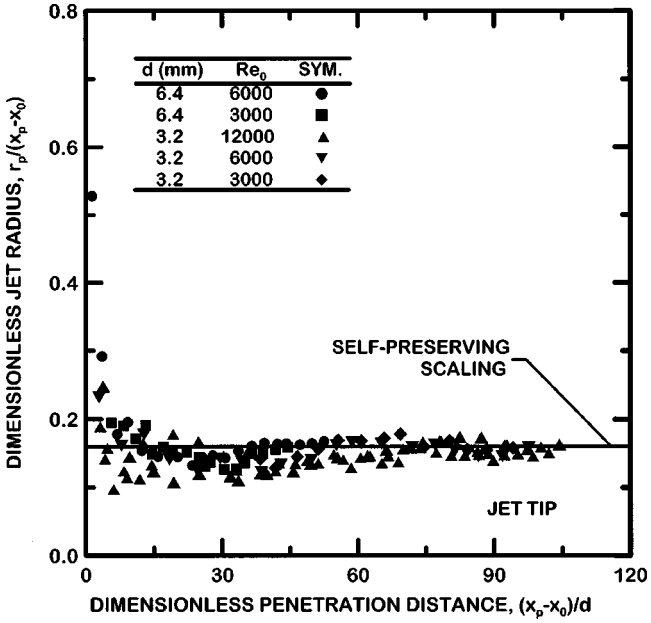

Fig. 6 Radial penetration distances of jet tips as a function of streamwise penetration distances for round nonbuoyant turbulent starting jets in still environments

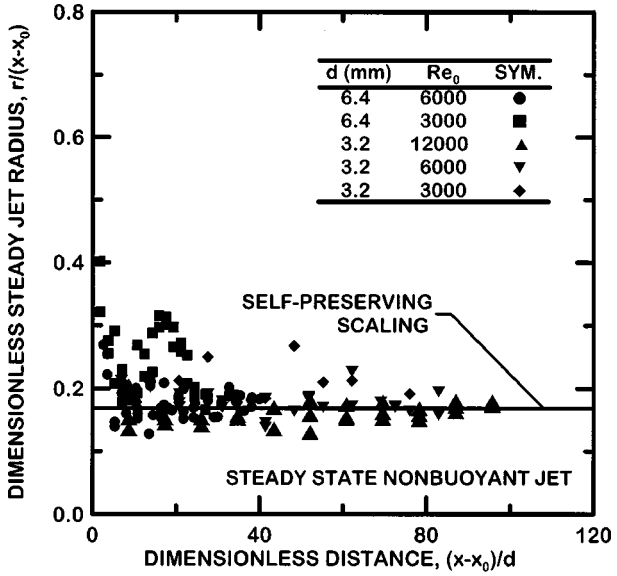

Fig. 8 Radial penetration distances of jets as a function of streamwise distances for steady turbulent round nonbuoyant jets in still environments

vortex was called the trailing jet (i.e., from the nozzle exit up to this location). The radius of the trailing jet was measured as a function of the streamwise distance and time. As can be seen from Fig. 7, the dimensionless trailing jet radius eventually reaches a mean value of $r_p/(x-x_0)$ of 0.18 for $(x_p-x_0)/d>30$ and generally behaves similar to the jet tip radius. The scatter in the data is due to the turbulent edges of the trailing jet.

The second additional parameter of interest for describing the behavior of nonbuoyant starting jets was the steady state jet radius. The starting nonbuoyant jet was allowed to run for a while. After the leading vortex has passed by, the turbulent jet becomes steady or stationary. The radius of this jet was measured as a function of streamwise distance and normalized to obtain values of the reduced steady jet radius illustrated in Fig. 8. The reduced steady state jet radius (the ordinate of Fig. 8) decreases with streamwise distance much like the maximum radial penetration distance and eventually settles down to a constant value of $r_p/(x-x_0)$ of 0.17 for $(x-x_0)/d>30$, which is very close to the trailing jet and maximum jet tip radii. This radial penetration distance is comparable to steady state jet radii measured during earlier studies, see [28] and references cited therein. It should be noted the present radial penetration distances are visible radii and are likely to be larger than the e^{-1} radius based on reduction of normalized distributions of velocities and concentrations of source fluid that are mentioned in the literature. The starting turbulent jet is not much wider than the steady state jet although there seems to be a trend for the steady state jet to be narrower. The trailing jet also seems to be very much like the steady state jet.

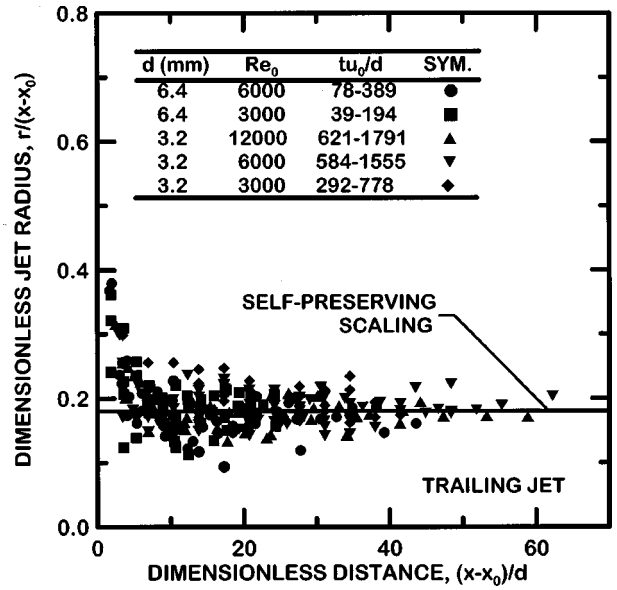

Fig. 7 Radial penetration distances of trailing jets as a function of streamwise penetration distances for round nonbuoyant turbulent starting jets

Nonbuoyant Puffs. Video images of a typical round nonbuoyant turbulent puff at various times after initiation of the flow are illustrated in Fig. 9. The present observations of puffs are qualitatively similar to earlier observations of thermals in the literature due to Scorer [31] and Turner [32]. The appearance of flow in the early stages when the source flow is maintained is naturally identical to the starting jet, as noted earlier. When the source flow is terminated, however, the leading turbulent vortex and the starting jet continue to penetrate into the still liquid with a thin stem connecting the base of the interrupted jet to the source. The stem continues to be stretched as the vortex and starting jet move away from the jet exit but the fluid velocity within the stem appears to be small and only a small fraction of the injected fluid was associated with the stem for most of the test conditions considered during the present investigation. The main difference between the motion of the upper regions of a starting jet and a puff is that the latter has a much smaller velocity once the source flow has been interrupted, which is evident from the different scaling rules of starting jets and puffs from Eqs. (1), (2), and (4), e.g., $x_p \sim t^n$ with $n=1/2$ and 1/4 respectively for starting jets and puffs. Another interesting difference between the behavior of starting jets and puffs is that the properties of the latter are affected by the amount of source fluid used to form the puff. Relatively large amounts of source fluid, as in Fig. 9, yield a leading vortex followed by an extended trailing jet-like region, whereas reduced amounts of source fluid tend to reduce the extent of he trailing

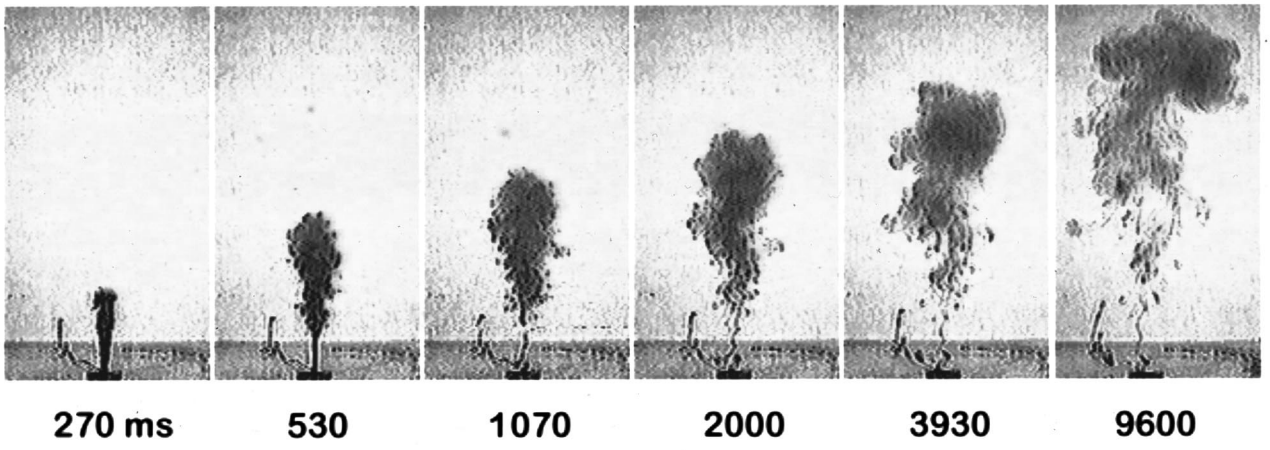

Fig. 9 Visualization of a round turbulent nonbuoyant puff in a still environment ($d=6.4$ mm, $u_0=930$ mm/s, $\mathrm{Re}_0=6000$, $Q_0/(A_0 d)=50$)

jet-like region, see [31]. In addition, continued penetration of the puff implies continued increases in the volume of the leading vortex; this causes the trailing jet to eventually be engulfed by the leading vortex followed by continued dilution of the leading vortex. Thus, there is significant potential for several different flow regimes during both the development and eventual self-preserving flow periods of the puff lifetime.

Normalized streamwise penetration distances of puffs are plotted according to the self-preserving scaling of Eqs. (1), (2), and (4) in Fig. 10. Present measurements agree reasonably well with self-preserving scaling of puffs for $(t-t_d)u_0/d>100$, and $(x_p-x_0)/d>20-30$, similar to the starting jet as long as $Q_0/(A_0 d)<127$. Flows having $Q_0/(A_0 d)\geqslant 127$, however, have sufficient time to approach self-preserving starting jet behavior (see Fig. 5) which delays the onset of self-preserving behavior. These flows really should be characterized as interrupted jets rather than puffs; treatment of interrupted jets by adjusting the location of the virtual origin will be discussed later. The different powers of the temporal growth of puffs compared to the starting jets, $n=1/4$ compared to 1/2, results in a much slower streamwise growth rate for puffs because the momentum supplied by the source is interrupted. Furthermore, there was no apparent change in self-preserving scaling when the trailing wake became fully engulfed by the leading vortex; this convenient state of affairs occurs, no doubt, because the self-preserving scaling of starting vortices and puffs as a function of time is the same, see [12,15].

A puff does not have any organized pattern of vorticity at injection. This is how it differs from a vortex ring. Puffs usually have been generated by placing a mesh/gauze at the exit of the injector to smooth out any existing flow patterns. This was not found to be necessary in the present tests because the flow at the jet exit corresponded to a fully developed turbulent pipe flow and was reasonably turbulent and disturbed. However, in spite of the differences between the structure and mechanism of growth of puffs and vortex rings, they follow the same scaling laws given by Eqs. (1), (2), and (4), as noted earlier.

Normalized maximum radial penetration distances for puffs are plotted according to the self-preserving scaling of Eq. (3) in Fig. 11. As before, more near-source points are plotted for the radial penetration results appearing in Fig. 11 than are shown in Fig. 10; these points are omitted from Fig. 10 to reduce overlap and improve clarity. The behavior here is qualitatively similar to results for the starting jet illustrated in Fig. 6; the main difference is that the normalized maximum radial penetration distance in the self-preserving region is larger for puffs than starting jets, e.g., $r_p/(x_p-x_0)=C_r=0.18$ compared to 0.16. These radial penetration distances for puffs and jets are comparable to results for buoyant thermals and plumes, however, from Sangras and Faeth [23], e.g., $r_p/(x_p-x_0)=0.22$ and 0.20, for thermals and plumes, respectively.

A summary of the properties measured during present and past studies of puffs, interrupted jets and vortex rings is given in Table 3. Grigg and Stewart [9] has been the only study, other than the present, that reports values of C_x, and this value differs from the present measurements by about 50 percent. This difference is probably explained by the relatively small source Reynolds number and modest distances from the source where the measurements of Grigg and Stewart [9] were made compared to the present measurements. The present radial penetration distances were measured and these results are also smaller than earlier measurements of Richards [10] and Kovasznay et al. [11] as shown in Table 3; a possible explanation for this behavior is that the earlier studies did not extend far enough from the source to reach self-preserving conditions. In addition, the characteristics of the puffs are likely to depend on $Q_0/(A_0 d)$ values, which is a measure of the amount of fluid used to form the puff, and the effect of this

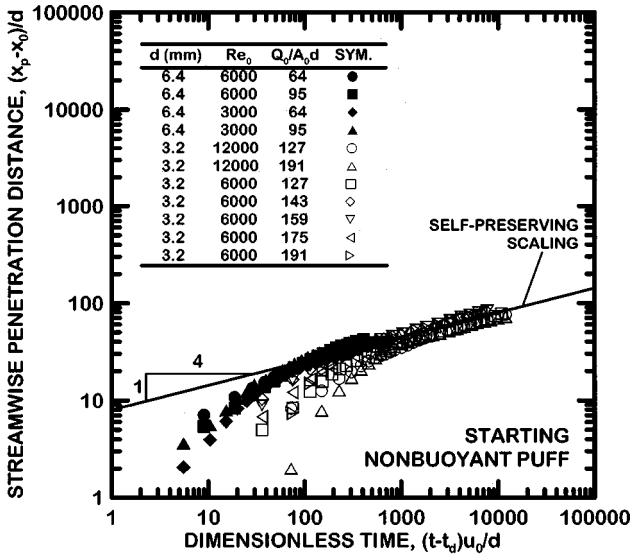

Fig. 10 Streamwise penetration distances of puffs as a function of time for round nonbuoyant turbulent puffs in still environments

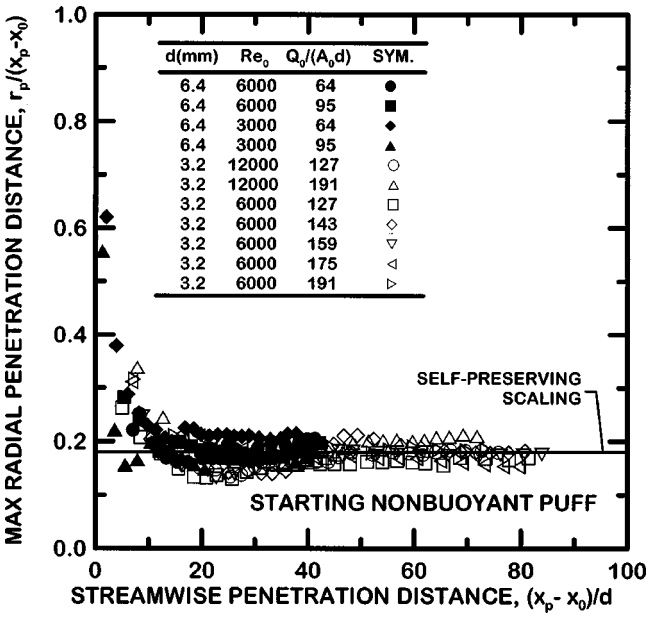

Fig. 11 Radial penetration distances of puffs as a function of streamwise penetration distances for round nonbuoyant turbulent puffs in still environments

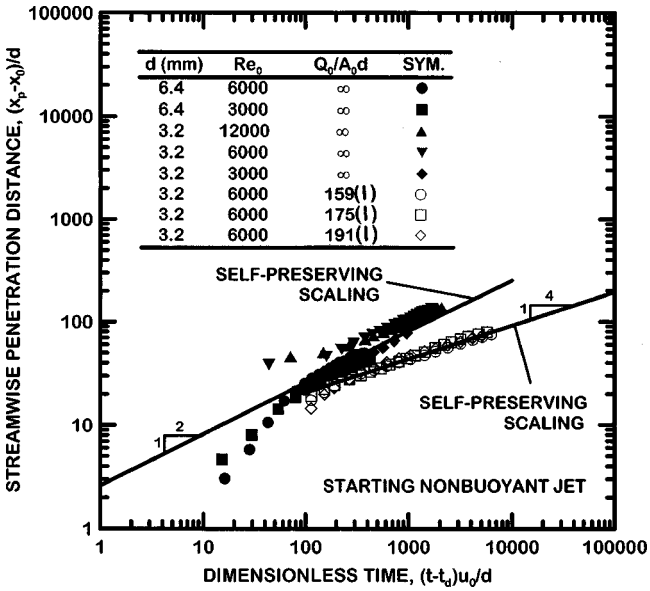

Fig. 12 Streamwise penetration distances as a function of time for round nonbuoyant turbulent starting ($Q_0/(A_0d)=\infty$) and interrupted (I) jets in still environments

parameter has only been studied to a limited degree thus far. Finally, the C_x value for a vortex ring reported by Glezer and Coles [12] is unusually large, $C_x=32$; the reasons for this unusually large value of C_x clearly merit consideration in view of existing observations of puffs.

Nonbuoyant Interrupted Jets. Normalized streamwise penetration distances of interrupted jets (denoted (I)) are plotted according to the self-preserving scaling of Eqs. (1), (2), and (4) in Fig. 12, along with results for starting jets ($Q_0/(A_0d)=\infty$) already shown in Fig. 5. Also note that the present results for interrupted jets are included in Fig. 10, along with the results for puffs. In this case, $Q_0/(A_0d)=159-191$ for the interrupted jets, so that the starting jet phase actually reached self-preserving behavior for nonbuoyant starting jets and $t^{1/2}$ scaling is achieved for a time. The flow to the starting jets was terminated at a values of dimensionless time of roughly 200. Then after a transition period, the flow proceeds according to the $t^{1/4}$ scaling expected for self-preserving puffs. Naturally, this period of transition is an exception to the observation that self-preserving behavior is observed for these flows at distances greater than 20–30 source diameters from the source. The net effect of this transition is to eventually achieve self-preserving puff behavior but with a virtual origin that is significantly displaced downstream from the source exit compared to puffs that do not have enough source fluid to reach self-preserving starting jet behavior. Thus, the boundary between puff and interrupted jet behavior can be conveniently defined by a transition of the virtual origin, as discussed next.

In order to resolve the behavior of displaced virtual origins with increasing amounts of injected fluid for interrupted jets, the location of the virtual origins are plotted as a function of the volume of injected fluid represented by the number of passage lengths of injected fluid, $Q_0/(A_0d)$, in Fig. 13. All data for puffs and interrupted jets obtained during the present investigation are shown in this figure. For small values of injected fluid, there is little influence of injected fluid volume on the location of the virtual origin (i.e., $Q_0/(A_0d)$ of up to roughly 120) and flows in this region can be conveniently defined as puffs. For large injected volumes, however, the virtual origin progressively increases as the injected volume increases and flows in this region are best described as interrupted jets. This behavior is easily explained when the injection

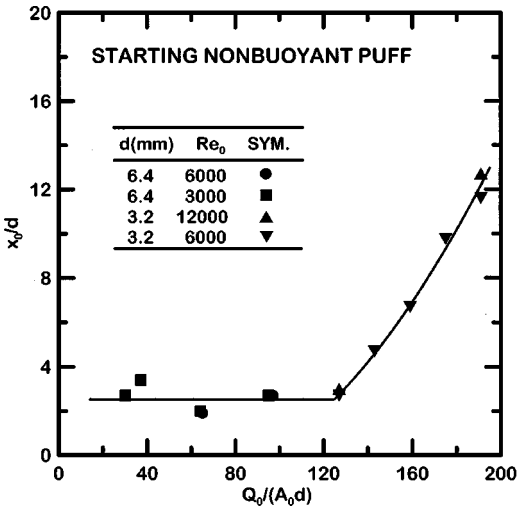

Fig. 13 Virtual origin locations of interrupted jets as a function of injected liquid volume for round nonbuoyant turbulent puffs and interrupted jets in still environments

times exceed times required for achieving self-preserving jet behavior for starting jets. At long times, however, the finite quantity of fluid injected by an interrupted jet dominates flow properties and transition to puff behavior is eventually completed at distances that are large compared to the location of the virtual origin.

Conclusions

The temporal development of round nonbuoyant turbulent starting jets, puffs and interrupted jets was studied both theoretically and experimentally. Conditions far from the source were emphasized where effects of source disturbances are lost, where the conserved properties of the flow control flow structure and where self-preserving behavior is approximated. The test conditions consisted of dye-containing fresh water sources injected into still fresh water with injector passage length/diameter ratios of 50 and

100 and other conditions as follows: jet exit diameters of 3.2 and 6.4 mm, jet exit Reynolds numbers of 3000–12,000, volume of injected fluid for puffs and interrupted jets of 30–191 passage diameters long and penetration lengths up to 140 source diameters. The major conclusions of the study are as follows:

1. The flows became turbulent near the jet exit, at distances of 0–5 source diameters; although near-source behavior varied significantly with source properties, self-preserving behavior was generally observed at distances greater than 20–30 source diameters from the source.
2. Within the self-preserving region, the dimensionless penetration distance, $(x_p - x_0)/d$, generally varied as a function of time in agreement with self-preserving predictions. This implies that the maximum penetration distance varied as a function of time to the following powers: 1/2 for nonbuoyant starting jets and 1/4 for nonbuoyant puffs.
3. Within the self-preserving region, the normalized maximum radius of the flow generally grew as a function of time in the same manner as the normalized penetration distance. This implies the following normalized values of maximum flow radius, $r_p/(x_p - x_0)$: 0.16 for nonbuoyant starting jets and 0.18 for nonbuoyant puffs. These maximum radii were observed at the position of the leading vortex.
4. For dimensionless source quantities of $Q_0/(A_0 d) = 120$ and greater, self-preserving starting jet behavior is reached before the source flow is interrupted. This flow eventually underwent transition to self-preserving puff behavior which exhibited a virtual source that was displaced considerably downstream from conditions where source quantities of the puffs were small; i.e., the virtual origin progressively increases as the injected volume increases, see Fig. 13. This transition period clearly is an exception of self-preserving behavior at distances larger than 20–30 source diameters from the source that were observed for the other flows considered during this investigation. The virtual origin for puffs for $Q_0/(A_0 d)$ less than 120, however, was independent of the injected fluid volume.

Acknowledgments

This research was supported by the United States Department of Commerce, National Institute of Standards and Technology, Grant Nos. 60NANB8D0081 and 60 NANB1D0006, with H. R. Baum of the Building and Fire Research Laboratory serving as Scientific Officer.

Nomenclature

A_0 = source cross sectional area
C_r = radial penetration coefficient, Eq. (3)
C_x = streamwise penetration coefficient, Eq. (1)
d = source diameter
L = source passage length
n = time exponent, Eq. (4)
Q_0 = volume of injected source fluid
$\dot{Q}_0$ = volumetric rate of injection of source fluid
Re_0 = source Reynolds number, $u_0 d/v_0$
r = radial distance
t = time
t^* = self-preserving time scale, Eqs. (1) and (4)
u = streamwise velocity
x = streamwise distance
v = kinematic viscosity
ρ = density

Subscripts

d = delay
max = maximum value
p = maximum penetration location
stop = effective end of source flow
0 = initial or virtual origin value
∞ = ambient value

References

[1] Kouros, H., Medina, R., and Johari, H., 1993, "Spreading Rate of an Unsteady Turbulent Jet," AIAA J., **31**, pp. 1524–1526.
[2] Witze, P. O., 1983, "Hot-Film Anemometer Measurements in a Starting Turbulent Jet," AIAA J., **21**, pp. 308–309.
[3] Kato, S. M., Groenwagen, B. C., and Breidenthal, R. E., 1987, "On Turbulent Mixing in Nonsteady Jets," AIAA J., **25**, pp. 165–168.
[4] Hyun, G. S., Nogami, M., Hosoyama, K., Senda, J., and Fujimoto, H., 1995, "Flow Characteristics in Transient Gas Jet," SAE Technical Paper 950847.
[5] Adriani, R., Coghe, A., and Cossali, G. E., 1996, "Near-Field Entrainment in Unsteady Gas Jets and Diesel Sprays: A Comparative Study," *Proceedings of the Combustion Institute*, Vol. 26, pp. 2549–2556.
[6] Hill, P. G., and Ouelette, P., 1999, "Transient Turbulent Gaseous Fuel Jets for Diesel Engines," ASME J. Fluids Eng., **121**, pp. 93–101.
[7] Rubas, P. J., Paul, M. A., Martin, G. C., Coverdill, R. E., Lucht, R. P., and Peters, J. E., 1998, "Methane Jet Penetration in a Direct-Injection Natural Gas Engine," SAE Technical Paper 980143.
[8] Birch, A. D., Brown, D. R., Dodson, M. G., and Swaffield, F., 1984, "The Structure and Concentration Decay of High Pressure Jets of Natural Gas," Combust. Sci. Technol., **36**, pp. 249–261.
[9] Grigg, H. R., and Stewart, R. W., 1962, "Turbulent Diffusion in a Stratified Fluid," J. Fluid Mech., **15**, pp. 174–186.
[10] Richards, J. M., 1965, "Puff Motions in Unstratified Surroundings," J. Fluid Mech., **21**, pp. 97–106.
[11] Kovasznay, L. S. G., Fujita, H., and Lee, R. L., 1974, "Unsteady Turbulent Puffs," Adv. Geophys., **18B**, pp. 253–263.
[12] Glezer, A., and Coles, D., 1990, "An Experimental Study of a Turbulent Vortex Ring," J. Fluid Mech., **211**, pp. 243–283.
[13] Maxworthy, T., 1974, "Turbulent Vortex Rings," J. Fluid Mech., **64**, pp. 227–239.
[14] Maxworthy, T., 1977, "Some Experimental Studies of Vortex Rings," J. Fluid Mech., **81**, pp. 465–495.
[15] Johnson, G. M., 1971, "An Empirical Model of the Motion of Turbulent Vortex Rings," AIAA J., **9**, pp. 763–764.
[16] Shariff, K., and Leonard, A., 1992, "Vortex Rings," Annu. Rev. Fluid Mech., **24**, pp. 235–279.
[17] Dai, Z., Tseng, L.-K., and Faeth, G. M., 1994, "Structure of Round, Fully-Developed, Buoyant Turbulent Plumes," ASME J. Heat Transfer, **116**, pp. 409–417.
[18] Dai, Z., Tseng, L.-K., and Faeth, G. M., 1995, "Velocity Statistics of Round, Fully-Developed Buoyant Turbulent Plumes," ASME J. Heat Transfer, **117**, pp. 138–145.
[19] Sangras, R., Dai, Z., and Faeth, G. M., 1998, "Mixing Structure of Plane Self-Preserving Buoyant Turbulent Plumes," ASME J. Heat Transfer, **120**, pp. 1033–1041.
[20] Sangras, R., Dai, Z., and Faeth, G. M., 1999, "Mixture Fraction Statistics of Plane Self-Preserving Buoyant Turbulent Adiabatic Wall Plumes," ASME J. Heat Transfer, **121**, pp. 837–843.
[21] Sangras, R., Dai, Z., and Faeth, G. M., 1999, "Buoyant Turbulent Jets and Plumes: I. Adiabatic Wall Plumes," Report No. NIST GCR CO-796, NIST, Gaithersburg, MD.
[22] Sangras, R., Dai, Z., and Faeth, G. M., 2000, "Velocity Statistics of Plane Self-Preserving Buoyant Turbulent Adiabatic Wall Plumes," ASME J. Heat Transfer, **122**, pp. 693–700.
[23] Sangras, R., and Faeth, G. M., 2000, "Round Turbulent Nonbuoyant Starting Jets and Puffs and Buoyant Starting Plumes and Thermals," *Proceedings of the 34th National Heat Transfer Conference*, Paper No. NHTC 2000-12174, ASME, New York.
[24] Steckler, K. D., Baum, H. R., and Quintiere, J. G., 1986, "Salt Water Modeling of Fire Induced Flows in Multicomponent Enclosures," Proceedings of the Combustion Institute, **21**, pp. 143–149.
[25] Wu, P.-K., Miranda, R. F., and Faeth, G. M., 1995, "Effects of Initial Flow Conditions on Primary Breakup of Nonturbulent and Turbulent Round Liquid Jets," Atomization Sprays, **5**, pp. 175–196.
[26] Johari, J., and Paduano, R., 1987, "Dilution and Mixing in an Unsteady Turbulent Jet," Exp. Fluids, **23**, pp. 272–280.

[27] List, E. J., 1982, ''Turbulent Jets and Plumes,'' Annu. Rev. Fluid Mech., **14**, pp. 189–212.
[28] Hinze, J. O., 1975, *Turbulence*, 2nd ed., McGraw-Hill, New York, pp. 534–585.
[29] Lahbabi, F. Z., Botee, J., Nuglisch, H. J., and Charnay, G., 1993, ''Analysis of Starting and Steady Turbulent Jets by Image Processing Techniques,'' *Experimental and Numerical Flow Visualization*, ASME Fluids Engineering Division, Vol. 172, pp. 315–321.
[30] Rizk, W., 1958, ''Experimental Studies of the Mixing Process and Flow Configurations in Two-Cycle Engine Scavenging,'' *Proceedings of the Institution of Mechanical Engineering*, Series E, Vol. 172, pp. 417–424.
[31] Scorer, R. S., 1957, ''Experiments on Convection of Isolated Masses of Buoyant Fluid,'' J. Fluid Mech., **2**, pp. 583–594.
[32] Turner, J. S., 1962, ''The Starting Plume in Neutral Surroundings,'' J. Fluid Mech., **13**, pp. 356–368.

Transient Coupled Radiation and Conduction in a Three-Layer Composite With Semitransparent Specular Interfaces and Surfaces

He-Ping Tan
e-mail: tan heping@power.hit.edu.cn

Jian-Feng Luo
e-mail: luo_jianfeng@yahoo.com

Xin-Lin Xia

Harbin Institute of Technology,
School of Energy Science and Engineering,
92 West Dazhi Street,
150001, Harbin,
People's Republic of China

Transient coupled radiative and conductive heat transfer in a three-layer absorbing and isotropically scattering composite with semitransparent specular interfaces and surfaces is investigated. The transient energy equation is solved by the full implicit control-volume method in combination with spectral band model. The radiative heat source term is calculated by the radiative transfer coefficients (RTCs), which are deduced by the ray tracing method in combination with Hottel and Sarofim's zonal method (Hottel H. C., and Sarofim A. F., 1967, Radiative Transfer, McGraw-Hill Book Company, New York). The effects of extinction coefficient, refractive index, and scattering albedo etc., on coupled heat transfer are studied under radiative and convective boundary conditions. The effect of isolating space on coupled heat transfer and the appearance of temperature peaks within the composite are investigated. It is found that temperature peaks also appear in the inner parts of an inhomogeneous semitransparent medium layer even though there is no convection cooling on the surfaces. This occurs when the absorbing coefficient of inner parts is higher than that of the parts close to the surfaces, and the two surfaces are semitransparent and subjected to an external radiation. [DOI: 10.1115/1.1418699]

Keywords: Composites, Conduction, Heat Transfer, Participating Media, Radiation, Transient

1 Introduction

In recent years, many researchers investigated transient coupled radiation and conduction heat transfer in a two-layer or multi-layer semitransparent composite. Gilpin et al. [1] presented a theoretical energy transfer model for the radiative transfer process within ice. Ignoring scattering and interface reflection, Tsai and Nixon [2] investigated transient coupled heat transfer in a multi-layer semitransparent composite with diffuse surfaces by the Runge-Kutta method in combination with the finite difference method. For a multi-layer absorbing-emitting composite with diffuse surfaces, using the finite variational-grid difference method, Timoshenko and Trener [3] analyzed radiative heat transfer under the condition of each layer being separated from another. Ho and Özisik [4,5] investigated transient coupled heat transfer in a two-layer isotropically scattering gray composite by the Galerkin method in combination with the finite difference technique. They considered the opaque surfaces and the unit refractive index value of each layer. Song and Viskanta [6] studied experimentally and numerically the melting and removal process of ice from a plastic slab by radiation heating. Siegel and Spuckler used diffuse approximate method and two-flux method in combination with Green's function to study steady and transient coupled heat transfer in a two-layer [7,8] or a multi-layer [9] absorbing and isotropically scattering semitransparent composite. Recently, Siegel [10] studied transient coupled heat transfer in two isotropically scattering gray layers with diffuse surfaces and separated by vacuum or transparent gas.

Using the ray tracing method in combination with Hottel and Sarofim's zonal method [11], Tan et al. [12] investigated the transient coupled heat transfer in a single absorbing and isotropically scattering layer. They divided the radiative transfer process into two subprocesses: emitting-attenuating-reflecting subprocess and absorbing-scattering subprocess. By tracing the transfer process layer by layer, Tan et al. [13] investigated the transient coupled heat transfer in a two-layer absorbing and isotropically scattering composite with semitransparent surfaces and interfaces.

The two-layer coupled heat transfer model has many restrictions for engineering application. For example, the optical window composed of two glass layers separated by vacuum or by air, is typically a three-layer condition. Therefore, in this paper, the transient coupled heat transfer in a three-layer absorbing and isotropically scattering composite with semitransparent and specular surfaces and interfaces is investigated. For multi-layer composites, it is difficult to trace layer by layer as Ref. [13] does. Therefore one-layer and two-layer radiative intensity quotient transfer models are put forward here to improve the tracing method. The two models are very convenient for solving the RTCs for the emitting-attenuating-reflecting subprocess in a three-layer composite, and based on this, the RTCs for the absorbing-scattering subprocess can be calculated. The radiative heat source term is calculated by the radiative transfer coefficients, and the transient energy equation is solved by the control volume method. With external radiation and convection boundary conditions, the effects of the refractive index, extinction coefficient, and the scattering albedo etc., on coupled heat transfer are investigated.

2 Physical Model and Governing Equation

2.1 Physical Model. As shown in Fig. 1, a three-layer absorbing and isotropically scattering semitransparent composite is located between two black surfaces $S_{-\infty}$ and $S_{+\infty}$, which denote the surroundings outside the two semitransparent boundary surfaces S_1 and S_2. The temperatures of $S_{-\infty}$ and $S_{+\infty}$ are $T_{-\infty}$ and $T_{+\infty}$, respectively. Surfaces S_1 and S_2 as well as interfaces P and Q are semitransparent and specular. The optical and thermal properties of the medium differ in each layer. The thickness, refractive index, and extinction coefficient of each layer are $L_b(b=1,2,3)$,

Contributed by the Heat Transfer Division for publication in the JOURNAL OF HEAT TRANSFER. Manuscript received by the Heat Transfer Division August 28, 2000; revision received July 25, 2001. Associate Editor: R. Skocypec.

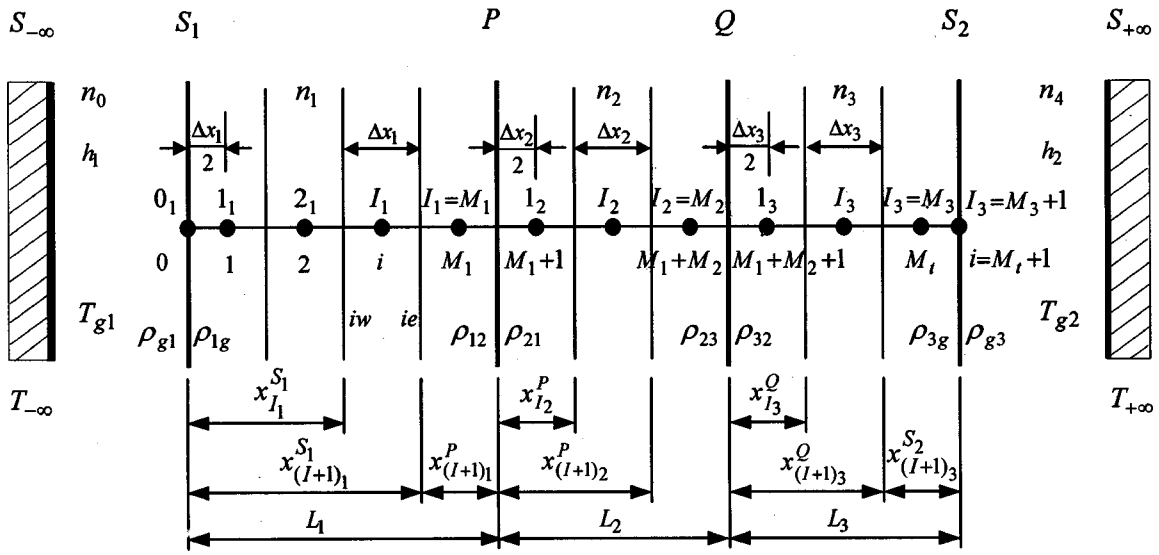

Fig. 1 Physical model of a three-layer semitransparent composite

n_b, and κ_b, respectively. The refractive indexes of the surroundings are n_0 and n_4 (equal to the refractive index of air n_g). Along the thickness, the three layers can be divided into M_1, M_2, and M_3 control volumes respectively. I_1, I_2, and I_3 are used to denote the I^{th} node in the first, second and third layer respectively. Let $M_t=M_1+M_2+M_3$, then the total node number is $M_t+2(0,1,\ldots,M_t+1)$ with node 0 locating S_1 and node M_t+1 locating S_2. For convenience, all the nodes are denoted by i except for the RTC expressions. If $i\leqslant M_1$, i represents the node in the first layer and $b=1$. If $M_1<i\leqslant M_1+M_2$, i represents the $(i-M_1)^{\text{th}}$ node in the second layer and the subscript $b=2$. Analogously, if $M_1+M_2<i\leqslant M_t$, i represents the $(i-M_1-M_2)^{\text{th}}$ node in the third layer and the subscript $b=3$. The parameters, such as κ_b, α_b, n_b, and ω_b etc., change with the wavelength, and they can be approximately expressed by a series of rectangular spectral bands. The total spectral band number is NB.

2.2 Discrete Governing Equation. The full implicit discrete energy equation of the i^{th} control volume of b^{th} layer is

$$\rho_b c_b \Delta x_b (T_i^{m+1}-T_i^m)/\Delta t = k_{ie}^{m+1}(T_{i+1}^{m+1}-T_i^{m+1})/(\delta x)_{ie} - k_{iw}^{m+1}(T_i^{m+1}-T_{i-1}^{m+1})/(\delta x)_{iw}+\Phi_i^{r,m+1}, \quad (1)$$

where $(\delta x)_{ie}$ and $(\delta x)_{iw}$ represent the distances between nodes i and $i+1$, and that between nodes i and $i-1$, respectively. For one-dimensional problem, the radiative heat source Φ_i^r of i^{th} control volume is equal to the difference of radiative heat fluxes at interfaces ie and iw. When the boundary surfaces S_1 and S_2 are semitransparent, the source term can be written as follows [14]:

$$\Phi_i^r = q_{ie}^r(T)-q_{iw}^r(T)=q_{ie}^r(T)-q_{(i-1)e}^r(T) = \sigma\sum_{k=1}^{NB}\left\{\sum_{j=1}^{M_t}[n_{j,k}^2[V_jV_i]_{k,t-t}^s A_{k,T_j}T_j^4-n_{i,k}^2[V_iV_j]_{k,t-t}^s A_{k,T_i}T_i^4] + [[S_{+\infty}V_i]_{k,t-t}^s A_{k,T_{+\infty}}T_{+\infty}^4-n_{i,k}^2[V_iS_{+\infty}]_{k,t-t}^s A_{k,T_i}T_i^4] + [[S_{-\infty}V_i]_{k,t-t}^s A_{k,T_{-\infty}}T_{-\infty}^4-n_{i,k}^2[V_iS_{-\infty}]_{k,t-t}^s A_{k,T_i}T_i^4]\right\} \quad 1\leqslant i\leqslant M_t, \quad (2)$$

where subscript k denotes the k^{th} spectral band.

3 RTCs for a Three-Layer Absorbing and Isotropically Scattering Semitransparent Composite

The RTC of element (surface or control volume) i versus element j is defined as the quotient that is absorbed by element j of the radiative energy emitted by element i. For the absorbing-scattering semitransparent medium, the transfer process includes (1) the radiative energy directly reaching element j, (2) the reflection by surfaces once or many times, and (3) the scattering by the media once or many times. The transfer process of radiative energy in absorbing scattering media can be divided into two subprocesses [12]: (1) emitting-attenuating-reflecting subprocess, for which the RTCs are presented by $(S_uS_v)_{k,t-t}^s$, $(S_uV_i)_{k,t-t}^s$, $(V_iS_u)_{k,t-t}^s$, and $(V_iV_j)_{k,t-t}^s$; (2) absorbing-scattering subprocess, for which the RTCs are presented by $[S_uS_v]_{k,t-t}^s$, $[S_uV_i]_{k,t-t}^s$, $[V_iS_u]_{k,t-t}^s$, and $[V_iV_j]_{k,t-t}^s$.

The specular reflectivity is calculated by the method used in Ref. [15], where Siegel divided the unpolarized radiative incidence into two equal, parallel and perpendicular components. And corresponding to the two components, the reflectivity is classified as parallel and perpendicular components, respectively, as shown in Appendix A.1.3.

3.1 RTCs for Emitting-Attenuating-Reflecting Subprocess. One-layer and two-layer basic radiative intensity transfer models are presented in Appendix A, where symbols **F** and **E**, respectively, represent the radiative intensity quotient transfer functions of the two models. For example, $\mathbf{E}_{P_2,2\sim3,k}^{Q_3}$ denotes the ratio of k^{th} spectral band radiative intensity emitted by P_2 to the amount arriving at Q_3 during the transfer process, in which the radiative intensity is reflected, attenuated by the second and the third layers for such many times that it can finally be ignored (almost to be zero). The ratio relates to the second and the third layers as well as their interfaces P_2, Q_2, Q_3, and S_2, but it doesn't relate to the other layer and interfaces. The subscript P_2 denotes the emitting surface; the superscript Q_3 denotes the receiving surface, and the subscript "2~3" denotes that the two-layer model is composed of the second and the third layers.

The total $(M_t+2)(M_t+2)$ RTCs of the three-layer composite can be classified into $(\text{number of layer}+2)^2=25$ categories and in theory, the following relations should be satisfied:

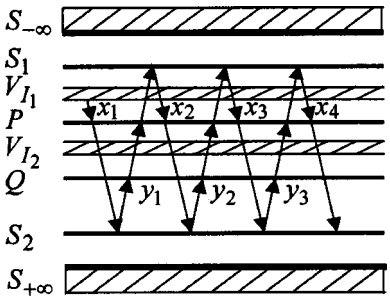

Fig. 2 Evaluation sketch map of RTC $(V_{I_1}V_{I_2})^s_{k,t-t}$

$$
\begin{aligned}
(S_{-\infty}V_{I_1})^s_{k,t-t} &= n^2_{1,k}(V_{I_1}S_{-\infty})^s_{k,t-t}\\
n^2_{1,k}(V_{I_1}S_{+\infty})^s_{k,t-t} &= (S_{+\infty}V_{I_1})^s_{k,t-t}\\
(S_{-\infty}V_{I_2})^s_{k,t-t} &= n^2_{2,k}(V_{I_2}S_{-\infty})^s_{k,t-t}\\
n^2_{2,k}(V_{I_2}S_{+\infty})^s_{k,t-t} &= (S_{+\infty}V_{I_2})^s_{k,t-t}\\
(S_{-\infty}V_{I_3})^s_{k,t-t} &= n^2_{3,k}(V_{I_3}S_{-\infty})^s_{k,t-t}\\
n^2_{3,k}(V_{I_3}S_{+\infty})^s_{k,t-t} &= (S_{+\infty}V_{I_3})^s_{k,t-t}\\
(V_{I_1}V_{J_1})^s_{k,t-t} &= (V_{J_1}V_{I_1})^s_{k,t-t}\\
n^2_{1,k}(V_{I_1}V_{I_2})^s_{k,t-t} &= n^2_{2,k}(V_{I_2}V_{I_1})^s_{k,t-t}\\
(V_{I_2}V_{J_2})^s_{k,t-t} &= (V_{J_2}V_{I_2})^s_{k,t-t}\\
n^2_{1,k}(V_{I_1}V_{I_3})^s_{k,t-t} &= n^2_{3,k}(V_{I_3}V_{I_1})^s_{k,t-t}\\
(V_{I_3}V_{J_3})^s_{k,t-t} &= (V_{J_3}V_{I_3})^s_{k,t-t}\\
n^2_{2,k}(V_{I_2}V_{I_3})^s_{k,t-t} &= n^2_{3,k}(V_{I_3}V_{I_2})^s_{k,t-t}
\end{aligned}
\tag{3}
$$

Fifteen of the 25 categories are listed in Appendix B, and the other ten can be obtained from Eq. (3).

The detailed deductive process of RTC $(V_{I_1}V_{I_2})^s_{k,t-t}$ is exemplified as following. For convenience, the subscript k is omitted in the deduction. As shown in Fig. 2, three basic radiative intensity transfer models are employed, which are the one-layer model composed of the first layer, the one-layer model composed of the second layer, and the two-layer model composed of the second and the third layers.

1 The total quotient of the radiative intensity emitted by V_{I_1} and finally arriving at P_1
   - *a* In the first layer, the quotient of the radiative intensity emitted by V_{I_1} at angle θ and arriving at P_1 for the first transfer process is expressed as $x_1=\mathbf{F}^{P_1}_{V_{I_1}}$.
   - *b* $\gamma(\theta)_{12}$ part of the above quotient penetrates into the two-layer model from interface P. After transferring in the two-layer model, a quotient of $x_1\gamma(\theta)_{12}\mathbf{E}^{P_2}_{P_2,2\sim3}$ reaches interface P_2, then $\gamma(\theta)_{21}$ part of the quotient returns into the first layer. And then after transferring again in the first layer, the quotient of the intensity arriving at P_1 for the second time becomes $x_2=x_1\gamma(\theta)_{12}\mathbf{E}^{P_2}_{P_2,2\sim3}\gamma(\theta)_{21}\mathbf{F}^{P_1}_{P_1}$.
   - *c* Repeat step 2, the quotient of the radiative intensity arriving at P_1 for the third time can be obtained, which is $x_3=x_2\gamma(\theta)_{12}\mathbf{E}^{P_2}_{P_2,2\sim3}\gamma(\theta)_{21}\mathbf{F}^{P_1}_{P_1},\ldots$. Where $x_1,x_2,x_3,\ldots$, is an infinite geometric series with a common ratio $\beta_3=\gamma(\theta)_{12}\mathbf{E}^{P_2}_{P_2,2\sim3}\gamma(\theta)_{21}\mathbf{F}^{P_1}_{P_1}(\beta_3<1)$. So, the total quotient of the intensity emitted by V_{I_1} and finally arriving at P_1 is derived as $x=\Sigma^{\infty}_{i=1}x_i=\mathbf{F}^{P_1}_{V_{I_1}}/(1-\beta_3)$.

2 Similarly, the total quotient of the radiative intensity emitted by V_{I_1} at angle θ and finally reaching Q_3 can be expressed as

$$y=\sum_{i=1}^{\infty}y_i=\left(\sum_{i=1}^{\infty}x_i\right)\gamma(\theta)_{12}\mathbf{E}^{Q_3}_{P_2,2\sim3}=\mathbf{F}^{P_1}_{V_{I_1}}\gamma(\theta)_{12}\mathbf{E}^{Q_3}_{P_2,2\sim3}/(1-\beta_3)$$

3 Parts of the total quotients x and y, denoted by $\gamma(\theta)_{12}$ and $\gamma(\theta)_{32}$, respectively, penetrate into the second layer. Applying the one-layer model function to the second layer, then the final quotient of the radiative intensity emitted by V_{I_1} and finally attenuated by V_{I_2} can be expressed as

$$
\begin{aligned}
\Gamma &= x\gamma(\theta)_{12}\mathbf{F}^{V_{I_2}}_{P_2}+y\gamma(\theta)_{32}\mathbf{F}^{V_{I_2}}_{Q_2}\\
&=\left(\mathbf{F}^{P_1}_{V_{I_1}}\gamma(\theta)_{12}\mathbf{F}^{V_{I_2}}_{P_2}+\mathbf{F}^{P_1}_{V_{I_1}}\gamma(\theta)_{12}\mathbf{E}^{Q_3}_{P_2,2\sim3}\gamma(\theta)_{32}\mathbf{F}^{V_{I_2}}_{Q_2}\right)\Big/(1-\beta_3)
\end{aligned}
\tag{4}
$$

The transmissivity $\gamma(\theta)$ and reflectivity $\rho(\theta)$ in Eq. (4) are functions of the parallel and the perpendicular components, as shown in Appendix A.1.3. So, corresponding to the two components, the attenuation quotient Γ can be divided into two parallel and the perpendicular components $\Gamma_{\parallel}$ and $\Gamma_{\perp}$. Therefore, for the incidence of an unpolarized radiative intensity, the total attenuation quotient can finally be expressed as $(\Gamma_{\parallel}+\Gamma_{\perp})/2$. Then by integrating the equation over the hemispherical space, the RTC $(V_{I_1}V_{I_2})^s_{k,t-t}$ can be solved. The integrating limits are closely related to the total reflection, and so they are related to the relative magnitude of the refractive indexes of the layers. The three integrating results for different relative relations of the refractive indexes are presented below.

a When $n_1<n_2<n_3$,

$$
\begin{aligned}
(V_{I_1}V_{I_2})^s_{k,t-t} &= \int_0^{\theta_{1g}}(\Gamma_{\parallel}+\Gamma_{\perp})\sin\theta\cos\theta d\theta\\
&\quad+\int_{\theta_{1g}}^{\pi/2}(\Gamma_{\parallel}+\Gamma_{\perp})\sin\theta\cos\theta d\theta
\end{aligned}
\tag{5a}
$$

b When $n_2<n_1<n_3$,

$$
\begin{aligned}
(V_{I_1}V_{I_2})^s_{k,t-t} &= \int_0^{\theta_{1g}}(\Gamma_{\parallel}+\Gamma_{\perp})\sin\theta\cos\theta d\theta\\
&\quad+\int_{\theta_{1g}}^{\theta_{12}}(\Gamma_{\parallel}+\Gamma_{\perp})\sin\theta\cos\theta d\theta
\end{aligned}
\tag{5b}
$$

c When $n_1>n_2>n_3$,

$$
\begin{aligned}
(V_{I_1}V_{I_2})^s_{k,t-t} &= \int_0^{\theta_{1g}}(\Gamma_{\parallel}+\Gamma_{\perp})\sin\theta\cos\theta d\theta\\
&\quad+\int_{\theta_{1g}}^{\theta_{13}}(\Gamma_{\parallel}+\Gamma_{\perp})\sin\theta\cos\theta d\theta\\
&\quad+\int_{\theta_{13}}^{\theta_{12}}(\Gamma_{\parallel}+\Gamma_{\perp})\sin\theta\cos\theta d\theta
\end{aligned}
\tag{5c}
$$

In Eq. (4), the values of $\gamma(\theta)$ and $\rho(\theta)$ may change if total reflection occurs, so this causes Γ to be an incontinuous function with respect to the variable $\theta\in[0,\pi/2]$. But if the integrating region $[0,\pi/2]$ is divided into many integrating intervals according to the values of critical angles arranged from small to large, then Γ becomes a continuous function within any of the intervals and differs from each other within different intervals. For example, in Eq. (5*b*), the integrating region $[0,\pi/2]$ is divided into three inter-

vals of $[0,\theta_{1g}]$, $[\theta_{1g},\theta_{12}]$ and $[\theta_{12},\pi/2]$, and $\int_{\theta_{12}}^{\pi/2}(\Gamma_{\parallel}+\Gamma_{\perp})\sin\theta\cos\theta d\theta=0$ because of the total reflection.

Because the arrangement of refractive index is very complex for a three-layer composite, only the RTCs for $n_2<n_1<n_3$ are presented in Appendix B. For other arrangements, however, the function Γ in each RTC formulation is of the same form but of different integrating limits, as shown in Eq. (5). If a criterion is defined as that in Appendix A.1.3, and the integrating limits are arranged from small to large according to the values of the critical angles, all the expressions in Appendix B can fit the cases with other refractive index arrangement as well.

3.2 RTCs for Absorbing-Scattering Subprocess. The RTCs deduced above only validate for an absorbing-emitting composite. For an absorbing and isotropically scattering composite, however, the quotient of radiative energy represented by RTCs $(S_uS_v)^s_{k,t-t}$, $(S_uV_i)^s_{k,t-t}$, etc., will be redistributed. For convenience, subscripts k, $t-t$ and superscript s are omitted in following deduction, and subscript a is introduced to denote the absorption quotient.

Let $\eta_i=1-\omega_i$, and notice that only the media scatters but the surfaces and interfaces don't. The isotropically scattering effect can be considered as follows (Take $[V_iV_j]$ as an example). After the first scattering, $[V_iV_j]_a^{1^{st}}=(V_iV_j)\eta_j$. After the second scattering, $[V_iV_j]_a^{2^{nd}}=[V_iV_j]_a^{1^{st}}+\Sigma_{l_2=1}^{M_t}(V_iV_{l_2})\omega_{l_2}(V_{l_2}V_j)\eta_j$. After the third scattering,

$$[V_iV_j]_a^{3^{rd}}=[V_iV_j]_a^{2^{nd}}+\Sigma_{l_2=1}^{M_t}(V_iV_{l_2})\omega_{l_2}[\Sigma_{l_3=1}^{M_t}(V_{l_2}V_{l_3})\omega_{l_3}(V_{l_3}V_j)\eta_j].$$

Then, by induction, after the n^{th} scattering,

$$[V_iV_j]_a^{n^{th}}=[V_iV_j]_a^{(n-1)^{th}}+\sum_{l_2=1}^{M_t}(V_iV_{l_2})\omega_{l_2}\left\{\sum_{l_3=1}^{M_t}(V_{l_2}V_{l_3})\omega_{l_3}\left\{\sum_{l_4=1}^{M_t}(V_{l_3}V_{l_4})\omega_{l_4}\cdots\left\{\sum_{l_{n-1}=1}^{M_t}(V_{l_{n-2}}V_{l_{n-1}})\omega_{l_{n-1}}\left[\sum_{l_n=1}^{M_t}(V_{l_{n-1}}V_{l_n})\omega_{l_n}(V_{l_n}V_j)\eta_j\right]\right\}\right\}\right\}. \tag{6a}$$

The deducing process of the rest RTCs $[S_uS_v]$, $[S_uV_i]$, and $[V_iS_u]$ is similar, so after the n^{th} scattering,

$$[S_uV_j]_a^{n^{th}}=[S_uV_j]_a^{(n-1)^{th}}+\sum_{l_2=1}^{M_t}(S_uV_{l_2})\omega_{l_2}\left\{\sum_{l_3=1}^{M_t}(V_{l_2}V_{l_3})\omega_{l_3}\left\{\sum_{l_4=1}^{M_t}(V_{l_3}V_{l_4})\omega_{l_4}\cdots\left\{\sum_{l_{n-1}=1}^{M_t}(V_{l_{n-2}}V_{l_{n-1}})\omega_{l_{n-1}}\left[\sum_{l_n=1}^{M_t}(V_{l_{n-1}}V_{l_n})\omega_{l_n}(V_{l_n}V_j)\eta_j\right]\right\}\right\}\right\} \tag{6b}$$

$$[V_iS_u]_a^{n^{th}}=[V_iS_u]_a^{(n-1)^{th}}+\sum_{l_2=1}^{M_t}(V_iV_{l_2})\omega_{l_2}\left\{\sum_{l_3=1}^{M_t}(V_{l_2}V_{l_3})\omega_{l_3}\left\{\sum_{l_4=1}^{M_t}(V_{l_3}V_{l_4})\omega_{l_4}\cdots\left\{\sum_{l_{n-1}=1}^{M_t}(V_{l_{n-2}}V_{l_{n-1}})\omega_{l_{n-1}}\left[\sum_{l_n=1}^{M_t}(V_{l_{n-1}}V_{l_n})\omega_{l_n}(V_{l_n}S_u)\right]\right\}\right\}\right\} \tag{6c}$$

$$[S_uS_v]_a^{n^{th}}=[S_uS_v]_a^{(n-1)^{th}}+\sum_{l_2=1}^{M_t}(S_uV_{l_2})\omega_{l_2}\left\{\sum_{l_3=1}^{M_t}(V_{l_2}V_{l_3})\omega_{l_3}\left\{\sum_{l_4=1}^{M_t}(V_{l_3}V_{l_4})\omega_{l_4}\cdots\left\{\sum_{l_{n-1}=1}^{M_t}(V_{l_{n-2}}V_{l_{n-1}})\omega_{l_{n-1}}\left[\sum_{l_n=1}^{M_t}(V_{l_{n-1}}V_{l_n})\omega_{l_n}(V_{l_n}S_v)\right]\right\}\right\}\right\}, \tag{6d}$$

where subscripts $u,v=-\infty$ or $+\infty$.

In fact, before calculating the RTCs for the absorbing-scattering subprocess, the RTCs for the emitting-attenuating-reflecting subprocess must be first normalized as follows.

$$(V_iV_j)^*=(V_iV_j)/(4\kappa_b\Delta x_b)\quad V_i\in b^{th}\ \text{layer} \tag{7a}$$

$$(V_iS_u)^*=(V_iS_u)/(4\kappa_b\Delta x_b)\quad V_i\in b^{th}\ \text{layer} \tag{7b}$$

$$(S_uV_i)^*=(S_uV_i) \tag{7c}$$

$$(S_uS_v)^*=(S_uS_v), \tag{7d}$$

where superscript "*" denotes the normalized values, and subscripts $i,j=1\sim M_t$. The inverse operation will be done after the calculation of the n^{th} scattering.

3.3 Validation of RTCs and Numerical Method. In theory, the correctness of RTCs can be validated by Eq. (3) and the following equations:

$$\sum_{j=1}^{M_t}(V_iV_j)^s_{k,t-t}+(V_iS_{-\infty})^s_{k,t-t}+(V_iS_{+\infty})^s_{k,t-t}=4\kappa_{b,k}\Delta x_b \qquad V_i\in b^{th}\ \text{layer} \tag{8a}$$

$$(S_{-\infty}S_{-\infty})^s_{k,t-t}+\sum_{j=1}^{M_t}(S_{-\infty}V_j)^s_{k,t-t}+(S_{-\infty}S_{+\infty})^s_{k,t-t}=1 \tag{8b}$$

$$(S_{+\infty}S_{-\infty})^s_{k,t-t}+\sum_{j=1}^{M_t}(S_{+\infty}V_j)^s_{k,t-t}+(S_{+\infty}S_{-\infty})^s_{k,t-t}=1. \tag{8c}$$

Equation (3) and Eq. (8) are examined during our calculation, and they are satisfied. This proves that the RTC expressions are correct in theory.

Table 1 Effect of control volume number on dimensionless temperature and heat flux at steady state

$M_b(b=1,2,3)$	dimensionless temperature Θ		dimensionless steady state heat flux $\tilde{q}^t$
	$X=1/6$	$X=5/6$	
50	0.8557432	0.9057453	0.076933
100	0.8558607	0.9059406	0.077056
150	0.8558832	0.9059781	0.077080

The radiative heat source term Φ_i^r is a nonlinear function of temperature, so it should be linearized by Patankar method [16]:

$$\Phi_i^{r,m,n+1}=\Phi_i^{r,m,n}+(d\Phi_i^r/dT_i)^{m,n}(T_i^{m,n+1}-T_i^{m,n})$$
$$=Sc_i^{m,n+1}+Sp_i^{m,n+1}T_i^{m,n+1}, \quad (9)$$

where superscript n and $n+1$ denote the n^{th} and $(n+1)^{\text{th}}$ iterative calculation, respectively; Sc_i represents the constant part of Φ_i^r; Sp_i is the modulus of T_i, and $Sp\leqslant 0$ [14]. By solving the linearized equations by tri-diagonal matrix algorithm (TDMA), the temperatures of all nodes can be evaluated.

The RTC expressions, such as Eq. (5), are numerically calculated by a 30-point improved Gaussian quadrature scheme. Except for special indication, the precision ($eps0$) chosen for the Gaussian quadrature scheme is $eps0=10^{-8}$ in the following calculations.

The solution is assumed to converge at each time step, m, when, for each node, the difference in temperatures between iterations n, and $n+1$ satisfies $|T_i^{m,n+1}-T_i^{m,n}|<10^{-5}$ K. A constant time step $\Delta t=t/100$ or $\Delta t^*=t^*/100$ is applied. The field of temperature is assumed to be stabilized when the difference of the temperatures between two time steps m and $m+1$ satisfies $|T_i^{m+1,nf}-T_i^{m,nf}|<10^{-5}$ K at each node. Here, the superscript nf designates the final iterative solution.

In all calculations, the convergence of the solution with respect to the grid size is also assured. The node number of each layer M_b is chosen until the total heat flux and the temperature at each node almost reaches a constant value, as shown in Table 1.

4 Results and Discussion

4.1 Comparison With Ref. [15]. Siegel [15] investigated the effects of refractive index, specular and diffuse surfaces on radiative heat transfer in an isothermal layer. Using a three spectral band model: $\alpha_k=20$, 400, 10000 m^{-1}, for $\lambda=0\sim2.7$, $2.7\sim4.4$, $4.4\sim\infty$ μm respectively, he considered the radiative cooling in detail. As shown in Fig. 3, the dotted lines are the results of Ref. [15] with respect to specular reflection, and the solid lines are the results of this paper. The calculating parameters are as following: $T_{-\infty}=T_{+\infty}=300$ K, $T_r=T_0$, $L_1=L_3=0.0025$ m, $L_2=10^{-10}$ m, and $M_1=M_2=M_3=1$. The other corresponding parameters of the three layers are the same. The initial temperature T_0 and refractive index values are presented in the figure. And then the temperature result $T_1(=T_3)$ of this paper is equivalent to the temperature of an isothermal layer. As shown in Fig. 3, the solid lines agree very well with the dotted lines. This proves that the specular model presented in this paper is correct.

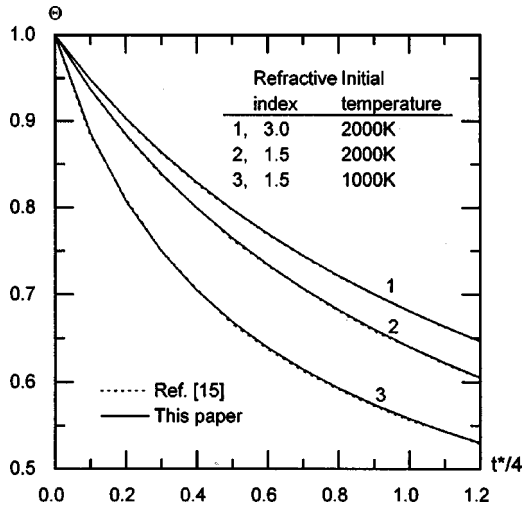

Fig. 3 Radiative heat transfer in an isothermal layer with specular surfaces

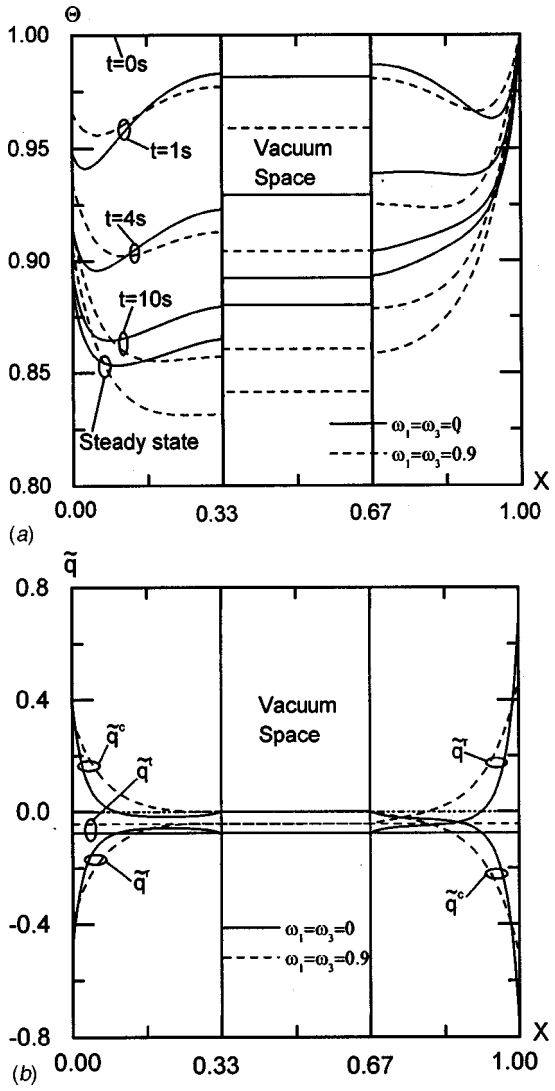

Fig. 4 Heat transfer in two semitransparent layers separated by vacuum space: (*a*) temperature distributions; and (*b*) heat fluxes at steady state

4.2 Effect of Isolating Space on Transient Coupled Heat Transfer. The three-layer model can be applied to investigate the condition that two layers are separated by a vacuum space. Assume the conductivity and specific heat capacity of the second layer to be infinitesimal, such as 10^{-100}, the optical thickness to be chosen as $\tau_2=10^{-8}$ with the thickness $L_2=L_1=L_3=0.01$ m, and let $n_2=1$, then the second layer actually is a vacuum space. Assuming that h_2 is an infinite, such as $h_2=10^{10}$ W m^{-2} K^{-1},

then the temperature of the surface S_2 is a constant value $T_{S_2} = T_{g2}$. The other calculating parameters are $n_1 = 1.8$, $n_3 = 1.5$, $\kappa_1 = \kappa_3 = 500\,\mathrm{m}^{-1}$, $\omega_1 = \omega_3 = 0$, or 0.9, $h_1 = 200\,\mathrm{W\,m^{-2}\,K^{-1}}$, $N_1 = N_3 = 0.07$, $\rho_1 c_1 = \rho_3 c_3 = 10^5\,\mathrm{J\,m^{-3}\,K^{-1}}$, $T_0 = T_r = 1000\,\mathrm{K}$, $T_{-\infty} = T_{+\infty} = 300\,\mathrm{K}$, and $T_{g1} = T_{g2} = 1000\,\mathrm{K}$. The temperature distribution and heat flux results are presented in Fig. 4(*a*) and Fig. 4(*b*), in which the solid lines are for $\omega_1 = \omega_3 = 0$, and the dashed lines are for $\omega_1 = \omega_3 = 0.9$.

The number of control volumes of each sublayer is chosen as $M_1 = M_2 = M_3 = 100$, which can make enough precision for the calculation, as shown in Table 1. The precision for Gaussian quadrature scheme is chosen as $eps0 = 10^{-5}$, with which the maximal absolute error for Eq. (3) and Eq. (8) is about 4.0×10^{-8}, and this is precise enough for the calculations.

As shown in Fig. 4(*a*), in the early stage of the process, the region influenced by convective boundary condition is only a very small part adjacent to the surface, while that affected by the radiative boundary condition is all over the composite because the radiative transfer rate is much greater than the conductive diffusion rate. Therefore, under the coupling effect of the radiative cooling and the convective heating on both surfaces, two minimum temperatures appear in the first and the third layer. With the evolution of the process, the intensive convection heating on the right surface not only results in a constant high temperature of the surface but also overcomes the effect of the radiative cooling and causes the minimum temperature to disappear in the third layer. For the first layer, however, when the media don't scatter (solid lines), the convection heating on the left surface is not strong enough to overcome the cooling effect of the radiation, and the minimum temperature remains until the steady state is reached; when the media scatters (dashed lines), the radiative cooling effect decreases, and the minimum temperature may disappear with the evolution of the process.

The abrupt change of the thermal properties on both sides of each interface causes the temperature to change abruptly therein. The temperature gradients in the first and the third layers tend to be zero at the two interior interfaces (Fig. 4(*a*)). This indicates that there is no conductive heat flux passing through the interfaces, as shown in Fig. 4(*b*). It should be pointed out that the temperature distributions of the vacuum space shown in Fig. 4(*a*) are just linking lines, and its effects on the temperature distributions of the first and the third layers are equivalent to those of vacuum. When the media scatter, as shown by the dashed lines in Fig. 4(*a*), the temperatures of surface S_1 and its nearby regions become higher and the central temperatures become lower.

As shown in Fig. 4(*b*), the emitting capacity of the third layer is stronger than that of the first layer because of its higher temperature, so a negative heat flux passes through the composite at the steady state. Within the vacuum space, there is no conductive heat flux but a constant negative radiative heat flux. This agrees with the vacuum assumptions. The dimensionless steady heat flux is $\tilde{q}^t = -0.07706$ for the solid lines, and that is $\tilde{q}^t = -0.04356$ for the dashed lines.

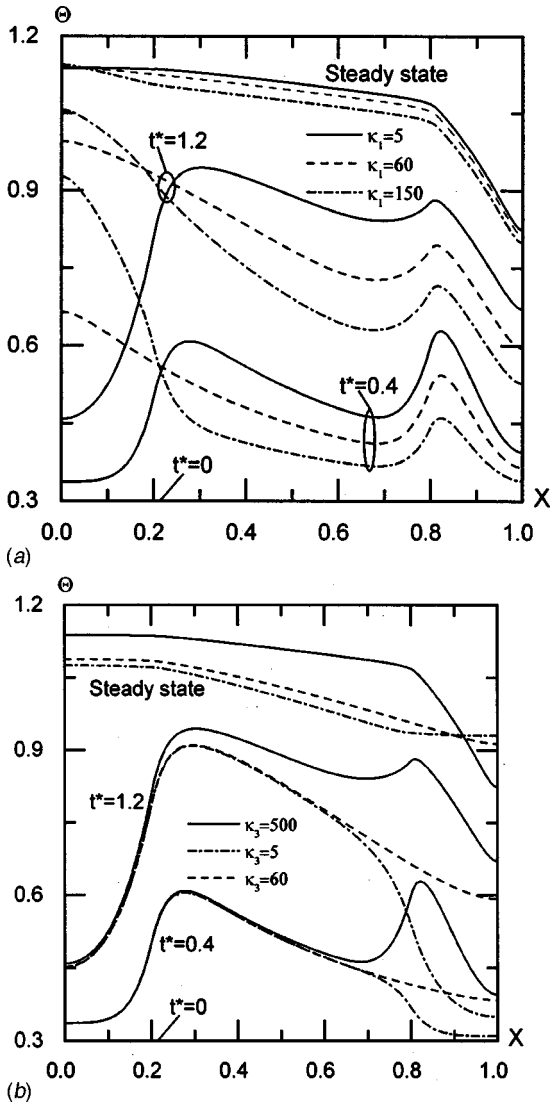

Fig. 5 Effect of extinction coefficient on temperature peaks when $\omega_1 = \omega_2 = \omega_3 = 0$: (*a*) extinction coefficient κ_1; and (*b*) extinction coefficient κ_3

4.3 Effect of Inhomogeneous Properties of Medium on Temperature Distribution. In infrared heating technology, sometimes it is discovered by experiment that the inner temperature of the heated material is higher than that of the surfaces although no inner heat source exists there [17].

The influence of evaporation and transfer of moisture within the material on temperature distribution is ignored in following analysis because this effect is similar to those caused by conduction and convection, that is, only the nearby regions are influenced. When there are no inner heat sources in the infrared heated material, the external energy transferred by coupled conduction, convection and moisture transfer can only penetrate into the material layer by layer from the surface, and the temperature decreases gradually along the transfer path. As for the semitransparent spectral bands, however, by radiation transfer, the energy can penetrate into any region of the material rapidly from the surfaces, and this may cause the maximum temperature to appear in the position where the maximum amount of energy accumulates.

It is pointed out in Ref. [18] that for the coupled conductive and radiative heat transfer, the main cause for a temperature peak appearing in a material with homogeneous property is radiation. It is also pointed that four conditions have to be satisfied simultaneously: (1) the medium being semitransparent; (2) the boundary surfaces being semitransparent; (3) the surfaces being subjected to external radiation; (4) the heated surface being cooled by surrounding convection.

Further analyzing, for an inhomogeneous medium, if the absorption coefficient of the inner regions are greater than those of the outer regions, the inner regions will absorb more radiative energy. Under this condition, can the temperature peak appear even though the surfaces are not cooled by convection? A two-layer semitransparent medium model has been employed in Ref. [13] to investigate this problem. The investigation showed that, for a two-layer composite, a temperature peak would appear if the

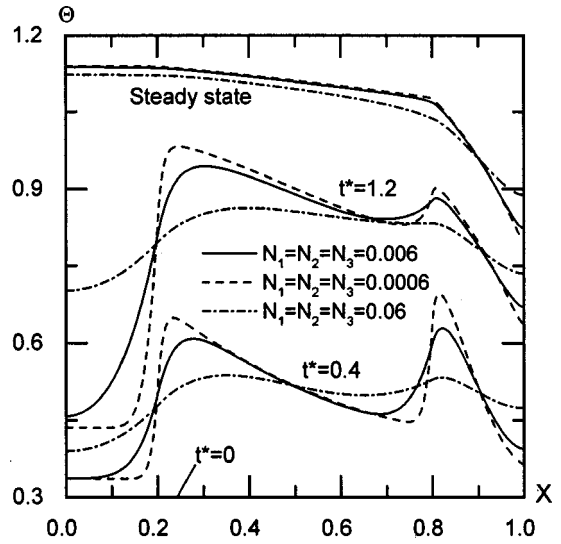

Fig. 6 Effect of conductivity on temperature peaks when $\kappa_1 = 5\ \mathrm{m}^{-1}$, $\kappa_2 = 60\ \mathrm{m}^{-1}$, and $\kappa_3 = 500\ \mathrm{m}^{-1}$

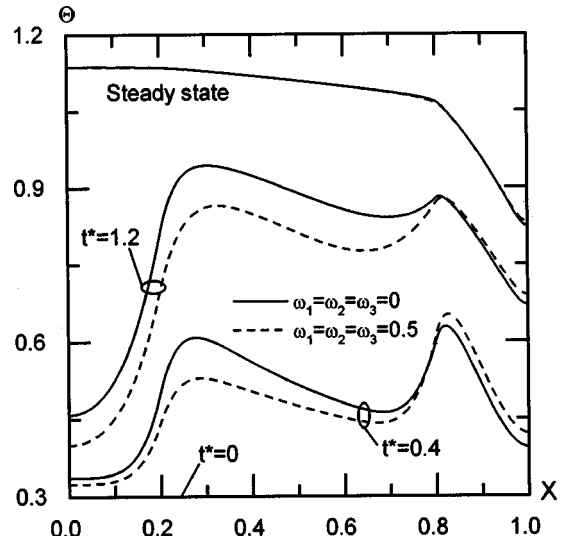

Fig. 8 Effect of scattering albedo on temperature peaks when $\kappa_1 = 5\ \mathrm{m}^{-1}$, $\kappa_2 = 60\ \mathrm{m}^{-1}$, and $\kappa_3 = 500\ \mathrm{m}^{-1}$

absorption coefficient of the second layer were greater than that of the first layer even though the heated surfaces were not cooled by convection.

When the physical properties of the three layers are different, the three-layer composite is equivalent to a single semitransparent layer with inhomogeneous physical properties. The temperature peak phenomenon is studied further here when the surfaces are not cooled by convection, and the results are shown in Figs. 5–8.

The common calculating parameters are $h_1 = h_2 = 0\ \mathrm{W\,m^{-2}\,K^{-1}}$, $T_{-\infty} = 1200\ \mathrm{K}$, $T_{+\infty} = T_0 = 300\ \mathrm{K}$, $T_r = 1000\ \mathrm{K}$, $L_1 = L_3 = L_2/3 = 0.005\ \mathrm{m}$, $\rho_1 c_1 = \rho_2 c_2 = \rho_3 c_3$, and $M_1 = M_2/3 = M_3 = 50$.

Taking the case of $n_1 = n_2 = n_3 = 1.1$, $\omega_1 = \omega_2 = \omega_3 = 0$, $N_1 = N_2 = N_3 = 0.006$, $\kappa_1 = 5\ \mathrm{m}^{-1}$, $\kappa_2 = 60\ \mathrm{m}^{-1}$, and $\kappa_3 = 500\ \mathrm{m}^{-1}$ as a reference working condition, the effects of extinction coefficient, thermal conductivity, refractive index, and scattering albedo on temperature peaks are investigated as follows.

The effect of κ_1 on temperature peaks is shown in Fig. 5(*a*). The solid lines denote the reference working condition with $\kappa_1 = 5\ \mathrm{m}^{-1}$; the dashed lines are for the case of $\kappa_1 = 60\ \mathrm{m}^{-1}$, and the dash-dot lines are for the case of $\kappa_1 = 150\ \mathrm{m}^{-1}$. As shown by the solid line, two obvious temperature peaks appear in the second and the third layers during the transient course, and the two temperature peaks are just about the maximum temperatures in the composite. For this condition, there is $\kappa_1 < \kappa_2 < \kappa_3$, so, when the radiative energy emitted by $S_{-\infty}$ traverses S_1 and transfers along the thickness, the first layer absorbs a little of the radiative energy because of the small $\kappa_1 (= 5\ \mathrm{m}^{-1})$ and L_1, and lots of the radiative energy reaches the second layer and is absorbed intensively by the layer because of the bigger $\kappa_2 (= 60\ \mathrm{m}^{-1})$. This causes the first peak temperature to appear near the interface P in the second layer. When the radiative energy transfers through the second layer, it is attenuated gradually, so the temperatures in the second layer decrease gradually along the thickness. But when the rest radiative energy reaches the third layer, it is intensively absorbed once again by the layer because of the biggest $\kappa_3 (= 500\ \mathrm{m}^{-1})$, and this causes the second temperature peak to appear near the interface Q in the third layer. We can foresee that the second temperature peak will be bigger than the first temperature peak if the κ_3 is big enough and κ_2 small enough. If $\kappa_1 \geqslant \kappa_2$ and $\kappa_2 < \kappa_3$, as shown by the dashed and dash-dot lines, only one temperature peak appears in the third layer. But it is not always the maximum temperature in the composite; the maximum temperature perhaps appears at the left surface. As shown in the figure, the big extinction coefficient in one layer causes the big temperature gradient therein because of the intensive absorption of the radiative energy.

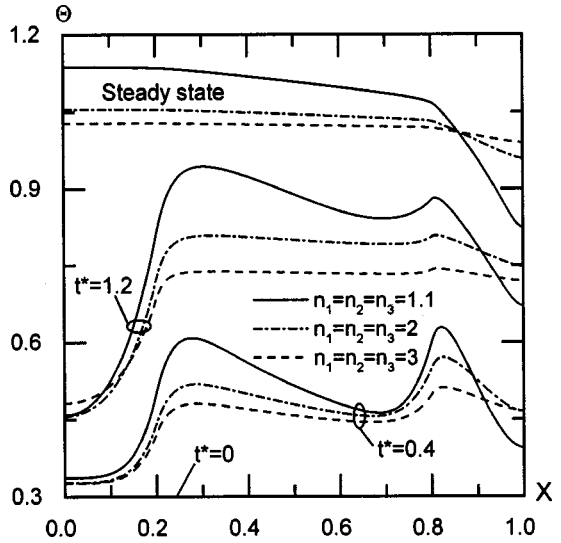

Fig. 7 Effect of refractive index on temperature peaks when $\kappa_1 = 5\ \mathrm{m}^{-1}$, $\kappa_2 = 60\ \mathrm{m}^{-1}$, and $\kappa_3 = 500\ \mathrm{m}^{-1}$

The effect of κ_3 on the temperature peaks is shown in Fig. 5(*b*). The solid lines denote the reference working condition with $\kappa_3 = 500\ \mathrm{m}^{-1}$; the extinction coefficients of the third layer for the dashed and the dash-dot lines are $\kappa_3 = 5\ \mathrm{m}^{-1}$ and $\kappa_3 = 60\ \mathrm{m}^{-1}$, respectively. As expected, when $\kappa_1 < \kappa_2$ and $\kappa_3 \leqslant \kappa_2$, only one temperature peak appears in the second layer during the transient course, and the peak temperature is just about the maximum temperature in the composite. As κ_3 decreases, the reemission of the third layer decreases, and causes the temperature to decrease.

The effect of thermal conductivity on temperature peaks is shown in Fig. 6. The solid lines still denote the reference working condition with $\kappa_1 = 5\ \mathrm{m}^{-1}$, $\kappa_2 = 60\ \mathrm{m}^{-1}$, $\kappa_3 = 500\ \mathrm{m}^{-1}$, and $N_1 = N_2 = N_3 = 0.006$. The dashed lines represent the case of $N_1 = N_2 = N_3 = 0.0006$, and the dash-dot lines represent that of $N_1 = N_2 = N_3 = 0.06$. As shown in the figure, the temperature peaks become more obvious during the transient course when the conductivities decrease. The reason is that heat conduction tends to

smoothen the temperature distribution in the composite, so the smoothening effect is weakened when the conduction-radiation parameter decreases.

The effect of refractive index on temperature peaks is shown in Fig. 7. The solid lines still represent the reference working condition with $\kappa_1=5\ \mathrm{m}^{-1}$, $\kappa_2=60\ \mathrm{m}^{-1}$, $\kappa_3=500\ \mathrm{m}^{-1}$ and $n_1=n_2=n_3=1.1$. The dash-dot lines and the dashed lines denote the cases of $n_1=n_2=n_3=2$ and $n_1=n_2=n_3=3$, respectively. As the refractive index increases, the reflection of surface S_1 is intensified, so more radiative energy emitted by $S_{-\infty}$ is reflected back, and this causes the whole temperature of the composite to decrease. Two temperature peaks still appear in the second and the third layers during the transient course, but they are obviously smaller than those of the reference case. The peak temperature in the third layer is just about the maximum temperature of the composite, and the bigger the refractive index is, the more uniform the temperature distribution is.

With the reference working condition of $\kappa_1=5\ \mathrm{m}^{-1}$, $\kappa_2=60\ \mathrm{m}^{-1}$, and $\kappa_3=500\ \mathrm{m}^{-1}$, the effect of the scattering albedo on temperature peaks is shown in Fig. 8. Similarly, the solid lines denote the reference working condition, and the dashed lines represent the case of $\omega_1=\omega_2=\omega_3=0.5$. As shown in the figure, when the media scatter, the temperature peaks still appear in the composite, and that in the first layer decreases.

5 Conclusions

In this paper, the transient coupled radiation and conduction heat transfer in a three-layer absorbing, and isotropically scattering composite is investigated. The correctness of the investigation is validated by Eq. (3) and Eq. (8) and by the comparison with Ref. [15]. From this investigation, following conclusions can be obtained.

1 For an inhomogeneous semitransparent media with semitransparent surfaces and subjected to external radiation, if the absorption coefficient of the inner regions is greater than that of the outer regions, the temperature peaks can appear even though the surfaces are not cooled by convection.
2 The temperature distribution and the appearance of temperature peaks are affected by the extinction coefficient, thermal conductivity, scattering albedo and refractive index of the layers and their arrangement.
3 By extending the one-layer and the two-layer radiative intensity quotient transfer models, multi-layer radiative intensity quotient transfer model can be created, and in combination with emitting-attenuating-reflecting subprocess and absorbing-scattering subprocess, the radiative transfer in multi-layer absorbing, isotropically scattering composite can be solved.

Acknowledgments

This research is supported by the Chinese National Science Fund for Distinguished Young Scholars (No. 59725617), the Science & Technology Foundation of Heilongjiang, and the National Natural Science Foundation of China (No. 59806003).

Nomenclature

A_{k,T_i} = fractional spectral emissive power of spectral band k at nodal temperature T_i, $\int_{\Delta\lambda_k} I_{\lambda,b}(T_i)d\lambda/(\sigma T_i^4)$
A, B = interface of the fundamental model
c_b = specific heat capacity of b^{th} layer, J $\mathrm{Kg}^{-1}\ \mathrm{K}^{-1}$
$eps0$ = precision of Gaussian quadrature scheme
h_1, h_2 = convective heat transfer coefficient at surfaces S_1 and S_2, respectively, W $\mathrm{m}^{-2}\ \mathrm{K}^{-1}$
k_b = thermal conductivity of b^{th} layer, W $\mathrm{m}^{-1}\ \mathrm{K}^{-1}$
L_b = thickness of b^{th} layer in composite, m
L_t = total thickness of composite, $L_1+L_2+L_3$, m
M_b = number of control volumes of b^{th} layer
M_t = total number of control volumes of composite, $M_1+M_2+M_3$
N_b = dimensionless thermal conductivity of b^{th} layer, $k_b/(4\sigma T_r^3 L_t)$
$n_{b,k}$ = spectral refractive index of b^{th} layer
$n_{i,k}$ = refractive index of i^{th} control volume, when $i\leqslant M_1$, $n_i=n_{1(b=1)}$, when $M_1<i\leqslant M_1+M_2$, $n_i=n_2$, when $M_1+M_2<i\leqslant M_t$, $n_i=n_3$
NB = total number of spectral bands
P, Q = interfaces in the composite
P_1, P_2 = interface P facing the first and the second layer, respectively
Q_2, Q_3 = interface Q facing the second and the third layer, respectively
q^c, q^r = heat fluxes of thermal conduction, radiation, respectively, $\mathrm{W}\cdot\mathrm{m}^{-2}$
q^t = total heat flux, $q^t=q^c+q^r$, $\mathrm{W}\cdot\mathrm{m}^{-2}$
$\tilde{q}$ = dimensionless heat flux, $q/(\sigma T_r^4)$
$S_{-\infty}$, $S_{+\infty}$ = left and right black surfaces representing the surroundings (Fig. 1)
S_1, S_2 = boundary surfaces (Fig. 1)
S_u, S_v = black surfaces, $u,v=-\infty$, or $+\infty$
$(S_uS_v)_k$, $(S_uV_j)_k$ $(V_iS_v)_k$, $(V_iV_j)_k$ = radiation transfer coefficients in non-scattering media relative to the spectral band $k(\Delta\lambda_k)$
$[S_uS_v]_k$, $[S_uV_j]_k$ $[V_iS_v]_k$, $[V_iV_j]_k$ = radiation transfer coefficients in isotropically scattering media relative to the spectral band $k(\Delta\lambda_k)$
T = absolute temperature, K
T_0 = uniform initial temperature, K
T_r = reference temperature, K
T_{S_1}, T_{S_2} = temperatures of the boundary surfaces S_1 and S_2, respectively, K
$T_{-\infty}$, $T_{+\infty}$ = temperatures of the black surface $S_{-\infty}$ and $S_{+\infty}$, respectively, K (Fig. 1)
T_{g1}, T_{g2} = gas temperature for convection at $x=0$ and L_t, respectively, K
t = physical time, s
t^* = dimensionless time, $4\sigma T_r^3 t/(\rho_1 c_1 L_t)$
V_i = i^{th} control volume, $i=1\sim M_t$
V_{1_b} = I^{th} control volume of the b^{th} layer, $I=1\sim M_b$
X = dimensionless coordinate, $X=x/L_t$
x = coordinate in direction across composite, m
x_a^b = distance between surface a and b, m
$\alpha_{b,k}$, $\sigma_{s,b,k}$ = spectral absorbing coefficient and scattering coefficient of b^{th} layer, m^{-1}
Γ = absorbed quotient of radiative intensity by control volume or surface, (Eq. (4))
$\gamma(\theta)$ = transmissivity at angle θ, $1-\rho(\theta)$
Δt = time interval, s
Δx_b = control volume thickness of b^{th} layer, m
η_i = $1-\omega_i$, when $i\leqslant M_1$, $\omega_i=\omega_1$, when $M_1<i\leqslant M_1+M_2$, $\omega_i=\omega_2$ when $M_1+M_2<i\leqslant M_t$, $\omega_i=\omega_3$
Θ = dimensionless temperature, T/T_r
θ = angle of reflection or incidence

$\kappa_{b,k}$ = extinction coefficients of b^{th} layer, $\alpha_{b,k}+\sigma_{s,b,k}$, m^{-1}
λ = wavelength, μm
ρ_b = density of b^{th} layer, kg/m^3
$\rho(\theta)$ = reflectivity at angle θ
σ = Stefan-Boltzmann constant, $\text{W m}^{-2}\ \text{K}^{-4}$
$\tau_{b,k}$ = spectral optical thickness of b^{th} layer, $\kappa_b L_b$
Φ_i^r = radiative heat source of control-volume i
$\omega_{b,k}$ = spectral scattering albedo of b^{th} layer, $\sigma_{s,b,k}/\kappa_{b,k}$

Superscripts

m = time step
r = radiation
s = specular reflection
t = total heat flux

Subscripts

b = layer index, $b=1,2,3$
i, j = number of node
iw, ie = left and right interfaces of control volume i
k = relative to spectral band k
S_1, S_2 = relative to S_1 and S_2
$-\infty, +\infty$ = relative to $S_{-\infty}$ and $S_{+\infty}$
$t-t$ = refer to a composite with semitransparent surfaces
$\parallel, \perp$ = component for parallel and perpendicular polarization

Appendix A Basic Radiative Intensity Transfer Models

For specular reflection, we can trace a ray emitting with an arbitrary angle and get the attenuation expression for a transfer path. One-layer and two-layer basic radiative intensity transfer models are put forward here for solving the three-layer problem. Symbol F and E are introduced to represent the radiative intensity quotient transfer functions of the two models respectively, whose subscript denotes the emitting element (surface or control volume), and superscript denotes the receiving element (surface or control volume).

The detailed deducing process of the radiative intensity quotient transfer functions for the two models is presented below for a typical example of $(V_{I_1}V_{I_2})^s_{k,t-t}$. For convenience, the subscript k is omitted here.

A.1 One-Layer Basic Radiative Intensity Transfer Model

A.1.1 Transfer of External Incident Radiative Intensity Within a Single Layer. As shown in Fig. 9, the b^{th} sublayer is chosen arbitrarily from a composite. The external radiative intensity emitted by the j^{th} element (surface or control volume) with angle θ, enters the b^{th} sublayer through the interfaces A or B. According to the Snell's refractive law, the relation between the refractive angle θ_b and the emitting angle θ is

$$\theta_b=\arcsin(n_j\sin\theta/n_b) \tag{A1}$$

(1) Transfer of the Radiative Intensity Traversing the Interface B. As shown in Fig. 9(*a*) the radiative intensity traversing the interface B, will be reflected by the interfaces A and B for many times, and finally attenuated to 0, and during this process the quotient $\mathbf{F}_{B_b}^{V_{I_b}}$, absorbed by control volume V_{I_b} of the intensity, can be expressed as

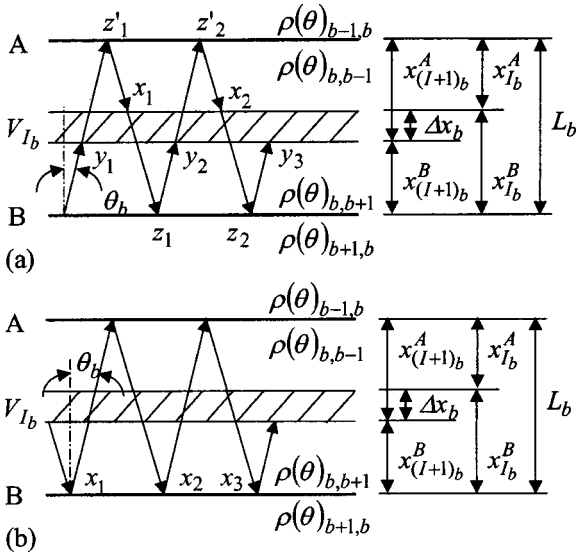

Fig. 9 One-layer basic radiative intensity transfer model: (*a*) transfer process of external incident radiative intensity; and (*b*) transfer process of radiative intensity emitted by a control volume

$$\begin{aligned}\mathbf{F}_{B_b}^{V_{I_b}}&=\left[\sum_{i=1}^{\infty}x_i+\sum_{j=1}^{\infty}y_j\right][1-\exp(-\kappa_b\Delta x_b/\mu_b)]\\&=(x_1+y_1)/(1-\beta_1)\cdot[1-\exp(-\kappa_b\Delta x_b/\mu_b)]\\&=\{\rho(\theta_b)_{b,b-1}\exp[-\kappa_b(L_b+x^A_{I_b})/\mu_b]\\&\quad+\exp(-\kappa_b x^B_{(I+1)_b}/\mu_b)\}[1-\exp(-\kappa_b\Delta x_b/\mu_b)]/(1-\beta_1),\end{aligned} \tag{A2}$$

where x_1 and y_1 are the first terms of two infinite geometric progressions of x_i and y_j, respectively. The common ratios of the two series are the same, $\beta_1=\exp(-2\kappa_b L_b/\mu_b)\rho(\theta_b)_{b,b-1}\times\rho(\theta_b)_{b,b+1}$ $(\beta_1<1)$; $\mu_b=\cos\theta_b$, substituting Eq. (*A*1) into it, then it can be written as $\mu_b=\cos[\arcsin(n_j\sin\theta/n_b)]$; $\rho(\theta_b)$ is the interface reflectivity, whose subscript writing order denotes the transfer direction of the ray traversing the interface. Similarly,

$$\mathbf{F}_{B_b}^{B_b}=\sum_{i=1}^{\infty}z_i=\exp(-2\kappa_b L_b/\mu_b)\rho(\theta_b)_{b,b-1}/(1-\beta_1) \tag{A3}$$

$$\mathbf{F}_{B_b}^{A_b}=\sum_{i=1}^{\infty}z'_i=\exp(-\kappa_b L_b/\mu_b)/(1-\beta_1). \tag{A4}$$

(2) Transfer of the Radiative Intensity Traversing the Interface A. By an analysis similar to that for (1), the following equation can be deduced:

$$\begin{aligned}\mathbf{F}_{A_b}^{V_{I_b}}&=\{\rho(\theta_b)_{b,b+1}\exp[-\kappa_b(L_b+x^B_{(I+1)_b})/\mu_b]\\&\quad+\exp(-\kappa_b x^A_{I_b}/\mu_b)\}[1-\exp(-\kappa_b\Delta x_b/\mu_b)]/(1-\beta_1)\end{aligned} \tag{A5}$$

$$\mathbf{F}_{A_b}^{A_b}=\exp(-2\kappa_b L_b/\mu_b)\rho(\theta_b)_{b,b+1}/(1-\beta_1) \tag{A6}$$

$$\mathbf{F}_{A_b}^{B_b}=\exp(-\kappa_b L_b/\mu_b)/(1-\beta_1) \tag{A7}$$

A.1.2 Transfer of Radiative Intensity Emitted by Control Volume Within a Single Layer. The energy emitted by a control volume will transfer towards its two sides, so two conditions should be considered, respectively.

As shown in Fig. 9(*b*) the radiative intensity emitted by control volume V_{I_b} and transferring towards the interface B, is attenuated, reflected for infinite times within the layer until it finally attenuates to 0. The total quotient of the radiative intensity, which finally reaches the interface B, is the sum of a geometric progression, that is

$$\eta' = \sum_{i=1}^{\infty} x_i = x_1/(1-\beta_1) \tag{A8}$$

$$x_1 = \exp(-\kappa_b x^B_{(I+1)_b}/\mu_b)[1-\exp(-\kappa_b \Delta x_b/\mu_b)], \tag{A9}$$

where x_1, is the first term of the geometric progression, and β_1 is the same parameter as stated in A.1.1.

The radiative intensity emitted by the control volume V_{I_b} towards the interface A finally attenuates to 0 after transferring within the layer, and then the total quotient of the radiative intensity finally reaching the interface B is the sum of another geometric progression

$$\eta'' = \sum_{i=1}^{\infty} y_i = y_1/(1-\beta_1) \tag{A10}$$

$$y_1 = \rho(\theta_b)_{b,b-1} \exp[-\kappa_b(L_b + x^A_{I_b})/\mu_b][1-\exp(-\kappa_b \Delta x_b/\mu_b)], \tag{A11}$$

where y_1, is the first term of the geometric progression. So the total quotient of the radiative intensity emitted by the control volume V_{I_b}, transferring towards its both sides and finally reaching the interface B can be expressed as

$$\begin{aligned}\mathbf{F}^{B_b}_{V_{I_b}} = \eta' + \eta'' = \{&\exp(-\kappa_b x^B_{(I+1)_b}/\mu_b) + \rho(\theta_b)_{b,b-1} \\ &\times \exp[-\kappa_b(L_b + x^A_{I_b})/\mu_b]\} \\ &\times [1-\exp(-\kappa_b \Delta x_b/\mu_b)]/(1-\beta_1).\end{aligned} \tag{A12}$$

A.1.3 Interface Reflectivity and Total Reflection. The reflectivity $\rho(\theta_b)$ in above equations is functions of the perpendicular and parallel components. So each function F in Eq. (*A*2) to Eq. (*A*12) has different forms corresponding to the two components. For a perfect dielectric medium, the effect of the extinction coefficient in the complex index of refraction can be neglected. When a radiative intensity transfers from b^{th} layer of refractive index n_b towards its adjacent o^{th} ($o=b-1$ or $b+1$) layer of refractive index n_o, the interface reflectivity $\rho(\theta_b)_{bo}$ is

$$\rho_{\parallel}(\theta_b)_{bo} = [\tan(\theta_b - \varphi_o)/\tan(\theta_b + \varphi_o)]^2 \quad \text{(for parallel component)} \tag{A13a}$$

$$\rho_{\perp}(\theta_b)_{bo} = [\sin(\theta_b - \varphi_o)/\sin(\theta_b + \varphi_o)]^2 \quad \text{(for perpendicular component)}, \tag{A13b}$$

where θ_b is the incident angle and φ_o is the refractive angle. According to the Snell's refractive law, the relationship between the two angles is

$$\varphi_o = \arcsin(\sin\theta_b n_b/n_o). \tag{A14}$$

Substituting Eq. (*A*1) into Eq. (*A*13) and (*A*14), the reflectivity $\rho(\theta_b)_{bo}$ can be written as $\rho(\theta)_{bo}$, which is only the function of angle θ. When $n_b > n_o$, and if $\theta_b > \arcsin(n_o/n_b)$, the total reflection occurs, and $\rho(\theta)_{bo}=1$. When a radiative intensity transfers in the reverse direction, the reflectivity $\rho(\theta)_{ob}$ is $\rho(\theta)_{ob}=\rho(\theta)_{bo}$, if the total reflection ($\rho(\theta)_{ob}=1$) does not occur. And if $n_b=n_o$, then $\rho(\theta)_{ob}=\rho(\theta)_{bo}=0$.

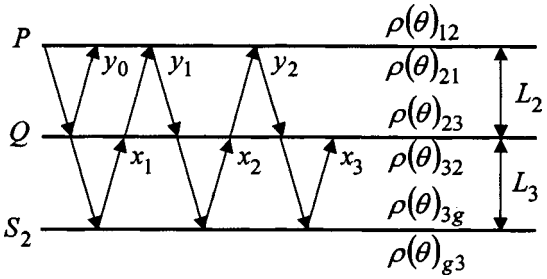

Fig. 10 Two-layer basic radiative intensity transfer model

A.1.4 The Radiative Intensity Quotient Transfer Functions for Each Layer. If the following replacement is made to Eq. (*A*2)~Eq. (*A*12), the radiative intensity quotient transfer functions for each layer can be obtained: (1) for the first layer, $A_b=S_1$ and $B_b=P_1$; (2) for the second layer, $A_b=P_2$, $B_b=Q_2$, and $V_{I_b}=V_{I_2}$; (3) for the third layer, $A_b=Q_3$ and $B_b=S_2$.

A.2 Two-Layer Basic Radiative Intensity Transfer Model Based on the one-layer basic radiative intensity transfer model, the two-layer basic radiative intensity transfer model can be created. As shown in Fig. 10 the radiative intensity emitted by V_{I_1} enters the two-layer model through the interface *P*, so $\mathbf{E}^{Q_3}_{P_2,2\sim3}$ and $\mathbf{E}^{P_2}_{P_2,2\sim3}$ are employed in the deduction of RTC $(V_{I_1}V_{I_2})^s_{k,t-t}$, and an analysis on the two quotient functions is presented below.

The radiative intensity traversed from the interface *P*, will be attenuated and reflected repeatedly within the two layers until it attenuates to 0. During the process, the total quotients of the radiative intensity reaching the interfaces Q_3 and P_2 can be written as $\mathbf{E}^{Q_3}_{P_2,2\sim3}$ and $\mathbf{E}^{P_2}_{P_2,2\sim3}$ respectively, where subscript "2~3" denotes that the two-layer model is composed of the second and the third layers. And their detailed expressions are

$$\mathbf{E}^{Q_3}_{P_2,2\sim3} = \sum_{i=1}^{\infty} x_i = x_1/(1-\beta_2) = \mathbf{F}^{Q_2}_{P_2}\gamma(\theta)_{23}\mathbf{F}^{Q_3}_{Q_3}/(1-\beta_2) \tag{A15}$$

$$\mathbf{E}^{P_2}_{P_2,2\sim3} = y_0 + \sum_{i=1}^{\infty} y_i = \mathbf{F}^{P_2}_{P_2} + \mathbf{E}^{Q_3}_{P_2,2\sim3}\gamma(\theta)_{32}\mathbf{F}^{P_2}_{Q_2}, \tag{A16}$$

where x_1 is the first terms of the geometric progression x_i with a common ratio $\beta_2 = \gamma(\theta)_{32}\mathbf{F}^{Q_2}_{Q_2}\gamma(\theta)_{23}\mathbf{F}^{Q_3}_{Q_3}$ ($\beta_2<1$). The relation between geometric progression y_i and x_i is $y_i = x_i\gamma(\theta)_{32}\mathbf{F}^{P_2}_{Q_2}$.

Appendix B RTCs for a Three-Layer Semitransparent Composite

The following RTC expressions fits for the condition that all the surfaces and interfaces are semitransparent and specular as well as $n_2<n_1<n_3$. And in following expressions, $\xi_1 = 1-\gamma(\theta)_{21}\mathbf{F}^{P_1}_{P_1}\gamma(\theta)_{12}\mathbf{E}^{P_2}_{P_2,2\sim3}$, and $\xi_2 = 1-\mathbf{F}^{Q_3}_{Q_3}\gamma(\theta)_{32}\mathbf{E}^{Q_2}_{Q_2,1\sim2}\times\gamma(\theta)_{23}$.

$$(S_{-\infty}S_{+\infty})^s_{k,t-t} = \int_0^{\pi/2} (\Gamma_{\parallel} + \Gamma_{\perp})\sin\theta\cos\theta d\theta, \tag{B1}$$

where $\Gamma = \gamma(\theta)_{3g}\gamma(\theta)_{g1}\mathbf{E}^{Q_2}_{S_1,1\sim2}\gamma(\theta)_{23}\mathbf{F}^{S_2}_{Q_3}/\xi_2$.

$$(S_{-\infty}V_{I_1})^s_{k,t-t} = \int_0^{\pi/2} (\Gamma_{\parallel} + \Gamma_{\perp})\sin\theta\cos\theta d\theta, \tag{B2}$$

where $\Gamma = \gamma(\theta)_{g1}\mathbf{F}^{V_{I_1}}_{S_1} + \gamma(\theta)_{g1}\mathbf{F}^{P_1}_{S_1}\gamma(\theta)_{12}\mathbf{E}^{P_2}_{P_2,2\sim3}/\xi_1\gamma(\theta)_{21}\mathbf{F}^{V_{I_1}}_{P_1}$.

$$(S_{+\infty}V_{I_3})^s_{k,t-t}=\int_0^{\pi/2}(\Gamma_{\parallel}+\Gamma_{\perp})\sin\theta\cos\theta d\theta, \qquad (B3)$$

where $\Gamma=\gamma(\theta)_{g3}\mathbf{F}^{V_{I_3}}_{S_2}+\gamma(\theta)_{g3}\mathbf{F}^{Q_3}_{S_2}\gamma(\theta)_{32}\mathbf{E}^{Q_2}_{Q_2,1\sim2}/\xi_2\gamma(\theta)_{23}\mathbf{F}^{V_{I_3}}_{Q_3}$.

$$(V_{I_1}V_{J_1})^s_{k,t-t}=\begin{cases}(V_{I_1}V_{J_1})'' & (I\neq J)\\ 4\kappa_1\Delta x_1-2[1-2\mathbf{E}_3(\kappa_1\Delta x_1)]+(V_{I_1}V_{J_1})'' & (I=J),\end{cases} \qquad (B4)$$

where

$$(V_{I_1}V_{J_1})''=\int_0^{\theta_{1g}}(\Gamma_{\parallel}+\Gamma_{\perp})\sin\theta\cos\theta d\theta+\int_{\theta_{1g}}^{\theta_{12}}(\Gamma_{\parallel}+\Gamma_{\perp})\sin\theta\cos\theta d\theta+\int_{\theta_{12}}^{\pi/2}(\Gamma_{\parallel}+\Gamma_{\perp})\sin\theta\cos\theta d\theta,$$

and $\Gamma=\mathbf{F}^{V_{J_1}}_{V_{I_1}}+\mathbf{F}^{P_1}_{V_{I_1}}\gamma(\theta)_{12}\mathbf{E}^{P_2}_{P_2,2\sim3}/\xi_1\gamma(\theta)_{21}\mathbf{F}^{V_{J_1}}_{P_1}$.

$$(V_{I_2}V_{J_2})^s_{k,t-t}=\begin{cases}(V_{I_2}V_{J_2})'' & (I\neq J)\\ 4\kappa_2\Delta x_2-2[1-2\mathbf{E}_3(\kappa_2\Delta x_2)]+(V_{I_2}V_{J_2})'' & (I=J)\end{cases} \qquad (B5)$$

where $(V_{I_2}V_{J_2})''=\int_0^{\theta_{2g}}(\Gamma_{\parallel}+\Gamma_{\perp})\sin\theta\cos\theta d\theta+\int_{\theta_{2g}}^{\pi/2}(\Gamma_{\parallel}+\Gamma_{\perp})\sin\theta\cos\theta d\theta$, and

$$\Gamma=\mathbf{F}^{V_{J_2}}_{V_{I_2}}+\mathbf{F}^{P_2}_{V_{I_2}}\gamma(\theta)_{21}\mathbf{F}^{P_1}_{P_1}\gamma(\theta)_{12}(\mathbf{F}^{V_{J_2}}_{P_2}+\mathbf{E}^{Q_3}_{P_2,2\sim3}\gamma(\theta)_{32}\mathbf{F}^{V_{J_2}}_{Q_2})/\xi_1+\mathbf{F}^{P_2}_{V_{I_2}}\gamma(\theta)_{23}\mathbf{F}^{Q_3}_{Q_3}\gamma(\theta)_{32}(\mathbf{E}^{P_1}_{Q_2,1\sim2}\gamma(\theta)_{12}\mathbf{F}^{V_{J_2}}_{P_2}+\mathbf{F}^{V_{J_2}}_{Q_2})/\xi_2$$

$$(V_{I_3}V_{J_3})^s_{k,t-t}=\begin{cases}(V_{I_3}V_{J_3})'' & (I\neq J)\\ 4\kappa_3\Delta x_3-2[1-2\mathbf{E}_3(\kappa_3\Delta x_3)]+(V_{I_3}V_{J_3})'' & (I=J)\end{cases} \qquad (B6)$$

where

$$(V_{I_3}V_{J_3})''=\int_0^{\theta_{1g}}(\Gamma_{\parallel}+\Gamma_{\perp})\sin\theta\cos\theta d\theta+\int_{\theta_{1g}}^{\theta_{31}}(\Gamma_{\parallel}+\Gamma_{\perp})\sin\theta\cos\theta d\theta+\int_{\theta_{31}}^{\theta_{32}}(\Gamma_{\parallel}+\Gamma_{\perp})\sin\theta\cos\theta d\theta+\int_{\theta_{32}}^{\pi/2}(\Gamma_{\parallel}+\Gamma_{\perp})\sin\theta\cos\theta d\theta$$

and $\Gamma=\mathbf{F}^{V_{J_3}}_{V_{I_3}}+\mathbf{F}^{Q_3}_{V_{I_3}}\gamma(\theta)_{32}\mathbf{E}^{Q_2}_{Q_2,1\sim2}/\xi_2\gamma(\theta)_{23}\mathbf{F}^{V_{J_3}}_{Q_3}$.

$$(V_{I_1}V_{I_2})^s_{k,t-t}=\int_0^{\theta_{1g}}(\Gamma_{\parallel}+\Gamma_{\perp})\sin\theta\cos\theta d\theta+\int_{\theta_{1g}}^{\theta_{12}}(\Gamma_{\parallel}+\Gamma_{\perp})\sin\theta\cos\theta d\theta \qquad (B7)$$

where $\Gamma=[\mathbf{F}^{P_1}_{V_{I_1}}\gamma(\theta)_{12}\mathbf{F}^{V_{I_2}}_{P_2}+\mathbf{F}^{P_1}_{V_{I_1}}\gamma(\theta)_{12}\mathbf{E}^{Q_3}_{P_2,2\sim3}\gamma(\theta)_{32}\mathbf{F}^{V_{I_2}}_{Q_2}]/\xi_1$.

$$(S_{-\infty}S_{-\infty})^s_{k,t-t}=\int_0^{\pi/2}(\Gamma_{\parallel}+\Gamma_{\perp})\sin\theta\cos\theta d\theta \qquad (B8)$$

where $\Gamma=[\gamma(\theta)_{g1}\mathbf{F}^{S_1}_{S_1}+\gamma(\theta)_{g1}\mathbf{F}^{P_1}_{S_1}\gamma(\theta)_{12}\mathbf{E}^{P_2}_{P_2,2\sim3}\gamma(\theta)_{21}\mathbf{F}^{S_1}_{P_1}/\xi_1]\times\gamma(\theta)_{1g}+\rho(\theta)_{g1}$.

$$(S_{+\infty}S_{+\infty})^s_{k,t-t}=\int_0^{\pi/2}(\Gamma_{\parallel}+\Gamma_{\perp})\sin\theta\cos\theta d\theta \qquad (B9)$$

where $\Gamma=[\gamma(\theta)_{g3}\mathbf{F}^{S_2}_{S_2}+\gamma(\theta)_{g3}\mathbf{F}^{Q_3}_{S_2}\gamma(\theta)_{32}\mathbf{E}^{Q_2}_{Q_2,1\sim2}\gamma(\theta)_{23}\mathbf{F}^{S_2}_{Q_3}/\xi_2]\times\gamma(\theta)_{3g}+\rho(\theta)_{g3}$.

$$(V_{I_3}V_{I_2})^s_{k,t-t}=\int_0^{\theta_{3g}}(\Gamma_{\parallel}+\Gamma_{\perp})\sin\theta\cos\theta d\theta+\int_{\theta_{3g}}^{\theta_{31}}(\Gamma_{\parallel}+\Gamma_{\perp})\sin\theta\cos\theta d\theta+\int_{\theta_{31}}^{\theta_{32}}(\Gamma_{\parallel}+\Gamma_{\perp})\sin\theta\cos\theta d\theta \qquad (B10)$$

where $\Gamma=[\mathbf{F}^{Q_3}_{V_{I_3}}\gamma(\theta)_{32}\mathbf{F}^{V_{I_2}}_{Q_2}+\mathbf{F}^{Q_3}_{V_{I_3}}\gamma(\theta)_{32}\mathbf{E}^{P_1}_{Q_2,1\sim2}\gamma(\theta)_{12}\mathbf{F}^{V_{I_2}}_{P_2}]/\xi_2$.

$$(V_{I_1}V_{I_3})^s_{k,t-t}=\int_0^{\theta_{1g}}(\Gamma_{\parallel}+\Gamma_{\perp})\sin\theta\cos\theta d\theta+\int_{\theta_{1g}}^{\theta_{12}}(\Gamma_{\parallel}+\Gamma_{\perp})\sin\theta\cos\theta d\theta \qquad (B11)$$

where $\Gamma=\mathbf{F}^{P_1}_{V_{I_1}}\gamma(\theta)_{12}\mathbf{E}^{Q_2}_{P_2,2\sim3}/\xi_1\gamma(\theta)_{23}\mathbf{F}^{V_{I_3}}_{Q_3}$.

$$(S_{-\infty}V_{I_2})^s_{k,t-t}=\int_0^{\pi/2}(\Gamma_{\parallel}+\Gamma_{\perp})\sin\theta\cos\theta d\theta \qquad (B12)$$

where $\Gamma=\gamma(\theta)_{g1}\mathbf{F}^{P_1}_{S_1}\gamma(\theta)_{12}/\xi_1(\mathbf{F}^{V_{I_2}}_{P_2}+\mathbf{E}^{Q_3}_{P_2,2\sim3}\gamma(\theta)_{32}\mathbf{F}^{V_{I_2}}_{Q_2})$.

$$(S_{+\infty}V_{I_2})^s_{k,t-t}=\int_0^{\pi/2}(\Gamma_{\parallel}+\Gamma_{\perp})\sin\theta\cos\theta d\theta \qquad (B13)$$

where $\Gamma=\gamma(\theta)_{g3}\mathbf{F}^{Q_3}_{S_2}\gamma(\theta)_{32}/\xi_2[\mathbf{F}^{V_{I_2}}_{Q_2}+\mathbf{E}^{P_1}_{Q_2,1\sim2}\gamma(\theta)_{12}\mathbf{F}^{V_{I_2}}_{P_2}]$.

$$(S_{-\infty}V_{I_3})^s_{k,t-t}=\int_0^{\pi/2}(\Gamma_{\parallel}+\Gamma_{\perp})\sin\theta\cos\theta d\theta \qquad (B14)$$

where $\Gamma=\gamma(\theta)_{g1}\mathbf{E}^{P_2}_{S_1,1\sim2}\gamma(\theta)_{23}\mathbf{F}^{V_{I_3}}_{Q_3}/\xi_2$.

$$(S_{+\infty}V_{I_1})^s_{k,t-t}=\int_0^{\pi/2}(\Gamma_{\parallel}+\Gamma_{\perp})\sin\theta\cos\theta d\theta \qquad (B15)$$

where $\Gamma=\gamma(\theta)_{g3}\mathbf{E}^{P_2}_{S_2,2\sim3}\gamma(\theta)_{21}\mathbf{F}^{V_{I_1}}_{P_1}/\xi_1$.

References

[1] Gilpin, R. R., Robertson, R. B., and Singh, B., 1977, "Radiative Heating in Ice," ASME J. Heat Transfer, **99**, pp. 227–232.

[2] Tsai, C. F., and Nixon, G., 1986, "Transient Temperature Distribution of A Multilayer Composite Wall with Effects of Internal Thermal Radiation and Conduction," Numer. Heat Transfer, **10**, No. 1, pp. 95–101.

[3] Timoshenko, V. P., and Trener, M. G., 1986, "A Method for Evaluation Heat Transfer in Multilayer Semitransparent Materials," Heat Transfer-Sov. Res., **18**, No. 5, pp. 44–57.

[4] Ho, C. H., and Özisik, M. N., 1987, "Combined Conduction and Radiation in A Two-Layer Planar Medium with Flux Boundary Condition," Numer. Heat Transfer, **11**, No. 3, pp. 321–340.

[5] Ho, C. H., and Özisik, M. N., 1987, "Simultaneous Conduction and Radiation in A Two-Layer Planar Medium," J. Thermophys. Heat Transfer, **1**, No. 2, pp. 154–161.

[6] Song, D., and Viskanta, R., 1990, ''Deicing of Solids Using Radiant Heating,'' J. Thermophys. Heat Transfer, **4**, pp. 311–317.
[7] Siegel, R., and Spuckler, C. M., 1993, ''Refractive Index Effects on Radiation in an Absorbing, Emitting, and Scattering Laminated Layer,'' ASME J. Heat Transfer, **115**, No. 1, pp. 194–200.
[8] Siegel, R., 1996, ''Two-Flux Green's Function Analysis for Transient Spectral Radiation in a Composite,'' J. Thermophys. Heat Transfer, **10**, No. 4, pp. 681–688.
[9] Siegel, R., and Spuckler, C. M., 1993, ''Variable Refractive Index Effects on Radiation in Semitransparent Scattering Multilayered Regions,'' J. Thermophys. Heat Transfer, **7**, No. 4, pp. 624–630.
[10] Siegel, R., 1999, ''Transient Thermal Analysis of Parallel Translucent Layers by Using Green's Functions,'' J. Thermophys. Heat Transfer, **13**, No. 1, pp. 10–17.
[11] Hottel, H. C., and Sarofim, A. F., 1967, *Radiative Transfer*, McGraw-Hill Book Company, New York.
[12] Tan, H.-P., Tong, T. W., Ruan, L.-M., Xia, X.-L., and Yu, Q.-Z., 1999, ''Transient Coupled Radiative and Conductive Heat Transfer in an Absorbing, Emitting and Scattering Medium,'' Int. J. Heat Mass Transf., **42**, No. 15, pp. 2967–2980.
[13] Tan, H.-P., Wang, P.-Y., and Xia, X.-L., 2000, ''Transient Coupled Radiation and Conduction in an Absorbing and Scattering Composite Layer,'' J. Thermophys. Heat Transfer, **14**, No. 1, pp. 77–87.
[14] Tan, H.-P., and Lallemand, M., 1989, ''Transient Radiative-Conductive Heat Transfer in Flat Glasses Submitted to Temperature, Flux and Mixed Boundary Conditions,'' Int. J. Heat Mass Transf., **32**, No. 5, pp. 795–810.
[15] Siegel, R., 1994, ''Effects of Refractive Index and Diffuse or Specular Boundaries on a Radiating Isothermal Layer,'' ASME J. Heat Transfer, **116**, pp. 787–790.
[16] Patankar, S. V., 1980, *Numerical Heat Transfer and Fluid Flow*, McGraw-Hill, New York.
[17] Гинзрург А. С., 1973, Основы теории и техники сушки пищевых продукмое Москва Пищеая Промышлен носмъ, translated by K. Y. Gao, *Mechanism and Technology on Food Torrefaction*, published by Chinese Beijing Industry Publishing Company, 1986, pp. 468–503.
[18] Tan, H.-P., and Yu, Q.-Z., 1991, ''Numerical Analysis of Temperature Field in Materials During Infrared Heating,'' Chinese J. Infrared and Millimeter Waves, **10**, No. 2, pp. 169–178.

Ben-Wen Li
e-mail: heatli@hotmail.com

Hai-Geng Chen

Thermal Engineering Department,
School of Materials & Metallurgy,
Northeastern University,
Shenyang, Liaoning 110004, China

Jun-Hu Zhou

Xin-Yu Cao

Ke-Fa Cen

Institute for Thermal Power Engineering,
Zhejiang University,
Hangzhou, Zhejiang 310027, China

The Spherical Surface Symmetrical Equal Dividing Angular Quadrature Scheme for Discrete Ordinates Method

A new angular quadrature scheme named Spherical surface Symmetrical equal Dividing (abbreviated to SSD_N) is presented. The evaluations of double moments by SSD_N and other traditional quadrature sets show that the new SSD_N is able to provide good accuracy and compete well with others (as for example the S_N and LS_N method). Radiative predictions in a black-walled rectangular enclosure containing absorbing-emitting medium indicate that, compared with S_N, LS_N, T_N, and $SRAP_N$, the SSD_N can give higher accuracy than S_N under some order numbers N. Numerical experiments demonstrate the computational economy of SSD_N for some cases. [DOI: 10.1115/1.1459731]

Keywords: Computational, Heat Transfer, Modeling, Numerical Methods, Radiation

Introduction

During the last two decades, among many available approximate solution methods for radiative heat transfer, the discrete ordinates method (DOM) [1–4] has enjoyed many applications and extensions. The reasons are the following: (1) The DOM can be easily incorporated into computational fluid dynamic (CFD) for the purpose of a complete description of thermal and fluid dynamical process in the furnaces or combustor chambers; (2) the DOM has the potential of highly accurate predictions even for multi-dimensional systems because it has been developed with much effort in the past. Based on the above-stated points, the DOM has a promising future and has achieved much progress in the application in arbitrary geometrical enclosures [5–11].

The selection of the angular quadrature scheme plays a fundamental role in the application of DOM. Up to now several kinds of quadrature schemes have been proposed or used [2,12–23]. In principle, the quadrature scheme can be chosen arbitrarily. However, a diligent choice of the quadrature set can positively affect both the accuracy of the solution and the economy of computation. Restrictions, including both symmetry under reflection and 90 deg rotation of the coordinate axes [1], must be imposed on the direction set to preserve labeling and prevent biasing of any computed quantity in orthogonal coordinate systems. One commonly used criterion to check the quality of quadrature scheme is moment-matching. Truelove [3] further emphasized that the chosen quadrature scheme should also match the half range first moment to improve the low-order discrete ordinate solutions of the radiative transport equation.

It is worthwhile to note that the YIX quadrature, proposed first by Tan and Howell [17] and applied to multi-dimensional problems with participating media by Hsu et al. [18] later, has the flexibility to use multiple discrete ordinates sets to deal with the ray effect which is an advantage over conventional quadrature sets.

From the view of geometrical and physical considerations, Wakil and Sacadura [20] proposed the LS_N quadrature set which can feed high order approximation for anisotropic phase function with high accuracy.

Another very useful quadrature is the ''Double Cyclic Triangles (DCT)'' proposed by Koch et al. [21]. The authors presented a sound mathematical methodology for the derivation of angular quadrature. Due to this analysis, one can identify the computational errors using the collocation principle and the theory of orthogonal polynomials.

Among the several quadrature schemes proposed in the past, the LS_N [20], the T_N [22], and $SRAP_N$ [23] schemes have some advantages over the conventional level symmetric sets as they are more accurate in computing the first-order moment and have no upper limit for the number of directions. However, as pointed by Thurgood et al. [22], the T_N is less accurate than the S_N when the discrete directions are the same. On the other hand, the $SRAP_N$ cannot exactly satisfy the rotational invariance emphasized by Koch et al. [21] to be of particular importance when the DOM is applied to non-orthogonal grids.

The purpose of this study is to present a new Spherical surface Symmetrical equal Dividing (SSD_N, N is a n-order level integer and equal to 0–4) angular quadrature scheme that has a different arrangement of directions than the standard level symmetric sets. Using double moment checking and one radiative heat transfer case comparing to benchmark or exact solutions, the new scheme is shown to be competitive with the LS_N sets, even more accurate than the S_N sets for the same number of directions up to its limit. As well as DCT sets, the SSD_N sets satisfy the general principles listed in Reference [21], and also the rotational invariance emphasized by Koch [21]. Finally, same as those of $SRAP_N$, all directions of SSD_N have the same corresponding weights for the same order N.

The SSD_N Angular Quadrature Scheme

Because of symmetry it is sufficient to construct the SSD_N quadrature scheme for one octant. Similar to the $SRAP_N$ set, the surface of the unit sphere is divided into equal contiguous elements. But different than $SRAP_N$, the whole octant spherical surface division is symmetrical along all three *x, y, z* axes, respectively. Furthermore, the division is also symmetrical along the direction $\overrightarrow{OG}$ which passes through the centroid of the whole octant (see Fig. 1). Thus, the total direction number in one octant can be three times an integer or three times an integer plus one, i.e., $3\times N$ (denoted by index *a* in the following) or $3\times N+1$ (denoted by the index *b*).

Contributed by the Heat Transfer Division for publication in the JOURNAL OF HEAT TRANSFER. Manuscript received by the Heat Transfer Division October 6, 2000; revision received October 8, 2001. Associate Editor: R. D. Skocypec.

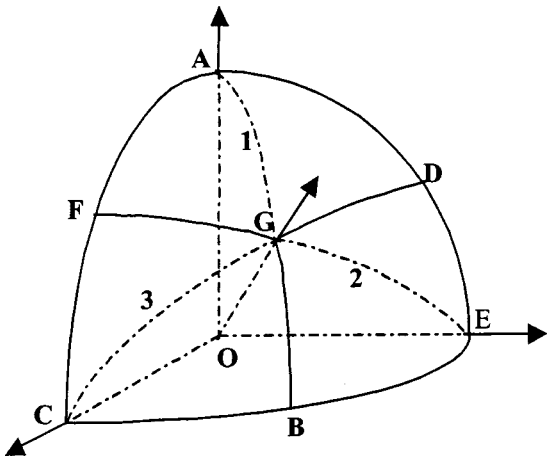

Fig. 1 Spherical surface dividing of SSD_{1a} quadrature set

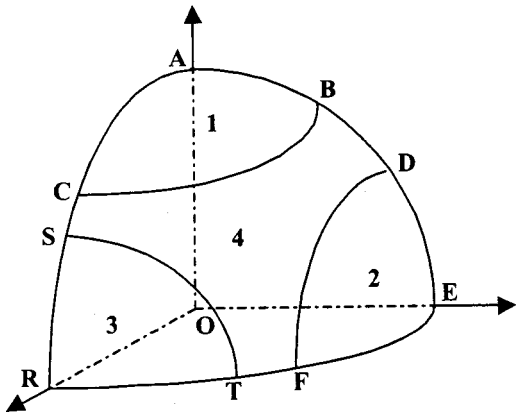

Fig. 2 Spherical surface dividing of SSD_{1b} quadrature set

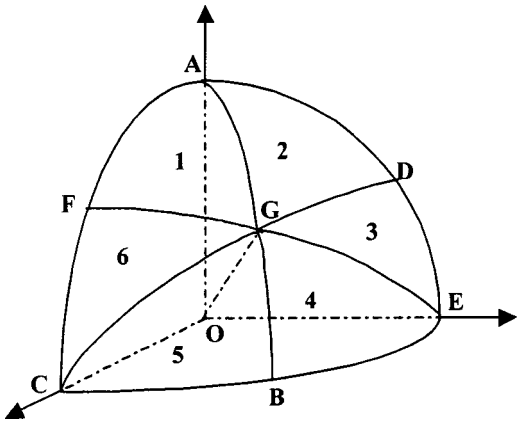

Fig. 3 Spherical surface dividing of SSD_{2a} quadrature set (method 1)

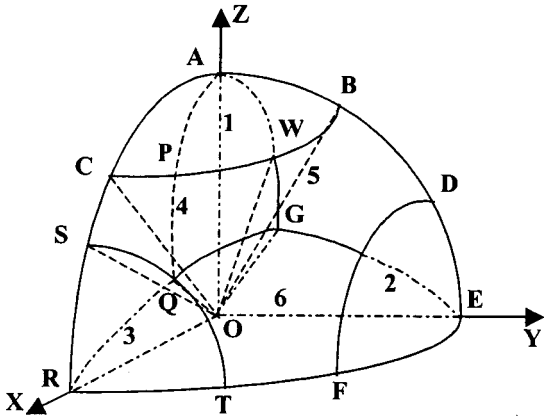

Fig. 4 Spherical surface dividing of SSD_{2a} quadrature set (method 2)

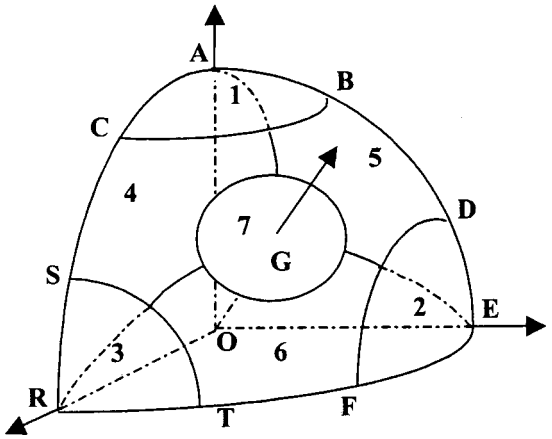

Fig. 5 Spherical surface dividing of SSD_{2b} quadrature set

In the SSD_N method only one direction exists ($\overrightarrow{OG}$ in Fig. 1) for which the index N is equal to 0. This direction is the same as in S_2.

For the order $N=1$ there are two cases: one with three directions and one with 4 directions shown in Figs. 1 and 2. In the first situation, three areas—enclosed by solid arc lines and numbered 1, 2, and 3—are arranged on the octant spherical surface. G on the center of the octant surface is the intersection point of three angular bisectors of spherical right-angled triangle AEC. Then, three spherical pyramids, O—ADGF, O—FGBC, and O—DGBE can be regarded as three solid angles in which three discrete directions pass through their centroids. For the second situation three quartered spherical crowns—numbered 1, 2, and 3—whose area is a quarter of the whole octant spherical surface, can be defined. In this way the three quartered tapers together with the residual part of the octant constitute four solid angles. Then four discrete directions can be constructed connecting the origin point O and four centroids of each solid angle.

For the order $N=2a$ six discrete directions can be constructed by two dividing methods, see Figs. 3 and 4. In the first method (Fig. 3), the spherical surface of the octant is directly divided into 6 equal areas (numbered 1 to 6) by three angular bisectors of the spherical right-angled triangle AEC. Then each spherical wedge, e.g., O—AGF numbered 1, is the solid angle in which the discrete direction passes through the origin point O and its centroid. In the second method (Fig. 4) three quartered spherical crowns—numbered 1, 2, and 3—whose area is one sixth of the whole octant spherical surface are defined. The rest of the octant spherical surface is divided into three equal parts—numbered 4, 5, and 6—by three arcs and three angular bisectors. As follows from the comparison in this paper, the accuracy of the two methods is very different.

For the order $N=2b$ the dividing method is very similar to that of $N=2a$ (method 2) except for two aspects: first, the three quartered spherical crowns—numbered 1, 2, and 3—the area is one seventh instead of one sixth of the whole octant spherical surface (shown in Fig. 5); second, another taper around the direction

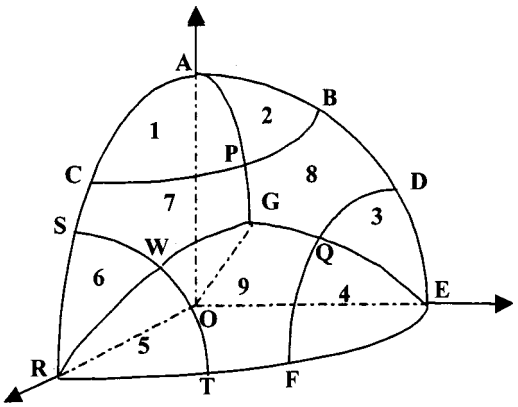

Fig. 6 Spherical surface dividing of SSD_{3a} quadrature set

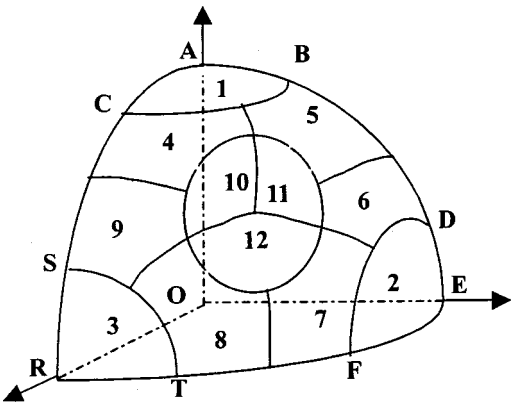

Fig. 8 Spherical surface dividing of SSD_{4a} quadrature set

$\overrightarrow{OG}$ is added. It has a spherical crown area (numbered 7) of one seventh of the octant spherical area.

Figure 6 shows the order $N=3a$. The dividing method is also similar to that of $N=2a$ (method 2) except that all three quartered spherical crowns have two ninths of the octant spherical surface area, and each quartered spherical crown is divided into two equal parts by the bisector.

Figure 7 shows the order $N=3b$. Based on Fig. 6 one taper around the direction $\overrightarrow{OG}$ which has a spherical crown area (numbered 10) of one tenth of the octant spherical area is added.

Let us return to Fig. 5. First, let all three quartered spherical crowns have one twelfth of the octant spherical surface; second, let the crown area (numbered 7 in Fig. 5) of the taper around $\overrightarrow{OG}$ be one fourth of the octant spherical surface. In this way this crown can be divided into three equal parts (numbered 10, 11, and 12 in Fig. 8) by three bisectors. Consequently, the remaining three parts (numbered 4, 5, and 6 in Fig. 5) all have an area of one sixth of the octant spherical surface and hence each one can be divided into two equal parts by the bisector again. The deduced Fig. 8 shows the order $N=4a$.

As can be seen from the illustration of the SSD_N sets, all discrete directions can be calculated after the evaluation of the corresponding centroids. The corresponding weights, i.e., the areas of spherical surface element, can also easily be carried out. Using spherical geometry one can compute the direction cosines of the centroid by integration. For example, we will demonstrate the computation on surface elements 1 and 4 from Fig. 4. For other surface elements in Fig. 4 the direction cosines then follow from symmetry. We first compute the centroid coordinates $(\overline{x_m},\overline{y_m},\overline{z_m})$, then determine the corresponding direction cosine. The geometrical meaning and the transformations between Cartesian and spherical coordinates systems are shown in Fig. 9.

Assuming a unit sphere the volume of the quartered taper O $\sim$ ABC corresponding to surface 1 in Fig. 4 is

$$V_1=\frac{1}{48}\times\frac{4}{3}\times\pi \tag{1}$$

Using elementary geometry one finds the equation of the tamper plane OCB in Cartesian coordinates system as

$$z^2=\frac{25}{11}(x^2+y^2) \tag{2}$$

which is

$$\varphi=arctg\frac{\sqrt{11}}{5} \tag{3}$$

in spherical coordinates system.

Then $\overline{x_1}$, $\overline{z_1}$ can be calculated as integral over the domain of O$\sim$ABC (indicated by down case of 1)

$$\overline{z_1}=\frac{\iiint z\,d\nu}{V_1}=\frac{1}{V_1}\int_0^{\pi/2}d\theta\int_0^{arctg\sqrt{11}/5}\sin\varphi\cos\varphi\,d\varphi\int_0^1 r^3dr \tag{4a}$$

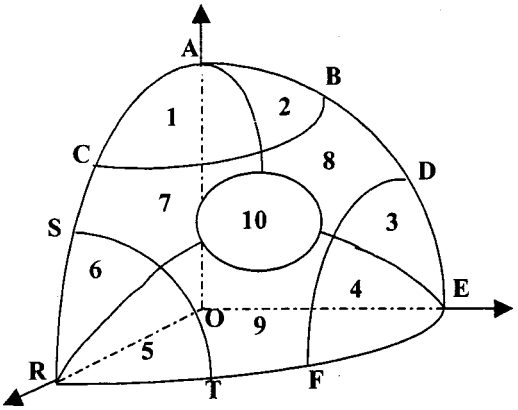

Fig. 7 Spherical surface dividing of SSD_{3b} quadrature set

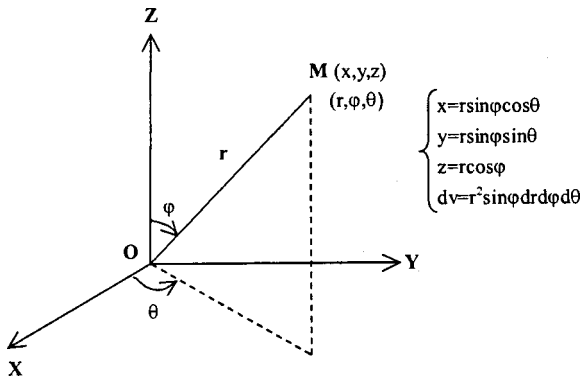

Fig. 9 Equalities between the Cartesian and spherical coordinates

Table 1 Partial ordinates and weights for SSD_N

Direction number	μ_m	η_m	ξ_m	ω_m
		SSD_{1a}		
1	0.3496826	0.3496826	0.8691629	0.5235988
2	0.3496826	0.8691629	0.3496826	
3	0.8691629	0.3496826	0.3496826	
		SSD_{2a}		
1	0.2444608	0.2444608	0.9383378	0.2617994
2	0.2444608	0.9383378	0.2444608	
3	0.9383378	0.2444608	0.2444608	
4	0.6775659	0.2860224	0.6775659	
5	0.2860224	0.6775659	0.6775659	
6	0.6775659	0.6775659	0.2860224	
		SSD_{3b}		
1	0.3739117	0.1548794	0.9144411	0.1570796
2	0.1548794	0.3739117	0.9144411	
3	0.1548794	0.9144411	0.3739117	
4	0.3739117	0.9144411	0.1548794	
5	0.9144411	0.3739117	0.1548794	
6	0.9144411	0.1548794	0.3739117	
7	0.6861174	0.2418386	0.6861174	
8	0.2418386	0.6861174	0.6861174	
9	0.6861174	0.6861174	0.2418386	
10	0.5773503	0.5773503	0.5773503	

$$\overline{x_1}=\frac{\int\int\int x\,d\nu}{V_1}=\frac{1}{V_1}\int_0^{\pi/2}\cos\theta d\theta\int_0^{arctg\sqrt{11}/5}\sin\varphi\sin\varphi d\varphi\int_0^1 r^3dr \quad (4b)$$

and due to the symmetry

$$\overline{y_1}=\overline{x_1} \quad (4c)$$

Evaluating the integrals one finds the centroid coordinates (0.1791112, 0.1791112, 0.6875000).

To find $(\overline{x_4},\overline{y_4},\overline{z_4})$ is more complicated than that of $(\overline{x_1},\overline{y_1},\overline{z_1})$. The volume O~CWGQS is surrounded by five side planes and one spherical surface numbered 4 in Fig. 4. The equations in spherical coordinates system for each side plane are

$$\varphi=arctg\frac{5}{\sqrt{11-36\sin^2\theta}} \quad \text{for tamper plane OSQ,}$$

$$\varphi=arctg(\csc\theta) \quad \text{for plane OQG,}$$

$$\theta=\frac{\pi}{4} \quad \text{for plane GOW,}$$

$$\varphi=arctg\frac{\sqrt{11}}{5} \quad \text{for tamper plane COW,}$$

$$\theta=0 \quad \text{for plane COS.}$$

Furthermore the volume O~CWGQS can be divided into two parts by plane OAPQ which has the following constant angle of $\theta=arctg\sqrt{22}/10$. Thus the integral over the whole domain of O ~CWGQS (indicated by law case of 4) divides up itself into a sum of two parts:

$$\overline{x_4}=\frac{\int\int\int x\,d\nu}{V_4}=\frac{1}{V_4}\left[\int_0^{arctg\sqrt{22}/10}\cos\theta d\theta\times\int_{arctg\sqrt{11}/5}^{arctg5/\sqrt{11-36\sin^2\theta}}\sin\varphi\sin\varphi d\varphi\int_0^t r^3dr+\int_{arctg\sqrt{22}/10}^{\pi/4}\cos\theta d\theta\int_{arctg\sqrt{11}/5}^{arctg(\csc\theta)}\sin\varphi\sin\varphi d\varphi\int_0^1 r^3dr\right] \quad (5a)$$

Table 2 Percent error in estimating $\int_{2\pi}\mu^a\eta^b\xi^c d\Omega$ for a variety of quadrature sets

Quadrature set	No. Of directions	Percent relative error in the moment (a, b, c)								
		(1,0,0)*	(3,0,0)*	(1,2,0)	(4,0,0)*	(2,2,0)	(5,0,0)*	(3,2,0)	(1,4,0)	(1,2,2)*
S_4&LS_4	24	0	6.804	-6.804	15.969	-23.953	24.517	-28.621	12.302	-20.490
SSD_{1a}	24	4.569	-1.051	10.188	0.100	-0.150	1.297	-5.745	16.153	24.158
T_2	32	1.717	1.807	1.628	5.636	-8.454	10.396	-15.370	1.747	35.264
SSD_{1b}	32	4.071	-0.981	9.122	0.205	-0.307	2.038	-7.020	10.158	38.299
$SRAP_2$	40	3.120	-2.627	8.868	-3.957	3.652	-6.429	4.975	10.814	10.814
S_6	48	0	0	0	-1.332	1.998	-3.397	6.795	2.485	-21.044
LS_6	48	0	2.152	-2.152	4.050	-6.076	5.409	-4.444	3.955	-15.727
$SSD_{2a}{}^1$	48	2.839	-1.367	7.045	-2.390	3.586	-3.954	3.807	12.852	-3.902
$SSD_{2a}{}^2$	48	2.280	0.063	4.498	0.885	-1.327	1.672	-3.156	7.032	12.207
SSD_{2b}	56	2.113	-0.895	5.121	-1.525	2.288	-2.046	1.407	4.466	14.513
T_3	72	0.102	1.618	-1.413	3.236	-4.854	4.411	-3.969	3.518	-11.082
$SRAP_3$	72	1.606	-0.319	3.531	-0.309	0.010	-0.649	0.341	5.126	5.126
SSD_{3a}	72	1.766	-0.101	3.633	0.293	-0.446	0.487	-1.278	7.741	1.131
S_8	80	0	0	0	0	0	0.646	-1.291	-5.829	20.069
LS_8	80	0	0.823	-0.823	1.134	-1.701	1.072	0.326	2.015	-11.636
SSD_{3b}	80	1.558	-0.245	3.360	-0.177	0.265	-0.238	-0.257	6.166	2.179
SSD_{4a}	96	1.209	-0.387	2.806	-0.665	0.997	-0.866	0.569	2.500	8.193
Exact		π	$\pi/2$	$\pi/4$	$2\pi/5$	$2\pi/15$	$\pi/3$	$\pi/12$	$\pi/8$	$\pi/24$

1. Method 1 of SSD_{2a} shown in Fig.3
2. Method 2 of SSD_{2a} shown in Fig.4
*Independent moments

Table 3 Dimensionless data for three-dimensional rectangular system fed to DOM program

Dimensions of the furnace	$\widetilde{L}_x=1, \widetilde{L}_y=1, \widetilde{L}_z=6$
Optical thickness	$\tau_0=1/6$
Wall black-body intensities	$\left(\widetilde{I}_{bw}\right)_{side}=0.0020$
	$\left(\widetilde{I}_{bw}\right)_{burner}=0.0574$
	$\left(\widetilde{I}_{bw}\right)_{end}=0.0167$
Gas temperature	$\widetilde{T}_i=0.1775$
	$\widetilde{T}_e=0.6222$
	$\widetilde{T}_{\max}=1$
Position of the peak	$Z'_{\max}=0.8$
Slope of gas temperature distribution at furnace exit	$d_e=-0.220$

$$\overline{y}_4=\frac{\int\int\int y\,d\nu}{V_4}=\frac{1}{V_4}\left[\int_0^{arctg\sqrt{22}/10}\sin\theta d\theta \times\int_{arctg\sqrt{11}/5}^{arctg5/\sqrt{11-36\sin^2\theta}}\sin\varphi\sin\varphi d\varphi\int_0^1 r^3dr+\int_{arctg\sqrt{22}/10}^{\pi/4}\sin\theta d\theta\int_{arctg\sqrt{11}/5}^{arctg(\csc\theta)}\sin\varphi\sin\varphi d\varphi\int_0^1 r^3dr\right] \tag{5b}$$

and due to the symmetry

$$\overline{z}_4=\overline{x}_4 \tag{5c}$$

Finally, the centroid of O~CWGQS is (0.4971973, 0.2098830, 0.4971973). The centroid coordinates determine the corresponding direction cosines.

It should be noted that formulas (5) are much more complicated than formulas (4). As the volume faces become more and more complicated the evaluation of the integrals becomes more and more difficult, especially for the highest order case of SSD_N. Thus the computation of the direction cosines can be complicated. But this work only has to be done once. When all discrete directions are determined, they can be used as common data for all. Those cases SSD_{1a}, SSD_{2a}, and SSD_{3b} that will be used for radiative heat transfer prediction in this paper are listed in Table 1 together with the corresponding weights.

Double Moment Test for SSD_N Angular Quadrature Sets

In order to check the accuracy of the SSD_N method, a comparison between the SSD_N and other sets—including S_N [19], LS_N [20], T_N [22], and $SRAP_N$ [23]—is made to evaluate the double moments of the form $\int_{2\pi}\mu^a\eta^b\zeta^c d\Omega$ over a hemisphere. The highest value of N for SSD_N used in this paper is 4. The results are listed in Table 2. Like the T_N and the $SRAP_N$ quadrature sets, all SSD_N quadrature sets have been found to exactly satisfy the (0,0,0) moment and the (2,0,0) moment (the diffusion condition), and therefore have not been listed here.

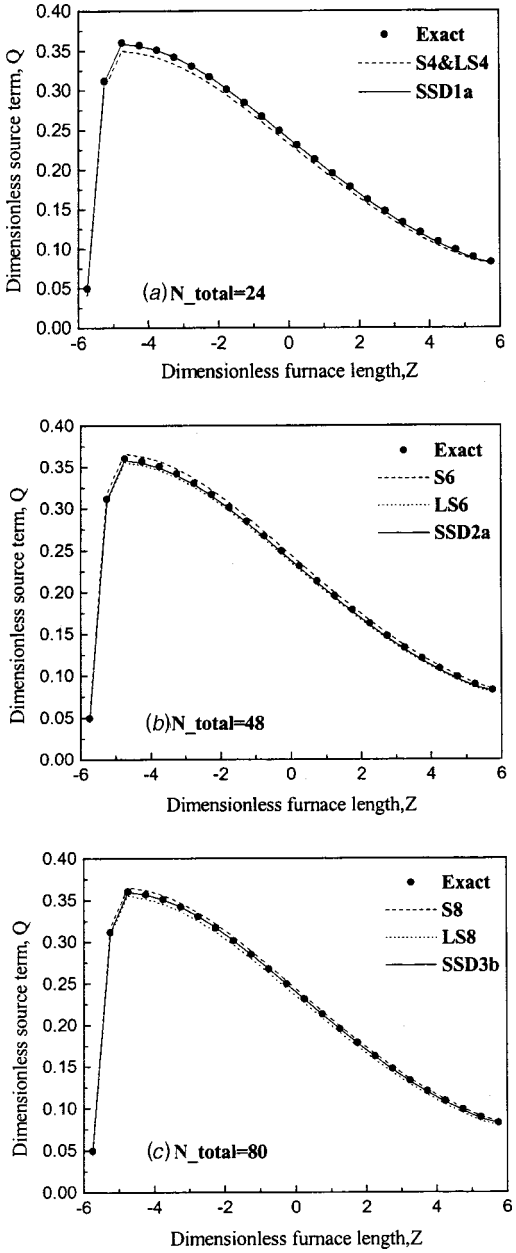

Fig. 10 Comparisons between the exact values and SSD_N, S_N and LS_N predictions of dimensionless radiative energy source terms along ($x=0.25, y=0.25, z$): (*a*) *N_total=24*; (*b*) *N_total=48*; (*c*) *N_total=80*.

From the results listed in Table 2 it can be seen that the SSD_N quadrature set globally matches the double moment very well. For the same discrete direction number, the accuracy of the SSD_N set is high and even close to those of S_N and LS_N on the whole. The SSD_N set can also give high accuracy for the half-range-fluxes ($\int_{2\pi}\mu d\Omega$, first-order moment) which was pointed out by Truelove [3] to be an indicator for the precision of DOM method. Therefore, there is another potential alternative quadrature set for DOM giving more accurate solution but using less number of discrete directions.

Prediction of Radiative Heat Transfer

In this section the DOM is evaluated for one typical case to compare the accuracy of different quadrature sets. The computation was performed with the same number of discrete directions

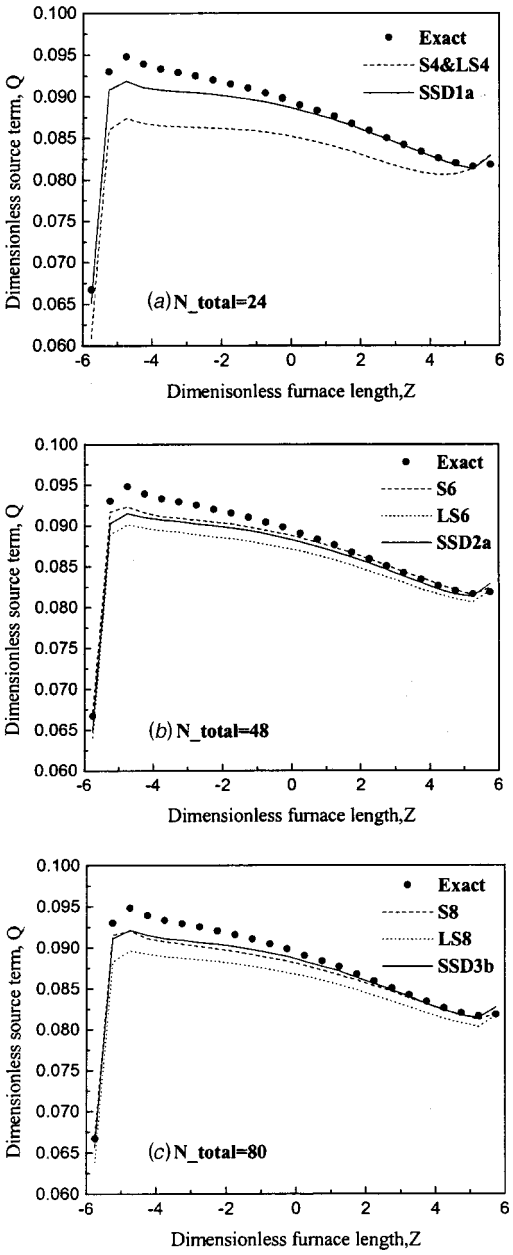

Fig. 11 Comparisons between the exact values and SSD_N, S_N, and LS_N predictions of dimensionless radiative energy source terms along ($x=0.75, y=0.25, z$): (*a*) *N*_total=24; (*b*) *N*_total =48; (*c*) *N*_total=80.

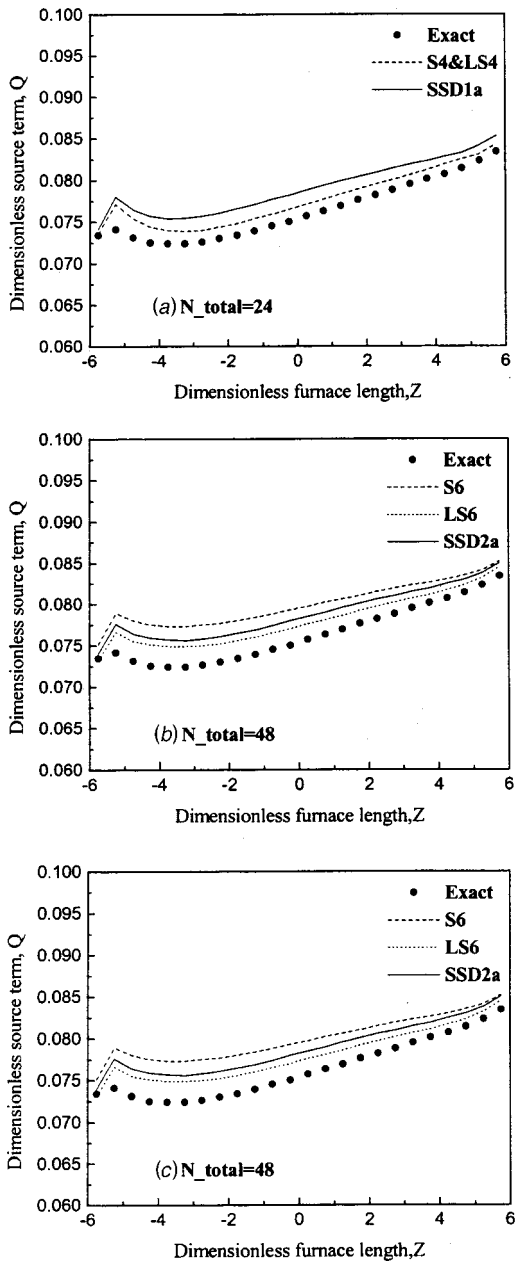

Fig. 12 Comparisons between the exact values and SSD_N, S_N and LS_N predictions of dimensionless radiative energy source terms along ($x=0.75, y=0.75, z$): (*a*) *N*_total=24; (*b*) *N*_total =48; (*c*) *N*_total=80.

for different quadrature sets so that the same quadrature set order and computer memory were employed. For the sake of briefness the discrete ordinates representations of RTE (radiative transfer equations) for an absorbing-emitting, no scattering medium in 3D system is not described here. Details about the execution of DOM is available in many previous published References [1–4], [21], [24]. In the present work the same weighted diamond-difference scheme which relates the cell edge radiant intensities to the cell center radiant intensity is used for different quadrature sets. Iteration was ended when the convergence criterion was satisfied [25]

$$|I^l_{m,p} - I^{l*}_{m,p}|/I_{m,p} \leqslant 10^{-6} \tag{6}$$

where the $I^1_{m,p}$ and $I^{1*}_{m,p}$ represent previous iteration intensity values in any direction l at the center location p of any control volume and its present one, respectively.

The test case employed here is a three-dimensional rectangular enclosure containing an absorbing-emitting medium with steep temperature gradients due to its available exact solution data. The input dimensionless data for DOM program are listed in Table 3. The detailed description of this problem together with its exact solutions can be found in References [26], [27]. As in [27], the test enclosure has been subdivided into $4\times4\times24$ control volumes in x, y, z directions respectively, but is solved only for $2\times2\times24$ volumes due to the symmetry of the enclosure [26].

Up to the discrete direction number limit of S_N Figs. 10–12 show the comparisons between the exact solution and the predictions of SSD_N, S_N, and LS_N of dimensionless radiative energy source terms along three lines within the enclosure. Figure 13 shows the comparison for radiative heat flux densities to the side

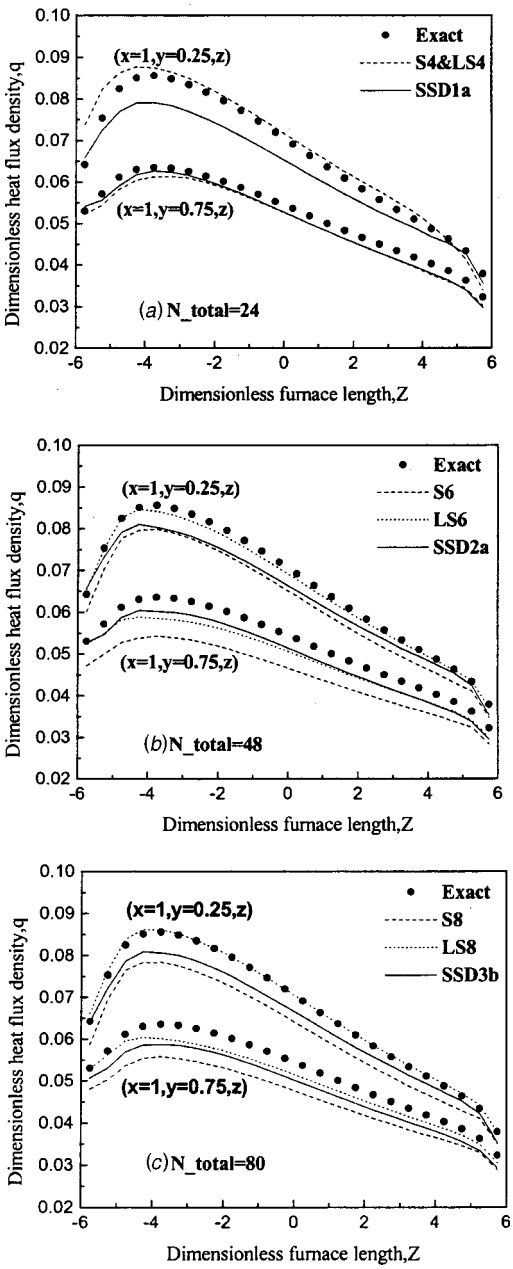

Fig. 13 Comparisons between the exact values and SSD_N, S_N, and LS_N predictions of dimensionless radiative heat flux densities to the side wall; (*a*) *N*_total=24; (*b*) *N*_total=48; (*c*) *N*_total=80.

wall alone two lines. *N*_total indicates the same total direction number discretized within the whole solid angle 4π for SSD_N, S_N, and LS_N.

From Figs. 10–13 it can be seen that different quadrature sets give different accuracies. Figure 10 shows the most accurate method is SSD_N. Figure 11 shows that SSD_N and S_N have almost identical accuracy, but the LS_N has the lowest accuracy. Figure 12 shows results contrary to Fig. 11. From Fig. 13, the results of dimensionless heat flux densities show LS_N has the highest accuracy, the SSD_N has the second, and the S_N does the third. Finally, the three sets can give excellent results competing well with exact solutions. For other pairs of quadrature sets with the same number of directions, say T_2 and SSD_{1b}, T_3 and $SRAP_3$ and SSD_{3a}, the differences between them are very small and not shown here.

A more condensed comparison of the results presented in Figures 10 to 13 are given in Tables 4 and 5. The first three columns give the average absolute errors compared to the exact solution, and the last column gives the maximum relative errors for every line. As can be seen in Table 4, all the maximum percentage errors produced by SSD_N are less than those produced by S_N and LS_N. Table 5 shows the LS_N can give the highest accuracy dimensionless heat flux densities. Finally, those comparative results are consistent with the trends shown in Figs. 10–13.

One important factor that largely affects the computational cost of DOM, is the iteration times under the same convergence criterion. A numerical comparison of iteration times between the SSD_N and S_N, LS_N, T_N, $SRAP_N$ was made. The CPU time is directly proportional to the iteration times, because the comparison was based on the same direction number for pairs of different quadrature sets. The comparison results are listed in Table 6. The results indicate that almost 10 percent of CPU time can be saved when using SSD_N instead of S_N, LS_N, T_N, $SRAP_N$ for coarse grid $4\times4\times12$. With increasing number of grid and discrete directions, even more CPU time can be saved. For the case investigated here the CPU time saved at most can amount up to 40 percent.

Conclusions and Discussions

A new spherical surface symmetrical equal dividing angular quadrature scheme (SSD_N) for discrete-ordinates method was developed. The double moment test and radiative heat transfer prediction of a black-walled rectangular enclosure, with available exact solution data for comparison, indicated that all results of SSD_N quadrature set agree well with the exact solution and are in excellent agreement with the results of S_N, LS_N, T_N, and $SRAP_N$. Comparison of computational iteration times showed that 10 percent CPU time can be saved by SSD_N relative to S_N, LS_N, T_N and $SRAP_N$ for the present case. It should be noted that the number of discrete directions of SSD_N investigated in this paper is limited to 96.

Table 4 Comparison of SSD_N, S_N, and LS_N predictions of dimensionless source term distributions for medium grid points

Method	Average absolute error (x=0.75,y=0.75,z)	(x=0.75,y=0.25,z)	(x=0.25,y=0.25,z)	Maximum Percentage error(%)
S_4&LS_4	0.001399	0.004291	0.006909	1.01
SSD_{1a}	0.002758	0.001102	0.000972	0.43
S_6	0.003664	0.000884	0.004129	0.63
LS_6	0.001730	0.002382	0.004159	0.48
SSD_{2a}	0.002539	0.001385	0.001822	0.44
S_8	0.003168	0.001304	0.003322	0.57
LS_8	0.001489	0.002742	0.004815	0.55
SSD_{3b}	0.002918	0.001058	0.000616	0.41

Table 5 Comparison of SSD_N, S_N, and LS_N predictions of dimensionless flux densities for surface grid points

Method	Average absolute error (x=1,y=0.75,z)	(x=1,y=0.25,z)	Side wall	Maximum Percentage error(%)
S_4&LS_4	0.002025	0.002254	0.002140	0.95
SSD_{1a}	0.001684	0.004132	0.002908	0.65
S_6	0.007132	0.004763	0.005948	0.94
LS_6	0.003401	0.000979	0.002190	0.51
SSD_{2a}	0.002731	0.003279	0.003005	0.54
S_8	0.006174	0.005624	0.005899	0.80
LS_8	0.002407	0.000433	0.001420	0.37
SSD_{3b}	0.003846	0.003149	0.003498	0.49

Table 6 Comparison of numbers of iterations between SSD_N and S_N, T_N, LS_N, $SRAP_N$

Quadrature sets	S_4&LS_4	SSD_{1a}	T_2	SSD_{1b}	S_6	LS_6	SSD_{2a}	T_3	$SRAP_3$	SSD_{3a}	S_8	LS_8	SSD_{3b}
Grid: 4×4×12													
Iteration	27	22	27	23	30	28	26	34	33	25	32	30	26
Grid: 12×12×72													
Iteration	65	47	58	51	68	61	54	92	85	51	80	88	65

Acknowledgments

This study was supported by the National Natural Science Foundation of China under the contracts No. 59876035 and No. 59974005. The first author gratefully acknowledges Dr. Egbert Zienicke for his help to improve the English text, and acknowledges Dr. R. D. Skocypec for his reasonable comments and great efforts to improve the total quality of this paper. The first author also would like to acknowledge Prof. J. F. Sacadura and Prof. J. R. Howell for providing their references.

Nomenclature

d = slope of the axial temperature curve
I = radiant intensity, $Wm^{-2}\,sr^{-1}$
L = half of the side lengths of the rectangular enclosure, m
N = order of quadrature set
r = radial distance in spherical geometry, m
T = temperature, K
V = volume, m^3
v = volume element, m^3
x, y, z = coordinates in Cartesian geometry, m
Z' = dimensionless axial distance

Greek Symbols

θ = azimuthal angles in spherical system
μ, η, ξ = direction cosines in x, y, z directions
τ = optical thickness
φ = polar angles in spherical system
Ω = integral domain, sr

Subscripts

burner = burner wall
bw = black wall
e = end-face
end = end wall
i = inlet
m = discrete direction
max = maximum
p = center location of control
side = side wall

Superscripts

a, b, c = double moments degree index
— = values of centroid
$*$ = present value
$\sim$ = dimensionless

References

[1] Carlson, B. G., and Lathrop, K. D., 1968, *Computing Methods in Reactor Physics*, H. Greenspan, C. N. Kelber, and D. Okrent, eds., Gordon and Breach, New York.
[2] Fiveland, W. A., 1984, "Discrete-Ordinates Solutions of the Radiative Transport Equation for Rectangular Enclosures," ASME J. Heat Transfer, **106**, pp. 699–706.
[3] Truelove, J. S., 1987, "Discrete-Ordinates Solutions of the Radiation Transport Equation," ASME J. Heat Transfer, **109**, pp. 1048–1051.
[4] Truelove, J. S., 1988, "Three-Dimensional Radiation in Absorbing-Emitting-Scattering Media Using the Discrete-Ordinates Approximation," J. Quant. Spectrosc. Radiat. Transf., **39**(1), pp. 27–31.
[5] Vaillon, R., Lallemand, M., and Lemonnier, D., 1996, "Radiative Heat Transfer in Orthogonal Cuvilinear Coordinates Using the Discrete Ordinates Method," J. Quant. Spectrosc. Radiat. Transf., **55**(1), pp. 7–17.
[6] Sakami, M., Charette, A., and Dez, V., 1996, "Application of the Discrete Ordinates Method to Combined Conductive and Radiative Heat Transfer in a Two-Dimensional Complex Geometry," J. Quant. Spectrosc. Radiat. Transf., **56**(4), pp. 517–513.
[7] Koo, H.-M., Chiong, K.-B., and Song, T.-H., 1997, "Schemes and Application of First and Second-Order Discrete Ordinates Interpolation Methods to Irregular Two-Dimensional Geometries," ASME J. Heat Transfer, **119**, pp. 730–737.
[8] Sakami, M., Charette, A., and Dez, V., 1998, "Radiative Heat Transfer in Three-Dimensional Enclosures of Complex Geometry by Using the Discrete-Ordinates Method," J. Quant. Spectrosc. Radiat. Transf., **59**(1/2), pp. 117–136.
[9] Coelho, P. J., Goncalves, J. M., and Carvalho, M. G., 1998, "Modelling of Radiative Heat Transfer in Enclosures with Obstacles," Int. J. Heat Mass Transf., **41**(1-4), pp. 745–756.
[10] Sakami, M., and Charette, A., 1998, "A New Differencing Scheme for the Discrete-Ordinates Method in Complex Geometries," Rev. Gen. Therm., **37**, pp. 440–449.
[11] Liu, J., and Chen, Y. S., 1999, "Examination of Conventional and Ever-Parity Formulations of Discrete Ordinates Method in A Body-Fitted Coordinates System," J. Quant. Spectrosc. Radiat. Transf., **61**(4), pp. 417–434.
[12] Lee, C. E., 1961, "The Discrete S_N Approximation to Transport Theory," LA-2595, Los Alamos Scientific Laboratory, NM.
[13] Lathrop, K. D., and Carlson, B. G., 1965, "Discrete Ordinates Angular Quadrature of the Neutron Transport Equation," LA-3168, Los Alamos Scientific Laboratory, NM.
[14] Fiveland, W. A., 1987, "Discrete-Ordinates Methods for Radiative Heat Transfer in Isotropically Scattering Media," ASME J. Heat Transfer, **109**, pp. 809–812.
[15] Jamaluddin, A. S., and Smith, P. J., 1988, "Predicting Radiative Transfer in Rectangular Enclosures Using the Discrete Ordinate Method," Combust. Sci. Technol., **59**, pp. 321–340.
[16] Jamaluddin, A. S., and Smith, P. J., 1988, "Predicting Radiative Transfer in Axisymmetric Cylindrical Enclosures Using the Discrete Ordinate Method," Combust. Sci. Technol., **62**, pp. 173–181.

[17] Tan, Z., and Howell, J. R., 1990, ''New Numerical Method for Radiation Heat Transfer in Nonhomogeneous Participating Media,'' J. Thermophys. Heat Transfer, **4**(4), pp. 419–424.
[18] Hsu, P.-F., Tan, Z., and Howell, J. R., 1993, ''Radiative Transfer by the YIX Method in Nonhomogeneous, Scattering, and Nongray Media,'' J. Thermophys. Heat Transfer, **7**(3), pp. 487–495.
[19] Fiveland, W. A., 1991, ''The Selection of Discrete Ordinate Quadrature Sets for Anisotropic Scattering,'' *Fundamentals of Radiation Heat Transfer*, ASME-HTD-**160**.
[20] Wakil, N. El., and Sacadura, J. F., 1992, ''Some Improvements of the Discrete Ordinates Method for the Solution of the Radiative Transport Equation in Multidimensional Anisotropically Scattering Media,'' *Developments in Radiative Heat Transfer*, ASME HTD-**203**, pp. 119–127.
[21] Koch, R., Krebs, W., Wittig, S., and Viskanta, R., 1995, ''Discrete Ordinates Quadrature Schemes for Multidimensional Radiative Transfer,'' J. Quant. Spectrosc. Radiat. Transf., **53**(4), pp. 353–372.
[22] Thurgood, C. P., Pollard, A., and Becker, H. A., 1995, ''The T_N Quadrature Set for the Discrete Ordinate Ordinates Method,'' ASME J. Heat Transfer, **117**, pp. 1068–1070.
[23] Li, Ben-Wen, Yao, Qiang, Cao, Xin-Yu, and Cen, Ke-Fa, 1998, ''A New Discrete Ordinates Quadrature Scheme for Three-Dimensional Radiative Heat Transfer,'' ASME J. Heat Transfer, **120**, pp. 514–518.
[24] Li, Ben-Wen, Zhou, Jun-Hu, Cao, Xin-Yu, and Cen, Ke-Fa, 2000, ''Successive Spherical Rings Arithmetic Progression Dividing Discrete Ordinates Method and Its Comparison with T_N Set,'' Int. J. Transport Phenomena, **2**, pp. 231–239.
[25] Chai, J. C., Lee, H. S., and Patankar, S. V., 1994, ''Improved Treatment of Scattering Using the Discrete Ordinates Method,'' ASME J. Heat Transfer, **116**, pp. 260–263.
[26] Selcuk, N., 1985, ''Exact Solution for Radiative Heat Transfer in Box-Shaped Furnaces,'' ASME J. Heat Transfer, **107**, pp. 648–655.
[27] Selcuk, N., and Kayakol, N., 1997, ''Evaluation of Discrete Ordinates Method for Radiative Transfer in Rectangular Furnaces,'' Int. J. Heat Mass Transf., **40**(2), pp. 213–222.

Falling Film Transitions on Plain and Enhanced Tubes

J. F. Roques

V. Dupont

J. R. Thome

Laboratory of Heat and Mass Transfer (LTCM),
Department of Mechanical Engineering,
Swiss Federal Institute of Technology Lausanne,
CH-1015 Lausanne, Switzerland

In falling film heat transfer on horizontal tube bundles, liquid flow from tube to tube occurs as a falling jet that can take on different flow modes. At low flow rates, the liquid film falls as discrete droplets. At higher flow rates, these droplets form discretely spaced liquid columns. At still higher flow rates, the film falls as a continuous sheet of liquid. Predicting the flow transitions between these flow modes is an essential step in determining the heat transfer coefficient for the particular flow mode, whether for a single phase process or for falling film condensation or evaporation. Previous studies have centered mostly on falling films on plain tube arrays. The objective of the present study is to extend the investigation to tubes with enhanced surfaces: a low finned tube, an enhanced boiling tube and an enhanced condensation tube. The effect of tube spacing on flow transition has also been investigated. The test fluids were water, glycol and a glycol-water mixture. The adiabatic experimental results show that the flow mode transition thresholds for the enhanced boiling tube are very similar to those of the plain tube while the fin structure of the other two enhanced tubes can significantly shift their transition thresholds.
[DOI: 10.1115/1.1458017]

Keywords: Enhancement, Film, Finned Surfaces, Heat Transfer, Visualization

1 Introduction

The Jakob [1] tube row equation for falling film condensation on plain tube bundles, i.e., the application of the Nusselt [2] vertical plate theory to a vertical array of horizontal tubes, is a classic in the heat transfer literature. In particular, Jakob modelled the condensate flow from one tube to the next as if it occurred on a continuous vertical plate formed of a series of half-tubes joined at their top and bottom, that is assuming that the condensate flows as a continuous sheet from the bottom of the upper tube onto the top of the lower tube, such that

$$\frac{\alpha(N)}{\alpha(N=1)} = N^{3/4} - (N-1)^{3/4}, \tag{1}$$

where $\alpha(N)$ is the local coefficient on tube N and $\alpha(N=1)$ is the Nusselt solution for the top tube. However, Kern [3] observed that condensers designed with the Jakob tube row expression were consistently oversurfaced and by inspection replaced the exponent with another to reduce the tube row effect with the following corresponding equation:

$$\frac{\alpha(N)}{\alpha(N=1)} = N^{5/6} - (N-1)^{5/6}. \tag{2}$$

Even so, as can be seen from Fig. 1 compiled by Marto [4], the tube row effect measured experimentally may deviate substantially from the two expressions of Jakob and Kern. Rather than interpreting the wide variation in the normalized data as only being experimental error, it is proposed here that the scatter in the data can be explained by the various film flow modes from tube to tube. For instance, it can be deduced that the sheet mode has the most severe tube row effect, i.e., that given by Jakob, since the lower tubes are inundated along their entire length by the condensate arriving from the tubes above. The column mode will have less of a tube row effect since a large portion of the surface of the lower tubes between the liquid columns is not inundated by condensate from above. Similarly, the droplet mode can be deduce to have an even weaker tuberow effect since the droplets are spaced apart like the columns and the flow rate of condensate is less than in the column mode and is also intermittent. On the other hand, the data falling below the Jakob curve at small tube row numbers are probably the result of small amounts of non-condensables in the vapor phase during those tests, which adversely affect heat transfer. (Photographs of these modes are shown later in Section 3).

It should be noted that falling film condensation can be modeled in terms of the film Reynolds number of the condensate, which can be either laminar or turbulent with or without interfacial ripples, and hence some of the scatter in Fig. 1 may also be due to this. For example, at large row numbers the film may have converted from laminar to turbulent flow with a sharp increase in local heat transfer, and, hence, these data would fall above the Jakob curve.

Despite numerous observations of condensation and falling film evaporation on rows of tubes, apparently no generalized flow mode map is currently available for either plain or enhanced types of tubes, although Honda et al. [5] have presented several transition expressions for fluids condensing on low finned tubes. These processes however are similar to that of an *adiabatic* falling film of liquid fed onto the top of a tube array, which has been studied extensively by Hu and Jacobi [6] on plain tubes for a variety of fluids, tube diameters, tube pitches and flow rates and with/without cocurrent gas flow. Based on their observations, they proposed a flow mode transition map with coordinates of film Reynolds number (Re) versus the Galileo number (Ga). The map delineates the transitions between the three dominant modes (sheet, column and droplet) with two mixed mode zones (column-sheet and droplet-column) in which both modes are present. Their corresponding four flow transition expressions between these five zones are given below for plain tubes (valid for passing through the transitions in either direction and hence the symbol $\Leftrightarrow$):

$$\text{Droplet} \Leftrightarrow \text{Droplet-Column:}\quad \mathrm{Re} = 0.074\ \mathrm{Ga}^{0.302} \tag{3}$$

$$\text{Droplet-Column} \Leftrightarrow \text{Column:}\quad \mathrm{Re} = 0.096\ \mathrm{Ga}^{0.301} \tag{4}$$

$$\text{Column} \Leftrightarrow \text{Column-Sheet:}\quad \mathrm{Re} = 1.414\ \mathrm{Ga}^{0.233} \tag{5}$$

$$\text{Column-Sheet} \Leftrightarrow \text{Sheet:}\quad \mathrm{Re} = 1.448\ \mathrm{Ga}^{0.236}, \tag{6}$$

where the modified Gallileo number of the liquid, which is the ratio between the gravity and the viscous force based on the capillary length scale, is defined as

Contributed by the Heat Transfer Division for publication in the JOURNAL OF HEAT TRANSFER. Manuscript received by the Heat Transfer Division November 7, 2001; revision received July 9, 2001. Associate Editor: G. P. Peterson.

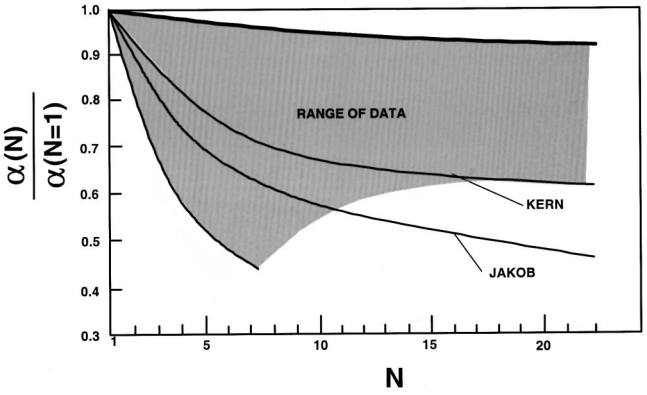

Fig. 1 Comparison of tuberow methods to experimental data by Marto [4]

$$\mathrm{Ga}=\frac{\rho\sigma^3}{\mu^4 g}, \tag{7}$$

and the liquid film Reynolds number is defined as

$$\mathrm{Re}=\frac{2\Gamma}{\mu}, \tag{8}$$

where Γ is the total flow rate on both sides of the tube [kg/m s], ρ is the density of the liquid, μ is liquid dynamic viscosity, σ is the surface tension, and g is the acceleration due to gravity. This map is applicable to plain tubes for cocurrent, i.e., downflow, air velocities less than 15 m/s.

An extensive investigation on falling film flow mode transitions of adiabatic and non-phase change films was presented for plain tubes by Mitrovic [7]. Various other studies have investigated the dynamics of transitions, droplet formation and column departure wavelengths, such as those of Taghavi and Dhir [8], Tang and Lu [9] and Mitrovic and Ricoeur [10]. Hu and Jacobi [11] have recently reported additional data on tube spacing effects on column and droplet departure wavelengths.

Hu and Jacobi [12] correlated their subcooled heat transfer data obtained with the same test stand by intertube flow mode, finding a separate, distinct correlation for the heat transfer data for each flow mode. Hence, the intertube flow mode approach appears to be the right flow regime based heat transfer model to apply to falling film condensation and falling film evaporation to obtain improved accuracy for bundle design methods. Refer to Thome [13] for a recent review of other work on falling film evaporation.

Hence, based on this approach, flow visualizations have been made here on four types of tubes with three different fluids under adiabatic flow conditions. The next sections present the experimental setup, test conditions and results. This work is a fundamental first step towards developing future general design methods for falling film condensation and evaporation on plain and enhanced tube bundles.

2 Description of the Test Facility

2.1 Test Facility. The test facility is shown in Figs. 2 and 3. It is composed of three main parts:

1 ***Fluid Circuit***: The fluid starts first from the *tank* that serves as a reservoir for the whole circuit, and then passes through a centrifugal pump. This type of pump was chosen to avoid oscillations in the mass flow and the pressure. A filter then eliminates any dust or particles in the fluid. The flow rate is measured with one of two rotameters, which are necessary because the ranges of mass flow and viscosity were too large for only one rotameter. The temperature in the liquid bath is measured with a thermocouple for calculation of the liquid properties.

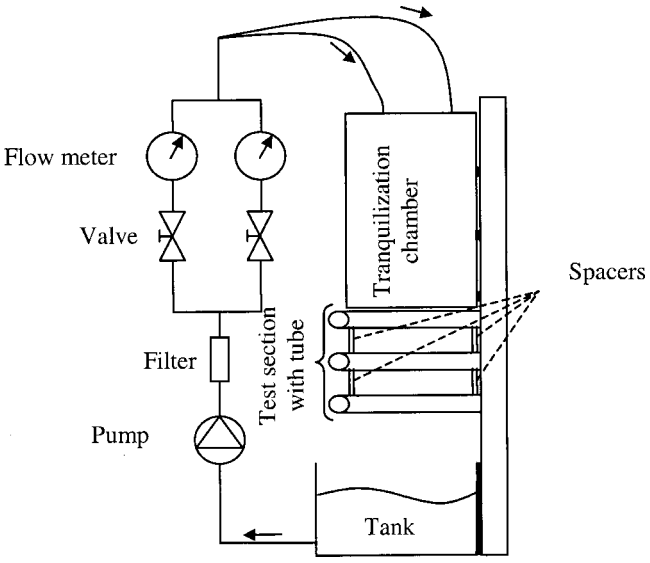

Fig. 2 Diagram of the rig test

2 ***Flow Tranquilization Chamber***: Its function is to insure a uniform flow from the top tube onto the second tube. It is a box of 300×260×10 mm (inside *Height*×*Width*×*Depth*) in which the flow enters at the top through two holes. For the lowest viscosity fluid in this study (water), a grid with foam is added in the middle of this chamber to increase the homogenization effect. The fluid leaves this box at the bottom through a flat plate with 1 mm diameter holes spaced 2 mm apart. The length of this distribution system (and the resulting film visualized) is 200 mm.

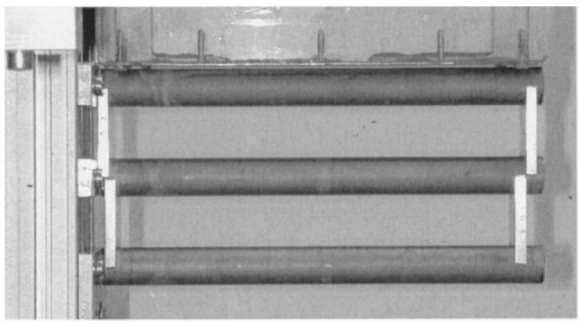

(*a*)

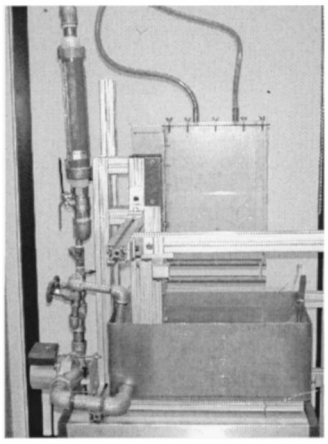

(*b*)

Fig. 3 Photos of the test section: (*a*) test section; and (*b*) overall view.

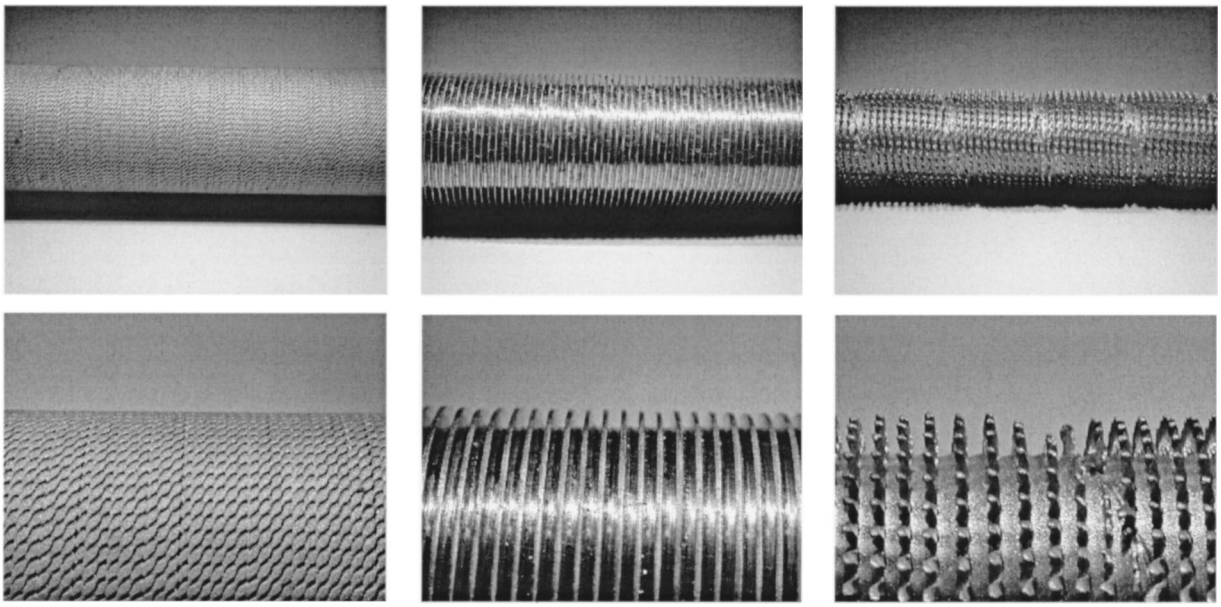

Fig. 4 Photographs of the enhanced tubes

Table 1 Fins dimensions of the enhanced tested tubes

	Fin height [mm]	Fin density [fpi] (fpm)
Turbo-BII	0.6	51 (2020)
Turbo-Chil	1.52	26 (1024)
Thermoexcel-C	1.96	24 (952)

3 ***Test Section***: It is comprised of three tubes on which the fluid flows. They are held at one end and the distance between them is fixed with appropriately manufactured *spacers*. Care is taken to obtain a precise alignment of the horizontal tubes into a vertical array.

2.2 Tested Tubes. Figure 4 depicts photographs of the Turbo-BII, Turbo-Chil and Thermoexcel-C tubes that were tested. The first is an enhanced boiling tube, the second is a commonly used integral low fin tube and the third is an enhanced condensation tube (the helical deformation observable on the Thermoexcel-C tube is from corrugation of the tube for inside enhancement).

Table 1 presents the fin dimensions of the enhanced tubes. The fin height is (outside diameter-root diameter)/2 while the fin density is the number of enhanced periodic patterns observable per inch.

All the tested tubes have been sanded before transition observations were made to remove any traces of oil. The result was an increase of the surface roughness from 0.3 μm to 2 μm (measurable only on plain tubes).

3 Measurements

3.1 Objectives of the Tests. The first objective was to observe the intertube flow modes and determine what transition takes place as the flow rate is varied. Secondly, the flow rate was measured in order to determine the flow rate at which the various transitions take place. For the plain and Turbo-BII types of tubes, the different flow modes are observed between the first tube (at the top) and the second tube as depicted in Fig. 2, i.e., similar to the test procedure utilized by Hu and Jacobi. This set up gives a uniform film on the top of the first tube and the intertube flow pattern between the first and second tube is that observed, and the third tube's purpose is to give continuation of the flow mode as if the tubes were in a large array. For the low fin and Thermoexcel-C tubes, the flow distribution from the tranquilization chamber onto the top tube is not uniform if the top tube has projecting fins. Hence, a plain tube was placed below the tranquilization chamber and above the three enhanced tubes in this case, such that the plain tube was in physical contact with the top of the upper enhanced tube. This gave a uniform film distribution onto the top of the upper enhanced tube and flow mode observations were made as before between the first and second enhanced tubes.

The flows between the tubes are classified into the five different modes described below. For each transition from one mode to another, the mass flow at which it occurs was recorded. A high speed Kodak digital video system was used to record and observe the phenomena in slow motion to facilitate detection of the mode. Some pictures of these videos are presented in Fig. 5 for plain tubes to illustrate the five different modes, where the dark zones are the three horizontal tubes and the transparent fluid is the falling film. These flow modes are also typical of those observed in condensation tests. The intertube flow modes have been defined as follows for categorization purposes:

A. Droplet Mode. The flow is in droplet mode when only droplets are falling between the tubes. To define this mode, the following rule was applied: the mode is Droplet when on all the video images (30 fps) it is always possible to draw a continuous curve from one side of the picture to the other without crossing any liquid. Note that the videos are essential to distinguish a rapid sequence of droplets from a continuous column of liquid.

B. Droplet-Column Mode. This is an intermediate mode that exists when there is at least one stable liquid column bridging from the upper tube to the lower tube and the other fluid flows as droplets. A column is a continuous liquid link between tubes. This column can move horizontally along the axis of the tubes but has to exist for at least 1 or 2 seconds to define this mode (otherwise these are counted as droplets).

C. Column Mode. This mode is when there are only liquid columns between the tubes.

D. Column-Sheet Mode. In this intermediate mode, fluid flows both in columns and as a liquid sheet simultaneously between the tubes. It is reached when at least one small sheet is visible. This small sheet is formed by the merging of two neighboring columns and has a triangular form (see photograph in Fig. 5).

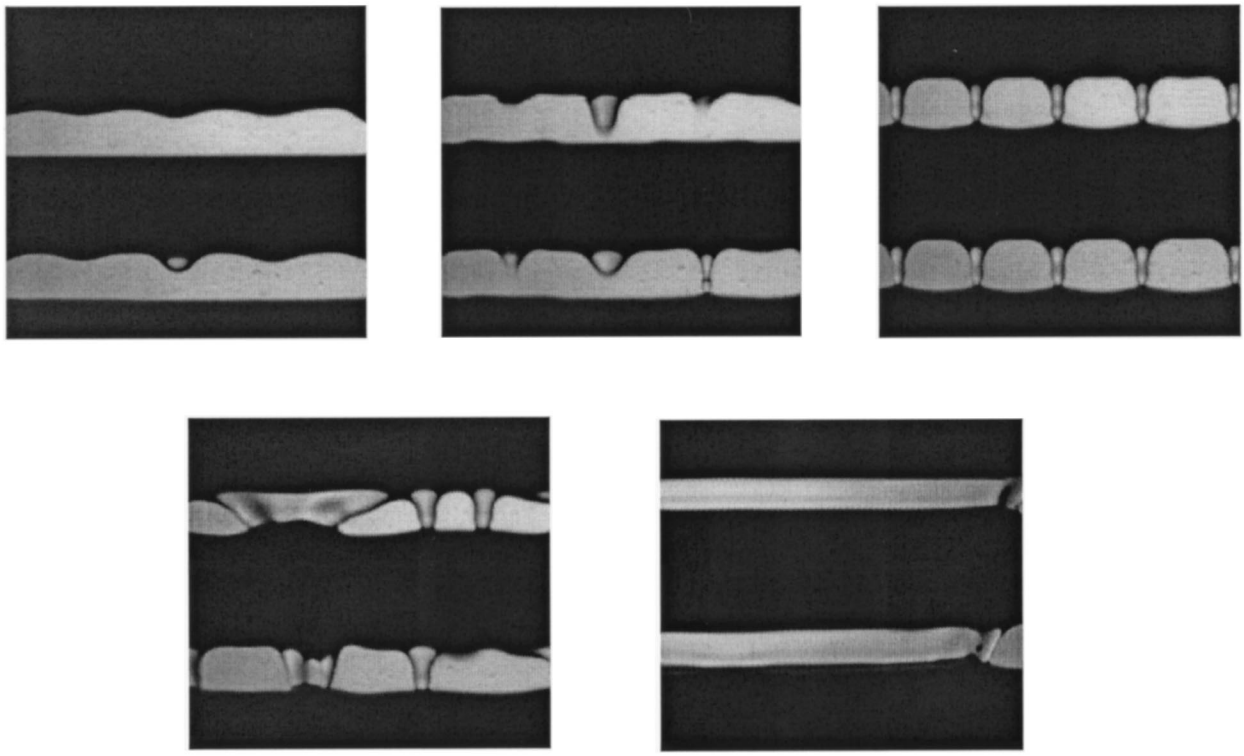

Fig. 5 Intertube flow modes on plain tubes: (*A*) droplet; (*B*) droplet-column; (*C*) column; (*D*) column-sheet; and (*E*) sheet.

E. Sheet Mode. This mode is when the fluid flows uniformly between the tubes as a continuous film or sheet.

The flow mode progresses from mode A to mode E as the mass flow rate is increased.

3.2 Test Matrix. All the mode transitions are observed for a variety of conditions. There are three main variables: tube spacing, type of fluid and the type of tube. The tests covered the following:

- Intertube spacings of 3.2, 4.8, 6.4, 9.5, 19.4, and 24.9 mm. These spacings were chosen to represent those that would be typical on an inline or staggered tube bundle.
- Four types of tubes. All are copper. First is a conventional 19.05 mm diameter plain tube, then a 19.05 mm Turbo BII™ tube (from Wolverine Tube Inc.), third a 19.05 mm Turbo-Chil™ tube (low finned with 28 fins/inch tube from Wolverine Tube Inc.) and finally a 12.7 mm Thermoexcel-C™ (from Hitachi). [™ Trademark of these companies].
- Three fluids were tested: water, reagent grade ethylene glycol and a 50 percent water/50 percent glycol mixture.

Typical fluid properties for the test fluids at 20°C are shown in Table 2. Since all the fluid properties change with temperature, the properties were measured over a range of temperatures and then these values were used to find temperature dependant, interpolating equations. The dynamic viscosity was measured with a capillary viscometer from 15°C to 35°C, the surface tension was measured with a wrenching tensiometer from 15°C to 45°C, and the density was measured by weighing a known volume of liquid from 15°C to 35°C. Uncertainties are specified in the Table 2. For every flow mode tested, the temperature was measured and then the physical properties of the fluid were determined for interpretation of the results. The other measurement uncertainties in the tests were: mass flow rate (±3 percent), temperature (±0.5°C) and tube spacings (±1.5 percent).

Table 2 Typical properties measured for the test fluids at 20°C and their resulting values of Galileo number

Physical properties at 20°C	Dynamic viscosity (μ)	Density (ρ)	Surface tension (σ)	Gallileo number $Ga^{1/4}$
Units	[Ns/m^2]	[kg/m^3]	[N/m]	-
Water	9.87×10^{-4}	9.98×10^{2}	7.37×10^{-2}	455
Ethylene glycol	2.34×10^{-2}	1.13×10^{3}	5.38×10^{-2}	17
Mixture 50% /50% mass of water and ethylene glycol	3.88×10^{-3}	1.06×10^{3}	5.14×10^{-2}	90
Uncertainty	±2%	±0.5%	±1%	±1.8%

As there are three main variables (type of tube, particular fluid and tube spacing), once these three parameters are chosen, we have a test configuration. For each configuration the mass flow rate is increased and then decreased to go through all the modes and also to detect any hysteresis effect on the transitions. This test cycle is made twice to include the effect of reproducibility. There are a total of about 1100 observations reported in this study, i.e., those required for observing 4 flow mode transitions (5 modes)×2 (two cycles of the tests)×2 types of flow (increasing and decreasing)×4 types of tubes×6 tube spacings×3 fluids. For each observation, a small video sequence has been taken. These videos last 1.3 s each (40 images obtained at 30 fps). They are used to keep a record of the observations and to compare the transitions for the different flow configurations.

3.3 Classification Difficulties. A sensitive point is the subjectivity of the observations. The modes are pretty well defined but what we are interested in are the transitions between modes and the transition is not always a discrete phenomenon. Sometimes, the change is continuous with the flow rate, so that it is difficult to choose one particular value for it. Another problematic point was to distinguish column mode from droplet mode at low Ga (viscous fluid) and small tube spacing. Indeed, at these conditions when a droplet departs, it does so quite slowly (due to viscosity and surface tension) and the liquid between the tubes remains a long time so large droplets grow that bridge between the two tubes, i.e., a large droplet itself bridges between the two tubes forming the equivalent of a column. Hence, it is not so obvious to say whether it is a column or a droplet in these cases.

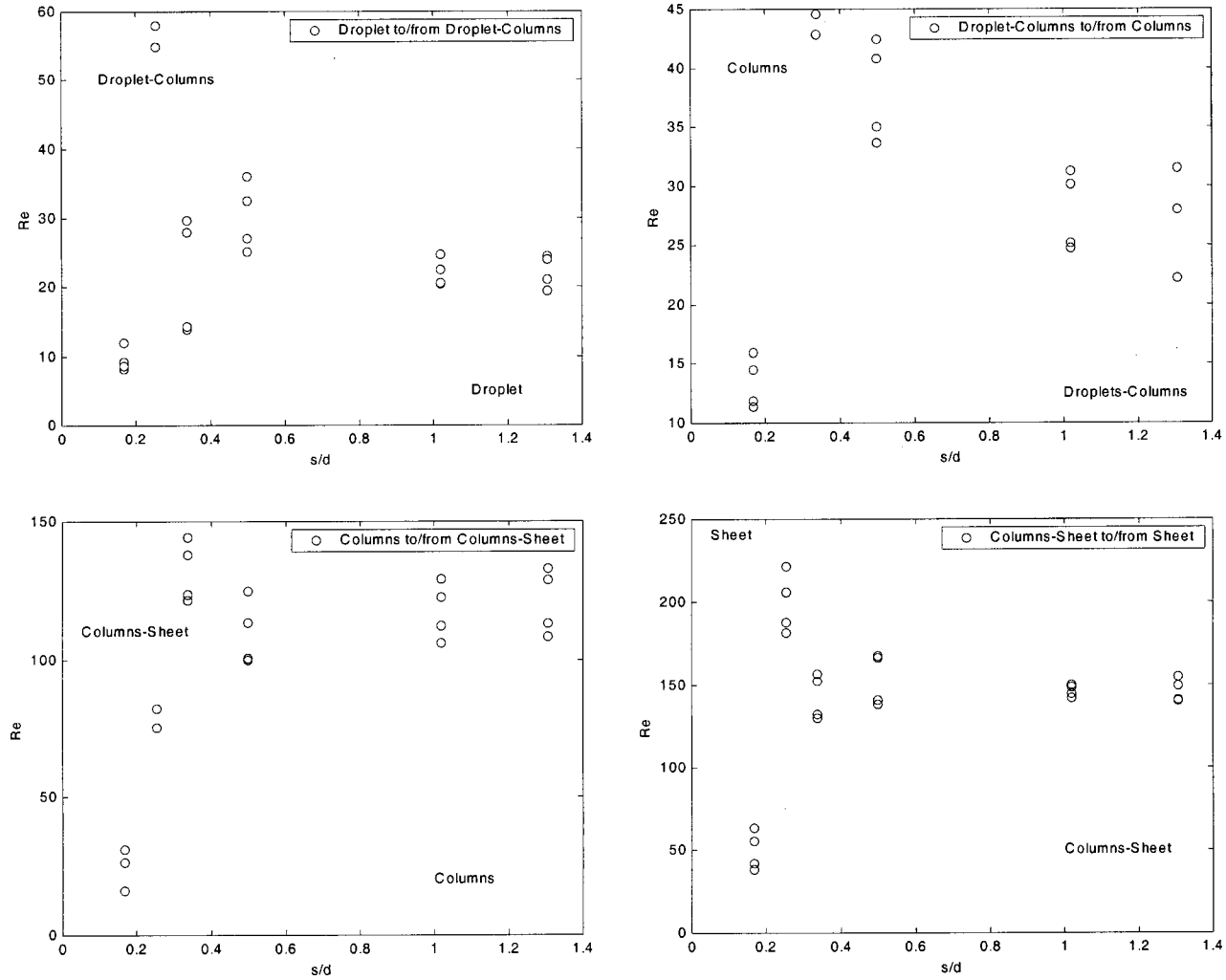

Fig. 6 Transition as a function of relative spacing for plain tube ($Ga^{0.25} \approx 90$)

4 Results and Discussion

The results have been analyzed using three dimensionless groups. The fluid type is characterized by the modified Gallileo number (Ga). The intertube spacing is represented by the ratio of s/d where s is the spacing between the tubes and d is the tube diameter. The mass flow rate is included in the film Reynolds number Re. The transition Reynolds number can thus be correlated as a function of the Galileo number as

$$\mathrm{Re} = a \ \mathrm{Ga}^b. \tag{9}$$

A transition is the change of the flow from one mode to another one. As there are five modes, there are of course four transitions or eight if one takes into account the variation of the flow rate (increasing or decreasing). Since we have observed only a small degree of hysteresis, the observations of these two cases are put together to find the following relations. In fact, neglecting the effect of hysteresis is also practical since it is impossible to know in an operating heat exchanger whether the flow was increasing or decreasing before reaching a particular operating condition.

4.1 Tube Spacing Effect. The tube spacing effect data are depicted for all the transitions for the plain tube in Fig. 6. The effect of tube spacing on transition Reynolds number is complex. At large s/d, it seems to be insensitive, at moderate values of s/d the Re transition threshold increases, and then it decreases rapidly at small s/d as the tubes approach one another. As visible on all the graphs, the effect of the tube spacing is most important for $s/d < 0.5$, which is also the domain where the modes are most difficult to distinguish from one another. As a first step, we will ignore the tube spacing effect and only correlate with Re versus Ga, which, hence, leads to some of the scatter in the resulting equations.

Figure 7 shows correlations (described in Section 4.2) of all the four transitions for a low fin tube compared to the observed data. The data are grouped in three zones on each graph representing each of the three fluids tested and also the small variations in fluid temperature from one test to another. The plots show the transitions ignoring the tube spacing effect, which is responsible for a good part of the vertical scatter. The other configurations give transitions with similar curvefits and trends.

4.2 Correlation of Transition Thresholds Without Tube Spacing Effect. The correlation of the measurements with an equation of the type $\mathrm{Re} = a\,\mathrm{Ga}^b$ as in Fig. 7 leads to the empirical coefficients listed in Table 3. The values of a and b were found by minimizing the log transformation of Eq. (9); that is

$$\ln(\mathrm{Re}) = \ln(a) + b \ln(\mathrm{Ga}). \tag{10}$$

A linear regression method has been used to calculate the relationship between Re and Ga. But since the original expression is a power law, the linear regression is between ln(Re) and ln(Ga) such that the coefficients a and b are chosen so as to minimize the variance S^2, which is the square of the difference between the predicted and measured values:

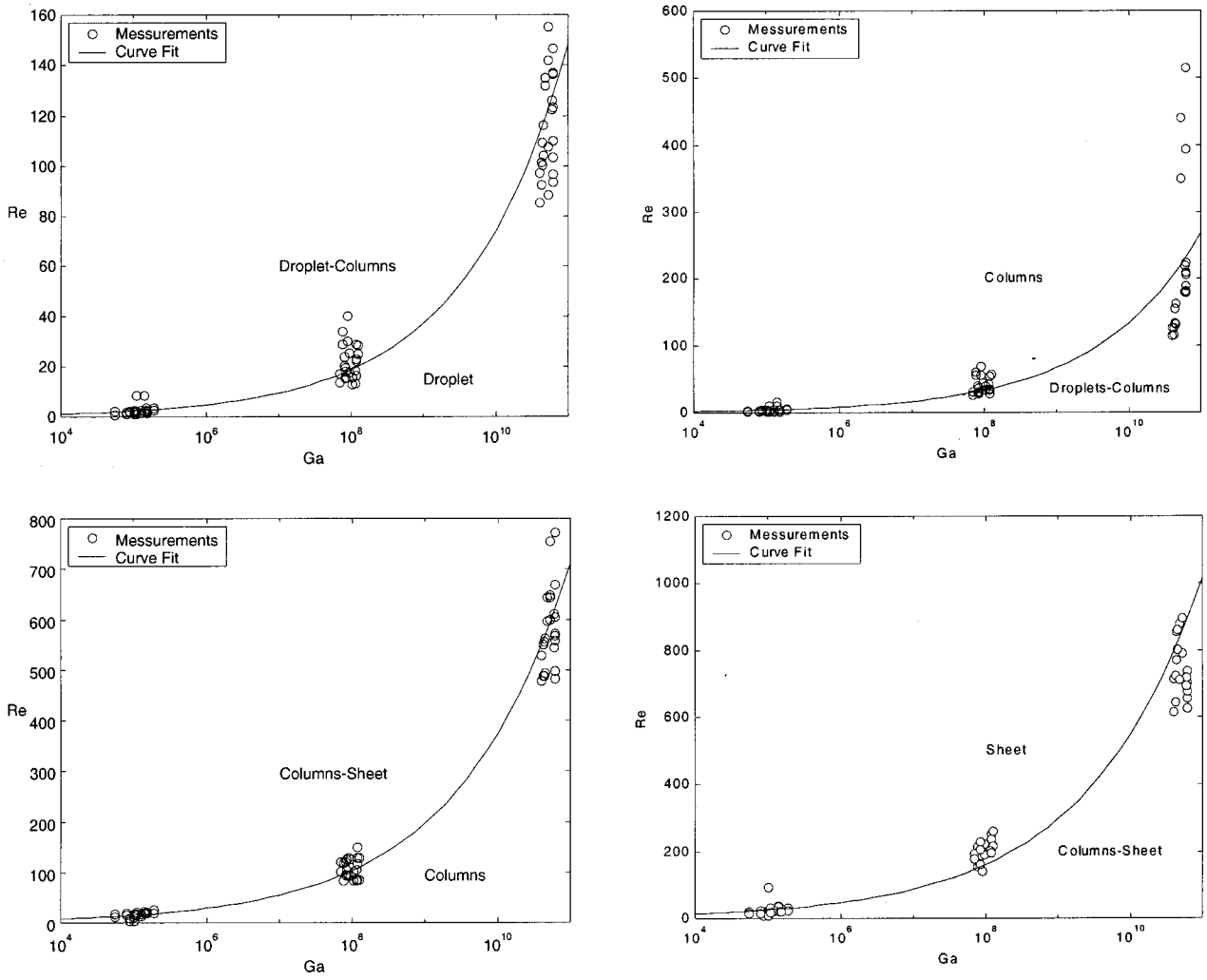

Fig. 7 Transition Reynolds number for low fin tube without spacing effect

$$S^2 = \frac{1}{N-1}\sum_n (\ln \mathrm{Re}_{\mathrm{meas}} - \ln \mathrm{Re}_{\mathrm{pred}})^2. \quad (11)$$

The standard deviation S has the same dimensions as the log values and hence we have referred to this as the log deviation, which is defined as

$$\text{log deviation} = e^{\left(\sqrt{(1/N-1)\Sigma_n (\ln \mathrm{Re}_{\mathrm{meas}} - \ln \mathrm{Re}_{\mathrm{pred}})^2}\right)} \propto \left[\left(\frac{\mathrm{Re}_{\mathrm{meas}}}{\mathrm{Re}_{\mathrm{pred}}}\right)\right]. \quad (12)$$

With this approach, we assume a Gaussian distribution of the measurements around the prediction. Thus, we have about a 68 percent chance that the measurements will be within the interval of $\pm S$ and about a 95 percent chance they will be within the interval $\pm 2S$. This means in our particular case that there is a 68 percent chance to have values within the log deviation shown in Table 3, i.e., for a log deviation of 1.3256 there is a 68 percent chance they fall within ± 32.56 percent of the predicted value.

In this table, the two last columns describe the accuracy of the relation. The first of these columns shows a comparison of our empirical fit to the data and the last column shows a comparison to the Hu-Jacobi transition equations. The closeness of the respective log deviation values for all four of the transitions illustrates the relatively good agreement between our data set and the Hu-Jacobi method.

It should be noted that the comparison of the Hu-Jacobi transition equations to the enhanced tube flow observations in Table 3 is an extrapolation of their method (it was developed only for plain tube observations) to determine the usefulness for these tubes. This extension of the method is successful except where the enhanced tube transition occurs at significantly different Ga numbers than for the plain tube.

Table 3 Coefficients for transition relation without spacing effect

				Log deviation between	
Tube	Transition	a	b	Our meas. and our prediction	Our meas. and Hu-Jacobi prediction
Plain	Droplet to/from Droplet-Column	0.0417	0.3278	1.3256	1.3669
	Droplet-Column to/from Column	0.0683	0.3204	1.2014	1.2151
	Column to/from Column-Sheet	0.8553	0.2483	1.3183	1.3958
	Column-Sheet to/from Sheet	1.068	0.2563	1.2238	1.2435
Low Fin	Droplet to/from Droplet-Column	0.0743	0.3	1.1386	1.1400
	Droplet-Column to/from Column	0.1263	0.3025	1.2425	1.3625
	Column to/from Column-Sheet	0.6172	0.2783	1.0804	1.1462
	Column-Sheet to/from Sheet	1.2015	0.2661	1.1159	1.2963
Turbo-BII	Droplet to/from Droplet-Column	0.0754	0.3007	1.1738	1.1739
	Droplet-Column to/from Column	0.1594	0.2748	1.2166	1.2440
	Column to/from Column-Sheet	0.7591	0.2482	1.4455	1.6447
	Column-Sheet to/from Sheet	1.3487	0.2453	1.1484	1.1625
Thermoexcel-C	Droplet to/from Droplet-Column	0.0975	0.2514	1.3512	2.1696
	Droplet-Column to/from Column	0.2293	0.2451	1.3486	1.4751
	Column to/from Column-Sheet	0.8146	0.2602	1.0721	1.0990
	Column-Sheet to/from Sheet	1.5859	0.2561	1.0496	1.3107

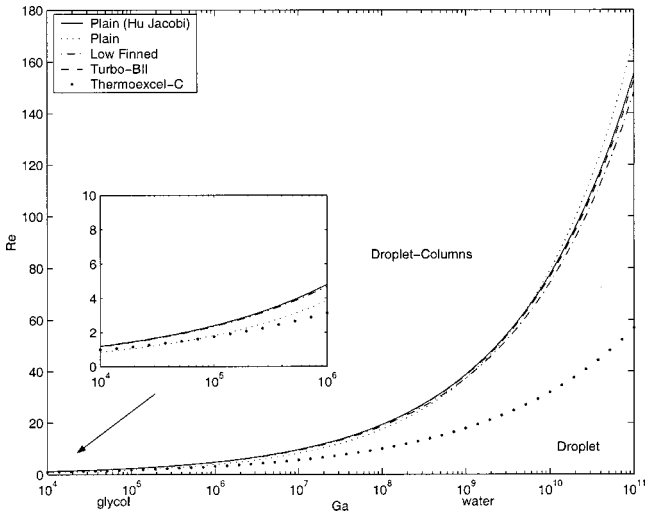

Fig. 8 Reynolds transition number for droplet to/from droplet-column transition

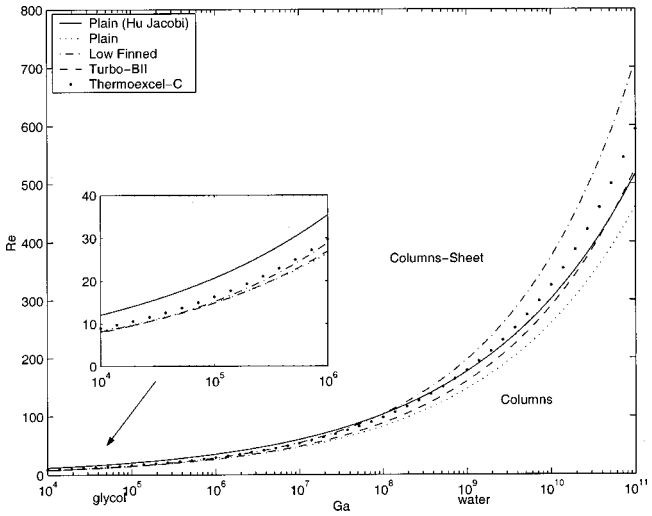

Fig. 10 Reynolds transition number for column to/from column-sheet transition

The transition relations with these coefficients are plotted in Figs. 8–11 to demonstrate the type of tube effect on the various flow mode transitions. Insets have been included in the graphs to give a better view at low Ga.

First of all, one can see that the predictions of Hu-Jacobi for a plain tube are similar to the curvefits of the present plain tube observations for all four transitions, which confirms the validity of their transition correlations. Secondly, the differences in transition thresholds between the Turbo-BII tube and the plain tube are small. This means that the pores in the Turbo-BII surface are too small to have an effect on the film flow regime. Since the Sheet mode is logically the most convenient mode of operation of a falling film evaporator tube bundle so as to avoid dry patch formation, the Turbo-BII tube benefits from its lower Re threshold into the Sheet mode compared to the other enhanced tubes.

As a third observation, in the two regimes involving columns (Droplet to/from Droplet-Column and Droplet-Column to/from Column), the Thermoexcel-C has a significantly lower transition Reynolds number than the other tubes. Observing the flow on this tube, one can in fact see that the columns are attached to the small pikes of the surface, i.e. the notched fin tips. This attachment point maintains the column mode stable to lower Reynolds numbers. That is, when Re is increased, if a column is created by instability, it is then attached and when Re is decreased, it has to reach a very low value to break up the column. In both cases, this means that the transition occurs at a low Re.

A fourth visible trend is the significantly higher Re number for the transition Column-Sheet to/from Sheet for the Thermoexcel-C and the low fin tubes. Due to surface tension forces, the interface of a liquid sheet at the fin tips is nonuniform in thickness at the fin tips and hence the film has to be thicker in order to be stable. Furthermore, the Column mode is advantageous for condensation compared to the Sheet mode because large parts of the surface are not inundated with condensate from the upper tubes. Consequently, the higher Re threshold of the Thermoexcel-C and low fin tubes means that more tube rows may operate in the Column mode than for a comparable plain tube bundle.

As a fifth point, it can be mentioned that the distance between columns, whose mode is controlled by the Taylor instability, is much larger than the low fin tube pitch and also larger than the fin pitches of the other two enhanced tubes. So for now there appears to not to be a fin pitch effect on column spacing.

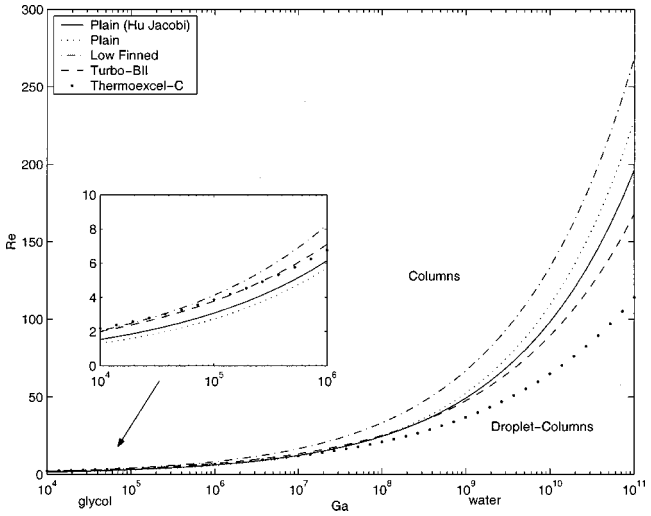

Fig. 9 Reynolds transition number for droplet-column to/from column transition

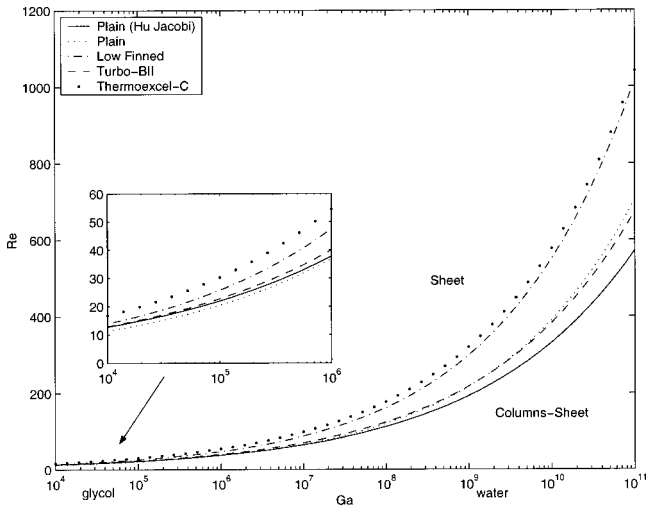

Fig. 11 Reynolds transition number for column-sheet to/from sheet transition

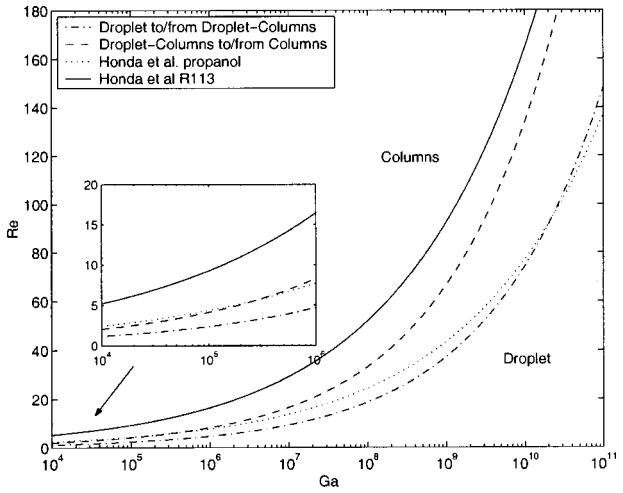

Fig. 12 Comparison with Honda's droplet to/from columns correlation

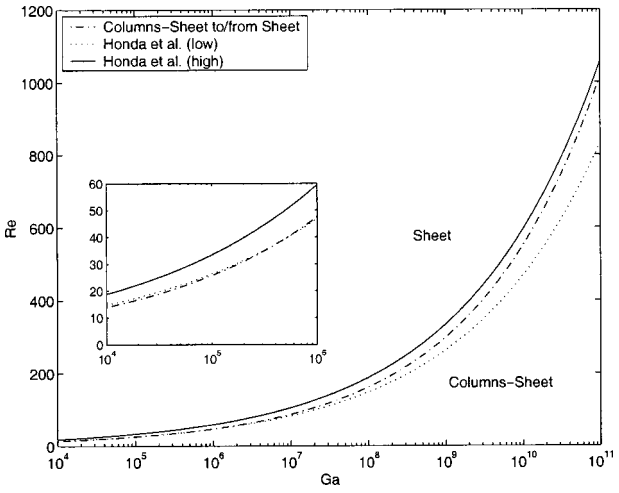

Fig. 14 Comparison with Honda's columns-sheet to/from sheet correlation

4.3 Comparison With Existing Correlation. Honda et al. [5] have presented correlations for flow pattern transitions for a low finned tube (27 fpi and 5/8 inch diameter). Their experiments were made with R113 ($Ga^{1/4}=240$), methanol ($Ga^{1/4}=310$) and Propanol ($Ga^{1/4}=82$) and with tube spacings of 22 and 44 mm. After rearrangements, their correlations lead to the following:

$$\text{Droplet}\Leftrightarrow\text{Columns for propanol:}\quad \mathrm{Re}=0.244\ \mathrm{Ga}^{0.25} \tag{13}$$

$$\text{Droplet}\Leftrightarrow\text{Columns for R113:}\quad \mathrm{Re}=0.52\ \mathrm{Ga}^{0.25} \tag{14}$$

Columns⇔Columns-Sheet for the three liquids:

$$\mathrm{Re}=1.28\ \mathrm{Ga}^{0.25} \tag{15}$$

Columns-Sheet⇔Sheet for the three liquids:

$$\mathrm{Re}=1.48 \text{ to } 1.88\ \mathrm{Ga}^{0.25} \tag{16}$$

Correlations (13) and (14) do not predict the intermediate mode Droplet-Columns so they have been compared in Fig. 12 with the two transitions Droplet to/from Droplet-Columns and Droplet-Columns to/from Columns. The extrapolated transition of Honda for propanol is close to the Droplet to/from Droplet-Columns transition of this study while the Honda value for R113 has the same shape as the Droplet-Columns to/form Columns curve but is shifted to higher Re. In Fig. 13 the curves for the Columns to/form Columns-Sheet transition are plotted. For this transition, Honda has found that there is only one equation for his three tested fluids which tends to prove that the Eq. (9) used in this study to describe transitions is correct. The agreement between his results and ours is very good for this transition. In Figure 14 the curves for the Columns-Sheet to/form Sheet transition are plotted. For this transition, Honda has found one lower value and one higher value for the coefficient in correlation (16). The resulting scatter in the transitions is small and the correlation of this study is in between the two Honda's curves.

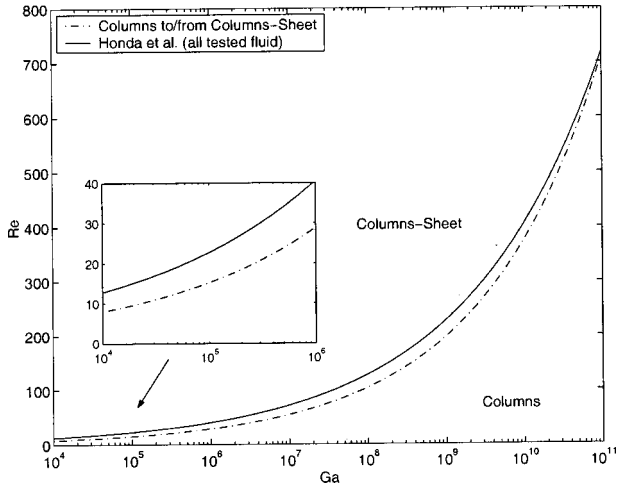

Fig. 13 Comparison with Honda's columns to/from columns-sheet correlation

4.4 Predictive Relationships Including Spacing Effect Some of the log deviation in Table 3 and scatter in Fig. 7 are from the tube spacing effect on transition as can be deduced by the results on spacing effect shown earlier in Fig. 6. Thus, tube spacing is now included in the relationship. As the tubes have significantly different surface geometries, it is not surprising that the spacing effects are not the same for the four types of tubes. In the new empirical relations, the spacing ratio is included in the *a* coefficient, such that *a* becomes a third order polynomial in order to fit the trends in the data in Fig. 6:

$$\mathrm{Re}=a\ \ \mathrm{Ga}^{b} \tag{17}$$

in which *a* is:

Table 4 Coefficients for transition relation with spacing effect

Tube	Transition	b	T	u	v	w	log deviation
Plain	Droplet to/from Droplet-Column	0.312	-1.427e-2	3.742e-1	-4.868e-1	1.856e-1	1.2277
	Droplet-Column to/from Column	0.319	2.158e-3	3.722e-1	-4.752e-1	1.799e-1	1.1551
	Column to/from Column-Sheet	0.248	-3.299e-1	6.445e0	-8.273e0	3.187e0	1.1446
	Column-Sheet to/from Sheet	0.253	3.011e-1	4.572e0	-5.649e0	2.086e0	1.1676
Low Fin	Droplet to/from Droplet-Column	0.302	1.053e-1	-7.475e-2	2.417e-2	6.745e-3	1.1272
	Droplet-Column to/from Column	0.304	2.993e-1	-6.308e-1	6.364e-1	-2.098e-1	1.1492
	Column to/from Column-Sheet	0.270	6.216e-1	4.830e-1	-5.220e-1	1.953e-1	1.0748
	Column-Sheet to/from Sheet	0.262	1.046e0	2.466e0	-3.592e0	1.615e0	1.1173
Turbo-BII	Droplet to/from Droplet-Column	0.293	-9.045e-1	1.056e1	-3.438e1	3.459e1	1.1139
	Droplet-Column to/from Column	0.269	5.530e-2	5.308e-1	0	-8.022e-1	1.1777
	Column to/from Column-Sheet	0.252	-1.786e0	1.766e1	-3.363e1	1.949e1	1.1295
	Column-Sheet to/from Sheet	0.233	-9.752e0	1.160e2	-3.596e2	3.480e2	1.0829
Thermoexcel-C	Droplet to/from Droplet-Column	0.258	4.463e-1	-2.165e0	3.561e0	-1.433e0	1.2160
	Droplet-Column to/from Column	0.246	1.110e0	-6.452e0	1.382e1	-8.638e0	1.2538
	Column to/from Column-Sheet	0.262	1.014e0	-1.265e0	9.238e-1	1.598e0	1.0643
	Column-Sheet to/from Sheet	0.253	6.465e0	-3.878e1	9.967e1	-8.092e1	1.0401

$$a = t + u\left(\frac{s}{d}\right) + v\left(\frac{s}{d}\right)^2 + w\left(\frac{s}{d}\right)^3. \quad (18)$$

To determine the values of these coefficients, a classical linear regression is not sufficient because the variables are linked by a combined addition and multiplication relationship. This problem has been confronted as follows: The power b on Ga has been changed from 0.2 to 0.4 in very small steps. At each step the coefficients t, u, v, and w are calculated with a classical regression method with s/d as the variable. With this, one gets a relation for each value of b. The relation that gives the lowest log deviation between the measured and the calculated Re values is selected as the best. The resulting coefficients are listed in Table 4. Compared to Table 3, there is a significant improvement by adding the spacing effect for the Column to/from Column-Sheet transition for the plain and Turbo-BII tubes and at low s/d for all tube types.

5 Conclusions

In this study, observations of the adiabatic flow modes between horizontal tubes oriented in a vertical array have been made. Based on these observations, relations to predict the flow mode transitions between droplet, column and sheet flows are presented. These relations concern four types of tubes: a low fin tube, a Turbo-BII, a Thermoexcel-C and a plain tube. The plain tube correlation allows a validation of the observation procedure by a comparison with the existing correlation from Hu and Jacobi, which are quite favorable. The four transition correlations per tube are based on 350 observations each. Relations including the tube spacing effect are also presented for all the tubes. They improve the predictions for all the transitions, particularly at very small tube spacings.

Acknowledgments

This research was sponsored by the EPFL/LTCM Falling Film Research Club together with a financial contribution by the EPFL. Club members are: Axima Refrigeration, Dunham-Bush Inc., UOP Inc., Wieland-Werke and Wolverine Tube Inc.

Nomenclature

α = local heat transfer coefficient ($W/m^2\,K$)
μ = dynamic viscosity (Ns/m^2)
ρ = density (kg/m^3)
σ = surface tension (N/m)
Γ = total flow rate on both sides of the tube (kg/m s)
a = multiplicative factor in relations
b = power of Ga number
d = tube diameter (m)
g = gravitational constant ($9.81\ m/s^2$)
t, u, v, w = coefficients of the polynomial decomposition
Ga = modified Gallileo number
N = tube number
Re = film Reynolds number
s = intertube spacing (m)
S = standard deviation

References

[1] Jakob, M., 1936, Mech. Eng. (Am. Soc. Mech. Eng.), **58**, p. 163.
[2] Nusselt, W., 1916, "Die oberflächenkondensation des wasserdampfes," Zeitschr. Ver. Deutch. Ing., **60**, pp. 541–569.
[3] Kern, D. Q., 1958, "Mathematical Development of Loading in Horizontal Condensers," AIChE J., **4**, No. 2, pp. 157–160.
[4] Marto, P. J., 1986, "Recent Progress in Enhancing Film Condensation Heat Transfer on Horizontal Tubes," Heat Transfer Eng., **7**, pp. 53–63.
[5] Honda, H., Nozu, S., and Takeda, Y., 1987, "Flow Characteristics of Condensation on a Vertical Column of Horizontal Tubes," *Proc. 1987 ASME-JSME Thermal Engineering Joint Conference*, Honolulu, Vol. **1**, pp. 517–524.
[6] Hu, X., and Jacobi, A. M., 1996, "The Intertube Falling Film Part 1—Flow Characteristics, Mode Transitions and Hysteresis," ASME J. Heat Transfer, **118**, pp. 616–625.
[7] Mitrovic, J., 1986, "Influence of Tube Spacing and Flow Rate on Heat Transfer From a Horizontal Tube to a Falling Liquid Film," *Proc. 8th International Heat Transfer Conf.*, San Francisco, **4**, pp. 1949–1956.
[8] Taghavi, K., and Dhir, V. K., 1980, "Taylor Instability in Boiling, Melting, Condensation or Evaporation," Int. J. Heat Mass Transf., **23**, pp. 1433–1445.
[9] Tang, Z., and Lu, B. Y. C., 1991, "Droplet Spacing of Falling Film Flow on Horizontal Tube Bundles," *Proc. 18th International Congress of Refrigeration*, Montreal, **2**, pp. 474–478.
[10] Mitrovic, J., and Ricoeur, A., 1995, "Fluid Dynamics and Condensation Heating of Capillary Liquid Jets," Int. J. Heat Mass Transf., **38**, pp. 1483–1494.
[11] Hu, X., and Jacobi, A. M., 1998, "Departure-Site Spacing for Liquid Droplets and Jets Falling Between Horizontal Circular Tubes," Exp. Therm. Fluid Sci., **16**, pp. 322–331.
[12] Hu, X., and Jacobi, A. M., 1996, "The Intertube Falling Film Part 2—Mode Effects on Sensible Heat Transfer to a Falling Liquid Film," ASME J. Heat Transfer, **118**, pp. 626–633.
[13] Thome, J. R., 1999, "Falling Film Evaporation: A State-of-the-Art Review of Recent Work," J. Enhanced Heat Transfer, **6**, No. 2-4, pp. 263–277.

J. H. Kim
The University of Texas at Arlington,
Department of Mechanical and
Aerospace Engineering,
P.O. Box 19023,
Arlington, TX 76019-0023

K. N. Rainey
Los Alamos National Laboratory,
P.O. Box 1663, MS-B258,
Los Alamos, NM 87545-1663

S. M. You
e-mail: you@uta.edu
The University of Texas at Arlington,
Department of Mechanical and
Aerospace Engineering,
P.O. Box 19023,
Arlington, TX 76019-0023

J. Y. Pak
Behr America Inc.,
2700 Daley Dr.,
Troy, MI 48033

Mechanism of Nucleate Boiling Heat Transfer Enhancement From Microporous Surfaces in Saturated FC-72

The present study is an experimental investigation of the nucleate pool boiling heat transfer enhancement mechanism of microporous surfaces immersed in saturated FC-72. Measurements of bubble size, frequency, and vapor flow rate from a plain and microporous coated 390 μm diameter platinum wire using the consecutive-photo method were taken to determine the effects of the coating on the convective and latent heat transfer mechanisms. Results of the study showed that the microporous coating augments nucleate boiling performance through increased latent heat transfer in the low heat flux region and through increased convection heat transfer in the high heat flux region. The critical heat flux for the microporous coated surface is significantly enhanced over the plain surface due to decreased latent heat transfer (decreased vapor generation rate) and/or increased hydrodynamic stability from increased vapor inertia; both of which are a direct result of increased nucleation site density. [DOI: 10.1115/1.1469548]

Keywords: Boiling, Enhancement, Heat Transfer, Microstructures, Porous Media

Introduction

Efforts to maximize the boiling heat transfer efficiency have resulted in the development of many different surface enhancement techniques. One of the earliest methods used to produce an enhanced boiling surface was to roughen a plain surface using sandpaper or some other abrasive. Kurihara and Myers [1] showed that the nucleate boiling enhancement from roughening was the result of increased active nucleation site density. The increased number of nucleation sites may enhance the heat transfer by providing more convection heat transfer from increased bubble agitation and/or increased latent heat transport. With regard to CHF, the effects of surface roughening are much less clear. Many researchers have reported that CHF was independent of surface roughness (Berenson [2], Nishio and Chandratilleke [3]). Alternatively, Ramilison et al. [4], using data for various fluids, showed that surface roughness actually does influence CHF.

Griffith and Wallis [5] showed that the geometry of the microcavity containing trapped vapor was directly related to the bubble nucleation process. Most notably, they found that re-entrant type cavities were stable, easily activated boiling sites. From their study (as well as others), many enhancement techniques utilizing re-entrant type cavities or grooves have been developed. Since their first development, porous metallic coatings have received much attention. Formed by bonding metal particles with diameters ranging from 44 to 1000 μm to a base surface (coating thickness ranges from 250 to 2000 μm), porous metallic coatings have been shown to significantly enhance nucleate boiling heat transfer performance. Thome [6] concluded that the primary enhancement mechanisms for re-entrant type enhanced surfaces were: enhanced nucleation from the larger embryonic bubbles, increased thin film evaporation due to the large internal surface area of the porous structure, and two-phase convection within the porous structure. The porous metallic coatings were also found to significantly enhance CHF. Polezhaev and Kovalev [7] suggested that the enhancement was due to decreased vapor jet spacing (increased vapor jet velocity) while Tehver [8] proposed that the enhancement was due to increased macrolayer evaporation time.

A relatively new method for surface enhancement is the microporous coating introduced by O'Connor and You [9], refined by Chang and You [10,11] and patented by You and O'Connor [12]. The coating is a surface treatment technique used to increase vapor/gas entrapment volume and active nucleation site density by forming a porous structure of 1–20 μm particles with cavities of about 0.1–1 μm and bonded together with epoxy. The microporous coating is different from conventional metallic porous coatings because; (a) it uses much smaller particles; (b) the coating is much thinner ($\approx$50 μm), and (c) the resulting porous structure has a low effective thermal conductivity (estimated as approximately 0.95 W/m-K by O'Connor and You [9]). The microporous coating has already shown to significantly enhance the pool nucleate boiling heat transfer performance and critical heat flux (CHF) over plain surfaces in highly wetting fluids [13,14]. Chang and You [11] attributed the enhancement of nucleate boiling heat transfer performance to increased active nucleation site density; however, the enhancement mechanisms of the coating have not been thoroughly investigated.

The development of advanced surface microstructures for the enhancement of nucleate boiling requires an understanding of both the macro and micro-scale heat transfer mechanisms involved. The objective of the present study is to investigate the nucleate boiling and CHF enhancement mechanisms associated with the microporous coating in saturated FC-72. To study the nucleate boiling heat transfer mechanisms, plain and microporous coated 390-μm diameter platinum wires were tested in saturated FC-72 at atmospheric pressure. The consecutive-photo method developed by Ammerman and You [15] is utilized to determine the effect that the microporous coating has on the heat transfer mechanisms. To study the effect of the microporous coating on CHF, data from previous studies are compiled and analyzed.

Contributed by the Heat Transfer Division for publication in the JOURNAL OF HEAT TRANSFER. Manuscript received by the Heat Transfer Division April 26, 2001; revision received November 16, 2001. Associate Editor: V. P. Carey.

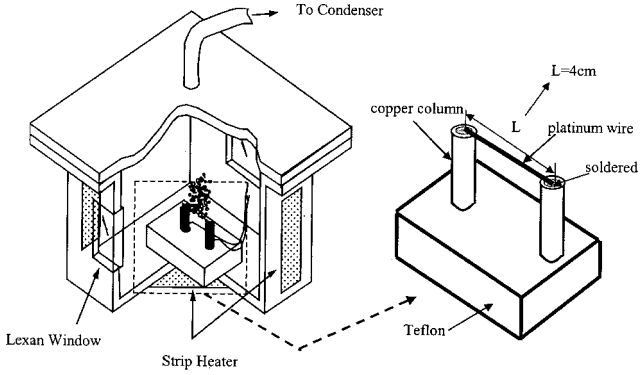

Fig. 1 Pool boiling test facility

Experimental Apparatus And Procedure

The experimental setup for this study is shown in Fig. 1. The test fluid, FC-72, is a highly-wetting dielectric perfluorocarbon produced by the 3M Industrial Chemical Products Division. The test liquid was contained within an aluminum vessel (200 mm wide×125 mm deep×200 mm high) with two tempered glass viewports, which was heated by band heaters located on the sides and bottom of the chamber. A cartridge heater was located in the bottom of the chamber to provide additional heating/stirring during the degassing process prior to testing. The test vessel was insulated with 15 mm thick foam insulation. An external, water-cooled condenser was used throughout the testing to prevent loss of test liquid. A copper-constantan thermocouple was placed within the test vessel to measure bulk liquid temperature. Atmospheric pressure was maintained by venting the vessel to ambient. The test heater assembly was mounted to a stainless steel support bar immersed in the test liquid.

The test heater assembly is also shown in Fig. 1. The 390 μm diameter platinum wire test heater was mounted horizontally between two 4 mm diameter copper posts spaced 4 cm apart. The heater wire was soldered to the top of each post. The electric circuit used to provide power to the heater consisted of a DC power supply connected in series with a precision shunt resistor and the test heater. The shunt resistor was used to determine the current in the electric circuit. The applied heat flux to the test heater was calculated from the measured voltage drop across the test heater and current through the shunt resistor. Since platinum has a repeatable temperature-resistance relationship, the wire itself was used to measure heater temperature. The wire was calibrated prior to testing and then checked after testing to ensure accuracy. For the microporous coated wire, the dielectric DOM (8-12 μm synthetic **D**iamond particles/**O**megabond 101 epoxy binder/**M**ethyl-ethyl-keytone carrier) microporous coating shown in Fig. 2 was used (the horizontal line at the top of the photograph is 50 μm long relative to the image). The coating thickness increased the wire diameter to $\approx$425 μm.

Prior to performing the experiments, the FC-72 test liquid was heated to its saturation temperature and boiled vigorously for two hours to remove noncondensible gases. Following this degassing process, the testing was initiated. The heat flux controlled boiling curves were generated by incrementally advancing the power supplied to the wire heater until CHF was detected at which point the power was shut off. Afterwards, the natural convection data was compared with the correlation of Kuehn and Goldstein [16] (not shown) to confirm that the calibration method was accurate. All measurements and control functions were performed through a computer-controlled data acquisition system. Hong et al. [17] should be referred to for a more detailed description of the test procedures used.

Measurements of the bubble departure diameter, frequency, and flow rate were performed at four different nucleate boiling heat

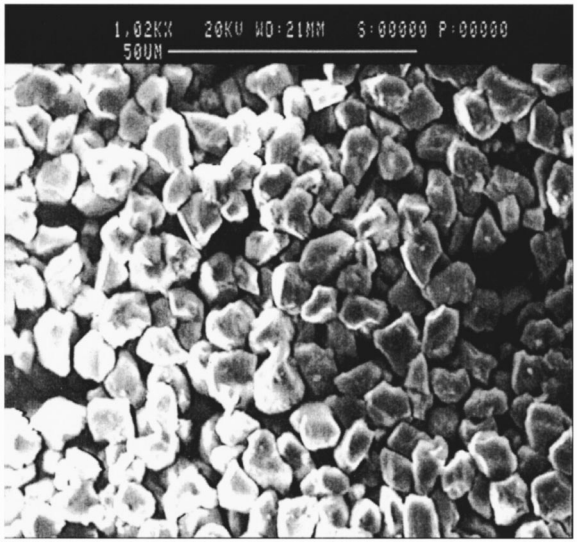

Fig. 2 SEM photo of DOM microporous coating (top view)

flux levels (6, 11, 13, and 16 W/cm^2) using the ''Consecutive-Photo Method'' developed by Ammerman and You [15]. Briefly, the consecutive-photo method uses consecutive images from a high-speed digital video camera and image processing software to measure bubble sizes and frequency. From this information the vapor volume flow rate leaving the wire is calculated. The latent heat flux contribution is then calculated from the following equation:

$$q''_{\mathrm{LH}}=\frac{\rho_g \dot{V}_g h_{1g}}{\pi D L} \tag{1}$$

For reference, the bubble measurements are taken at an imaginary control line located 2 mm above the wire heater. A more detailed description of the method is given by Ammerman and You [15].

Uncertainties for this study were estimated using the method of Kline and McClintock [18]. Considering the uncertainty in calibration, the uncertainty in heater surface temperature measurement was $\pm$0.2 K. The total nucleate boiling heat flux uncertainty (taking into account uncertainties in voltage, current, and area) is estimated as $\pm$4.1 percent. With regard to the uncertainties in vapor volume flow rate and latent heat flux for the consecutive-photo method, Ammerman and You [15] found that the uncertainty was mainly due to image resolution and bubble shape irregularity. The uncertainties in vapor volume flow rate and latent heat flux for the present study were estimated to be no more than $\pm$6.6 percent and $\pm$7.8 percent, respectively.

Results And Discussion

The present study is to understand the nucleate pool boiling and CHF enhancement mechanisms of the microporous coating. In general, the heat transfer mechanisms associated with pool boiling are liquid convection and latent heat transfer. Liquid convection could be further subdivided into natural convection (where nucleation does not occur), micro-convection (due to bubble motion), and Marangoni convection; however, only the total convective heat transfer contribution is considered in the present study to simplify the analysis. To determine the latent heat contribution to heat transfer, the vapor flow rate leaving the test heater was measured using the consecutive-photo method developed by Ammerman and You [15]. From a practical viewpoint, it would have been preferable to test flat, square heater surfaces; however, the consecutive-photo method can only be used in situations where the bubbles can be clearly seen in the photos such as the quasi-

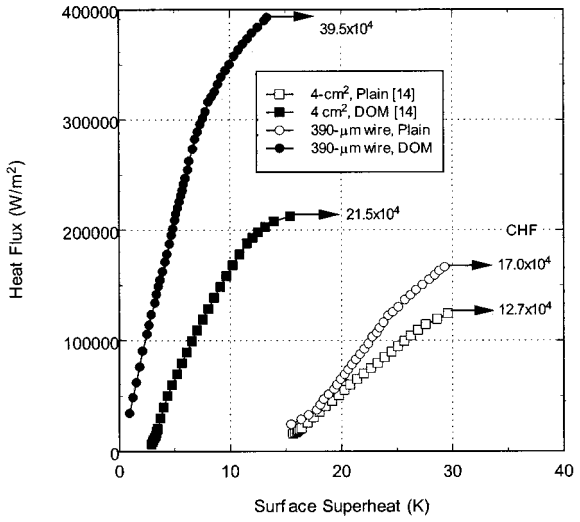

Fig. 3 Reference pool boiling curves

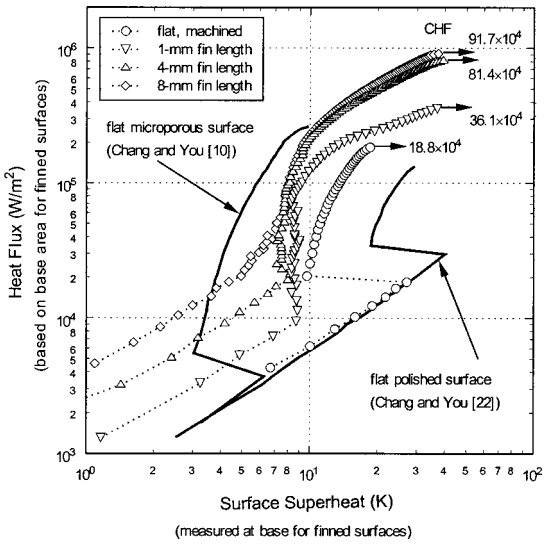

Fig. 4 Effect of area (fins) on boiling curve (Rainey and You [21])

two-dimensional, 390 μm wire heater chosen for the present study. All testing was performed in a pool of saturated FC-72 at atmospheric pressure.

Reference Boiling Curves. Figure 3 illustrates the present plain and microporous wire surfaces' nucleate boiling heat transfer test results. In addition, nucleate boiling curves of plain and microporous coated 2 cm×2 cm flat copper surfaces from Rainey and You [14] are shown for comparison. The single-phase natural convection data have been removed for clarity. Throughout the nucleate boiling regime, the microporous coating consistently augmented the heat transfer coefficients of the wire surface by more than 600 percent when compared to those of the plain wire surface which is similar but higher than the enhancement of +300 percent reported by Rainey and You for their 4 cm^2 surfaces. O'Connor and You [9] attributed the enhancement from the microporous coating to dramatically increased active nucleation site density but gave no indication to the main enhancement mechanism. In addition, the microporous coating enhanced the wire surface CHF values by about 130 percent which is also similar but higher than the enhancement of about 70 percent observed for the 4 cm^2 surfaces. It has already been shown that below a certain heater size (length-scale), the nucleate boiling heat transfer coefficient and CHF will increase with decreasing heater size (Hong [19], Bar-Cohen and McNeil [20]). In addition, the wire surfaces show higher levels of enhancement of nucleate boiling and CHF with the addition of the microporous coating. This may be due to increased sensitivity to changes in convection heat transfer from the length-scale effects just mentioned. However, the important observation to make from Fig. 3 is that the 390 μm wire surface behaves in a similar manner to the larger 4 cm^2 flat surface with regard to microporous coating enhancement, therefore, the conclusions drawn from the present heat transfer mechanism analysis of 390 μm wire heaters can be applied to relatively larger, flat surfaces.

The increased heat transfer coefficients of the microporous surface are not due to increased surface area generated by the microporous coating. Fig. 4, previously reported by Rainey and You [21], shows the effect of adding square pin fins to a 1 cm^2 machine roughened base surface along with a polished [22] and a microporous coated [10] 1 cm^2 flat surface for comparison. For reference, all of the data in Fig. 4 was tested in saturated FC-72 at atmospheric pressure and, for the finned surfaces, the heat flux is based on the base area and the surface superheat is calculated from the base of the fins. As can be seen from Fig. 4, an increase in surface area shifts the boiling curve vertically, not horizontally and has a significant effect on single-phase natural convection heat transfer.

Visual Observations of Boiling Behavior. Figure 5 shows photos of the plain and microporous wire heaters at 6 and 16 W/cm^2. At 6 W/cm^2, the photos show a much higher active nucleation site density on the microporous wire compared to the plain wire as previously reported by O'Connor and You [9]. When the heat flux is increased to 16 W/cm^2, the plain surface photos exhibit an increase in active nucleation site density while the microporous wire site density appears unchanged (but still appears to be higher than the plain wire). This indicates that the active nucleation site density of the microporous wire is already at or near a maximum value at 6 W/cm^2. Observations of bubble behavior near the wire surface revealed that most of the bubbles would merge with neighboring bubbles prior to or just after departure at all analyzed heat fluxes for both the plain and microporous wires. Very little bubble merging occurred at distances greater than about 2 mm above the wire surface. This means that the bubble diameters and frequencies measured in the present study represent secondary or tertiary bubbles rather than departure bubbles. Rainey and You [14] found that the transition from the isolated bubbles regime to the slugs and columns regime (or regime of mutual bubble interaction) for FC-72 occurred at a very low heat flux of about 3 W/cm^2 which is consistent with the observations of significant bubble merging and means that the four heat fluxes analyzed in the present study are in the regime of mutual bubble interaction.

Nucleate Boiling Enhancement Mechanisms. To determine the relative contributions of convective and latent heat transfer to the total heat transfer, measurements of vapor volume flow rate from the plain and coated wire heaters were made at four different total heat flux levels: 6, 11, 13, and 16 W/cm^2. A plot of the measured latent heat flux versus total heat flux is shown in Fig. 6. The heavy solid line indicates the total heat flux or theoretical upper limit on the latent heat flux. The present plain wire results in Fig. 6 show that the latent heat flux contribution steadily increases from about 40 percent of the total heat flux at 6 W/cm^2 to about 94 percent near CHF at 16 W/cm^2. The increased latent heat contribution with increased heat flux is attributed to the increased number of active nucleation sites. Paul and Abdel-Khalik [23] also observed a steady increase in latent heat flux contribution towards CHF for their plain 300 μm wire in saturated water at atmospheric

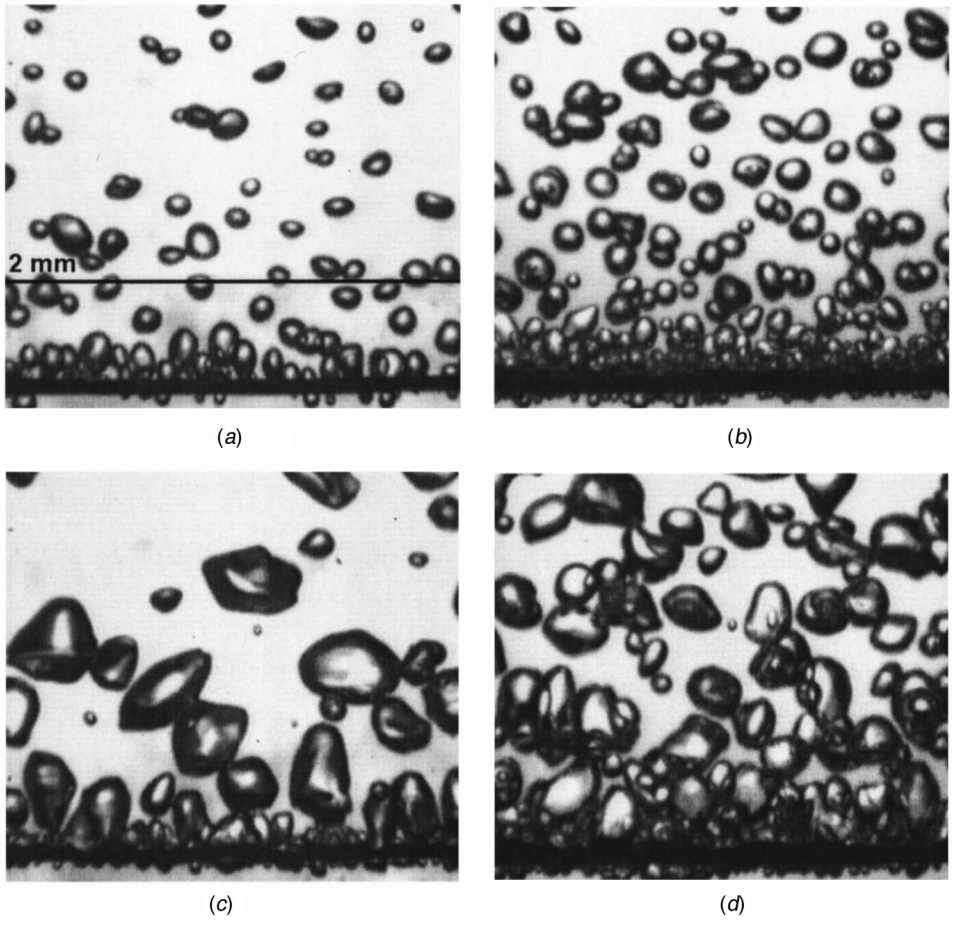

Fig. 5 Photographs of boiling behavior from plain and microporous wires: (*a*) plain wire, 6.0 W/cm^2; (*b*) microporous wire, 6.2 W/cm^2; (*c*) plain wire; 16.0 W/cm^2; and (*d*) microporous wire, 16.2 W/cm^2.

pressure. In contrast, the microporous wire results show a relatively constant latent heat flux contribution of around 70 percent for the heat flux range tested. The relatively constant latent heat flux contribution for the microporous wire appears to be consistent with the observed lack of significant change in active nucleation site density mentioned previously. When comparing the plain to the microporous wire at 6 W/cm^2 in Fig. 6, the microporous coating appears to augment heat transfer through increased latent heat transfer from the higher active nucleation site density. Due to its lower site density, the plain surface must dissipate more heat through convection heat transfer, which in turn requires a higher surface temperature to dissipate the same amount of heat as the microporous surface. Conversely, at 16 W/cm^2, the microporous coating appears to augment heat transfer through increased convection and is most likely from higher bubble departure frequencies.

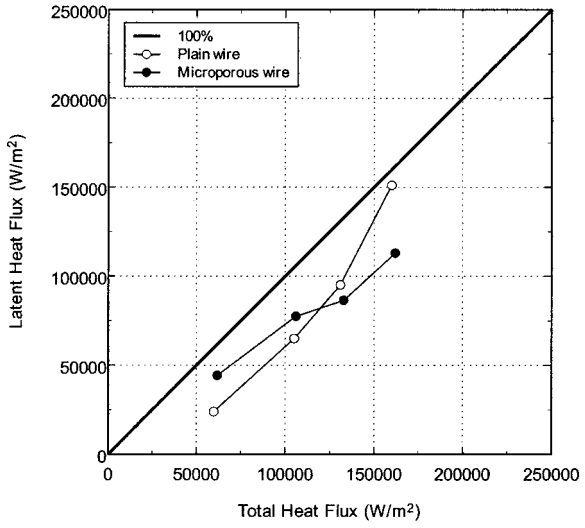

Fig. 6 Latent heat flux contribution for plain and microporous wires (increasing heat flux)

To help explain the results from Fig. 6, the bubble diameter and frequency versus total heat flux and the bubble frequency versus size range for the two wires are plotted in Figs. 7 and 8, respectively. As previously mentioned, the bubble diameters and frequencies shown in Figs. 7 and 8 are not considered ''departure'' diameters and frequencies because most of the departing bubbles (even at the lowest heat flux) had already merged with one or more neighboring bubbles prior to being measured. From Fig. 7 at 6 W/cm^2, the average bubble diameters for the plain and microporous wires were nearly the same, however, the frequency for the microporous wire was 2.5 times higher due to its higher active nucleation site density. As the heat flux is increased, the average bubble diameters increased while the bubble frequencies decreased. Previous studies have shown that the departure diameter remains relatively constant [24,25] in the isolated bubble regime and then decreases [26,27] with increasing heat flux. This means that the increased average bubble diameter and subsequent de-

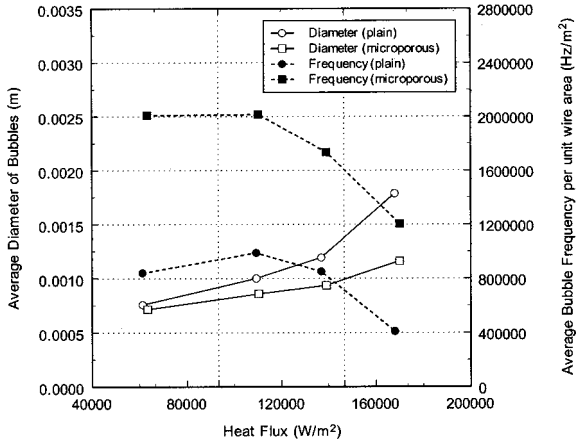

Fig. 7 Average diameter and frequency of bubbles departing from the wire

creased frequency shown in Fig. 7 for both wires is mainly due to increased bubble merging near the wire surface, which was visually confirmed from the videos.

Another observation from Fig. 7 is that the average bubble diameter of the plain wire becomes much larger than the average bubble diameter of the microporous wire as the heat flux is increased which at first appears counter-intuitive because of the plain wire's lower active nucleation site density (less bubble crowding). It is expected that more merging among bubbles will occur at higher heat fluxes due to a higher vapor flow rate (higher departure frequency), however, this does not offer an explanation for the difference in plain and microporous wire bubble behavior seen in Fig. 7. The following three possible bubble mechanisms, which could explain this behavior: (1) First, consider that the bubble will detach once it reaches the ''critical'' diameter when the buoyancy and/or inertia force are greater than the surface tension force holding the bubble to the surface. When two bubbles of the same size merge, the resulting bubble is twice the volume but the diameter only changes by 26 percent. Since buoyancy is related to the bubble volume and the surface tension force is related to bubble perimeter in contact with heater surface (bubble diameter), merging of bubbles will significantly accelerate the departure process. Therefore, when neighboring bubbles merge while still attached to the wire, it is expected that the new, larger bubble would become greater than the critical diameter and immediately depart. The lower active site density of the plain wire would allow an individual bubble to grow to a larger diameter prior to merging with neighboring bubbles and thus have a larger diameter upon departure than the microporous wire. (2) A second possible explanation would be that increased bubble interaction on the microporous wire from its higher active site density might cause the bubbles to depart earlier. In other words, the effective critical bubble diameter would become smaller due to more turbulence caused by more frequent and crowded bubble departures. A smaller critical diameter due to a higher active site density for the microporous wire may partially offset the effect of increased merging at higher heat fluxes. (3) A third possible explanation concerns the vapor behavior within the microporous coating. O'Connor and You [9] estimated a low thermal conductivity for the microporous coating layer, therefore, the majority of nucleation/phase change is expected to occur inside the coating near the heating surface. The rest of the coating would act to distribute the vapor to all of the openings on the top surface (the cavities within the coating are interconnected). This would provide many more apparent nucleation sites than even a roughened plain surface and would cause the bubble to be formed by a relatively high velocity jet of vapor normal to the surface. The addition of internal vapor inertia on the bubbles could cause premature

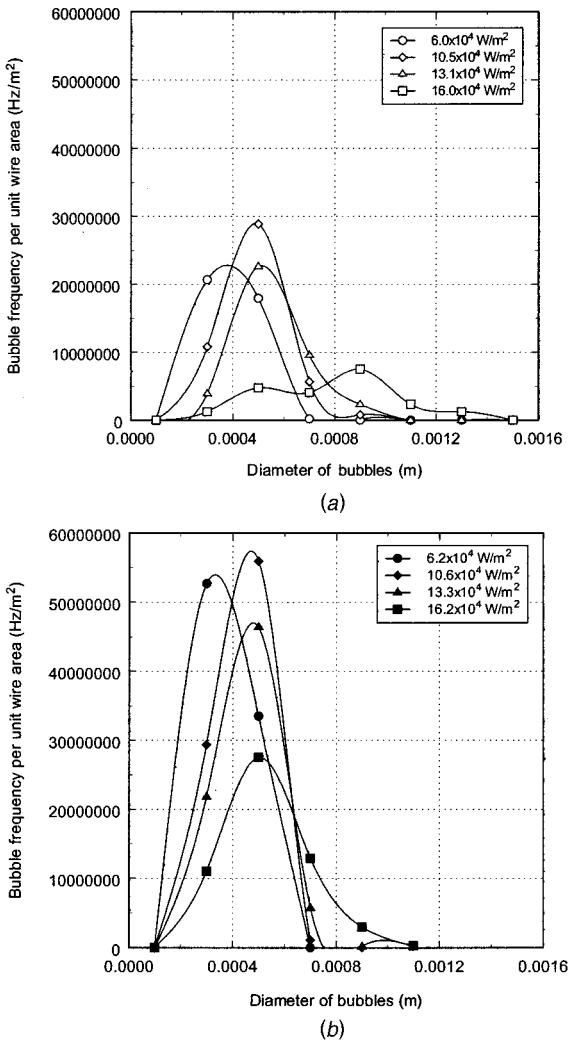

Fig. 8 Bubble frequency distributions: (*a*) plain wire; (*b*) microporous wire.

departure. Evidence of this effect can be seen when comparing the plain and microporous photos of Fig. 5. The microporous photos show many bubbles protruding from the bottom of the wire while the plain surface bubbles appear to slide upward before becoming large. The addition of vapor inertia directed downward for the microporous wire may delay the bubble from sliding upward until the bubble is larger. Regardless of the actual explanation(s) for the difference in average bubble size behavior between the plain and microporous wire, the effect appears to be a direct result of differences in the active or apparent nucleation site density which in turn improves the convection heat transfer mechanism of the microporous wire over the plain wire at higher heat fluxes.

The enhancement of nucleate boiling performance from the microporous wire over the plain wire is surprisingly similar to the enhancement from the addition of surfactant to water observed by Ammerman and You [28]. Ammerman and You found that by decreasing the surface tension of water the average bubble diameter was reduced while the average bubble frequency per unit length of wire increased. From their boiling photos, the active nucleation site density appears to be significantly increased as well. Ammerman and You further found that these effects on bubble dynamics caused the enhancement of nucleate boiling from increased latent heat at low heat fluxes and from increased convection at high heat fluxes, which is strikingly similar to the present results from Fig. 6. Ammerman and You attributed the

increased latent heat at low heat fluxes to the activation of normally dormant nucleation sites (increased active nucleation site density). At high heat fluxes, Ammerman and You said that the reduction in surface tension decreased the amount of bubble agglomeration at the surface (decreased diameter/increased frequency). The increased frequency was thought to reduce the superheated liquid layer thickness at the surface, which would inhibit boiling but increase the effective temperature gradient at the surface and ultimately trade latent heat transfer for convection heat transfer. Although the cause for the reduced bubble diameters and increased bubble frequencies is different between the present study and Ammerman and You's study, the resulting effect on the heat transfer mechanisms appears to be the same.

From the frequency plots in Fig. 8, some of the effects previously discussed can be seen. In Fig. 8(*a*), the plain wire shows a slight increase in the peak diameter from 6 to 10 W/cm^2, remains constant from 10 to 13 W/cm^2, and then increases dramatically at 16 W/cm^2. The dramatic change from 13 to 16 W/cm^2 for the plain wire can also be seen in Fig. 7 as a large increase in average bubble diameter with a corresponding decrease in bubble frequency. For the microporous wire in Fig. 8(*b*), the frequency behavior from 6 to 10 W/cm^2, is similar although with higher frequencies. From 10 to 16 W/cm^2, the microporous wire shows a different behavior. The peak bubble diameter remains relatively constant while the frequency decreases. This is showing a more gradual increase in average bubble diameter through increased bubble merging than the plain wire. Paul and Abdel-Khalik's [23] data also shows a relatively constant peak bubble diameter regardless of heat flux in saturated water. It is also interesting to observe that at 6, 10 and 13 W/cm^2 the peak diameters of the plain and microporous wires are the same.

Critical Heat Flux Behavior. As previously mentioned, it has already been shown that the microporous coating significantly enhances CHF in saturated pool boiling of highly-wetting fluids [13,14], and is also observed in Fig. 3. Recently, using data from their flat polished, roughened, and microporous surfaces, Rainey and You [21] showed that the surface microstructure significantly affects CHF in FC-72. They further suggested that the enhancement was a direct result of increased active nucleation site density. Combining Rainey and You's observations with the results of the present study allows for a more complete view of the CHF enhancement mechanism of the microporous coating.

As the heat flux approaches CHF for the plain wire, the latent heat contribution increases towards 100 percent as shown in Fig. 6. Visual observations of the plain wire showed that the wire surface became increasingly obscured by large vapor bubbles until complete dryout occurred at CHF. The obscuring of the wire surface by the bubbles from increased vapor generation rate would increase the blockage to the fluid re-wetting the surface, which in turn would reduce the convection heat transfer. Increased vapor generation from the wire along with decreased convection would also produce more vapor flow instability. Unfortunately the latent heat contribution of the microporous wire could not be measured close to CHF due to excessive bubble crowding in the photos so its behavior near CHF is not known, however, it is expected that the microporous wire latent heat contribution will eventually approach 100 percent at CHF similar to the plain wire. As previously discussed, the microporous coating enhances nucleate boiling at higher heat fluxes by providing better convection heat transfer. Its increased active nucleation site density appears to prevent the bubbles from becoming too large prior to departure and produces significantly greater bubble departure frequencies which in turn provides better convection heat transfer. In addition, if there is a significant amount of vapor inertia normal to the surface as postulated above, this may increase the hydrodynamic stability of the vapor flow from the surface and thus allow for higher vapor flow generation rates prior to CHF which was previously proposed by Polezhaev and Kovalev [7] for porous surfaces. From these discussions, it appears that the microporous coating delays CHF through decreased bubble diameters and increased bubble frequencies, which ultimately provides significantly more convection heat transfer contribution than the plain surface and/or increased hydrodynamic stability from increased vapor bubble inertia. These phenomena would allow for the extension of the nucleate boiling regime before hydrodynamic instability occurs (CHF).

Conclusions

The macro and micro-scale heat transfer mechanisms of pool boiling heat transfer from microporous surfaces immersed in saturated FC-72 at atmospheric pressure were investigated using 390 μm diameter platinum wires (one plain and one coated with the DOM microporous coating). The consecutive-photo method developed by Ammerman and You [15] was utilized to determine the differences in latent heat contribution as well as bubble diameter and frequency leaving the surface. The effects of the coating on CHF are also discussed. Following are the primary conclusions made from this study:

1 It was confirmed that the microporous coating enhances nucleate boiling heat transfer as a direct result of its significantly higher active nucleation site density and is not due to an increase in surface area.

2 Compared to the plain surface, the higher active nucleation site density of the microporous coating reduces bubble diameters while increases bubble frequency. At low heat fluxes (below about 12 W/cm^2), this produces more latent heat contribution by activating normally dormant nucleation sites. At high heat fluxes (above about 12 W/cm^2), this reduces the superheated liquid layer at the surface, which inhibits latent heat transfer but promotes convection heat transfer. In addition, the phenomenon is very similar to the enhancement of nucleate boiling from the addition of surfactant to water.

3 The microporous coating appears to delay CHF by increasing the convection heat transfer contribution with a subsequent decrease in latent heat (vapor generation) and/or increasing the hydrodynamic stability of the vapor leaving the surface from increased bubble vapor inertia, which would allow for more vapor generation from the surface. Either or both of these possible explanations would extend the nucleate boiling curve prior to CHF.

Nomenclature

D = wire diameter, [m]
h_{1g} = latent heat of vaporization, [J/kg]
L = length of wire examined, [m]
q''_{LH} = latent heat flux, [W/m^2]
$\dot{V}_g$ = vapor volumetric flow rate, [m^3/s]
ρ_g = density of saturated vapor, [kg/m^3]

References

[1] Kurihara, H. M., and Myers, J. E., 1960, "The Effects of Superheat and Surface Roughness on Boiling Coefficients," AIChE J., **6**(1), pp. 83–91.
[2] Berenson, P. J., 1962, "Experiments on Pool-Boiling Heat Transfer," Int. J. Heat Mass Transf., **5**, pp. 985–999.
[3] Nishio, S., and Chandratilleke, G. R., 1989, "Steady-State Pool Boiling Heat Transfer to Saturated Liquid Helium at Atmospheric Pressure," JSME Int. J., Ser. II, **32**(4), pp. 639–645.
[4] Ramilison, J. M., Sadasivan, P., and Lienhard, J. H., 1992, "Surface Factors Influencing Burnout on Flat Heaters," ASME J. Heat Transfer, **114**(1), pp. 287–290.
[5] Griffith, P., and Wallis, J. D., 1960, "The Role of Surface Conditions in Nucleate Boiling," *Chemical Engineering Progress Symposium Series No. 49*, **56**, pp. 49–63.
[6] Thome, J. R., 1992, "Mechanisms of Enhanced Nucleate Pool Boiling," *Proceedings of the Engineering Foundation Conference on Pool and External Flow Boiling*, ASME, New York, pp. 337–343.
[7] Polezhaev, Y. V., and Kovalev, S. A., 1990, "Modeling Heat Transfer with Boiling on Porous Structures," Thermal Engineering, **37**(12), pp. 617–620.
[8] Tehver, J., 1992, "Influences of Porous Coating on the Boiling Burnout Heat Flux," *Recent Advances in Heat Transfer*, B. Sundén et al., eds., Elsevier Science Publishers, pp. 231–242.
[9] O'Connor, J. P.,, and You, S. M., 1995, "A Painting Technique to Enhance

Pool Boiling Heat Transfer in FC-72,'' ASME J. Heat Transfer, **117**(2), pp. 387–393.
[10] Chang, J. Y., and You, S. M., 1997, ''Boiling Heat Transfer Phenomena From Microporous and Porous Surfaces in Saturated FC-72,'' Int. J. Heat Mass Transf., **40**(18), pp. 4437–4447.
[11] Chang, J. Y., and You, S. M., 1997, ''Enhanced Boiling Heat Transfer From Microporous Surfaces: Effects of a Coating Composition and Method,'' Int. J. Heat Mass Transf., **40**(18), pp. 4449–4460.
[12] You, S. M. and O'Connor, J. P. 1998, ''Boiling Enhancement Paint,'' U. S. Patent #5814392.
[13] Chang, J. Y., and You, S. M., 1997, ''Enhanced Boiling Heat Transfer From Micro-Porous Cylindrical Surfaces in Saturated FC-87 and R-123,'' ASME J. Heat Transfer, **119**(2), pp. 319–325.
[14] Rainey, K. N., and You, S. M., 2001, ''Effects of Heater Orientation on Pool Boiling Heat Transfer from Microporous Coated Surfaces,'' Int. J. Heat Mass Transf., **44**(14), pp. 2589–2599.
[15] Ammerman, C. N., and You, S. M., 1998, ''Consecutive-Photo Method to Measure Volume Flow Rate During Boiling From a Wire Immersed in Saturated Liquid,'' ASME J. Heat Transfer, **120**(3), pp. 561–567.
[16] Kuehn, T. H., and Goldstein, R. J., 1976, ''Correlating Equations for Natural Convection Heat Transfer Between Horizontal Circular Cylinders,'' Int. J. Heat Mass Transf., **19**, pp. 1127–1134.
[17] Hong, Y. S., Ammerman, C. N., and You, S. M., 1997, ''Boiling Characteristics of Cylindrical Heaters in Saturated, Gas-Saturated, and Pure-Subcooled FC-72,'' ASME J. Heat Transfer, **119**(2), pp. 313–318.
[18] Kline, S. J., and McClintock, F. A., 1953, ''Describing Uncertainties in Single-Sample Experiments,'' Mech. Eng. (Am. Soc. Mech. Eng.), **75**(1), pp. 3–8.
[19] Hong, Y. S., ''Pool Boiling Heat Transfer for Cylindrical Heaters Immersed in Gas-Saturated FC-72,'' Ph.D. thesis, The University of Texas at Arlington, Arlington, TX.
[20] Bar-Cohen, A., and McNeil, A., 1992, ''Parametric Effects on Pool Boiling Critical Heat Flux in Dielectric Liquids,'' *Proceedings of the Engineering Foundation Conference on Pool and External Flow Boiling*, ASME, Santa Barbara, CA, pp. 171–175.
[21] Rainey, K. N., and You, S. M., 2000, ''Pool Boiling Heat Transfer From Plain and Microporous, Square Pin-Finned Surfaces in Saturated FC-72,'' ASME J. Heat Transfer, **122**(3), pp. 509–516.
[22] Chang, J. Y., and You, S. M., 1996, ''Heater Orientation Effects on Pool Boiling of Microporous-Enhanced Surfaces in Saturated FC-72,'' ASME J. Heat Transfer, **118**(4), pp. 937–943.
[23] Paul, D. D., and Abdul-Khalik, S. I., 1983, ''A Statistical Analysis of Saturated Nucleate Boiling Along a Heated Wire,'' Int. J. Heat Mass Transf., **26**, pp. 509–519.
[24] Gaertner, R. F., 1965, ''Photographic Study of Nucleate Pool Boiling on a Horizontal Surface,'' ASME J. Heat Transfer, **87**, pp. 17–29.
[25] Rini, D. P., Chen, R. H., and Chow, L. C., 2001, ''Bubble Behavior and Heat Transfer Mechanism in FC-72 Pool Boiling,'' Exp. Heat Transfer, **14**(1), pp. 27–44.
[26] Gaertner, R. F., and Westwater, J. R., 1960, ''Population of Active Sites in Nucleate Boiling Heat Transfer,'' *Chemical Engineering Progress Symposium Series*, **56**(30), pp. 39–48.
[27] Kolev, N. I., 1994, ''The Influence of Mutual Bubble Interaction on the Bubble Departure Diameter,'' Exp. Therm. Fluid Sci., **8**, pp 167–174.
[28] Ammerman, C. N., and You, S. M., 1996, ''Determination of the Boiling Enhancement Caused by Surfactant Addition to Water,'' ASME J. Heat Transfer, **118**, pp. 561–567.

Self-Organization and Self-Similarity in Boiling Systems

L. H. Chai
e-mail: lhchai@photon.t.u-tokyo.ac.jp
Post-Doctoral Research Fellow
Shoji Laboratory,
Department of Mechanical Engineering,
The University of Tokyo,
Hongo 7-3-1, Bunkyo-ku,
Tokyo 113-8656, Japan

M. Shoji
Professor
Department of Mechanical Engineering,
The University of Tokyo,
Hongo 7-3-1, Bunkyo-ku,
Tokyo 113-8656, Japan

Boiling system is a typical open dissipative structure. Focusing on the investigation of boundary adjacent to heating plate surface in boiling system, nonlinear non-equilibrium statistical thermodynamics theory of open systems was originally constructed. The competitive bubble formation was realized by non-equilibrium phase transition caused by the interactions among active sites or bubbles. The "natural selection" among all possible sites was mathematically outlined. It was by the means of "natural selection" that a kind of self-organized and self-similar structure was formed. The present studies theoretically explained the experimental observations from other researchers, and gave more reasonable guidance of enhancing boiling heat transfer, such as by way of installing artificial cavities. Beyond the scope of boiling systems, the present studies not only have far-reaching theoretical implications on explaining time, life, thermodynamic, self-similar, fluctuation, order and chaos etc., but also can find many promising applications from new perspectives, such as wider industrial optimization, the recognitions of pattern and reproduction pattern of by computer etc. [DOI: 10.1115/1.1470490]

Keywords: Boiling, Non-Equilibrium, Optimization, Thermodynamics, Nonlinear Statistical

Introduction

Boiling process is encountered in a number of applications, including not only in traditional industry such as metallurgical quenching processes, flooded tube and shell evaporator, immersion cooling of industrial components, to name only a few, but also in modern heat transfer technologies related to space, electronics component and nuclear reactors etc. The importance of boiling in a wide variety of applications has provided the incentive for numerous investigations of its basic mechanisms over the past several decades. A substantial number of such efforts have been devoted to the understanding and modeling of the transport during boiling process. A plethora of empirical correlations are now available in the literature [1]. The characteristic of boiling process varies considerably depending on the conditions at which boiling occurs. The heat flux level, the thermo-physical properties of medium, the wall material and finish, and size of heated wall all may have an effect on the boiling processes. Because of the multiplicity of variables of boiling systems, it is more difficult to suggest equations for the calculation of heat transfer coefficients than it is in the case of other problems of heat transfer such as conduction, convection and radiation. Also, we are far from having worked out a complete theory, because the physical phenomena are too complicated and in no way have been sufficiently understood. Therefore, a satisfactory mechanism and modeling description remain elusive though boiling phenomena have been studied extensively for several decades.

It is becoming apparent that traditional methods still remain principally an empirical art and traditional modeling efforts thus far typically use a linearized approach [2]. For example, physical phenomena and heat transfer are analyzed on the basis of a single site or vapor bubble, by assuming uniform condition to obtain results with a given active site density distribution. It is implied that the formation of active sites or bubbles has no effect on the formation of adjacent active sites or bubbles. Consequently potential important interactions between active sites are ignored. Traditional linear approaches provide doubtful mechanistic models [3].

It is necessary to look at the whole picture of boiling process, that is to say, to see the forest rather than the tree [4]. Considering that the boiling system is characterized by the existence of nonlinear, non-equilibrium, complexity and stochastic, it is necessary to deal with potential nonlinear effects in boiling systems. Introduction of nonlinear nonequilibrium statistical perspectives may promise the eventual and complete understanding of boiling processes.

In our viewpoints, among three zones of boiling system, as shown in Fig. 1, the two-phase zone above heater surface could be predicted by turbulent models, and the solid zone below the heater surface could be modeled by conductive equation providing that the boundary conditions at heater surface are known. Therefore, the central point is how to model the coupled heater surface. The present authors focus on analyzing the nonlinear interactions on coupled complex heater surface caused all possible nonlinear factors by use of non-equilibrium statistical theories, which are still elusive to this day [5,6]. Firstly, the nonlinear nonequilibrium statistical theory of arbitrary open systems is originally constructed basing upon optimization viewpoints. Self-organized boiling processes by means of non-equilibrium phase transition are then revealed. It is mathematically demonstrated that the boiling process is a kind of evolution by ''natural selection.'' The self-similar dissipative structure is accordingly formed. Beyond the scope of boiling systems, the present studies not only have far-reaching theoretical implications on explaining time, life, thermodynamic, self-similar, fluctuation, order and chaos etc., but also can find many promising applications from new perspectives, such as wider industrial optimization, the recognitions of pattern and reproduction of pattern by computer etc.

Boiling System: A Typical Complex System

The nonlinear effects involved in boiling systems include nonuniform site distribution, the on/off behavior of sites, the formation and evaporation of micro-layers and macro-layers, bubble generation, growth, departure and coalescence, and interactions between bubbles or sites etc. Note that these nonlinear effects are concentrated in the boundary layer near the heater surface. Therefore, the nonlinear behavior of pool boiling systems can be partially investigated by solving the controlling equations in a control volume of the two-phase system in the boundary layer adjacent to the heater surface [7].

More importantly, in the boiling process, the parameters of heater surface, such as temperature is extremely nonuniform and

Contributed by the Heat Transfer Division for publication in the JOURNAL OF HEAT TRANSFER. Manuscript received by the Heat Transfer Division December 18, 2000; revision received January 16, 2002. Associate Editor: V. P. Carey.

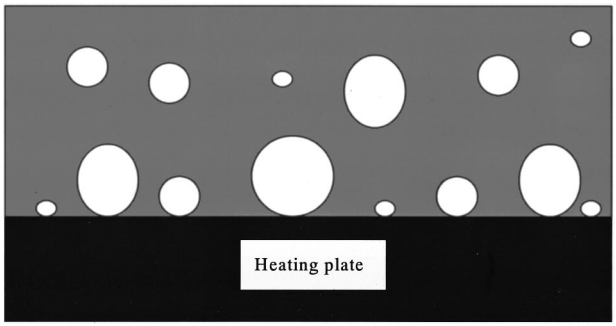

Fig. 1 Boiling system

rapidly varies with time for the nonlinear interactions within turbulent flow regime, heater regime and their interface [8]. It is necessary to analyze heater surface characteristics from microscopic view, for averaged ways would completely hide the nonlinear dynamic performance. Assuming macroscopic boundary systems adjacent to heater surface consist of a large number of objects, viewed as elementary, as shown in Fig. 2. Throughout the whole volume, within each subsystem, the parameters of the two-phase system near the surface are homogenized. Doubtless, for the other wide spectrum and complexity of any open systems, a sufficiently complete and adequate description in most cases can be achieved in same way, on the basis of the statistical theory.

General Description. In classical statistical physics, in order to describe a macroscopic system consisting of an enormous number of microscopic elements, the extremely complex motion of the microscopic elements has to be projected, so to speak, onto a much smaller number of macroscopic variables. The projection is necessarily of a statistical character. In this sense, it is statistical physics that synthesizes the microscopic world to the macroscopic world. Basing on the assumption of equal weights of microstates, the whole structure of the statistical mechanics for equilibrium state was beautifully constructed by Boltzmann and Gibbs [9]. For classical nonequilibrium statistical processes, there are two categories. One is kinetic method, such as Boltzmann-typed equation or Markovian equation. The other is linear-response theory. However, as far as open systems far from equilibrium are concerned, there is still lack of general methods [9].

Anyway, the situation for open systems far from equilibrium is completely different from that of equilibrium or near-equilibrium systems. How to develop a method for open systems far from equilibrium analogized to equilibrium systems then becomes a central problem. Similar to the assumption of equal a priori probability, from which the whole classical statistical mechanics was born, we propose the following assumption for open systems far from equilibrium.

An open system far from equilibrium always seeks an optimization process so that the obtained flux J from outside is maximal under given prices or constrains. Simultaneously, a kind of self-organized and self-similar fractal structure will be formed.

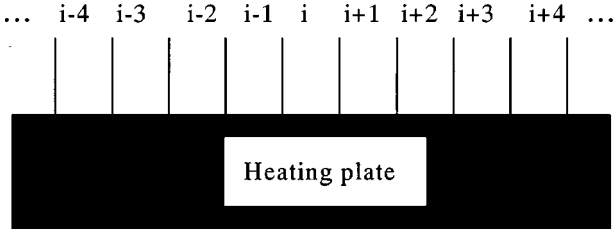

Fig. 2 Sub-elements adjacent to heating plate surface

We all know that the whole framework of equilibrium statistical mechanics is constructed on the basis of the principle of equal weights of microstates. Although the ergodic theories have progressed in recent years, we still lack a rigorous proof of the equal weight principle. Despite this fact, no one doubts the validity of equilibrium statistical mechanics. It is our idea that the nonequilibrium statistical theory of open systems can also be constructed by above assumption, which may be considered as a kind of thermodynamics law.

Assuming the driving forces of subsystems, as shown in Fig. 2, i.e., the cause of receiving flux from environment, can be expressed as $x_1, x_2, \cdots x_n$, which are lumped as a vector $\mathbf{x} = (x_1, x_2, \cdots x_n)$, the driving forces may indicate velocity difference, temperature difference, concentration difference, etc. Similar to classical statistical theory, here we can consider that all possible microstates compose a continuous scope in the Γ space. $d\mathbf{x} = dx_1 dx_2 \cdots dx_n$ is a volume unit in Γ space. The probability for the state of the system existing within the volume unit $d\mathbf{x}$ at time t is

$$\rho(\mathbf{x},t)d\mathbf{x} \tag{1}$$

$\rho(\mathbf{x},t)$ is distribution function of ensemble, which satisfies the normalization condition

$$\int \rho(\mathbf{x},t)d\mathbf{x} = 1 \tag{2}$$

Assuming that the generalized flux is J when the state of the system exists within the volume unit $d\mathbf{x}$ at time t, the averaged flux over all possible microstates is

$$\overline{J} = \int \rho(\mathbf{x},t)J(\rho)d\mathbf{x} \tag{3}$$

For discrete systems, Eq. (2) and Eq. (3) can be changed as

$$\sum_s \rho_s(t) = 1 \tag{4}$$

$$\overline{J} = \sum_s \rho_s(t)J(\rho_s) \tag{5}$$

By use of Lagrange multiplier, let us maximize the Eq. (3) or Eq. (5) under the following constraints (indicate given prices)

$$\langle x_i \rangle = f_1 \tag{6}$$

$$\langle x_i x_j \rangle = f_2 \tag{7}$$

$$\langle x_i x_j x_k \rangle = f_3 \tag{8}$$

$$\langle x_i x_j x_k x_l \rangle = f_4 \tag{9}$$

We obtain that

$$J(\rho) + \rho J'(\rho) - \alpha - \sum_i \beta_i x_i - \sum_{ij} \beta_{ij} x_i x_j - \sum_{ijk} \beta_{ijk} x_i x_j x_k - \sum_{ijkl} \beta_{ijkl} x_i x_j x_k x_l = 0 \tag{10}$$

Equation (10) yields

$$J = \alpha + \sum_i \beta_i x_i + \sum_{ij} \beta_{ij} x_i x_j + \sum_{ijk} \beta_{ijk} x_i x_j x_k + \sum_{ijkl} \beta_{ijkl} x_i x_j x_k x_l + \frac{c}{\rho} \tag{11}$$

where c is integration constant.

Equation (11) can be changed as

$$\rho=\frac{c}{J-\alpha-\sum_i \beta_i x_i-\sum_{ij} \beta_{ij}x_i x_j-\sum_{ijk} \beta_{ijk}x_i x_j x_k-\sum_{ijkl} \beta_{ijkl}x_i x_j x_k x_l} \tag{12}$$

It is noted that the generalized flux J can be described as

$$J=\eta+\sum_i \gamma_i x_i+\sum_{ij} \gamma_{ij}x_i x_j+\sum_{ijk} \gamma_{ijk}x_i x_j x_k+\sum_{ijkl} \gamma_{ijkl}x_i x_j x_k x_l+\cdots \tag{13}$$

Obviously, it is the extended relation of classical linear thermodynamics.

Substituting Eq. (13) into Eq. (12) yields

$$\rho=\frac{c}{\eta-\alpha+\sum_i (\gamma_i-\beta_i)x_i+\sum_{ij} (\gamma_{ij}-\beta_{ij})x_i x_j+\sum_{ijk} (\gamma_{ijk}-\beta_{ijk})x_i x_j x_k+\sum_{ijkl} (\gamma_{ijkl}-\beta_{ijkl})x_i x_j x_k x_l+\cdots} \tag{14}$$

As well known that

$$e^x=1+x+\frac{1}{2!}x^2+\frac{1}{3!}x^3+\cdots \tag{15}$$

Equation (14) can be changed as

$$\rho=\exp\left(\mu+\sum_i \sigma_i x_i+\sum_{ij} \sigma_{ij}x_i x_j+\sum_{ijk} \sigma_{ijk}x_i x_j x_k+\sum_{ijkl} \sigma_{ijkl}x_i x_j x_k x_l+\cdots\right) \tag{16}$$

The constants in Eq. (16) are determined by the constants in Eq. (14). The exponential term can be considered as a potential function, which guarantees the asymptotic stability of reference-state. It is interesting that Eq. (16) has the same form as the probability function for open systems proposed by Haken [10]. For the state that is far from the equilibrium-state, the sign of the potential function is not fixed, which can be positive or negative depending on specific situations. The characteristics of potential function depend on the sign of depends on constants. If the constants of second order terms would be less than zero, the bifurcation would occur and new dissipative ordered structure will correspondingly be formed.

Application to Boiling System. General description for arbitrary open systems is given above. Obviously, for boiling systems, the driving forces indicate temperature difference, while the generalized flux will be heat flow. As for the optimization law for boiling systems, we may say that the boiling systems are always seeking an optimization process so that the maximum heat can be transferred from the heater. All in same way, we can obtain the Eq. (16). By the diagnosis of the sign of second order term constants, we may judge the occurrence of bifurcation, i.e., bubble formation, which stands a new boiling mode.

The Competitive Incipience of Order: Bubble Formation for Boiling Systems

General Analysis. Ideal systems are composed of elements with negligible interactions and the treatments of these systems can be reduced essentially to that of a single element. Complex systems, in contrast to ideal systems, have strong interactions among constituent elements, which can never be ignored. A cooperative phenomenon called a phase transition will be exhibited. Through a phase transition, system will often acquire a new structure or a new property, which is absent before the phase transition.

According to above analyses, we have a general prescription for writing down the probability function, just as one did for thermal equilibrium systems in term of Gibbs statistical mechanics, providing that the elements of the system are known. The probability function can be used to give any nonequilibrium properties of the system, when suitably treated. Consequently, the feature for nonequilibrium phase transition can be analyzed.

Defining the exponential term of Eq. (16) as potential function

$$\mathbf{\Phi}(\boldsymbol{\sigma},\mathbf{x})=\mu+\sum_i \sigma_i x_i+\sum_{ij} \sigma_{ij}x_i x_j+\sum_{ijk} \sigma_{ijk}x_i x_j x_k+\sum_{ijkl} \sigma_{ijkl}x_i x_j x_k x_l+\cdots \tag{17}$$

Assuming [10]

$$\mathbf{x}=\mathbf{x_0}+\mathbf{w} \tag{18}$$

Here, potential function is most symmetric at point $\mathbf{x_0}$. Then

$$\mathbf{\Phi}(\boldsymbol{\sigma},\mathbf{x})=\overline{\mathbf{\Phi}}(\overline{\boldsymbol{\sigma}},\mathbf{w}) \tag{19}$$

and

$$\overline{\mathbf{\Phi}}(\overline{\sigma},\mathbf{w})=\overline{\mu}+\sum_{ij} \boldsymbol{\sigma}_{ij}w_i w_j+\cdots \tag{20}$$

Where the constants are determined as

$$\overline{\sigma}_{ij}=\frac{1}{2}\frac{\partial^2 \mathbf{\Phi}}{\partial x_i \partial x_j}\bigg|_{\mathbf{x}_0} \tag{21}$$

Matrix $\langle \overline{\sigma}_{ij} \rangle$ is diagonalizable under the transformation

$$w_i=\sum_k \psi_{ki}\xi_k \tag{22}$$

Accordingly, Eq. (20) can be changed as

$$\overline{\mathbf{\Phi}}(\boldsymbol{\lambda},\boldsymbol{\xi})=\zeta+\sum_k \lambda_k \xi_k^2+\cdots \tag{23}$$

Terms for $\lambda_k>0$ correspond to unstable modes and induce the occurrence of non-equilibrium phase transitions. From the mean molecular field of Van der Waals, Weiss, and Bethe to the phenomenological theory of phase transition of Landau, the equilibrium phase transitions theory was beautifully constructed in unifying fashion. In fact, here we try to show that non-equilibrium phase transition can be developed in a deep analogy with the equilibrium phase transitions. Furthermore, the present results shed new lights on the more complete understanding of equilibrium phase transitions.

Discussion on Boiling System. As far as boiling systems are concerned, the unstable modes mean the formations of bubbles, in other word, the appearances of a new boiling mode.

Natural Selection—Competition for Input Flux

General Analysis. Obviously, the generalized flux can be described by new variables as

$$\overline{J}=\int_{\xi}\rho(\xi,t)J(\xi)d\xi \tag{24}$$

Considering the identifiable contributions of stable modes and unstable modes, the potential function can be decomposed as [10]

$$\overline{\Phi}(\lambda,\xi)=\zeta+\overline{\Phi}_u(\lambda_u,\xi_u)+\overline{\Phi}_s(\lambda_u,\lambda_s;\xi_u,\xi_s) \tag{25}$$

where

$$\overline{\Phi}_u(\lambda_u,\xi_u)=\sum_u \lambda_u\xi_u^2+\sum_{uu'u''}\lambda_{uu'u''}\xi_u\xi_{u'}\xi_{u''}+\sum_{uu'u''u'''}\lambda_{uu'u''u'''}\xi_u\xi_{u'}\xi_{u''}\xi_{u'''}+\cdots \tag{26}$$

$$\begin{aligned}\overline{\Phi}_s(\lambda_u,\lambda_s;\xi_u,\xi_s)=&\sum_s(-|\lambda_s|\xi_s^2+\sum_{suu'}3\lambda_{suu'}\xi_s\xi_u\xi_{u'}\\&+\sum_{suu'u''}4\lambda_{suu'u''}\xi_s\xi_u\xi_{u'}\xi_{u''}\\&+\sum_{ss'u}\lambda_{ss'u}\xi_s\xi_{s'}\xi_u+\sum_{ss's''}\lambda_{ss's''}\xi_s\xi_{s'}\xi_{s''}\\&+\sum_{ss'uu'}\lambda_{ss'uu'}\xi_s\xi_{s'}\xi_u\xi_{u'}\\&+\sum_{ss's''u}\lambda_{ss's''u}\xi_s\xi_{s'}\xi_{s''}\xi_u\\&+\sum_{ss's''s'''}\lambda_{ss's''s'''}\xi_s\xi_{s'}\xi_{s''}\xi_{s'''}+\cdots\end{aligned} \tag{27}$$

Therefore

$$\rho(\mathbf{x})=\rho(\xi_u,\xi_s)=\exp[\overline{\Phi}(\lambda,\xi)]=\rho(\xi_u)\rho(\xi_s/\xi_u) \tag{28}$$

Defining

$$\int \exp(\overline{\Phi}_s)d^{N_s}\xi_s=g(\xi_u)=\exp[-h(\xi_u)] \tag{29}$$

N_s is the number of stable modes. Obviously

$$W_s=h(\xi_u)+\overline{\Phi}_s \tag{30}$$

$$W_u=\zeta+\overline{\Phi}_u-h(\xi_u) \tag{31}$$

then

$$\rho(\xi_u)=\exp(W_u) \tag{32}$$

$$\rho(\xi_s/\xi_u)=\exp[W_s(\xi_s/\xi_u)] \tag{33}$$

In order to show the competitive process, i.e., adiabatic elimination process in static mechanics and quantum mechanics [5,6], we now turn to the dynamics analyses. Equation (28) can be regarded as the solutions of Fokker-Planck equations, and therefore we write down the corresponding generalized Langivan equations as follows

$$\dot{\xi}_u=\lambda_u\xi_u+S_u(\xi_u,\xi_s)+F_u(t) \tag{38}$$

$$\dot{\xi}_s=\lambda_s\xi_s+T_s(\xi_u)+F_s(t) \tag{39}$$

Clearly, the functions S_u and T_s are known. In fact, we obtained the typical evolution equations for systems undergoing nonequilibrium phase transitions.

Detailed adiabatic elimination process analyses are as follows. According to Eq. (38) and Eq. (39), equations that describe the dynamic processes of subsystems are in the following form because of interactions among subsystems when considering the existence of multiple sub-elements

$$\begin{aligned}\dot{\xi}_1&=-\lambda_1\xi_1+f_1(\xi_1,\xi_2,\cdots\xi_n)\\\dot{\xi}_2&=-\lambda_2\xi_2+f_2(\xi_1,\xi_2,\cdots\xi_n)\\&\vdots\\\dot{\xi}_n&=-\lambda_n\xi_n+f_n(\xi_1,\xi_2,\cdots\xi_n)\end{aligned} \tag{40}$$

where first term on right side is linear effect, second term is nonlinear effect that is the function of multiple parameters when taking effects of interactions among subsystems into account. Equations (40) can be classified into two groups: one is $i=1,2,\cdots m$, which stands for small-damp modes, that is, small λ_i, even changes into unstable modes ($\lambda_i\approx 0$). Another is $s=m+1,m+2,\cdots n$, which stands for unstable modes, adiabatic elimination principle takes effects. Let $\dot{\xi}=0$, the following equation is obtained from Eqs. (40)

$$\lambda_s\xi_s=f_s(\xi_1,\xi_2,\cdots\xi_m,\xi_{m+1}(\xi_i),\cdots) \tag{41}$$

which means the mode $|\xi_s|$ induced by λ_s is far less than $|\xi_i|$. Thus for $s=m+1,m+2,\ldots n$, ξ_s in f_s can be neglected and ξ_s can be looked as known parameters.

In real evolution process in complex systems, as described above, only one or a few modes in a unit will become unstable while most other modes still remain damped. This gives the results that all damped modes follow the order parameters and even complicated systems exhibit ordered behaviors: system with disordered motion of subsystems will change into a well-organized system. Order parameter with less damped modes often dominants the whole system behaviors.

If damped coefficients satisfy the situation,

$$\lambda_1\gg\lambda_2\gg\lambda_3\gg\cdots \tag{42}$$

We can first eliminate variables related to ξ_1 with other variables remaining untouched and then eliminate variables related to ξ_2 with other variables untouched. Similar ways go on until only one variable remains.

Analysis above supposes that Eq. (40) can be classified into two groups by damp magnitude. Analyses of self-organization process in complex systems without such limits are as follows. Assuming arbitrary complex system, in which various parameters cannot be explicitly grouped, therefore can be applied to any open dissipative systems

$$\dot{r}_j=h_j(r_1,r_2,\cdots r_n) \tag{43}$$

where h_j is nonlinear function of $r_1,r_2,r_3,\cdots r_n$. Assuming stationary solution of Eq. (43) is r_j^0 and right side of Eq. (43) is dependent on a group of parameters, which are chose in a way so that r_j^0 stands for static value and satisfies the condition when moving r coordinate

$$r_j^0=0 \tag{44}$$

It stands for stationary state without any motion, let

$$r_j(t)=r_j^0+u_j(t) \tag{45}$$

$$\vec{r}(t)=\vec{r}^0+\vec{u}(t) \tag{46}$$

which mean r is decomposed into base and perturbed components. It is useful to do linear stability analysis of Eq. (43). Considering the system is stable and thus u_j is small enough, Eq. (43) is lineaized by substituting Eq. (46) into Eq. (43)

$$\dot{u}_j = \sum_{j'} L_{jj'} u_{j'} \tag{47}$$

Matrix L_{jj} depends on $\vec{r}^{\,0}$ and controlling parameters. Equation (47) is substituted by

$$\dot{\vec{u}} = L\,\vec{u} \tag{48}$$

Equation (47) or Eq. (48) is one order ordinal differential equation and the solution is the form

$$\vec{u} = \vec{u}^{(\mu)}(0)\exp(\lambda_\mu t) \tag{49}$$

where λ_μ is eigenvalue of the following equation

$$\lambda_\mu \vec{u}^{(\mu)}(0) = L\vec{u}^{(\mu)}(0). \tag{50}$$

$\vec{u}^{(\mu)}(0)$ is right eigen vector, generalized solution of Eq. (47) or Eq. (48) is the superimposition of Eq. (49)

$$\vec{u} = \sum_{\mu} \xi_\mu \exp(\lambda_\mu t)\vec{u}_\mu(0). \tag{51}$$

ξ_μ is an arbitrary constant. Introducing left eigen vector $\vec{v}^{(\mu)}$. and requiring

$$\lambda_\mu \vec{v}^{(\mu)} = \vec{v}^{(\mu)} L. \tag{52}$$

For the system is stable, the real parts of λ_μ are all negative. If we require that Eq. (48) satisfy the nonlinearity, Eq. (48) will have the form

$$\dot{\vec{u}} = L\,\vec{u} + \vec{N}(\vec{u}). \tag{53}$$

$\vec{N}(\vec{u})$ results from nonlinear contribution. We can still express u in a form as Eq. (51) by finding appropriate expression $\xi(t)$ so that the following relation is satisfied when left multiplying Eq. (53)

$$\langle \vec{v}^{(\mu)}, \vec{u}^{(\mu')} \rangle = \delta_{\mu\mu'}. \tag{54}$$

Equation (54) simply becomes as

$$\dot{\xi}_\mu = \lambda_\mu \xi_\mu + g_\mu(\xi_1, \xi_2, \ldots \xi_n) \tag{55}$$

where $g_\mu = \langle \vec{v}^{(\mu)}, \vec{N}(\Sigma_\mu \xi_\mu u^{(\mu)}) \rangle$.

Equation (55) is thoroughly same as Eq. (40) in form, which implies that analysis in similar way as Eq. (40) can be conducted. We can change parameters and thus destabilize Eq. (55), that is to say, let one or a few λ_μ equal to or greater than zero with others having negative real part and thus being relating to damped modes. Considering that mode ξ_r for $\mathrm{Re}(\lambda_\mu) \geqslant 0$ acts as order parameter and dominants other modes, adiabatic elimination principle is effective. When adiabatic elimination principle takes no effects, flashing phenomena will occur and chaos may follow. The condition of chaos incipience is $\lambda_1 \approx \lambda_2 \approx \lambda_3 \approx \cdots \lambda_n$.

According to above analysis of adiabatic elimination principle, simultaneously, considering the decompositions of $J(\xi_u, \xi_s)$, Eq. (24) can be changed as

$$\overline{J} = \int_{\xi_u, \xi_s} \prod_s \rho_s(\xi_s/\xi_u)\rho(\xi_u)\left[J(\xi_u) + \sum_s J_s(\xi_s/\xi_u) \right] d\xi \tag{56}$$

It is known that

$$\int_{\xi_s} \rho_s(\xi_s/\xi_u)]\, d\xi_s = 1 \tag{57}$$

Equation (56) can be changed as

$$\overline{J} = \int_{\xi_u} \rho(\xi_u) J(\xi_u) d\xi_u + \int_{\xi_{u,s}} \rho(\xi_u) \int_{\xi_s} \rho_s(\xi_s/\xi_u) J_s(\xi_s/\xi_u) d\xi. \tag{58}$$

That is

$$\overline{J} = \int_{\xi_\mathbf{u}} \rho(\xi_u) J(\xi_u) d\xi_u + \int_{\xi_u} \rho(\xi_u) \int_{\xi_{s,s}} \rho_s(\xi_s/\xi_u) J_s(\xi_s/\xi_u) d\xi \tag{59}$$

We now turn to considering the case of nonequilibrium phase transition. If the system is controlled externally by a control parameter, then all the quantities on the right hands of Eq. (38) and Eq. (39) depend on that control parameter, but in different ways.

When we normalize the control parameter such that the instability occurring at $\alpha = 0$, then λ_u and λ_s depend on α in the following manners.

$$\lambda_u = \alpha^k \tag{60}$$

$$\lambda_s = \lambda_s(0) + 0(\alpha) \approx \lambda_s(0) \tag{61}$$

where k is some positive number. Obviously, λ_u depends very sensitively on α, whereas λ_s depends only weakly on it because the leading term is a no vanishing constant. Similarly, the functions S_u, T_s, F_u, and F_s depend also only weakly on α.

According to adiabatic elimination technique [5,6], we have

$$\dot{\xi}_s = 0. \tag{62}$$

In term of Eq. (39), we have

$$\xi_s = -\frac{T_s(\xi_u)}{\lambda_s(0)} - \frac{F_s(t)}{\lambda_s(0)}. \tag{63}$$

In other words,

$$F_s = -\lambda_s(0)\left[\xi_s + \frac{1}{\lambda_s(0)} T_s(\xi_u) \right] \tag{64}$$

The fluctuation forces, as usual, Gaussian distribution, i.e., the probability of finding F_s within the internal $F \leqslant F_s \leqslant F + dF$ is given by

$$\rho(F \leqslant F_s \leqslant F + dF) = N \exp(-F_s^2/Q) dF. \tag{65}$$

Therefore, the conditional probability can be expressed as

$$\rho(\xi_s/\xi_u) = N \exp\left\{ -\left[\xi_s + \frac{T_s(\xi_u)}{\lambda_s(0)} \right]^2 Q^{-1} \right\}. \tag{66}$$

Obviously, by introducing the new variables, we can eliminate the dependence of the probability distribution of the enslaved variables on ξ_s so that J_s becomes independent of ξ_u, therefore, in Eq. (59) we may perform the integration over ξ_u in the second term of the right hand. We thus obtain that

$$\overline{J} = J_u + \sum_s J_s \tag{67}$$

where the second part does not depend on α, at least in the present approximation. Therefore, the flux change close to the instability point is governed by that of the order parameter alone

$$\overline{J}(\alpha_1) - \overline{J}(\alpha_2) \approx J_u(\alpha_1) - J_u(\alpha_2). \tag{68}$$

Equation (68) provides vivid physical picture: only unstable subsystem with stronger ability can get flux and grow. For open complex system that consists of many subsystems, some of them can use the input of energy or matter better. In other words, energy is concentrated in one or a few subsystems, which may dominant the macroscopic behavior of the whole system. Equation (68) is basic equation of analyzing synergetic phenomena in complex system. Basic ideas of cooperative effects are intuitively incorporated in Eq. (68).

Self-organization transition process from one state to another state by symmetry breaking is analyzed above, which is a transition from a disordered state to another ordered state. Above analysis provides a vivid picture of formation of this kind of ordered dissipative structure: during the process of transition, system is extremely non-uniform and subsystems exist at random. However,

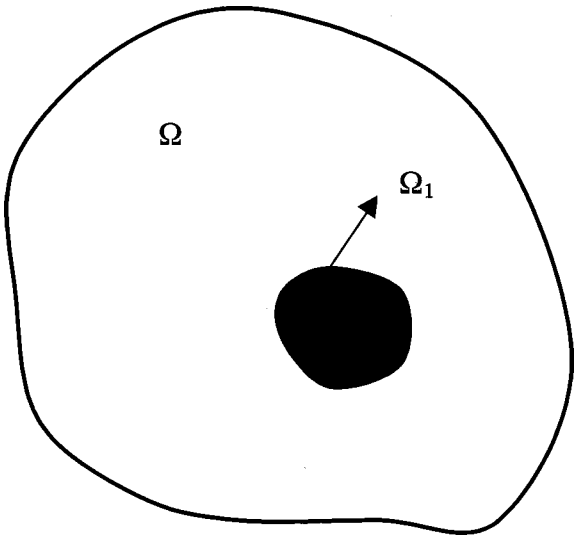

Fig. 3 Arbitrary open system

most subsystems will disappear rapidly for continuously being damped. They can be eliminated by adiabatic principle for their greater damped coefficients and thus be dominated by one or a few subsystems with smaller damped coefficients. These predominant subsystems can grow steadily and eventually promise the transition from disordered state to ordered state. It is a kind of self-organized transition.

With the development of modern measurement and calculation techniques, studies on view of self-organization process and cooperative effects are available in microscopic levels.

In a word, the development of complex systems, as Darwin's picture of a flexible, continuously changing and adapting biosphere under the selection pressure of competition and changing environment conditions [11], is an evolution kinetic process. Nonlinear characteristic existing in complex systems promises the synergetic or cooperative effects and guarantees a certain self-organized behaviors and functions. The evolution can be treated as a sequence of nonequilibrium phase transitions leading to more order and more organized structures.

Discussions on Boiling Phenomena. Above analysis can be applied to the analysis of boiling system and is in good agreement with actual boiling phenomena that we often observed. Numerous sites exist on a unit volume or a unit area. However, only one or a few can be destabilized and become visible bubbles while most others will remain damped. Obviously, if we considered specific boiling system, as shown in Fig. 2, by the "natural selection" principle analyzed above, we demonstrate that some subsystems can use the input of heat better and generate bubbles, in other word, heat is concentrated in a few subsystems, i.e., nucleate bubble mode regimes, which dominate the macroscopic behavior of the whole system.

The Formation of Self-Similar Structures

General Analysis. Based on the above mathematical theory of natural selection, we turn to the analysis of the formation of fractal self-similar structures, i.e., the increasing complex structures in boiling system and other systems we often observe in our common experience: trees, blood vessels, nervous, streams, streets, etc. We want to mathematically derive the geometric forms of these natural structures.

Considering a finite-size system Ω, which may be a certain volume in heater surface when boiling system is considered, for as shown in Fig. 3. We first choose a small unit Ω_1, which contains $m1$ subsystems (the unit is chosen so that it contains potential unstable subsystem, i.e., potential fast mode). For simplicity, we assume that the unit Ω_1 is rectangle, as shown in Fig. 4.

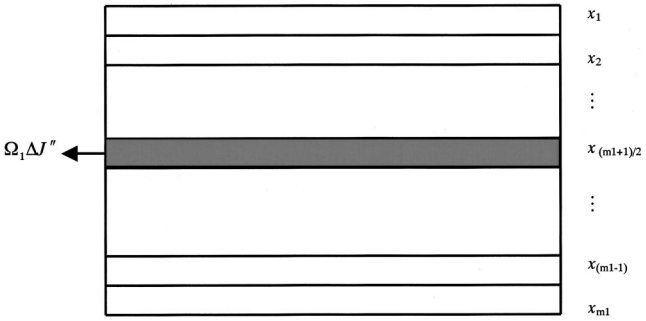

Fig. 4 Enlarged unit Ω_1

Symmetry suggests that the unstable mode is placed in the middle of unit Ω_1 and is indicated by the number $(m1+1)/2$. According to the above analyses, the change of the flux before and after undergoing nonequilibrium phase change is mostly transferred through this section, that is

$$\Omega_1\Delta J''=\overline{J_1}(\alpha_1)-\overline{J_1}(\alpha_2)\approx J_{u1}(\alpha_1)-J_{u1}(\alpha_2) \tag{69}$$

where $\Delta J''$ is the flux density change before and after undergoing nonequilibrium phase transition. The structure formed here is the innermost one.

Noticing the Fig. 3, with the growth of system, the smallest element may continuously develop until the eventual coverage of the total element the unit Ω. Obviously, we can repeat the above process several times, each time for a larger element, until the total element Ω is reached.

Similarly, as time passes, Ω_1 will develop in a larger space, which may contain several Ω_1. We correspondingly have the second element regime Ω_2, which contains $m2$ subsystems, as shown in Fig. 5. Symmetry suggests again that the unstable mode is placed in the middle of unit Ω_2 and is indicated by the number $[(m2+m1)+1]/2$. According to the natural selection principle, the change of the flux before and after undergoing nonequilibrium phase change is mostly transferred through this section and equal to

$$\Omega_2\Delta J''=\overline{J_2}(\alpha_1)-\overline{J_2}(\alpha_2)\approx J_{u2}(\alpha_1)-J_{u2}(\alpha_2). \tag{70}$$

Again, as time passes, Ω_2 will develop in a larger space, which may contain several Ω_2. We correspondingly have the third element regime Ω_3, which contains m_3 subsystems, as shown in Fig. 6. Symmetry suggests again that the unstable mode is placed in the middle of unit Ω_3 and is indicated by the number $[(m3+m2)+1]/2$. According to the natural selection principle, the

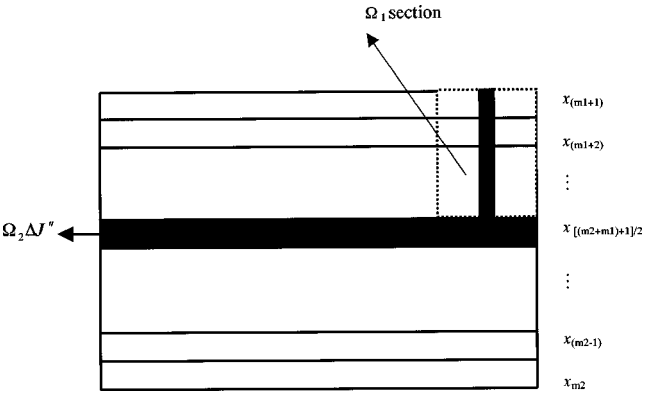

Fig. 5 Enlarged unit Ω_2

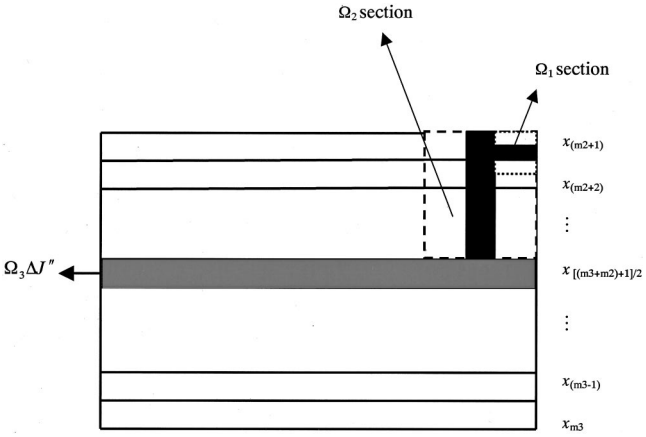

Fig. 6 Enlarged unit Ω_3

change of the flux before and after undergoing nonequilibrium phase change is mostly transferred through this section and equal to

$$\Omega_3\Delta J''=\overline{J}_3(\alpha_1)-\overline{J}_3(\alpha_2)\approx J_{u3}(\alpha_1)-J_{u3}(\alpha_2). \quad (71)$$

Similarly, for n-order element, we can obtain the tree-like structure as shown in Fig. 7. Again, we have

$$\Omega_n\Delta J''=\overline{J}_n(\alpha_1)-\overline{J}_n(\alpha_2)\approx J_{un}(\alpha_1)-J_{un}(\alpha_2). \quad (72)$$

Obviously, we can write down

$$\frac{\overline{J}_n(\alpha_1)-\overline{J}_n(\alpha_2)}{\overline{J}_{(n-1)}(\alpha_1)-\overline{J}_{(n-1)}(\alpha_2)}\approx\frac{J_{un}(\alpha_1)-J_{un}(\alpha_2)}{J_{u(n-1)}(\alpha_1)-J_{u(n-1)}(\alpha_2)}=\frac{\Omega_n}{\Omega_{(n-1)}}. \quad (73)$$

Where $\overline{J}_i$ and $\overline{J}_{ui}$ are the flux for the whole system and unstable sub-systems with order parameter respectively, α is the control parameter, Ω is growth unit. Eq. (73) evidently reveals the similar fractal characteristics.

The simplified tree-like network is shown in Fig. 8. Obviously, the network generated here from pure theoretical umbrella will look more ''natural'' with the increase of given conditions.

Application to Boiling Systems. Obviously, we can conduct similar analysis on boiling systems and surely the same results as above will be yielded. Providing that the detailed conditions were given, a certain expression for bubble distribution might be derived. More importantly, according to present analysis, physical interest may be found that the bubble distribution may exhibit self-organized and self-similar performance. It is definitely necessary for the available boiling models to incorporate the nonlinear and nonequilibrium features of boiling processes.

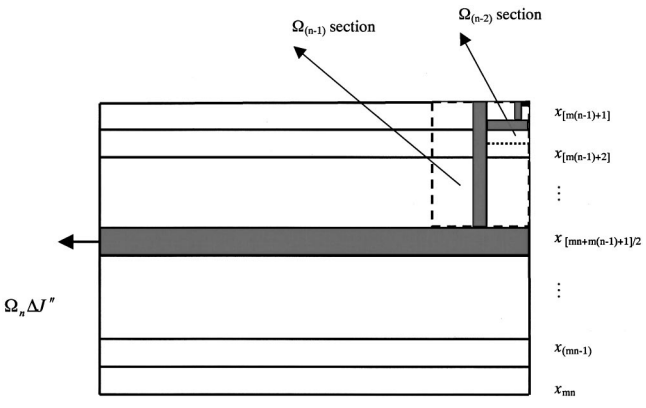

Fig. 7 Tree-like structure after n-order growth

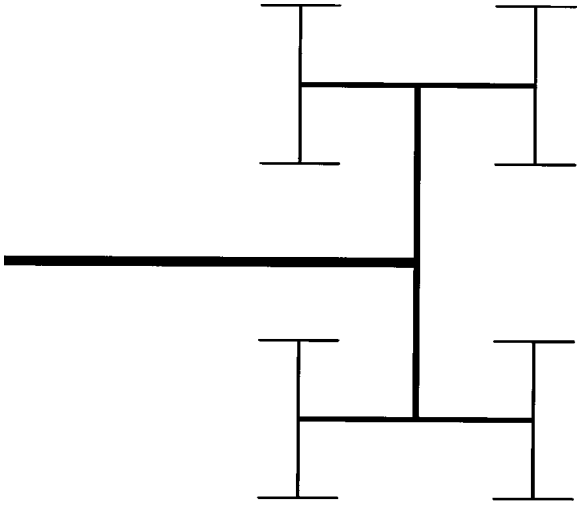

Fig. 8 Tree-like network after n-order growth

Concluding Remarks

Boiling is a typical open system with input of heat from environment. Focusing on the investigation of heater surface in boiling system, nonlinear nonequilibrium statistical thermodynamics theory is originally constructed. We show that the competitive bubble formation is realized by non-equilibrium phase transition caused by the interactions among lots of active sites or bubbles. The natural selection among all possible sites is then mathematically outlined. It is by the means of natural selection that a kind of self-organized and self-similar structure is formed.

In fact, to this end, our theory is very general. Beyond the scope of boiling systems, our theory can be applied for any dissipative open systems far from equilibrium, i.e., regardless what they are, living or not living, discrete or continuous.

Academic Implications. The present paper has far-reaching implications in unifying the natural science on both living and not living:

1. Different from fossils and genetic analysis, the present paper elaborates a complete mathematical theory on evolution of living and not living systems by natural selection.
2. We mathematically demonstrated that the complex natural occurrence of self-similar structures is realized by fluctuations
   and continuous bifurcations. In other word, we mathematically find the role of fluctuation and bifurcation in the processes of evolution.
3. We mathematically demonstrated that the formation of increasing complex natural self-similar structure is a process of evolving growth, i.e., from small scale to large scale. The process evidently reveals a direction of time. In other word, the present theory brings the time into natural science and provides a bridge between physics or chemistry and biology. The law of thermodynamics, as proposed in section 1, means that optimizing is to survive and persist in time, i.e., the favored one replaces the old one. It is in this way that time comes into our theory.
4. There is no difference between living systems and not living systems when facing to competition for obtaining flux from environment. The stronger and more efficient subsystems can get more flux from environment, and then survive to dominate the development of other subsystems.

5. We demonstrate that the dominant subsystems often get more flux by competition among enormous subsystems and by symmetry breaking. In other word, order comes out of chaos. The present paper not only reveals the origin of ordered structures, including the animate and inanimate, but also sheds on new light on the reasons for the coexistence of order and disorder in nature.
6. Compared to available theories, we may say that the dissipative structure proposed by Prigogine [12] and Nicolis and Prigogine [13] is mathematically obtained in the umbrella of mathematical theory presented in this paper. The fractal geometry proposed by Mandelbrot [14] can be mathematically derived in present theoretical fashions.

Industrial Implications. From optimization perspectives, the present theory can give more reasonable guidance of enhancing boiling heat transfer, such as by way of installing artificial cavities. Among other things, i.e., beyond the boiling systems, the present investigation may find lots of practical implications in wider scopes:

1. In nature, for one example, the streams often develop their own network system, i.e., the coexistence of river having high flux transfer rate with wet soil having low seeping flux transfer rate. For another example, cities often form their own network system, i.e., the coexistence of street having high flux transfer rate with small roads having low flux transfer rate. For one more example in living system, the blood vessels, tissues etc., form their tree-like networks too. Learning from natural complexity, there is great reason for optimism. Natural systems display such a large number of remarkable capabilities (and capabilities that are so clearly complex) that their analysis will unquestionably be a rich source of models for new areas of engineering. In Benard flow system, the coexistence of the roll and diffusion parts tends to transport heat most efficiently [15,16]. Doubtless, design of artificial tree-like structures can often greatly promote the system performance in fluid or heat transfer systems and other systems.
2. The law for the natural selection proposed here can guide us to recognize and reproduce pattern by the use of computers.
3. According to the present theory, natural selection can greatly decrease system freedoms. This makes it possible for one to easily analyze the key aspects of problems.
4. The present analyses provide theoretical and quantity basis for the actual sizes design of the tree-like network.

Concluding Remarks. Most natural systems, regardless of living or not living, are often open and dissipative structure far from equilibrium through the exchange of generalized flux from environment. Actually, the present paper proposed a universal non-equilibrium statistical theory of open system and discussed non-equilibrium phase transitions characteristics. Evolution process by means of ''natural selection'' was mathematically revealed. The formation of natural self-similar fractal structure was then mathematically derived, which was a kind of self-organized growth processes from small to large caused by the interactions among sub-systems. The present studies not only have far-reaching theoretical implications on explaining time, life, thermodynamic, self-similar, fluctuation, order and chaos etc., but also can find many promising applications from new perspective, such as industrial optimization, the recognitions and reproduction of pattern by computers etc.

In reality, the present investigation introduced new ideas of exploring the theories of complex systems. The present investigations not only provide clear physical picture, but also are based on firm theoretical foundation. The new theory of complex system presented here significantly wins the advantage over the traditional theory.

From reductive science and the mechanized materialism of the industrial revolution, and the reductionisms of modern physics and chemistry, to the evolution theory of Darwin and self-organization nonlinear sciences theories appearing in 1970s, the continuous debate have taken place on whether the nature is reductive or holistic [17]. According to the present paper, we show that, in closed systems, things tend to be equilibrate, but for open systems far from equilibrium, regardless of living or non-living, equilibration means death. Molecular biology was born with the recognition that the large molecular structures essential to living cells give rise to autonomous feedback systems. All open systems far from equilibrium can be seen as an interacting hierarchy of feedback systems, from cells to individuals, and from populations to communities and ecosystems.

Where to lead the developing the theories of complex system is a serious problem. Currently, many problems, such as the reasons for the formation of fractal structure, self-organization, etc., still remain elusive. The present investigations provide a renewed effort in understanding these problems. The essence of fractal structure formation is a process of nonequilibrium phase change. However, the studies of the nonequilibrium phase change are far behind the studies on phase change in thermal states. This paper virtually provides instruction for investigations of more universal nonequilibrium phase change.

Acknowledgment

The project is currently supported by Japan Society for the Promotion of Science.

Nomenclature

c = constant
$f_1 \sim f_4$ = constants
f_i = functions introduced in Eq. (40)
F_u, F_s = fluctuation forces introduced in Eq. (38) and Eq. (39)
g, h = functions defined in Eq. (29) and Eq. (55)
$J, \overline{J}$ = flux, W
J'' = flux density, W/m^2
L = matrix defined in Eq. (47)
$\vec{N}$ = function defined in Eq. (53)
N_s = the number of stable modes
Q = fluctuation coefficient
r = function defined in Eq. (43)
S = function defined in Eq. (38)
t = time, s
T = function introduced in Eq. (39)
u, v = vectors defined in Eq. (45) and Eq. (52), respectively
$\mathbf{w}$ = variables defined in Eq. (20)
$\mathbf{W}_s, \mathbf{W}_u$ = potential functions of stable modes and unstable modes
x = driving force
$\mathbf{x}$ = driving force vector

Greek Symbols

ρ = probability density
$\boldsymbol{\sigma}, \overline{\boldsymbol{\sigma}}$ = constants
η = constants
λ = constants
α = controlling parameter defined in Eq. (60)
α, β, γ = constants
$\boldsymbol{\Phi}, \overline{\boldsymbol{\Phi}}$ = potential functions
ζ = constant
ξ = variables defined in Eq. (22)
μ = constant
Ω = area or volume unit

Subscripts

0 = reference state
μ = integer

i,j,k,l = integer
s = integer
s,s',s'',s''' = stable modes
u,u',u'',u''' = unstable modes

References

[1] Carey, V. P., 1992, *Liquid Vapor Phase-Transition Phenomena*, Hemisphere Publishing Corporation, Washington, pp. 222–246.
[2] Sadasivan, P., Unal, C., and Nelson, R. A., 1995, ''Nonlinear Aspects of High Heat Flux Nucleate Boiling Heat Transfer,'' ASME J. Heat Transfer, **117**, pp. 981–989.
[3] Keening, D. B. R., and Yan, Y. Y., 1996, ''Pool Boiling Heat Transfer on a Thin Plate: Features Revaled by Liquid Crystal Thermography,'' Int. J. Heat Mass Transf., **39**, pp. 3117–3137.
[4] Shoji, M., 1998, ''Boiling Chaos and Modeling,'' in *Proceeding of 11th International Heat Transfer Conference*, **1**, Taylor and Francis, London, (Invited Keynotes), pp. 3–21.
[5] Haken, H., 1977, *Synergetics*, Springer, Berlin.
[6] Haken, H., 1983, *Advanced Synergetics*, Springer, Berlin.
[7] Chai, L. H., Peng, X. F., and Wang, B. X., 2000, ''Nonlinear Aspects of Boiling Systems and a New Method for Predicting the Pool Nucleate Boiling Heat Transfer,'' Int. J. Heat Mass Transf., **43**, pp. 75–84.
[8] Chai, L. H., Peng, X. F., and Wang, B. X., 2000, ''Nucleation Site Interaction During Boiling,'' Int. J. Heat Mass Transf., **43**, pp. 4249–4258.
[9] Toda, M., Kubo, R., and Saito, N., 1992, *Statistical Physics I*, Springer, Berlin.
[10] Haken, H., 2000, *Information and Self-Organization*, Springer, Berlin.
[11] Darwin, C., 1859, *The Origin of Species by Means of Natural Selection*, Murry, London.
[12] Prigogine, I., 1980, *From Being to Becoming*, W. H. Freeman, San Francisco, CA.
[13] Nicolis, G., and Prigogine, I., 1977, *Self-Organization in Nonequilibrium Systems*, Wiley, New York.
[14] Mandelbrot, B., 1982, *The Fractal Geometry of Nature*, W. H. Freeman, San Francisco, CA.
[15] Bejan, A., 1997, *Advanced Engineering Thermodynamics*, Wiley, New York, Chap. 13.
[16] Nelson, R. A., and Bejan, A., 1998, ''Constructal Optimization of Internal Flow Geometry in Convection,'' ASME J. Heat Transfer, **120**, pp. 357–364.
[17] Davies, K. G., 2000, ''Creative Tension—What Links Aristotle, William Blake, Darwin and GM Corps?'' Nature, **407**(6807), pp. 135–135.

Experimental Investigation of Convective Melting of Granular Packed Bed Under Microgravity

J. Jiang

Y. Hao[1]

Y.-X. Tao[1]

Department of Mechanical Engineering,
Tennessee State University,
Nashville, TN 37209

To improve the understanding of convective melting of packed solid particles in a fluid, an experimental investigation is conducted to study the melting characteristics of a packed bed by unmasking the buoyancy forces due to the density difference between the melt and solid particles. A close-loop apparatus, named the particle-melting-in-flow (PMF) module, is designed to allow a steady-state liquid flow at a specified temperature. The module is installed onboard NASA's KC-135 reduced gravity aircraft using ice particles of desired sizes and water as the test media. Experimentally determined melting rates are presented as a function of upstream flow velocity, temperature and initial average particle size of the packed bed. It is found that the melting rate is influenced mainly by the ratio of the Reynolds number (Re, based on the initial particle diameter) to the square of the Froude number (Fr), and the Stefan number (Ste). In general, the dimensionless melting rate decreases as Re/Fr^2 increases and increases as Ste increases. With the absence of gravity, i.e., as the Froude number approaches infinity, a maximum melting rate can be achieved. The increase in the melting rate proportional to the Stefan number also becomes more pronounced under the zero gravity condition. The trend of average and local Nusselt number of the melting packed bed under microgravity, as a function of Reynolds number and Prandtl number, is discussed and compared with the case of nonmelting packed bed.
[DOI: 10.1115/1.1469521]

Keywords: Convection, Heat Transfer, Melting, Microgravity, Packed Beds

Introduction

Melting heat transfer that involves phase change of a porous media matrix occurs in many industrial and environmental processes. Examples include manufacturing of alloys, treatment of hazardous waste, air conditioning, and melting of accumulated packs of ice in rivers. In material processing and treatment of hazardous waste, smelting, alloying, and nitrification operations involve the melting of a packed bed of solids. Melting of materials in the low gravity conditions of space finds applications in both space-based materials processing and in space system thermal management. Materials processing applications can be greatly enhanced by the use of the microgravity conditions available in Earth orbit to reduce impurity levels in semiconductors, superconductors, superalloys, and other potentially important materials. Recent studies include processing via containerless floating techniques that can be used to grow single, high-mass crystals [1], comparison of eutectic structures which were formed in microgravity and earth gravity [2], numerical solution on the effect of vibration on melting of unfixed rectangular phase-change material under variable-gravity environment [3]. The use of phase change materials (PCM) as heat transfer media has been studied for thermal management in space. In cold region applications, the melting of accumulated ice packs occurs in rivers, and packed ice frequently forms in water pipes. To avoid a sudden release of water as a result of an ice jam in a river or explosion of frozen water pipes, accurate prediction of melting ice-water flow is required [4].

In this study, the melting rate in nonthermal equilibrium, convective conditions is studied by unmasking the buoyancy effects in coupled flow, phase change and heat transport phenomena. To achieve this, a series of experiments are conducted under microgravity conditions created onboard a KC-135 research aircraft. In such an experiment involving melting solid particles and fluid flow, the buoyancy effects include both thermal buoyancy, due to temperature gradients in the fluid, and the buoyancy force due to the density difference between solid and liquid phases, which is more pronounced than the thermal buoyancy in our study. It is expected that under any gravitational condition the solid particle packing in a flow results from both the buoyancy force and inertial force of flow, while under zero gravity, only inertial force influences the packing. To develop a correlation that could be used to represent the melting characteristics, a generalized momentum equation is derived from the fluidized bed theory. Results are presented in terms of functional relationships between the Nusselt number, Reynolds number, Froude number and Stefan number. This study of melting of dispersed or packed solid particles in a fluid under microgravity condition provides benchmark information for various applications that involves packed or dispersed solid particles interacting with fluid flow at above-melting temperatures.

Experimental Apparatus and Procedures

We first construct a flight module that consists of a flow system, a heating control system, and a data recording system. Figure 1(*a*) is an overview of the flow system. There are three flow paths in the flow system, consisting of the main flow path, bypass path, and drainage path. The main flow path is used to supply a controlled constant-rate flow to the test section after the test section is initially filled with ice particles. The bypass path is used to set the liquid to the desired temperature. The drainage path is used to drain liquid out of the test section and return it to the storage tank after completion of a test. The test section consists of a Nylon body with Plexiglas sidewindows for video imaging. On the top of the test section, there are one sapphire window for infrared imaging and one opening for ice feeding. The effective dimensions of the test section for imaging melting packed bed and flow are 0.059

[1]Present Address: Department of Mechanical Engineering, Florida International University, Miami, FL 33174.

Contributed by the Heat Transfer Division for publication in the JOURNAL OF HEAT TRANSFER. Manuscript received by the Heat Transfer Division August 10, 2000; revision received November 1, 2001. Associate Editor: M. L. Hunt.

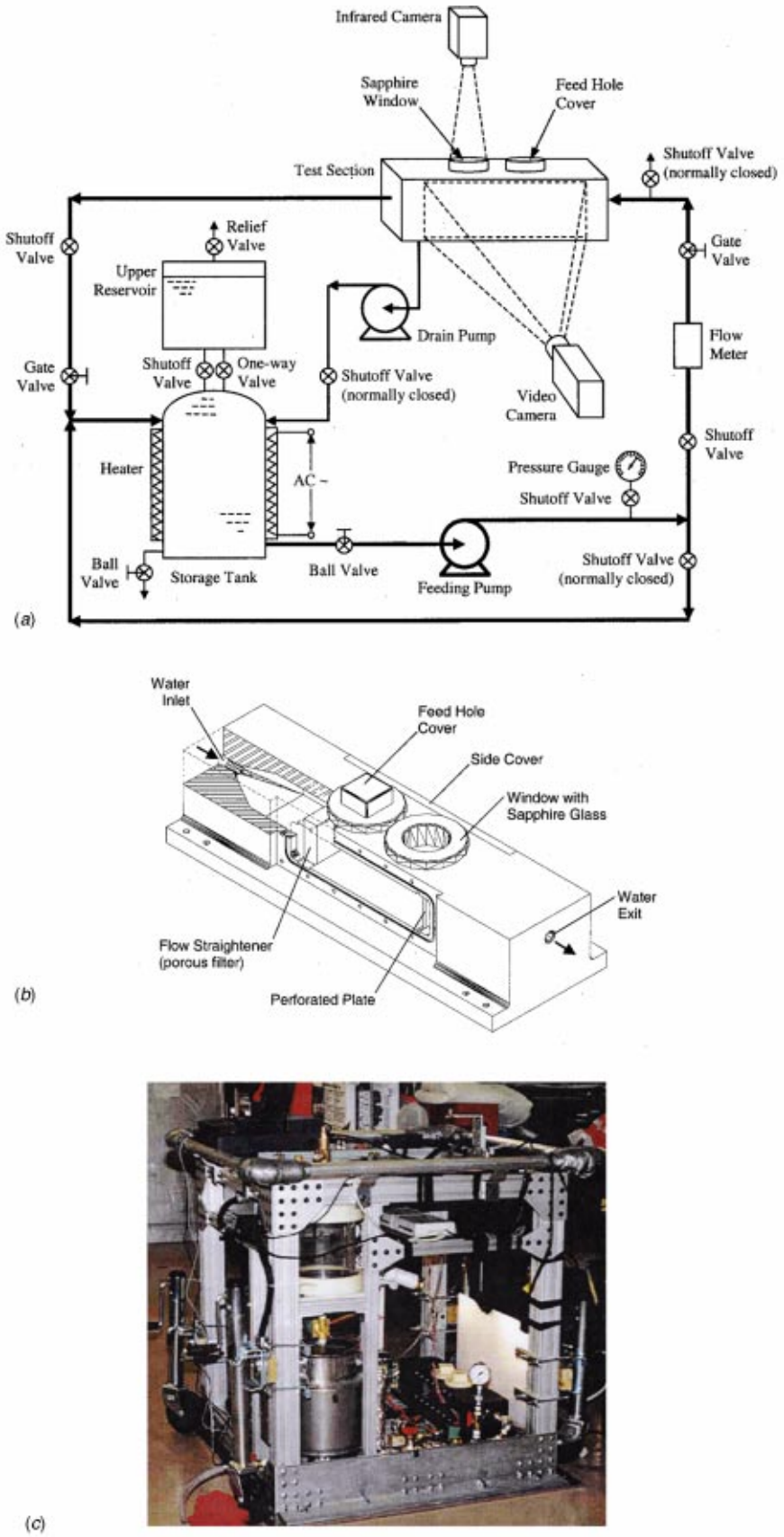

Fig. 1 (*a*) **Schematic,** (*b*) **test section, and** (*c*) **the photo of the Particle-Melting-in-Flow** (**PMF**) **flight test module**

m in height and 0.229 m in length. The width of the flow cross-section is 0.127 m. There is an additional 0.25 m long flow path, including a divergent connector, before flow reaches a porous metal plate and enters the packed bed. The porous plate has a thickness of 0.0125 m and acts as a flow straightener. A perforated Plexiglas plate is installed downstream of the packed bed to stop the melting particles. Figures 1(*b*) and 1(*c*) show the configuration of the test section and the photograph of entire system, respectively.

Nineteen T-type thermocouples are placed in the inlet, outlet and sidewall of the test section to measure the two-dimensional liquid temperature distribution (in vertical and axial directions). The liquid temperature is recorded automatically through a data acquisition unit connected to a laptop computer. The data acquisition unit has a maximum speed of 2 Hz, and the maximum resolution is 0.0015 percent. A large aluminum isothermal plate is mounted in the data acquisition unit to improve accuracy by attenuating temperature differences at the cold junction connector. The uncertainty in the temperature measurement is ± 0.7°C. A gear-type flow meter is used to measure the flow rate, and a Crossbow CXL02LF3-R accelerometer is mounted on the test module to record *in situ* the vertical component of the acceleration force acting on the test module. The readings from flow meter and accelerometer are sent to the laptop computer through the data acquisition unit. The uncertainty of the flow rate is ± 0.013 GPM, and for acceleration it is ± 0.01 g. A digital video camera is placed at the side of the test section to record the ice melting process in the vertical and axial directions.

An infrared camera is mounted over the test section to obtain the local thermal image of the liquid-solid mixture at a certain location downstream from the entrance of the test section. To achieve this, a sapphire window of 0.0765 m in diameter is designed and mounted on the top surface of the test section. The thermal image of ice-water mixture is taken every 5 sec. The thermal image has a resolution of 0.1°C and accuracy of ± 0.5°C. The emissivity of both water and ice is very close to unity (0.95–0.98), and the transmissivity of sapphire window is also close to unity (at a thickness of 2 mm, it is greater than 0.9). In addition, the temperature difference between ice and water alone will be used to reduce data, which further reduces the overall error by subtracting the absolute error in temperature difference readings. Therefore, the overall accuracy of the infrared imaging system is reasonably acceptable.

In the present study, ice particles with square shape and controllable thickness are produced using a portable icemaker and filtered water. Four different thickness are used, which translates into four volume-based equivalent particle diameters of $D = 13$ mm, 16.4 mm, 20.6 mm, and 26 mm, respectively. Four different flow rates (0.0423, 0.0839, 0.126, and 0.158 liter per sec, respectively) are tested. The supply liquid temperature ranges from 278 K to 298 K. An error analysis, according to [5] yields the N^{th} order uncertainty in the obtained Nusselt numbers that lie in between $\pm$ 3.2 and $\pm$ 7 percent, whereas that in the Reynolds numbers is between $\pm$ 4.5 and $\pm$ 8.2 percent. The uncertainty in displacement measurement, resulting from the video image analysis, was established to be less then $\pm$ 5 percent.

The flight module achieves a typical test duration of 150 sec. For a KC-135 flight test, this test duration is further divided into a number of time periods corresponding to periodic, variable gravity conditions. For example, after an initial high gravity (1.8 g) period, a 25 sec, microgravity time segment is maintained, followed by a 30 sec, high gravity duration, and again followed by a 25 sec, microgravity period, and so on. Depending on the flow rate and supply water temperature, a complete melting process typically needs three to six parabola cycles. Before a parabolic flight starts, the water is pumped through the bypass path to obtain the desired supply temperature. A control valve is preset at the desired flow rate position. For each melting experiment, a predetermined amount of packed ice is fed to the test section, and a switch on the control panel is then turned on to allow water flowing steadily through the test section filled with packed ice. All the variables are recorded automatically as described above. A test matrix is developed to cover a range of variables parameters.

Results and Discussion

A. Melting Characteristics. Experiments are carried out for packed beds of different initial particle sizes and different supply water flow rates and temperatures. The initial mass and volume fraction of particles in a full test section are determined in separate experiments. The test section holds different initial mass of ice particles if the different ice particle size is used. This is because the ice volume fraction is different if the particle size is different. Figure 2 shows typical melting phenomena of the packed beds under gravity and microgravity condition, as viewed from the side. Shown in Fig. 2(*a*) the thickness of the packed bed at a given time is determined by first dividing the *x*-axis into a number of equal intervals at locations of x_1, x_2, etc. At each x_i, the number of pixels (calibrated against the physical distance) between the top border of the top ice and bottom border of bottom ice is measured from the digital image. As mentioned in the previous section, the accuracy of such a measurement is within $\pm$ 5 percent. The variation of bed thickness in the third dimension, i.e., the direction parallel to the video camera is negligible under gravity conditions, as confirmed by visual observation. This leads to a reasonable assumption of two-dimensional flow and melting. Under microgravity conditions, however, the bed thickness variation is three-dimensional, as will be discussed later. Figure 2(*b*) shows that under near-zero gravity conditions, the packed bed does not float to the top as in gravity conditions; instead, the center of the particles tend to remain at the same horizontal position when melting occurs and may be inclined to move downstream under the velocity pressure.

Figure 3 shows the typical infrared image of ice-water mixture. The image is a top view of the ice-liquid through the top sapphire window at a location centered in the flow axis and with a distance about one third of test section length from the downstream stop plate. Through an image analysis software, the local temperature difference between the solid phase and liquid phase can be determined, and therefore the local Stefan and Nusselt numbers are calculated, as will be discussed in the next section.

In Figure 4, the typical evolution of the arithmetically averaged packed bed thickness is shown for the packed beds at a moderate liquid velocity ($v_\ell = 0.0175$ m/s). The initial particle diameter

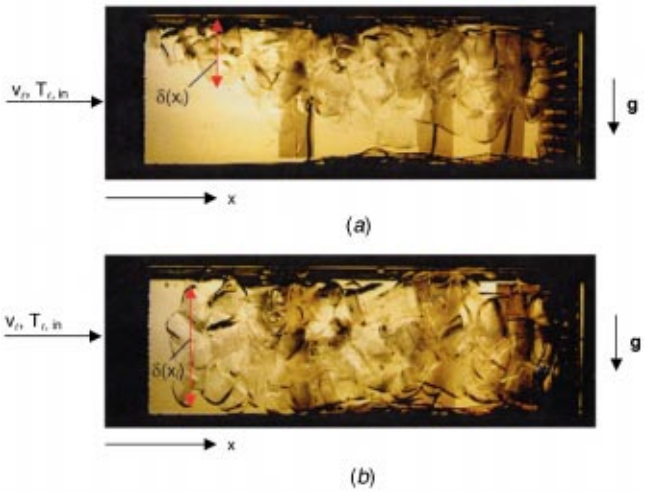

Fig. 2 (*a*) Melting of packed bed under gravity condition, and (*b*) under microgravity condition

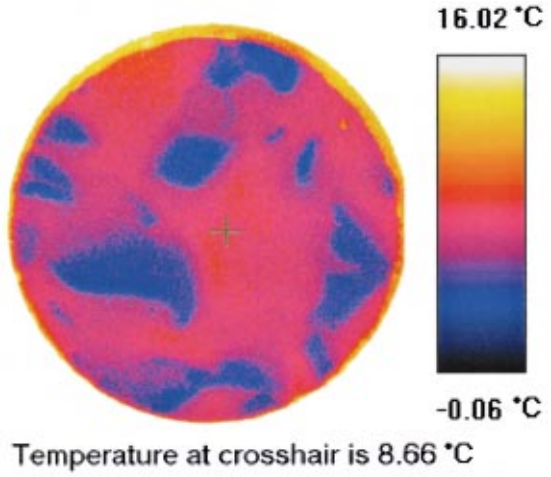

Fig. 3 Typical thermal image of ice-water mixture

and mass of ice are 16.4 mm and 750 g, respectively. The averaged thickness $\overline{\delta}$ is calculated from the following equation.

$$\overline{\delta}=\frac{\sum_{i=1}^{n} x_i \delta_i}{\sum_{i=1}^{n} x_i}, \tag{1}$$

where δ_i is the packed bed thickness measured at the ith point on a video image, n is the total number of the measurement points, and x_i is the grid coefficient, the value of which depends on the measurement location. If the grid of the measurement point is uniform, the value for x_1 (at the inlet of the test section) and x_n (at the outlet of the test section) is equal to 0.5, and the value for the others is equal to 2. The graph shown in the up-right insert of Fig. 4 is the measured vertical acceleration history during a typical test. From the acceleration data, it can be determined whether the corresponding time segment of the test is conducted under microgravity or high gravity (1.8 g) conditions. Under high gravity conditions, the ice particles are quickly packed at the top of the test section (Fig. 2(*a*)). Under microgravity conditions, the packed ice bed is suspended in the water. From data shown in Fig. 4, the average packed bed thickness actually increases during the microgravity process. This indicates that the ice particles are packed

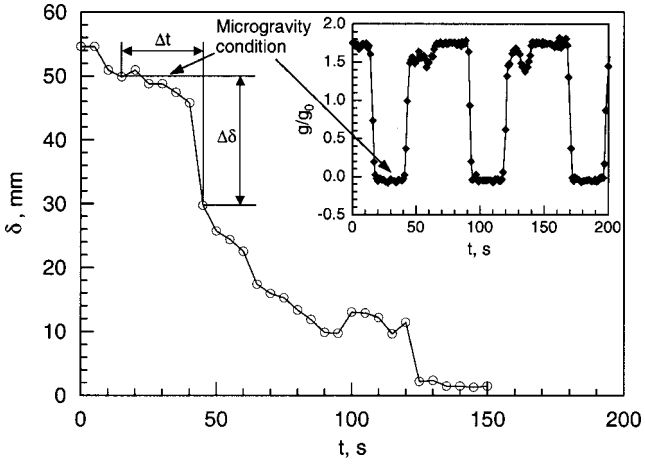

Fig. 4 Time variation of the packed bed thickness: D =16.4 mm, Re=275, $T_{\ell,\mathrm{in}}$=293 K

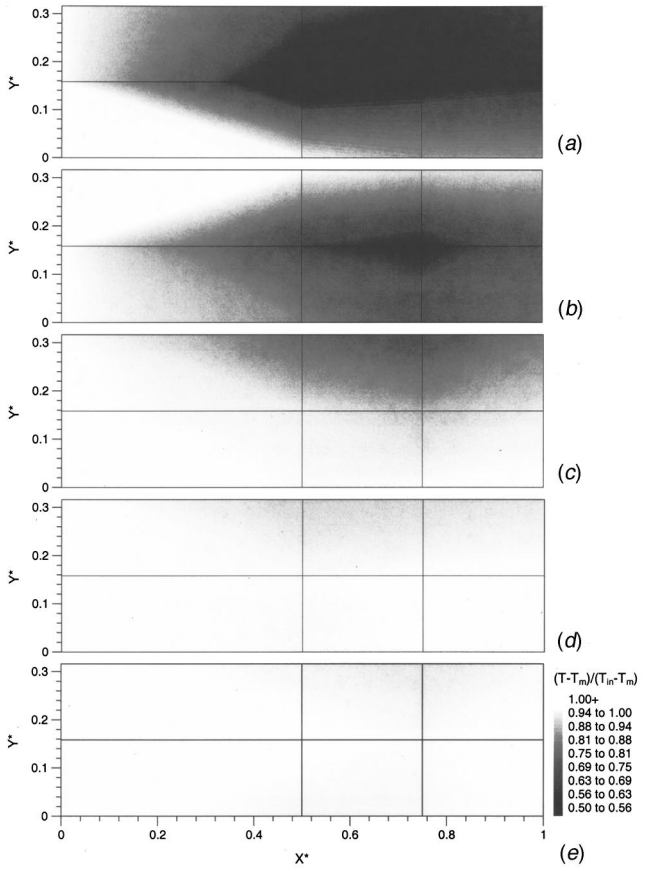

Fig. 5 Time variation of liquid temperature distribution near the side window: D=16.4, Re=275, $T_{\ell,\mathrm{in}}$=293 K, t=(*a*) 10 s, (*b*) 30 s , (*c*) 70 s , (*d*) 110 s, and (*e*) 150 s.

loosely without the presence of buoyancy force. The interface area between solid and liquid, therefore, increases. As a result, the melting rate under microgravity conditions should be greater than that under high gravity conditions. Assisted by those observations, we may conclude that the two-dimensional melting pattern is only valid for the conditions of gravity or high gravity. Under this condition, we can estimate the melting rate by calculating the slope of the curve shown in Fig. 4 (also see Eq. (2) below). Under microgravity conditions, we calculate the average melting rate using the value of $\Delta\delta/\Delta t$, where $\Delta\delta$ is the thickness difference between the beginning of the microgravity condition and the end of microgravity condition, and Δt is the duration of microgravity time period.

B. Temperature and Nusselt Number. Figure 5 show the typical liquid temperature distribution near the backside wall at 10 s, 30 s, 70 s, 110 s, and 150 s, respectively, for the conditions of D=16.4, Re=275, $T_{\ell,\mathrm{in}}$=293 K. The nondimensional temperature scale is defined as $(T-T_m)/(T_{\ell,\mathrm{in}}-T_m)$ where $T_{\ell,\mathrm{in}}$ is the inlet liquid temperature (293 K) and T_m is the melting temperature (273 K). From the acceleration graph (see Fig. 4), it can be seen that at 30 s and 110 s, the experiment proceeds under microgravity conditions. For the rest of time indicated, the experiment is under high gravity conditions. At 10 s, the low temperature region is at the downstream upper corner. This indicates that the ice particles are packed towards the upper side under high gravity conditions. At 30 s, the low temperature region is the downstream, near the center of the test section. From this temperature distribution, it can also be seen that the packed ice bed is suspended in the test section under microgravity conditions. At 70 s, it can be seen that the lowest temperature region is not close to the outlet of the test section, as observed in ground tests, but rather is at the upper

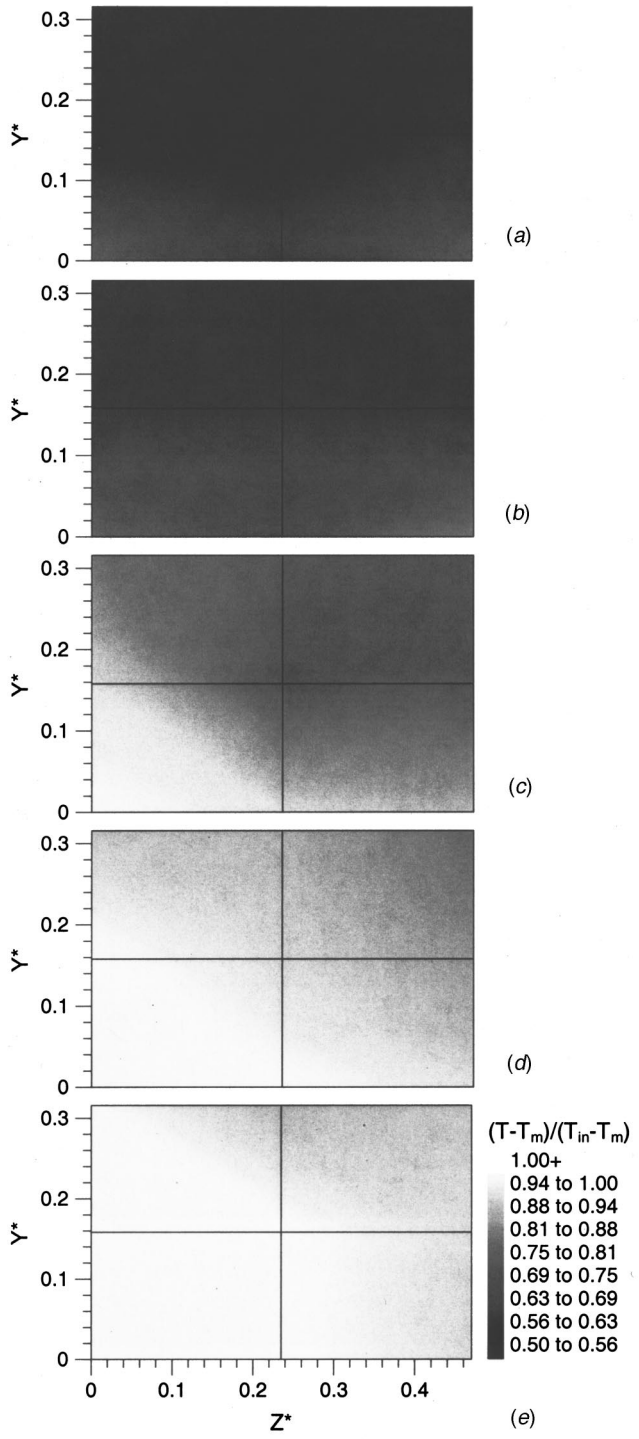

Fig. 6 Time variation of liquid temperature distribution at the outlet of test section: $D=16.4$, Re=275, $T_{\ell,\mathrm{in}}=293$ K: t=(*a*) 10 s, (*b*) 30 s, (*c*) 70 s, (*d*) 110 s, and (*e*) 150 s.

region about one third of the test section length away from the downstream (Fig. 5(*c*)). Again, this indicates that the ice particles are more packed at the low temperature location, and not at the outlet as occurs in ground test conditions. After 70 s, there exists a distance between the side wall and the packed ice bed, which is why the temperature distribution is uniform and the value is near the supply water temperature (recall that the temperature was measured by the thermocouples mounted on the side wall).

Figure 6 shows the temperature distribution of the cross section

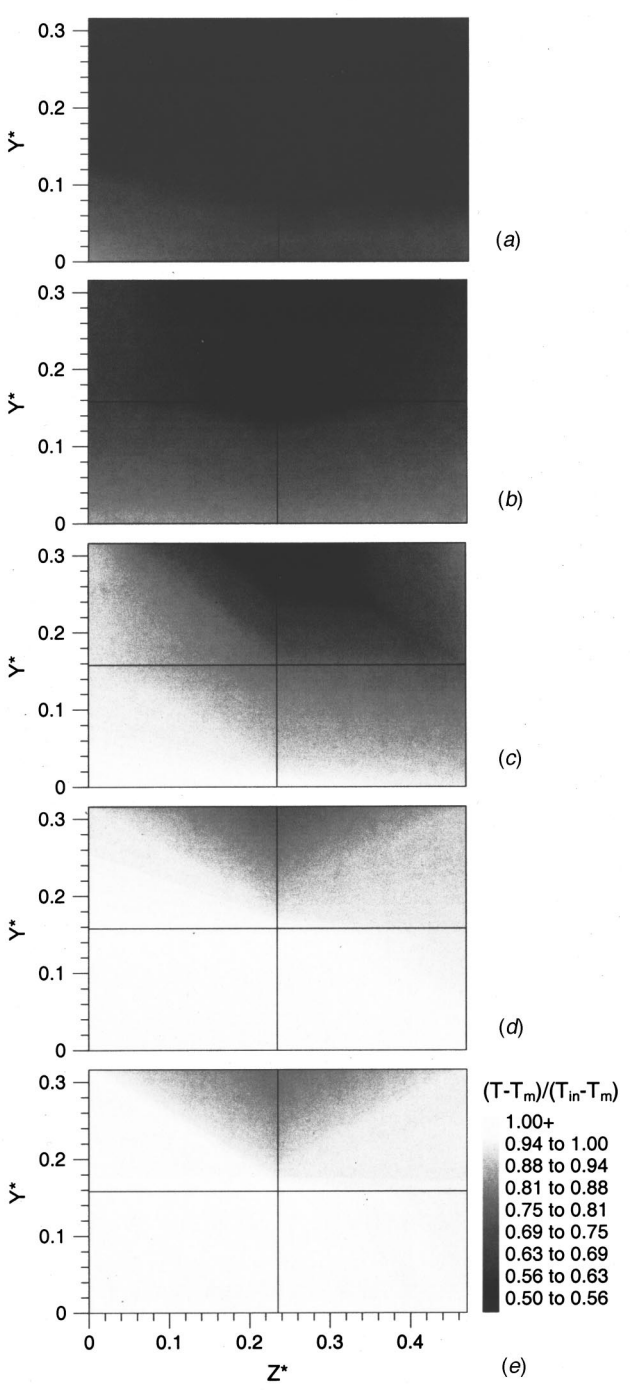

Fig. 7 Time variation of liquid temperature distribution at the outlet of test section for ground tests: (the other conditions are the same as those in Fig. 6)

at the outlet. No matter whether the melting process occurs under high gravity condition or microgravity condition, the temperature distribution is symmetrical about the vertical center line at 10 s and 30 s (see Fig. 6(*a*) and 6(*b*)), and the temperature decreases from bottom to top. This means that the packed ice bed is distributed symmetrically, and the melting rate increases from bottom to top. After 70 s, the temperature distribution becomes asymmetrical (see Fig. 6(*c*), 6(*d*), and 6(*e*)); in other words, the packed ice bed is asymmetrical about the center of the test section. In order to explain this phenomenon, the ground test is processed at the same test condition, and the temperature distribution at the outlet is shown in Fig. 7. It can be seen that the temperature distribution is

almost symmetrical during the entire test. By comparing Fig. 6 with Fig. 7, we can conclude that the asymmetrical temperature distribution in the traverse direction is due to the fact that there exist additional acceleration components in the traverse direction of the test section after a few parabolas, causing the packing pattern to deviate from the two-dimensional assumption. This deviation is, however, only significant during the later period of melting process where the mass of ice particle is relatively small. Based on this observation, we decide to use the results during the first microgravity period to calculate the value of melting rate.

The melting rate of ice particles in an interval of time Δt can be determined in terms of the volume variation in the same interval of time:

$$\dot{m} = -\varepsilon_s \rho_s \frac{A \Delta \delta}{\Delta t}, \tag{2}$$

where A is the area of the top face of the test section, and ε_s is the average volume fraction of ice particles during Δt. It is assumed that under the gravity condition the packing of ice particles yields a statistically constant volume fraction that only depends on the ice particle size. This value can be determined separately by a series of ground tests. In this study, the following specific melting rate (melting rate per unit volume) is defined by

$$\dot{m}''' = \frac{\dot{m}}{V_s} = -\frac{\rho_s}{\delta} \frac{\Delta \delta}{\Delta t}, \tag{3}$$

where V_s is the volume of ice phase.

Based on the energy balance, the heat transfer rate from the water to the ice particle should be equal to the rate used to melt the ice particles (although, strictly speaking, a small portion of less than 1 percent of energy is transferred to warm up the ice particle from the initial temperature to the melting temperature), and its value is estimated by considering that the melt flows into the liquid phase at the melting temperature T_m:

$$\dot{m} h_{s\ell} = h A_{s\ell} (T_{\ell,\mathrm{in}} - T_m), \tag{4}$$

where h is the average heat transfer coefficient assumed constant over the area of interface between water and ice particles, and $T_{\ell,\mathrm{in}}$ is the supply water temperature. Using Eq. (4) as a guide, the time (and spatially) averaged Nusselt number is, therefore, determined as follow

$$\mathrm{Nu} = \frac{hD}{k} = \frac{\dot{m}''' h_{s\ell} \delta D}{k(T_{\ell,\mathrm{in}} - T_m)}, \tag{5}$$

where D is the initial ice particle diameter.

Figure 8 shows the Nusselt number versus Reynolds number for different initial ice particle size at range of Prandtl number from 7 to 10.5 and under the microgravity condition. The solid straight line in the figure is for the correlation obtained from the single ice particle melting experiment by Hao and Tao [6]. From Fig. 8, it can be seen that for the same Reynolds number, the value of average Nusselt number (Fig. 8(*a*)) for the packed ice bed is lower than that for the single ice particle, but the slope of average Nusselt number versus Reynolds number for the packed ice bed is greater than that for the single particle. This means that the total heat transfer rate from water to the ice for packed ice bed is smaller than that for single ice particle if the Reynolds number and the temperature difference between solid and liquid are held the same. It can also be concluded that the dependence of the Nusselt number on the Reynolds number in the case of the packed bed is stronger than that in the case of single ice particle. Considering that the average heat transfer coefficient is defined using the supply temperature of liquid at the inlet of the packed bed (Eq. 5), the above conclusion may need further investigation. The heat transfer coefficient obtained from the single particle melting experiment [6] may be closer to the definition of the local heat transfer coefficient in a no-phase-change packed bed, as will be discussed later. This is because the temperature of liquid flowing

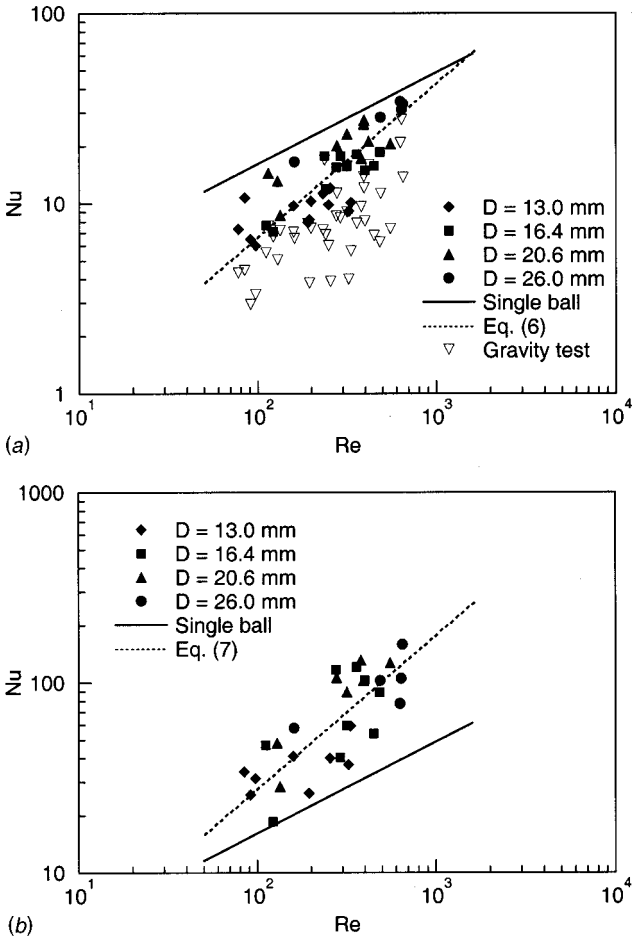

Fig. 8 Nusselt number variation with Reynolds number for (*a*) average Nu, and (*b*) local Nu

in the space between particles in a packed bed is conceptually similar to the supply temperature in a single-particle experiment [6]. It should be noted, however, that the comparison of the trend in Nu-Re relation between the packed bed and single particle shown here (i.e., the average Nu is lower for the packed bed) is similar to the comparison between a fluidized bed and a single particle [7]. The average Nusselt number obtained under gravity conditions is also shown in Fig. 8(*a*). In general, the average Nusselt number under gravity conditions is lower than that under microgravity.

To further facilitate the discussion, we develop the following correlation between the average Nusselt number versus Reynolds number and Prandtl number from the experimental data:

$$\mathrm{Nu} = 1.5 + 0.085\,\mathrm{Re}^{0.808}\,\mathrm{Pr}^{1/3} \quad (7 < \mathrm{Pr} < 10.5). \tag{6}$$

The dotted line in Fig. 8(*a*) show this equation at the average Pr $= 8.5$. In Fig. 8(*a*), the supplied liquid temperature is used to calculate the heat transfer coefficient and Nusselt number (see Eqs. 4 and 5). To illustrate the equivalency between the local Nusselt number of a packed bed and Nu for a single melting particle (as mentioned above), we calculate the local Nusselt number using local liquid temperature measured from the infrared image (see Fig. 3). For microgravity conditions, the correlation for Nusselt number versus Reynolds number and Prandtl number using local liquid temperature is obtained and shown as follows:

$$\mathrm{Nu} = 1.25 + 0.35\,\mathrm{Re}^{0.808}\,\mathrm{Pr}^{1/.3} \quad (7 < \mathrm{Pr} < 10.5). \tag{7}$$

The results are shown in Fig. 8(*b*). It can be seen that the Nusselt number using local liquid temperature is four times that of the

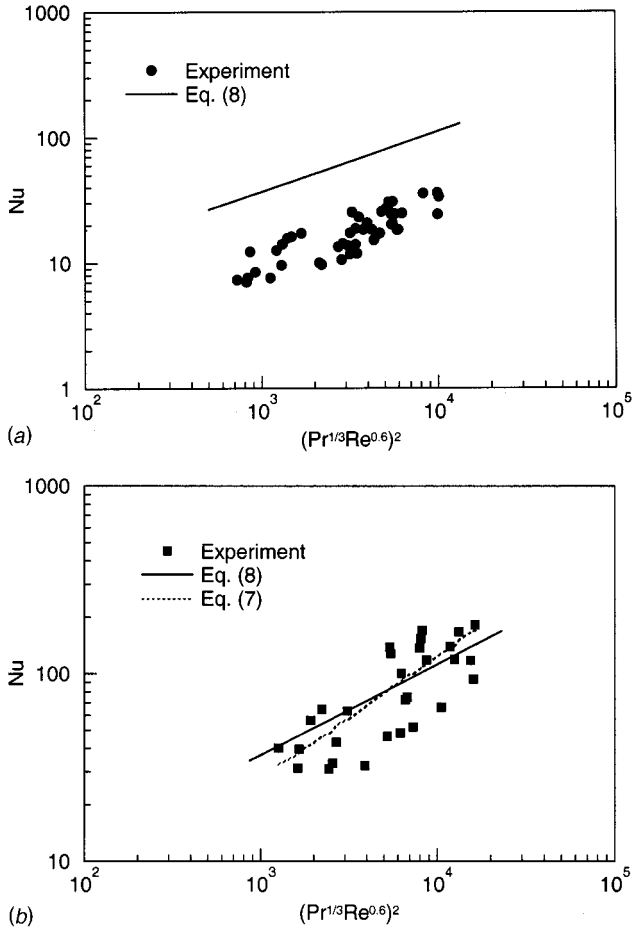

Fig. 9 Nusselt number versus $(Pr^{1/3}\,Re^{0.6})^2$ for (*a*) average Nu, and (*b*) local Nu [$(Pr^{1/3}\,Re^{0.6})^2$ instead of $Pr^{1/3}\,Re^{0.6}$ shown here for illustration only]

value obtained by using the supplying liquid temperature and higher than that obtained from the correlation for a single melting particle.

Wakao and Kaguei [8] have critically examined the experimental results on the Nusselt number and have selected experiments (steady state and transient) that they found to be reliable. They achieved an improvement over the continuous-solid model for the evaluation of Nu and have found the following correlation for Nu for spherical particles

$$\mathrm{Nu} = 2 + 1.1\,\mathrm{Re}^{0.6}\,\mathrm{Pr}^{1/3}. \tag{8}$$

The above equation is widely used in simulation to calculate the heat transfer coefficient h for both no-phase-change and phase-change cases. Figure 9 shows the value of Nu calculated using Eq. (8) with a comparison with our experimental data. To view the comparison more clearly in Fig. 9, the squares of $(\mathrm{Re}^{0.6}\,\mathrm{Pr}^{1/3})$ are plotted in the horizontal axis. Figure 9(*a*) shows experimental data obtained by using the supply liquid temperature, and Fig. 9(*b*) shows data using local liquid temperatures. It can be seen that the results using the local temperature are reasonably close to the correlation for the no-phase-change packed bed consisting of spherical particles (Eq. 8), although the slope of the curve is different. This comparison is interesting because Eq. (8) is used for heat transfer problems in constant matrix porous media. Only recently, the same correlation is extended to the numerical simulation of heat transfer in packed beds with melting solid phase [9–11]. This study presents for the first time an experimental comparison made to confirm that Eq. (8) could be used to estimate the local heat transfer coefficient from melting particles only under microgravity conditions. Under gravity conditions, Eq. (8) tends to overestimate the Nusselt number because the Nusselt number under gravity conditions is lower than that under microgravity (see Fig. 8(*a*). Because these observations are purely empirical, further study is needed to explain the physical reasons behind the phenomenon.

C. A Generalized Functional Relation for Nu. It can be seen from Figs. 7–9 that there exists a significant scatter of data in the Nu-Re, Pr relations. This suggests important effects of other physical phenomena such as gravity and temperature difference between two phases. In order to work towards obtaining a more generalized correlation that includes all the dimensionless numbers, we first develop a functional relationship using the theoretical foundation laid by the work in multiphase system modeling [10,11,12]. Nondimensional, liquid and solid momentum equations in a phase change, packed bed are given as:

$$\frac{\partial}{\partial t}(\varepsilon_\ell \mathbf{v}_\ell) + \mathrm{Re}\,\nabla\cdot(\varepsilon_\ell \mathbf{v}_\ell \mathbf{v}_\ell) = -\nabla p + \nabla\cdot[\mu_\ell(\nabla \mathbf{v}_\ell + \nabla \mathbf{v}_\ell{}^T)] + P_1 \varepsilon_\ell \mathbf{g} - P_3(\mathbf{v}_\ell - \mathbf{v}_s) + \varepsilon_s D^* \frac{d}{dt}(\mathbf{v}_\ell - \mathbf{v}_s) + \dot{m}^* \mathbf{v}_\ell, \tag{9a}$$

$$\frac{\partial}{\partial t}(\varepsilon_s \rho_s \mathbf{v}_s) + \mathrm{Re}\,\nabla\cdot(\varepsilon_s \rho_s \mathbf{v}_s \mathbf{v}_s) = -\varepsilon_s \nabla p + \nabla\cdot[\varepsilon_s \mu_s(\nabla \mathbf{v}_s + \nabla \mathbf{v}_s{}^T)] + P_1 \varepsilon_s \rho_s \mathbf{g} - P_2 \nabla \varepsilon_s + P_3(\mathbf{v}_\ell - \mathbf{v}_s) - \varepsilon_s D^* \frac{d}{dt}(\mathbf{v}_\ell - \mathbf{v}_s) - \dot{m}^* \mathbf{v}_s. \tag{9b}$$

The dimensionless parameters in Eq. (9) are defined as follows:

P_1 = Gravitational dimensionless number

$$= \frac{\rho g D^2}{\mu U} \rightarrow \frac{\rho U D/\mu}{\frac{U^2}{gD}}$$

$$= \frac{\text{Body force}}{\text{Viscous force}} = \frac{\mathrm{Re}}{\mathrm{Fr}^2}$$

P_2 = Particle interaction factor. For the liquid phase momentum equation, $P_2 = 0$.

P_3 = Dimensionless drag coefficient.

Also, we have

$$|\mathbf{g}| = \begin{cases} 1 & \text{in } y \\ 0 & \text{in } x,z \end{cases},$$

where y is in the vertical direction, and x,z are the axial and traverse directions, respectively. The definition of the other dimensionless variables is listed in the Appendix, under Nomenclature.

The energy balance Eq. (4) also yields the following dimensional form of the interfacial boundary condition between the solid and liquid phases:

$$\dot{m} h_{s\ell} = k A_{s\ell} \left| \frac{dT}{dn} \right|, \tag{10}$$

where the fluid temperature gradient is normal to the fluid-solid interface. Equation (10) indicates the local energy balance between phase change energy and thermal diffusion. The differential equation of energy equation of a local averaged volume for a porous medium [10] also points to the coupled transport mecha-

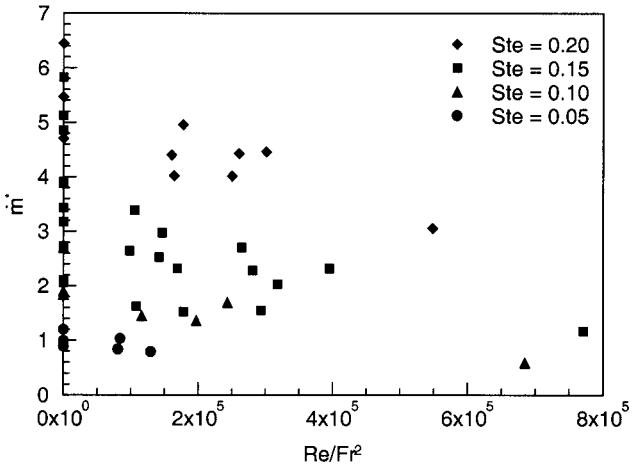

Fig. 10 Dimensionless average mass melting rate as a function of Re/Fr^2

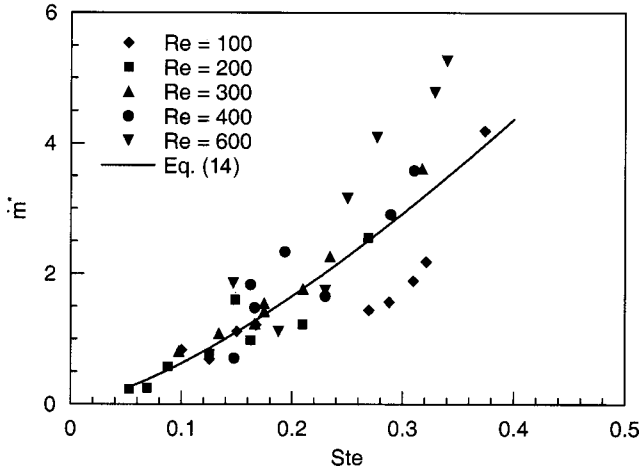

Fig. 11 Dimensionless average mass melting rate as a function of Stefan number

nism in convective melting phenomena. To further assist in the understanding of such complex phenomena, we define an average Stefan number as follows

$$\mathrm{Ste} = c_p(T_{\ell,\mathrm{in}} - T_m)h_{s\ell}\,. \tag{11}$$

Equations 9 to 11 and the above discussion lead us to the following functional relationship:

$$\text{Dimensionless melting rate } \dot{m}^* = f(\mathrm{Re}, \mathrm{Re/Fr^2}, \mathrm{Ste}, P_2, P_3). \tag{12}$$

Due to the limited range of experiments, we do not attempt to achieve the complete correlation, Eq. (12). Instead, we present some trends in terms of the effect of each variable. In Fig. 10, the dimensionless melting rate is presented as a function of gravitational dimensionless number, Re/Fr^2, at different Stefan numbers. It can be seen that the melting rate decreases with the increase in Re/Fr^2 for the same Ste. The increase in the gravity acceleration results in the increase in Re/Fr^2. Under those conditions, the ice particles are packed tightly, which causes the interfacial area between the water and ice particle to decrease, and therefore, reduces the mass melting rate. On the other hand, for the same Re/Fr^2, the increase in Ste corresponds to an increase in water temperature. For the range of liquid velocities studied, it can be seen that gravity plays a very important role in non-thermal equilibrium, convective melting of a packed bed. Near the zero gravity range, the thermal diffusion effect is more pronounced, and the melting rate reaches a maximum value under otherwise the same condition.

Under microgravity condition, the Froude number becomes infinity, and therefore, Re/Fr^2 reaches zero. Figure 10 cannot show how the Reynolds number influences the melting rate. We then plot in Fig. 11 the dimensionless melting rate versus the Stefan number at different Reynolds numbers. The increase in the Stefan number results in an increase in the dimensionless melting rate regardless the Reynolds number. For the region of Stefan number less than 0.25, there is no major difference in the melting rate for different Reynolds number from 100 to 600. When the Stefan number (Ste) is greater than 0.25, it is shown that for the same Stefan number the increase in Reynolds number causes the increase in the melting rate. Based on the experimental data, the following correlation for the dimensionless melting rate can be obtained:

$$\dot{m}^* = (0.04\,\mathrm{Re} + 2.1)\,\mathrm{Ste}^{(-0.355\ln \mathrm{Re} + 3.275)} \quad (\mathrm{Ste} < 0.4), \tag{13}$$

which is a reasonable representation of the trend of $\dot{m}^* = f(\mathrm{Ste}, \mathrm{Re})$

It can be seen that the Reynolds number does not greatly influence the melting rate in the region of Stefan numbers less than 0.4 and low Reynolds numbers. For the sake of simplicity, the dimensionless melting rate may be calculate by the following correlation:

$$\dot{m}^* = 15.75\ \ \mathrm{Ste}^{1.4}. \quad (\mathrm{Ste} \leqslant 0.4 \ \text{ and } \mathrm{Re} \leqslant 600) \tag{14}$$

Conclusions

Based on the above discussion, the following conclusions may be drawn:

1 Under the nonthermal equilibrium, convective melting conditions, the packed bed tends to melt faster as the gravity decreases. The maximum melting rate can be achieved under the zero gravity condition. This finding provides an important experimental benchmark for validation of numerical simulation results.

2 For relatively low Stefan numbers (water), thermal diffusion proves to be an important factor contributing to the melting rate of a packed bed. The dimensionless melting rate is directly proportional to the Stefan number. Under the zero gravity condition, the trend of increase in melting with the Stefan number is more pronounced than normal and high gravity conditions.

3 Under the zero gravity condition, for Stefan numbers less than 0.25 and for relative low Reynolds numbers ($\mathrm{Re} \leqslant 600$), the melting rate does not depend on the Reynolds number and is only influenced by the supply liquid temperature.

4 For the first time, an experimental comparison is made to confirm that under microgravity conditions, the correlation of local Nusselt number versus Prandtl and Reynolds numbers follows closely the correlation for non-melting packed bed of spherical particles. Further theoretical studies are needed to explain the physical mechanisms

Acknowledgment

The authors thank A. A. Siddiqui, C. Stewart, and K. Scrimpsher for their assistance in design and assembly of the apparatus and collecting and reducing experimental data. The grant supports from NASA (#NAG3-1797) and NSF (#HRD-676268) are greatly appreciated.

Nomenclature

A = top test section area, m^2
c_p = specific heat at constant pressure, J/kg K
D = initial average solid particle diameter, m

D^* = virtual mass coefficient (dimensionless)
Fr = Froude number, $U/(gD)^{1/2}$
g = gravitational acceleration, m/s^2
h = heat transfer coefficient, W/m^2 K
$h_{s\ell}$ = latent heat, J/kg
$\dot{m}$ = mass melting rate, kg/s
$\dot{m}'''$ = melting mass per unit ice volume, kg/m^3 s
$\dot{m}^*$ = dimensionless melting rate, $\overline{\dot{m}'''}D^2/\mu$
p = pressure, Pa
Re = Reynolds number, $\rho UD/\mu$
Ste = Stefan number, $c_p(T_{\ell,\mathrm{in}}-T_m)/h_{s\ell}$
T = temperature, K
t = time, s
V = volume, m^3
ν = velocity, m/s
U = inlet liquid velocity, m/s

Greek Symbols

α = thermal diffusivity, m^2/s
δ = packed ice bed thickness, m
ε = volume fraction
μ = viscosity, kg/m^2 s
ν = kinematic viscosity, m^2/s
ρ = density, kg/m^3

Subscripts

D = particle diameter
in = test section inlet
ℓ = liquid phase
$s\ell$ = solid-liquid interface
m = melting
s = solid phase

Superscripts

* = non-dimensional

Others

$\bar{}$ = dimensional (overbar)

Appendix

Table 1 lists the definitions of the variables appearing in Eq. (9).

Table 1 Dimensionless variables

Dimensionless variables	t	v	ρ	T	p	$\dot{m}^*$
Dimensional variables	$\frac{\alpha t}{D^2}$	$\frac{\bar{\nu}}{U}$	$\frac{\bar{\rho}}{\rho_\ell}$	$\frac{\bar{T}}{\Delta T}$	$\frac{\bar{p}}{p_0}$	$\frac{\overline{\dot{m}'''}D^2}{\mu}$

References

[1] Feuerbacher, B., Hamacher, H., and Naumann, R. J., 1986, *Material Science in Space*, Springer-Verlag, Berlin.
[2] Barbieri, F., and Patuelli, C., 1988, "Eutectic Structures of Ag-Cu after Melting and Solidification in Microgravity and on Earth," Metall. Trans. A, **19**, pp. 2659–2668.
[3] Shirvanian, A., Faghri, M., Zhang, Z., and Asako, Y., 1998, "Numerical Solution of the Effect of Vibration on Melting of Unfixed Rectangular Phase-Change Material Under Variable-Gravity Environment," Numer. Heat Transfer, Part A, pp. 257–278.
[4] Fukusako, S., and Yamada, M., 1993, "Recent Advances in Research on Water-Freezing and Ice-Melting Problems," Exp. Therm. Fluid Sci., **6**, pp. 90–105.
[5] Moffat, R. J., 1988, "Describing the Uncertainties in Experimental Results," Exp. Therm. Fluid Sci., **1**, pp. 3–17.
[6] Hao, Y. L., and Tao, Y.-X., 1999, "Heat Transfer Characteristics in Convective Melting of a Solid Particle in a Fluid," *Proc., 1999 International Mechanical Engineering Congress and Exposition*, ASME, New York, HTD-Vol. **364-2**, pp. 113–121.
[7] Kunii, D., and Levenspiel, O., 1991, *Fluidization Engineering*, 2nd Edition, Butterworth-Heinemann.
[8] Wakao, N., and Kaguei, S., 1982, *Heat and Mass Transfer in Packed Beds*, Gordon and Breach, New York.
[9] Plumb, A., 1994, "Convective Melting of a Packed Bed," Int. J. Heat Mass Transf., **37**, pp. 829–836.
[10] Bouré, J. A., and Delhaye, J. M., 1982, "General Equations and Two-Phase Flow Modeling," *Handbook of Multiphase Systems*, G. Hestroni, ed., Hemisphere Publishing Corp., Washington, pp. 36–95, Chap. 1.
[11] Hao, Y. L., and Tao, Y.-X., 1999, "Three-Dimensional Numerical Simulation of Convective Melting of Solid Particles in a Fluid," *Proc. 1999 International Mechanical Engineering Congress and Exposition*, ASME, New York, HTD-Vol. **364-2**, pp. 213–220.
[12] Garg, S. K., and Pritchett, J. W., 1975, "Dynamics of Gas-Fluidized Beds," J. Appl. Phys., **46**, pp. 4493–4500.

Exact Solution for Determination of the Maximum Sublimation Rate in a Porous Medium

Sui Lin
Department of Mechanical and Industrial Engineering,
Concordia University,
Montreal, Quebec, Canada H3G 1M8

The optimum condition for the sublimation process taking place in a porous half space are determined in this paper. The vapor mass concentration at the surface of the porous medium and the initial frozen mass concentration in the frozen region are predetermined. The optimum condition is found by determining the vapor mass concentration at the sublimation front between the vapor and frozen phases, that yields the maximum flux of the vapor mass at the sublimation front. Exact solutions of the temperature and vapor mass concentration as well as the location of the moving sublimation front are obtained. The surface temperature used as the thermal controller is also determined to match the optimum sublimation condition. [DOI: 10.1115/1.1470168]

Keywords: Heat Transfer, Moving Boundaries, Phase Change, Porous Media

1 Introduction

The heat and mass transfer in a porous medium, such as evaporation, condensation, sublimation and de-sublimation, have wide applications in separation processes, food technology, heat and moisture migration in soil and grounds, and so forth. Due to the nonlinearity of the moving boundary problem, solutions usually involve mathematical difficulties. Only a few exact solutions have been obtained for idealized situations [1–6].

The complication involved in the heat and mass transfer with phase change is that the location of the moving phase boundary is unknown. This is important because at this moving boundary the heat transfer and mass transfer are related. In Refs. [4] and [5], the characteristics of the sublimation process were investigated. However, the optimum condition and thermal control of the sublimation process were not addressed in these two studies.

The optimum condition and the thermal control of the sublimation process in engineering applications are emphasized in the present study. The optimum condition defines the maximum flux of the vapor mass at the sublimation front. The surface temperature that is used as a thermal controller has to be determined to match the optimum condition.

2 Mathematical Formulation of the Problem

A rigid, solid, porous half-space is considered, as shown in Fig. 1, initially containing a uniform frozen moisture C_i and having an initially uniform temperature T_i. In order to define the sublimation process, the vapor mass concentration at the surface, $x=0$, is specified as a fixed value of C_0. The vapor mass concentration C_s and the corresponding equilibrium temperature T_s at the sublimation front, $x=s(t)$, for the optimum condition are unknown. They will be determined as a part of the solution. After the determination of the optimum condition, the surface temperature T_0 at $x=0$, will then be determined. In order to formulate the sublimation problem, the following assumptions are made:

1. In the frozen region, $s(t)<x<\infty$, there is no moisture movement, where $x=s(t)$ locates the sublimation front.
2. The convection in the vapor region and the heat transferred by radiation are negligible.
3. The change of pressure caused by the nonuniformity of the curvature of the frozen-moisture at the sublimation front may be neglected.
4. The sensible heat absorbed by the vapor mass diffusing through the vapor region is small in comparison with the latent heat of sublimation, and may be neglected.
5. The properties of each phase remain constant but may differ for different phases.
6. The Soret effect, or the thermal diffusion, gives rise to a mass flux, which is usually very small relative to the normal Fickian flux, and may be neglected.

The sublimation process can be described by three differential equations.
For the frozen region, Region 1:

$$\frac{\partial T_1(x,t)}{\partial t}=a_1\frac{\partial^2 T_1(x,t)}{\partial x^2},\quad s(t)<x<\infty \tag{1}$$

For the vapor region, Region 2:

$$\frac{\partial T_2(x,t)}{\partial t}=a_2\frac{\partial^2 T_2(x,t)}{\partial x^2},\quad 0<x<s(t) \tag{2}$$

$$\frac{\partial C(x,t)}{\partial t}=a_m\frac{\partial^2 C(x,t)}{\partial x^2},\quad 0<x<s(t) \tag{3}$$

where a_1 and a_2 are the volume averaged thermal diffusivities in the frozen and vapor regions, respectively, and a_m is the volume averaged mass diffusivity of the vapor moisture in the porous medium. The method described by Slattery [7] may be used for evaluation of the values of a_1, a_2, and a_m.

The sublimation process in the two regions is subject to initial and boundary conditions:

$$T_1(x,0)=T_1(\infty,t)=T_i \tag{4}$$

$$s(t=0)=0 \tag{5}$$

$$T_2(0,t)=T_0 \tag{6}$$

$$C(0,t)=C_0 \tag{7}$$

$$T_1(s,t)=T_2(s,t)=T_s \tag{8}$$

$$C(s,t)=C_s \tag{9}$$

Contributed by the Heat Transfer Division for publication in the JOURNAL OF HEAT TRANSFER. Manuscript received by the Heat Transfer Division June 1, 2001; revision received December 3, 2001. Associate Editor: B. T. F. Chung.

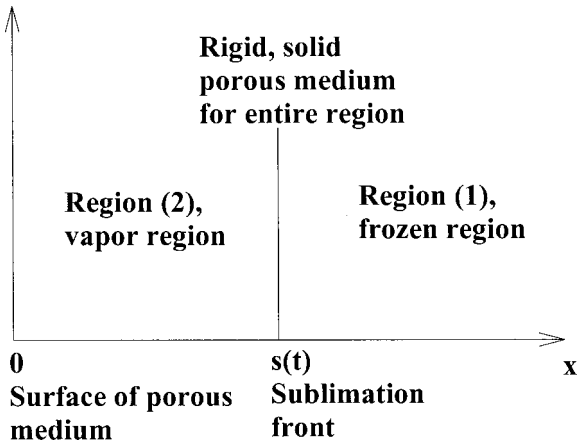

Fig. 1 Two regions in sublimation process

The surface temperature T_0 in Eq. (6), the temperature at the sublimation front T_s in Eq. (8) and the vapor mass concentration at the sublimation front C_s in Eq. (9) are unknown. They will be determined as a part of the solution.

The energy and moisture mass balances at the sublimation front can be expressed as

$$-k_2\frac{\partial T_2(s,t)}{\partial x}+k_1\frac{\partial T_1(s,t)}{\partial x}=C_iL\frac{ds(t)}{\partial t} \tag{10}$$

$$a_m\frac{\partial C(s,t)}{\partial x}=(C_i-C_s)\frac{\partial s(t)}{\partial t} \tag{11}$$

where k_1 and k_2 are the volume averaged thermal conductivities in the frozen and vapor regions, respectively, and L is the latent heat of sublimation of the moisture.

3 Solution of The Problem

The system of Eqs. (1–9) describing the distributions of the temperature and vapor mass concentration in the frozen and vapor regions in the sublimation process in a porous medium is similar to that for the distributions of the temperatures in the solid and liquid regions in a melting process for a pure substance used in Reference [8]. Therefore, Neumann's solution presented in Reference [8] can be used to obtain the temperature and vapor mass concentration distributions.

Assume that the vapor mass concentration *Cs* at the sublimation front is known. The solution of Eq. (3) for the vapor mass concentration that satisfies the boundary conditions of equations (7) and (9) is

$$C(x,t)=C_0+\frac{C_s-C_0}{erf(p)}erf\left(\frac{x}{2\sqrt{a_mt}}\right) \tag{12}$$

where p is a dimensionless constant defined as

$$p=\frac{s(t)}{2\sqrt{a_mt}} \tag{13}$$

The definition of p presented in Eq. (13) is used to satisfy the boundary condition of Eq. (9). Substitution of Eqs. (12) and (13) into Eq. (11) gives the constant p implicitly as

$$\sqrt{\pi}pe^{p^2}erf(p)=\frac{C_s-C_0}{C_i-C_s} \tag{14}$$

Assume that the temperatures at the surface, $x=0$, and at the sublimation front, $x=s(t)$, are known. Then the solutions of Eqs. (1) and (2) for the temperature distributions in the frozen and vapor regions that satisfy the initial and boundary conditions of Eqs. (4), (6), and (8), can be determined to be

$$T_1(x,t)=T_i+\frac{T_s-T_i}{erfc\left(p\sqrt{\frac{a_m}{a_1}}\right)}erfc\left(\frac{x}{2\sqrt{a_1t}}\right) \tag{15}$$

$$T_2(x,t)=T_0-\frac{T_0-T_s}{erf\left(p\sqrt{\frac{a_m}{a_2}}\right)}erf\left(\frac{x}{2\sqrt{a_2t}}\right) \tag{16}$$

The surface temperature T_0 in Eq. (16) can be determined by substituting Eqs. (13), (15) and (16) into Eq. (10) to obtain

$$\frac{k_2(T_0-T_s)}{a_2C_iL}\left[\frac{\exp\left(-p^2\frac{a_m}{a_2}\right)}{erf\left(p\sqrt{\frac{a_m}{a_2}}\right)}\right]-\frac{k_1(T_s-T_i)}{\sqrt{a_1a_2}C_iL}\left[\frac{\exp\left(-p^2\frac{a_m}{a_1}\right)}{erfc\left(p\sqrt{\frac{a_m}{a_1}}\right)}\right]=\sqrt{\pi}p\sqrt{\frac{a_m}{a_2}} \tag{17}$$

At this point, the solution of the sublimation process, with assumed values of C_s, T_s, and T_0, is obtained.

4 Determination of the Optimum Condition

The optimum condition for the sublimation process is considered as a condition at which the maximum flux of the vapor mass occurs at the sublimation front. Equation (11) gives the moisture mass balance at the sublimation front. The left-hand side of Eq. (11) shows the flux of the vapor mass at the sublimation front. Substitution of Eq. (13) into Eq. (11) yields

$$a_m\frac{\partial C(s,t)}{\partial x}=(C_i-C_s)p\sqrt{\frac{a_m}{t}} \tag{18}$$

From Eq. (14) it can be seen that an increase of the value of (C_i-C_s) results in a decrease of the value of p if the left-hand side is considered to be nearly constant. Therefore it is expected that the flux of the vapor mass at the sublimation front on the left-hand side of Eq. (18) has an optimum value. Differentiating Eq. (18) with respect to C_s gives

$$\frac{d}{dC_s}\left[a_m\frac{\partial C(s,t)}{\partial x}\right]=\sqrt{\frac{a_m}{t}}\left[(C_i-C_s)\frac{dp}{dC_s}+p(-1)\right] \tag{19}$$

When the right-hand side of Eq. (19) equals zero, the optimum condition for the sublimation process is obtained. In this case

$$(C_i-C_s)\frac{dp}{dC_s}=p \tag{20}$$

Utilization of Eq. (14) in the derivative dp/dC_s in the above equation gives

$$\frac{dp}{dC_s}=\left[\frac{1}{2p+(2p^2+1)\sqrt{\pi}\exp(p^2)erf(p)}\right]\frac{C_i-C_0}{(C_i-C_s)^2} \tag{21}$$

Substitution of Eq. (21) into Eq. (20) yields

$$\frac{C_s-C_0}{C_i-C_s}=\frac{1}{2p^2}-1 \tag{22}$$

Utilization of Eq. (14) again in Eq. (22) gives

$$\sqrt{\pi}p\exp(p^2)erf(p)=\frac{1}{2p^2}-1 \tag{23}$$

The numerical solution of Eq. (23) gives the optimum value of p to be

$$p_{\text{opt}} = 0.540388 \tag{24}$$

With this value of p, the value of the left-hand side of Eq. (22) for the optimum condition is

$$\left(\frac{C_s - C_0}{C_i - C_s}\right)_{\text{opt}} = 0.712216 \tag{25}$$

or

$$(C_s)_{\text{opt}} = 0.416 C_i + 0.584 C_0 \tag{26}$$

Note that the sum of the coefficients of C_i and C_0 in Eq. (26) is equal to unity. Equation (26) can be written in dimensionless form as

$$\left(\frac{C_s}{C_i}\right)_{\text{opt}} = 0.416 + 0.584 \frac{C_0}{C_i} \tag{27}$$

With the known value of $(C_s)_{\text{opt}}$, the value of the corresponding equilibrium temperature, $(T_s)_{\text{opt}}$ at the sublimation front, can be determined by using the Clapeyron-Clausius equation that describes a pure substance undergoing a phase change process [9]. The Clapeyron-Clausius equation is

$$\frac{dP_s}{dT_s} = \frac{L}{T_s(v_s''' - v_s')} \tag{28}$$

where P_s is the vapor pressure; while v_s' and v_s''' are the specific volumes of the frozen and vapor mass at the sublimation front, respectively. Since the vapor pressure is small during the sublimation process, v_s' is much smaller than v_s''' and, therefore, may be neglected. Equation (28) becomes

$$\frac{dP_s}{dT_s} = \frac{L}{T_s v_s'''} \tag{29}$$

Considering the vapor at the sublimation front to be an ideal gas, we have

$$v_s''' = \frac{RT_s}{P_s} \tag{30}$$

where R is the gas constant. Substitution of Eq. (30) into Eq. (29) gives

$$\frac{dP_s}{dT_s} = \frac{LP_s}{RT_s^2} \tag{31}$$

Integration of Eq. (31) yields

$$\ln \frac{P_s}{P_3} = \frac{L}{R}\left(\frac{1}{T_3} - \frac{1}{T_s}\right)$$

or

$$\frac{C_s T_s}{C_3 T_3} = \exp\left[\frac{L}{R}\left(\frac{1}{T_3} - \frac{1}{T_s}\right)\right] \tag{32}$$

where P_3, T_3, and C_3 are the pressure, temperature and vapor mass concentration at the triple point of the moisture, respectively. When the value of C_s in Eq. (32) is set to the value of $(C_s)_{\text{opt}}$, the value of T_s determined from Eq. (32) is the value of the corresponding optimum equilibrium temperature $(T_s)_{\text{opt}}$. With the optimum values of $(C_s)_{\text{opt}}$ and $(T_s)_{\text{opt}}$, the optimum surface temperature $(T_0)_{\text{opt}}$, acting as the thermal controller to match the optimum condition, can be determined from Eq. (17). In order to simplify Eq. (17), the following dimensionless parameters are introduced:

$$p^* = p_{\text{opt}} \sqrt{\frac{a_m}{a_2}}, \quad a_{21} = \frac{a_2}{a_1} \tag{33}$$

$$(T_0^*)_{\text{opt}} = \frac{k_2[(T_0)_{\text{opt}} - (T_s)_{\text{opt}}]}{a_2 C_i L} \frac{\exp(-p^{*2})}{erf(p^*)} \tag{34}$$

and

$$(T_s^*)_{\text{opt}} = \frac{k_1[(T_s)_{\text{opt}} - T_i]}{\sqrt{a_1 a_2} C_i L} \frac{\exp(-p^{*2} a_{21})}{erfc(p^* \sqrt{a_{21}})} \tag{35}$$

Equation (17) then becomes

$$(T_0^*)_{\text{opt}} = (T_s^*)_{\text{opt}} + \sqrt{\pi} p^* \tag{36}$$

Substitution of the optimum value of p_{opt} into Eqs. (13), (12), (15), and (16) gives the optimum distributions of the location s_{opt} of the sublimation front, the optimum vapor mass concentration C_{opt}, the optimum temperatures in the frozen region $(T_1)_{\text{opt}}$, and in the vapor region $(T_2)_{\text{opt}}$, respectively, as

$$s_{\text{opt}}(t) = p_{\text{opt}} \sqrt{4 a_m t} \tag{37}$$

$$\frac{C_{\text{opt}}(x,t) - C_0}{(C_s)_{\text{opt}} - C_0} = \frac{erf\left(\dfrac{x}{\sqrt{4 a_m t}}\right)}{erf(p_{\text{opt}})} \tag{38}$$

$$\frac{(T_1)_{\text{opt}}(x,t) - T_i}{(T_s)_{\text{opt}} - T_i} = \frac{erfc\left(\dfrac{x}{\sqrt{4 a_1 t}}\right)}{erfc(p_{\text{opt}} \sqrt{a_{m1}})} \tag{39}$$

$$\frac{(T_2)_{\text{opt}}(x,t) - (T_s)_{\text{opt}}}{(T_0)_{\text{opt}} - (T_s)_{\text{opt}}} = 1 - \frac{erf\left(\dfrac{x}{\sqrt{4 a_2 t}}\right)}{erf(p_{\text{opt}} \sqrt{a_{m2}})} \tag{40}$$

where

$$a_{m1} = \frac{a_m}{a_1}, \quad a_{m2} = \frac{a_m}{a_2} \tag{41}$$

For the purpose of presentation of the results, dimensionless parameters are introduced:

$$C_{\text{opt}}^* = \frac{C_{\text{opt}}(x,t) - C_0}{(C_s)_{\text{opt}} - C_0} \tag{42}$$

$$(T_1^*)_{\text{opt}} = \frac{(T_1)_{\text{opt}}(x,t) - T_i}{(T_s)_{\text{opt}} - T_i} \tag{43}$$

$$(T_2^*)_{\text{opt}} = \frac{(T_2)_{\text{opt}}(x,t) - (T_s)_{\text{opt}}}{(T_0)_{\text{opt}} - (T_s)_{\text{opt}}} \tag{44}$$

$$\eta_0 = \eta = \frac{x}{\sqrt{4 a_m t}}, \quad p_0 = p_{\text{opt}} \tag{45}$$

$$\eta_1 = \eta \sqrt{a_{m1}}, \quad p_1 = p_{\text{opt}} \sqrt{a_{m1}} \tag{46}$$

$$\eta_2 = \eta \sqrt{a_{m2}}, \quad p_2 = p_{\text{opt}} \sqrt{a_{m2}} \tag{47}$$

With these dimensionless parameters, the optimum vapor mass concentration C_{opt}, the optimum temperatures in the frozen region $(T_1)_{\text{opt}}$, and in the vapor region $(T_2)_{\text{opt}}$ defined in Eqs. (38), (39) and (40) can be written in dimensionless forms as

$$C_{\text{opt}}^* = \frac{erf(\eta_0)}{erf(p_0)} \tag{48}$$

$$(T_1^*)_{\text{opt}} = \frac{erfc(\eta_1)}{erfc(p_1)} \tag{49}$$

$$(T_2^*)_{\text{opt}} = 1 - \frac{erf(\eta_2)}{erf(p_2)} \tag{50}$$

The advantage of using the dimensionless expressions in Eqs. (48), (49), and (50) is that they can be all plotted in one diagram.

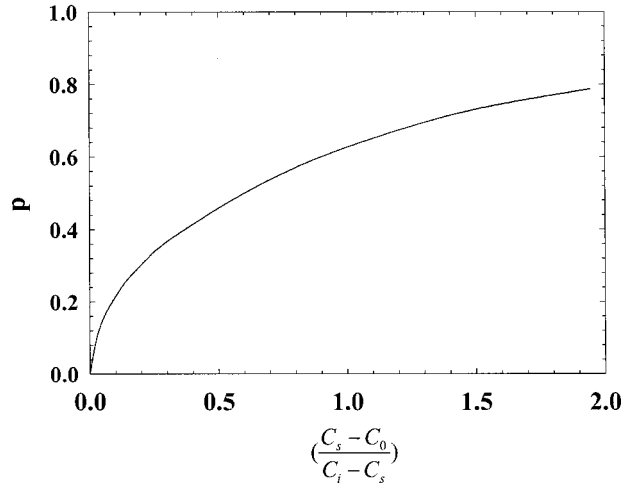

Fig. 2 p **as a function of** $(C_s - C_0)/(C_i - C_s)$

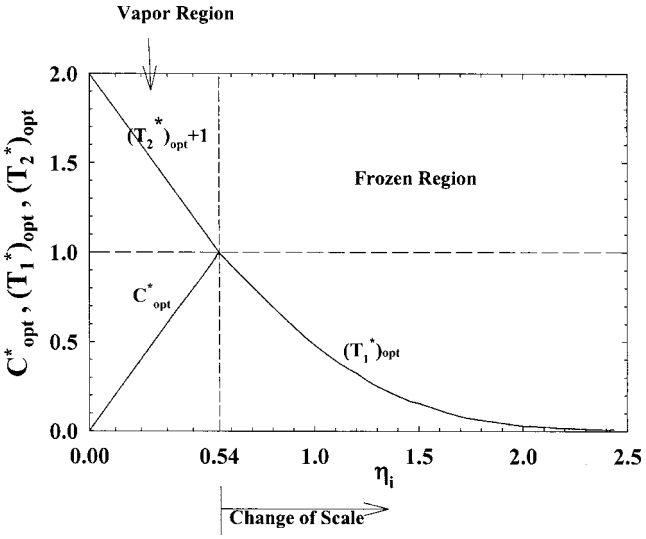

Fig. 4 C^*_{opt}, $(T_1^*)_{opt}$ **and** $(T_2^*)_{opt}$ **as functions of** η_i **for** $i=0$, **1, and 2 with** $p_i=0.540$

5 Discussion and Conclusions

The functional relationship between the ratio of the moisture mass concentration, $(C_s - C_0)/(C_i - C_s)$, and the dimensionless constant p presented in Eq. (14) is shown in Fig. 2. It can be seen that the vapor mass concentration at the sublimation front has two limiting values: one is $C_s = C_0$, and the second $C_s = C_i$.

In the first case for which $C_s = C_0$, p is equal to 0 as shown in Fig. 2. In this case, the vapor mass flux at the sublimation front presented in Eq. (18) is equal to zero.

In the second case for which C_s approaches C_i, $(C_s - C_0)/(C_i - C_s)$ approaches a very large value, and the curve shown in Fig. 2 has a very small slope. This means that the growth of the value of $(C_s - C_0)/(C_i - C_s)$ is much faster than that of p. For example, when $(C_s - C_0)/(C_i - C_s)$ reaches a value of the order of 6E11, the corresponding value of p is only about 5. Therefore it is expected that when C_s approaches the value of C_i, or $(C_s - C_0)/(C_i - C_s)$ approaches infinity as a limit, p will approach a finite value. This indicates that the flux of the vapor mass at the sublimation front presented in Eq. (18) also approaches zero.

From the above discussion it can be concluded that the two extreme cases all result in zero values for the flux of the vapor mass at the sublimation front. Hence there exists an optimum condition to have a maximum value of the flux of the vapor mass at the sublimation front. The optimum condition is determined in Eqs. (24) and (26) as

$$p_{\text{opt}} = 0.540 \tag{24}$$

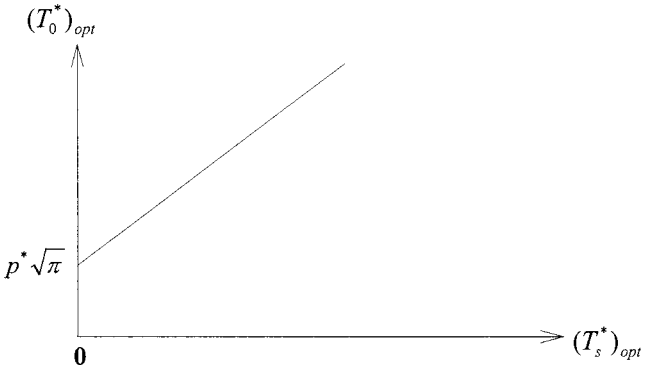

Fig. 3 $(T_0^*)_{\text{opt}}$ **as function of** $(T_s^*)_{\text{opt}}$

$$(C_s)_{\text{opt}} = 0.416C_i + 0.584C_0 \tag{26}$$

Substitution of Eqs. (24) and (26) into Eqs. (18) gives the optimum flux of the vapor mass at the sublimation front to be

$$\left[a_m \frac{\partial C(s,t)}{\partial x}\right]_{\text{opt}} = 0.2628\sqrt{\frac{a_m}{t}}(C_i - C_0) \tag{51}$$

The optimum surface temperature $(T_0)_{\text{opt}}$, or the dimensionless optimum surface temperature $(T_0^*)_{\text{opt}}$ appearing in Eq. (36), acts as a thermal controller in matching the optimum condition for the sublimation process. Its value as a function of $(T_s^*)_{\text{opt}}$, the dimensionless optimum temperature at the sublimation front, is plotted in Fig. 3. Based on Eq. (35), it is seen that the initial frozen temperature T_i should be equal to $(T_s)_{\text{opt}}$ so that the dimensionless temperature $(T_s^*)_{\text{opt}}$ at the sublimation front is zero in order to achieve the most optimum condition. For such a case, the dimensionless optimum surface temperature, $(T_0^*)_{\text{opt}}$, shown in Eq. (36) has a minimum value of $p^*\sqrt{\pi}$.

The dimensionless optimum vapor mass concentration C^*_{opt}, as well as the temperatures $(T_1^*)_{\text{opt}}$ and $(T_2^*)_{\text{opt}}$ in Eqs. (48), (49), and (50), respectively, are plotted in Fig. 4 with η_i as an abscissa for $i=0$, 1, and 2. The frozen mass concentration C_i in the frozen region is constant and is not shown in Fig. 4 because it does not fit the ordinate scale in Fig. 4.

Acknowledgment

The present work was supported by the Natural Sciences and Engineering Research Council of Canada under grant No. OGP0007929

Nomenclature

a = thermal diffusivity [m^2/s]
a_m = mass diffusivity of vapor [m^2/s]
a_{21} = dimensionless thermal diffusivity ratio defined by Eq. (33)
a_{m1}, a_{m2} = dimensionless diffusivity ratios defined by Eq. (41)
C = vapor mass concentration [kg/m^3]
$erf(\,)$ = error function
$erfc(\,)$ = complimentary error function
k = thermal conductivity [W/Km]
L = latent heat of sublimation [kJ/kg]

p = dimensionless constant defined by Eq. (13)
p_i = $i=0,1,2$, defined by Eqs. (45), (46), and (47), respectively
p_s = vapor pressure at sublimation front
R = gas constant [kJ/kgK]
$s(t)$ = position of sublimation front [m]
t = time [s]
T = temperature [K]
v_s', v_s''' = specific volumes of frozen and vapor mass at sublimation front [m^3/kg]
x = space coordinate [m]

Greek Symbols

η = dimensionless variable defined by Eq. (45)
η_i = $i=0,1,2$ defined by Eqs. (45), (46), and (47), respectively

Subscripts

0 = at surface, $x=0$
1 = frozen region, $s(t)<x<\infty$
2 = vapor region, $0<x<s(t)$
3 = triple point
i = initial condition in frozen region
opt = optimum condition
s = at sublimation front

Superscript

* = dimensionless quantity

References

[1] Cho, S. H., 1975, "An Exact Solution of the Coupled Phase Change Problem in a Porous Medium," Int. J. Heat Mass Transf., **18**, pp. 1139–1142.
[2] Mikhailov, M. D., 1975, "Exact Solution of Temperature and Moisture Distributions in a Porous Half-Space With Moving Separation Front," Int. J. Heat Mass Transf., **18**, pp. 797–804.
[3] Mikhailov, M. D., 1976, "Exact Solution for Freezing of Humid Porous Half-Space," Int. J. Heat Mass Transf., **19**, pp. 651–655.
[4] Lin, S., 1981, "An Exact Solution of the Sublimation Problem in a Porous Medium," ASME J. Heat Transfer, **103**, pp. 165–168.
[5] Lin, S., 1982, "An Exact Solution of the Sublimation Problem in a Porous Medium, Part II—With an Unknown Temperature and Vapor Concentration at the Moving Sublimation Front," ASME J. Heat Transfer, **104**, pp. 808–811.
[6] Lin, S., 1982, "An Exact Solution of the Desublimation Problem in a Porous Medium," Int. J. Heat Mass Transf., **25**, pp. 625–630.
[7] Slattery, J. C., 1972, *Momentum, Energy and Mass Transfer in Continua*, McGraw-Hill, New York, Sections 7.3 and 10.3.
[8] Carslaw, H. S., and Jager, J. C., 1959, *Conduction of Heat in Solids*, Oxford University Press, London, Chap. XI.
[9] Cengel, Y. A., and Boles, M. A., 1994, *Thermodynamics—An Engineering Approach*, McGraw-Hill, New York, Section 11.3.

Empirical Evaluation of Convective Heat and Moisture Transport Coefficients in Porous Cotton Medium

Kamel Ghali
Beirut Arab University,
Faculty of Engineering,
Beirut, Lebanon
e-mail: amro@aub.edu.lb

Nesreen Ghaddar
American University of Beirut,
Faculty of Engineering and Architecture,
P.O. Box 11-236,
Riad ElSolh,
Beirut 1107 2020, Lebanon
e-mail: farah@aub.edu.lb

Byron Jones
Kansas State University,
College of Engineering,
148 Rathbone Hall,
Manhattan, KS 66506-5202
e-mail: jones@ksu.edu

The air penetration within a porous clothing system on a moving human being is an important physical process that considerably affects the heat and moisture resistance of the textile material. This effect of the coupled convection heat and mass exchange within the clothing system is experimentally investigated and theoretically modeled to determine the heat and mass transfer coefficients between the air penetrating the void space and the solid fiber as a function of the velocity of penetrating air. Experiments were conducted inside environmentally controlled chambers to measure the transient moisture uptake of untreated cotton fabric samples as well as the outer fabric temperature using an infrared pyrometer. The moisture uptake was conducted at three different volumetric flow rates of 0.0067, 0.018 and 0.045 $m^3/sec/m^2$ of fabric area to represent airflow penetrations that could result from slow, medium, and vigorous walking, respectively. The theoretical analysis is based on a two-node adsorption model of the fibrous medium. A set of four coupled differential equations were derived describing time-dependent convective heat and mass transfer between the penetrating air and the solid fiber in terms of relevant unknown transport coefficients. The unknown model parameters were adjusted to fit the experimental data. The outer heat and mass transfer coefficients were found to increase with the air penetration flow rate. [DOI: 10.1115/1.1471524]

Keywords: Absorption, Mass Transfer, Porous Media

Introduction

The clothing system plays a very important role in human thermal responses because it determines how much of the heat generated in the human body can be exchanged with the environment. With the development of new technology, it is becoming important to know how the human body will behave thermally under different environmental conditions with various clothing systems. Examples include working in a spaceship or in a harmful environment with special protective clothing.

The first clothing model that describes the mechanism of transient diffusion of heat and moisture transfer into an assembly of hygroscopic textile materials was introduced and analyzed by Henry [1]. He developed a set of two differential coupled governing equations for the mass and heat transfer in a small flat piece of clothing material. Henry's analysis was based on a simplified analytical solution. In order to describe the complicated process of adsorption behavior in textile materials, David and Nordon [2] presented a model in terms of experimentally adjustable parameters appropriate for a first stage of rapid moisture sorption followed by a second stage of slow moisture sorption. However, their model did not take into account the physical mechanisms of the sorption process. For this reason, Li and Holcombe [3] introduced a new two-stage adsorption model to better describe the coupled heat and moisture transport in fabrics.

In addition to the above-mentioned models, which describe the heat and mass transfer in a piece of a clothing material, there are models that describe these processes in the whole clothing system. Farnworth [4] developed a numerical model that takes into account the condensation and adsorption in a multi-layered clothing system. Jones [5] developed another new unsteady-state thermal model for the whole clothing system. The whole clothing system model was based on simplified expressions of Henry's model. Recently, Li and Holocombe [3] presented a transient mathematical clothing model that describes the dynamic heat and moisture transport behavior of clothing and human body.

The above-mentioned models, whether developed for a piece of clothing material or for the whole clothing system, focused on the diffusion process of heat and water vapor transport and assumed instantaneous equilibrium between the local relative humidity of the penetrating air and the moisture content of the fiber. However, the hypothesis of local equilibrium was shown to be invalid during periods of rapid transient heating or cooling in porous media as reported by Minkowycz et al. [6]. Their results for a one-dimensional porous layer show that in the presence of flow, local thermal equilibrium is not valid if the ratio of the Sparrow number to the Peclet number is small. In the absence of local thermal equilibrium, the solid and fluid should be treated as two different constituents. Gibson [7] conducted a two-dimensional numerical modeling and experimental testing of steady diffusion/convection processes in textiles, where pressure drops and relative humidities across the fabric are compared. He used a dynamic moisture permeation cell for experimental testing [8–11], where concentration differences between top and bottom of the fabric were imposed, induced by convective air flow streams above and below the fabric that are parallel to the fabric surface. The numerical model of Gibson included diffusion and convective transport of heat and moisture as well as liquid water wicking through a porous textile material. Gibson model was based on Whitaker's theory for mass and energy transport through porous media that assumes local thermal equilibrium between the three phases of solid, liquid and gas that could exist in the porous textile material and ignored the possible existence of micro-scale pore-level heat and mass transfer coefficients. Under vigorous movement of a relatively thin porous textile material, the air will pass quickly between the fibers, invalidating the local thermal equilibrium assumption. Dur-

Contributed by the Heat Transfer Division for publication in the JOURNAL OF HEAT TRANSFER. Manuscript received by the Heat Transfer Division February 7, 2001; revision received January 25, 2002. Associate Editor: J. G. Georgiadis.

ing body motion, air must go in and out, and ventilation is obtained without gross environmental air movement. Harter et al. [12] called this particular aspect in clothing comfort ''ventilation of the microclimate within clothing.'' The ventilation rate is affected mainly by the walking velocity as described by Lotens [13] who derived empirically the steady ventilation rate as function of the air permeability of the fabric and the effective wind velocity.

The objective of this research is to develop a new simple one-dimensional model that takes into account the ventilation effect on the heat and mass transport through fibrous materials, and does not assume local thermal equilibrium in the fiber. The airflow through the fiber is induced by a bulk pressure gradient generated by air with an elevated velocity impinging normal to the fabric. Our purpose is not to perform the definitive description of adsorption/desorption processes, but to develop a simulation model that can accurately reflect the heat and mass transport behavior for fabrics or other similar highly porous adsorbing media with bulk airflow. Such a model could be ultimately incorporated into human body simulations to better predict the transient response of a walking human.

Mathematical Formulation

The Two-Node Model. The theoretical analysis is based on a two-node adsorption model of the fibrous medium. The outer node represents the exposed surface of the yarns (yarns that are woven into a fabric), which is in direct contact with the penetrating air in the void space between the yarns. The inner node represents the inner portion of the ''solid'' yarn (fibers on the interior of the yarn), which is completely surrounded by the outer node. The outer node exchanges heat and moisture transfer with the flowing air and with the inner node, while the inner node exchanges heat and moisture by diffusion only with the outer node. The moisture uptake in the fabric is initially very fast due to the convection effect at the yarns surface, followed by diffusion to the yarn interior. The relation of the outer-node to the inner-node size is designated by the mass fraction γ of the outer node mass of the fabric to the total fabric mass. The parameter γ is related to the internal porosity of the fiber, and reflects the mass of the fiber with effective large size pores which the air penetrates to the mass of the fiber that contains the micro pores in which diffusion process dominates. The parameter γ, will be dependent on fabric type and possibly the air flow rate. A cylindrical representation of the two-node model is shown in Fig. 1, where the air-fiber model can hypothetically be visualized as an external flow of air around cylinders (yarns) in cross flow. The fabric is represented by a large number of these two-node modules in cross flow depending on the fabric porosity. The fabric area is $L \times W$ and the fabric thickness is t_f. The airflow is normal to the fabric plane.

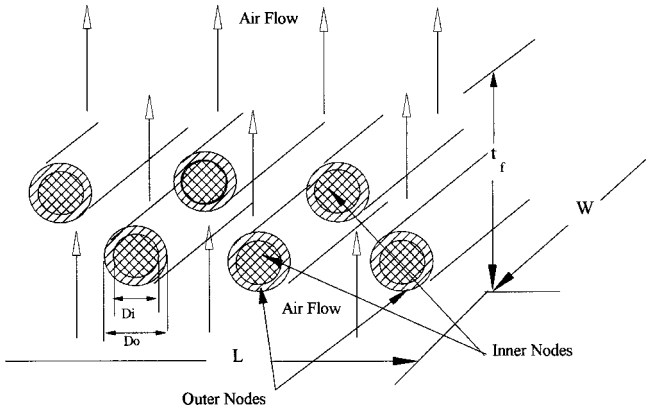

Fig. 1 A cylindrical representation of the two-node model as cross flow over cylinders

Governing Equations. The time-dependent mass and energy balances are derived for the outer and inner nodes of the fabric yarn in terms of the relevant unknown heat and mass transport coefficients between the penetrating air and the outer node and between inner and outer nodes. The outer node and the inner node mass balances of moisture are given in Eqs. (1) and (2), respectively:

$$\rho \gamma t_f A_f \left(\frac{dR_o}{dt} \right) = H_{mo} A_o (P_a - P_o) + H_{mi} A_i (P_i - P_o) \tag{1}$$

$$\rho (1-\gamma) t_f A_f \left(\frac{dR_i}{dt} \right) = H_{mi} A_i (P_o - P_i) \tag{2}$$

where R_o is the regain of the outer node, R_i is the regain of the inner node, and H_{mo} is the mass transfer coefficients between the outer node and the penetrating air, and H_{mi} is the mass diffusion coefficient between the outer node and the inner node. The total regain R in the fiber, which is the mass of adsorbed water per unit mass of the fiber, is then given by:

$$R = \gamma R_o + (1-\gamma) R_i \tag{3}$$

where γ is the fraction of mass in the outer node. An energy balance on the outer nodes gives:

$$\begin{aligned} \rho \gamma t_f A_f \left(\frac{du_f}{dt} \right) = {} & H_{mo} A_o (P_a - P_o) h_{fg} + H_{mi} A_i (P_i - P_o) h_{fg} \\ & + H_{co} A_o (T_a - T_o) + H_{ci} A_i (T_i - T_o) \\ & + h_r A_f (T_a - T_o) \end{aligned} \tag{4a}$$

where H_{co} is the heat transfer coefficients between the outer node and the penetrating air, H_{ci} is the diffusion coefficient between the outer node and the inner node, respectively and h_r is the linearized radiation heat transfer coefficient based on average temperature given by Holman [14]:

$$h_r = 4 \sigma \varepsilon \left(\frac{T_o + T_a}{2} + 273 \right)^3 \tag{4b}$$

The view factor for the fabric in its climatic enclosure is taken as unity with the assumption that the walls of the climatic chamber are at T_a. The radiative heat transfer at the level of temperatures present in the problem is fairly small compared to convective transfer but it is simple to incorporate radiation heat transfer effects in the model for more accuracy of the heat balance on the outer node as reported by Gibson [9] and Zhao [15]. The enthalpy of the water vapor in air is approximated by the heat of vaporization, h_{fg}. The internal energy of the fabric can be divided into two components, the internal energy of the solid fiber and the internal energy of the adsorbed water vapor so that the rate of internal energy change is expanded to:

$$\frac{du_f}{dt} = c_f \frac{dT_o}{dt} + \frac{d(R u_{ad})}{dt} \tag{5a}$$

and

$$\frac{d(R u_{ad})}{dt} = u_{ad} \frac{dR}{dt} + R \frac{du_{ad}}{dt} \tag{5b}$$

The enthalpy of the adsorbed phase depends primarily on the fabric regain, and to a much lesser extent on the fabric temperature. Therefore, Eq. (5*b*) can be approximated as:

$$\frac{d(R u_{ad})}{dt} = u_{ad} \frac{dR}{dt} + R \frac{\partial u_{ad}}{\partial R} \frac{dR}{dt} \tag{6}$$

The density of the adsorbed phase of water is similar to that of liquid water. The high density results in the enthalpy and internal energy of the adsorbed phases being very nearly the same. Therefore, the internal energy, u_{ad}, can be replaced with the enthalpy of the adsorbed water. Since liquid water represents the state of zero

enthalpy, then for consistency, the enthalpy of the adsorbed state is $(h_{fg}-h_{ad})$. Data on h_{ad} as a function of relative humidity was obtained from the work of Morton and Hearle [16]. Except for very low regain values corresponding to very low relative humidities, the value of $\partial h_{ad}/\partial R$ is on the order of, or less than the value of h_{ad}. The regain is typically less than 0.1, which implies that $R(dR/dt) \ll (dR/dt)$ and this term can be dropped from Eq. (6). Substituting back in Eq. (5*a*) and then in the heat balance of the outer node (Eq. (4*a*)) leads to:

$$\rho \gamma t_f A_f \left[c_f \frac{dT_o}{dt} + (h_{fg}-h_{ad}) \frac{dR_o}{dt} \right] = H_{mo} A_o (P_a - P_o) h_{fg} + H_{mi} A_i (P_i - P_o) h_{fg} + H_{co} A_o (T_a - T_o) + H_{ci} A_i (T_i - T_o) + h_r A_f (T_a - T_o) \quad (7)$$

The mass balance of the outer node given in Eq. (1) can be substituted in Eq. (7) to express the terms that have the mass transfer coefficients H_{mo} and H_{mi} in terms of the rate of change of the outer regain dR_o/dt. Then Eq. (7) simplifies to:

$$c_f \frac{dT_o}{dt} = h_{ad} \frac{dR_o}{dt} + \frac{1}{\rho \gamma t_f} \left[H_{co} \frac{A_o}{A_f} (T_a - T_o) + H_{ci} \frac{A_i}{A_f} (T_i - T_o) + h_r (T_a - T_o) \right] \quad (8)$$

To generalize the mass and heat balances of the outer node, effective heat and mass transfer coefficients are defined such that these equations are independent of the geometric model used to visualize the system. The effective transport and diffusion coefficients are defined as follows:

$$H'_{mo} = H_{mo} \frac{A_o}{A_f}, \quad H'_{co} = H_{co} \frac{A_o}{A_f}, \quad H'_{mi} = H_{mi} \frac{A_i}{A_f}, \quad H'_{ci} = H_{ci} \frac{A_i}{A_f} \quad (9)$$

The effective transport and diffusion coefficients are relevant to what can be measured experimentally rather than being tied to a specific micro-model. Substituting the effective coefficients in Eq. (1) and Eq. (8) yields to the following general mass and heat balance equations for the outer node:

$$\frac{dR_o}{dt} = \frac{1}{\rho \gamma t_f} [H'_{mo}(P_a - P_o) + H'_{mi}(P_i - P_o)] \quad (10)$$

$$\frac{dT_o}{dt} = \frac{h_{ad}}{c_f} \frac{dR_o}{dt} + \frac{1}{\rho c_f \gamma t_f} [H'_{co}(T_a - T_o) + H'_{ci}(T_i - T_o) + h_r (T_a - T_o)] \quad (11)$$

A similar derivation for the energy balance on the inner node is done. The mass and heat transport equations are given in terms of the effective diffusion coefficients as follows:

$$\frac{dR_i}{dt} = \frac{1}{(1-\gamma)\rho t_f} [H'_{mi}(P_o - P_i)] \quad (12)$$

$$c_f \frac{dT_i}{dt} = h_{ad} \frac{dR_i}{dt} + \frac{1}{(1-\gamma)\rho t_f} [H'_{ci}(T_o - T_i)] \quad (13)$$

The previous set of four coupled differential Eqs. (10) to (13) describes the time-dependent convective mass and heat transfer between the penetrating air and the solid fiber in terms of the moisture regain in the outer and inner nodes and the temperature of the inner and outer nodes. To numerically solve the equations for the transient response, the mass fraction of the exposed yarn "γ" and the four unknown diffusion and transport coefficients, namely H'_{mi}, H'_{ci}, H'_{mo}, and H'_{co}, have to be determined. The determination of these coefficients is done with the aid of experimental measurements of the moisture regain and fabric temperature under forced air flow as a function of time as will be explained in the next section.

Using the Lewis relation for the heat and mass transfer, the unknown model parameters can be reduced to the internal heat or mass diffusion coefficient, the outer heat or mass transfer coefficient and the mass fraction of the exposed "solid" yarn. The Lewis relation for heat and mass transfer is given by:

$$H_c = H_m \frac{h_{fg}}{i_{cl}(16.5 \text{ K/kPa})} \quad (14)$$

where i_{cl} is the permeation efficiency factor and (16.5 K/kPa) is the so-called Lewis constant [17]. For the outer transport coefficients, the situation is that of surface convection to air and the value of i_{cl} is unity. However, the heat and mass transfer mechanism in the inner node is different. The relationship between heat transport and water vapor mass transport in stagnant air layers can be derived from a more fundamental consideration of heat conduction and mass diffusion without bulk flow of air. However, this relationship is numerically nearly identical to the Lewis relation modified with the permeation efficiency factor, i_{cl}. Mathematically, the vapor permeation efficiency is defined as: $i_{cl} = (R_d/E_r)/LR$, where R_d is the thermal resistance of a fabric (m^2 K/W), E_r is the evaporative resistance of the fabric (m^2 kPa/W) and LR is referred to as the Lewis ratio [17]. Consequently, it is common in the field of clothing heat and mass transport to refer to the relationship between heat transport and water vapor mass transport in stagnant air layers as the Lewis relationship [18]. The fabric is normally constructed of yarns (threads) where each yarn consists of many fibers. The outer node consists of fibers on the surface of the yarn and the interior node represents the interior of the yarn. The interior node transport process is dominated by diffusion/conduction within the yarn that still has the very small pores of air. The value of i_{cl} (0.3–0.8) is less than unity because the presence of the fibers increases conduction and decreases the moisture diffusion.

In the next section, a description is given of the experiments carried out at various penetrating airflow rates to measure the transient moisture regain and fabric temperature. The experimental data is combined with the solution of the coupled transport equations of the two-node model to determine the unknown transport parameters.

Experimental Setup and Procedure

Untreated cotton was chosen as a representative of a most common worn fabric to test the model and determine the necessary unknown parameters (the heat and mass transfer coefficients for the inner and outer nodes as well as the mass fraction of the two nodes). The cotton was obtained from Test fabrics Inc. (Middlesex, NJ 08846), and is made of unmercerized cotton duck, style #466.

Ten different fabric samples, each having an area of 0.457×0.457 m^2 and thickness of 0.0010 m, were cut from different locations in the fabric sample to minimize the effect of any local nonhomogeneity that may exist within the cotton fabric sample. The fabric samples were conditioned inside an environmental chamber at an air temperature of 30°C and relative humidity of 30 percent for at least 24 hours. Following this conditioning period, the fabric was weighed to determine their weight at these dry conditions. After establishing the dry weight of the fabric at 30 percent relative humidity, these fabric samples were taped to a steel frame by an aluminum tape. The fabric steel frame was fixed to the top of a Styrofoam box having dimensions of 0.762×0.762 m^2 and a depth of 0.457 meter. The top opening of the box had some clearance to allow the fabric sample to be easily placed and removed as shown in Fig. 2. The box also had an air connection to a flow calibrator that allows the generation of very low air flow rates at a reading accuracy of ± 0.02 liter/min (± 0.00000333 m^3/s). Before each experiment, the steel supported

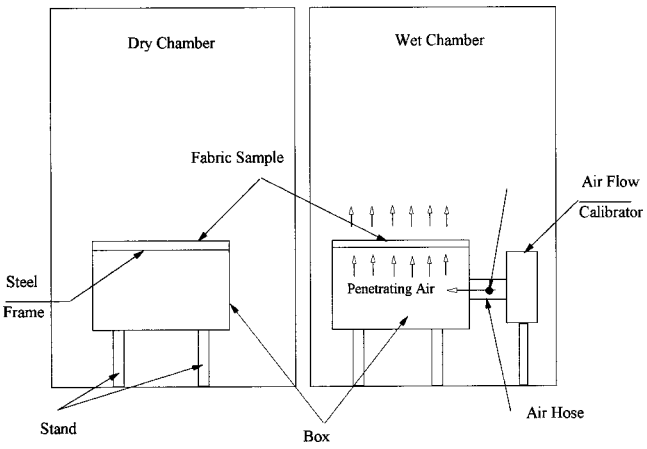

Fig. 2 A schematic of the experimental setup and the Styrofoam box

fabric samples were conditioned inside the dry chamber for at least 16 hours and weighed. Inside the dry chamber, the fabric sample was supported to the top of the Styrofoam box and the whole box was covered by a plastic bag and carried to an adjacent environmental chamber whose conditions were set at 30°C and 80 percent humidity. The precision in the set conditions of the climatic chamber temperature was ±0.5°C and chamber relative humidity was ±2 percent. Inside the moist chamber, the plastic bag was quickly removed and air hose connection was quickly attached to the calibrator. The whole process of moving the sample box from the dry chamber to the moist chamber and attaching the air hose took 25 sec. The sample is subject to the desired flow rate for a designated length of time after which it would be weighed. A different sample would then be used to get results for a longer period of time. The experiments were conducted and repeated at the following lengths of time in the moist chamber: 1, 2, 3, 4, 5, 6, 8, 10, 12, 14, 16, 18, 20, 25, and 30 min. At the end of each designated length of time for the test, the fabric would quickly be removed and placed inside a plastic bag for weighing using a sensitive scale of accuracy ±0.01 gram. The weight gain of moisture was determined at the end of each specified length of time for the test. The weighing of the fabric is a straightforward and reliable method to measure moisture gain in the fabric, particularly when moisture content of the air stream exiting the fabric is not measured. To reduce uncertainty in the measurements, each data point was repeated at least three times for three different samples and the uncertainty in the repeated measurements of weight gain was less than 5 percent.

The fabric temperature was recorded using an infrared Omega pyrometer to determine the fabric temperature during the absorption process. The accuracy in temperature readings of the pyrometer was ±0.55°C. The pyrometer was pointed normally to the fabric and the surface temperature of the fabric was recorded every 5 sec for the initial fifteen minutes of the moisture adsorption process. The measurement of the fabric surface temperature may not be exactly relevant to the predicted outer and inner node temperatures of the fabric; rather it will be a combination of both at the fabric surface temperature due to the fact that the fabric has a high porosity close to 80 percent. It is not known what portion of the radiation detected originates from the outer node and what portion originates from the inner node, so the measured temperature could represent a value bounded between the inner and outer nodes' temperatures.

The whole experimental procedure was carried out for three different flow rates of 0.0014, 0.00376, and 0.0094 ($\pm 0.00000333 m^3/s$) m^3/sec, corresponding to flow rates per unit area of 0.0067, 0.018, and 0.045 ($m^3/sec \cdot m^2$), respectively. The selected airflow rates represent flow rates movement through a clothing system that could be generated during low, medium and vigorous human activity, respectively.

Methodology for Calculation of the Transport Parameters

The coupled mass and heat transport Eqs. (10) through (13) of the outer and inner nodes of the fabric are integrated numerically using a time step size of 0.1 second. Initial values of the effective mass transport parameters H'_{mi} and H'_{mo} are assumed. The effective heat transport coefficients H'_{ci} and H'_{co} are then calculated using the modified Lewis equation (14) with $i_{cl}=1$ for the outer node coefficient and $i_{cl}=0.7$ for the inner node coefficient. The mass fraction of the outer node, γ, is taken as 0.6, although other values have been also considered. The vapor pressure of the flowing air, P_a, is related to the air relative humidity, *RH*, and temperature and is calculated using the psychometric formulas of Hyland and Wexler [19] to predict the saturation water-vapor pressure and the hence the vapor pressure at the specified relative humidity. The regain of the cotton material has a definite relation to the relative humidity of the water vapor through a property curve of regain versus relative humidity [16]. The graphical relation of *R* as a function of relative humidity, *RH*, has been interpolated with 3rd order polynomials for 10 relative humidity intervals from zero to 100 percent. The interpolation functions are used in the simulation to calculate the inner and outer nodes' relative humidities corresponding to the values obtained of inner and outer regains, respectively. The vapor pressures in the outer node P_o and the inner node P_i are then obtained from the inner and outer nodes' relative humidities. A first order Euler-Forward numerical integration is used as follows:

$$R_o^{n+1}=R_o^n+\frac{\Delta t}{\gamma\rho t_f}[H'_{mo}(P_a-P_o^n)+H'_{mi}(P_i^n-P_o^n)] \quad (15)$$

$$R_i^{n+1}=R_i^n+\frac{\Delta t}{(\gamma-1)\rho t_f}[H'_{mi}(P_o^n-P_i^n)] \quad (16)$$

$$T_o^{n+1}=T_o^n+\frac{h_{ad}}{c_f}(R_o^{n+1}-R_o^n)+\frac{\Delta t}{\gamma\rho t_f c_f}[H'_{co}(T_a-T_o^n) + H'_{ci}(T_i^n-T_o^n)+h_r^n(T_a-T_o^n)] \quad (17)$$

where Δt is the time step, and n is the time step number ($t=n\Delta t$). Once the updated value of outer node regain R_o^{n+1} is obtained, then the corresponding relative humidity is found from the cotton *R-RH* function and the vapor pressure P_o^{n+1} is evaluated at T_o^{n+1} and RH_o^{n+1}. The outer node vapor pressure is then used in the inner-node energy equation to update the inner temperature value at time t^{n+1}.

$$T_i^{n+1}=T_i^n+\frac{h_{ad}}{c_f}(R_i^{n+1}-R_i^n)+\frac{\Delta t}{\gamma\rho t_f c_f}[H'_{ci}(T_o^{n+1}-T_i^n)] \quad (18)$$

The inner node regain at t^{n+1} is used to find the new relative humidity RH_i^{n+1} and hence update the inner node vapor pressure P_i^{n+1} at T_i^{n+1}. At every time step, the total regain can be evaluated using Eq. (3).

Experimental data of the total regain and fabric temperature are fed into the simulation program with their respective times. For any assumed set of effective transport parameters, the simulation program calculates the average relative regain error between the measured regain and calculated regain. The simulations are repeated many times for each experiment, by assuming a different set of effective transport parameters and mass fraction of the outer node. In every run, the regain relative error is calculated as:

Table 1 Effective heat transport parameters of the two-node adsorption model.

Flow rate (m^3/sec.m^2)	H'_{mi} (kg/m^2 kPa.sec)	H'_{ci} (W/m^2 K)	H'_{mo} (kg/m^2 kPa.sec)	H'_{co} (W/m^2 K)
0.0067	7.58×10^{-06}	1.574	1.14×10^{-5}	1.64
0.018	7.58×10^{-06}	1.574	1.52×10^{-5}	2.18
0.045	7.58×10^{-06}	1.574	3.03×10^{-5}	4.36

$$e_R=\frac{1}{mt_m}\sum_{i=1}^{m}\frac{|R^i_{\text{experimental}}-R^i_{\text{numerical}}|\Delta t^i}{R^i_{\text{experimental}}} \tag{19}$$

where "i" is the measurement number of total number of m measurements conducted over a period of time t_m. The simulation results are then used to determine the effective heat and mass transfer coefficients by finding those transport coefficients that best fit and predict the experimentally measured transient regain. The results will be discussed in the next section.

Results and Discussion

Empirical Evaluation of Effective Transport Parameters Using the Two-Node Model and Experimental Data. The fabric in the two-node model can be visualized to be consisting of an outer node, an inner node and a void space. The effective heat and mass transfer coefficients for the outer node, H'_{co} and H'_{mo}, are dependent on the external air bulk flow in the void space. The inner coefficients H'_{ci} and H'_{mi} are independent of the external flow rate since the process here is diffusion. The other parameters will be kept fixed at all flow rates, with the condition that they are selected to give a good fit of the experimental data at any flow rate. An initial good guess for the internal node effective mass transfer coefficient H'_{mi} is derived from the known and experimentally measured evaporative resistance "E_r" through the fabric. The mass transfer diffusion coefficient H'_{mi} in the inner node is diffusion through solid yarn that encloses the micro pores of air and it can be assumed to be an order of magnitude smaller than the overall conductance of the whole fiber. So H'_{mi} can be taken as:

$$H'_{mi}=\frac{1}{k_1E_rh_{fg}} \tag{20}$$

where E_r is the evaporative resistance of the cotton fiber ($E_r=0.00505$ m^2K/W, extracted from [17]), and k_1 is an empirical factor that has been selected to be equal to 10 (other values of k_1 have also been tested). The mass fraction of the outer node, γ, which depends on the fabric type and fabric porosity, was taken as 0.6. It is not intended in the model to consider γ as flow dependent parameter, but rather as design parameter for the fabric. This parameter is empirically determined such that a small or close to minimum relative error is introduced in the predicted regain as compared to the experimental results in the range of the imposed flow rates. The permeability efficiency factor i_{cl} is taken as 0.4. When the values of i_{cl} are varied from 0.05 to 0.7, the relative error in the regain between predictions and experiment does not significantly change at the flow rates under consideration. The value of $i_{cl}=0.4$ is selected as optimal parameter, because a best fit is obtained when predicted and measured temperatures are compared. Experimentally it was evident that most of the regain uptake occurred within the initial 3–5 minutes of the transient uptake indicating that the mass fraction of the outer node is substantial. A high value of i_{cl} produces a higher inner node temperature because the effective conductive coefficient H'_{ci} becomes lower. The values of the effective external transport coefficients H'_{mo} and H'_{co} are then found as given in Table 1, at each of the three flow rates such that the relative regain error is minimum while keeping all other parameters fixed (γ and i_{cl}).

Figure 3 shows the average regain relative error at the flow rates per unit area of 0.0067, 0.018, and 0.045 m^3/sec.m^2 for different values of H'_{co} at $i_{cl}=0.4$ and $\gamma=0.6$. Figure 4 shows the *measured* total regain and the predicted total regain as a function of time at various flow rates. The average regain relative error for the cases presented in Fig. 4 are 0.067, 0.0744, and 0.0501 at the flow rates of 0.0067, 0.018, and 0.045 m^3/sec.m^2, respectively. The correlation factor calculated for the predicted regains to measured data for the two-node model are 0.9525, 0.9236, and 0.96107 at the flow rates of 0.0067, 0.018, and 0.045 m^3/sec.m^2, respectively. The correlation factors are calculated using Pearson's method as reported by Walpole and Myers [20]. A sensitivity analysis is performed on the predicted regain of the model to ±20 percent variation in the convective heat flux coefficients and results are shown in Fig. 5. The maximum variations were of ±6.5

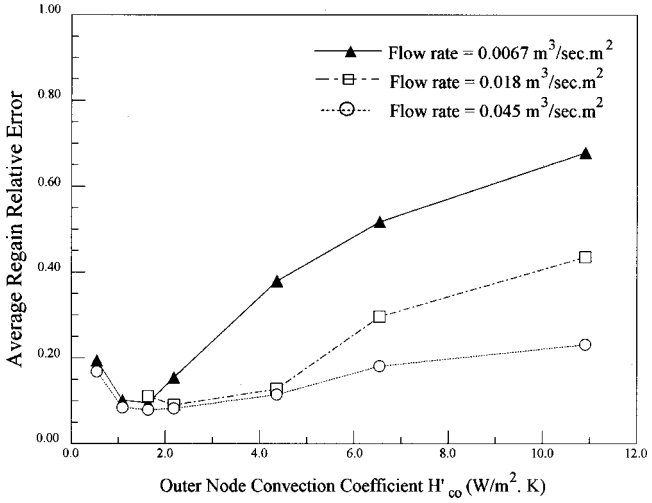

Fig. 3 The average regain relative error at the flow rates per unit area of 0.0067, 0.018, and 0.045 m^3/sec.m^2 for different values of H'_{co} at $i_{cl}=0.4$ and $\gamma=0.6$

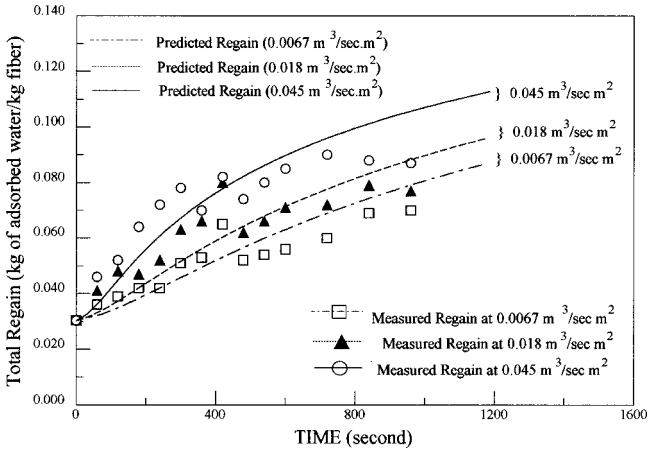

Fig. 4 A plot of the predicted total regain and the measured regain as a function of time at different flow rates.

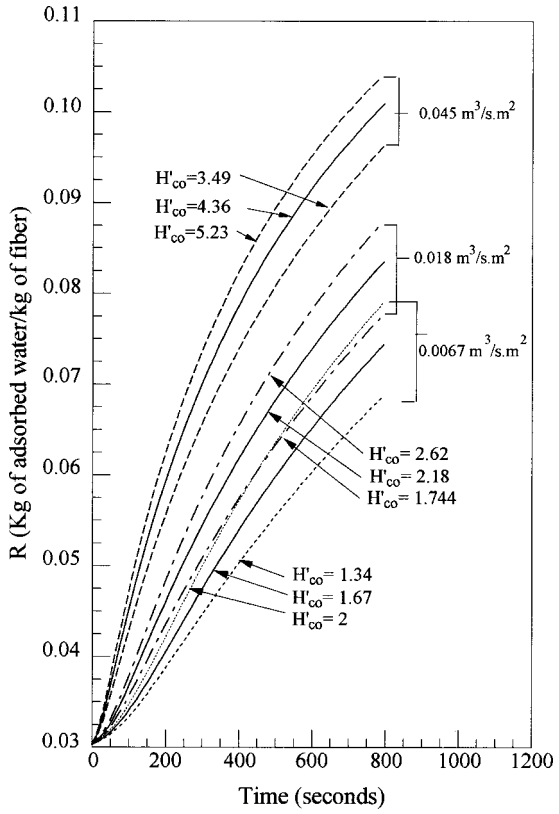

Fig. 5 (a) The predicted regain at optimal H'_{co}, $0.8H'_{co}$, and $1.2H'_{co}$ at the flow rates of 0.0067, 0.018, and 0.045 m^3/sec.m^2

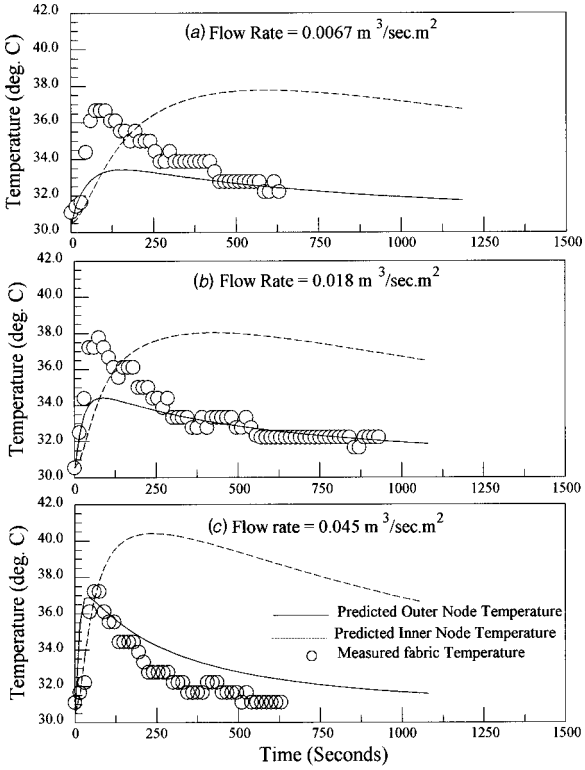

Fig. 6 The predicted inner and outer node temperatures and the measured fabric temperatures as a function of time at the flow rates of (*a*) 0.0067 m^3/sec.m^2, (*b*) 0.018 m^3/sec.m^2, and (*c*) 0.045 m^3/sec.m^2

percent, ±5.3 percent, and 3.4 percent from the optimal predicted regain at the flow rates of 0.0067, 0.018, and 0.045 m^3/sec.m^2, respectively. Another sensitivity analysis is performed on the predicted regain of the model to check the effect of varying the outer node mass fraction γ by ±20 percent from its value of 0.6 at the selected empirical transport coefficients. Results show that the maximum variations were of ±7.5 percent, ±8.7 percent, and 9.3 percent from the predicted regain at $\gamma=0.6$ for the flow rates of 0.0067, 0.018, and 0.045 m^3/sec.m^2, respectively.

The predicted inner and outer nodes' temperatures are shown as a function of time in Figs. 6(*a*), 6(*b*), and 6(*c*) at the flow rates of 0.0067, 0.018, and 0.045 m^3/sec.m^2, respectively. On the same Figs. 6(*a–c*), the measured fabric temperatures are plotted as a function of time at the respective flow rates. The model does show that both the inner and outer nodes temperatures experience an initial increase due to the release of heat from adsorption of the water vapor and then the temperature curves drop gradually in time to approach the chamber temperature after a relatively long period of time. The inner node temperature is substantially higher than the outer node temperature as should be expected. The higher the flow rate, the smaller is the peak temperature in the fabric and temperature transient is faster to reach the chamber air temperature. The measured fabric temperature should be more representative of the outer node than it is for the inner node. The fabric is relatively thick and when there is initially no airflow through the fabric, there may exist some temperature gradient in the fabric. Once the airflow is established, the temperature gradients in the fabric become minimal and the inner and outer nodes temperature should approach equilibrium with the air stream. The predicted peak outer node temperature is lower than the measured one. The average relative error in the Celsius temperature between the measured and the predicted one at the optimal assumed parameters is calculated for the three flow rates as 0.0641, 0.0609, and 0.0235 at the flow rates of 0.0067, 0.018, and 0.045 m^3/sec.m^2, respectively. The fabric has a high porosity close to 80 percent, and it is not known which portion of the radiation detected originates from the outer node and which portion originates from the inner node, so the measured temperature could represent some temperature that is bounded between the inner and outer nodes' temperatures. When the values of measured temperature are compared with the predicted inner and outer temperature, the agreement is fair, particularly for the first few minutes. The discrepancy during the initial period is attributed to the fact that when the fabric box was placed in the humid chamber, the box was full of dry air. Once the high humidity conditioned airflow started, the dry air passed first into the fabric, followed by the humid air, which delayed the rise in the fabric temperature due to moisture adsorption. Note that this delay decreases as the flow rate increases. The other factor that may cause some deviation of results after the initial period is the precision at which ambient conditions are maintained in the climatic chamber with an error of ±0.5°C.

Limiting Values of the Empirical Transport Parameters: Outer Heat Transfer Coefficient. The fabric yarns may be modeled as a group of cylinders in cross flow. Although heat and mass transfer through hygroscopic textiles such as cotton are very complicated, it is important to check if the coefficients obtained in the model are not higher than what is expected in the simplest case of cross flow around cylinders. The actual outer heat transport coefficient "H_{co}" can be evaluated from the outer effective heat transfer coefficient H'_{co} using Eq. (9). The ratio of A_f/A_o is the key factor in the physical verification of the two-node model. The area A_o is the surface area of the exposed yarns to the airflow. The fabric is visualized as made up of N outer node cylinders of diameter D_o. Woven fabrics are 1–2 yarn diameter in thickness. If the fabric is treated as two layers of equally spaced parallel yarns running in perpendicular directions, then the cylinders diameter can be reasonably taken as half the thickness ($D_o=t_f/2$),

i.e., the yarns that make up the fabric are on the order of 0.5 mm diameter which is of the same order as the fabric thickness or less. The fabric effective porosity ε_f can then be used to find N as:

$$N = 2\frac{(1-\varepsilon_f)Wt_f}{\pi D_o^2} \tag{21a}$$

Then using Eq. (10), the external heat transfer coefficient becomes:

$$H_{Co} = H'_{Co}\frac{LW}{\pi D_o LN}, \quad A_f = LW \ \& \ A_o = \pi D_o LN \tag{21b}$$

Using $D_O = t_f/2$, the area ratio A_f/A_o becomes:

$$\frac{A_f}{A_o} = \frac{1}{4(1-\varepsilon_f)} \tag{21c}$$

Much of the porosity comes from the void space within the yarn. However, the restriction to flow within the yarn is much greater than the restriction to flow between the yarns. Most of the airflow will go through the lager pores between the yarns and the air within the yarn is treated as immobile and does not contribute to the external convection. So the effective porosity, ε_f, would only reflect the space between the yarns and it is of the order of 50 percent of the volume compared to the total porosity of 80 percent. The Nusselt number correlation for laminar cross-flow around cylinders, presented in ASHRAE Handbook of Fundamentals [17] is given by:

$$(\mathrm{Nu}_{Do})_{CF} = 0.32 + 0.43\,\mathrm{Re}_{Do}^{(0.52)} \tag{22}$$

where Re_{Do} is the air flow Reynolds number. The tube flow heat transfer coefficient can then be found as $(H_{co})_{CF} = \mathrm{Nu}_{Do}.k_{\mathrm{air}}/D_o$, where k is the thermal conductivity of air. The calculations are done for air properties at 300 K, effective porosity of 0.5 and for D_o/t_f ratio of 0.5. The accuracy of general, wide-range correlations is often only about ± 30 percent. Figure 7 shows a plot of the heat transfer coefficients obtained from the experimental model and from the cross flow and internal flow models. The predicted convective heat transfer coefficients by cross flow physical model is substantially higher than our empirical model. It is expected to measure lower heat transfer coefficients through the fabric considering that the correlations used were based on aligned cylinders in two rows, while the exact physical situation has these cylinders woven perpendicular to each other. This imposes additional resistance to heat convection. Note that the two-node empirical results are still within the same order of magnitude of the physical cross flow over cylinders indicating a strong relationship to the real physical aspects of the flow in such a complex domain as the fabric. At high flow rate, the measured and predicted outer-node temperatures are better correlated. Generalization of the model can be done when more experiments are performed on other types of fabric material.

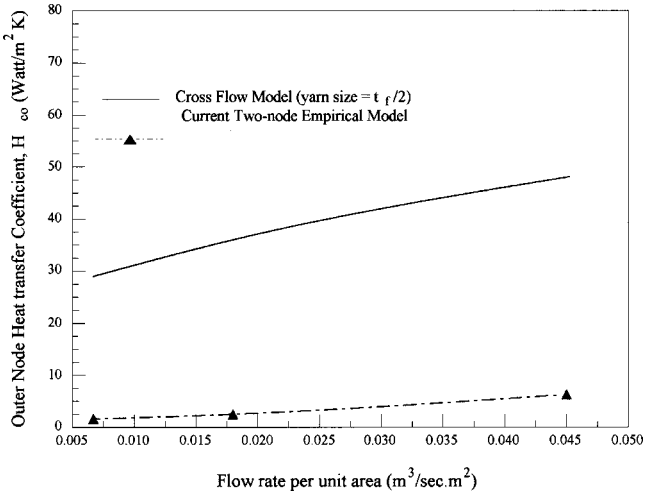

Fig. 7 Plot of the heat transfer coefficients obtained from the experimental model and from the cross flow model at $D_o/t_f = 0.5$

Inner Heat Conductance Model. The internal conductance coefficient H_{ci} for the inner node must be smaller than the overall conductance of the fabric solid, since the inner node encloses the micro immobile air pores. This will be a check on the limiting value of H_{ci}. The internal node size, $(D_i \cong 0.63D_o)$, is based on the fact that the mass fraction of the outer node γ is taken as 0.6. The value of H_{ci} was 2.35 W/K m^2 at $D_o/t_f = 0.5$. From the dry resistance data of the fabric, which is 0.029 m^2°C/Watt, the conductance of the solid fabric can be found and compared to H_{ci}. Taking the fabric total porosity ε_t of 0.8, $t_f = 0.001$ and $k_{\mathrm{air}} = 0.027$ W/Km, and considering the solid yarn and void space represent layers in parallel, then thermal conductance can be found from:

$$\frac{1}{0.029} = \frac{(1-\varepsilon_t)k_{\mathrm{yarn}}}{t_f} + \frac{k_{\mathrm{air}} \times \varepsilon_t}{t_f} \tag{23}$$

Solving for conductivity of the solid yarn gives $k_{\mathrm{yarn}} = 0.016$ W/Km and a yarn conductance $U_{\mathrm{yarn}} = (k_{\mathrm{yarn}}/t_f) = 6.1$ W/K m^2. The solid yarn conductance is higher than the empirical H_{ci}, which is expected.

Conclusion

The effect of the coupled convection heat and mass exchange within the clothing system is experimentally investigated and theoretically modeled to determine the heat and mass transfer coefficients between the air penetrating the void space and the solid fiber as a function of the velocity of penetrating air. The theoretical analysis is based on a two-node adsorption model of the fibrous medium. The simulation results are used for determining the heat and mass transfer coefficients between the air penetrating the void space and the solid fiber as function of the velocity of penetrating air by finding those transport coefficients that best fit and predict the experimentally measured transient regain in the fiber.

The heat and mass transfer coefficients that are determined empirically from the model and experiment are then compared with limiting values that are expected when a simple physical model of the fiber and airflow within it is used. The physical model of the system as a cross flow of air over a group of cylinders (yarns) has given higher coefficients than the empirical values of the two-node model as it should.

The developed model could be ultimately incorporated into human body simulations to better predict the transient response of a walking human. The ventilation parameters, when evaluated for other types of fabrics, may also be used in fabric selection of garment design for various human activities.

Acknowledgments

The authors wish to thank the Institute of Environmental Research at Kansas State University for allowing the use of their facilities. The authors greatly acknowledge the support of the University Research Board of the American University of Beirut Grant DCU-179960-73417. In addition, the help of Mr. Nizar Awar in performing the simulations is greatly acknowledged.

Nomenclature

A_f = area of the fabric (m^2)
A_i = inner node area in contact with the outer node (m^2)
A_o = outer-node exposed surface area to air flow (m^2)
C_f = fiber specific heat (J/kg K)
D_o = outer-node diameter or yarn diameter

Er = evaporative resistance of the cotton fiber (=0.00505 m^2kPa/W)
h_{fg} = heat of vaporization of water (J/kg)
h_{ad} = heat of adsorption (J/kg)
H_{ci} = conduction heat transfer coefficient between inner node and outer node (W/m^2K)
H_{co} = convection heat transfer coefficient between outer node and air flowing through fabric (W/m^2K)
H_{mi} = diffusion mass transfer coefficient between inner node and outer node (kg/m^2 kPa sec)
H_{mo} = convection mass transfer coefficient between outer node and air flowing through fabric (kg/m^2 kPa sec)
k_{air} = air thermal conductivity (W/mK)
L = fabric length (m)
N = number of cylindrical yarns in the fabric sample
P_a = air vapor pressure (kPa)
Nu = Nusselt number
P_i = vapor pressure of water vapor adsorbed in inner node (kPa)
P_o = vapor pressure of water vapor adsorbed in outer node (kPa)
Pr = Prandtl number
R = total regain in fabric (kg of adsorbed H_2O/kg fiber)
Re_{Do} = Reynolds number of the air flow based on the effective pore size
RH = relative humidity
t = time (s)
T = Temperature (°C or K)
t_f = fabric thickness (m)
u_{ad} = internal energy of water in adsorbed state (J/kg H_2O)
u_f = total internal energy of fiber containing adsorbed H_2O (J/kg of dry fiber)
W = fabric width (m)

Greek

ε = fabric emissivity
ε_f = fabric effective porosity
ε_t = fabric total porosity
ρ = mass density of fabric (kg/m^3)
γ = outer node mass fraction
σ = Stefan-Boltzman constant= 5.669×10^{-8} W/m^2K^4

Subscripts:

a = air
CF = cross flow over group of cylinders
i = inner node
o = outer node

References

[1] Henry, P. S. H., 1939, ''Diffusion in Absorbing Media,'' Proc. R. Soc. London, Ser. A, **171A**, pp. 215–241.
[2] Nordan, P., and David, H. G., 1967, ''Coupled Diffusion of Moisture and Heat in Hygroscopic Textile Mafariah,'' Int. J. Heat Mass Transf., **10**, pp. 853–866.
[3] Li, Y., and Holcombe, B. V., 1992, ''A Two Stage Sorption Model of the Coupled Diffusion of Moisture and Heat in Wool Fabrics,'' Text. Res. J., **62(4)**, pp. 211–217.
[4] Farnworth, B., 1986, ''A Numerical Model of Combined Diffusion of Heat and Water Vapor Through Clothing,'' Textile Res. Inst., **56**, pp. 653–655.
[5] Jones, B. W., and Ogawa, Y., 1993, ''Transient Interaction Between the Human and the Thermal Environment,'' ASHRAE Trans., **98**, Part 1, pp. 189–195.
[6] Minkowycz, W. J., Haji-Sheikh, A., and Vafai, K., 1999, ''On Departure From Local Thermal Equilibrium in Porous Media Due to a Rapidly Changing Heat Source: The Sparrow Number,'' Int. J. Heat Mass Transf., **42**, pp. 3373–3385.
[7] Gibson, P. 1996, ''Governing Equations for Multiphase Heat and Mass Transfer in Hydroscopic Porous Media With Applications to Clothing Materials,'' Technical Report NATICK/TR-95/004 by United States Army Natick Research, pp. 105; 115–117.
[8] Gibson, P., Kendrick, C., Rivin, D., Sicuranza, L., and Charmchi, M., 1995, ''An Automated Water Vapor Diffusion Test Method for Fabrics, Laminates, and Films,'' Journal of Coated Fabrics, **24**.
[9] Gibson, P., and Charmchi, M., 1996, ''Convective and Diffusive Energy and Mass Transfer in Hygroscopic Porous Textile Materials,'' *Proceedings of the 1996 International Congress & Exposition*, ASME Winter Annual Meeting, No. 96-WA/HT-27, Atlanta, GA, November 17–22.
[10] Gibson, P., and Charmchi, M., 1997, ''The Use of Volume-Averaging Techniques to Predict Temperature Transients Due to Water Vapor Sorption in Hygroscopic Porous Polymer Materials,'' J. Appl. Polym. Sci., **64**, pp. 493–505.
[11] Gibson, P., and Charmchi, M., 1997, ''Coupled Heat and Mass Transfer Through Hygroscopic Porous Materials—Application to Clothing Layers,'' J. of the Society of Fiber Science and Technology, Japan, **35**, pp. 183–194.
[12] Harter, K. L., Spivak, S. M., and Vigo, T. L., 1981, ''Applications of the Trace Gas Technique in Clothing Comfort.'' Textile Research, **51**, pp. 345–355.
[13] Lotens, W., 1993, ''Heat Transfer from Humans Wearing Clothing,'' Doctoral thesis, published by TNO Institute for Perception, Soesterberg, The Netherlands, pp. 34–37.
[14] Holman, J. P. 1997, *Heat Transfer*, McGraw-Hill, 8th ed., New York, p. 488, Ch. 8.
[15] Zhao J., 1995, ''Computer Modeling for Estimation of Effect of Walking on Clothing Insulation,'' M. S. thesis, Kansas State University, Manhattan, KS.
[16] Mortan, W. E., and Hearle, L. W., 1975, *Physical Properties of Textile Fibers*, Heinemann, London.
[17] *ASHRAE Handbook of Fundamentals*, 1997, American Society of Heating, Refrigerating and Air conditioning Engineers, Atlanta.
[18] Oohori, T., Brglund, L. G., and Gagge, A. P., 1985, ''Comparison of Current Two Parameters Indices of Vapor Permeation of Clothing—As Factors Governing Thermal Equilibrium and Human Comfort,'' ASHRAE Trans., **90**, Part II, pp. 85–101.
[19] Hyland, R. W., and Wexler, A., 1983, ''Formulations for the Thermodynamic Properties of the Saturated Phases of H_2O From 173.15 K to 473.15 K,'' ASHRAE Trans., **89**, pp. 500–519.
[20] Walpole, R. E., and Meyers, R. 1985, *Probability and Statistics for Engineers and Scientists*, Third Edition, Collier Macmillan, New York, p. 347.

M. Greiner
ASME Mem.
Professor of Mechanical Engineering,
University of Nevada,
Reno, NV 89557
e-mail: greiner@unr.edu

P. F. Fischer
Mathematics and Computer Science Division,
Argonne National Laboratory,
Argonne, IL 60439
e-mail: fischer@mcs.anl.gov

H. M. Tufo
Department of Computer Science,
University of Chicago,
Chicago, IL 60637
e-mail: hmt@cs.uchicago.edu

Two-Dimensional Simulations of Enhanced Heat Transfer in an Intermittently Grooved Channel

Two-dimensional Navier-Stokes simulations of heat and momentum transport in an intermittently grooved passage are performed using the spectral element technique for the Reynolds number range $600 \leqslant Re \leqslant 1800$. The computational domain has seven contiguous transverse grooves cut symmetrically into opposite walls, followed by a flat section with the same length. Periodic inflow/outflow boundary conditions are employed. The development and decay of unsteady flow is observed in the grooved and flat sections, respectively. The axial variation of the unsteady component of velocity is compared to the local heat transfer, shear stress and pressure gradient. The results suggest that intermittently grooved passages may offer even higher heat transfer for a given pumping power than the levels observed in fully grooved passages. [DOI: 10.1115/1.1459730]

Keywords: Channel Flow, Computational, Enhancement, Forced Convection, Instability

Introduction

Engineering devices frequently employ enhanced heat transfer surfaces [1]. Fins are typically used to extend surface areas while offset strips are commonly used to promote thin boundary layers. In recent years, a number of configurations that increase fluid mixing by triggering flow instabilities have been considered. Transversely grooved channel [2–5] passages with eddy promoters [6,7] and communicating channels [8] all contain fairly large features whose sizes are roughly half the channel wall to wall spacing. These structures are designed to excite normally damped Tollmien-Schlichting waves at moderately low Reynolds numbers.

The current authors have presented a series of articles on heat transfer augmentation in rectangular cross section passages with contiguous grooves cut into the walls. Experimental flow visualizations in a long grooved channel downstream of a laminar flat passage show that two-dimensional waves appear after an initial quiescent development length [9]. Unsteadiness is first observed thirty-five hydraulic diameters downstream of the first groove at a Reynolds number of $Re=350$. As the Reynolds number is increased, the onset moves upstream and the flow behavior at a given location becomes increasingly three-dimensional. Experimental and numerical results in a passage with eddy promoters indicate that the instability that leads to unsteady flow is convective rather than absolute in nature [10]. Measurements using air show that fully developed heat transfer is enhanced relative to laminar flat channel flow by as much as a factor of 4.6 at equal Reynolds numbers and by a factor of 3.5 at equal pumping powers [11,12].

Numerical simulations of fully developed convection in transversely grooved passages were performed using the spectral element technique for $Re \leqslant 2000$ [13,14]. Those simulations employed three-dimensional computational domains that represented one periodicity cell of the contiguously grooved passage. The pressure gradient and heat transfer results were within 20 percent of the measured values. At $Re=1000$ *two*-dimensional simulations gave Nusselt number values that were 20 percent below *three*-dimensional results while friction factors were smaller by a factor of two. This suggests that three-dimensionality strongly affects the transport characteristics of these flows, especially drag.

Experimental measurements in a flat passage downstream of a grooved channel were performed for Reynolds number range $1500 \leqslant Re \leqslant 5000$ [15,16,17]. These measurements show that the heat transfer coefficient remained high for a substantial distance in the flat region. The pressure gradient dropped down to the flat passage value much more rapidly, especially for $Re > 2500$. As a result, the heat transfer for a given pumping power was even greater in the first five hydraulic diameters of the decay region than in the grooved passage itself.

Three-dimensional Navier-Stokes simulations in a flat passage downstream of a *fully developed* grooved channel were performed for $405 \leqslant Re \leqslant 764$ [17]. The grooved channel had transverse grooves cut symmetrically into both walls. Two different computational sub-domains were employed. The first represented one periodicity cell of a continuously grooved passage. It had periodic inflow/outflow boundary conditions in order to simulate fully developed flow. The second sub-domain consisted of a single groove cell coupled to a flat passage at the downstream end. The inflow conditions to the grooved/flat sub-domain were taken from the outflow of the fully developed domain. Unsteady flow from the grooved region persisted several groove-lengths into the flat passage. This unsteadiness increased both local heat transfer and pressure gradient relative to steady flat passage flow. Moreover, the heat transfer for a given pumping power in the first three groove-lengths of the flat passage was even greater than the high levels observed in a fully developed grooved passage. However, the numerical Nusselt number decayed more rapidly in the flat passage than was expected from measurements.

The favorable heat transfer versus pumping power performance of flat passages downstream from grooved channels suggests that intermittently grooved passages, in which flat regions separate grooved sections, may have significant advantages in engineering heat transfer devices. However, the development of unsteady flow in grooved regions as well as the decay of unsteady flow exiting from a short grooved section must be investigated before the design of intermittently grooved passages can be optimized.

The current work is a two-dimensional numerical investigation of heat transfer in an intermittently grooved passage for the Reynolds number range $600 \leqslant Re \leqslant 1800$. The grooved portions of this passage have seven right-triangular slots cut symmetrically into opposite walls. The flat portion is also seven groove-lengths long

Contributed by the Heat Transfer Division for publication in the JOURNAL OF HEAT TRANSFER. Manuscript received by the Heat Transfer Division February 6, 2001; revision received October 17, 2001. Associate Editor: M. Faghri.

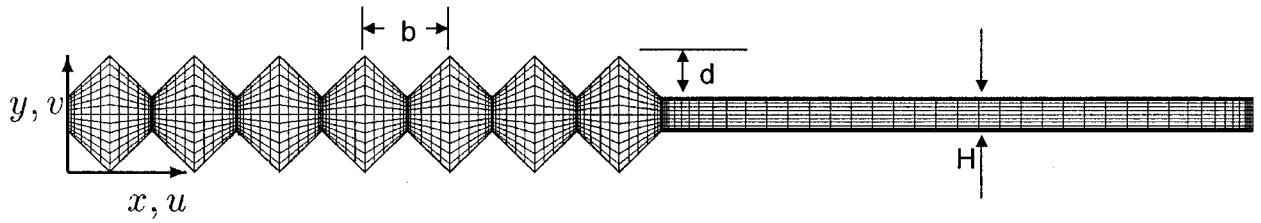

Fig. 1 Computational domain and spectral element mesh

and its wall to wall spacing is the same as the minimum spacing in the grooved section. The study of an intermittently grooved passage requires a very long computational domain. As pointed out earlier, three-dimensional simulations predict the pressure gradient in fully developed grooved passages much more accurately than two-dimensional calculations [13,14]. However, the resources to perform three-dimensional simulations in this large domain are not available at the current time. The current two-dimensional simulations afford an opportunity to learn more about this flow and provide guidance to future three-dimensional calculations.

Numerical Method

Computational Domain. Figure 1 shows the two-dimensional spectral element mesh employed in this work. The upper and lower boundaries are solid walls, and the flow is from left to right. The domain consists of seven grooves, each of length $b=0.024$ m and depth $d=0.012$ m, followed by a flat section of length $7b$. The total domain length is $L_d=14b$ and the minimum passage wall to wall spacing is $H=0.01$ m. The groove length, b, was chosen to be compatible with the wavelength of the most slowly decaying Tollmien-Schlichting waves of the outer channel flow [2]. Moreover, the groove and passage dimensions are the same as the geometries studied in our earlier work on decaying unsteadiness downstream of a grooved passage [12,16,17]. However, the current domain uses periodic inlet/outlet boundary conditions and thus models fully developed flow in an *array* of alternating grooved and flat channels.

In the spectral element method [18,19] the velocity, data and geometry are expressed as tensor-product polynomials of degree N in each of K quadrilateral spectral elements, corresponding to a total grid point count of roughly KN^2. Numerical convergence is achieved by increasing the spectral order N. The present calculations were carried out at a base resolution of $K=1960$, $N=7$ (Fig. 1 shows the K spectral elements but not the KN^2 grid points). Resolution tests were performed for $\mathrm{Re}=1200$ and $\mathrm{Re}=1800$ at $N=8$ and $N=9$, respectively. The present simulations use consistent approximation spaces for velocity and pressure, with pressure represented as polynomials of degree $N-2$ [19,20]. The momentum equations are advanced by first computing the convection term, followed by a linear Stokes solve for the viscous and pressure terms. The decoupling allows for convective Courant numbers greater than unity while maintaining second-order accuracy in time. Full details of the method can be found in [20].

The Periodic Domain. The flow is driven from left to right in the periodic domain by applying a uniform body force. The level of forcing is adjusted at each time step to ensure that the mass flow rate through the domain is invariant with time. The approach is outlined in Ghaddar et al. [21] and Fischer and Patera [22]. It exploits the linearity of the implicit Stokes problem. One first computes, in a preprocessing step, velocity and pressure fields for the Stokes problem that result from application of unit forcing, corresponding to a mean pressure gradient, in the absence of nonlinear terms. Then, at each time step, the implicit Stokes problem is solved with the nonlinear terms treated explicitly, in the absence of any mean pressure gradient. To this second solution, we add a multiple of the first that yields the desired flow rate. The multiplier corresponds to the mean pressure gradient.

The thermal problem for the periodic domain requires careful treatment. If one simply specifies zero-temperature conditions on the walls then the solution eventually decays to zero. To produce the desired spatially fully-developed state requires that the temperature profiles at the inlet and outlet be self-similar, that is,

$$T(x=L_d,y,t)=C\,T(x=0,y,t), \tag{1}$$

with $T\geqslant 0$ and $C<1$. The solution technique for computing the fully developed temperature field for constant temperature boundary conditions follows the analysis of Patankar et al. [23]. The energy equation (neglecting viscous dissipation) and associated initial and boundary conditions are

$$\frac{\partial T}{\partial t}+\vec{U}\cdot\nabla T=\alpha\cdot\nabla^2 T \tag{2a}$$

$$T(x,y,t=0)=T_{\mathrm{init}}(x,y) \tag{2b}$$

$$T(x,y,t)=0 \ \text{ on the walls} \tag{2c}$$

$$T(x=L_d,y,t)=e^{-cL_d}T(x=0,y,t) \tag{2d}$$

where $\vec{U}=(u,v)$ is the convecting velocity field determined by the hydrodynamic part of the computation. Equation $(2d)$ corresponds to the fully developed condition where the temperature profile is self-similar in each successive domain in the periodic sequence, that is $T(x+L_d,y,t)=e^{-cL_d}T(x,y,t)$ for all (x,y,t), where $e^{-cL_d}=C$. The constant c is unknown and is a parameter to be determined as part of the computation. The fact that each domain independently satisfies the homogeneous set in Eq. (2) and that we are considering fully developed solutions that are independent of T_{init} implies that the solution to Eq. (2) for each domain would yield the same value of c. Hence, c cannot be a function of x. Moreover, an energy balance on the computational domain shows that c is proportional to the log-mean Stanton number. Since the Stanton number is constant c is not function of time even when the flow is itself unsteady.

Any function satisfying the above self-similar condition has the unique decomposition $T(x,y,t)=e^{-cx}\theta(x,y,t)$, where $\theta(x+L_d,y,t)=\theta(x,y,t)$ is a periodic function. Thus, the computation of T is reduced to the computation of the periodic function θ, and the constant c. Substituting this decomposition into Eq. (2) yields:

$$\frac{\partial\theta}{\partial t}+\vec{U}\cdot\nabla\theta-\alpha\cdot\nabla^2\theta=(\alpha\cdot c^2+uc)\theta-2\alpha\cdot c\frac{\partial\theta}{\partial x} \tag{3a}$$

$$\theta(x,y,t=0)=\theta_{\mathrm{init}}(x,y) \tag{3b}$$

$$\theta(x,y,t)=0 \ \text{ on the walls} \tag{3c}$$

$$\theta(x=L_d,y,t)=\theta(x=0,y,t) \tag{3d}$$

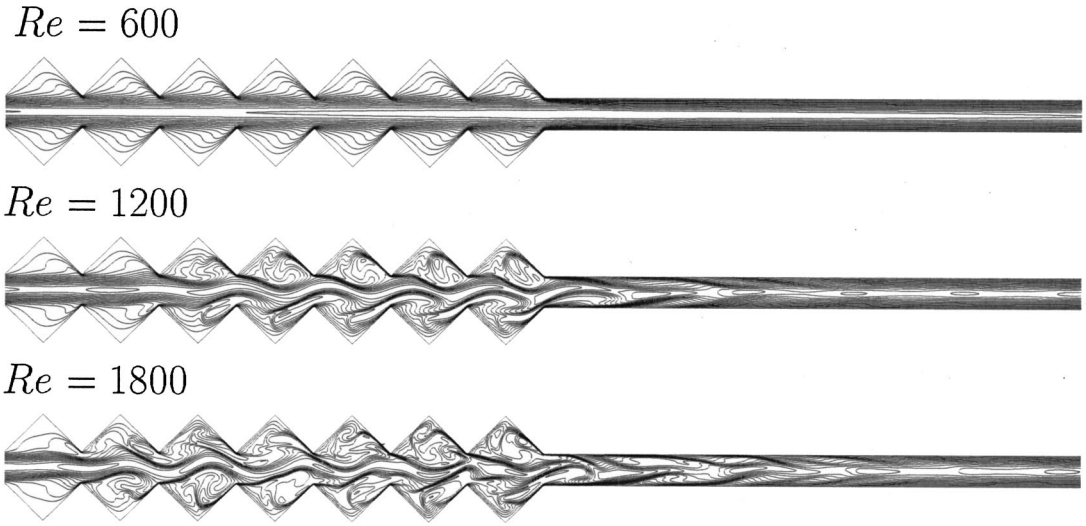

Fig. 2 Snapshot contour plots of periodic temperature θ at Re=600, 1200 and 1800

Since the fully developed solution is independent of the initial condition we may arbitrarily assign θ_{init}, which is typically set to unity when starting from rest, or to a prior converged result when starting from an existing flow-field. Equation $(3a)$ is solved using a semi-implicit time-stepping procedure similar to that of our Navier-Stokes solver. The diffusive terms are treated implicitly while the convective terms are treated explicitly. In addition, all terms on the right of Eq. $(3a)$ are treated explicitly using the latest available value for c.

In the steady state case $(\partial/\partial t=0)$, Eq. (3) constitutes an eigenproblem for the eigenpair (c,θ). The constant c corresponds to the decay rate of the mean temperature in the x-direction. As such, a larger value of c implies more rapid decay and more effective heat transfer (larger Stanton number). In the convection-dominated limit where the Peclet number $U_m D_h/\alpha$ is large, Eq. $(3a)$ becomes a linear eigenvalue problem. In this case, standard iterative methods for computing the lowest value of c (corresponding to the most slowly decaying mode in x) can be used even when the nonlinear (c^2) term in Eq. $(3a)$ is not identically zero. We find that this method accurately computes the decay rate and Nusselt numbers for steady flows in square and round ducts [24].

For steady-periodic flows with period τ, the temperature is periodic in time, implying $T(x,y,t+\tau)=T(x,y,t)$. Since c is independent of time, this implies that $\theta(x,y,t+\tau)=\theta(x,y,t)$. If the value of c is not chosen correctly, this condition will not be satisfied. Unfortunately, τ is not known a priori but is a result of the hydrodynamic part of the calculation. A robust approach to computing c is obtained by multiplying Eq. $(3a)$ by θ, integrating over the domain Ω, and simplifying to yield:

$$\frac{1}{2}\frac{d}{dt}\int_{\Omega}\theta^2 dV=\int_{\Omega}[(\alpha c^2+uc)\theta^2-\alpha\nabla\theta\cdot\nabla\theta]dV \qquad (4)$$

While we do not expect the time derivative of the average temperature (represented by the left-hand side of Eq. (4)) to be identically zero, it will in general be less than the time derivative of θ at any one point in the domain. Moreover, if we integrate the right-hand side of Eq. (4) from time t to $t+\tau$, the resultant quantity must be zero due to the temporal periodicity.

This suggests a two-tier strategy for computing c in the unsteady case. Initially, we determine c such that the right hand side of Eq. (4) is identically zero at each time step. This permits a relatively coarse but quick determination of c and θ. Once τ is well established, we use this value of c to advance θ for one or more periods, and monitor the decay or growth of $\int\theta^2\,dV$. At the end of each trial period, we adjust c until convergence is attained. Typical values of cL_d over the range of Re considered are 0.55 to 1.0, corresponding to 42 percent to 63 percent drops in mean temperature over the domain length.

The simulations at Re=600 were initialized using $u=0$ and $\theta=1$. Subsequent cases were initialized from converged results at lower Reynolds numbers. Because of the extreme length of the domain ($14b$, versus b for our earlier computations [13,14]), very long time integrations were required to reach a quasi-steady-periodic state at the higher Reynolds numbers. For example, the Re=1800 case was initiated from the Re=1200 final solution and run for a physical time of 2.9 sec (corresponding to 9.6 convective passages through the domain based on mean flow-rate and domain length) before ''steady state'' statistics were calculated. The statistics were calculated based on a simulation with spectral order $N=9$ and a time step of 0.000016 sec (corresponding to a convective Courant number of 3.0). Solution files were extracted every 100 time steps, and a total of 580 such files were used to compute the time-averaged and rms data. This sampling rate corresponds to roughly 50 samples per oscillation in the solution signal.

Adequacy of the spatial resolution was determined by comparing the results for the most difficult case (Re = 1800) computed using polynomial order $N=7$ with those obtained using $N=9$. Figures 4 and 5 show the axial variations of the fluctuating velocity and the bulk Nusselt number. The results for $N=7$ and 9 are virtually indistinguishable. The maximum difference in the fluctuating velocity is less than 4 percent of the average value. The Nusselt number is based on the *derivative* of temperature. The maximum difference is always less than 3 percent, except at the singular points located at the groove peaks. Given the unsteady nature of these flows, this close agreement indicates both adequate spatial resolution and sufficiently long time integration to obtain meaningful statistics.

The simulations were performed on 8, 16, and 32 processors of a 96 processor SGI Origin2000. Each processor is a MIPS R10000 running at 250 MHz and shares 24 GB of memory. The Re=1800, $N=9$ computation required 2.5 CPU sec/step on 32 nodes.

Results

Figure 2 shows three contour plots of the dimensionless periodic temperature θ. These plots are typical snapshots at Reynolds numbers Re=600, 1200, and 1800. In this work the Reynolds number is $\text{Re}=U_m D_H/\nu$. The average velocity through the mini-

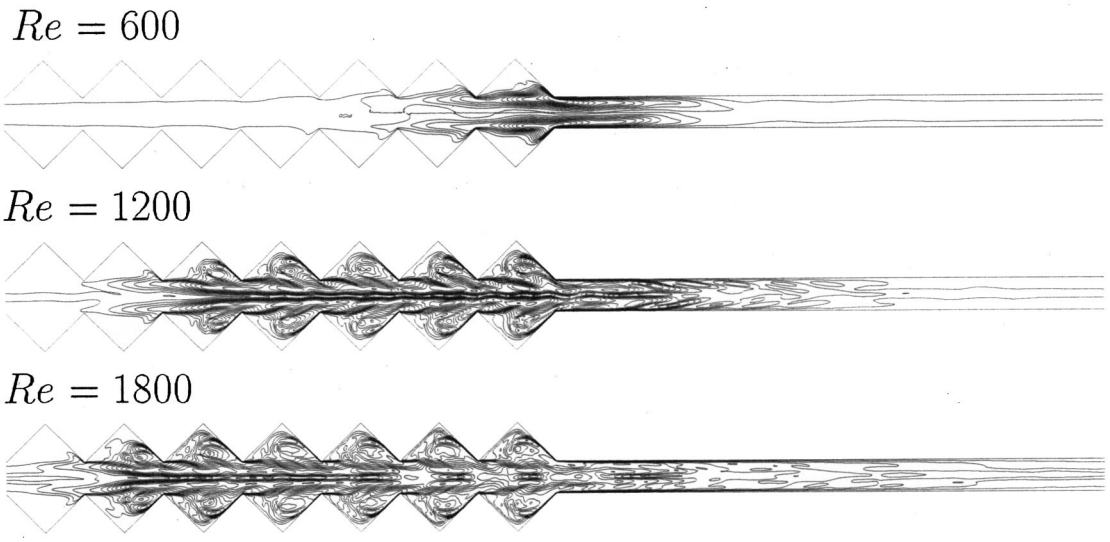

Fig. 3 Contour plots of the root-mean-squared component of periodic temperature θ_{rms} at Re=600, 1200, and 1800

mum channel cross section is $U_m=(\int_\Omega u dA)/(14bH)$, where the integration is taken over the entire area of the computational domain, Ω. The minimum channel hydraulic diameter is $D_H=2H$, and ν is the fluid kinematic viscosity. Other researchers have used the Orr-Sommerfeld definition of the Reynolds number, which is $\mathrm{Re}_{OS}=(3/8)\mathrm{Re}$ [2].

For Re=600, temperature contours lines in the open passage are virtually parallel to the x-axis. Streamline plots (not shown) indicate that the central portion of the passage has essentially no transverse motion and the grooves contain slowly turning vortices. The effect of the vortices on the contour lines in the grooves is evident. In contrast, long contiguously grooved channels exhibit two-dimensional waves for Re$\geqslant$350 [9,13,14]. The steady behavior of the current intermittently grooved passage indicates that the development length for unsteady flow at Re=600 is longer than the groove section length, $7b$. This result is consistent with the convective nature of the instability [10].

At Re=1200 a wavy structure develops in the third groove and its amplitude grows in the x-direction. This transverse motion persists for the remainder of the grooved section and for several groove-lengths into the flat region. At Re=1800, the transverse motion is stronger and more irregular than it is at Re=1200. It develops more rapidly in the grooved section and decays more slowly in the flat region.

Figure 3 shows contours plots of the root-mean-squared component of the dimensionless periodic temperature θ_{rms}, for Re =600, 1200, and 1800. While the isotherms for Re=600 in Fig. 2 are nearly parallel to the x-axis, Fig. 3 shows that some unsteadiness develops in the fifth groove and persists roughly three groove lengths into the flat region. This unsteadiness is concentrated in the region across the groove opening, and does not penetrate deeply into the grooves. The contour plots for Re=1200 and 1800 show that as the Reynolds number is increased, unsteadiness appears closer to the first groove and it persists further into the flat region. Moreover, the flow exhibits high levels of unsteadiness deep in the grooves. For Re=1800 a significant level of unsteadiness is present at the end of the flat section (entrance to the groove region).

Figure 4 shows dimensionless axial velocity unsteadiness u'/U_m versus location and Reynolds numbers. This unsteadiness is defined as $u'/U_m=(1/D_h)\int(u_{\mathrm{rms}}/U_m)dy$, where u_{rms} is the root-mean-squared deviation of the axial velocity from its local time mean value, and the integration is taken from the bottom to the top of the channel. The region $0\leqslant x/b\leqslant 7$ corresponds to the grooved portion of the domain, while $7\leqslant x/b\leqslant 14$ represents the flat section. Two traces are included for Re=1800 with spectral orders of $N=7$ and 9.

At Re=600, the velocity unsteadiness reaches maximum values of less than 2 percent near the end of the grooved section. For Re=1200, the unsteadiness grows in the first four grooves ($0\leqslant x/b\leqslant 4$), drops off slightly in the next groove ($4\leqslant x/b\leqslant 5$), and then increases in the two last grooves. The unsteadiness remains near the high values observed in the grooved section for the first half-groove-length of the flat region. It drops off very rapidly for the next two groove-lengths and then decreases at a much slower rate. For Re=1800, the unsteadiness grows rapidly in the first three grooves, drops off in the fourth groove, grows again in the next two grooves and then drops off slightly in the last groove. Once again the unsteadiness remains high in the first half-groove-length of the flat region before dropping off. Time dependent streamline plots show that the velocity field exhibits a traveling wave structure. In Fig. 4, the local rises and dips in the time-averaged data indicate that the flow field exhibits standing waves as well.

The thinner solid lines in Fig. 5 show bulk Nusselt number versus axial location and Reynolds number. A dashed horizontal line in the region $7\leqslant x/b\leqslant 14$ shows the Nusselt number in a fully developed flat passage. The thicker line in the domain $5\leqslant x/b$

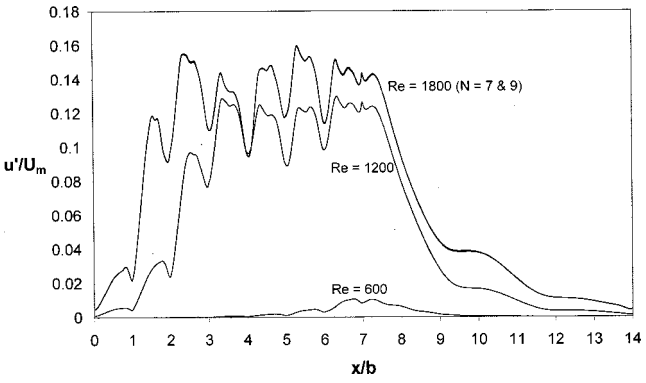

Fig. 4 Unsteady component of axial velocity versus location and Reynolds number

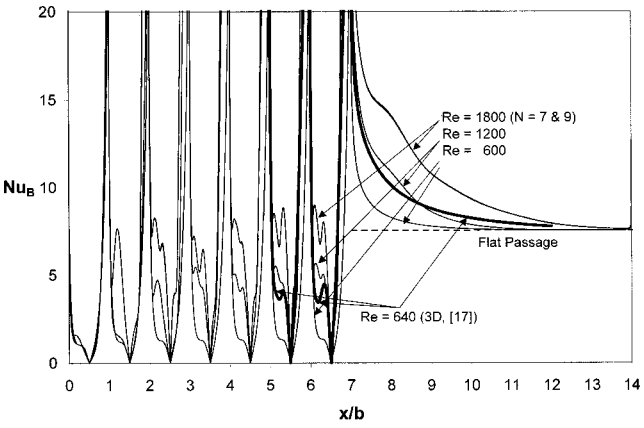

Fig. 5 Bulk Nusselt number versus location and Reynolds number

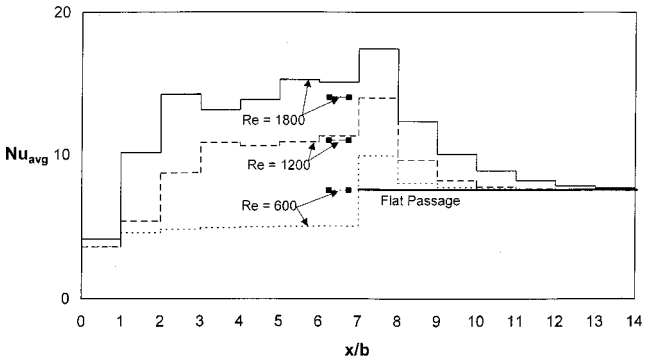

Fig. 6 Groove-length averaged Nusselt number versus location and Reynolds number

$\leqslant 12$ shows results at Re=640 from a *three-dimensional* simulation of a flat passage downstream of a *fully developed* grooved channel [17].

The bulk Nusselt number is defined as $\mathrm{Nu}_B=(D_h/k)\times(\langle q''/\Delta T_B\rangle)$, where the pointed brackets ($\langle\ \rangle$) indicate a time average. In this expression the fluid thermal conductivity is k and ΔT_B is the local temperature difference between the surface and bulk fluid. The bulk temperature at any axial location x and time t is defined as $T_B(x,t)=(\int uT\,dy)/(\int u\,dy)$, where both integrations in the y direction are taken from the bottom to the top of the domain. The heat transfer to the fluid per unit *projected* surface area is $q''(x,t)=-k(dT/dn)_{\mathrm{wall}}/m$, where T is temperature, n is the direction normal to the wall, m is the wall surface direction cosine, and the temperature gradient is evaluated at the wall. The direction cosine in the flat region is $m=1$, while it is $m=0.7071$ in the grooved region. Two traces are included for Re=1800 with spectral orders of $N=7$ and 9.

The strong singularities at $x/b=0$, 1, 2, 3, 4, 5, 6, and 7 are caused by the sharp edges of the groove peaks. At all other locations Nu_B increases with Reynolds number. The heat transfer in the first groove is very similar for all three Reynolds numbers. We see that the Nusselt number on the downstream (windward) surface ($0.5\leqslant x/b\leqslant 1$) is significantly higher than that on the upstream (leeward) side ($0\leqslant x/b\leqslant 0.5$). This is due to the location and rotation direction of the groove vortex flow. The upstream surface exhibits a local plateau centered at $x/b=0.3$. The groove vortex impinges against the wall at that location.

For Re=600, the shape of the Nusselt number profile is similar in all seven grooves. At Re=1200 the profile shape in the second groove is similar to that in the first. Its shape then changes substantially in subsequent grooves and its magnitude increases. The heat transfer on the windward side of each groove is greater than the level exhibited at Re=600. Moreover, the groove vortex impingement plateau grows stronger in the third through fifth groove. Its shape is essentially the same in the fifth, sixth and seventh grooves, indicating that the heat transfer has approached its fully developed condition. The profile shape has a number of local peaks especially on the leeward face. This suggests the time-averaged flow field has small secondary vortices that impinge against the walls at the locations of the peaks. For Re=1800, the Nusselt number profile in the second groove is substantially different form its shape in the first groove. Moreover, its shape does not appear to stabilize until the sixth or seventh groove, although it is difficult to say whether it would continue to change if the grooved section were longer.

The heat transfer at the inlet of the flat region ($x/b=7$) is well above the fully developed flat passage value for all three Reynolds numbers. Very steep velocity and temperature gradients near the walls cause this. The heat transfer for Re=600 drops to the flat passage value after three groove lengths as its wall gradients approach the fully developed levels. Examining the Re=1200 and 1800 traces shows that both the level of heat transfer enhancement and the length of the flat region where augmentation is observed increase with Reynolds number. The steeper velocity and temperature gradients as well as the higher levels of unsteadiness cause these increases. For Re=1200 and 1800, the heat transfer drop off is inflected one-half of a groove-length downstream from the grooved section. This corresponds to the location where the velocity unsteadiness in Fig. 4 begins to decrease. At Re=1800, heat transfer enhancement persists for the full length of the flat region.

The three-dimensional results for Re=640 (thicker line, Greiner et al. [17]) give heat transfer levels that are substantially higher than the current Re=600 data. As mentioned earlier, the three-dimensional results are for a flat passage downstream of a *fully developed* grooved channel. The flow in a fully developed grooved channel is unsteady for $\mathrm{Re}\geqslant 350$, while the current intermittently grooved passage is essentially steady at Re=600. The unsteady structure of the three-dimensional simulation increases the heat transfer level well beyond that predicted by the current work for Re=600. In fact, its level is closer to the current Re=1200 results. Moreover, the three-dimensional simulations do not predict the inflection at $x/b=7.5$ or the secondary vortices in the grooves.

Figure 6 shows the bulk Nusselt number averaged over different groove-length regions of the domain. A thicker solid line shows the fully developed flat passage Nusselt number. The horizontal line segments with solid squares represent *fully developed* grooved channel results from two-dimensional simulations at Re=600, 1200 and 1800 [14]. Those simulations employed a computational domain that represents one periodicity cell of the grooved channel and periodic inlet/outlet boundary conditions.

For Re=600 the average Nusselt number increases slightly for the first four grooves and then reaches a fully developed value. This value is below the flat passage level. The thermal resistance of the slowly turning groove-vortices causes this reduction in heat transfer. For Re=1200, the average heat transfer in the first groove is the same as that at Re=600, but its value increases substantially in the second, third and fourth grooves. After reaching a local maximum the heat transfer drops slightly in the fifth notch and then rises slightly in the sixth and seventh grooves. However, the heat transfer level in the last four groove-lengths is fairly uniform. Moreover, this level is greater than the value for a fully developed flat passage. The unsteady mixing at Re=1200 is sufficient to overcome the thermal resistance of the groove vortices.

At Re=1800 the heat transfer in the first groove is slightly higher than the level exhibited at Re=600 and 1200. This may be caused by the unsteadiness at the exit of the flat section (Figs. 3 and 4). The heat transfer exhibits a substantial rise in the next two

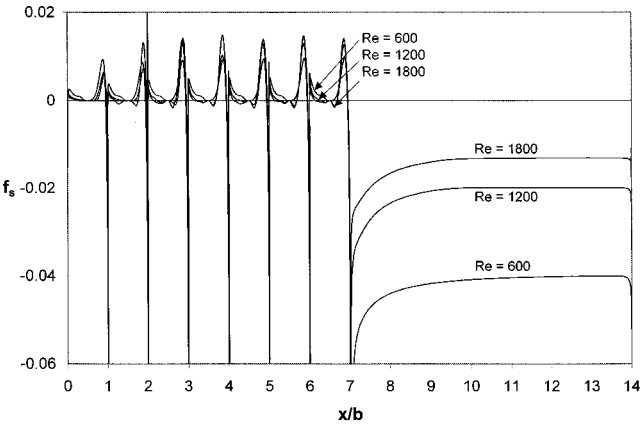

Fig. 7 Dimensionless axial shear stress versus location and Reynolds number

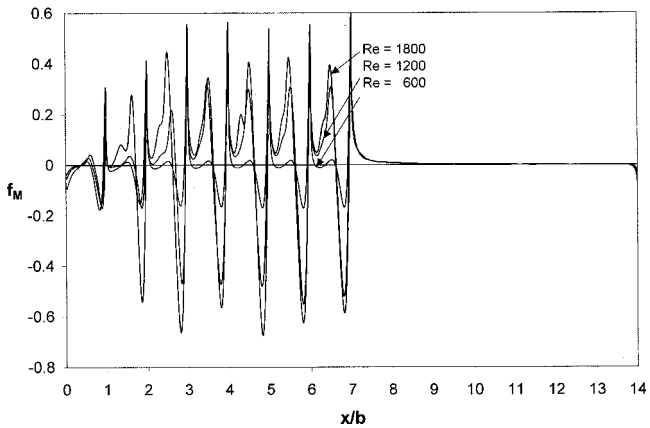

Fig. 8 Dimensionless momentum flux gradient versus location and Reynolds number

grooves. It drops in the fourth groove and rises for the next two grooves before dropping slightly in the final groove. The average Nusselt numbers in all but the first groove are greater than the fully developed flat passage value. The rise and fall of heat transfer in the interior grooves at Re=1200 and 1800 are closely correlated with the unsteady velocity levels described in Fig. 4.

At Re=600, the heat transfer in the seventh groove is substantially less than the level predicted for fully developed flow. The unsteadiness present in the fully developed simulation causes this difference. At Re=1200 and 1800 the heat transfer in the seventh groove is, respectively, 2 percent and 7 percent higher than the fully developed values.

In the flat region ($7 \leqslant x/b \leqslant 14$), the heat transfer begins at very high levels. It decreases as distance from the grooves increases, eventually approaching the fully developed rate. The heat transfer development length in the grooved region (as demonstrated by a rise in heat transfer) *decreases* as Reynolds number increases, while the heat transfer decay-length in the flat region *increases*. As a result, the length of the region of enhanced heat transfer increases with Reynolds number.

Figure 7 shows the dimensionless x-component of shear stress $f_S = 2\tau_x/\rho U_m{}^2$ versus axial location and Reynolds number. In this expression the x-component of wall shear stress is $\tau_x = -\mu(du_t/dn)_{\text{wall}}/m$, where u_t is time average component of fluid velocity tangential to the wall, ρ is the fluid density, and μ is the fluid dynamic viscosity. The strong negative singularities are caused by the sharp groove peaks at $x/b = 0$, 1, 2, 3, 4, 5, 6, and 7.

For Re=600, the shape of the shear stress profile in the grooves ($0 \leqslant x/b \leqslant 7$) has a number of similarities to the Nusselt number profiles seen in Fig. 5. For instance, the shear stress is significantly higher on the downstream surface of each groove than it is on the upstream side. Moreover, the shear stress exhibits a plateau 0.3-groove-lengths downstream from the leading edge of each groove. These similarities are caused by the analogous behavior of heat and momentum transport in the absence of strong pressure gradients.

At Re=600 the shear stress is positive throughout the grooved region (with the exception of the singular points). This indicates that the fluid near the groove surfaces is always moving in the negative x-direction. For Re=1200 and 1800, on the other hand, the shear stress is negative in certain locations. This implies that fluid in these regions moves in the *positive* x-direction, indicating the existence of secondary vortices, as described in connection with Fig. 5. In the flat region downstream of the grooves, the dimensionless shear stress is in the negative x-direction. The magnitude of the shear stress in the flat region is much higher than it is in the grooved region.

Comparing Figs. 5 and 7 shows that the wall shear stress is analogous to heat transfer. However, the *pressure gradient* is the drag characteristic that affects the pumping power per unit passage volume required of the prime mover, $(dp/dx)U_m$. This prime mover power is of great importance to many engineering devices. We now relate the Fanning pressure gradient $f_P = (-dF_p/dx)(1/2\rho U_m{}^2)$ to the wall shear stress. In this expression the time averaged pressure force is $F_p = \langle \int p\, dy \rangle$, where p is the local pressure and the integration is performed from the top to the bottom of the channel. A time-averaged force balance on a control volume of axial length dx shows that the Fanning pressure gradient is composed of wall shear stress and momentum flux gradient components, that is $f_P = f_M - f_S$. The axial gradient of the momentum flux is defined as $f_M = d/dx[\int(\langle u^2 \rangle/U_m{}^2)dy]$, where $\langle u^2 \rangle$ is the time average of the square of the x-velocity, and the integration is performed from the bottom to the top of the passage.

Figure 8 shows the axial gradient of the momentum flux f_M versus location and Reynolds number. In the first groove, the momentum flux gradient is similar for all three Reynolds numbers. In subsequent grooves, the magnitude of f_M increases with Reynolds numbers. This indicates that the fluid experiences large levels of acceleration and deceleration. In the flat region downstream of the grooves, the axial variation of the velocity is small and f_M drops to zero very quickly. Comparing Figs. 7 and 8 (and noting the y-axis scales), we see that the magnitude of the momentum flux gradient is much larger than that of the shear stress in the grooved regions, while the opposite is true in the flat portion of the passage. The local Fanning pressure gradient is the difference between the traces in these figures, $f_P = f_M - f_S$.

Figure 9 shows the product $f_{P,\text{avg}}\,\text{Re}$ versus location and Reynolds number. In this product, $f_{P,\text{avg}}$ is the Fanning pressure gradient averaged over different groove-length regions. The dotted

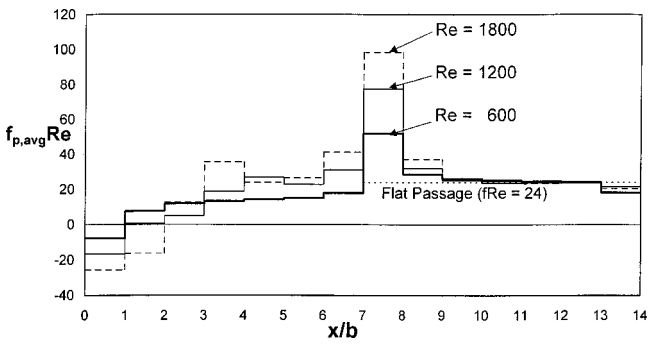

Fig. 9 Groove-length average Fanning pressure gradient versus location and Reynolds number

horizontal line in the region $7 \leqslant x/b \leqslant 14$ shows the fully developed flat channel value $f_{P,\mathrm{avg}}\,\mathrm{Re}=24$. In the first groove $f_{P,\mathrm{avg}}\,\mathrm{Re}$ is negative for all three Reynolds numbers indicating that the dimensional pressure actually *increases* across this region. This pressure rise is caused by fluid deceleration. The expansion of the channel cross section as the flow exits a flat passage and enters the grooved region causes this deceleration. For $\mathrm{Re}=600$, the friction factor becomes positive in the second groove and continues to increase with distance from the inlet of the grooved section. The increment in $f_{P,\mathrm{avg}}\,\mathrm{Re}$ decreases with increasing x/b until the last groove. The pressure decrease across the last groove is larger than in the internal grooves because the flow accelerates as it exits the grooved section and enters the flat region.

For $\mathrm{Re}=1200$, $f_{P,\mathrm{avg}}\,\mathrm{Re}$ increases for the first five grooves, then decreases in the next groove, and finally increases in the last groove. The pressure gradient for $\mathrm{Re}=1800$ increases for the first four grooves, decreases in the next groove, and rises in the final two grooves. We see that the pressure gradient development length in the grooved section decreases with Reynolds number.

In the first groove-length of the flat region, $f_{P,\mathrm{avg}}\,\mathrm{Re}$ is very high for all three Reynolds numbers due to the high shear stress (sharp velocity gradients) at $x/b=7$. The pressure gradients then approach their fully developed values after only three groove lengths. The pressure gradient in the last groove-length of the flat region is below the fully developed flat passage value. This is due to the decelerating flow caused by the expanding cross sectional area at $x/b=14$.

Comparing Figs. 6 and 9, we see that while the heat transfer remains enhanced for up to six groove-lengths in the flat region, the pressure gradient drops back to the flat passage value in only three groove lengths. Moreover, while the decay length for heat transfer increases with Reynolds numbers, the pressure gradient decay length is rather insensitive to Reynolds number.

Conclusions

Two-dimensional Navier-Stokes simulations of heat and momentum transport in an intermittently grooved passage were performed using the spectral element technique for the Reynolds number range $600 \leqslant \mathrm{Re} \leqslant 1800$. The computational domain had seven contiguous transverse grooves cut symmetrically into opposite walls, followed by a flat section of the same length. This domain employed periodic inflow/outflow boundary conditions.

The flow is essentially steady at $\mathrm{Re}=600$. However, traveling waves develop near the inlet of the grooved section at $\mathrm{Re}=1200$ and 1800 and persist several groove lengths into the flat region. The axial variation of unsteady velocity within the grooved section is closely correlated with increases in heat transfer, shear stress and pressure gradient. In the grooved region the development lengths for heat transfer and pressure gradient both decrease with increasing Reynolds number. While the length of the flat region where heat transfer augmentation is observed increases with Reynolds number, the pressure gradient returns to the flat passage value in roughly three groove lengths for the entire Reynolds number range considered in this work.

The current two-dimensional simulations in an intermittently grooved passage exhibit a number of differences from three-dimensional results in fully developed grooved channels and downstream flat passages. However the current calculations will provide guidance for future three-dimensional calculations in intermittently grooved passages. Finally, these results suggest that intermittently grooved passages may offer very favorable heat transfer versus pumping power performance for engineering devices.

Acknowledgments

National Science Foundation Grant CTS-9501502 supported this work. The work of P.F. Fischer was supported by the Mathematical, Information, and Computational Sciences Division subprogram of the Office of Advanced Scientific Computing Research, U.S. Department of Energy, under Contract W-31-109-Eng-38. The work of H.M. Tufo was supported by the Department of Energy under Grant number B341495 to the Center on Astrophysical Thermonuclear Flashes at University of Chicago, and by the University of Chicago.

Nomenclature

b = groove length
c = decay constant
d = groove depth
D_h = minimum hydraulic diameter, $2H$
f_M = dimensionless momentum flux gradient
f_P = fanning pressure gradient
f_S = dimensionless axial shear stress
H = minimum channel wall to wall spacing
k = fluid thermal conductivity, 0.0263 W/m°C
K = number of spectral elements
L_d = domain length, $14b$
N = spectral element order
Nu_B = bulk Nusselt number based on projected area
Pr = fluid molecular Prandtl number, 0.70
Re = Reynolds number, $U_m D_h/\nu$
t = time
T = temperature
T_b = bulk temperature
u, v = velocity components in the x and y directions
u' = axial velocity unsteadiness
U_m = mean x-velocity at the minimum channel cross-section

Greek

α = thermal diffusivity, 2.63×10^{-5} m^2/s
ν = fluid kinematic viscosity, 1.84×10^{-5} m^2/s
θ = periodic temperature
ρ = fluid density, 1.006 kg/m^3
τ = period of local time variations
τ_x = x-component of wall shear stress
Ω = computation domain

References

[1] Webb, R. L., 1994, *Principles of Enhanced Heat Transfer*, John Wiley & Sons, New York.
[2] Ghaddar, N. K., Korczak, K., Mikic, B. B., and Patera, A. T., 1986, "Numerical Investigation of Incompressible Flow in Grooved Channels. Part 1: Stability and Self-Sustained Oscillations," J. Fluid Mech., **168**, pp. 541–567.
[3] Greiner, M., 1991, "An Experimental Investigation of Resonant Heat Transfer Enhancement in Grooved Channels," Int. J. Heat Mass Transf., **24**, pp. 1383–1391.
[4] Roberts, E. P. L., 1994, "A Numerical and Experimental Study of Transition Processes in an Obstructed Channel Flow," J. Fluid Mech., **260**, pp. 185–209.
[5] Lee, B. S., Kang, I. S., and Lim, H. C., 1999, "Chaotic Mixing and Mass Transfer Enhancement by Pulsatile Laminar Flow in an Axisymmetric Wavy Channel," Int. J. Heat Mass Transf., **42**, pp. 2571–2581.
[6] Kozlu, H., Mikic, B. B., and Patera, A. T., 1988, "Minimum-Dissipation Heat Removal by Scale-Matched Flow Destabilization," Int. J. Heat Mass Transf., **31**, pp. 2023–2032.
[7] Karniadakis, G. E., Mikic, B. B., and Patera, A. T., 1988, "Minimum-Dissipation Transport Enhancement by Flow Destabilization: Reynolds Analogy Revisited," J. Fluid Mech., **192**, pp. 365–391.
[8] Amon, C. H., Majumdar, D., Herman, C. V., Mayinger, F., Mikic, B. B., and Sekulic, D. P., 1992, "Experimental and Numerical Investigation of Oscillatory Flow and Thermal Phenomena in Communicating Channels," Int. J. Heat Mass Transf., **35**, pp. 3115–3129.
[9] Greiner, M., Chen, R.-F., and Wirtz, R. A., 1990, "Heat Transfer Augmentation Through Wall-Shaped-Induced Flow Destabilization," J. Heat Transfer , **112**, pp. 336–341.
[10] Schatz, M. F., Tagg, R. P., Swinney, H. L., Fischer, P. F., and Patera, A. T., 1991, "Supercritical Transition in Plane Channel Flow with Spatially Periodic Perturbations," Phys. Rev. Lett., **66**, No. 12, pp. 1579–1582.
[11] Greiner, M., Chen, R.-F., and Wirtz, R. A., 1991, "Enhanced Heat Transfer/Pressure Drop Measured From a Flat Surface in a Grooved Channel," J. Heat Transfer, **113**, pp. 498–500.
[12] Wirtz, R. A., Huang, F., and Greiner, M., 1999, "Correlation of Fully Devel-

oped Heat Transfer and Pressure Drop in a Symmetrically Grooved Channel,'' J. Heat Transfer, **121**, pp. 236–239.
[13] Greiner, M., Spencer, G., and Fischer, P. F., 1998, ''Direct Numerical Simulation of Three-Dimensional Flow and Augmented Heat Transfer in a Grooved Channel,'' J. Heat Transfer, **120**, pp. 717–723.
[14] Greiner, M., Faulkner, R. J., Van, V. T., Tufo, H. M., and Fischer, P. F., 2000, ''Simulations of Three-Dimensional Flow and Augmented Heat Transfer in a Symmetrically Grooved Channel with Constant Temperature Walls,'' J. Heat Transfer, **122**, pp. 653–660.
[15] Greiner, M., Chen, R.-F., and Wirtz, R. A., 1995, ''Augmented Heat Transfer in a Recovery Passage Downstream From a Grooved Section: An Example of Uncoupled Heat/Momentum Transport,'' J. Heat Transfer, **117**, pp. 303–308.
[16] Huang, F., 1998, ''Experimental Investigation of Fully-Developed Augmented Convection in a Symmetrically Grooved Channel,'' Masters of Science Degree thesis, University of Nevada, Reno, NV, May 1998.
[17] Greiner, M., Fischer, P. F., Tufo, H. M., and Wirtz, R. A., 2002, ''Three Dimensional Simulations of Enhanced Heat Transfer in a Flat Passage Downstream From a Grooved Channel,'' J. Heat Transfer, **124**(1), pp. 169–176.
[18] Patera, A. T., 1984, ''A Spectral Element Method for Fluid Dynamics; Laminar Flow in a Channel Expansion,'' J. Comp. Phys., **54**, pp. 468–488.
[19] Maday, Y., and Patera, A. T., 1989, ''Spectral Element Methods for the Navier-Stokes Equations,'' *State of the Art Surveys on Computational Mechanics*, A. K. Noor and J. T. Oden, eds., ASME, New York, pp. 71–143.
[20] Fischer, P. F., 1997, ''An Overlapping Schwarz Method for Spectral Element Solution of the Incompressible Navier-Stokes Equations,'' J. Comp. Phys., **133**, pp. 84–101.
[21] Ghaddar, N. K., Karniadakis, G. E., and Patera, A. T., 1986, ''A Conservative Isparametric Spectral Element Method for Forced Convection: Application to Fully Developed Flow in Periodic Geometries,'' Numer. Heat Transfer, **9**, pp. 277–300.
[22] Fischer, P. F., and Patera, A. T., 1992, ''Parallel Spectral Element Solutions of Eddy-Promoter Channel Flow,'' *Proc. of the European Research Community on Flow Turbulence and Computation Workshop*, Lausanne, Switzerland, Cambridge University Press, pp. 246–256.
[23] Patankar, S. V., Liu, C. H., and Sparrow, E. M., 1977, ''Fully Developed Flow and Heat Transfer in Ducts Having Streamwise Periodic Variations of Cross-Sectional Area,'' J. Heat Transfer, **99**, pp. 180–186.
[24] Kays, W. M., and Crawford, M. E., 1993, *Convection Heat and Mass Transfer*, 3rd edition, McGraw-Hill, New York.

Local and Average Characteristics of Heat/Mass Transfer Over Flat Tube Bank Fin With Four Vortex Generators per Tube

L. B. Wang

F. Ke

S. D. Gao

Y. G. Mei

Department of Mechanical Engineering,
Lanzhou Railway Institute,
Lanzhou, Gansu 730070, P. R. of China

The analogy between heat and mass transfer has been used to obtain local and average heat transfer characteristics over a complete flat tube-fin element with four vortex generators (VGs) per tube. Several types of surfaces involved in heat transfer process such as fin surface mounted with VGs, its back surface (mounted without VGs) and flat tube surface are considered. The mass transfer experiments are performed using naphthalene sublimation method. The effects of the fin spacing and VG parameters such as height and attack angle on heat transfer and pressure drop are investigated. The comparisons of heat transfer enhancement with flat tube-fin element without VG enhancement under three constraints are carried out. The local Nusselt number distribution reveals that VGs can efficiently enhance the heat transfer in the region near flat tube on fin surface mounted with VGs. On its back surface the enhancement is almost the same as on the fin surface mounted with VGs but enhanced region is away from flat tube wall with some distance. Average results reveal that increasing of VG height and attack angle increases the enhancement of heat transfer and pressure drop, whereas small fin spacing causes greater increase of pressure drop. The heat transfer performance, correlations of Nusselt number and friction factor are also given. [DOI: 10.1115/1.1423905]

Keywords: Enhancement, Finned Surfaces, Heat Transfer, Heat Exchangers, Vortex

Introduction

Fin and tube heat exchangers are employed in a wide variety of engineering applications. Flat tube bank fin heat exchangers (typically shown in Fig. 1) are frequently used in transportation equipment due to their significant advantages comparing with circular tube bank fin heat exchangers. Generally, a flat tube has a smaller hydraulic diameter than that of a circular tube with the same cross section area; and in particular the flat tube bank fin heat exchanger has a small pressure drop characteristic. Louvred fins have been frequently used in flat tube bank fin heat exchangers to enhance heat transfer, but the heat transfer enhancement can be achieved only at the very beginning of the leading edges of Louvred fin [1–3] and the pressure drop increases greatly [2,3]. Since flat tube bank fin has small fin efficiency, the heat transfer enhancement on large part of louvred fin is inefficient comparing with the penalty of pressure drop increase.

Wing-type vortex generators (VGs), which have been intensively investigated recently [4–7], can generate developing boundary layers, swirl and flow destabilization mechanisms for passive heat transfer enhancement. Many research works on heat transfer enhancement with VGs have been carried out for plate heat exchangers and finned circular tubes. For a finned flat tube with a mounted delta winglet pair, experimental investigations show that the effect of delta winglet type VG pair on heat transfer enhancement is more pronounced than that of a finned circular tube and the VG pair should be located at the upstream side of the flat tube with a distance of two tube widths between the winglets [6,7]. Liquid crystal thermography is used to deduce the local heat transfer rate in these studies. In order to get local heat transfer coefficient, heat conduction on the fin surface and temperature gradient over the fin thickness is neglected and heat transfer coefficients on studied fin surface (mounted with VGs) and its back surface is assumed the same. However our experiments show somewhat large differences between the heat transfer coefficients on fin surface mounted with VGs and its back surface mounted without VGs.

Regarding a complete flat tube-fin element, several types of surfaces are involved in heat transfer process: fin face mounted with VGs (fin surface I in Fig. 2(*d*)), back surface of fin mounted with VGs (fin surface II in Fig. 2(*e*)) and flat tube surface (Fig. 2(*f*)). In the references [6,7] only surface I was studied. The characteristics of heat transfer enhancement of VGs on all the surfaces and the effects of VG parameters (attack angle, height) and fin spacing on heat transfer performance are very important in engineering application. To the best of our knowledge, nobody has reported these effects in published literature so far. It motivates us to carry out the present experiments to study them. The local and average heat transfer coefficients are measured by using naphthalene sublimation method. The heat transfer enhancements are

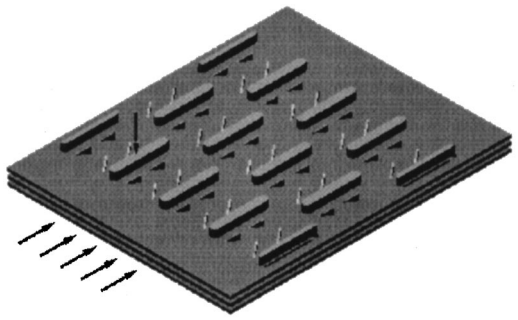

Fig. 1 Schematic view of flat tube bank fin arrays embedded with vortex generators

Contributed by the Heat Transfer Division for publication in the JOURNAL OF HEAT TRANSFER. Manuscript received by the Heat Transfer Division December 15, 2000; revision received September 24, 2001. Associate Editor: G. P. Peterson.

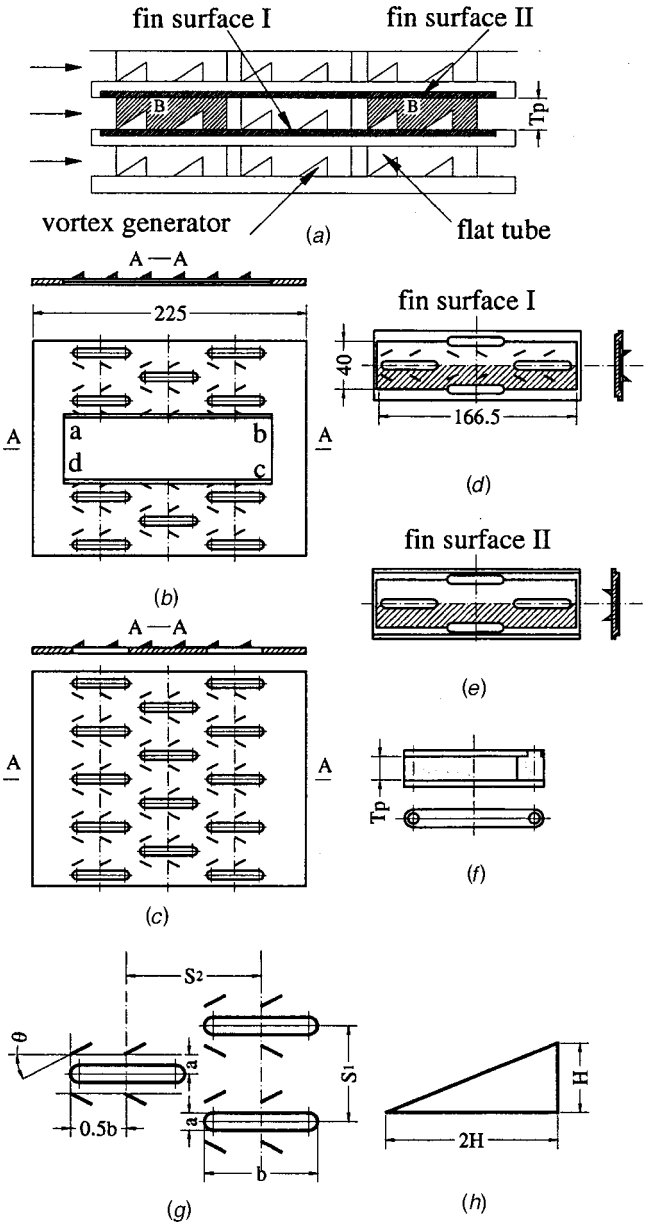

Fig. 2 Experimental setup: (*a*) flow passages; (*b*) measured plate supporting; (*c*) plate constructing flow passage; (*d*) fin surface I; (*e*) fin surface II; (*f*) flat tube cast from naphthalene; (*g*) flat tube bank parameters and positions of vortex generators; and (*h*) geometry of vortex generator.

evaluated by comparison of flat tube-fin element with and without VG enhancement under the identical mass flow rate, pumping power and pressure drop constraints.

Test Apparatus and Experimental Methods

The description of the experimental test setup is facilitated by reference to Fig. 2. As shown in Fig. 2(*a*), the flow passages walled with flat tube and plates (to model the fins) mounted with VGs are presented. Two plates with 6 mm thickness shown in Fig. 2(*b*) and one plate with same thickness shown in Fig. 2(*c*) are used in test channel. On the plate shown in Fig. 2(*b*), there is a void region marked with *abcd* on which we put the experimentally measured plates which are presented in Fig. 2(*d*) named with "fin surface I" and Fig. 2(*e*) named with "fin surface II". One of the surfaces of experimentally measured plates is cast from naphthalene. The depth of naphthalene is about one half of the plate thickness. VGs are mounted on the fin surface I and the back surface of fin surface II. Fin surfaces I and II are arranged face to face, as Fig. 2(*a*) shows, so that fin surface II can be used for modeling the back side surface of the fin mounted with VGs. The stakes with 8 mm in width and 4 mm, 5 mm, and 6 mm in heights are used to set up the fin spacing (T_p). Two flat tubes cast from naphthalene shown in Fig. 2(*f*) are put in the regions labeled with *B* in Fig. 2(*a*) to measure the sublimation of flat tubes. Other flat tubes and plates except the parts of fin surface I and fin surface II serve only to model the fluid mechanics of the tubes and fins in a fin and tube heat exchanger, they do not participate directly in the mass transfer process.

The flat tube fin geometries and positions of VGs are presented in Fig. 2(*g*). In the present study the geometrical parameters are $S_1=40$ mm, $S_2=55$ mm, $b=46.3$ mm and $a=6.3$ mm. As shown in Fig. 2(*g*), the leading points of first VG pair are on the line tangent to the flat tube and two tube widths apart. The leading points of second VG pair are located on the mid line of the flat tube with the same width apart as that of the first pair. The geometry of VG is a delta winglet (see Fig. 2(*h*)) with the base side edge length twice the trailing edge length.

In this study, the average experiments are carried out for parameter combinations of three attack angles ($\theta=25$ deg, 35 deg, and 45 deg), three relative heights of VG ($H/T_p=0.6$, 0.8, and 0.975), and three types of fin spacings ($T_p=4$ mm, 5 mm, and 6 mm). Thus the total experimental data sets are 3^3.

The experimental method used in the present study is the naphthalene sublimation technique via the heat-mass transfer analogy. The preparation of naphthalene plates is as follows. Firstly the naphthalene plates (fin surfaces I and II) are cast in a specially designed mold. Using this mold, the surface of the cast plates possess a high quality of flatness and smoothness. Secondly, the VGs are mounted at the given positions on the fin surfaces I and fin surface II by quick-drying glue. With special care, the use of this glue does not damage naphthalene surface. Finally, each cast plate is sealed in a special glass container and placed in a temperature-controlled experimental room having temperature fluctuation less than ± 0.1°C for a time period of about 24 hours prior to a test run.

Measurements of the surface contour of the naphthalene plates before and after a test run are made with a sensitive dial gauge with the resolution of 1 μm. The dial gauge is mounted on a fixed strut that over hung a movable coordinate table. The coordinate table enables the surface to be independently traversed in two directions in the horizontal plane. The traversing is controlled by a micrometer head and can be read with a resolution of 0.05 mm. The sublimation depth on the plate is measured on the entire surface and a symmetrical mass transfer is obtained in some pre-test experiments. In the formal experiments, only half of fin surfaces I and II are measured (hatched areas in Fig. 2(*d*) and (*e*)) due to symmetry. The total measured points are 3300 on the half fin surfaces I or II. The interval of any two neighboring points is 1 mm in both the streamwise direction (y) and spanwise direction (x).

The net change in local elevation of the naphthalene surface resulting from the mass transfer during a test run is determined by the contour measurements. The measured local elevation should be corrected due to the natural convection sublimation from the surface during the contour measurements. The mass loss caused by natural convection sublimation is estimated by measuring the weight of the naphthalene plates before and after a measurement of local elevation. We assume the mass loss at any measured point is the same and then an average height reduction can be calculated. From this average height reduction and the time needed for counter measurement, we can get the average height reduction rate. We assume also the natural convection sublimation is linearly proportional to the time needed for counter measurement. The real elevation of the naphthalene is corrected by subtracting a value which is average height reduction rate multiplied by time interval

between the beginning of counter measurement and when the corrected point is measured. In the present experiments, the mass loss by natural convection sublimation is below 1.5 percent of the mass sublimated in the test run. The local changes in elevation are integrated over the surface of the plates in order to yield the overall mass transfer. This overall mass transfer is compared with the average mass transfer obtained by directly weighing with a sensitive balance before and after the test run. The difference of these two overall mass transfers is well below 8 percent.

The average mass transfer is measured with a precision balance capable of discriminating to within 0.1 mg for specimens having a mass up to 200 g. A volumetric flow meter is used to measure the flow with precision of 0.1/3600 m^3/s. The temperature of air entering test section is sensed by a precision grade laboratory thermometer, which can be read to 0.1°C. A digital timer is used to measure the duration of a test run as well as the time required for setting up the experiment and for executing the surface contour measurements. The pressure drops are measured by a micro pressure gauge with a precision of 0.2 mm water column. VGs are manufactured with copper plate of 0.8 mm thickness by a line milling method.

Data Reduction

The surface profile measurements yield the surface distribution of the sublimation depth δz. Using the density ρ_s of the solid naphthalene and the sublimation time interval $\delta\tau$, the local mass sublimation rate per unit area is evaluated from

$$m' = \rho_s \delta z / \delta\tau. \tag{1}$$

Then the local mass transfer coefficient h_m can be determined as:

$$h_m = m'/(\rho_{n,w} - \rho_{n,b}), \tag{2}$$

where $\rho_{n,w}$, is determined by using the perfect gas law and the vapor pressure-temperature relation for naphthalene [8]

$$\rho_{n,w} = P_{n,w}/(RT_w) \tag{3}$$

$$\log P_{n,w} = 11.55 - 3765/T_w. \tag{4}$$

The local Sherwood number is defined as

$$\mathrm{Sh} = h_m \cdot D/D_{\mathrm{naph}}, \tag{5}$$

where D_{naph} is diffusion of naphthalene, and D the hydraulic diameter of flat tube bank fin channel. The diffusion of naphthalene is calculated by

$$D_{\mathrm{naph}} = 0.0681(T/298.10)^{1.93}(1.013\times 10^5/P_{\mathrm{atm}})\times 10^{-6}. \tag{6}$$

The definition of D in the present study is

$$D = 4(S_1 - a)T_p/(2(S_1 - a) + 2T_p). \tag{7}$$

It should be noted that in the subsequent section of comparison with different types of fin spacing, the hydraulic diameter is simply set to the width of flat tube a. The reason is that the changes of fin spacing make the hydraulic diameter, see Eq. (7), to get different values and then comparison with different hydraulic diameters becomes meaningless.

Average mass transfer coefficient and Sherwood number are defined as

$$h_m = \delta m/((\rho_{n,w} - \rho_{n,b}) \cdot \delta\tau \cdot A) \tag{8}$$

$$\mathrm{Sh} = h_m D/D_{\mathrm{naph}}. \tag{9}$$

After obtaining the local and average Sherwood number, the analogy between heat and mass transfers is employed to determine the local and average Nusselt number by

$$\mathrm{Nu} = \mathrm{Sh}(\mathrm{Pr}/\mathrm{Sc})^n, \tag{10}$$

where Sc and Nu are defined as

$$\mathrm{Sc} = 2.28(T/298.10)^{-0.1526} \tag{11}$$

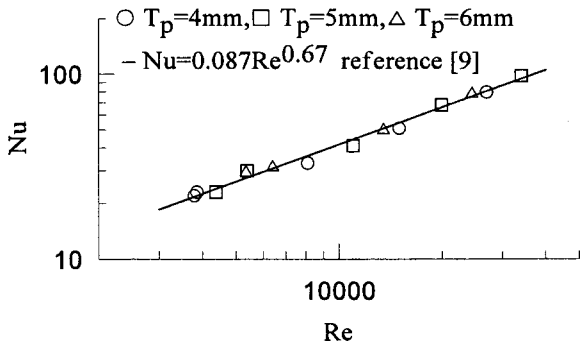

Fig. 3 Validation of experimental method

$$\mathrm{Nu} = \alpha \cdot D/\lambda. \tag{12}$$

The exponent n is in the range of 1/3 to 0.4. According to the suggestion of [8] $n = 0.4$ is adopted in this study.

The Reynolds number and the friction factor are defined as

$$\mathrm{Re} = \rho \cdot u_{\max} \cdot D/\mu \tag{13}$$

$$f = \Delta p D/(L\rho u_{\max}^2/2), \tag{14}$$

where $u_{\max} = Q/A_{\min}$.

Validation of Experimental Method and Uncertainty

The validation of experimental method has been carried out by a group of test runs for the flat tube bank fin without VG enhancement. We compared our results with the published data in [9]. The experimental results shown in Fig. 3 are found in good agreement with the published data, which indicates the following experimental data obtained by using the present experimental apparatus and methods are convincible.

The data uncertainty is estimated by a single sample theory of [10]. The uncertainties of sublimation depth δz, average mass transfer coefficient h_m, Sherwood number Sh, Nusselt number Nu and friction factor f are 4, 5.78, 5.86, 5.86, and 7.3 percent, respectively.

Experimental Results

The presentation of the results will begin with the local Nusselt number, followed by the spanwise integrated local Nusselt number results, the average Nusselt number and friction factor for the entire flat fin-tube element with different parameters of VG (attack angle, height) and fin spacing, and finally the comparison of heat transfer performance between flat fin-tube elements with and without VG enhancement.

Local Results. In Fig. 4, a presentation of representative results for the distribution of the local Nusselt number on the fin surfaces is given. Figure 4(*a*) is the image figure of local Nusselt number distribution on the fin surface I without VG enhancement. With VG enhancement, the image figures of local Nusselt number distribution on the fin surfaces II and I are presented in Fig. 4(*b*) and Fig. 4(*c*), respectively. As Fig. 4(*a*) shows, without VG enhancement, the Nusselt number on the fin surface has large value only at the leading edge of the flat tube and the small region near the flat tube. Whereas, large part of the fin surface has small value of Nusselt number. Figures 4(*b*) and 4(*c*) show the Nusselt number distributions on fin surface II and fin surface I change drastically. On the fin surface I, the enhancement is appreciable, especially around flat tube. The area with larger Nusselt number increases distinctly. On fin surface II, the enhancement of heat transfer is also quite distinct, but in a region away from the flat tube. On this surface, between the enhanced narrow region and the flat tube, there exists a region with lower Nusselt number. Unlike on the surface I, in the region between the first pair VGs and

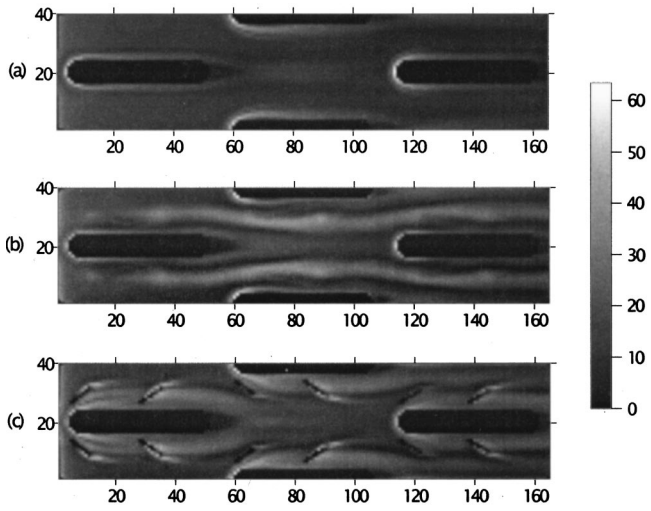

Fig. 4 Comparison of local Nu distribution on fin surfaces: (*a*) fin surface I, without VGs enhancement Re=2681, T_p=5 mm; (*b*) fin surface II, with VGs enhancement Re=2739, T_p=5 mm, θ=35 deg, H/t_p=0.8; and (*c*) fin surface I, with VGs enhancement Re=2739, T_p=5 mm, θ=35 deg, H/t_p=0.8.

second pair VGs, the enhancement is not so significant. The main reason is that the vortex is in its developing process and its intensity is not strong.

The local distributions of Nusselt number along 18 spanwise cross sections as labeled in Fig. 5 are presented in Fig. 6. The compared base is the flat tube-fin without VG enhancement. From Fig. 6, it can be seen that VGs have changed the Nusselt number distribution drastically and enhanced the Nusselt number efficiently. At enhanced and un-enhanced surfaces, irrespective of surfaces I or II, the Nusselt numbers have nearly the same amplitudes near flat tube, whereas the distribution of Nusselt number along spanwise direction is different. On fin surfaces II, VGs can enhance the region beside the flat tube and there is a small Nusselt number region near flat tube, the Nusselt number on cross sections of first tube row is small comparing with that of other two rows. The peak position of Nusselt number is at about $0.2\,S_1$ from flat tube wall for all of the cross sections. The width of the region having larger Nusselt number is about $0.2\,S_1$. On the fin surface I, the region of enhanced Nusselt number is near the flat tube. This enhancement becomes weaker for the region far from the flat tube. This is very important since large fin efficiency exists in the region near flat tube. The peak position of Nusselt number is at about $0.11\,S_1$ from flat tube wall for most of the cross sections. The width of the region having larger Nusselt number is also about $0.2\,S_1$. On this surface, immediately after vortex generators, the Nusselt number has two peak values (see Fig. 6 labeled with 4, 11, and 16). This is the effect of vortex generated by the trailing edge of VGs.

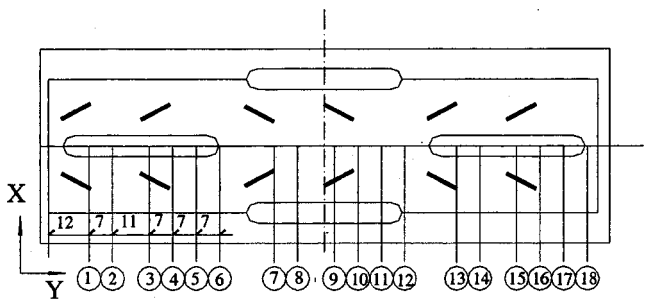

Fig. 5 Cross section position labels for local Nu number presentation

In Fig. 7, the spanwise average Nusselt number along stream wise direction on the fin surfaces I and II is presented. This figure shows that without VG enhancement Nusselt number at leading edge of flat tube is large but decreases rapidly along the streamwise direction. After mounting of VGs on fin surface, Nusselt number has large value both on the fin surfaces I and II. There exist periodic peak values for Nusselt number near the positions mounted with VGs. The peaks around the second row tube are much larger on fin surface II. As for fin surface I, the similar trend has been reported in [6]. We do not try to compare the present results with the published ones [6] as there are large differences in geometrical parameters in both the cases.

Average Results. The effects of attack angle θ, relative height H/T_p of VG and fin spacing T_p on average Nusselt number and friction factor are presented in Figs. 8–10. The results of flat tube-fin element without using VG enhancement are also presented in these figures for comparison. As the attack angle increases from 25 deg to 45 deg at fixed H/T_p and T_p, shown in Fig. 8(*a*), the average Nusselt number increases slightly. With the increase of attack angle, the friction increases as shown in Fig. 8(*b*). The enhancement of Nusselt number and increase of friction factor are clearly compared with flat tube-fin element without VG enhancement.

In Fig. 9(*a*), the effects of relative height H/T_p of VG on the Nusselt number and friction factor at θ=45 deg, and T_p=4 mm are presented. It is seen that as H/T_p increases, the Nusselt number has weaker enhancement. The reason may be that the fin surface has dominant effect on the formation and developing of vortex when the T_p is small enough. Compared with the results of flat tube-fin element without VG enhancement the Nusselt number also increases. Figure 9(*b*) shows that the friction factor increases with the increase of H/T_p due to the increase of flow blockage in flow passage.

In Fig. 10, the effects of fin spacing T_p on the Nusselt number and friction factor at θ=45 deg, H/T_p=0.6 are presented. Note that in this figure the width of the flat tube is used as a characteristic length to evaluate the Nusselt number, Reynolds number and friction factor. Figure 10(*a*) shows that the Nusselt number is almost independent to the T_p as it increases from 4 mm to 6 mm, which agrees with the results reported in [11]. The friction factors for T_p=5 mm and T_p=6 mm are almost the same, but the friction factor for T_p=4 mm is much larger than those for T_p=5 mm and 6 mm, especially in the small Re number region. In the present study, a scale factor of 2.5 is adopted to model the practical flat tube bank geometries. T_p=4 mm means 1.6 mm fin spacing in real geometry, which may be too small to be used in the practical engineering application.

Considering the practical application, it is useful to correlate the average results. The experimental average Nusselt number and friction factor are correlated by a least square curve-fitting method and the resulted correlation equations are

$$\mathrm{Nu}=0.128\,\mathrm{Re}^{0.674}\left(\frac{T_p}{a}\right)^{0.455}\left(\frac{H}{T_p}\right)^{0.299}\left(\frac{\theta}{45}\right)^{0.131}. \qquad (15)$$

$$f=6.23\,\mathrm{Re}^{-0.464}\left(\frac{T_p}{a}\right)^{0.593}\left(\frac{H}{T_p}\right)^{0.618}\left(\frac{\theta}{45}\right)^{0.270}. \qquad (16)$$

$$500<\mathrm{Re}<4100,\quad 25\ \mathrm{deg}\leqslant\theta\leqslant 45\ \mathrm{deg},\quad 0.635\leqslant T_p/a\leqslant 0.952.$$

The maximum deviations are 7.6 and 8.3 percent for Nusselt number and friction factor, respectively.

Performance Comparison. There are many constraints and criteria for heat transfer performance comparison. The heat transfer boundary condition simulated by naphthalene sublimation can be considered as constant wall temperature. So the identical mass flow rate constraint, the identical pumping power constraint, and the identical pressure drop constraint are used to evaluate the heat transfer enhancement compared with flat tube-fin element without

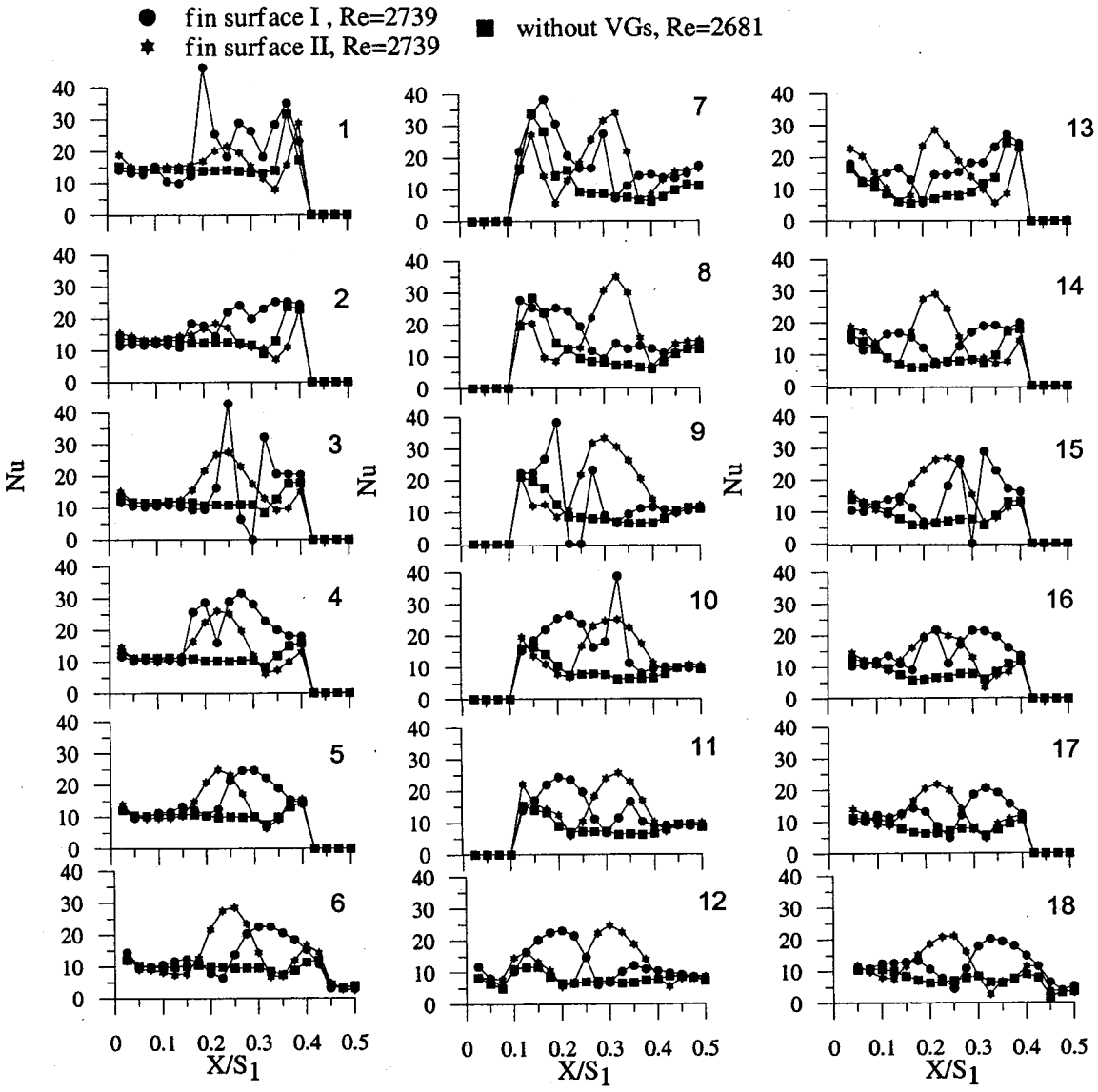

Fig. 6 Comparison of span wise local Nu on fin surfaces

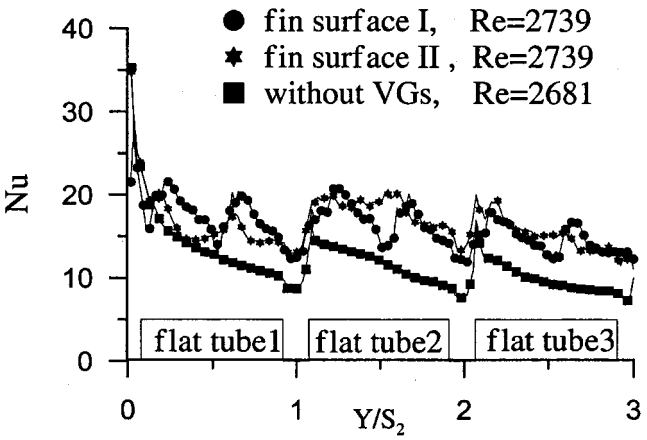

Fig. 7 Comparison of span wise average Nu along streamwise

VG enhancement. The comparisons of heat transfer performance under identical mass flow rate, pumping power and pressure drop are given below.

(1) Identical Mass Flow Rate Constraint.

$$(m)^* = m \tag{17}$$

$$\mathrm{Re}^* = \mathrm{Re}\, D^*/D \tag{18}$$

(2) Identical Pumping Power Constraint.

$$(\Delta pm/\rho)^* = (\Delta pm/\rho) \tag{19}$$

$$\mathrm{Re}^* = \mathrm{Re}\cdot(D^*/D)\sqrt[3]{D^*(Af)/((Af)^*D)} \tag{20}$$

(3) Identical Pressure Drop Constraint.

$$(\Delta p)^* = (\Delta p) \tag{21}$$

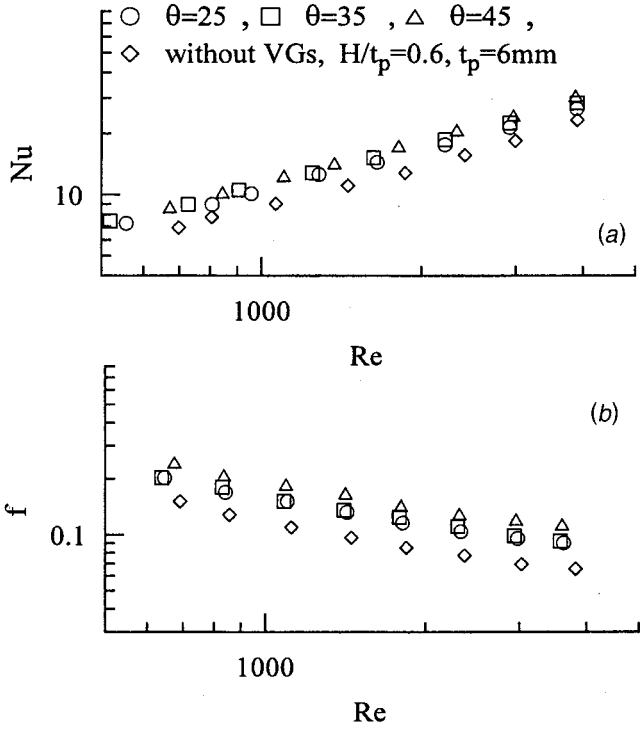

Fig. 8 Effect of attack angle on the average Nu and *f*

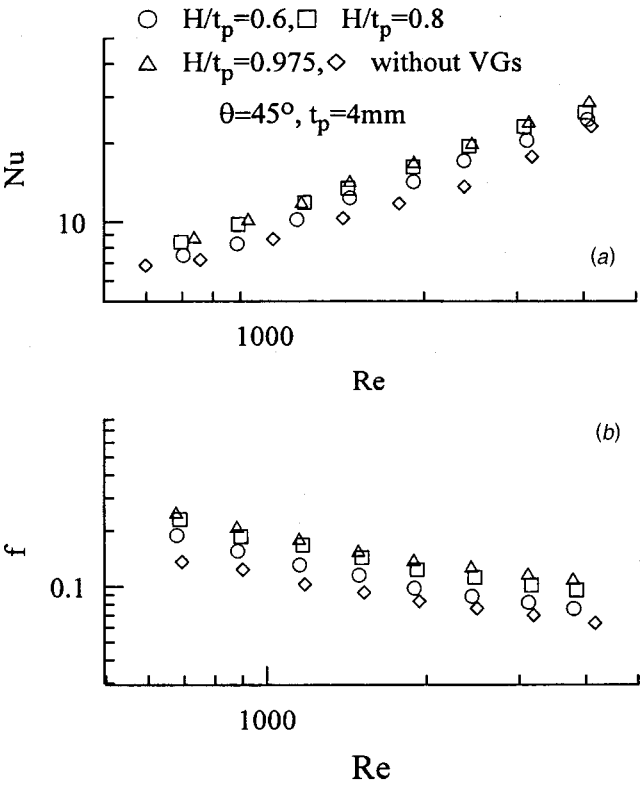

Fig. 9 Effect of relative height of vortex generator on the average Nu and *f*

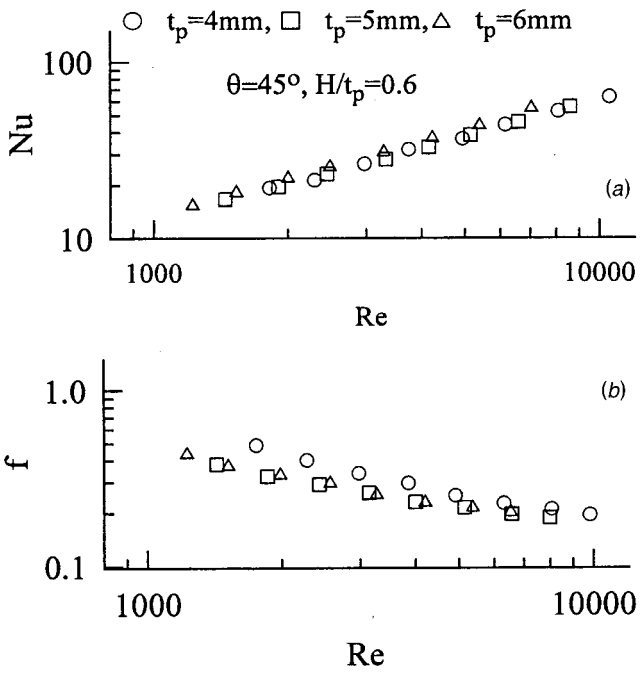

Fig. 10 Effect of fin spacing on the average Nu and *f*

Table 1 Heat transfer enhancement under identical mass flow rate constraint $H/T_p=0.975$, and $T_p/a=0.952$

$\theta/45^o$	Re					
	900	1450	1900	2450	3100	4050
0.556	1.358	1.360	1.362	1.363	1.364	1.366
0.778	1.419	1.420	1.423	1.424	1.426	1.427
1.000	1.466	1.468	1.470	1.472	1.473	1.475

Table 2 Heat transfer enhancement under identical pumping power constraint $H/T_p=0.975$, and $T_p/a=0.952$

$\theta/45^o$	Re					
	900	1450	1900	2450	3100	4050
0.556	1.250	1.285	1.306	1.326	1.344	1.366
0.778	1.275	1.311	1.332	1.352	1.371	1.393
1.000	1.294	1.331	1.352	1.372	1.392	1.414

Table 3 Heat transfer enhancement under identical pressure drop constraint $H/T_p=0.975$, and $T_p/a=0.952$

$\theta/45^o$	Re					
	900	1450	1900	2450	3100	4050
0.556	1.184	1.239	1.271	1.302	1.331	1.366
0.778	1.189	1.244	1.276	1.307	1.337	1.371
1.000	1.193	1.248	1.280	1.311	1.341	1.375

$$\mathrm{Re}^* = \mathrm{Re}\cdot D^*/D \sqrt{\frac{Af}{(Af)^*}\frac{D^*}{D}}, \tag{22}$$

where the superscript* refers to flat tube fin with VG enhancement. The ratio of heat transfer at the same temperature difference can be evaluated by

$$\frac{\dot{Q}^*}{\dot{Q}} = \frac{A^*\,\mathrm{Nu}^*(\mathrm{Re}^*)}{A\,\mathrm{Nu}(\mathrm{Re})}\frac{D}{D^*}. \tag{23}$$

The performance comparisons are presented in Tables 1–3. In these tables, the enhancements of heat transfer at some geometri-

cal combinations with different Reynolds numbers are given. As Tables 1–3 show, with $T_p/a=0.952$ ($T_p=6$ mm), $H/T_p=0.975$, $\theta=45$ deg, and Re=4050, the heat transfer enhancement is about 47.5, 41.4, and 37.5 percent for identical mass flow rate, identical pumping power, and identical pressure drop constraints, respectively. From Table 1, it is clear that at identical mass flow rate constraint, heat transfer enhancement weakly depends on the Re, but it depends largely on attack angle of VGs. Tables 2 and 3 reveal that heat transfer enhancement has a strong dependence on Re, but a weak dependence on attack angle of VG, especially for the identical pressure drop constraint.

Conclusions

Local and average heat transfer characteristics over a complete flat tube-fin element with four vortex generators per tube have been measured by using the naphthalene sublimation method. The effects of fin spacing and VGs parameters such as height and attack angle on heat transfer and pressure drop are investigated. The comparisons of heat transfer enhancement with flat tube-fin element without VG enhancement under three constraints are carried out. The following conclusion can be drawn:

1. The use of VGs can efficiently enhance the heat transfer on both fin surface mounted with VGs and its back surface.
2. VGs can greatly enhance the heat transfer in the region near flat tube with $2\times0.2\,S_1$ width per tube on the fin surface mounted with VGs.
3. On the fin surface mounted without VGs, heat transfer can be enhanced in the region with $2\times0.2\,S_1$ width per tube, but the centerline of this region is away from flat tube wall with $0.2\,S_1$ distance.
4. Increasing of VG height and attack angle increases the enhancements of heat transfer and pressure drop.
5. The Nusselt number is almost independent of T_p with flat tube width as the characteristic length.
6. Small fin spacing causes great increase of pressure drop.
7. Compared with the flat tube-fin element without VG enhancement, the heat transfer enhancement can reach 47.5, 41.4, and 37.5 percent at identical mass flow rate, identical pumping power and identical pressure drop constraints, respectively.

Acknowledgments

This research was partly supported by Natural Science Foundation of Gansu Province. We also thank Dr. Bo Yu for useful discussions.

Nomenclature

A = area of heat/mass transfer [m^2]
A_{mim} = minimum flow area [m^2]
a = width of flat tube [m]
b = length of flat tube [m]
D = hydraulic diameter of flow channel [m]
D_{nath} = diffusion of naphthalene [m^2/s]
f = friction factor
h_m = local mass transfer coefficient [m/s]
H = height of winglet type vortex generators [m]
L = stream wise length of fin [m]
m = mass [kg]
m' = mass sublimation rate of naphthalene [$kg/(m^2\cdot s)$]
Nu = Nusselt number
P = pressure of naphthalene vapor [Pa]
Pr = Prandlt number
Q = volumetric flow rate of air [m^3/s]
$\dot{Q}$ = heat transfer rate [W]
R = universal gas constant [$m^2/s^2\cdot K$]
Re = Reynolds number
S_1 = transversal distance of flat tubes [m]
S_2 = longitudinal distance of flat tubes [m]
Sc = Schmidt number
Sh = Sherwood number
T_p = fin spacing [m]
T = temperature [K]
u_{max} = maximum velocity [m/s]
x,y = coordinates
z = sublimation depth [m]

Greek

α = heat transfer coefficient [$W/m^2\cdot K$]
λ = heat conductivity [$W/m\cdot K$]
μ = viscosity [$kg/m\cdot s$]
ρ = density [kg/m^3]
θ = attack angle of vortex generator [deg]
τ = time interval for naphthalene sublimation [s]
δ = small value or interval when combine with other characters
Δp = pressure drop [Pa]

Subscript

a = characteristic length based on flat tube width a
atm = atmosphere
naph = naphthalene
m = average
w = wall
n,b = naphthalene at bulk flow temperature
n,w = naphthalene at wall temperature

References

[1] Atkinson, K. N., Drakulic, R., Heikal, M. R., and Cowell, T. A., 1998, "Two and Three-Dimensional Numerical Models of Flow and Heat Transfer Over Louvred Fin Arrays in Compact Heat Exchangers," Int. J. Heat Mass Transf., **41**, pp. 4063–4080.

[2] Wang, L. B., Jiang, G. D., Tao, W. Q., and Ozoe, H., 1998, "Numerical Simulation on Heat Transfer and Fluid Flow Characteristics of Arrays With Non-Uniform Plate Length Positioned Obliquely to the Flow Direction," ASME J. Heat Transfer, **120**, pp. 991–998.

[3] Wang, L. B., and Tao, W. Q., 1995, "Heat Transfer and Fluid Flow Characteristics of Plate-Array Aligned at Angles to the Flow Direction," Int. J. Heat Mass Transf., **38**, No. 16, pp. 3053–3063.

[4] Fiebig, M., 1995, "Vortex Generators for Compact Heat Exchangers," J. of Enhanced Heat Transfer, **2**, Nos. 1-2, pp. 43–61.

[5] Fiebig, M., 1995, "Embedded Vortices in Internal Flow: Heat Transfer and Pressure Loss Enhancement," Int. J. Heat Mass Transf., **16**, pp. 376–388.

[6] Fiebig, M., Valencia, A., and Mitra, N. K., 1994, "Local Heat Transfer and Flow Losses in Fin-Tube Heat Exchanger With Vortex Generators: A Comparison of Round and Flat Tubes," Exp. Therm. Fluid Sci., **8**, pp. 35–45.

[7] Fiebig, M., Valencia, A., and Mitra, N. K., 1993, "Wing Type Vortex Generators for Fin-Tube Heat Exchangers," Proc. 1st International Conference on Aerospace Heat Exchanger Technology, Palo Alto, CA, pp. 467–485.

[8] Goldstein, R. J., 1993, "A Review of Mass (Heat) Transfer Measurements Using Naphthalene Sublimation," in *Experimental Heat Transfer, Fluid Mechanics, and Thermodynamics*, Elsevier Science Publishers, B. v. pp. 21–40.

[9] Kylikof, U. A., 1988, *The Cooling System of Diesel Locomotive*, Moscow (in Russian).

[10] Moffart, R. J., 1982, "Contribution to the Theory of Single-Sample Uncertainty Analysis," ASME J. Heat Transfer, **104**, pp. 250–260.

[11] Rich, D. G., 1973, "The Effect of Fin Spacing on Heat Transfer and Friction Performance of Multi-Row, Smooth Plate Fin and Tube Heat Exchanger," ASHRAE Trans., **79**, No. 2, pp. 137–145.

Detailed Numerical and Experimental Investigation of Non-Isothermal Sintering of Amorphous Polymer Material

R. M. Tarafdar
Novellus Systems, Inc.
3940 North First Street,
San Jose, CA 95134

T. L. Bergman
Professor and Head Fellow ASME,
Department of Mechanical Engineering,
191 Auditorium Drive, Unit 3139,
University of Connecticut,
Storrs, CT 06269
e-mail: tberg@engr.uconn.edu

Simulations and experiments are performed to investigate the coupled thermal and morphological response of polymer material during non-isothermal sintering. The experimental results are utilized to validate a numerical model that describes the response of the system. Predictions of the material expansion, its subsequent contraction due to sintering, and the temperature evolution are obtained and favorably compared with experimental results. Parametric simulations are performed to acquire additional insight into the dynamics of non-isothermal sintering while a relationship is established to describe the ratio of the sintering penetration depth to the thermal penetration depth and its dependence upon the boundary and initial temperatures. [DOI: 10.1115/1.1459732]

Keywords: Heat Transfer, Materials, Moving Boundaries, Polymers, Porous Media

Introduction

Sintering of powder occurs in a variety of industrial processes including glass fiber manufacturing [1], rotational molding [2] and fabrication of net shape structures [3,4]. In these operations, the initially-porous material is heated and the powder particles coalesce, leading to shrinkage and densification of the bulk matter. The change in the porosity modifies the internal temperature distribution, which in turn changes local sintering rates. In general, prediction of the porosity distribution within, as well as the overall shape of the bulk material after thermal processing involves a coupled analysis.

Historically, most studies of powder sintering have dealt with microscale (particle-to-particle) material flow that leads to the change of the geometric shape of adjacent particles. Since many powders are micron-sized, spatial temperature gradients are negligible and heat transfer is of no concern [5,6]. Frenkel [7] first analyzed the coalescence of two isothermal spheres as representative of the initial sintering of a powder material. It was postulated that densification occurred by Newtonian viscous flow driven by surface tension forces, and it was suggested that the rate of deformation of the adjacent particles could be found by equating the time rate of change in the surface energy to the rate of energy dissipation due to liquid flow. Frenkel's model did not accurately account for mass conservation, and was later corrected by Eshelby [8] and the correction is known as the Frenkel-Eshelby model. Subsequently, Scherer [9] also corrected Frenkel's analysis. More recently, Pokluda et al. [10] developed a sintering model that describes the complete fusing of two spherical particles where the completion of the process is defined as the ultimate formation of a single, large spherical particle from adjacent particles.

A number of detailed particle-level modeling efforts [5,6,11–13] have been made. Jagota and Dawson [11] as well as Martinez-Herrera and Derby [5] used finite element methods to describe the shape evolution of adjacent sintering particles. Other studies have concentrated on the final stages of sintering when closed pores develop during multiple-particle sintering [14]. The influence of the geometry of the microstructure on the sintering rate has also been investigated [15,16] and it has been found that, for many different particle geometries, sintering relationship based upon an assumed spherical particle shape can be applied successfully to predict sintering dynamics.

Macroscopic sintering has received little attention due to the difficulty of describing the geometrical response of the bulk matter in terms of local material transport associated with sintering at the particulate level [17]. Several models exist to describe the macroscopic shape evolution of isothermally sintered materials. For example, Reid [18] developed a model that treats the powder as a continuous medium with spatially varying porosity. This approach allows description of the macroscopic sintering response using equations for mass conservation and force balances coupled with a microscale sintering submodel.

Although no industrial sintering process occurs under spatially isothermal conditions, non-isothermal macroscopic sintering has received little attention until recently. As the material sinters, morphological changes at the microscale affect heat transfer internal to the material and, in turn, modify local temperatures. Local sintering rates are usually highly dependent upon the local temperature [19]. Kandis and Bergman [20] experimentally observed and numerically predicted the shape evolution induced by non-isothermal sintering of polymer powder. The model was extended to consider highly non-isothermal sintering of polycarbonate powder. In these models, temperature distributions were predicted within the bulk material by application of a porous medium based analysis using the continuum approach, local sintering rates were predicted using Frenkel's equation, and solid as well as interstitial gas phase velocities were predicted using a novel computational method described in detail by Kandis and Bergman [20]. Because of the modeling and experimental approaches taken, however, conclusions regarding (for example) the interplay between thermal expansion of the powder at low temperatures and the coalescence of particles induced by high temperatures which may occur simultaneously in different regions of the bulk matter could not be drawn. Although insight was gained regarding the connection between penetration depths associated with the thermal and morpho- logical response of the material, no general relationships were developed. Existing models for the effective thermal conductivity of the porous medium were employed.

Contributed by the Heat Transfer Division for publication in the JOURNAL OF HEAT TRANSFER. Manuscript received by the Heat Transfer Division April 5, 2000; revision received October 9, 2001. Associate Editor: C. T. Avedisian.

The objectives of this study are to (1) develop a non-isothermal sintering model that explicitly accounts for variations in local morphologies on the effective transport properties (density and thermal conductivity) of the bulk matter, (2) acquire data regarding the expansion and contraction of material undergoing highly non-isothermal sintering, (3) use the experimentally-generated data to validate the sintering model, (4) perform parametric simulations to observe the influence of particle diameters and applied thermal boundary and initial conditions on the mechanical response of the material, and finally (5) develop a correlation that relates the sintering penetration depth to the thermal penetration depth for various dimensionless thermal conditions. The material considered here is amorphous polycarbonate, a material used in commercial fabrication of net shape structures [21].

Mathematical Model

A one-dimensional, non-isothermal sintering situation is shown schematically in Fig. 1. A loosely packed powder is initially at a temperature below T_g and is of height, h_i. Consider the case where the bottom surface of the powder region is raised to a temperature above T_g. Warm temperatures propagate into the powder, resulting in the thermal expansion of the material which induces an increase of the powder bed height (see time t_1). Sintering begins as local temperatures exceed T_g, resulting in local densification of the medium in the lower regions of the domain. With loss of porosity, the effective thermal conductivity and thermal capacitance of the medium increase. A thermal penetration depth (δ_T) may be defined as the z location where $(T-T_b)/(T_i-T_b)=0.99$, and a sintering penetration depth (δ_s) may be defined as the location where $x/a \neq 0$ where x/a is the dimensionless neck radius of two particles that are in contact.

In this study, the sintering rate is determined using an analytical relationship developed by Pokluda et al. [10] that has been verified experimentally and relevant definitions are shown in Fig. 2. The neck radius between adjacent spherical particles of instantaneous radius $a > a_i$ is determined by integrating the time history of the neck radius angle, θ which is described by

$$\frac{d\theta}{dt} = \frac{\Gamma}{a_i \eta} \frac{2^{-5/3} \cos(\theta)\sin(\theta)[2-\cos(\theta)]^{1/3}}{[1-\cos(\theta)][1+\cos(\theta)]^{1/3}}. \tag{1}$$

Equation (1) takes into account the driving forces associated with surface tension and the resistances to material flow associated with the viscosity of the material. The sintering rate, $d\theta/dt$, increases as the surface tension of the material is increased, and decreases as the viscosity of the material increases or as θ becomes larger. Ultimately, a single solid sphere of radius a_f is formed. For polymeric materials, η is expected to follow anArrhenius form [21] with $\eta = A_v \exp(E_v/RT)$. The relationship between $a(t)$ and $\theta(t)$ is obtained from the conservation of mass principle using the assumption of a constant density

$$a(t) = a_i \left(\frac{4}{\{1+\cos[\theta(t)]\}^2 \{2-\cos[\theta(t)]\}} \right)^{1/3} \tag{2}$$

while the half distance between the centers of the two adjacent spheres is expressed as

$$d(t) = a(t)\cos\theta(t) \tag{3}$$

Thermal expansion occurs during the heating of the material from the initial temperature to T_g and is expressed as $\Delta V/V = \chi_x \Delta T$ where, $\chi_v = \chi_x + \chi_y + \chi_z$ [22]. In this case the material is isotropic so $\chi_v = 3\chi$ [22]. Consistent with the use of Eq. (2), thermal expansion after the onset of sintering is neglected. Note that sintering causes changes in the size and shape of individual spheres that are several orders of magnitude larger than changes due to thermal expansion.

The one-dimensional sintering model may be developed by coupling a straightforward heat transfer analysis to the sintering and thermal expansion analysis for a column composed of spherical particles. The material (powder and air) is treated as a continuum (pseudo single phase system). Heat transfer is assumed to be one-dimensional and occurs by combined conduction and surface radiation across interstitial regions. Convection in the interstitial regions and advection (of the solid and the air) associated with shrinkage of the column of spheres due to sintering are assumed to be negligible. Therefore, the one-dimensional

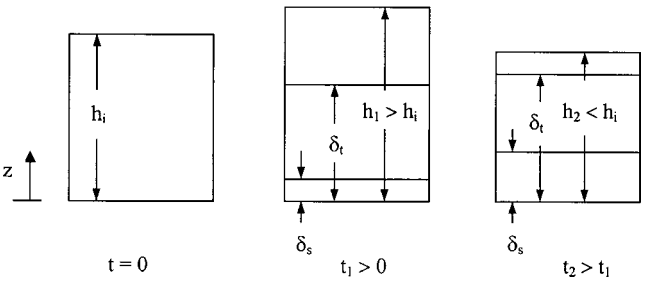

Fig. 1 Schematic diagram of one dimensional sintering of a porous medium. The conditions illustrated are the initial condition (left) an intermediate time (middle) and later time (right). Thermal and sintering penetration depths are noted.

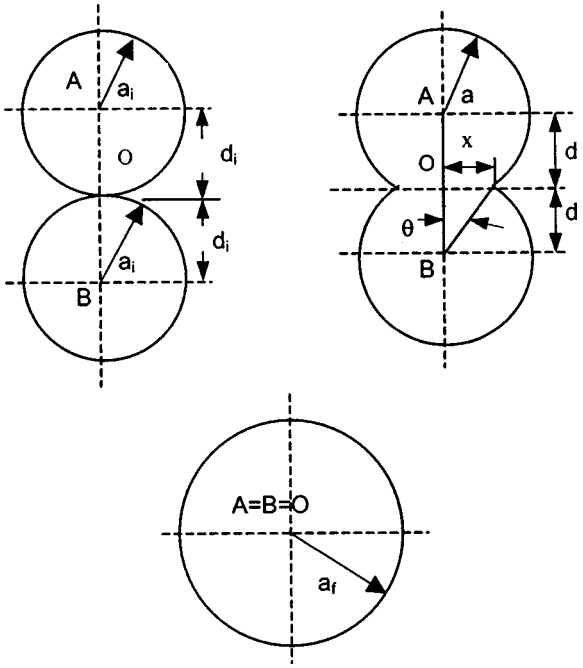

Fig. 2 Shape evolution of two equal sized spheres with definitions of variables. The initial (top left), intermediate (top right) and complete (bottom) sintering conditions are shown.

temperature distribution is obtained from the heat diffusion equation

$$\frac{\partial}{\partial z}\left(k_{\text{eff}}\frac{\partial T}{\partial z}\right)=c_p\frac{\partial T}{\partial t} \tag{4}$$

Numerical Model

Features of the heat transfer model are shown in Fig. 3(*a*). Note that a continuum approach is used with a (cylindrical) control volume placed about each sphere. Each control volume consists ofthe solid material and air. The integrated form of Eq. (4) is used to predict the temperature distribution. The boundary conditions are applied to the bottom and top surfaces of the column of spheres as shown in Fig. 3(*a*). With this approach, the midpoint temperature of each control volume is predicted. Specifically,

$$\left(k_{\text{eff}}A\frac{dT}{dz}\right)_{\text{in}}-\left(k_{\text{eff}}A\frac{dT}{dz}\right)_{\text{out}}=m_{\text{eff}}c_{p,\text{eff}}\frac{dT}{dt} \tag{5}$$

is solved where m_{eff} and $c_{p,\text{eff}}$ are expressed as $m_{\text{eff}}=m_s+m_a$ and $c_{p,\text{eff}}=c_{p,s}\rho_s(1-\phi)/\rho_{\text{eff}}+c_{p,a}\rho_a\phi/\rho_{\text{eff}}$. Note that $\rho_{\text{eff}}=\rho_s(1-\phi)+\rho_a\phi$. The porosity of each control volume is determined by a straightforward calculation based upon the instantaneous shape of the solid particle that is predicted by time integration of Eqs. (1–3). A piecewise linear temperature distribution is assumed to exist between the center points of the control volumes. As will be described shortly, k_{eff} is evaluated by taking into account both conduction and surface radiative heat transfer.

Initially, due to the rise of temperatures within each control volume the spheres thermally expand as shown in Fig. 3(*b*). Therefore, during the thermal expansion phase both the temperatures and the sizes of the spheres will increase and as a result the control volumes surrounding the spheres are allowed to increase in size. The expansion of the spheres will continue until the sphere temperature reaches T_g.

Once local sintering begins, the value of x/a becomes non-zero, and the morphology of the column evolves to one that can no longer be characterized by packed spheres. Rather, each sintered interface is similar to the one shown in the RHS of Fig. 2 and values of x/a can be significantly different at various locations within the porous medium. Note that the effective diameter (a) of the spheres increases upon sintering, as required by conservation of mass principles. Because of the evolution of the morphology, the effective density within each control volume increases. More important, k_{eff} increases because constriction resistances associated with the particle-to-particle interfaces are reduced as x/a becomes larger. The augmentation of conduction heat transfer by radiation across the air gap is reduced as x/a increases and at small initial sphere diameters.

Because of the strong dependence of k_{eff} upon x/a, values of k_{eff} were calculated for a range of x/a values, temperatures, and sphere sizes using a commercial CFD package. To do so, temperatures at the horizontal planes associated with points A and B (Fig. 2) were specified and heat transfer rates from or to horizontal

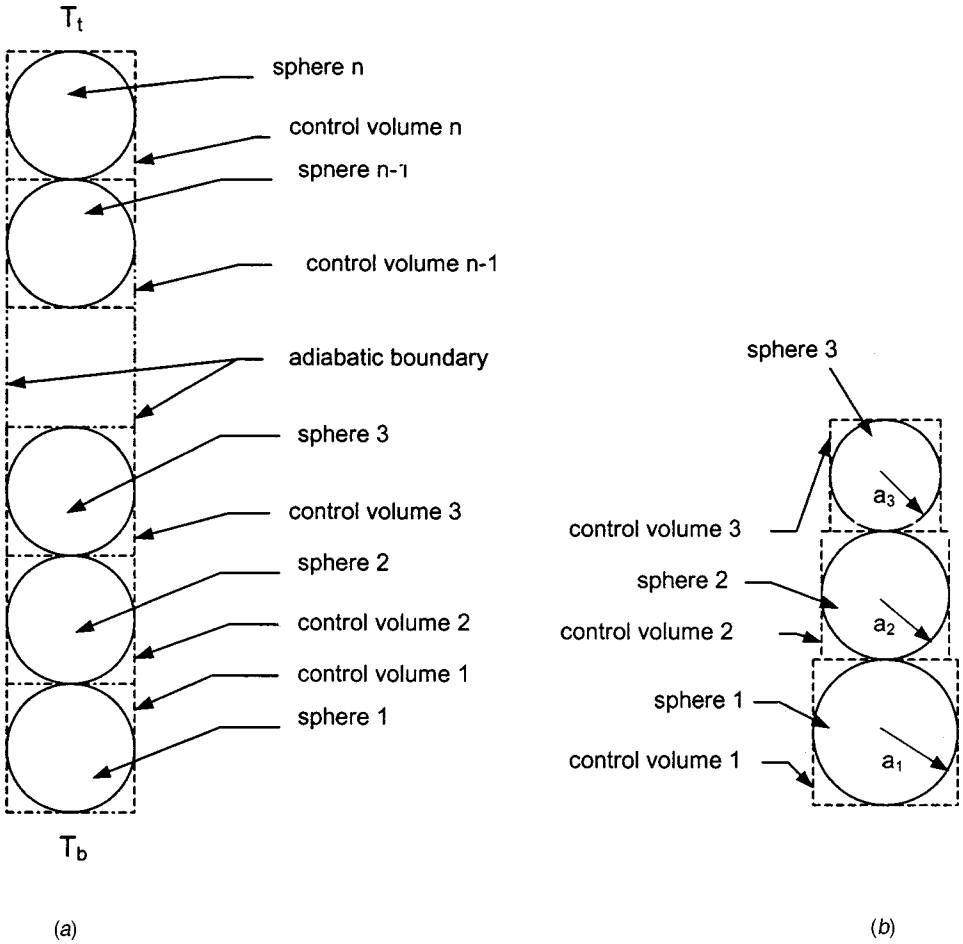

Fig. 3 Diagram of (*a*) control volumes associated with a column of spheres and (*b*) thermal expansion of the lower spheres in the column

planes at A to B were calculated. Conduction in the solid and in the air was accounted for, as was gray, diffuse surface-to-surface radiation heat transfer across the air gap. The cylindrical surface of the surrounding integral control volume was considered to be adiabatic and re-radiating. Values of k_{eff} were found based upon the predicted heat transfer rates and the separation distance, $2d$, associated with various x/a. Predictions of k_{eff} values associated with $0<x/a<0.8$ and for $290\ \text{K}<T_{\text{avg}}<475\ \text{K}$ where $T_{\text{avg}}=(T_A+T_B)/2$ for sphere sizes ranging from 0.03 mm to approximately 3 mm were obtained. The resulting values of k_{eff} range from approximately 0.12 W/mK (for the lowest average temperature, the smallest sphere size and $x/a=0$) to approximately 0.23 W/mK (for the highest average temperature, the largest particle size, and $x/a=0.8$). The predictions were correlated, and the correlations were used in the sintering model described here. Details of the prediction method, the grid size independence study, sample results, and correlations for k_{eff} are included in [23]. Note that for sphere radii less than approximately 0.3 mm, radiation heat transfer across the air gap is negligible for the temperature ranges of interest here. With the approach taken to evaluate the effective thermal conductivity, constriction resistances are taken into account.

Several assumptions are employed to predict the contraction of the particles associated with sintering. They are (1) sintering will start when the average temperature of two adjacent spheres or particles reach T_g, (2) sintering rates are evaluated using the average radius of two adjacent particles, (3) k_{eff} is evaluated using the average radius of two adjacent particles, and (4) the flattening of the bottom surface of sphere 1 (Fig. 3) is predicted by assuming that it sinters to an adjacent (underlying) particle at the same temperature as sphere 1. Note that Eq. (1) is singular at $\theta=0$. A discussion regarding treatment of the singularity in the intitial stages of the simulation is included in [23]. This study is limited to polycarbonate material and air as the interstitial gas. With the numerical approach taken here, one control volume is associated with each particle (and as will become evident, hundreds of particles will be considered in each parametric simulation). Therefore, the grid dependence of the solution is not relevant. The discretized form of Eq. (5) was solved using numerical time steps of 0.0001 and 0.0005 s with no discernable difference in the predictions. A time step of 0.0001 s was used here. Properties are listed in Table 1.

Experimental Apparatus and Procedure

The model described above includes a number of assumptions and, as such, an experiment was conducted to validate the model to the extent possible. Specifically, a test procedure was designed to measure the values of x/a that develop at the interfaces between adjacent spheres in a column that is heated beyond the glass transition temperature in a highly non-isothermal fashion. In addition, the evolution of the overall height of the column of spheres due to thermal expansion at local temperatures below T_g and sintering at local temperatures exceeding T_g was measured. Note that accurate and non-intrusive measurement of internal temperatures within individual, small diameter and low thermal conductivity spheres is not considered feasible.

Non-intrusive measurement of local temperatures and sintering rates is difficult due to the particles' low thermal conductivity and small size. In order to acquire meaningful data the experiment was conducted using larger spheres (3.175 mm diameter, grade2 polycarbonate spheres with $T_g=418$ K).

The spheres were placed in a test cell constructed of a bakelite cylinder (Fig. 4(*a*)). Rather than measure the temperature of individual spheres, the temperature distribution in the bakelite was measured and it is assumed that $T(z,t)$ within the sphere column is approximately equal to $T(z,t)$ within the bakelite. The test cell is placed upon a bottom, multipass aluminum heat exchanger while a top multipass aluminum heat exchanger is set atop the bakelite cylinder. The cylinder (25.25 mm diameter by 27.4 mm long) is molded from black bakelite powder and is made of a large diameter to promote one dimensional heat transfer in the *z* direction. The cavity that houses the spheres is 3.3 mm in diameter and was sized as a compromise between (1) ensuring a nearly colinear column of spheres, and (2) (as will become evident) maximizing the degree of sintering that could be observed in a typical experiment. Eight 0.9 mm diameter, 8 mm deep holes are drilled (3.175 mm apart) along the height of the cylinder and house *K*-type thermocouples. The test cell and the heat exchangers were insulated with approximately 15 loose wraps of aluminum foil and glass wool board to minimize heat losses and further promote one-dimensional heat transfer in the bakelite.

The entire experimental apparatus (Fig. 4(*b*)) consists of the test cell, a stand to hold a LVDT that is used to measure the height of the sphere column, the two heat exchangers, and *K*-type thermocouples embedded in the bakelite and in the heat exchangers. A pulley arrangement was used to counterbalance the weight of the core of the LVDT so that sintering proceeds with minimal applied compressive force on the spheres. Each heat exchanger is supplied by hot fluid from two high temperature circulating baths. The fluids used are ethylene glycol and silicone oil in the top (cool) and bottom (hot) heat exchangers, respectively.

To conduct an experiment, eight spheres are placed in the test cell. The 1 mm diameter copper tube that connects the LVDT to the column of spheres is then placed through the top heat exchanger to rest on the top sphere. In the meantime, the fluids are pre-heated in the high temperature baths until they reached a desired temperature. At the onset of the experiment, the hot fluids

Table 1 Actual and effective thermophysical properties [21,23,24]

Property	Value
Polycarbonate [21]	
A_v	1.027×10^{-12} N•s/m^2
c_p	1395.4 J/kg•K
E_v	35.9 Kcal/mol
k_s	$0.025 + (5 \times 10^{-4})$•T
ε	0.95
ρ_s	1278 kg/m^3
Γ	0.025 N/m
χ	68×10^{-6} K^{-1}
Air [24]	
c_p	1017 J/kg•K
k_a	$0.004372 + (7.38 \times 10^{-5})$ •T
ρ_a	from ideal gas law
Bakelite [24]	
c_p	1465 J/kgK
k	1.4 W/mK
ρ	1300 kg/m^3

Table 1 Continued.

Effective Properties of Polycarbonate and Air [23]

$k_{eff} = 1.2827x10^{-10}(T_m)^4 - 1.8198x10^{-7}(T_m)^3 + 9.6385x10^{-5}(T_m)^2 - 2.2260x10^{-2}(T_m) + 1.9734$

$(x/a = 0, 290K < T_m < 418K, a_i = 3.175x10^{-3}\ m)$

$k_{eff} = 1.4521x10^{-3} + 1.6047x10^{-4}(T_m) + 3.7680x10^{-2}(x/a) - 2.6212x10^{-5}(T_m)(x/a)$

$+ 3.2694x10^{-7}(T_m)^2 + 9.0412x10^{-2}(x/a)^2$

$(0 < x/a < 0.8, 418K < T_m < 475K, a_i = 3.175 \times 10^{-3}\ m)$

$k_{eff} = -1.5841x10^{-10}(T_m)^4 + 2.2807x10^{-7}(T_m)^3 - 1.2256x10^{-4}(T_m)^2 + 2.9374x10^{-2})(T_m) - 2.5649$

$(x/a = 0, 290K < T_m < 418K, a_i < 3.175x10^{-4}\ m)$

$k_{eff} = -0.1746 + 1.1352x10^{-3}(T_m) - 6.3833x10^{-2}(x/a) + 2.0577x10^{-4}(T_m)(x/a)$

$- 1.0314x10^{-6}(T_m)^2 + 0.1071(x/a)^2$

$(0 < x/a < 0.8, 418K < T_m < 475K, a_i < 3.175 \times 10^{-4}\ m)$

Note 1: The disparity between the curve fits and predicted quantitities is typically less than 1 percent.

Note 2: T_m is in kelvins

are diverted to the heat exchangers. A Keithley Metrabyte data acquisition system is used to acquire thermocouple and LVDT data. The thermal expansion of the bottom heat exchanger is taken into account when interpreting the LVDT measurements and estimates of the uncertainty are determined using standard methods.

Results

Experimental conditions (in terms of the maximum top and bottom heat exchanger temperatures) are listed in Table 2. To compare predictions and experimental measurements, the heat transfer model was modified to predict the transient temperature distribution within the bakelite (properties are listed in Table 1.) Measured temperature histories in the top and bottom heat exchangers were used as boundary conditions in the model. As expected, because of the straightforward nature of this heat transfer analysis, the predicted temperatures within the bakelite are in excellent agreement with measured values [23] and are not reported here.

Measurements and predictions for the expansion and contraction of the polycarbonate column height are presented in Fig. 5. Overall, good agreement exists between the measurements and the predictions, except at times greater than indicated by the vertical mark shown on each predicted response.

The column of spheres is measured and predicted to expand until approximately 900 s in Experiment 1, 700 s in Experiment 2 and 600 s in Experiment 3. The accelerated transition from expansion to contraction is due to the higher operating temperatures associated with Experiments 2 and 3. The degree of column shrinkage is different in the various experiments and is maximum for Experiment 3. Because the contraction is proportional to the sintering rate, it is expected that Experiment 1 and Experiment 3 will have the minimum and maximum rates of contraction, respectively.

As previously noted, the experimental results and numerical predictions deviate after approximately 2400 s in Experiment 1, 1950 s in Experiment 2 and 1800 s in Experiment 3 as indicated by the vertical marks. The deviation is attributed to the fact that, as sintering progresses the diameter of the spheres increase in the manner shown in Fig. 2. At these particular times, the largest sphere diameters are predicted to be equal to the diameter of the cavity in the bakelite test cell. Hence, after this time there will be no increase in the diameter of the largest particles, and shrinkage of the sphere column will be suppressed. The duration of non-interference between the spheres and the bakelite test cell could be increased, but only at the expense of reducing the co-linearity of the column of spheres.

At the conclusion of each experiment, the sintered columns of spheres were carefully removed from the test cell. A Nikon Metaphot Reflected Light microscope (model VMS) was used to observe the structurally-intact, sintered particles. Clear evidence of the interference described in the previous paragraph was noted with the bottom most spheres taking on a more cylindrical shape. More important, the neck radii at each interface were measured and compared with the predicted values of x. Note that each interface was viewed from orthogonal directions and no dependence of the measured neck radius with viewing angle could be observed.

Figure 6 shows the measured and predicted neck radii for Experiments 1, 2, and 3. Note that interface number "n" corresponds to the junction between sphere "n" and sphere "$n+1$." The small differences between the predicted and the measured values of the neck radii are due to various reasons. In the model, it is assumed that two adjacent spheres begin sintering when the average center

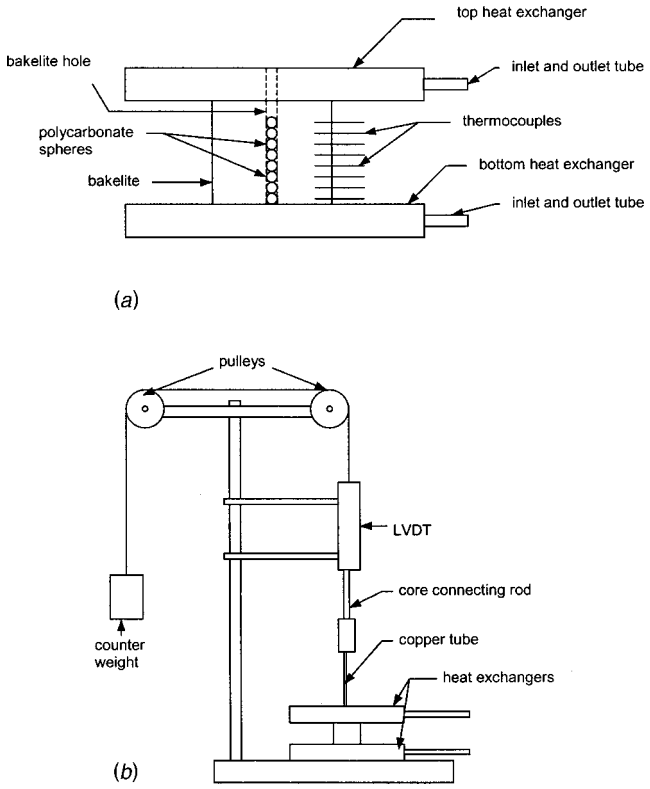

Fig. 4 Diagram of (*a*) the test cell and (*b*) the experimental apparatus

Table 2 Maximum temperatures applied to bottom and top heat exchangers for Experiments 1, 2, and 3

Experiment	T_b, °C	T_t, °C
1	167	150
2	187	150
3	198	150

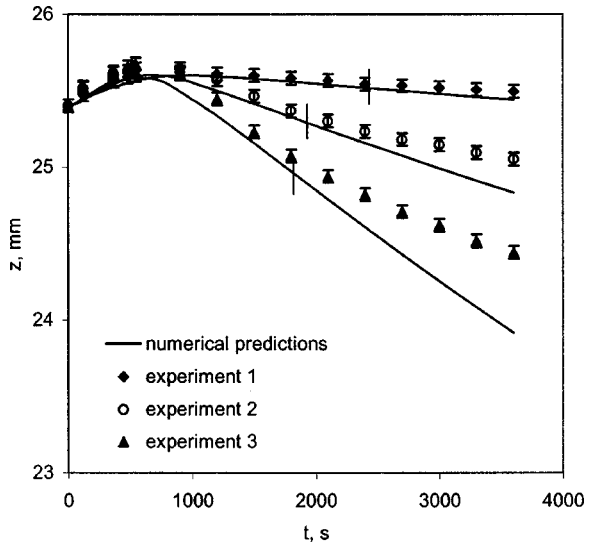

Fig. 5 Experimental measurements and predictions of the expansion and contraction of the column of spheres for Experiments 1, 2, and 3. The vertical fiducial marks are associated with the time when there is predicted interference between the medium and the walls of the test cell.

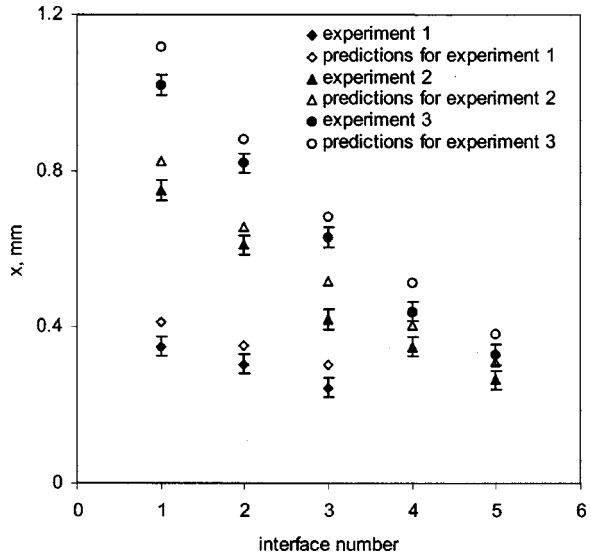

Fig. 6 Predicted and measured neck radii for Experiments 1, 2, and 3

point temperature of the two particles reaches T_g. Because the particles used in the experiments are relatively large, spatial temperature variations will exist within each sphere, leading to some discrepancy between measurement and prediction. As previously discussed, the diameter of the sintering spheres is restricted by the test cell hole dimension and, as a result, smaller x/a values are expected in the experiments. Despite the potential for discrepancies, the comparison between actual and predicted morphological evolution of the medium in response to heating is deemed to be very good.

Parametric Simulations

With agreement between the predictions and the measurements established, the model was then used to conduct parametric investigations. For these simulations, a domain filled with spherical polycarbonate powder in a column was considered. The bottom and the top surfaces of the domain are subjected to two different temperatures. The physical processes (heat transfer and sintering) are considered to be one-dimensional. The initial height of the powder layer is 25 mm and three different sized particles (diameters of 50, 100, and 250 μm) are considered. As before, each computational control volume is associated with an individual powder particle, necessitating predictions using 500, 250, and 100 control volumes.

Predicted temperature distributions associated with a 100 μm particle case are shown in Fig. 7. In this result, $T_b = 180°C$, $T_t = 30°C$, and $T_i = 30°C$. The temperature distributions are nearly independent of the particle size [23].

Neck radii at the particle interfaces at various times for 50, 100, and 250 μm particle powder layers are presented in Figs. 8(*a*)–8(*c*). For each case, the degree of sintering increases at any location with time, but the sintering rate decreases with increasing x/a and concurrent loss of surface energy. The smallest particles undergo more extensive sintering, as anticipated by inspection of Eq. (1). In each case, a sintering penetration depth of approximately 12 percent of the initial powder layer thickness exists at $t = 300$ s.

Figure 8(*d*) shows the changes in the height of the powder region for the different diameter particles. Here, ΔL is the difference between the height at any instant and the initial height. At 300 s the powder bed associated with 50 μm and 100 μm particles contract from the initial height (this contraction can be noted upon

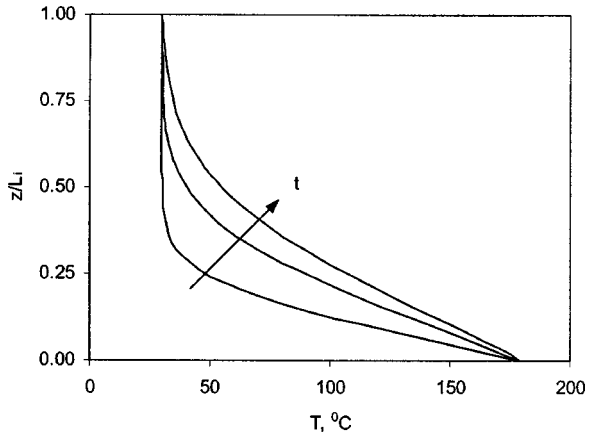

Fig. 7 The predicted temperature distributions for a medium composed of 100 μm particles with 180°C bottom surface temperature. Distributions are shown at 60 s, 180 s, and 300 s.

careful inspection of Fig. 7), while the powder bed composed of 250 μm particles is slightly larger than its initial thickness. This behavior is directly related to the degree of sintering noted in Figs. 8(*a*)–8(*c*).

Additional simulations were performed with various initial and boundary thermal conditions applied to the system. In the cases that follow, adiabatic conditions were applied to the top surface of the powder layer, and the simulations were curtailed prior to the top surface temperature rising by more than 0.1°C. Because $\delta_T > \delta_s$, the following results are associated with a semi-infinite medium. The following predictions are associated with two dimensionless temperatures that are defined as

$$\theta_1 = \theta_2 \equiv (T_g - T_i)/(T_b - T_i) \tag{6}$$

where θ_1 is used to denote cases where T_b is varied, and T_i is held constant, while θ_2 is defined for cases when T_i is varied and T_b is held constant.

Figure 9 includes x/a_i distributions as well as the change in

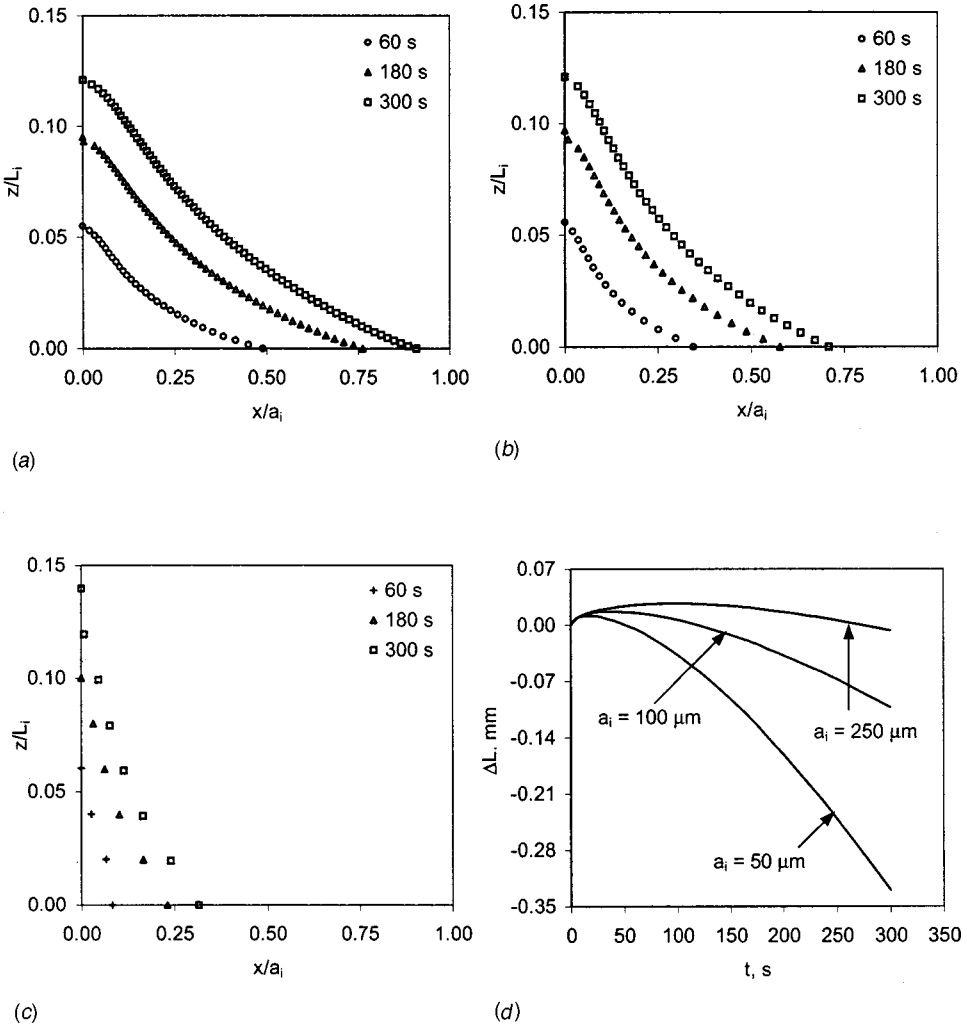

Fig. 8 Dimensionless neck radii distributions for media composed of (*a*) 50 μm, (*b*) 100 μm, and (*c*) 250 μm particles at different times with 180°C and 30°C bottom and initial temperatures. Also shown is (*d*) the change in the height of the medium with time.

height of the powder layer height for different diameter particles. Here, $T_b=170°C$ and $T_i=30°C$ yielding $\theta_1=\theta_2=0.82$. A comparison of Figs. 9(*a*) through 9(*c*) with Figs. 8(*a*) through 8(*c*) shows that x/a_i is reduced as the bottom surface temperature is decreased as expected. In addition, changes in the powder layer thickness are less significant as the bottom temperature is reduced, as noted by comparing Fig. 9(*d*) with Fig. 8(*d*).

The dynamic response of the semi-infinite medium may be illustrated by inspecting the time variation of δ_T and δ_s. Analytical expressions for the thermal penetration depth may be used yielding

$$0.99 \equiv \mathrm{erf}(0.5\delta_T/(\alpha_{\mathrm{eff}}t)^{1/2}) \tag{7}$$

In addition, the sintering penetration depth may be approximated as the vertical location at which the medium reaches T_g

$$(T_g-T_b)/(T_i-T_b) \equiv \mathrm{erf}(0.5\delta_s/(\alpha_{\mathrm{eff}}t)^{1/2}) \tag{8}$$

where α_{eff} is evaluated at $(T_i+T_b)/2$ and $x/a=0$ in Eqs. (8) and (9).

Predicted and calculated δ_T histories for different θ_1 values associated with a medium composed of 100 μm diameter particles are presented in Fig. 10(*a*). Three different values of T_b (158°C, 170°C, and 183°C) lead to $\theta_1=0.75$, 0.82, and 0.9 respectively. The analytical and predicted values of δ_T are slightly different because of the variable properties used in the numerical solution.

Inspection of Fig. 10(*b*) shows that the predicted value of δ_s is greater than the analytical value, and the predicted value exhibits a high frequency response. The fluctuating response is related to the particulate nature of the medium. Specifically, the predicted value of δ_s is defined as the height where the neck radius at the interface between the particles of the column is minimum but not equal to zero. Hence, as sintering propagates upward from interface-to-interface, discontinuous behavior occurs. The predicted value of δ_s is greater than the analytical value because the thermal diffusivity in the sintered region is larger than the value used in the analytical expression.

The value of $\Re \equiv \delta_s/\delta_T$ for the 100 μm particle size medium is presented in Fig. 10(*c*). The analytical value of $\Re$ is found by manipulating Eqs. (7) and (8) yielding

$$\Re \equiv 0.55\,\mathrm{erf}^{-1}((T_g-T_b)/(T_i-T_b)) = 0.55u \tag{9}$$

where erf^{-1} is defined as follows. If $y=\mathrm{erf}(x)$, then $x=\mathrm{erf}^{-1}(y)$. Because the predicted value of δ_s exceeds the analytical value, the predicted value of $\Re$ exceeds its analytical value as well. Note that the results for the 50 and 250 μm particle diameter cases are similar to those shown in Fig. 10, except the response of the

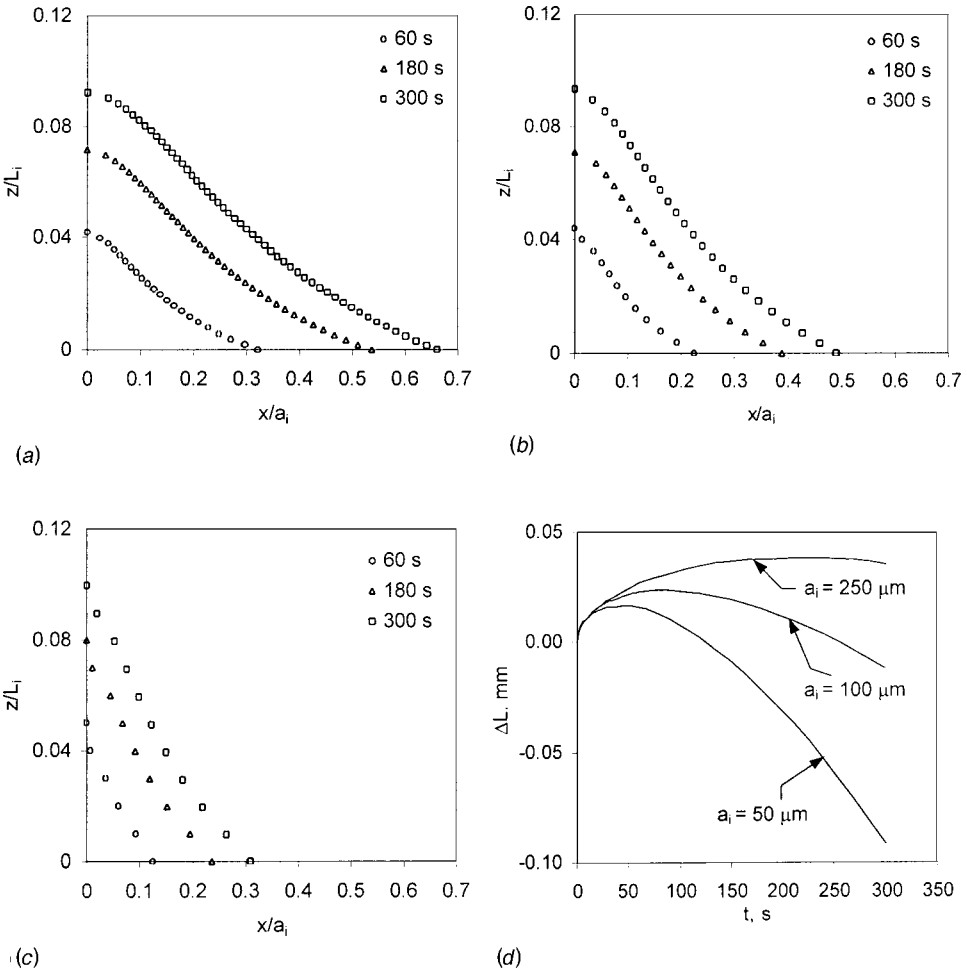

Fig. 9 Dimensionless neck radii distributions for media composed of (*a*) 50 μm, (*b*) 100 μm, and (*c*) 250 μm particles at different times with 170°C and 30°C bottom and initial temperatures yielding $\theta_1=0.82$. Also shown is (*d*) the change in the height of the medium with time.

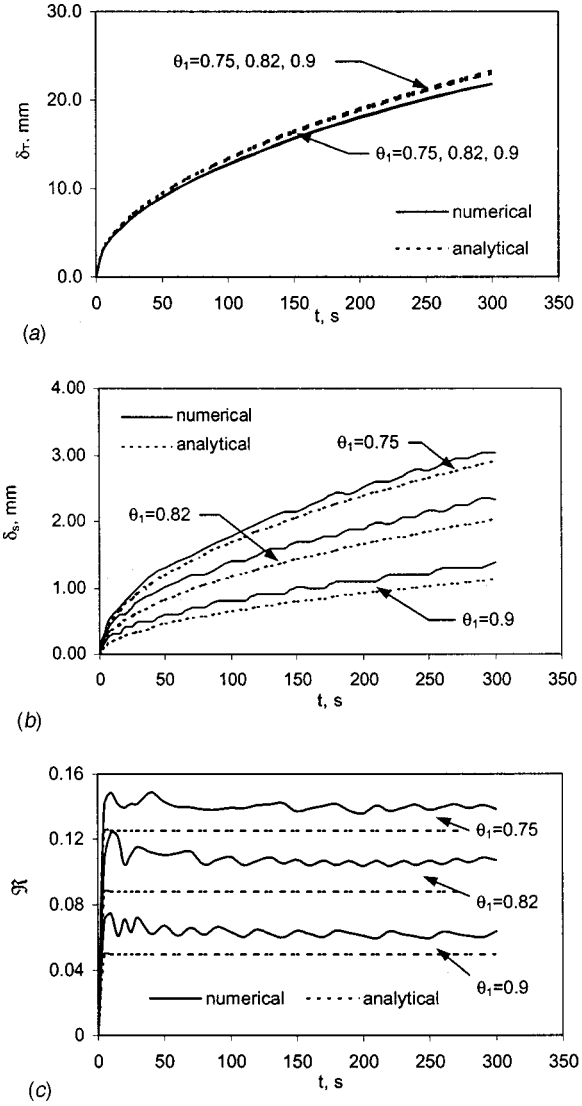

Fig. 10 Results showing (*a*) the thermal penetration depth (*b*) the sintering penetration depth and (*c*) ratio of the penetration depths for a medium composed of 100 μm particles column with different θ_1

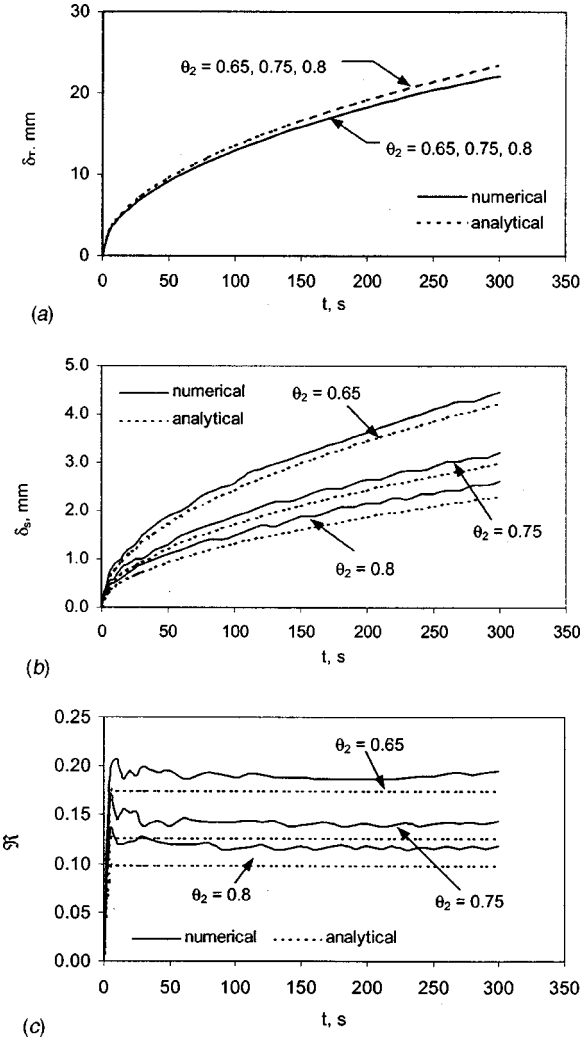

Fig. 11 Results showing (*a*) the thermal penetration depth (*b*) the sintering penetration depth and (*c*) ratio of the penetration depths for a medium composed of 100 μm particles column with different θ_2.

sintering penetration depth is of lower (higher) amplitude and higher (lower) frequency for the medium composed of smaller (larger) particle [23].

Figure 11 is included to show the effect of different values of θ_2 on the δ_T, δ_s, and $\Re$ behavior for the medium composed of 100 μm diameter particles. In this case three different values of T_i were used (98.57°C, 70°C, and 45°C) while T_b was held at 170°C. As required, the predicted δ_T values are same for $\theta_2 = 0.65$, 0.75, and 0.8 as evident in Fig. 11(*a*). The results of Fig. 11(*b*) suggest that δ_s becomes larger as θ_2 is reduced. That is, higher initial temperatures promote larger sintering penetration depths. The larger values of δ_s associated with smaller values of θ_2 induce higher values of $\Re$ for smaller values of θ_2 (Fig. 11(*c*)).

From the practical point of view, it is desirable to be able to predict the value of δ_S for purposes of controlling thermal processing conditions, especially in net shape manufacturing processes. To this end, a relationship between $\Re$ and θ_1 (as well as θ_2) is presented in Fig. 12. The predicted values of $\Re$ for different values of θ_1 and θ_2 are associated with the ratio of penetration depth averaged over the time span 5 s$\leq t \leq$300 s and are shown as data points. Slight variations in the predicted values of $\Re$ occur due to the highly variable properties and the discontinuous nature of the medium. The average predicted value of $\Re$ was used to construct the curve fit shown in Fig. 12. Agreement between the curve fit and any predicted value of $\Re$ is within 3 percent. The analytical expression for $\Re$ is taken from Eq. (9). The predicted and the analytical relationship are within 20 percent of each other. Note that these relationships are valid for a packing of spherical polycarbonate particles with $0 < x/a_i \leq 0.8$, 158°C$\leq T_b \leq$183°C, and 30°C$\leq T_i \leq$98°C.

Conclusions

A model has been developed to analyze the coupled thermal and morphological response of polycarbonate powder subjected to spatially non-isothermal conditions. Experiments were performed to generate data that was subsequently used to validate the model. A number of interesting features (expansion and contraction of powder during non-isothermal heating) are predicted using the model and these predicted features were corroborated with the experimental results. Parametric simulations were performed to examine the physical and thermal responses to various initial and thermal conditions and also to different sizes of the powder. From

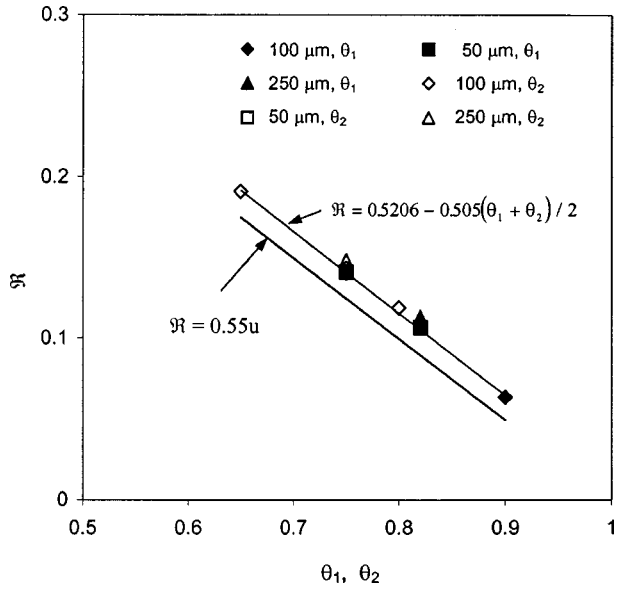

Fig. 12 The ratio of sintering penetration depth to the thermal penetration depth for different dimensionless temperatures. Numerical predictions are denoted by the data points.

the parametric investigations it was concluded that by controlling the boundary and initial conditions one can control the sintering penetration depth in the porous medium. A relationship was established between the ratio of the sintering penetration depth to the thermal penetration depth and the non-dimensional boundary and initial temperatures, allowing easy estimation of sintering penetration depths given knowledge of the thermal processing temperatures.

In actual sintering processes the particles may be arranged in a random manner which may affect the results presented here. In addition, due to the thermal and contraction of the particles, multi-dimensional mechanical responses are likely to occur, even in systems characterized by one-dimensional heat transfer. Additional areas of investigations might include sintering of different types of amorphous, crystalline or semi-crystalline materials, sintering of randomly-shaped particles, or processing of particles that have a wide size and shape distribution.

Acknowledgment

This material is based upon work supported by the National Science Foundation under Grant No. CTS-9796186.

Nomenclature

A = cross-sectional area, m^2
a = sphere radius, m
A_v = viscosity rate constant, $N \cdot s/m^2$
c_p = specific heat, $J/kg \cdot K$
d = particle separation half distance, m
E_v = activation energy, kcal/mol
k = thermal conductivity, $W/m \cdot K$
h = medium height, m
ΔL = change in height, m
m = mass, kg
R = universal gas constant, $kcal/mol \cdot K$
$\Re$ = ratio of penetration depths
T = temperature, K
t = time, s
V = volume, m^3
x = neck radius, m
z = vertical coordinate direction

Greek Symbols

α = thermal diffusivity, m^2/s
δ_s = sintering penetration depth, m
δ_T = thermal penetration depth, m
ε = emissivity
ϕ = porosity
η = viscosity, $N \cdot s/m^2$
Γ = surface tension, N/m
ρ = density, kg/m^3
θ = angle of intersection, dimensionless temperature
χ = linear expansion coefficient, K^{-1}

Subscripts

a = air
b = bottom
eff = effective
f = final
g = glass transition
i = initial
m = mean
s = solid
t = top

References

[1] Rabinovich, E. M., 1985, ''Preparation of Glass by Sintering,'' J. Mater. Sci., **20**, pp. 4259–4297.
[2] Crawford, R. J., 1992, *Rotational Molding of Plastics*, John Wiley & Sons, Inc., New York.
[3] Kipphut, C. M., Bose, A., Farooq, S., and German, R. M., 1988, ''Gravity and Configurational Energy Induced Microstructural Changes in Liquid Phase Sintering,'' Metall. Trans. A, **19A**, pp. 1905–1913.
[4] Conley, J. G., and Marcus, H. L., 1997, ''Rapid Prototyping and Solid Free Form Fabrication,'' ASME J. Manuf. Sci. Eng., **119**, pp. 811–816.
[5] Martinez-Herrera, J. I., and Derby, J. J., 1994, ''Analysis of Capillary-Driven Viscous Flows During the Sintering of Ceramic Powders,'' AIChE J., **40**, pp. 1794–1803.
[6] Martinez-Herrera, J. I., and Derby, J. J., 1995, ''Viscous Sintering of Spherical Particles via Finite Element Analysis,'' J. Am. Ceram. Soc., **78**, pp. 645–649.
[7] Frenkel, J., 1945, ''Viscous Flow of Crystalline Bodies Under the Action of Surface Tension,'' Journal of Physics, **9**, pp. 385–391.
[8] Eshelby, J. D., 1949, ''Discussions of Seminar on the Kinetics of Sintering,'' Metall. Trans., **185**, pp. 796–813.
[9] Scherer, G. W., 1992, ''Constitutive Models for Viscous Sintering,'' *Mechanics of Granular Materials and Powder Systems*, M. M. Mehrabadi, ed. ASME, MD-Vol. 37, New York, pp. 1–18.
[10] Pokluda, O., Bellehumeur, C. T., and Vlachopoulos, J., 1997, ''Modification of Frenkel's Model for Sintering,'' AIChE J., **43**, pp. 3253–3256.
[11] Jagota, A., and Dawson, P. R., 1988, ''Micromechanical Modeling of Powder Compacts-I. Unit Problems for Sintering and Traction Induced Deformation,'' Acta Metall., **36**, pp. 2551–2561.
[12] Rosenzweig, N., and Narkis, M., 1981, ''Dimensional Variations of Two Spherical Polymeric Particles During Sintering,'' Polym. Eng. Sci., **21**, pp. 582–585.
[13] Van de Vorst, G. A. L., 1994, ''Numerical Simulation of Axisymmetric Viscous Sintering,'' Eng. Anal. Boundary Elem., **14**, pp. 193–207.
[14] MacKenzie, J. K., and Shuttleworth, R., 1949, ''Phenomenological Theory of Sintering,'' Proc. Phys. Soc. London, Sect. B, **62**, pp. 833–852.
[15] Scherer, G. W., 1977, ''Sintering of Low-Density Glass: I, Theory,'' J. Am. Ceram. Soc., **60**, pp. 236–239.
[16] Bellehumeur, C. T., Bisaria, M. K., and Vlachopoulos, J., 1996, ''An Experimental Study and Model Assessment of Polymer Sintering,'' Polym. Eng. Sci., **36**, pp. 2198–2207.
[17] Reid, C. R., and Oakburg, R. G., 1990, ''A Continuum Theory for the Mechanical Response of Materials to the Thermodynamic Stress of Sintering,'' Mech. Mater., **10**, pp. 201–213.
[18] Reid, C. R., 1992, ''Application of a Continuum Theory for Sintering to Densification Rates,'' *Mechanics of Granular Materials and Powder Systems*, M. M. Mehrabadi, ed. ASME, MD-Vol. 37, New York, pp. 19–27.
[19] Beruto, D., Botter, R., and Searcy, A. W., 1989, ''Influence of Temperature Gradients on Sintering: Experimental Tests of a Theory,'' J. Am. Ceram. Soc., **72**, pp. 232–235.
[20] Kandis, M., and Bergman, T. L., 1997, ''Observation, Prediction, and Corre-

lation of Geometric Shape Evolution Induced by Non-Isothermal Sintering of Polymer Powder,'' ASME J. Heat Transfer, **119**, pp. 824–831.
[21] Nelson, J. C., Xue, S., Barlow, J. W., Beaman, J. J., Marcus, H. L., and Bourell, D. L., 1993, ''Model of the Selective Laser Sintering of Bisphenol-A Polycarbonate,'' Ind. Eng. Chem. Res., **32**, pp. 2305–2317.
[22] Van Vlack, L. H., 1989, *Elements of Materials Science and Engineering*, 6th edition, Addison-Wesley Publishing Company, Inc., Reading, MA.
[23] Tarafdar, R. M., 2001, ''Numerical and Experimental Study of One-Dimensional, Non-Isothermal Sintering of Amorphous Polymer Materials,'' M. S. thesis, University of Connecticut, Storrs, CT.
[24] Incropera, F. P., and DeWitt, D. P., 1996, *Introduction to Heat and Mass Transfer*, 4th edition, John Wiley & Sons, Inc., New York.

Flow Visualizations and Transient Temperature Measurements in an Axisymmetric Impinging Jet Rapid Thermal Chemical Vapor Deposition Reactor

A. G. Mathews

J. E. Peterson
e-mail: pete@cimar.me.ufl.edu

Department of Mechanical Engineering,
University of Florida,
Gainesville, FL 32611

Carrier gas flow in a rapid thermal chemical vapor deposition (RTCVD) reactor was studied using flow visualization and laser induced Rayleigh light scattering (RLS). The flow field consists of a downward axisymmetric jet of carrier gas impinging on a wafer which undergoes transient heating. Flow visualization results showed three stable flow regimes as the surface rose from ambient to high temperature: momentum dominated, buoyancy dominated, and a second momentum dominated regime at high temperature; each separated by unstable, chaotic flows. RLS temperature measurements provided transient gas temperature histories, documenting flow visualization results. Regions of momentum dominated, buoyancy dominated, and unstable flows were defined as a function of Grashof number, Reynolds number, pressure, and wafer temperature.
[DOI: 10.1115/1.1469525]

Keywords: Experimental, Mixed Convection, Temperature, Thin Films, Transient

Introduction

The formation of thin films of semiconductors is an important technology to the microelectronics industry. The most common processes of depositing thin silicon films are by quasi-steady state chemical vapor deposition (CVD) and by transient rapid thermal chemical vapor deposition (RTCVD). In RTCVD, a non-reactive carrier gas is used to deliver silicon to the surface of a single substrate wafer. Transient radiative heating of the wafer surface causes the silicon to automatically deposit on the wafer surface. This technology has several advantages, including short processing times and the ability to form high quality films because of better control of temperature and carrier gas behavior (Fair [1]). There are many different geometries used in CVD and RTCVD processing, including, for example, horizontal reactors, vertical pedestal reactors and barrel reactors. Two commonly studied reactor configurations are the horizontal duct and the vertical axisymmetric because of their fundamental nature. Regardless of geometry, however, knowledge of conditions leading to carrier gas stability is critical for film uniformity, and the goal of many numerical and experimental projects.

The focus of the present work is the experimental simulation and characterization of carrier gas fluid mechanics in a vertical axisymmetric impinging jet reactor during a transient heating process. A schematic of the test section is seen in Fig. 1. When the disc surface is heated, the flow field consists of an opposition of downward jet momentum versus upward disc buoyancy. The numerous length scales required to define the geometry in Fig. 1 make clear the complexity of the problem, and an objective of the project was to find which of these lengths is useful to characterize flow transitions. Flow visualizations were performed first to obtain an overall picture of flow field stability and transitions under conditions typical of the RTCVD transient heating process. Laser induced Raleigh light scattering temperature measurements were then used to provide quantitative documentation of gas transient temperatures and transitions.

Contributed by the Heat Transfer Division for publication in the JOURNAL OF HEAT TRANSFER. Manuscript received by the Heat Transfer Division March 28, 2001; revision received November 19, 2001. Associate Editor: C. Amon.

Rapid Thermal Chemical Vapor Deposition

Numerical simulations of the CVD and RTCVD processes are limited by the inherent complexity of the problem. While Coltrin [2,3] focused on the chemical kinetics and rate equations, most simulations decouple the chemical rate equations, or neglect them completely. This is an appropriate simplification because the silicon laden reactants are present in the carrier gas only in dilute amounts, and the heats of reaction during RTCVD do not contribute significantly to the energy conservation equation (Jensen [4]).

However, the carrier gas is usually numerically modeled as non-Boussinesq, thus other simplifications are required to make the problem tractable. Evans and Grief [5–7] focused on instabilities and asymmetries resulting from buoyancy in both horizontal and vertical axisymmetric CVD reactors. Mahajan and Wei [8] examined buoyancy as well as Soret, Dufour and variable property effects commonly neglected in other models. Fotiadis et al. [9–11] established CVD operation regions where multiple steady flows are possible. Many of these were unsteady and asymmetric, and some depended on flow history. Jensen et al. [4] provide an excellent summary and discussion of the modeling of the CVD and RTCVD process including sections on both horizontal and vertical geometries and effects of boundary conditions, the existence of multiple stable flows, lack of symmetry and the dependence of start up procedure. Merchant [12] developed a systematic modeling approach to aid in design and optimization of CVD reactors. Hebb and Jensen [13] used a detailed radiation model to examine the effect of variable radiative properties of a patterned wafer on temperature distribution in RTCVD. More recently two-dimensional (2D) and three-dimensional (3D) models have been compared by Kelkar and Mahajan [14] and Mihopoulos et al. [15]. Soong et al. [16] numerically studied a rotating disc CVD reactor and created a parameter map that showed transitions between three different types of flows: rotational, buoyant and plug.

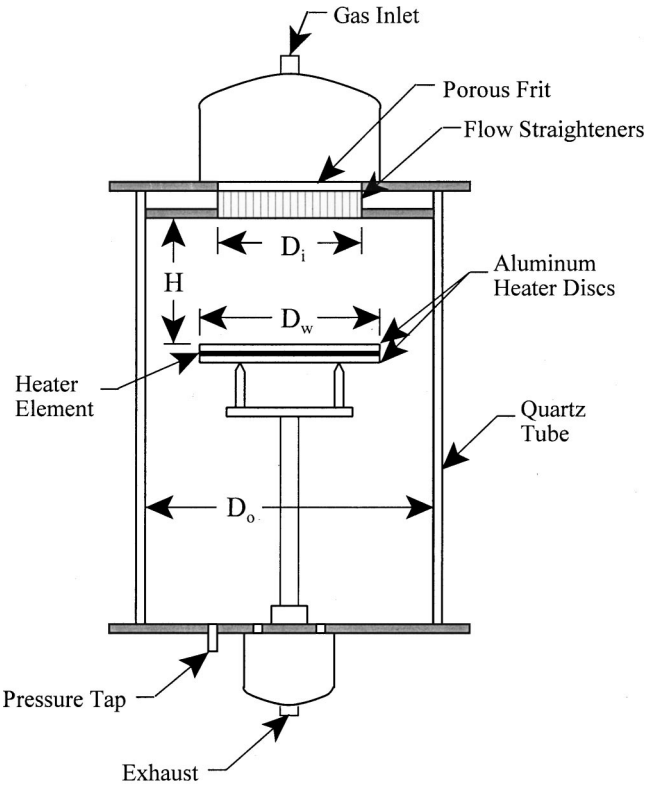

Fig. 1 Schematic of test section used to simulate an axisymmetric, impinging jet RTCVD reactor

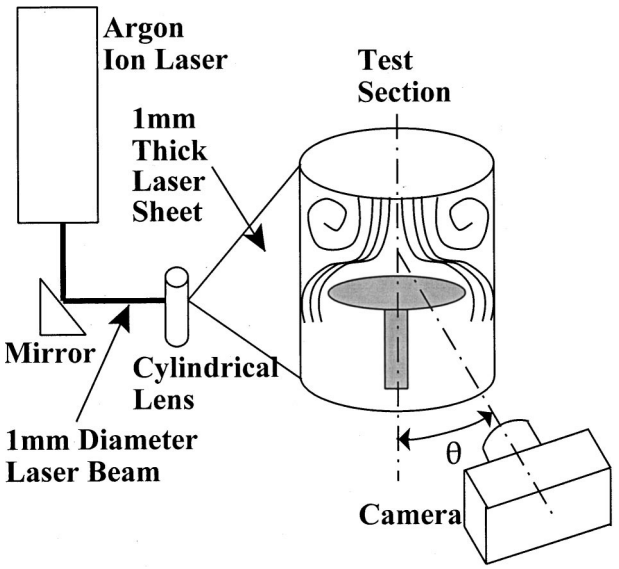

Fig. 2 Schematic of flow visualization apparatus

Experimental verification of carrier gas flow and temperature has been limited. Flow visualizations were used to study effects of reactor geometry and wafer rotation (Wang et al. [17], Gadgil [18]). Fotiadis et al. [10,11] used flow visualization and Raman light scattering to find CVD reactor gas flow patterns and temperature. The weak signal characteristic of Raman scattering required long averaging times and made transient effects impossible to distinguish. Salim et al. [19] used infrared spectroscopy to obtain path averaged information in a vertical rotating CVD reactor, while Johnson et al. [20] evaluated infrared thermography for CVD applications. Laser induced Rayleigh scattering (RLS) was used by Horton and Peterson [21,22] to find transient carrier gas temperature in a RTCVD reactor. This method yielded real time transient temperature measurements in a discrete control volume, and established the method as a viable one for non-invasively finding temperature with high temporal and spatial resolution.

Experimental Apparatus

Flow Visualization. Flow visualizations were used to obtain overall information about flow phenomenon in the test section. Apparatus consisted of a 4 watt argon ion laser beam of 1 mm diameter which was expanded into a light sheet using a cylindrical lens, as illustrated in Fig. 2. The flow visualizations were conducted by first establishing the target mass flow rate and pressure in the test section. The carrier gas was seeded with smoke particles. The disc heater was turned on and a step power input of 825 watts was applied to the heater. This power level, test section pressure and inlet flow rate remained constant until the end of the test. When the disc reached T_{max} the power was turned off and the test ended. Each test run was video taped or photographed for subsequent analysis. Transients were characterized in terms of Grashof number, Gr_H, based on inlet to disc distance, H, with both the thermal expansion coefficient and the kinematic viscosity evaluated at a film temperature $T_{film} \equiv (T_w - T_{in})/2$. The Reynolds number, Re_{in}, was based on test section inlet diameter and fluid properties evaluated at the inlet temperature. Numerical simulations have well established the non-Boussinesq nature of this problem, thus non-dimensionalization of the governing equations indicates a third parameter of importance; dimensionless temperature ratio defined as:

$$\chi = \frac{T_w - T_{in}}{T_{in}}. \tag{1}$$

In the present work, Reynolds number and maximum Grashof number were chosen to simulate typical RTCVD operating conditions and to match the large body of existing numerical studies. Maximum value of χ was limited to 1.6 by the melting temperature of the aluminum disc. Typical test section pressures studied in numerical works ranged from 0.05 ATM to 1 ATM, and typical Reynolds numbers ranged from 1 to 100. Preliminary flow visualizations revealed that for pressures above 0.3 ATM the flow was very strongly dominated by buoyant forces. Limits on the capabilities of the vacuum pump also restricted the upper limit of the inlet flow rate. From this a test matrix was developed and flow visualization were conducted at Reynolds numbers of 15, 30, 45, and 60, at pressures of 0.05, 0.1, 0.15, and 0.2 ATM and for inlet to disc ratios of $H/D_w = 0.35$ and 0.55. Flow visualizations were also conducted for $Re_{in} = 30$, $H/D_w = 0.28$, and pressures of 0.05, 0.1, 0.15, and 0.2 ATM.

The dominant uncertainty was estimation of the disc temperature when transitions in gas flow occurred. Transitions occurred over a period of time, usually less than 5 sec, while the disc surface temperature was constantly increasing. Therefore the transition temperature was estimated to be the disc temperature at the midpoint of the transition period. The uncertainty in the disc transition temperature due to estimation of the instant of transition was approximately ± 12°C. The following values for uncertainty were used to calculate uncertainty of the Grashof number: disc temperature ± 12°C, gas inlet temperature ± 5°C, inlet to disc distance ± 0.0025 m, pressure $\pm .002$ ATM, and fluid dynamic viscosity ± 1.5 percent. Using a propagated error analysis (Holman [23]), uncertainty in transitional Grashof number was found to be ± 7 percent at test section pressures of 0.2 ATM, 8 percent at 0.15 ATM, 12 percent at 0.1 ATM and 23 percent at 0.05 ATM, with the dominant uncertainty due to run to run variation in transition temperature.

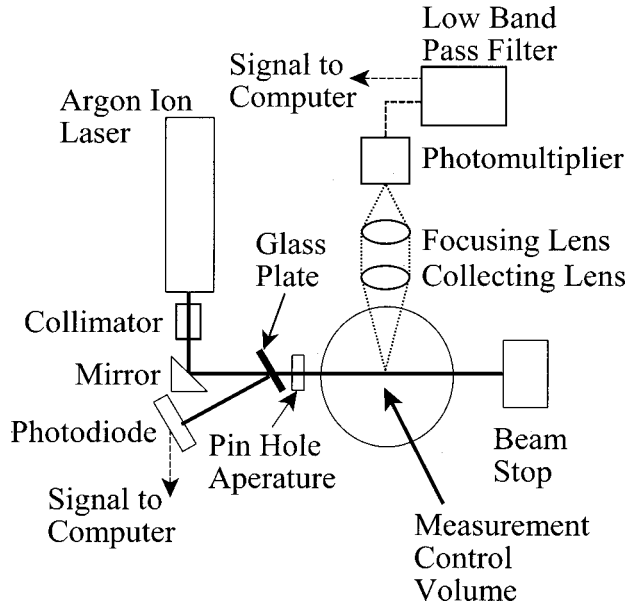

Fig. 3 Schematic of laser induced Rayleigh light scattering optical components

Rayleigh Light Scattering

Laser-induced Rayleigh light scattering occurs when the electric field of gas molecules interacts with the electric field of an incident laser beam, causing the gas molecules to resonate in unison with the laser. This causes a small amount light to be scattered in directions other than that of the incident beam. The total amount of light scattered is directly proportional to the molecular number density inside the control volume formed by the laser and the collection optics. Hence if the pressure is known, the temperature can be determined from the intensity of the scattered light. By first measuring the scattered light as a known reference temperature, T_{ref}, and pressure, the instantaneous temperature, T_j, can be determined as:

$$T_j = \frac{T_{\text{ref}} I_{\text{scat,ref}}}{I_{\text{scat}j}} \tag{2}$$

where I_{scat} is the intensity of scattered light.

The basics of Mie and Rayleigh light scattering theory are given in Van de Hulst [24], Kerker [25], and Bohren and Huffman [26]. Rayleigh light scattering has been used to study gas concentrations in turbulent mixing (Pitz et al. [27], by Pitz and Kashiwagi [28]) and a good background discussion can be found in those works. A schematic of the RLS system is seen in Fig. 3, and detailed description and evaluation of the system used in the present work is found in [21]. The control volume is defined by the laser beam diameter and collection optics, and was a 1 mm diameter by 0.15 mm in length.

The RLS signal is contaminated by glare reflected off the disc and test section. Glare is measured by filling the test section with helium as the initial step of each test run. The scattering cross section of helium is only about 0.015 of that of air, so intensity of scattered light from a helium filled test section is an excellent estimate of glare. The test section is refilled with air, a reference voltage at known ambient temperature is recorded, and the transient heating process initiated. The instantaneous gas temperature is found as:

$$T_j = T_{\text{ref}} \left[\frac{V_{\text{scat,ref}} - V_{\text{glare}}}{V_{\text{scat},i} - V_{\text{glare}}} \right] \tag{3}$$

Disc surface temperature was allowed to rise to 500 °C, and at each half second interval four PMT readings were sampled at 12 Hz and averaged to get a data point. Data from the photodiode (monitoring incident laser light power) pressure transducer and thermocouple were also stored in the computer for later analysis. The uncertainty in the RLS gas temperature measurements is discussed in detail by Horton and Peterson [21,22], and was estimated at $\pm 2-4$ °C.

Results: Flow Visualization

Flow visualization results showed three stable flow regimes during the transient heating process, and also unstable transitional flows. The flow visualizations were carried out for each set of parameters given in the test matrix and the Grashof number at each transition was calculated. Flow visualization photographs are seen in Figs. 4(*a–e*). In these photographs, the vertical dark line near the middle of the photograph is a test section support structure, and the horizontal lines are shadows from the extruded quartz cylinder wall. Bright regions show the highly seeded inlet flow. Smoke particles used to seed the flow were driven away from the heater surface by thermophoretic forces, thus dark areas in Figs. 4(*b–e*) show high temperature fluid. While the flow structures were all initially momentum dominated (Fig. 4(*a*), in most cases the flow became unstable, and then either dominated by a stable buoyant regime or a stable momentum flow regime as the disc temperature rose. These transitions are best interpreted in terms of Grashof number as a function of dimensionless temperature, χ. Transitions are graphed in Fig. 5(*a–e*) for the five Reynolds numbers tested, and discussed below. Also graphed in Figs. 5 is disc Grashof number based on film properties. It is seen that peak buoyancy occurs at $\chi \approx 0.58$, and that decreased fluid density at higher temperature causes buoyancy at the surface to decrease. When as discussed below are examined together, regions of momentum dominated flows (shown shaded gray in Fig. 5), and buoyancy dominated (cross hatched area) could be estimated. These are separated by a region where fluid is unstable or, at times, in unstable equilibrium—either momentum or buoyancy dominated. The various areas and transitions were evaluated as follows:

Momentum Dominated. At test initiation, the wafer was at ambient temperature, and a stable momentum dominated flow regime formed (Fig. 4(*a*)). Carrier gas entered the test section and impinged smoothly on the wafer surface, remaining laminar to exit. Recirculation regions were caused by the sudden expansion inlet geometry.

First Instability: Momentum⇒Buoyant. After initiation of heating, buoyancy increased at the wafer surface, opposing the downward impinging jet momentum. The first instability was defined as the Grashof number when the system became unstable. As seen in Fig. 4(*b*), the impinging jet flow was disrupted by periodic thermal plumes bursting up from the surface due to the classic Rayleigh-Benard instability. These plumes formed at the stagnation region where the inlet air met the disc. Figure 5(*a*) shows this first instability occurs at Grashof numbers below 5000 when $\text{Re}_{\text{in}} = 15$. The Grashof number of the first instability increased with Reynolds number. Figure 5(*d*) shows the highest Reynolds number tested ($\text{Re}_{\text{in}} \approx 60$), where stable momentum flow was retained to Grashof numbers in the order of 25,000 at higher pressures.

Analysis of this initial instability showed the complexity of this problem. The relative importance of the four principle variables (pressure, Reynolds number, temperature ratio χ, and geometric ratio H/D_w) was assumed to be exponential. A four factor, multilevel analysis of the experimental data was performed. A multiple regression of the four parameters and their cross products was used to evaluate their importance and their interaction. Results shows all terms and cross products were of approximately equal significance. Figure 6 shows the initial instability for all test conditions, along with a correlation for $H/D_w = 0.3526$ stating the initial instability as a function of Grashof number. The *y*-axis in-

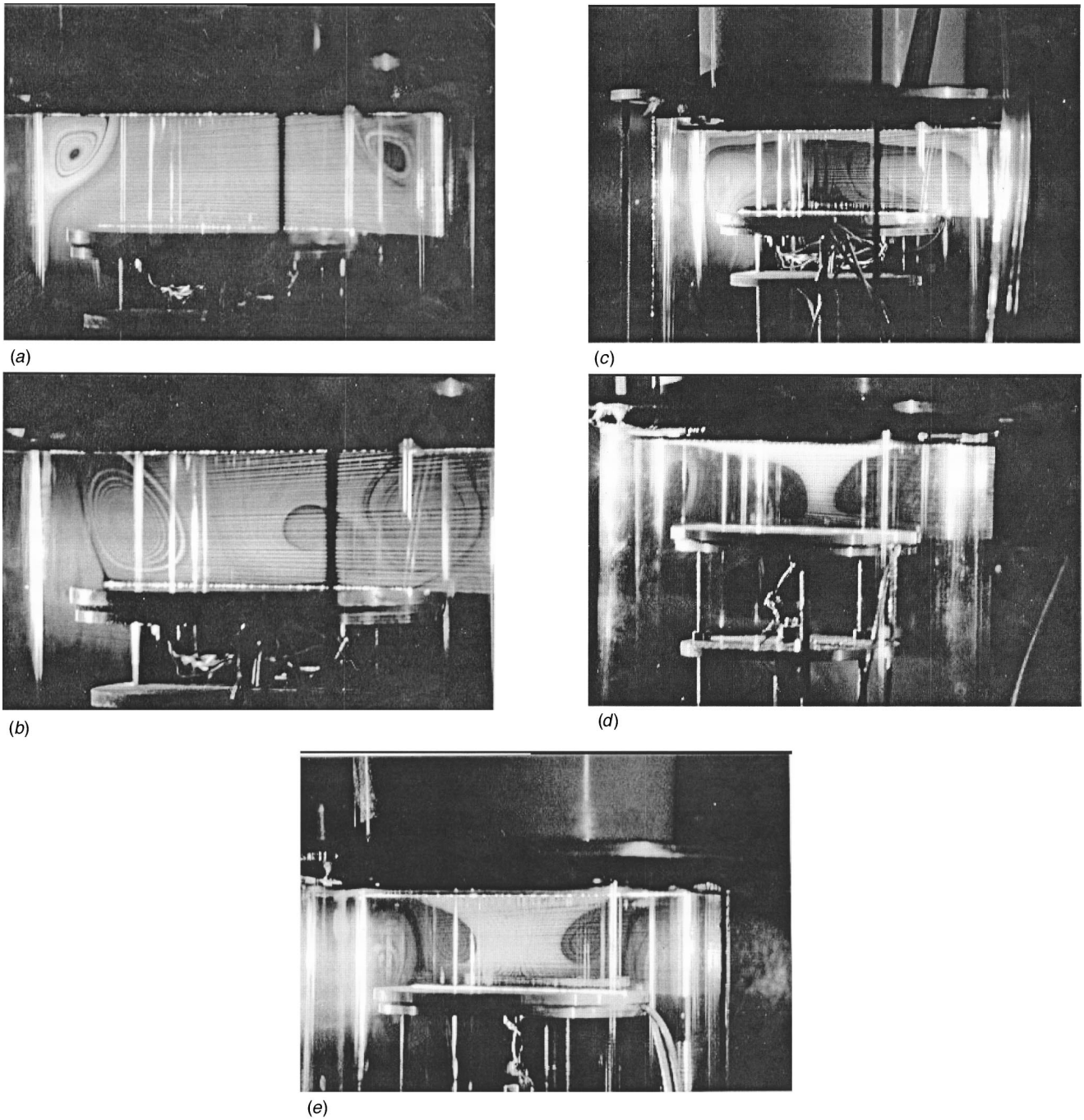

Fig. 4 (*a*) **Momentum dominated flow** ($Re_i=30$; $Gr_H=0$); (*b*) **first instability** ($Re_i=30$; $Gr_H\approx3500$); (*c*) **stable buoyant flow** ($Re_i=45$; $Gr_H\approx31{,}000$); (*d*) **second instability** ($Re_i=45$; $Gr_H\approx30{,}000$); **and** (*e*) **momentum dominated, high temperature** ($Re_i=30$; $Gr_H\approx11{,}500$)

tercept (for $Re_{in}=0$) of 1950 compares well with estimates of Behringer and Ahlers [29], who used instability theory to analytically predict critical Grashof number for the onset of convection in shallow cylinders. Their results applied to the current geometry predicts at transition at $Gr_H=2188$, only 1 percent higher than that predicted in Fig. 6. Figure 6 shows considerable scatter because the pressure dependence of this transition has not been considered; that is all pressures have been lumped together. Even so, it is clear that the two lower aspect ratios ($H/D_w=0.3526$ and 0.2756) are similar, while the highest aspect ratio has significantly higher transitions and does not appear to be headed towards the *y* intercept predicted by the other data and from shallow cylinder theory.

Depending on the test parameters this first unstable flow preceded either a buoyancy dominated or a high temperature momentum dominated flow as described below.

Buoyancy Dominated. Continued temperature increase led to formation of a stable buoyancy dominated flow easily seen in the strong thermal plume rising from the hot disc surface (Fig. 4(*c*)). The buoyant hot air would rise from the center of the disc surface almost to the inlet where it would meet the cool incoming air and deflect to the walls of the test section. The cool inlet air was deflected from the wafer surface, and would flow radially

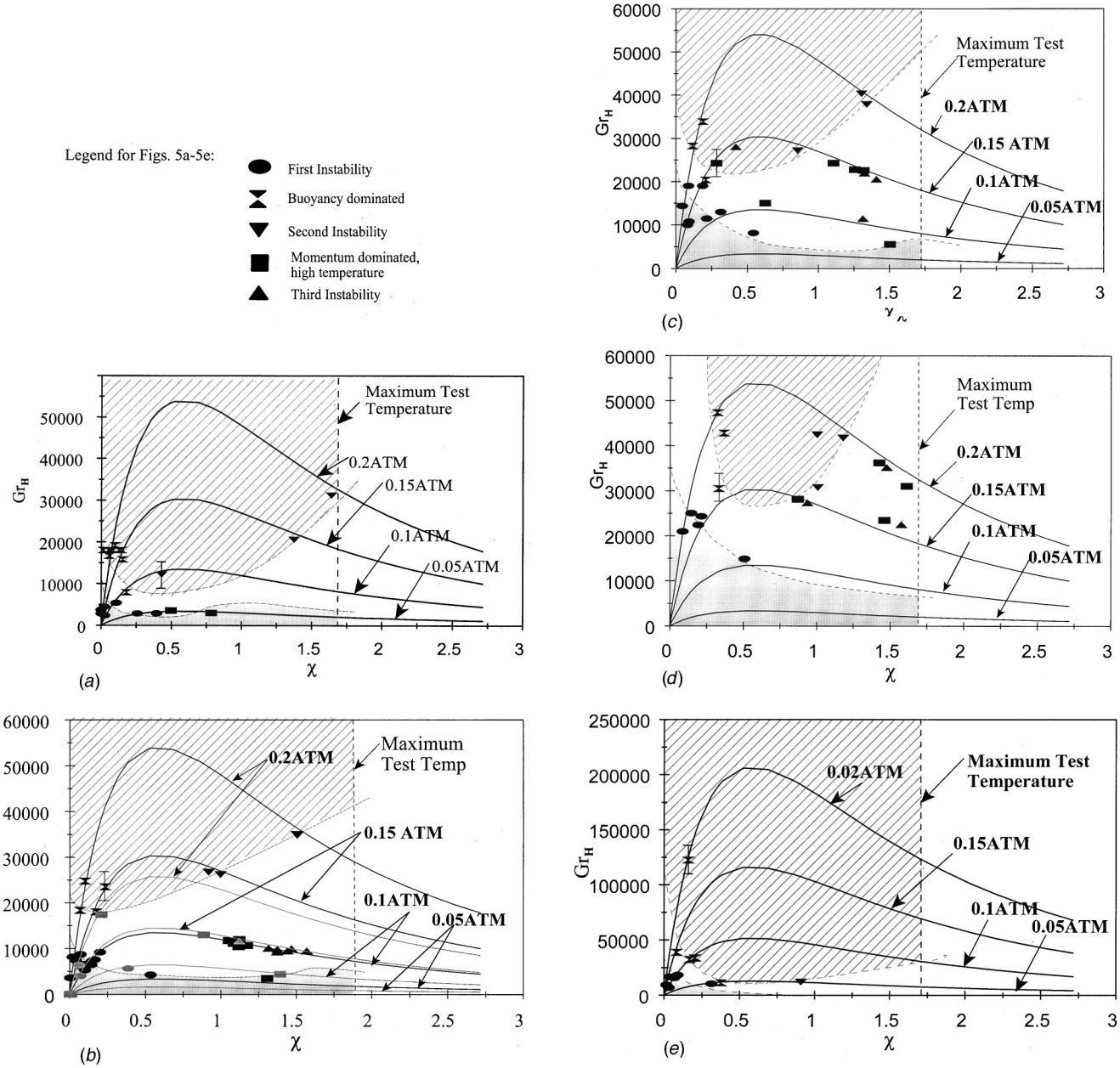

Fig. 5 Flow transitions as a function of Grashof and dimensionless wafer temperature for Reynolds numbers from 15 to 60, H/Dw=0.2756 to 0.5513, and pressures of 0.02 ATM to 0.05 ATM. The shaded area at the bottom of each graph indicates stable momentum driven flow, and the striped area at the top is a region of stable, buoyancy dominated flow. The central white area flow conditions create either unstable flows, or in some cases apparently stable momentum dominated flow which subsequently becomes unstable. (*a*) Re_i=15, H/D_w=0.3526; (*b*) Re_i=30, H/D_w=0.2756 (gray symbols), H/D_w=0.3526 (black symbols); (*c*) Re_i=45, H/D_w=0.3526; (*d*) Re_i=60, H/D_w=0.3526; and (*e*) Re_i=30, H/D_w=0.5513.

outward and down the walls and out the exhaust. Figure 5(*a*) shows stable buoyant flow was established below Grashof number of 20,000 at low Reynolds number, but is increasingly delayed (Figs. 5(*b*), 5(*c*)), not forming until Grashof numbers of 40000 to 50000 for an inlet Reynolds number of 60 (Fig. 5(*d*). Figure 5(*e*) shows the highest aspect ratio examined (H/D_w=0.5513). In this case, buoyancy was very strong, and buoyant flow dominated throughout the majority of the test space. In all cases buoyant flow occurred before the temperature of peak buoyancy.

Second Instability, Buoyant⇒Momentum. At high temperatures (χ>0.58) the maximum Grashof number had been exceeded, and decrease in fluid density at the disc surface resulted in decreased buoyancy. Density of the hot rising fluid decreased to the point that buoyant forces weakened and could no longer deflect the momentum driven gas. The interface where the hot, rising air met the cool inlet air would then deform, waiver and a column of denser inlet air would periodically pierce the rising hot air and reach the disc (Fig. 4(*d*)). This unstable flow continued until the maximum test temperature was reached in some tests. The instability marks the end of buoyancy dominated flow, and entry to the unstable (white) graph areas of Fig. 5.

Momentum Dominated, High Temperature. A second momentum dominated regime formed in some tests, and is seen in Fig. 4(*c*). As the disc temperature rose past temperature of peak buoyancy, jet momentum is again important. The impinging jet stabilized and formed momentum dominated flow, this time at

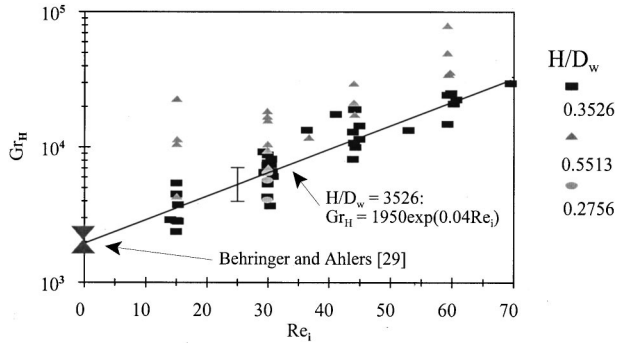

Fig. 6 Initial instability (all pressures included). The two lower length ratios approach the analytic solution for a cylinder heated from below [29]. The highest length ratio appears significantly different.

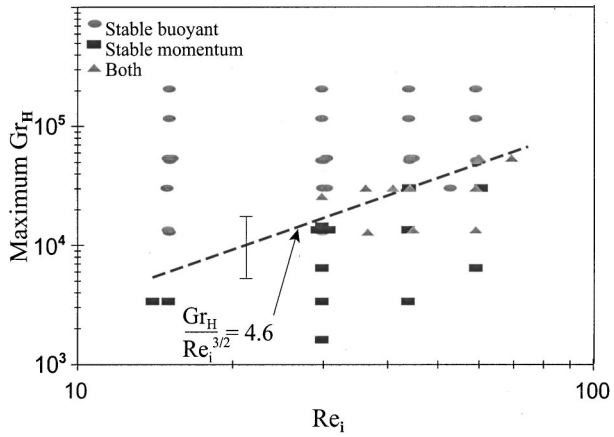

Fig. 7 Stable flows at peak Gr_H for various Reynolds numbers. Triangles indicate conditions that led to first a stable buoyant flow followed by a high temperature momentum dominated flow.

high temperature. Stable flows in this regime are short lived, seem to be in ''unstable equilibrium'', and the competition of buoyancy and momentum is well matched.

Third Instability, Momentum⇒Unsteady. The high temperature momentum driven flows became unstable as temperature continued to increase. Plumes would again begin bursting off the disc surface at the stagnation point of the impinging jet. Both the high temperature momentum dominated transition and the third instability are graphed in the white area of the graph. This region seems to be the region of multiple steady flow solutions mentioned by Fotiadis et al. [9] to exist for apparently identical operating conditions. In this region flow visualization showed that the buoyant forces and the momentum forces were well matched so that neither type of flow could dominate, hence the flow was an unstable momentum driven flow.

From Figs. 5, graph regions where certain types of flows occur can be seen. The regions were drawn so that as a test run followed the Grashof curve from left to right, the flow would be stable buoyant while in the striped region and stable momentum dominated while in the gray region. It should be stressed that the location of the borders is very approximate. On the left side of the Grashof number peak (prior to peak buoyancy) the first instability and buoyant stable flow occurs. These transitions do not occur past peak buoyancy. Conversely, the second instability, high temperature momentum dominated flow and the third instability transitions occur past peak Grashof number. As expected, the type of flow existing over the top of the Grashof number curve is either a buoyant flow or an unstable buoyancy/momentum driven flow.

In order to better understand the general trends, a graph was made mapping stable buoyant or stable momentum flow of Gr_{max} and Re_i (Fig. 7). Test runs marked as stable momentum were never dominated by buoyant forces. A line that estimates the approximate division of the parameters that produce a buoyant or a momentum dominated flow is stated as

$$\frac{Gr_H}{Re_{in}^2} = 4.6Re_{in}^{1/2} \tag{4}$$

Equation (4) is approximate and is likely to be specific to the exact geometry of the test section. A more universal method may not be possible because of the complexity of all the interrelated variables and lengths involved. It is interesting to note that Fig. 7 shows that test runs where a buoyant stable flow followed by a high temperature momentum stable flow (marked ''both'') were seen only at Reynolds numbers higher than 15. Multiple steady flow patterns at apparently identical boundary conditions were numerically predicted by Fotiadis et al. [9] at similar Reynolds number and χ values.

Results: Transient Temperature Measurements. Laser induced Rayleigh light scattering was used to measure instantaneous gas temperatures for two sets of flow parameters, and results are seen in Figs. 8(*a*) and 8(*b*). The results provide quantitative documentation of the events visualized previously. It should be emphasized that each RLS transient heating curve (two shown in Fig. 8(*a*) and three in 8(*b*)) is a different experimental test run.

Figure 8(*a*) shows that the boundary layer at the disc surface becomes unstable at 25 to 30 seconds as a couple of thermal

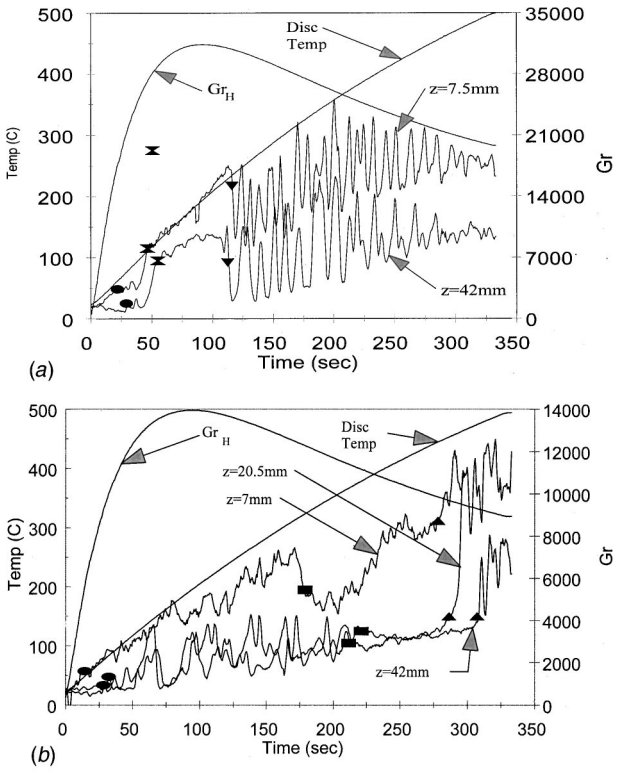

Fig. 8 (*a*) Rayleigh light scattering measurements of temperature for pressure of 0.15 ATM, $H/D_w = 0.3526$ and $Re_i = 45$. Symbols are the same as those used in Fig. 4; (*b*) Rayleigh light scattering measurements of temperature for pressure of 0.1 ATM, $H/D_w = 0.3526$ and $Re_i = 30$. Symbols are the same as those used in Fig. 4.

plumes rise. The temperature at both locations rises rapidly at about 50 seconds, indicating the establishment of stable buoyancy dominated flow. The thermal energy from the disc is convected directly up to the 42 mm location, and no low temperature entrance gas reaches either level. After the peak Grashof number is passed, however, the buoyant flow is no longer able to dominate the cool downward impinging jet, and large temperature oscillations begin to occur as the control volume is alternately exposed to thermal plumes from the surface and cool entrance gas. These oscillations continued to the end of these two test runs.

Figure 8(*b* shows transient gas temperature at 7.5 mm, 20.5 mm, and 42 mm above the wafer surface. Heating is initiated, and the momentum dominated flow becomes unstable at about 25 sec. Temperature in the boundary layer at the surface continues to rise, but by about 100 s has become increasingly unstable. This is seen in the temperature oscillations which occur as thermal plumes burst from the surface. At that time, temperature oscillations also begin at the 20.5 and 42 mm measurement heights, as the control volume is alternately exposed to a hot plume from the heated surface, or the cool downward entrance gas. At about 175 seconds, the high temperature momentum dominated regime forms. This is seen because the disc temperature continues to rise, but the temperature in the boundary layer as (7.5 mm) drops and stabilizes, indicating the cooler gas entering the test section is again reaching the disc surface. The temperature at the two upper measurement levels also stabilizes at close to the inlet temperature, clearly indicating the established momentum dominated flow at high disc temperature. Finally, around 275 and 300 sec, the high disc temperature momentum dominated flow becomes unstable, and large temperature oscillations are again seen at all three measurement locations.

Summary and Conclusions

A study has been conducted of an axisymmetric jet of gas impinging downward on a flat disc as the disc undergoes a transient heating process. This geometry is typical of that studied in relation to the rapid chemical vapor deposition process. The study involved flow visualization to find overall effects, and laser induced Rayleigh light scattering for transient temperature measurements.

Grashof number based on film temperature helped explain complicated transitions seen with increasing temperature. Momentum dominated flow was seen at low temperature and also at high temperature when fluid density at the disc surface was low and buoyancy thus reduced. Graphs of transitional Grashof number as a function of dimensionless disc temperature for a variety of pressures, height ratios and inlet Reynolds numbers describe stable momentum and stable buoyant flow regions separated by a region of chaotic and unstable flow. At higher inlet Reynolds number, this separation region at time showed different flows resulting from apparently identical flow histories and boundary conditions.

The characterization of the flow field as an enclosed heating from below (that is, basing Grashof number on H) appears to be appropriate for the two lower height ratios. Significant differences and much more scatter in transitions were seen at the greatest height ratio, indicating that it was not appropriately described as the other two. Laser induced Rayleigh light scattering was used for instantaneous temperature measurements. These quantitatively support the interpretations of flow visualization data.

Nomenclature

V = voltage (V)
χ = dimensionless surface temperature (Eq. 1)

Subscripts

ref = reference
scat = scatttered
w = wafer

References

[1] Fair, R. B., 1993, *Rapid Thermal Processing*, Academic Press, San Diego, CA.
[2] Coltrin, M. E., Kee, R. J., and Miller, J. A., 1984, ''A Mathematical Model of the Coupled Fluid Mechanics and Chemical Kinetics in a Chemical Vapor Deposition Reactor,'' J. Electrochem. Soc., **131**, pp. 425–434.
[3] Coltrin, M. E., Kee, R. J., and Miller, J. A., 1988, ''A Mathematical Model of Silicon Chemical Vapor Deposition,'' Journal of Electrochemical Society: Solid-State Science and Technology, **133**, pp. 1206–1213.
[4] Jensen, K. F., Einset, E. O., and Fotiadis, D. I., 1991, ''Flow Phenomena in Chemical Vapor Deposition of Thin Films,'' Annu. Rev. Fluid Mech., **23**, pp. 197–232.
[5] Evans, G., and Greif, R., 1987, ''A Numerical Model of the Flow and Heat Transfer in a Rotating Disk Chemical Vapor Deposition Reactor,'' ASME J. Heat Transfer, **109**, pp. 928–935.
[6] Evans, G., and Greif, R., 1989, ''A Study of Traveling Wave Instabilities in a Horizontal Channel Flow with Applications to Chemical Vapor Deposition,'' Int. J. Heat Mass Transf., **32**, pp. 895–911.
[7] Evans, G., and Greif, R., 1993, ''Thermally Unstable Convection with Applications to Chemical Vapor Deposition Channel Reactors,'' Int. J. Heat Mass Transf., **36**, pp. 2769–2781.
[8] Mahajan, R. L., and Wei, C., 1991, ''Buoyancy, Soret, Dufour and Variable Property Effects in Silicon Epitaxy,'' ASME J. Heat Transfer, **113**, pp. 688–696.
[9] Fotiadis, D. I., Kremer, A. M., McKenna, D. R., and Jensen, K. F., 1987, ''Complex Flow Phenomena in Vertical MOCVD Reactors: Effects on Deposition Uniformity and Interface Abruptness,'' J. Cryst. Growth, **85**, pp. 154–164.
[10] Fotiadis, D. I., Boekhold, M., Jensen, K. F., and Richter, W., 1990, ''Flow and Heat Transfer in CVD Reactors: Comparison and Raman Temperatures and Finite Element Model Predictions,'' J. Cryst. Growth, **100**, pp. 577–589.
[11] Fotiadis, D. I., Kieda, S., and Jensen, K. F., 1990, ''Transport Phenomena in Vertical Reactors for Metalorganic Vapor Phase Epitaxy,'' J. Cryst. Growth, **102**, pp. 441–470.
[12] Merchant, T. P., Cole, J. V., Knutson, K. L., Hebb, J. P., and Jensen, K. F., 1996, ''A Systematic Approach to Simulating Rapid Thermal Processing Systems,'' J. Electrochem. Soc. **143**, pp. 2035–2043.
[13] Hebb, J. P., and Jensen, K. F., 1996, ''The Effect of Multilayer Patterns on Temperature Uniformity During Rapid Thermal Processing,'' J. Electrochem. Soc. **143**, pp. 1142–1151.
[14] Kelkar, A. S., and Mahajan, R. L., 1997, ''Two and Three-Dimensional Transport Models for MOCVD Reactors: Effect of Boundary Conditions,'' *1997 National Heat Transfer Conference*.
[15] Mihopoulos, T. G., Hummel, S. G., and Jensen, K. F., 1998, ''Simulation of Flow and Growth Phenomena in a Close-Spaced Reactor,'' J. Cryst. Growth **195**, pp. 725–732.
[16] Soong, C. Y., Chyuan, C. H., and Tzong, R. Y., 1998, ''Thermo-Flow Structure and Epitaxial Uniformity in Large-Scale Metalorganic Chemical Vapor Deposition Reactors with Rotating Susceptor and Inlet Flow Control,'' Jpn. J. Appl. Phys., Part 1, **37**, pp. 5823–5834.
[17] Wang, C. A., Groves, S. H., Palmateer, S. C., Wayburne, D. W., and Brown, R. A., 1986, ''Flow Visualization Studies for Optimization of OMVPE Reactor Design,'' J. Cryst. Growth, **77**, pp. 136–143.
[18] Gadgil, P. N., 1993, ''Optimization of a Stagnation Point Flow Reactor Design for Metalorganic Chemical Vapor Deposition by Flow Visualization,'' J. Cryst. Growth, **134**, pp. 302–312.
[19] Salim, S., Wang, C. A., Driver, R. D., and Jensen, K. F., 1996, ''In situ Concentration Monitoring in a Vertical OMPVE Reactor by Fiber-Optics-Based Fourier Transform Infrared Spectroscopy,'' J. Cryst. Growth, **169**, pp. 443–449.
[20] Johnson, E. J., Hyer, P. V., Culotta, P. W., and Clark, I. O., 1998, ''Evaluation of Infrared Thermography as a Diagnostic Tool in CVD Applications,'' J. Cryst. Growth, **187**, pp. 463–473.
[21] Horton, J. F., and Peterson, J. E., 1999, ''Transient Temperature Measurements in an Ideal Gas by Laser-Induced Rayleigh Light Scattering,'' Rev. Sci. Instrum., **70**, pp. 3222–3226.
[22] Horton, J. F., and Peterson, J. E., 2000, ''Rayleigh Light Scattering Measurements of Transient Gas Temperature in a Rapid Chemical Vapor Deposition Reactor,'' ASME J. Heat Transfer, **122**, pp. 165–170.
[23] Holman, J. P., 1994, *Experimental Methods for Engineers*, McGraw-Hill, Inc., New York.
[24] Van de Hulst, H. C., 1953, *Light Scattering by Small Particles*, Chapmann & Hall, London.
[25] Kerker, M., 1969, *The Scattering of Light*, Academic Press, New York.
[26] Bohren, C. F., and Huffman, D. R., 1983, *Absorption and Scattering of Light by Small Particles*, John Wiley & Sons, New York.
[27] Pitz, R. W., Cattolica, R., Bobben, F., and Talbot, F., 1976, ''Temperature and Density in a Hydrogen-Air Flame From Rayleigh Light Scattering,'' Combust. Flame, **27**, pp. 313–320.
[28] Pitz, W. M., and Kashiwagi, T., 1984, ''The Application of Laser-Induced Rayleigh Light Scattering to the Study of Turbulent Mixing,'' J. Fluid Mech., **141**, pp. 391–429.
[29] Behringer, R. P., and Ahlers, G., 1982, ''Heat Transport and Temporal Evolution of Fluid Flow Near the Rayleigh-Benard Instability in Cylindrical Containers,'' J. Fluid Mech., **125**, pp. 219–258.

Journal of Heat Transfer

Technical Notes

This section contains shorter technical papers. These shorter papers will be subjected to the same review process as that for full papers.

Numerical Investigation of Forced Convection in a Horizontal Channel With a Built-In Triangular Prism

H. Abbassi, S. Turki, and S. Ben Nasrallah
Heat and Mass Transfer Laboratory, National Engineering High School of Monastir (Tunisia)

Keywords: Channel Flow, Computational, Forced Convection, Heat Transfer, Periodic

Introduction

Flow past bluff bodies between two parallel walls has been investigated by many researchers both numerically and experimentally. This flow situation is popular not only because of its academic attractiveness but also owing to its related technical problems associated with energy conservation and structural design. This type of flow is of relevance for many practical applications, such as electronic cooling and heat exchanger systems.

The incompressible flow around a circular cylinder represents one of the most investigated prototypes of bluff body wakes. The flow around a rectangular cylinder has received far less attention than the flow around a circular cylinder, but no references have been found which simulate the laminar flow around a triangular prism placed in a channel. Furthermore the effect of presence of bluff body in the heat transfer in a flow with heat source has not yet been investigated. This has motivated the present work that is concerned with structure of laminar flow and heat transfer in a two dimensional channel differentially heated with a built-in triangular prism. This specifically shaped cylinder is specially used in systems of vortex flowmeters and flame stabilizer in combustion chambers. The investigation is carried out from the numerical solutions of complete Navier-Stokes and energy equations by Control Volume Finite Element Method. The effects of presence of triangular prism on the flow structure and heat transfer are the subject of the present work.

Results and Discussion

The system of interest is a horizontal plane channel, a triangular prism is symmetrically placed in the channel axis as indicated in Fig. 1. Boundary conditions expressed in dimensionless form are as follows:

$$\text{at } 0 \leqslant x \leqslant L/B; y=0: u=v=0, \theta=1$$

$$\text{at } 0 \leqslant x \leqslant L/B; y=4: u=v=0, \theta=0$$

$$\text{at } x=0; 0 \leqslant y \leqslant 4: u=y(4-y)/4, v=0, \theta=0$$

$$\text{at } x=L/B; 0 \leqslant y \leqslant 4: \frac{\partial u}{\partial x}=\frac{\partial v}{\partial x}=\frac{\partial \theta}{\partial x}=0; \quad \int_0^4 u\,dy=8/3$$

The thermal heat flux transferred from the hot bottom wall to the flow is characterized by the space-averaged Nusselt number evaluated as follows:

$$\overline{\mathrm{Nu}}=\frac{1}{L/B}\int_0^{L/B}\mathrm{Nu}\,dx,$$

where Nu is the local Nusselt number defined as

$$\mathrm{Nu}=-\frac{\partial \theta}{\partial y}.$$

The space- and time-averaged Nusselt number is defined as

$$\langle\overline{\mathrm{Nu}}\rangle=\left(\frac{1}{\tau_2-\tau_1}\right)\int_{\tau_1}^{\tau_2}\overline{\mathrm{Nu}}\,d\tau,$$

where the time interval $(\tau_2-\tau_1)$ is the period of oscillation of the space-averaged Nusselt number Nu.

A modified version of Control Volume Finite-Element Method (CVFEM) of Saabas and Baliga [1] is adapted to the standard staggered grid for solving the dimensionless equations of continuity, momentum, and energy. The obtained numerical code was successfully validated with many standard test flows. We can quote the flow in a horizontal channel with a built-in square cylinder where results obtained are in good agreement with those reported by Davis et al. [2] as indicated in Table 1. The maximum error committed in the Strouhal numbers is less than 6.5 percent by report to numerical values and less than 9.3 percent in comparison with experimental measurements. We can also quote the Poiseuille-Benard channel flow at Re=10, Pe=20/3, and Ra $=10^4$ (see Table 2). Especially our results are close to that reported by Evans and Paolucci [3] where the errors in the period and in the space- and time-averaged Nusselt number are respectively 4.7 percent and 0.9 percent. These results demonstrate good accuracy and competence of our numerical code.

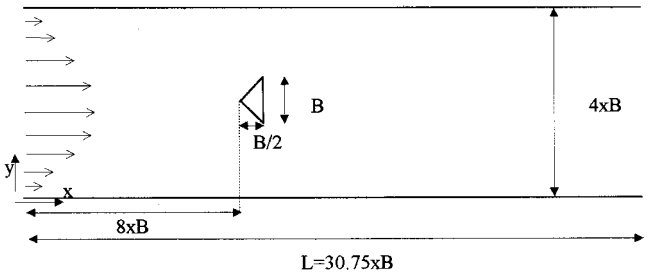

Fig. 1 Flow in a horizontal channel with built-in triangular prism

Contributed by the Heat Transfer Division for publication in the JOURNAL OF HEAT TRANSFER. Manuscript received by the Heat Transfer Division October 18, 1999; revision received November 13, 2000. Associate Editor: C. T. Avedisian.

Table 1 Flow in a horizontal channel with a built-in square cylinder: Variation of Strouhal numbers with Reynolds numbers.

Re	250	500	750
Present	0.188	0.200	0.190
Numerical values of Davis[2]	0.201	0.198	0.183
Experimental values of Davis[2]	-----	0.183	0.178

Table 2 Poiseuille-Benard channel flow at Re=10, Pe=20/3, and Ra=10^4

Reference	Present	Evans[3]	Comini[4]
Period Θ	1.395	1.332	1.273
$<\overline{Nu}>$	2.536	2.558	2.574

After verifying that the implemented numerical code gives accurate results for laminar two dimensional flows, a solution for the flow described in Fig. 1 is next sought. Grid refinement tests have been performed for the case Re=100 using three non uniform grids 72×13, 105×21, and 131×32. Results shows that when we pass from a grid of 105×21 to a grid of 131×32 the space and time-averaged Nusselt number $\langle\overline{Nu}\rangle$ and the Strouhal number St undergoes an increase of only 4.2 percent and 2.8 percent respectively, then, for reasons of calculation coast, the grid of 105×21 is retained.

Solutions are first obtained for Re=30. For this relatively low Reynolds number, the convergence of the numerical procedure is easily obtained. The velocity profiles at different axial locations in the channel are symmetrical about the channel axis. Two symmetrical vortices appear behind the triangular prism on each side of the wake turning in place in opposite sense. The flow is steady state.

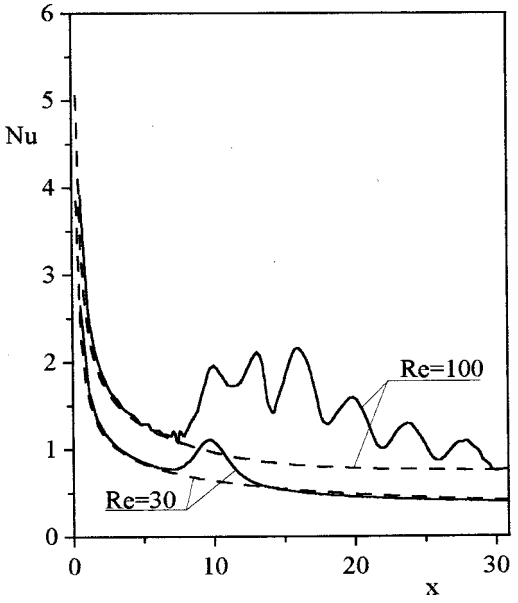

Fig. 2 Local Nusselt number distribution along the lower wall: Solid line: flow with triangular prism; dashed: flow without triangular prism

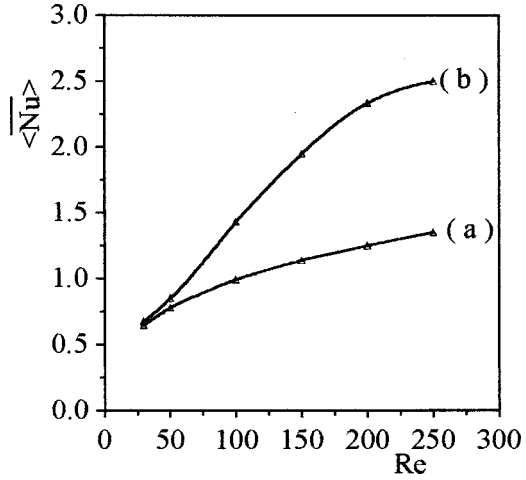

Fig. 3 Variation of the space and time-averaged Nusselt numbers with Reynolds numbers: (a) flow without; and (b) flow with triangular prism

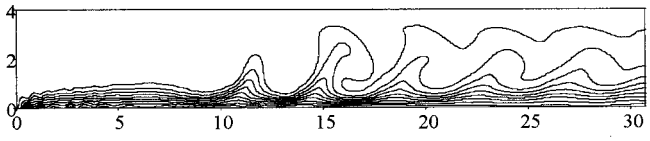

Fig. 4 Isotherms at Re=100 for the flow with triangular prism from 1 (at the bottom wall) to 0 (at the top wall) by interval 0.1

A series of computations were carried out, by increasing slowly the Reynolds number to determine the critical Reynolds number separating the symmetric and periodic flows. At Re=45 the wake loses its original symmetry. Oscillations in the wake grow in magnitude, and it begins to shed vortices into the stream. The flow in the wake becomes periodic. As in references [2,5], the destabilization of the flow happens without any need of imposing external perturbations, the action of small truncation errors and computer's round-off errors were sufficient to initiate vortex shedding. Jackson [6] report a critical Reynolds number of 31 from numerical investigation of flow around a triangular prism of the same geometry as ours but placed in an infinite medium (0 percent blockage). We estimate that this difference in Re_c is due to the presence of an important blockage (25 percent) in our configuration. As mentioned by Sohankar et al. [7], it may be conjectured that the critical Reynolds number characterizing the onset of vortex shedding increases with increasing blockage.

Recently, Fey et al. [8], based on their experiments, propose a new law for the vortex shedding from a circular cylinder which describes the Strouhal-Reynolds number dependency as: $St=a+b/\sqrt{Re}$. They have shown that such a formula seems to fit the data to some extent. In fact, this law, represents the first two terms of a series expansion in 1/root(Re) [$St=a+b/\sqrt{Re}+c/Re+\ldots$]. In the range $47<Re<180$, coefficients are $a=0.2684$ and $b=-1.0356$. For the triangular prism, this law is also in good agreement with numerical results, but coefficients are different and takes the values $a=0.2294$ and $b=-0.4736$. Comparing the coefficients b we deduce that the Strouhal number varies more quickly with Reynolds number for the circular cylinder placed in an infinite media than for triangular prism placed between two parallel plates.

In the following study our attention will be focused on the effect of the presence of the triangular prism on the heat transferred from the hot wall to the flow. Figure 2 is a plot of the local Nusselt number along the hot plate. At Re=30, the presence of triangular prism has just a little local effect by increasing slowly the local Nusselt number. In contrast, at Re=100 the effect of the presence of the triangular prism is more important, the solid line is well disturbed, but appears floating above the dashed line. An immediate conclusion can be made: the periodic flow leads to favor the heat transfer from the hot plate to the near flow, this heat is immediately transported by the Von Karmen street to the medium flow.

Figure 3 summarizes the variation of the space and time-averaged Nusselt numbers with Reynolds numbers. At relatively low Reynolds numbers corresponding to the symmetric and the beginning of periodic flows (Re$\leqslant$50) the presence of the triangular prism has no significant effect in the space and time-averaged Nusselt number $\langle\overline{\mathrm{Nu}}\rangle$. Increasing Reynolds number, curves start to separate, the presence of the triangular prism leads to an important increase of the space and time-averaged Nusselt number compared with that obtained without prism. At Re=250 this augmentation is about 85 percent. Indeed, in presence of the triangular prism, and for the fully periodic flow, the thermal boundary layer is well disturbed by the Von Karman street leading enhance heat transfer from the bottom wall to the flow (Fig. 4).

Conclusion

For the studied configuration shown in Fig. 1, results are summarized as follows: (1) the transition from symmetric flow to periodic flow is observed at Reynolds number in the vicinity of 45; (2) the Strouhal number of the periodic flow behaves as $\mathrm{St}=0.2294-0.4736/\sqrt{\mathrm{Re}}$; and (3) for the symmetric flow (Re$<$45) the presence of the triangular prism has only a local weak effects on the heat transfer and on the flow pattern, while, in periodic flow (Re$\geqslant$45), heat transfer is seen to increase strongly with Reynolds number in presence of the triangular prism. This result can be of interest in engineering.

References

[1] Saabas, H. J., and Baliga, B. R., 1994, ''Co-Located Equal-Order Control-Volume Finite-Element Method for Multidimensional, Incompressible, Fluid Flow Part I: Formulation,'' Numer. Heat Transfer, Part B, **26**, pp. 381–407.

[2] Davis, R. W., Moore, E. F., and Purtell, L. P., 1984, ''A Numerical-Experimental Study of Confined Flow Around Rectangular Cylinders,'' Phys. Fluids, **27**, No. 1, pp. 46–59.

[3] Evans, G., and Paolucci, S., 1990, ''The Thermoconvective Instability of Plane Poiseuille Flow Heated From Below: A Benchmark Solution for Open Boundary Flow,'' Int. J. Numer. Methods Fluids, **11**, pp. 1001–1013.

[4] Comini, G., Manzan, M., and Cortella, G., 1997, ''Open Boundary Conditions for the Streamfunction of Unsteady Laminar Convection,'' Numer. Heat Transfer, Part B, **31**, pp. 217–234.

[5] Persillon, H., and Braza, M., 1998, ''Physical Analysis of the Transition to Turbulence in the Wake of a Circular Cylinder by Three-Dimensional Navier-Stokes Simulation,'' J. Fluid Mech., **365**, pp. 23–88.

[6] Jackson, C. P., 1987, ''A Finite-Element Study of the Onset of Vortex Shedding in Flow Past Variously Shaped Bodies,'' J. Fluid Mech., **182**, pp. 23–45.

[7] Sohankar, A., Norberg, C., and Davidson, L., 1998, ''Low-Reynolds-Number Flow Around a Square Cylinder at Incidence: Study of Blockage, Onset of Vortex Shedding and Outlet Boundary Condition,'' Int. J. Numer. Methods Fluids, **26**, pp. 39–56.

[8] Fey, U., Konig, M., and Eckelmann, H., 1998, ''A new Strouhal-Reynolds-Number Relationship for the Circular Cylinder in the Range $47<\mathrm{Re}<2\times10^5$,'' Phys. Fluids, **10**, No. 7, pp. 1547–1549.

Combined Free and Forced Convection Film Condensation on a Finite-Size Horizontal Wavy Plate

Chi-Chang Wang
Postgraduate Student

Cha'o-Kuang Chen
e-mail: ckchen@mail.ncku.edu.tw
Professor

Department of Mechanical Engineering, National Cheng Kung University, Tainan,
Taiwan 701, Republic of China

Mixed-convection film condensation with downward flowing vapors onto a finite-size horizontal wavy plate is studied by a simple mathematical model and the spline alternating-direction implicit method. Effects of the wavy geometry, the interfacial vapor shear and the pressure gradient on the local condensate film thickness and the heat transfer characteristics have been studied independently. Results show that the pressure gradient tends to increase the heat transfer rate and to decrease the influence of the wavy amplitude. The appropriate wave number which can enhance the maximum condensation heat transfer rate is found in the neighborhood of lunder all circumstances. [DOI: 10.1115/1.1458019]

Keywords: Condensation, Film Cooling, Heat Transfer, Two-Phase, Wavy

Introduction

The problem of laminar film condensation of pure vapor on surfaces of various forms has been studied since Nusselt [1] obtained simple and explicit solutions for varied parameters. Following this, geometries such as plates and tubes have been studied under various conditions by many investigators. The free convection film condensation on the horizontal flat plate has been studied by Leppert and Nimmo [2] and Shigechi et al. [3]. Moreover, Shigechi proposed the following equation:

$$\mathrm{Nu}_m=0.82(\mathrm{Ra/Ja})^{0.2}. \tag{1}$$

In previous studies, the film condensation thickness at the plate edge (a necessary boundary condition) is either arbitrarily assumed or established by means of ''trial and error''. In fact, the above problem can be dealt with the concept of minimum mechanical energy in open-channel flow [4].

The prediction of heat transfer from irregular surface is a topic of fundamental importance. Irregularities frequently occur in the process of manufacture. Moreover, surfaces are sometimes intentionally roughened to enhance heat transfer since the presence of rough surfaces disturbs the flow and alter the heat transfer rate [5,6]. Another method to enhance heat transfer rate is about the velocity of the oncoming vapor. When the vapor surrounding a horizontal plate is moving with velocity, the problem becomes a type of mixed-convection film condensation and the analysis must consider the gravity, interfacial vapor shear force and the pressure gradient force. The objective of this study is to analyze the mixed-convection film condensation on a finite-size horizontal wavy plate, which is based on Nusselt's assumptions, together with

Contributed by the Heat Transfer Division for publication in the JOURNAL OF HEAT TRANSFER. Manuscript received by the Heat Transfer Division January 8, 2001; revision received July 31, 2001. Associate Editor: K. S. Ball.

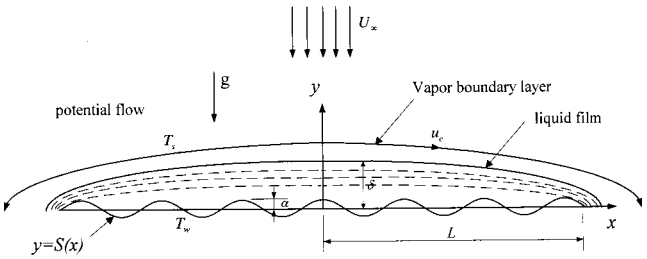

Fig. 1 Physic model and coordinate system

adopting the vapor shear model of Shekriladze and Gomelauri. Moreover, the film thickness at the plate edge will be determined by the concept of minimum mechanical energy.

Mathematical Formulation

The physical model and the coordinate system used are shown in Fig. 1. A wavy horizontal plate described by $S(x)=\alpha\cos(n\pi x/L)$ is immersed in downward flowing pure vapor which is at its saturation temperature T_s and moves at uniform velocity U_∞. This horizontal wavy plate is cooled internally thus the wall temperature T_w is uniform and lower than the vapor saturation temperature T_s. Therefore, a continuous condensate film will occur on the wall and run outward from the plate center to the plate edge under the combined effect of gravity, pressure gradient force, and interfacial vapor shear force. Based on these assumptions of Nusselt [1], the mass equation, momentum equations and the energy balance equation for the liquid laminar flow are described by the following equations:

$$\dot{m}=\int_{S(x)}^{\delta(x)}\rho u\,dy \tag{2}$$

$$0=-\frac{\partial p}{\partial x}+\mu\frac{\partial^2 u}{\partial y^2} \tag{3}$$

$$0=-\frac{\partial p}{\partial y}-\rho g \tag{4}$$

$$h'_{fg}\dot{m}'=k\left.\frac{\partial T}{\partial y}\right|_{y=S}\approx k\frac{T_s-T_w}{\delta-S}=k\frac{\Delta T}{\delta-S} \tag{5}$$

with the boundary and interface conditions

$$\text{(a)}\quad \text{at the wavy-wall (i.e., } y=S):u=0 \tag{6}$$

$$\text{(b)}\quad \text{at the interface (i.e., } y=\delta):\mu\frac{\partial u}{\partial y}\approx\dot{m}'u_e, \tag{7}$$

where $h'_{fg}=h_{fg}+3Cp\Delta T/8$ is the modified latent heat of condensate proposed by Rohsenow [7] to account for the effects of heat convection in the film. And at the liquid-vapor interface, the shear stress is equal to the loss of momentum flux of condensing vapor which is similar to that of Shekriladze and Gomelauri's [8].

Solve u in Eq. (3) and use Eqs. (4), (6) and (7), the following equation can be obtained:

$$u=\frac{1}{\mu}(\rho g\,\delta'-\rho_v u_e u'_e)\left(\frac{y^2+S^2}{2}-y\,\delta+\delta S\right)+\frac{\dot{m}'}{\mu}u_e(y-S), \tag{8}$$

where u_e is the tangential vapor velocity at the edge of the boundary layer. It can be obtained by potential flow theory.

Substitute Eqs. (2) and (8) into Eq. (5) and use the following dimensionless variables

Table 1 A comparison of δ and $\mathrm{Re}^{-1/2}\,\mathrm{Nu}_m$ for different grid numbers ($F=20$, $P=1$, $\alpha=0.05$, $n=5.5$)

Grid number	δ		$\mathrm{Re}^{-1/2}Nu_m$	
	x=0	x=1	x=0	x=4
100	0.696986	0.003280	1.545628	1.738114
300	0.684907	0.003291	1.575033	1.789175
500	0.684962	0.003324	1.574898	1.787904
300*	0.685141	0.003266	1.574454	1.765389

*:Uniform grid

$$\bar{x}=\frac{x}{L},\quad \bar{\delta}=\frac{\delta}{L}\sqrt{\mathrm{Re}},\quad \bar{\alpha}=\frac{\alpha}{L}\sqrt{\mathrm{Re}},\quad \bar{u}_e=\frac{u_e}{U_\infty},\quad \mathrm{Ja}=\frac{C_p\Delta T}{h'_{fg}}$$
$$\mathrm{Ra}=\frac{\rho^2 g\,\mathrm{Pr}\,L^3}{\mu},\quad \mathrm{Re}=\frac{\rho U_\infty L}{\mu},\quad \mathrm{Pr}=\frac{\mu C_p}{k},\quad F=\frac{\mathrm{Ra}}{\mathrm{Ja}\,\mathrm{Re}^{5/2}}, \tag{9}$$
$$P=\frac{\mathrm{Pr}}{\mathrm{Ja}}\frac{\rho_v}{\rho}.$$

The dimensionless governing equation may then become

$$(\bar{\delta}-\bar{S})\frac{d}{d\bar{x}}\left\{(F\bar{\delta}'-P\bar{u}_e\bar{u}'_e)\frac{(\bar{S}-\bar{\delta})^3}{3}+\bar{u}_e\frac{\bar{\delta}-\bar{S}}{2}\right\}=1 \tag{10}$$

with the following boundary conditions:

$$\text{(a)}\quad \text{at } \bar{x}=0:\frac{d\bar{\delta}}{d\bar{x}}=0 \tag{11}$$

$$\text{(b)}\quad \text{at } \bar{x}=1:3456\dot{\bar{m}}^3+180\dot{\bar{m}}^2\bar{u}_e-\left(2240\frac{\mathrm{Pr}}{\mathrm{Ja}}F\dot{\bar{m}}(\bar{\delta}-\bar{S})+\bar{u}_e^3\right)=0, \tag{12}$$

where

$$\dot{\bar{m}}=\frac{\bar{u}_e}{2}+\frac{1}{3}(P\bar{u}_e\bar{u}'_e-F\bar{\delta}')(\bar{\delta}-\bar{S})^2. \tag{13}$$

In Eq. (12), the film thickness at the plate edge is established by the application of minimum mechanical energy principle, i.e.,

$$\left[\frac{\partial}{\partial\delta}\int_S^\delta\left(\frac{u^2}{2}+gy+\frac{p}{\rho}\right)\rho u\,dy\right]\Bigg|_{\dot{m}_c}=0. \tag{14}$$

The mean Nusselt number is defined as

$$\mathrm{Nu}_m=\frac{h_m L}{k}\frac{\sigma(x)}{x}=\frac{\sqrt{\mathrm{Re}}}{\bar{x}}\int_0^{\bar{x}}\frac{1}{\bar{\delta}-\bar{S}}d\bar{x}, \tag{15}$$

where

$$h_m=\frac{-k}{\sigma(T_w-T_\infty)}\int_0^\sigma\sqrt{(\partial T/\partial x)^2+(\partial T/\partial y)^2}\,d\sigma \tag{16}$$

$$\sigma=\int_0^x(1+S'^2)^{1/2}dx. \tag{17}$$

Table 2 A comparison of mean Nusselt numbers, Nu_m, for natural film condensation on a horizontal flat plate ($F=20$, $P=1$, $\alpha=0.05$, $n=5.5$, grid number=300)

Ra/Ja	Present method			Shigechi(1990)
	Pr/Ja=1	Pr/Ja=10	Pr/Ja=100	
1×10^2	1.86924	2.03384	2.05738	2.0597
1×10^4	4.69501	5.10805	5.16716	5.1739
1×10^6	11.79302	12.83157	12.98005	12.996
1×10^8	29.62201	32.23073	32.60368	32.644

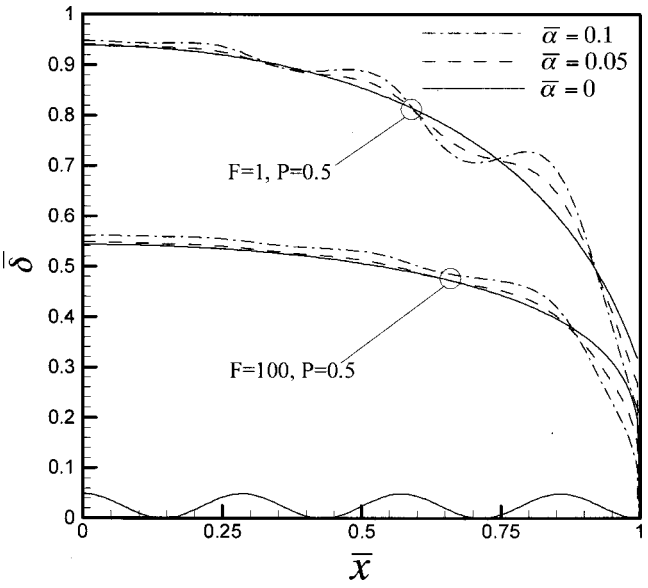

Fig. 2 Normalized film thickness along wavy plates for $P = 0.5$, $n = 7$, and Pr/Ja=50

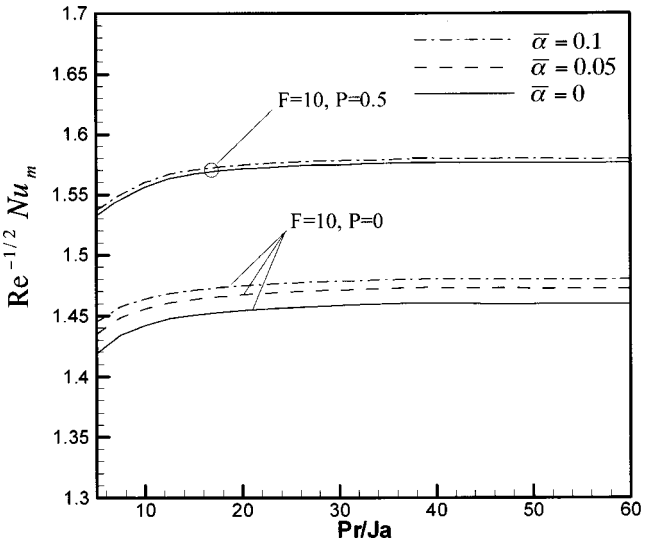

Fig. 4 A comparison of mean Nusselt numbers for a flat plate and wavy plates ($F = 10$, $n = 7$)

It should be noted that the mean Nusselt number is obtained by averaging the heat transfer flux over the surface from the plate center to $\sigma(x)$.

Results and Discussion

Equation (22) is solved numerically by using the cubic spline approximation [9]. This method can evaluate the spatial derivative terms directly without any finite difference discretization and the requirement of a uniform mesh is not necessary. As shown in Table 1, the test of grid independence, which shows that the difference between results of grids of 300 and 500 is less than 0.1 percent in both condensate film thickness and mean Nusselt number. Therefore, the nonuniform grid of 300 with smaller spacing mesh near the plate edge is employed in this study. To verify the accuracy of the present method, comparing with Shigechi [3] has also been shown in Table 2 and finds to agree favorably.

Figure 2 shows the variation of the film thickness along the wavy plate, the film thickness at the middle plate increases with the dimensionless wavy amplitude. Next, the dimensionless film thickness of the wavy plate tends to decrease rapidly near the plate edge as the fluid moves downstream, which is different from the behavior of the flat plate. It is also found that the amplitude of the dimensionless film thickness tends to increase with the axial coordinate $\overline{x}$ and the wavy amplitude.

Figure 3 shows the variation of $\mathrm{Re}^{-1/2}\,\mathrm{Nu}_m$ with $\overline{x}$. As the axial coordinate increases or the dimensionless wavy amplitude decreases, the amplitude of the mean Nusselt number will decrease. Therefore, we can observe that the variation of the mean Nusselt number only occurs near the plate center when larger wavy amplitudes are used. Also, a lower F results in a lower $\mathrm{Re}^{-1/2}\,\mathrm{Nu}_m$ for all wavy surfaces.

Figure 4 shows the variation of the mean Nusselt number with Pr/Ja. The parameter Pr/Ja is only found in Eq. (12) that can determine the film thickness $\overline{\delta}_{\min}$ at the plate edge. In cases of the

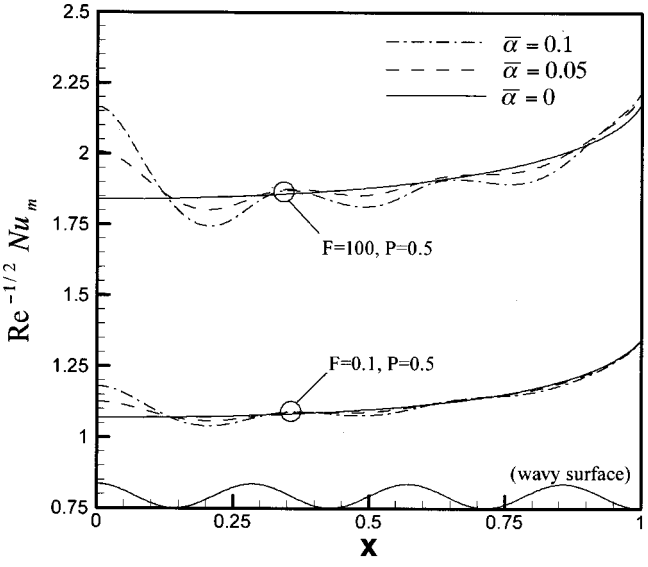

Fig. 3 Distribution of mean Nusselt number for $P = 0.5$, $n = 7$, and Pr/Ja=50

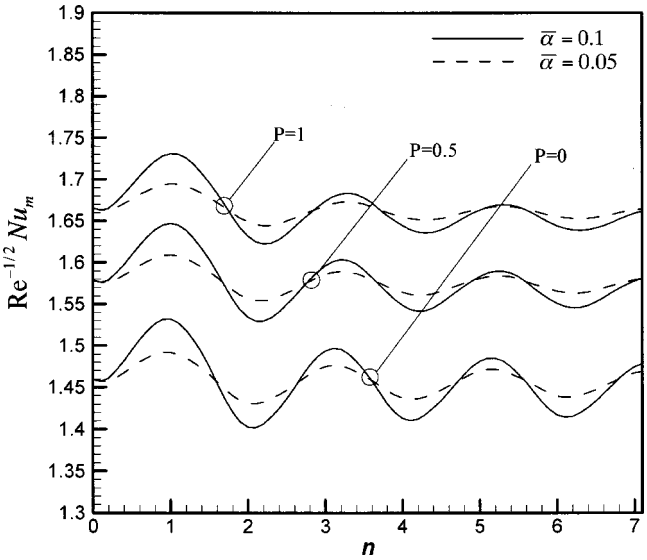

Fig. 5 Dependence of mean Nusselt number on wave number for $F = 10$ and Pr/Ja=100

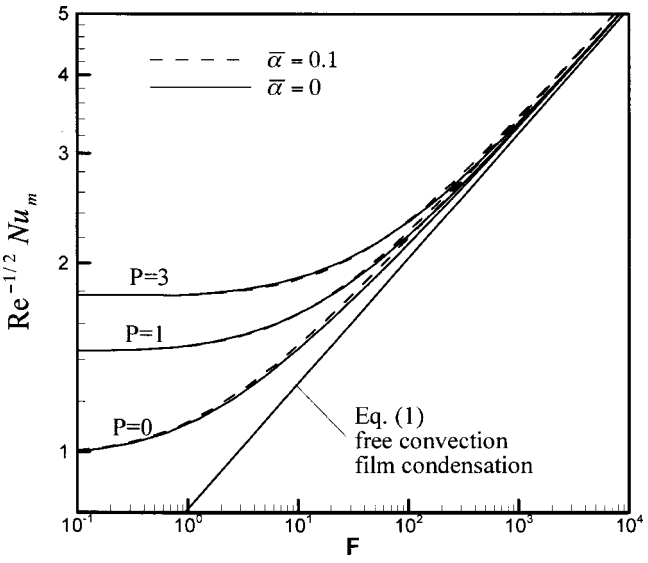

Fig. 6 Dependence of mean Nusselt number on *F* for combined forced and natural convection condensation (*n*=7, Pr/Ja =100)

flat surface and the wavy surface, both mean Nusselt numbers increase with parameter Pr/Ja and approach constant values. Moreover, the mean Nusselt number of wavy surface is higher than that of the flat plate, especially if the pressure gradient parameter is small.

Figure 5 show the dependence of the mean Nusselt number on the wave number. It is found that, for increasing the wave number the mean Nusselt numbers of the wavy surface show the sinusoidal curves, whose amplitudes decrease with the pressure gradient and increase with the wave amplitude. Peaks of the mean Nusselt number curres will occur under the wave number approaches to be odd (i.e., 1,3,5 . . .). As the wave number is quite large (i.e., the case of a rough surface), the mean Nusselt number tends to be a constant value, which equals that of the flat plate (i.e., $n=0$). This outcome is due to that although the wavy surface has a larger heat transfer area, the thermal resistance will also increase for the condensate accumulates between the trough and crest.

Figure 6 shows the dependence of the mean Nusselt number on *F*. It is seen that as *F* is greater than 100, all solutions in Eq. (10) tend to blend with the free convection (quiescent vapor) film condensation solution. For the other extreme, when *F* decreases to be zero (e.g., vapor velocity increases and the effect of gravity decreases), the mean heat transfer will change from the free-convection region into the forced-convection region through a transition zone. Moreover, increasing the pressure gradient makes the mean heat transfer coefficient increase, especially in the forced-condensation region.

Conclusions Remarks

1. The harmonic curves of the film thickness and mean Nusselt numbers have the same frequency as that of the wavy surface.
2. A larger pressure gradient will increase the total heat transfer rate but decrease the influence of wavy amplitude.
3. The maximum enhancement in heat transfer rate is found as only one wavy surface exists in the plate. It is due to that the special case has the smallest thermal resistance and the best angle to accelerate the flow outward at the plate edge.

Nomenclature

C_p = specific heat of the fluid at constant pressure
F = dimensionless parameter
g = acceleration of gravity
h_{fg} = latent heat of condensate
Ja = Jacob number
k = thermal conductivity of condensate
L = plate half length
$\dot{m}$ = condensate mass flow rate
n = wavy number
Nu_x, Nu_m = local and mean Nusselt number
p = pressure
P = dimensionless pressure gradient parameter
Pr = Prandtl number
Ra = Rayleigh number
Re = generalized Reynolds number
u_e = vapor velocity at the edge of the boundary layer
T = temperature
u,v = velocity components

Greek Symbols

α = amplitude of wavy surface
δ = condensate film thickness
μ = dynamic viscosity
ρ, ρ_v = density of condensate and vapor, respectively

Superscripts

$\bar{}$ = dimensionless variables
$'$ = derivative with respect to x, i.e., d/dx

References

[1] Nusselt, W., 1916, "Oberflachen Condensation Des Wasserdampfes," Zeitschrift des Vereines Deutscher Ininuere, **60**, pp. 541–569.
[2] Leppert, G., and Nimmo, B., 1968, "Laminar Film Condensation on Surfaces Normal to Body of Inertial Forces," ASME J. Heat Transfer, **80**, pp. 178–179.
[3] Shigechi, T., Kawa, N., Tokita, Y., and Yamada, T., 1990, "Film Condensation Heat Transfer on a Finite-Size Horizontal Plate Facing Upward," Trans. Jpn. Soc. Mech. Eng., Ser. B, **56**, pp. 205–210.
[4] Yang, S. A., and Chen, C. K., 1992, "Laminar Film Condensation on a Finite-Size Horizontal Plate with Suction at the Wall," Appl. Math. Model., **16**, pp. 325–329.
[5] Webb, R. L., Rudy, T. M., and Kedzierski, M. A., 1985, "Prediction of the Condensation Coefficient on Horizontal Integral-Fin Tubes," ASME J. Heat Transfer, **107**, pp. 369–376.
[6] Honda, H., Takamatsu, H., and Takata, N., 1999, "Experimental Measurements for Condensation of Downward-Flowing R123/R134a in a Staggered Bundle of Horizontal Low-Finned Tubes with Four Fin Geometries," Int. J. Refrig., **22**, 615–624.
[7] Rohsenow, W. M., 1956, "Heat Transfer and Temperature Distribution in Laminar Film Condensation on a Horizontal Tube," Int. J. Heat Mass Transf., **27**, pp. 39–47.
[8] Shekriladze, I. G., and Gomelauri, V. I., 1966, "The Theoretical Study of Laminar Film Condensation of a Flowing Vapor," Int. J. Heat Mass Transf., **9**, pp. 581–591.
[9] Rubin, S. G., and Graves, R. A., 1975, "Viscous Flow Solution with a Cubic Spline Approximation," Comput. Fluids, **1**, No. 5, pp. 1–36.

Enclosed Buoyant Convection With Internal Heat Generation Under Oscillating Sidewall Temperature

Gi Bin Kim

Jae Min Hyun
e-mail: jmhyun@cais.kaist.ac.kr

Department of Mechanical Engineering,
Korea Advanced Institute of Science & Technology,
373-1 Kusong-dong, Yusong-gu,
Taejon 305-701, South Korea

Ho Sang Kwak
School of Mechanical Engineering,
Kumoh National University of Technology,
188 Shinpyung-dong, Kumi,
Kyongbuk 730-701, South Korea

Keywords: Unsteady Buoyant Convection, Internal Heat Generation, Resonance

1 Introduction

Buoyant convection in an enclosure induced by uniform internal heat generation has been extensively studied (Acharya and Goldstein [1], Bergholz [3], Fusegi et al. [4], Kulacki and Goldstein [6], May [10]). One canonical layout is a rectangular cavity with two vertical sidewalls at constant temperatures and two insulated horizontal endwalls, with large Rayleigh number Ra ($>10^5$), Prandtl number O(1) and cavity aspect ratio O(1). In particular, when both vertical sidewalls are maintained at the same temperature T_0, the overall flow is expectedly symmetric about the vertical centerline. In each half-cavity, the fluid rises (sinks) near the centerline (near the vertical sidewall) region, which forms a single circulation cell.

Recently, buoyant flows induced by time-periodic boundary conditions, with no internal heat generation, emerge to be a subject of considerable interest (Antohe and Lage [2], Kwak and Hyun [7], Kwak et al. [8], Lage and Bejan [9]). The overriding concern here is the existence of resonance, which was first observed in the numerical studies of Lage and Bejan [9] and was corroborated later by Antohe and Lage [2]. It was illustrated that, when the frequency of the time-periodic boundary condition matches the proper resonance frequency, convective activities in the cavity are invigorated. This gives rise to a substantial increase in the amplitude of the fluctuating heat transfer coefficient in the cavity interior. The analytical endeavor of Lage and Bejan [9], based on the concept of a fluid wheel inside the cavity, suggested ways to make an order-of-magnitude estimate of the resonance frequency. In a related effort, Kwak and Hyun [7] and Kwak et al. [8] asserted that resonance is anticipated when the basic mode of the system eigenfrequencies is excited. They further argued that the system eigenfrequencies are characterized by the internal gravity oscillations in the interior, which are supported by the prevailing stratification.

This paper describes the time-dependent buoyant convection in an enclosure, with the presence of internal heat generation, under a time-periodic thermal boundary condition. Estimations of the resonance frequencies will be made, and physical explanations will be offered. This configuration simulates simplified models of post-accident heat removal in nuclear reactors and geophysical problems. Also, natural convection is important in fluids undergoing electrolytic processes or exothermic chemical reactions. As emphasized earlier, utilization of time-periodic thermal boundary conditions is explored as a possible means to control these processes or reactions. Convection in an air-conditioned room, subject to the daily-varying environmental temperature, provides an easy example of technological applications of the flow configuration under present study.

2 Formulation

Consider a square cavity, filled with an incompressible Newtonian fluid with spatially-uniform internal heat generation of constant strength q_0''', as sketched in Fig. 1. The left vertical sidewall is maintained at constant temperature T_0. The temperature T_r at the right vertical sidewall varies about T_0 sinusoidally with time, $T_r = T_0 + \Delta T' \sin(ft)$, in which $\Delta T'$ and f denote, respectively, the amplitude and frequency of oscillation.

Flow is governed by the time-dependent Navier-Stokes equations, with the invocation of the Boussinesq-fluid relationship $\rho = \rho_0[1-\beta(T-T_0)]$, which, after non-dimensionalization, read

$$\frac{\partial U}{\partial X} + \frac{\partial V}{\partial Y} = 0, \tag{1}$$

$$\frac{\partial U}{\partial t} + U\frac{\partial U}{\partial X} + V\frac{\partial U}{\partial Y} = -\frac{\partial P}{\partial X} + \left(\frac{\mathrm{Pr}}{\mathrm{Ra}_I}\right)^{1/2}\left(\frac{\partial^2 U}{\partial X^2} + \frac{\partial^2 U}{\partial Y^2}\right), \tag{2}$$

$$\frac{\partial V}{\partial t} + U\frac{\partial V}{\partial X} + V\frac{\partial V}{\partial Y} = -\frac{\partial P}{\partial Y} + \left(\frac{\mathrm{Pr}}{\mathrm{Ra}_I}\right)^{1/2}\left(\frac{\partial^2 V}{\partial X^2} + \frac{\partial^2 V}{\partial Y^2}\right) + \theta, \tag{3}$$

$$\frac{\partial \theta}{\partial t} + U\frac{\partial \theta}{\partial X} + V\frac{\partial \theta}{\partial Y} = \left(\frac{1}{\mathrm{Ra}_I\mathrm{Pr}}\right)^{1/2}\left(\frac{\partial^2 \theta}{\partial X^2} + \frac{\partial^2 \theta}{\partial Y^2}\right) + \left(\frac{1}{\mathrm{Ra}_I\mathrm{Pr}}\right)^{1/2}. \tag{4}$$

The associated boundary conditions can be expressed as

$$U = V = \frac{\partial \theta}{\partial Y} = 0, \quad \text{at } Y = 0,1; \tag{5}$$

$$U = V = \theta = 0, \quad \text{at } X = 0; \tag{6}$$

$$U = V = 0, \quad \theta = \varepsilon \sin(\omega\tau), \quad \text{at } X = 1. \tag{7}$$

In the above, dimensionless quantities are defined as

$$\tau = t(\mathrm{Ra}_I\mathrm{Pr})^{1/2}\frac{\kappa}{H^2}; \quad (X,Y) = \frac{(x,y)}{H};$$

$$(U,V) = (u,v)(\mathrm{Ra}_I\mathrm{Pr})^{-1/2}\frac{H}{\kappa};$$

$$\theta = \frac{k(T-T_0)}{H^2 q_0'''}; \quad P = \frac{(p+\rho_0 g y)H^2}{\rho_0 \kappa^2 \mathrm{Ra}_I\mathrm{Pr}}; \quad \mathrm{Pr} = \nu/\kappa; \tag{8}$$

$$\mathrm{Ra}_I = \frac{g\beta q_0''' H^5}{\kappa\nu k},$$

where (u,v) indicate dimensional velocity components in the horizontal (x) and vertical (y) directions, and ρ_0 the reference density evaluated at the cold-wall temperature (T_0), and ν and κ denote the kinematic viscosity and thermal diffusivity, respectively, and β the isobaric coefficient of volumetric thermal expansion. The strength of internal heat generation is represented by the internal Rayleigh number, Ra_I. All fluid properties are assumed to be constant.

Contributed by the Heat Transfer Division for publication in the JOURNAL OF HEAT TRANSFER. Manuscript received by the Heat Transfer Division April 3, 2001; revision received September 6, 2001. Associate Editor: M. Faghri.

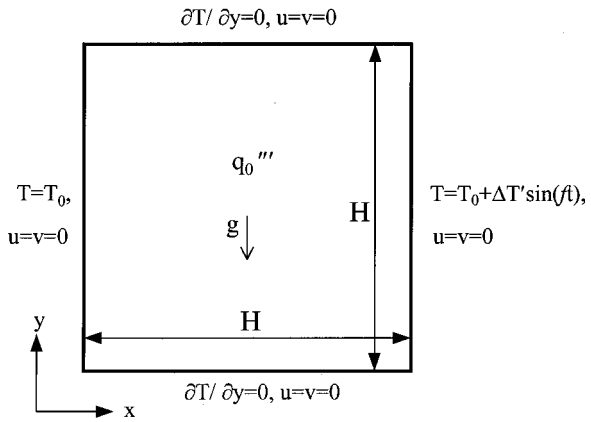

Fig. 1 Flow configuration

Time is nondimensionalized by using the system Brunt-Väisäla frequency N, i.e.,

$$N \equiv \left[\frac{g\beta(q_0'''H^2/k)}{H}\right]^{1/2} = (\mathrm{Ra}_I \mathrm{Pr})^{1/2}\frac{\kappa}{H^2}. \tag{9}$$

The nondimensional amplitude and frequency of the right-sidewall temperature fluctuation are

$$\varepsilon \equiv \frac{k\Delta T'}{q_0'''H^2}; \quad \omega \equiv \frac{f}{N}. \tag{10a,b}$$

In the above development, the system-wide temperature scale is derived from the internal heat generation, i.e., $q_0'''H^2/k$, and this scale is employed consistently, e.g., in Eqs. (8), (9), and (10*a*).

Numerical solutions are acquired by using the well-documented finite-volume computational procedure (e.g., Hayase et al. [5], Patankar [12]).

3 Results and Discussion

For all the computations, the Prandtl number was set Pr=7.0 to simulate water.

In the computations, the value of ε was set $\varepsilon/\theta_m = 0.3$. This choice of ε was based on the considerations explained below. First, ε should be small enough not to seriously distort the prevailing steady-state flow. In a series of detailed calculations, Kwak et al. [8] demonstrated that, when ε is small, i.e., $\varepsilon \leqslant 0.5$, the amplitude of fluctuating Nusselt number in the interior is approximately proportional to ε. Secondly, the presence of multiple resonance was observed by Antohe and Lage [2] when the nondimensional amplitude of wall heat flux oscillation was larger than 0.1. The value of $\varepsilon/\theta_m = 0.3$ was selected to meet the aforementioned two dynamical issues. The nondimensional frequency of oscillation ω encompasses a wide range, $0.005 \leqslant \omega \leqslant \mathrm{O}(1)$.

In the analysis of the computed results, it is advantageous to introduce the following notations, i.e.,

$$\mathrm{Nu}_X^*(\tau) \equiv \frac{\mathrm{Nu}_X(\tau) - \mathrm{Nu}_X^B}{\mathrm{Nu}_{X=1}^B}, \tag{11a}$$

$$A(\mathrm{Nu}_X^*) \equiv \frac{\mathrm{Max}\{\mathrm{Nu}_X^*(\tau)\} - \mathrm{Min}\{\mathrm{Nu}_X^*(\tau)\}}{2}, \quad \tau_0 \leqslant \tau \leqslant \tau_0 + \frac{2\pi}{\omega}. \tag{11b}$$

In the above, $\mathrm{Nu}_X^*(\tau)$ indicates the difference between the instantaneous Nu value (at $X=X$ and $\tau=\tau$) and the corresponding value Nu_X^B of the case of non-oscillating sidewall temperature ($\varepsilon=0$). The amplitude of Nu-value fluctuations is expressed by $A(\mathrm{Nu}_X^*)$.

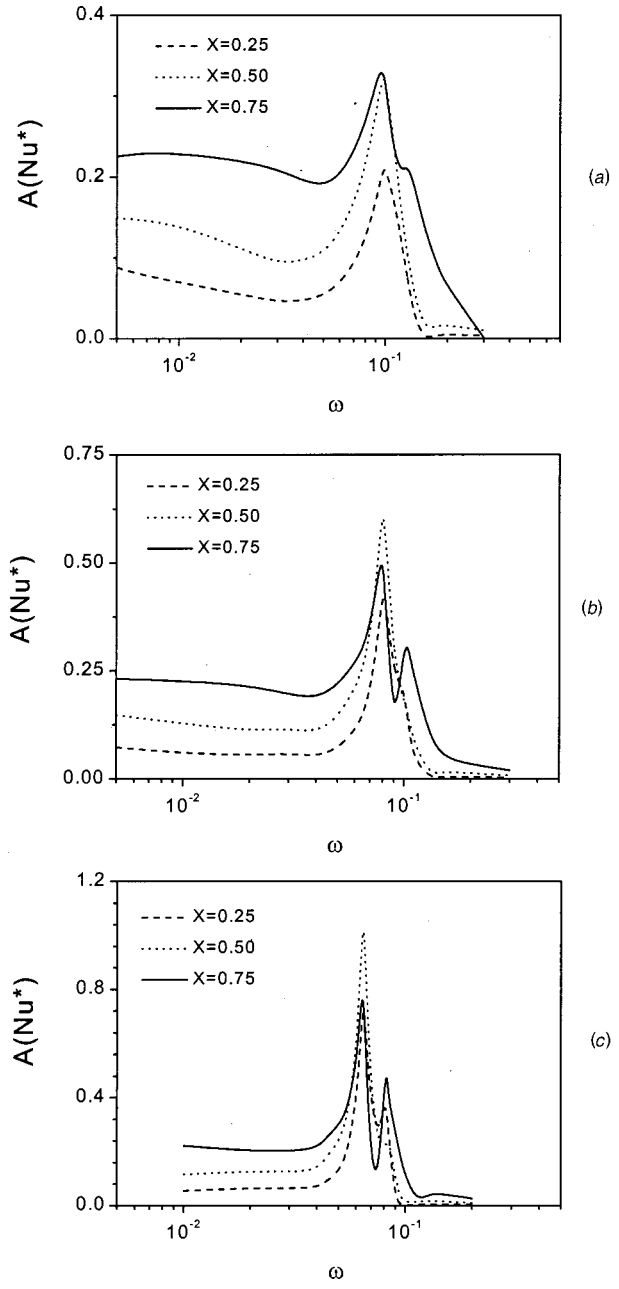

Fig. 2 *A*(Nu*) versus ω plots: (*a*) $\mathrm{Ra}_I = 10^8$; (*b*) $\mathrm{Ra}_I = 10^9$; and (*c*) $\mathrm{Ra}_I = 10^{10}$.

As stressed by Lage and Bejan [9], the amplitude of Nu-fluctuation, $A(\mathrm{Nu}^*)$, at the centerline ($X=0.5$) is of particular interest. This is representative of the intensity of time-dependent heat transfer activities in the interior core. Figure 2 displays the collection of numerical data of $A(\mathrm{Nu}_X^*)$ in the interior region versus ω for varying Ra_I. It is clear that the amplitude of Nu-fluctuation, $A(\mathrm{Nu}_X^*)$, peaks at certain particular frequencies; this was interpreted to manifest the existence of resonance in the context of enclosed buoyant convection (Lage and Bejan [9]). Frames (*a*), (*b*), and (*c*) of Fig. 2 show that the frequency at which the primary peak occurs, ω_{r1}, is largely unaffected by Ra_I. Furthermore, the secondary peak at ω_{r2} is visible for very high values of Ra_I, i.e., $\mathrm{Ra}_I \geqslant 10^9$.

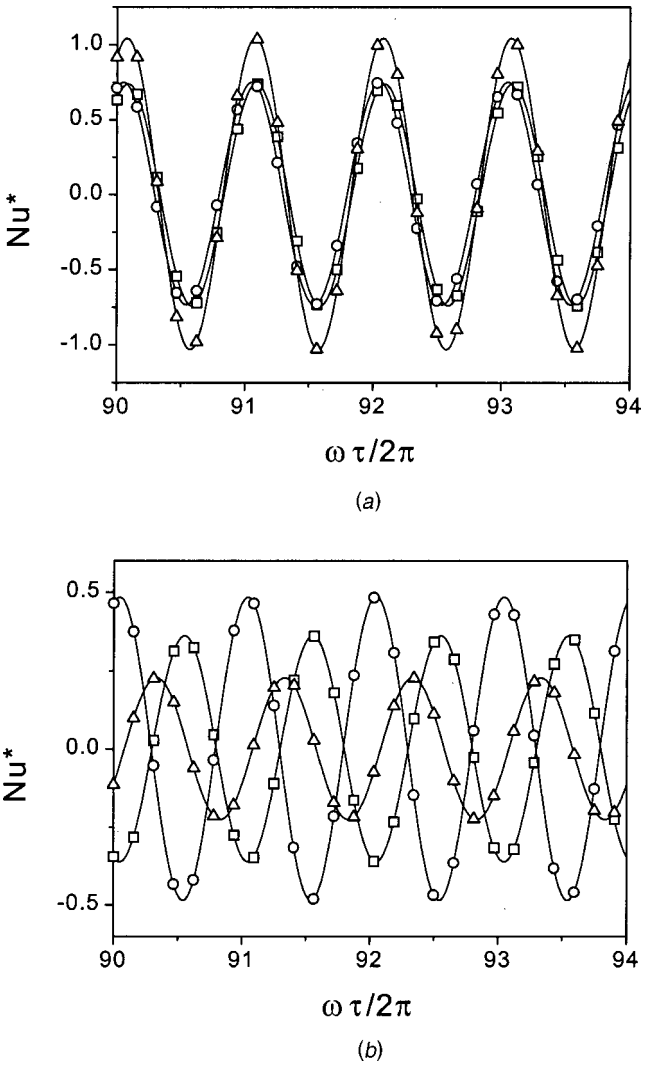

Fig. 3 Time history of Nu* at resonance frequencies. $Ra_I = 10^{10}$. Symbols □, △, and ○ denote the positions, $X = 0.25$, 0.5, and 0.75, respectively: (*a*) $\omega = 0.065(\approx \omega_{r1})$; and (*b*) $\omega = 0.082(\approx \omega_{r2})$.

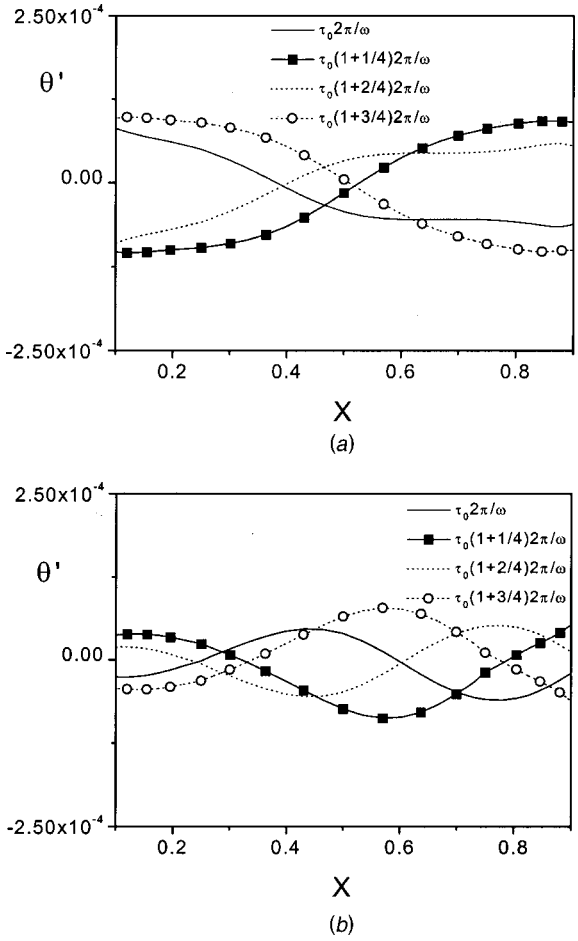

Fig. 4 Temperature fluctuations relative to the basic state. $Y = 0.5$, $Ra_I = 10^{10}$: (*a*) $\omega = 0.065(\approx \omega_{r1})$; and (*b*) $\omega = 0.082(\approx \omega_{r2})$.

The prior expositions by Kwak et al. [7–8] ascertained that resonance is anticipated when the eigenfrequencies of the system are excited. Furthermore, these intrinsic eigenfrequencies are characterized by the internal gravity oscillations in the stably stratified interior core. Paolucci and Chenoweth [11] calculated the modes of these oscillations, which, for a square cavity, can be expressed, in the present nondimensional form, as

$$\omega_n \equiv \frac{f_n}{N} = \frac{(\partial\theta/\partial Y)^{1/2}}{(1+1/n^2)^{1/2}}. \tag{12}$$

In the above, $\partial\theta/\partial Y$ denotes the average strength of stratification in the interior. In the practical calculation of $\partial\theta/\partial Y$, a linear curve-fitting was applied to the interior vertical temperature profile at a given location X. Here, n is the mode index, which is the ratio of the wave numbers in the horizontal and vertical directions. The primary mode is identified to be $n=1$, i.e., the scale of the whole cavity. The theoretical values of ω_1 obtainable from Eq. (12) are 0.098, 0.079, and 0.062 for $Ra_I = 10^8$, 10^9, and 10^{10}, respectively. The computed primary resonance frequencies ω_{r1}, as illustrated in Fig. 2, are respectively 0.098, 0.080, and 0.065, which are in close agreement with the results of Eq. (12). This comparison gives credence to the assertion that the resonance frequencies are determined by the modes of internal gravity oscillations. The secondary peak in Fig. 2 is identified to be the consequence of the excitation of ω_2 mode of Eq. (12). In this case, fluid motions based on $n=2$, which have the size of half-cavity, are under focus. Again, ω_2, calculated by Eq. (12), are 0.124, 0.100, and 0.078, while the present computed data for ω_{r2} are 0.123, 0.103, and 0.082, respectively, for $Ra_I = 10^8$, 10^9 and 10^{10}. As before, this favorable agreement reinforces the finding that the modes of internal gravity oscillations are the principal eigenfrequencies of the system.

The time histories of Nu_X^* are revealing. For the primary resonance mode ($\omega \cong \omega_{r1}$), as demonstrated in Fig. 3(*a*), convective fluid motions are intensified throughout the entire interior region of the cavity. Because of the dominant convective activities, the amplitudes of Nu-oscillation are substantial. The invigorated convective flows are propagated to the bulk of the interior from the sidewall of oscillating temperature; much of Nu in the cavity interior core does not show appreciable phase lags. When the sidewall temperature oscillates at the secondary resonance frequency ($\omega \cong \omega_{r2}$), as depicted in Fig. 3(*b*), considerable phase lags are discernible in the interior. The phase lag is π radian between $X = 0.25$ and $X = 0.75$. This implies that the convective motions at ω_{r2} take place with opposite phases between these two locations.

At higher values of ω, the effect of sidewall temperature oscillation is confined to the region close to the wall, and the influence of sidewall temperature oscillation is meager at far-away locations. As a result, the amplitude of Nu_X^* oscillation at $X=0.75$ is larger than at other locations.

The behavior of temperature fluctuation in the interior at resonance is plotted in Fig. 4. The horizontal profiles of interior temperature oscillation at mid-height ($Y=0.5$) clearly exhibit [see Fig. 4(a)] the periodic tilting with ω_{r1}, which points to the source of internal gravity oscillations. This pattern is qualitatively similar to the observations of Kwak and Hyun [7] for a differentially-heated cavity with $q_0'''=0$. The spatial behavior of thermal field fluctuations at the secondary resonance frequency (ω_{r2}) is slightly more complex. A closer inspection of Fig. 4(b) discloses that there exist two branches of tilting, with a phase difference of approximately π radian, in the left and right regions of the cavity. This points to the fact that the gradients of fluctuating temperature in both regions have opposite signs at each time instant.

4 Concluding Remarks

The primary-peak resonance at ω_{r1} is distinct. The secondary-peak resonance at ω_{r2} is detected for higher Ra_I. The instantaneous Nusselt number fluctuation at ω_{r1} indicates the presence of cavity—scale motions, which are qualitatively similar to those of a differentially—heated cavity. For the secondary resonance frequency ω_{r2}, the tilting of the interior isotherms is of a concave/convex shape. The theoretical predictions of the resonance frequencies, based on the modes of internal gravity oscillations, are in accord with the present numerical data.

Acknowledgment

This work was supported by the grants from NRL, South Korea.

References

[1] Acharya, S., and Goldstein, R. G., 1985, "Natural Convection in An Externally Heated Vertical or Inclined Square Box Containing Internal Energy Sources," ASME J. Heat Transfer, **107**, pp. 855–866.

[2] Antohe, B. V., and Lage, J. L., 1996, "Amplitude Effect on Convection Induced by Time-Periodic Horizontal Heating," Int. J. Heat Mass Transf., **39**, No. 6, pp. 1121–1133.

[3] Bergholz, R. F., 1980, "Natural Convection of a Heat Generating Fluid in a Closed Cavity," ASME J. Heat Transfer, **102**, pp. 242–247.

[4] Fusegi, T., Hyun, J. M., and Kuwahara, K., 1992, "Natural Convection in a Differentially Heated Square Cavity With Internal Heat Generation," Numer. Heat Transfer, **21**, pp. 215–229.

[5] Hayase, T., Humphery, J. A. C., and Grief, R., 1992, "A Consistently Formulated QUICK Scheme for Fast and Stable Convergence Using Finite-Volume Iterative Calculation Procedures," J. Comput. Phys., **98**, pp. 108–118.

[6] Kulacki, F. A., and Goldstein, R. J., 1972, "Thermal Convection in a Horizontal Fluid Layer With Uniform Volumetric Energy Sources," J. Fluid Mech., **55**, pp. 271–287.

[7] Kwak, H. S., and Hyun, J. M., 1996, "Natural Convection in an Enclosure Having a Vertical Sidewall With Time-Varying Temperature," J. Fluid Mech., **329**, pp. 65–88.

[8] Kwak, H. S., Kuwahara, K., and Hyun, J. M., 1998, "Resonant Enhancement of Natural Convection Heat Transfer in a Square Enclosure," Int. J. Heat Mass Transf., **41**, pp. 2837–2846.

[9] Lage, J. L., and Bejan, A., 1993, "The Resonance of Natural Convection in an Enclosure Heated Periodically From the Side," Int. J. Heat Mass Transf., **36**, pp. 2027–2038.

[10] May, H. O., 1991, "A Numerical Study on Natural Convection in an Inclined Square Enclosure Containing Internal Heat Sources," Int. J. Heat Mass Transf., **34**, No. 4, pp. 919–928.

[11] Paolucci, S., and Chenoweth, D. R., 1989, "Transition to Chaos in a Differentially Heated Vertical Cavity," J. Fluid Mech., **210**, pp. 379–410.

[12] Patankar, S. V., 1980, *Numerical Heat Transfer and Fluid Flow*, McGraw-Hill.

A Method to Accelerate Convergence and to Preserve Radiative Energy Balance in Solving the P_1 Equation by Iterative Methods

Genong Li and Michael F. Modest

Department of Mechanical Engineering, The Pennsylvania State University, University Park, PA 16802

An acceleration method is proposed particularly for the P_1 equation. The radiative energy balance is used as a constraint to correct iterative solutions. The method not only accelerates convergence but also preserves the radiative energy balance, the latter being of great importance when radiation calculations are coupled with flow calculations. This acceleration method can be applied to other elliptical problems with boundary conditions of the second and/or the third kind. [DOI: 10.1115/1.1423318]

Keywords: Computational, Numerical Methods, Radiation, Acceleration, Iterative Method

Introduction

The P_1 approximation reduces the equation of transfer from a very complicated integro-differential equation to a relatively simple partial differential equation (the P_1 equation). Yet, the P_1 approximation is powerful, allowing non-black surfaces, non-constant properties, anisotropic scattering, etc. For the vast majority of important engineering problems (i.e., in the absence of extreme anisotropy in the intensity field), the method provides high accuracy at very reasonable computational cost. Furthermore, the P_1 approximation can easily be combined with sophisticated spectral models such as the Weighted-Sum-of-Gray-Gases method (WSGG) [1]. Currently, many commercial CFD codes such as FLUENT [2] have the P_1 approximation as an optional solution technique for radiation calculations.

The P_1 equation is a Helmholtz equation and it is conceptually simple to solve numerically. The only problem is that the boundary condition for this equation is of the third kind, which causes the convergence of the solution, by even the most sophisticated iterative methods, to be quite slow, especially when the absorption coefficient of the medium is small. A parallel problem is that unconverged, intermediate solutions of the P_1 equation during the iterative process do not satisfy the basic energy balance–computed total radiative heat source within the medium is not equal to computed total radiative heat flux through boundaries. When such a radiation calculation, without a fully-converged solution, is coupled with a flow calculation, the total energy balance is destroyed during the iterative process and may not converge.

Many approaches have been devised to speed up convergence of iterative methods such as block correction [3] and multigrid acceleration techniques [4]. While these approaches are effective in general and are already widely used in commercial CFD codes, they are not efficient enough, in particular, for equations with boundary conditions of the second and/or the third kind only, e.g., the P_1 approximation. This is because boundary conditions of the second and third kind prescribe only the gradient of an unknown, or a relation between the gradient of an unknown and the unknown itself. A large number of iterations are required for interior nodes as well as boundary nodes to adjust themselves to satisfy

Contributed by the Heat Transfer Division for publication in the JOURNAL OF HEAT TRANSFER. Manuscript received by the Heat Transfer Division February 22, 2001; revision received August 30, 2001. Associate Editor: R. Skocypec.

their governing equations and boundary conditions. Traditional acceleration techniques such as block correction and multigrid acceleration speed up convergence by adding some corrections to drive the solution toward global conservation. Such techniques may not be effective for elliptic equations with boundary conditions of the second and/or third kind. Another acceleration approach is the mesh rebalance method, which was developed by Wachspress [5] and Reed [6] in the context of neutron transport. The characteristic of the mesh rebalance method is that it corrects base iterative results by multiplying with correction factors to speed up convergence. This method has been applied to the discrete ordinated method (DOM) to solve the radiative transfer equation (RTE) [7].

A reduced mesh rebalance acceleration method, which corrects intermediate iterations by a uniform multiplication factor to satisfy the total radiative energy balance, is proposed in this note specifically for the P_1 approximation (a Helmholtz equation with boundary conditions of the second and/or third kind). The method can be used in conjunction with any existing iterative method to achieve faster convergence when solving the P_1 equation.

The Correction Procedure

In the P_1 approximation, the incident radiation, G, is governed by the Helmholtz equation [1]

$$\nabla\cdot\left(\frac{1}{\kappa+\sigma}\nabla G\right)=-3\kappa(4\pi I_b-G) \tag{1}$$

subject to the boundary condition,

$$-\frac{2-\epsilon}{\epsilon}\frac{2}{3}\hat{n}\cdot\nabla G=(\kappa+\sigma)(4\pi I_{bw}-G), \tag{2}$$

where κ and σ are the absorption and scattering coefficients of the radiating gas, respectively, I_b is the Planck function, ϵ is the surface emissivity, and $\hat{n}$ is the surface normal. In practice, the discretized P_1 equation is solved by iterative methods. Due to the nature of the boundary condition of the third kind, convergence of the solution tends to be very slow.

Conservation of radiative energy states that total radiative heat source in a radiating medium is always equal to total radiative heat flux through its boundaries, i.e.,

$$\int\int\int_{\mathcal{V}}\nabla\cdot\underline{q}^R dV=-\int\int_{\mathcal{S}}\hat{n}\cdot\underline{q}^R dS, \tag{3}$$

where q^R is the radiative heat flux vector, which also follows from the divergence theorem. In the P_1 approximation, the divergence of the radiative heat flux vector and the radiative heat flux at the boundaries are calculated as [1]

$$\nabla\cdot\underline{q}^R=\kappa(4\pi I_b-G),\quad -\hat{n}\cdot\underline{q}^R=\frac{\epsilon}{2(2-\epsilon)}(G-4\pi I_{bw}). \tag{4}$$

In iterative methods the converged solution of the P_1 equation satisfies the above energy balance; intermediate solutions during iterative process, however, often do not. In any realistic fire/combustion simulation, the solution to radiative transfer equation is coupled with the solution to the overall energy equation. Since $\nabla\cdot\underline{q}^R$ enters the energy equation as a source, while $-\hat{n}\cdot\underline{q}^R$ appears in the boundary conditions of the energy equation, it is apparent that the total energy balance will also be destroyed during the iterative process, if a partially converged radiative solution is employed. This, in turn, may slow down convergence of the overall energy equation as well.

To speed up convergence and to preserve radiative energy balance, Eq. (3) can be used as a constraint to correct the computed incident radiation field. The computed incident radiation at any node i after the n^{th} iteration, $G_i^{(n)}$, is multiplied uniformly by a factor $f^{(n)}$ to satisfy the discretized form of the energy balance. That is,

$$\sum_{i=1}^{N}\kappa_i(4\pi I_{b,i}-f^{(n)}G_i^{(n)})V_i=\sum_{j=1}^{M}\frac{\epsilon_j}{2(2-\epsilon_j)}(f^{(n)}G_j^{(n)}-4\pi I_{bw,j})A_j, \tag{5}$$

where N is the total number of nodes throughout the whole computational domain and M is the total number of boundary nodes; and V_i and A_j are the nodal volume of the i^{th} node and the boundary surface area of the j^{th} node, respectively.

The correction factor for the n^{th} iteration, $f^{(n)}$, is determined from the above equation as

$$f^{(n)}=\frac{\sum_{i=1}^{N}4\pi\kappa_i I_{b,i}V_i+\sum_{j=1}^{M}\frac{\epsilon_j}{2-\epsilon_j}2\pi I_{bw,j}A_j}{\sum_{i=1}^{N}\kappa_i G_i^{(n)}V_i+\sum_{j=1}^{M}\frac{\epsilon_j}{2(2-\epsilon_j)}G_i^{(n)}A_j}. \tag{6}$$

To implement this method, after each iteration the correction factor is calculated based on Eq. (6). The whole incident radiation field is then corrected by multiplication with the correction factor, $f^{(n)}$, guaranteeing that Eq. (3) is satisfied. As the solution converges, the correction factor gradually moves toward unity. Therefore, the correction procedure does not change the converged incident radiation field.

This correction method not only preserves the total radiative energy balance for partially converged solutions, but also accelerates convergence of the P_1 equation. This is because the correction procedure connects the incident radiation at boundary nodes directly to those of interior nodes, allowing the boundary condition to propagate much more quickly to the inner points, which usually means that the solution converges faster.

Test Problem

A simple two-dimensional problem has been chosen to test the convergence rate of the method, namely a cylindrical combustion chamber, which is 4 m long and 1 m in radius. The temperature field is given by $T(x,r)=8000(x/L)(1-x/L)(1-r/R)$ (K), where x,r, are axial and radial coordinates, respectively. The incident radiation field is to be calculated for different constant absorption coefficients. The problem is axisymmetric and an equally-spaced nodal system with 20×20 nodes is used. The P_1 equation is discretized at these nodes and different iterative methods are used to solve the discretized linear equations. The initial field of incident radiation is set to zero and the convergence criterion is set to $|f-1|\leqslant 1.0\times10^{-5}$. The Gauss-Seidel and the alternating direction line-by-line TDMA iterative methods (supplemented with block correction [3]) will be used with and without our new acceleration scheme. The latter iterative method is widely used and is the main iterative method adopted by many commercial CFD codes. In this method one complete iteration consists of block corrections and line-by-line TDMA sweeps in the row direction and in the column direction. The computed radiative heat sources and the number of iterations to reach the converged solu-

Table 1 Summary of numerical results from test problem

κ	Gauss-Seidel iteration				Line-by-line TDMA iteration			
	$\iiint \nabla \cdot \underline{q}^R dV$ (W)		number of iterations		$\iiint \nabla \cdot \underline{q}^R dV$ (W)		number of iterations	
(1/m)	w/o corr.	with corr.	w/o corr.	with corr.	w/o corr.	with corr.	w/o corr.	with corr.
10	2726	2699	20	9	2716	2698	6	5
1	421869	421491	987	210	421868	421786	165	44
0.1	113773	113756	14474	771	113773	113768	2449	192
0.01	12292	12292	149537	934	12292	12292	25927	236

tion are summarized in Table 1. From the table it is seen that the correction procedure is very effective, especially for optically thin media. For an absorption coefficient of $\kappa = 0.01\ \mathrm{m}^{-1}$ the required number of iterations, or, essentially, the cpu time (since the overhead of cpu time spent in the correction procedure is small—only about five percent of that used in the original base iteration) is reduced to less than 1 percent, regardless of whether the Gauss-Seidel or the line-by-line TDMA iterative methods are employed. Although the line-by-line TDMA iterative method converges after fewer iterations than the Gauss-Seidel method, the correction procedure is equally effective with either one, especially for optically thin media. To further evaluate the performance gains from the correction method, a relative error, defined as $1/N\Sigma_{i=1}^{N}|G_i - G_{\mathrm{conv},i}|/G_{\mathrm{conv},i}$, where $G_{\mathrm{conv},i}$ denotes the converged solution at node i, is plotted versus the number of iterations in Fig. 1 for the case of $\kappa = 1\ \mathrm{m}^{-1}$. It is clear that the solution converges after fewer iterations to the exact solution if the correction procedure is applied. The evolution of the computed total radiative heat source and the total radiative heat flux along the iterative process is shown in Fig. 2. Although an energy balance is ultimately reached when the solution has converged, the total radiative heat source is not equal to the total radiative heat flux through the boundaries during the iterative process if the conventional method is used. In contrast, the method with correction procedure always maintains equilibrium between radiative heat source and the radiative wall flux throughout the iterative process.

While the P_1 approximation with its Helmholtz equation was of particular interest here, its applicability is not limited to this type of problem. The method should perform equally well for all elliptic problems with boundary conditions of the second (specified gradient) and/or third (mixed) kind. For example, applying the method to steady-state conduction of a two-dimensional cylinder with convective boundary conditions leads to very similar results and conclusions (i.e., best acceleration for small heat transfer coefficients, corresponding to small absorption coefficients in the P_1 approximation, and preservation of the conductive energy balance during iterative process).

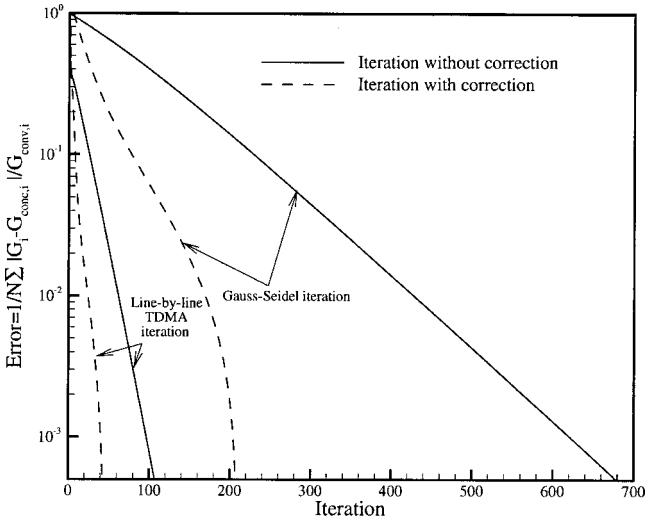

Fig. 1 Relative error change versus number of iterations

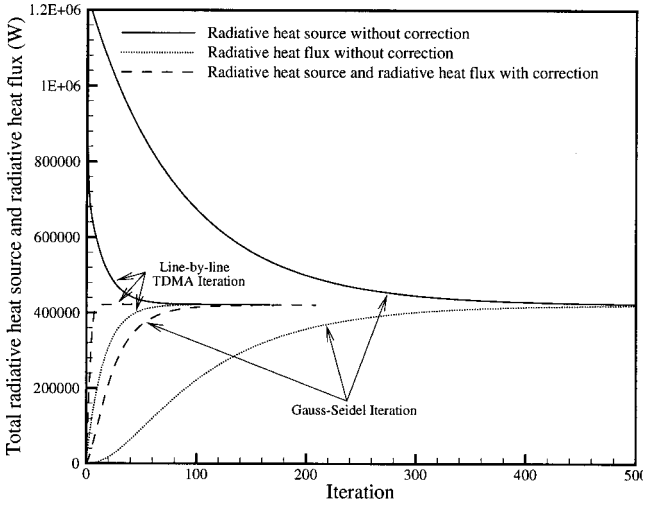

Fig. 2 Computed radiative heat source and radiative heat flux versus number of iterations

Conclusions

A corrective acceleration procedure is proposed for the iterative solution of the discretized P_1 equation (or any other elliptical partial differential equations subject to boundary conditions of the second or third kind), which can be used in conjunction with any iterative method. The procedure not only accelerates the convergence rate of the solution, but also preserves the radiative energy balance during the iterative process, which is desirable when radiation calculations are coupled with flow field calculations. A test problem demonstrated that accelerated iteration is achieved for all optical regimes, with speed-up of more than 100 times for optically thin situations.

Acknowledgment

This research is funded by the National Science Foundation through grant number CTS-9732223.

References

[1] Modest, M. F., 1993, *Radiative Heat Transfer*, McGraw-Hill, New York.
[2] FLUENT, 1995, "Computational Fluid Dynamics Software," Version 4.
[3] Patankar, S. V., 1981, "A Calculation Procedure for Two-Dimensional Elliptic Situations," Numer. Heat Transfer, **4**, pp. 409–425.
[4] Ferziger, J. H., 1998, *Numerical Methods for Engineering Application*, John Wiley & Sons, New York.
[5] Wachspress, E. L., 1966, *Iterative Solution of Elliptic Systems and Applications to the Neutron Diffusion Equations of Reactor Physics*, Prentice-Hall, Englewood Cliffs, NJ.
[6] Reed, W. H., 1971, "The Effectiveness of Acceleration Techniques for Iterative Methods in Transport Theory," Nucl. Sci. Eng., **45**, No. 3, pp. 245–254.
[7] Fiveland, W. A. and Jessee, J. P., 1996, "Acceleration Schemes for the Discrete Ordinates Method," J. Thermophys. Heat Transfer, **10**, No. 3, pp. 445–451.

Stagnation Line Heat Transfer Augmentation Due to Freestream Vortical Structures and Vorticity

Aung N. Oo
Graduate Student
e-mail: aung@engr.mun.ca
Faculty of Engineering and Applied Science,
Memorial University of Newfoundland,
St. John's, Newfoundland, A1B 3X5, Canada

Chan Y. Ching
Associate Professor
Department of Mechanical Engineering, McMaster University, Hamilton, Ontario, L8S 4L7, Canada

An experimental study has been performed to investigate the effect of freestream vortical structures and vorticity on stagnation region heat transfer. A heat transfer model with a cylindrical leading edge was tested in a wind tunnel at Reynolds numbers ranging from 67,750 to 142,250 based on leading edge diameter of the model. Grids of parallel rods were placed at several locations upstream of the heat transfer model in orientations where the rods were perpendicular and parallel to the stagnation line to generate freestream turbulence with distinct vortical structures. All three components of turbulence intensity, integral length scale and the spanwise and transverse vorticity were measured to characterize the freestream turbulence. The measured heat transfer data and freestream turbulence characteristics were compared with existing empirical models for the stagnation line heat transfer. A new correlation for the stagnation line heat transfer has been developed that includes the spanwise fluctuating vorticity components.
[DOI: 10.1115/1.1471526]

Keywords: Convection, Enhancement, Heat Transfer, Turbulence, Vortex

Introduction

Heat transfer augmentation in the stagnation region due to freestream turbulence has been studied extensively [1–7]. Several studies [1–3,6,7] have been performed to understand the physics of the turbulent heat transport mechanism in the stagnation region and to develop empirical models of the heat transfer augmentation due to freestream turbulence. In most studies, the freestream turbulence is nearly isotropic generated using square-meshed grids. However, isotropic turbulence is more the exception in real life engineering applications. It is well established that the coherent vortical structures in a turbulent flow play an important role in momentum and heat transfer. However, attempts to examine the relationship between freestream vortical structures and stagnation region heat transfer are very limited. Oo and Ching [8] performed an experiment where grids of parallel rods were used to generate freestream turbulence with different orientations of vortical structures. They determined that heat transfer in the stagnation region due to freestream turbulence with different coherent structures had distinct characteristics.

A knowledge of the interaction of freestream vortical structures with the stagnation region boundary layer should lead to improved models of stagnation region heat transfer. The vorticity field is closely related with the turbulence structure and dissipation rate [9]. Analyzing the correlation between the vorticity field and the heat transfer augmentation should, therefore, provide further insight to the turbulent heat transfer mechanism in the stagnation region. There are several empirical models [1–3,6,7] that relate stagnation line heat transfer with the characteristics of the freestream turbulence, namely Reynolds number, streamwise turbulence intensity and the integral length scale. These empirical models, however, fail to reveal the influence of vorticity and vortical structures of the freestream turbulence.

Characterizing freestream turbulence with Tu, Re_D, and λ_x does not provide a complete picture of the turbulence, especially when the turbulence is anisotropic. Freestream turbulence can be better described if information pertaining to the vorticity field and the coherent vortical structures are included. The objective of this technical note is to present a relationship between the characteristics of the freestream turbulence, including the vorticity field, and stagnation region heat transfer presented in a previous paper [8]. The freestream vorticity was measured and an empirical model for the heat transfer augmentation that includes the freestream vorticity field developed.

Experimental Details

Heat transfer in the stagnation region was measured using a model with a cylindrical leading edge in a low-speed wind tunnel. Freestream turbulence with different orientations of primary vortices was generated using grids of 2.86 cm, 1.59 cm, and 0.95 cm diameter parallel rods. The grids were arranged in two different orientations, perpendicular and parallel to the stagnation line (Fig. 1). Heat transfer measurements were made with the grids 25d to 125d upstream of the model at three different Re_D of 67,750, 108,350, and 142,250. The experimental details and data reduction for the turbulence intensity and integral length scale are given in Oo and Ching [8]. The spanwise fluctuating vorticity components, ω_z and ω_y, were measured using a vorticity probe similar to the design of Foss and Haw [10]. The vorticity probe consists of a pair of parallel wires and an X-wire. The two spanwise fluctuating vorticity components were obtained separately by rotating the vorticity probe 90 deg. The hot wires were operated using DANTEC 55M01 constant temperature bridges, and the output voltages of the anemometers were digitized using a 16 channel 12 bit Keithley 570 System A/D converter, interfaced to a personal computer. The frequency response of each circuit was determined by standard square-wave test, and found to be about 30 kHz. The sampling frequency of the study ranged from 20 to 30 kHz.

The spanwise vorticity components were measured using the vorticity probe and approximated by:

$$\Omega_z = \frac{\Delta V}{\Delta x} - \frac{\Delta U}{\Delta y} = -\frac{1}{U}\frac{\Delta V}{\Delta t} - \frac{\Delta U}{\Delta y} \tag{1.a}$$

$$\Omega_y = \frac{\Delta U}{\Delta z} - \frac{\Delta W}{\Delta x} = \frac{\Delta U}{\Delta z} + \frac{1}{U}\frac{\Delta W}{\Delta t} \tag{1.b}$$

where ΔU is the difference between the instantaneous streamwise velocity measured by a pair of parallel wires separated in spanwise directions, Δy and Δz. The spanwise velocity derivatives, $\Delta V/\Delta x$ and $\Delta W/\Delta x$, were estimated using Taylor's hypothesis, i.e., $\Delta/\Delta x = -U^{-1}\,\Delta/\Delta t$. The performance of the vorticity probe was tested in the wake of a circular cylinder and the results are in agreement with those of Antonia et al. [11]. Experimental uncertainties in fluctuating vorticity components based on the uncertainty analysis of hot wire data by Yavuzkurt [12], was estimated to be 9.43 percent. The details of the uncertainty analysis are provided in a later section and the results presented in Tables 1 and 2.

Contributed by the Heat Transfer Division for publication in the JOURNAL OF HEAT TRANSFER. Manuscript received by the Heat Transfer Division September 1, 2001; revision received February 1, 2002. Associate Editor: H. S. Lee.

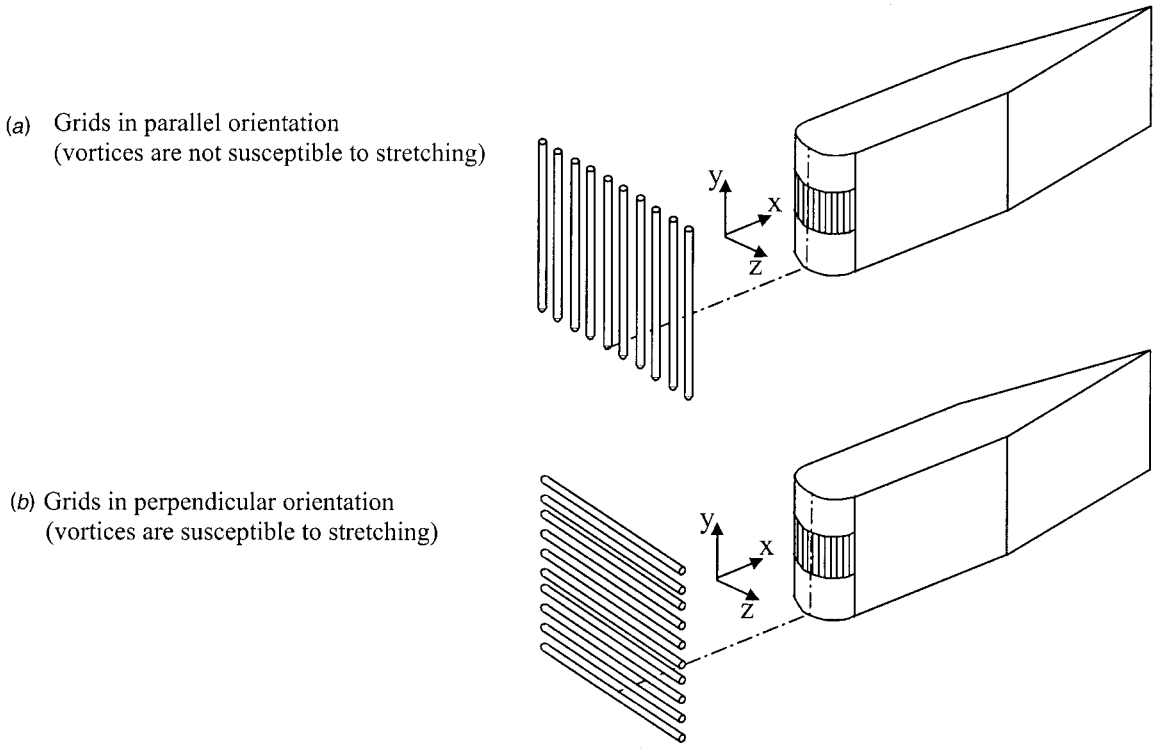

Fig. 1 Arrangements of grids

Table 1 Experimental uncertainty in Fr (percent)

Variable	Bias Error		Precision Error	
	Experimental Reynolds Number Range			
	Max.	Min.	Max.	Min.
Current I	0.18	0.26	0.53	0.51
Voltage Vo	0.06	0.08	0.20	0.21
Temperature difference ΔT	3.20	3.20	0.53	0.53
Conduction heat Q_{cond}	4.60	4.60	0.75	0.75
Radiation heat Q_{rad}	12.80	12.80	2.12	2.12
Convection heat Q_{cov}	1.61	2.10	0.55	0.60
Reynolds number Re_D	0.05	0.10	0.32	0.37
Frossling number *Fr*	3.58	3.83	0.79	0.82

Table 2 Experimental uncertainty in Tu, λx, and ω (percent)

	Experimental Reynolds Number Range	
	Maximum	Minimum
Velocity Calibration (Tu, λ_x)	0.07	0.14
Velocity Curve Fitting (Tu, λ_x)	2.18	2.18
Autocorrelation Curve Fitting (λ_x)	10.50	10.50
Turbulence Intensity *Tu*	3.09	3.09
Integral Length Scale λ_x	10.95	10.95
Fluctuating vorticity ω_z and ω_y	9.43	9.43

Results and Discussion

The turbulence intensity, integral length scale and spanwise velocity fluctuations downstream of the turbulence generating grids were presented in a previous paper [8]. The streamwise distribution of spanwise vorticity, normalized with the mean freestream velocity and diameter of the leading edge, are presented in Fig. 2 for Re_D=108,350. Since greater vorticity is usually associated with the smaller eddies in turbulence [9], the fluctuating vorticity component increases with smaller grid-rod for a given mean freestream velocity. For instance, at $x/d=25$, $\omega U/D$ ranges from about 20 to 25 for the 2.86 cm grid while it varies from about 32 to 39 for the 0.95 cm grid. An attempt to examine the isotropy of the rod-grid turbulence was made by estimating the degree of isotropy of the turbulence from the measurements taken with the single wire and the vorticity probe. For isotropic turbulence, $5\overline{(\partial u/\partial x)^2}$ is equal to $\overline{\omega_z^2}$ and $\overline{\omega_y^2}$ [13]. Therefore, the degree of isotropy is defined as:

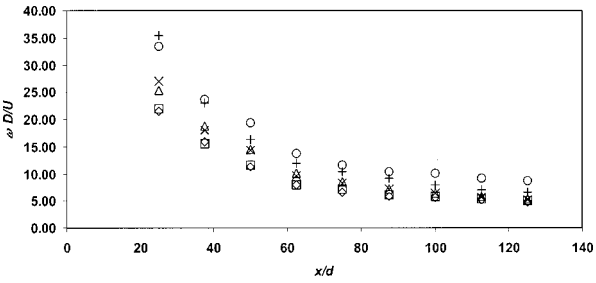

Fig. 2 RMS fluctuating vorticity components of grids in perpendicular orientation for Re_D=108,350 (2.86 cm rod-grid: ◇, ω_z; □, ω_y; 1.59 cm rod-grid: △, ω_z; ×, ω_y; 0.95 cm rod-grid: ○, ω_z; +, ω_y)

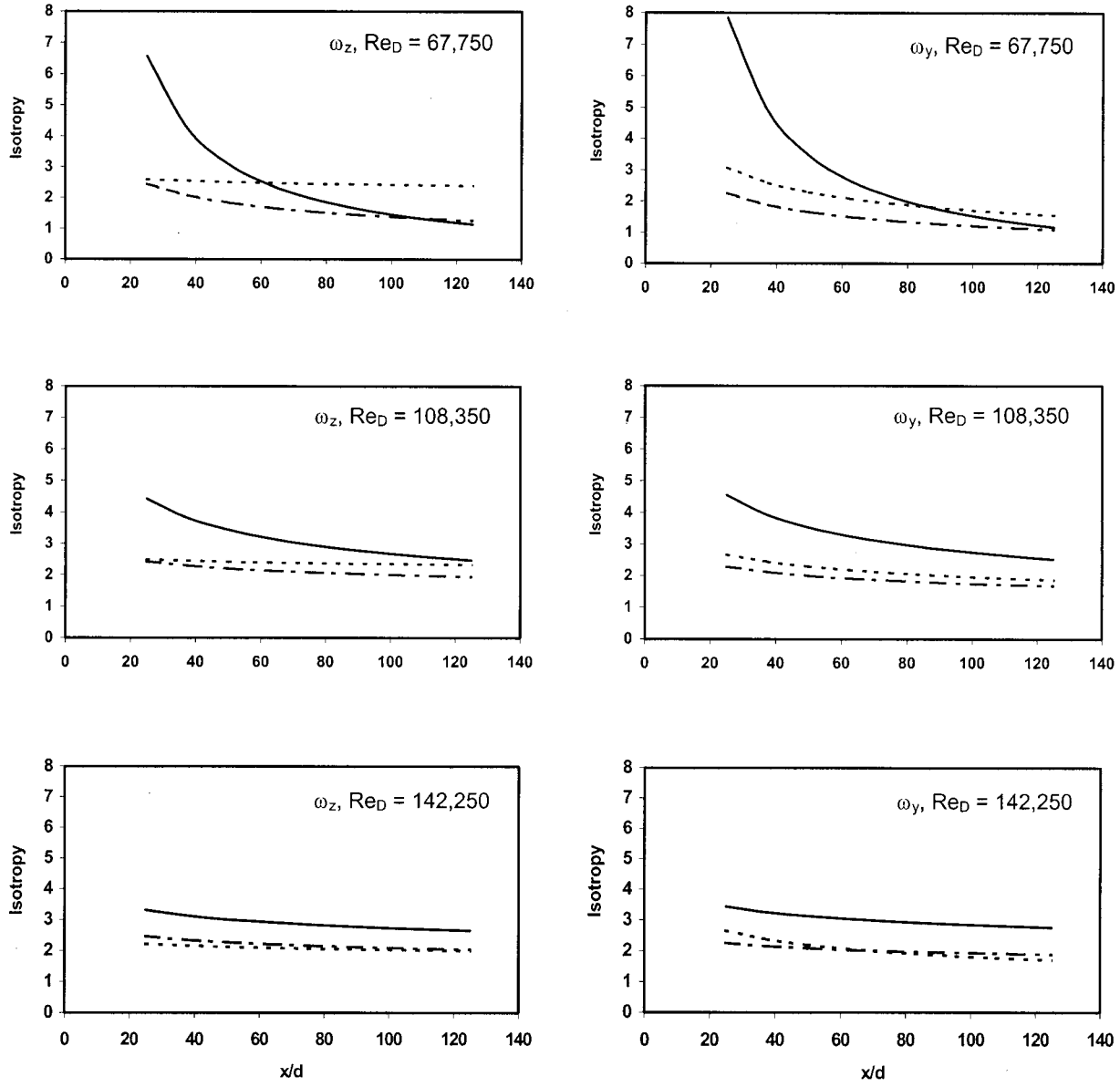

Fig. 3 Streamwise trends of the degree of isotropy (rod-grids of: —, 2.86 cm; - — -, 1.59 cm; - - -, 0.95 cm)

$$\mathrm{Iso} = \frac{\overline{\omega^2}}{5\left(\overline{\frac{\partial u}{\partial x}}\right)^2} \tag{2}$$

where $\overline{\omega^2}$ is the mean square value of fluctuating vorticity components and $\partial u/\partial x$ is estimated from single wire measurements. The streamwise distributions of the estimated degree of isotropy, which is calculated from the best-fit curves of vorticity components and $\partial u/\partial x$, are shown in Fig. 3. For the 2.86 cm rod-grid, deviation from isotropy is highest (Iso of an order of 7 at $x/d = 25$) at the lowest Reynolds number. At freestream Re_D of 67,750, the grid turbulence approaches isotropy with downstream distance for all grids (Iso$\sim$1 at $x/d = 125$). Deviation from isotropy is higher for the higher Reynolds numbers (Iso$\sim$2 at $x/d = 125$ for Re_D of 108,350 and 142,250). The general trend is that turbulence approaches isotropy as downstream distance increases, and the degree of anisotropy is highest with the biggest rod-grid.

The stagnation line heat transfer data from the three grids are compared with the correlation of VanFossen et al. [7] in Fig. 4.

$$\mathrm{Fr} = 0.008\sqrt{\mathrm{Tu}\ \mathrm{Re}_D^{0.8}\left(\frac{\lambda_x}{D}\right)^{-0.574}} + 0.939 \tag{3}$$

There is a significant discrepancy between the present experimental data and Eq. (3) for the 2.86 cm rod-grid, but the agreement improves with decreasing size of rod. For the 0.95 cm rod-grid, 87 percent of data falls within ± 4 percent of Eq. (3). It is clear from Fig. 4 that correlations developed for isotropic turbulence generated by square mesh grids should be corrected to predict the heat transfer due to turbulence with distinct coherent vortical structures. The errors are larger for the 2.86 cm rod-grid, where the freestream turbulence has a greater distinction between the primary and secondary vortices. It is unlikely that correlations developed for isotropic turbulence can be used to estimate heat transfer to gas turbine blades, where the turbulence from the combustor and wakes from the upstream blades is highly anisotropic and laced with well-defined vortical structures.

The freestream turbulence needs to be characterized more comprehensively to obtain more accurate empirical models. It seems plausible that incorporating the vorticity field and spanwise veloc-

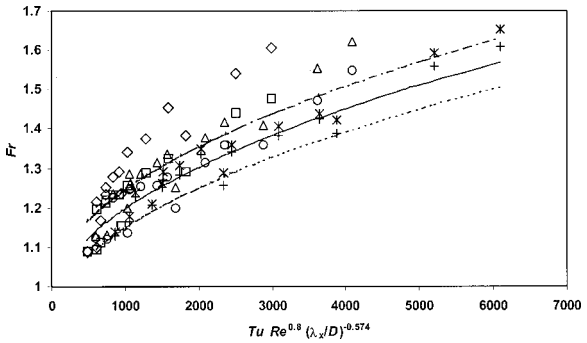

Fig. 4 Stagnation line Fr versus correlation parameter proposed by VanFossen et al. [7] (perpendicular Rod-grids: ◇, 2.86 cm; △, 1.59 cm; *, 0.95 cm; parallel rod-grids: □, 2.86 cm; ○, 1.59 cm; +, 0.95 cm; correlation lines: —, VanFossen et al. [7]; – – –, +4%; - - -, −4%)

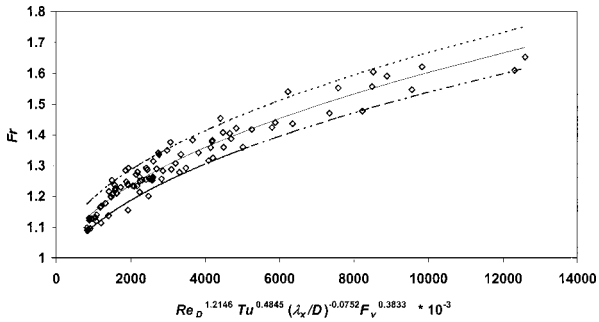

Fig. 5 Stagnation line Fr versus correlation parameter with spanwise vorticity and velocity fluctuations for both grid orientations (◇, data, correlation lines: —, Eq. (5); - - -, +4%; - · - ·, −4%)

ity fluctuations would improve the correlation, since they highlight the distinct structure of turbulence. Since vorticity amplification due to vortex stretching is hypothesized to influence the stagnation region heat transfer, the fluctuating vorticity component of primary vortices, i.e., ω_z and ω_y for turbulence generated by the rod-grids in perpendicular and parallel orientations, respectively, were considered to form a new turbulence parameter. The products of spanwise vorticity and velocity fluctuating components, $v\omega_z$ and $w\omega_y$, are taken as additional parameters to be included in the correlation. The products, $v\omega_z$ and $w\omega_y$, can be interpreted to represent the vortex forces in turbulence, which are analogous to the Coriolis forces [9]. The additional turbulence parameter used to develop a new correlation for the stagnation line heat transfer is defined as:

$$F_\nu = \frac{\nu\omega_z D}{U^2} \quad \text{for grid-rods in perpendicular orientation} \tag{4.a}$$

$$F_\nu = \frac{w\omega_y D}{U^2} \quad \text{for grid-rods in parallel orientation} \tag{4.b}$$

Therefore, the additional parameter is the vortex force due to primary vortices of freestream normalized by the diameter of the leading edge and the mean freestream velocity. The new correlation is obtained by a regression analysis and is presented in Fig. 5. It can be seen that 95 percent of experimental data fall within the ±4 percent of the new correlation given by:

$$\mathrm{Fr} = 0.00021\sqrt{\mathrm{Re}_D{}^{1.2146}\mathrm{Tu}^{0.4845}\left(\frac{\lambda_x}{D}\right)^{-0.0752} F_\nu^{0.3833}} + 0.939 \tag{5}$$

The improved correlation suggests that the inclusion of the vorticity field and spanwise velocity components takes into account the vortical structures of the freestream to a certain extent. It is clear that freestream turbulence with different orientations of coherent vortical structures have different influences over the heat transfer in the stagnation region, and the consideration of vortical structures of turbulence would improve the empirical models for prediction of gas turbine heat transfer.

Conclusions

Heat transfer enhancement in the stagnation region by freestream turbulence with distinct coherent vortical structures is different to that by turbulence generated using square-mesh grids. The present heat transfer data, obtained using an array of parallel rods in different orientations, are poorly predicted by existing correlation models. A new correlation model was developed by including the lateral fluctuating velocity and vorticity components of the freestream. The new correlation model predicts the heat transfer data of this study within ±4 percent. Any empirical model should take into account the distinct nature of the coherent vortical structures of the turbulence to improve its predictive capability.

Acknowledgments

The support of the Natural Sciences and Engineering Research Council (NSERC) of Canada is gratefully acknowledged.

Appendix

Analysis of Experimental Uncertainties. Following the uncertainty analysis methods of Moffat [14] the uncertainty in Fr can be expressed as:

$$(Un_{\mathrm{Fr}})^2 = (Un_{\mathrm{Nu}})^2 + 0.25(Un_{\mathrm{Re}D})^2$$

where Un_{Fr} = Uncertainty in Fr (%)
Un_{Nu} = Uncertainty in Nu (%)
$Un_{\mathrm{Re}\,D}$ = Uncertainty in Re_D (%)

The uncertainty in Fr and the influencing variables with 95 percent confidence levels are given in Table 1 for both maximum and minimum freestream velocities. Uncertainties in temperature were considered in estimating conduction heat loss, radiation heat losses and convection heat transfer. Uncertainties associated with leading edge diameter (D), thermal conductivity (k), and area (A) are assumed to be negligible since these values are based on the data specified by manufacturers.

The techniques proposed by Yavuzkurt [12] were used to estimate the uncertainties in Tu and λ_x and ω. The uncertainties are given in Table 2.

Nomenclature

d = diameter of a grid-rod (m)
D = diameter of cylindrical leading edge (m)
Fr = Frossling number ($\mathrm{Nu}/\sqrt{\mathrm{Re}_D}$)
F_ν = dimensionless vortex force
Iso = degree of isotropy
Re_D = Reynolds number based on D
t = time (s)
Tu = streamwise turbulence intensity
u = rms of fluctuating velocity component in streamwise direction (m/s)
U = mean freestream velocity (m/s)
v = rms of fluctuating velocity component in spanwise Y-direction (parallel to stagnation line) (m/s)
w = rms of fluctuating velocity component in spanwise Z-direction (m/s)
x = distance downstream of the grid (m)

Ω_y = instantaneous vorticity in spanwise *Y*-direction (l/s)
Ω_z = instantaneous vorticity in spanwise *Z*-direction (l/s)
λ_x = streamwise integral length scale of turbulence (m)
ω_y = rms of fluctuating vorticity component in spanwise *Y*-direction (l/s)
ω_z = rms of fluctuating vorticity component in spanwise *Z*-direction (l/s)

References

[1] Smith, M. C., and Kuethe, A. M., 1966, "Effects of Turbulence on Laminar Skin Friction and Heat Transfer," Phys. Fluids, **9**(12), pp. 2337–2344.
[2] Kestin, J., and Wood, R. T., 1971, "The Influence of Turbulence on Mass Transfer from Cylinders," ASME J. Heat Transfer, **93C**, pp. 321–327.
[3] Lowery, G. W., and Vachon, R. I., 1975, "Effect of Turbulence on Heat Transfer from Heated Cylinders," Int. J. Heat Mass Transf., **18**(11), pp. 1229–1242.
[4] O'Brien, J. E., and VanFossen, G. J., 1985, "The Influence of Jet-Grid Turbulence on Heat Transfer from the Stagnation Region of a Cylinder in Crossflow," ASME Paper 85-HT-58.
[5] Mehendale, A. B., Han, J. C., and Ou, S., 1991, "Influence of High Mainstream Turbulence on Leading Edge Heat Transfer," ASME J. Heat Transfer, **113**, pp. 843–850.
[6] Yeh, F. C., Hippensteele, S. A., VanFossen, G. J., Poinsatte, P. E., and Ameri, A. 1993, "High Reynolds Number and Turbulence Effects on Aerodynamics and Heat Transfer in a Turbine Cascade," Paper No. AIAA-93-2252.
[7] VanFossen, G. J., Simoneau, R. J., and Ching, C. Y., 1995, "Influence of Turbulence Parameters, Reynolds Number and Body Shape on Stagnation Region Heat Transfer," ASME J. Heat Transfer, **117**, pp. 597–603.
[8] Oo, A. N., and Ching, C. Y., 2001, "Effect of Turbulence with Different Vortical Structures on Stagnation Region Heat Transfer," ASME J. Heat Transfer, **123**, pp. 665–674.
[9] Tennekes, H., and Lumley, J. L., 1972, *A First Course in Turbulence*, The MIT Press, The Massachusetts Institute of Technology.
[10] Foss, J. F., and Haw, R. C., 1990, "Transverse Vorticity Measurements Using a Compact Array of Four Sensors," *The Heuristics of Thermal Anemometry*, D. E. Stock, S. A. Sherif, and A. J. Smits, eds., ASME-FED 97, pp. 71–76.
[11] Antonia, R. A., Browne, L. W. B., and Shah, D. A., 1988, "Characteristics of Vorticity Fluctuation in a Turbulent Wake," J. Fluid Mech., **189**, pp. 349–365.
[12] Yavuzkurt, S., 1984, "A Guide to Uncertainty Analysis of Hot-Wire Data," ASME J. Fluids Eng., **106**, pp. 181–186.
[13] Zhou, T., and Antonia, R. A., 2000, "Reynolds Number Dependence of the Small-Scale Structure of Grid Turbulence," J. Fluid Mech., **406**, pp. 81–107.
[14] Moffat, R. J., 1988, "Describing the Uncertainties in Experimental Results," Exp. Therm. Fluid Sci., **1**, pp. 3–17.

Similarity Solution for Marangoni Convection Over a Flat Surface

David M. Christopher
Associate Professor
Mem. ASME
e-mail: dmc@tsinghua.edu.cn

Buxuan Wang
Professor

Thermal Engineering Department, Tsinghua University, Beijing, 100084, China

A similarity solution is presented for Marangoni flow over a flat surface for both the velocity and temperature profiles assuming developing boundary layer flow along the surface with various imposed temperature profiles. Marangoni flow results from variations of the surface tension along a liquid-vapor interface and is especially noticeable in microgravity. Solutions are presented for the surface velocity, the total flow rate and the heat transfer for various temperature profiles and various Prandtl numbers. [DOI: 10.1115/1.1473143]

Keywords: Boiling, Convection, Heat Transfer, Thermocapillary

Introduction

Marangoni flow due to surface tension variations is of importance in various processes including the flow in crystal growth melts in both microgravity and normal earth gravity conditions where the Marangoni flow can affect crystal quality and in boiling where the Marangoni flow may significantly affect the heat transfer as shown by boiling tests in microgravity [1,2].

The numerous investigations of Marangoni flow have been reviewed in the literature (e.g., [3,4]) so only the studies most closely related to this paper are reviewed here. Okano et al. [5] presented an order-of-magnitude analysis of Marangoni flow that showed the general trends for the Grashof number, Marangoni number, and Prandtl number dependence on the Reynolds number. Banks and Zaturska [6] and Arafune and Hirata [7] presented a similarity solution for the momentum boundary layer equations with the flat surface velocity specified as a function of the distance along the surface. Arafune and Hirata [7] also presented experimental results for Marangoni flow along a flat surface. Schwabe and Metzger [8] experimentally investigated Marangoni flow on a flat surface combined with natural convection in a unique geometry where the Marangoni and buoyancy effects could be varied independently.

This paper presents a similarity solution for both the momentum and energy boundary layer equations for Marangoni flow over a flat surface with an imposed surface temperature gradient that is a power-law function of the location. The resulting family of solutions can also be applied qualitatively to other flows that have surface temperature variations that can be related to the assumed temperature variation as has been done with the Falkner-Skan family of flows [6]. The momentum and energy boundary layer equations are transformed to ordinary differential equations which are then solved using the Runge-Kutta method. The present results extend previous solutions by including the solution of the energy equation so that the velocity distribution is related to the specified temperature distribution through the Marangoni boundary condition rather than just specifying the surface velocity distribution as done previously.

Theoretical Analysis

The continuity equation and the momentum and energy equations are solved for laminar boundary layer flow of a Newtonian fluid in the half plane $0<y<\infty$ having a flat surface in the x direction starting at $x=0$. The boundary conditions at the surface are:

$$\mu \left.\frac{\partial u}{\partial y}\right|_{y=0} = -\frac{d\sigma}{dT}\left.\frac{\partial T}{\partial x}\right|_{y=0}$$
$$\nu(x,0)=0 \tag{1}$$
$$T(x,0)=T(0,0)+Ax^{k+1}$$

Far from the surface, the boundary conditions are:

$$u(x,\infty)=0$$
$$T(x,\infty)=T_\infty=T(0,0) \tag{2}$$

Using the standard definition of the stream function, similarity variables are introduced as:

$$\eta=C_1x^dy$$
$$f(\eta)=C_2x^a\psi(x,y) \tag{3}$$
$$\varphi(\eta)=(T(x,y)-T(0,0))x^h/A$$

so the governing equations can be written as:

Contributed by the Heat Transfer Division for publication in the JOURNAL OF HEAT TRANSFER. Manuscript received by the Heat Transfer Division April 11, 2000; revision received February 25, 2002. Associate Editor: S. S. Sadhal.

$$f^m = f'^2(d-a) + aff''$$
$$\varphi'' = \Pr(af\varphi' - hf'\varphi) \tag{4}$$

The coefficients are defined as:

$$C_1 = \sqrt[3]{\frac{\frac{d\sigma}{dT}A\rho}{\mu^2}}; \quad C_2 = \sqrt[3]{\frac{\rho^2}{\frac{d\sigma}{dT}A\mu}} \tag{5}$$

For similarity, the exponents are related to k in Eq. (1) by:

$$d = \frac{k-1}{3}; \quad a = \frac{-2-k}{3}; \quad h = -1-k \tag{6}$$

The boundary conditions are:

$$f(0) = 0; \quad f''(0) = -1; \quad f'(\infty) = 0 \tag{7}$$

$$\varphi(0) = 1; \quad \varphi(\infty) = 0 \tag{8}$$

The surface velocity given by the similarity solution is:

$$u(x,0) = \sqrt[3]{\frac{\left(\frac{d\sigma}{dT}A\right)^2}{\rho\mu}} f'(0)x^{(2k+1)/3} \tag{9}$$

The temperature gradient coefficient can be defined in terms of the total temperature difference along a surface of length L as $A = \Delta T/L^{k+1}$ so that the Marangoni number can then be defined for a general temperature profile as:

$$\mathrm{Ma}_L = \frac{\frac{d\sigma}{dT}\frac{\Delta T}{L^{k+1}}L^{k+2}}{\mu\alpha} = \frac{\frac{d\sigma}{dT}\Delta TL}{\mu\alpha} \tag{10}$$

The Reynolds number defined in terms of the surface velocity is then related to the Marangoni number as:

$$\mathrm{Re}_L = \frac{u(x,0)L}{\nu} = f'(0)\mathrm{Ma}_L^{2/3}\mathrm{Pr}^{-2/3} \tag{11}$$

The total mass flow in the boundary layer per unit width can be written as:

$$\dot{m} = \int_0^\infty \rho u dy = \sqrt[3]{\frac{d\sigma}{dT}A\rho\mu}x^{(k+2)/3} f(\infty) \tag{12}$$

The problem statement in this analysis differs in several ways from that used by Arafune and Hirata [7], Banks and Zaturska [6] and others. While the definitions of the similarity variables are only slightly different, the surface boundary condition for the momentum equation in this analysis is based on the Marangoni boundary condition rather than the specified velocity variation as in previous works. In addition, the current derivation is extended to include the energy equation so that the velocity distribution throughout the liquid region is a function of the temperature distribution. The surface velocity distribution given in Eq. (9), while similar to the form of the velocity distribution used by others, is a result of the derivation that clarifies the relationship between the velocity and temperature distributions.

Discussion of Similarity Results

The governing equations, Eq. (4), were solved numerically using the fourth-order Runge-Kutta method with at least 20,000 steps. The shooting method was used to determine the unknown boundary conditions at $\eta = 0$, $f'(0)$ for the momentum equation and $\phi'(0)$ for the energy equation. The maximum value for the independent variable, η, which was a function of the Prandtl number, was always chosen to be at least 4 times the maximum momentum or thermal boundary layer thickness. The results presented in the following section were all independent of the number of steps and the maximum value of η.

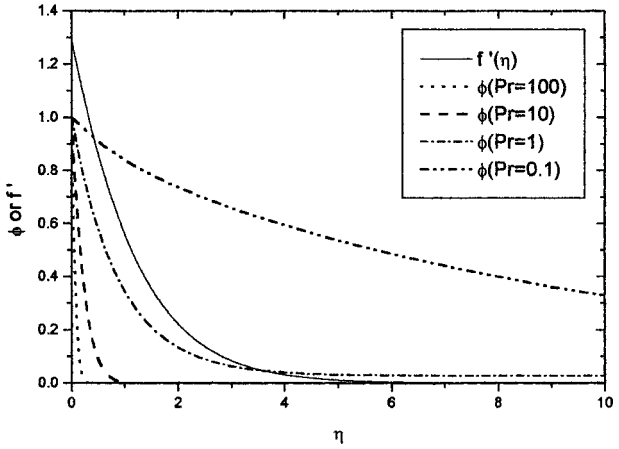

Fig. 1 Velocity and temperature profiles for $k=0$

The similarity stream function, f, is a function of the exponent, k, while the temperature function, ϕ, is a function of both k and the Prandtl number. The governing equations were solved subject to the boundary conditions in Eqs. (7) and (8) for various values of k and Pr. Typical velocity and temperature profiles are given in Fig. 1 for several representative values of the Prandtl number and for $k=0$ which is a linear surface temperature profile.

The variations of the surface velocity, the boundary layer thickness and the total flow rate in the boundary layer are given as functions of k in Fig. 2, of which $k=0$ refers to a linear profile and $k=1$ is quadratic, while $k=-0.5$ would be a temperature variation relative to the square root of x. The minimum value of k is -1, which results in no temperature variation on the surface and thus no Marangoni flow. The momentum boundary layer thickness is defined as the point where the velocity function, f, is 1 percent of the value at the surface. The surface velocity for small values of k is greater because for a fixed total temperature difference across the surface (i.e., fixed A), the profile for a small value of k is steeper near the leading edge which provides more flow. For larger values of k, the slope of the temperature profile is larger near the trailing edge where the boundary layer is thicker and the additional acceleration of the flow has less effect. The mass flow rate follows the same trend. The boundary layer thickness is greatest for the uniformly increasing temperature profile, $k=0$. For k greater than or less than 0, the temperature profile over part of the surface is relatively flat, so the flow does not accelerate much in that region and the boundary layer does not grow.

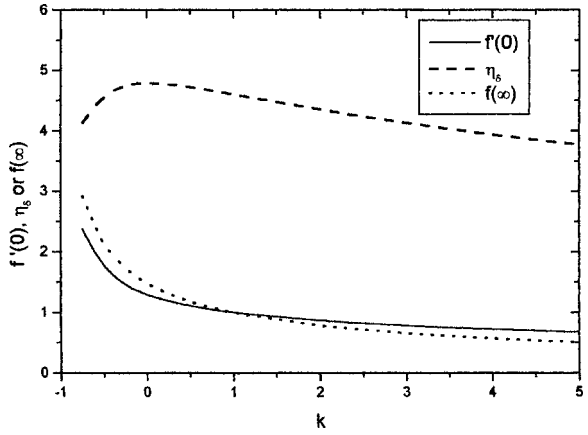

Fig. 2 Variations of surface velocity, boundary layer thickness, and flow rate for various temperature gradient exponents

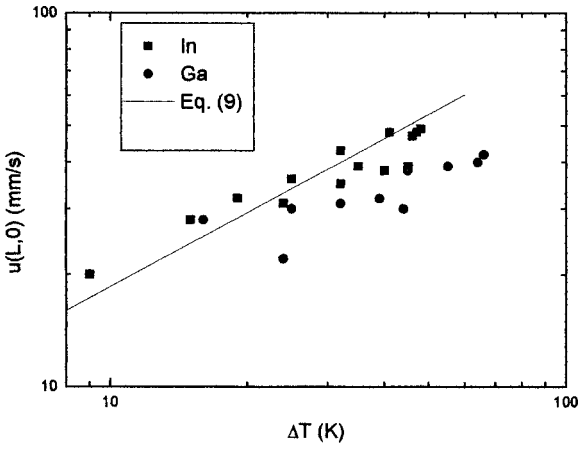

Fig. 3 Comparison of experimental results from Arafune and Hirata [7] with the predicted surface velocities for $k=0$

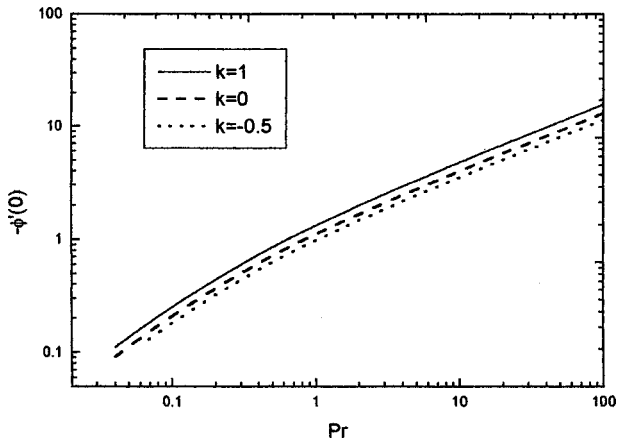

Fig. 4 Variation of the surface heat flux

The predicted surface velocities for $k=0$ agree well with the surface velocities measured by Arafune and Hirata [7] for Marangoni driven flow of gallium and indium in a shallow pool shown in Fig. 3. The slopes of the similarity and experimental results also agree with the analysis of Okano et al. [5] which showed that the Reynolds number should vary as the two-thirds root of the Marangoni number for large Reynolds numbers.

The variation of the surface heat flux as a function of the Prandtl number and the temperature gradient exponent is shown in Fig. 4. The local Nusselt number is:

$$\mathrm{Nu}_x=\frac{q''(x)x}{\lambda(T(x,0)-T(x,\infty))}=-\mathrm{Ma}_x^{1/3}\mathrm{Pr}^{-1/3}\left(\frac{x}{L}\right)^{(k+2)/3}\phi'(0) \tag{13}$$

The similarity analysis is based on the boundary layer equations which assume that the transverse derivatives of the velocity and temperature are much larger than their axial derivatives. Analysis of the similarity transformation shows that both are true if:

$$C_1L^{(k+2)/3}=\sqrt[3]{\frac{d\sigma}{dT}\frac{A\rho L^{k+2}}{\mu^2}}=\mathrm{Ma}_L^{1/3}\mathrm{Pr}^{-1/3}\gg 1 \tag{14}$$

Conclusions

A similarity solution was given for Marangoni boundary layer flow over a flat surface with an imposed temperature gradient. The predicted surface velocities agree well with measured values for shallow pools of liquid indium and gallium [7].

The analysis gives the variations of the velocity and temperature distributions in the boundary layer for power-law variations of the surface temperature gradient. Equations are then given for the surface velocity, the total mass flow rate and the heat flux at the interface as functions of the Marangoni, Prandtl and Reynolds numbers, the exponent k and the location. For $k=0$, the analysis agrees with previous results using a specified surface velocity distribution [5] that the Reynolds number based on the surface velocity varies as the two-thirds power of the Marangoni number.

Acknowledgment

The project was financially supported by the National Natural Science Foundation of China with grant number 59995550-3.

Nomenclature

a, d, h = exponents in similarity transformation
A = temperature gradient coefficient (K/m^{k+1})
C_1 = similarity transformation coefficient (m^a)
C_2 = similarity transformation coefficient ($s\ m^{(k-4)/3}$)
$f(\eta)$ = stream function similarity variable
k = temperature gradient exponent
$\dot{m}$ = mass flow rate per unit width (kg/m s)
Ma = Marangoni number, Eq. (10)
Nu = Nusselt number, Eq. (13)
Pr = Prandtl number
q'' = heat flux (W/m^2)
Re = Reynolds number, Eq. (11)
T = temperature (K)
u, v = velocities (m/s)
x, y = coordinates (m)

Greek

α = thermal diffusivity (m^2/s)
ϕ = dimensionless similarity temperature
η = location similarity variable
η_δ = dimensionless momentum boundary layer thickness
λ = thermal conductivity (W/mK)
μ = dynamic viscosity (Ns/m^2)
ν = kinematic viscosity (m^2/s)
ρ = density (kg/m^3)
σ = surface tension (N/m)
ψ = stream function (m^2/s)

Subscripts

L = average over surface length
x = local value

References

[1] Straub, J., 1994, "The Role of Surface Tension for Two-Phase Heat and Mass Transfer in the Absence of Gravity," Exp. Therm. Fluid Sci., **9**, pp. 253–273.
[2] Christopher, D., and Wang, B., 1998, "Marangoni Convection around a Bubble in Microgravity," *Heat Transfer, 1998, Proceedings 11th International Heat Transfer Conference*, J. S. Lee, ed., Taylor and Francis, Inc., Levittown, PA, **3**, pp. 489–494.
[3] Arafune, K., and Hirata, A., 1998, "Interactive Solutal and Thermal Marangoni Convection in a Rectangular Open Boat," Numer. Heat Transfer, Part A, **34**, pp. 421–429.
[4] Croll, A., Muller-Sebert, W., and Nitsche, R., 1989, "The Critical Marangoni Number for the Onset of Time-dependent Convection in Silicon," Mater. Res. Bull., **24**, pp. 995–1004.
[5] Okano, Y., Itoh, M., and Hirata, A., 1989, "Natural and Marangoni Convections in a Two-Dimensional Rectangular Open Boat," J. Chem. Eng. Jpn., **22**, pp. 275–281.
[6] Banks, W. H. H., and Zaturska, M. B., 1986, "Eigensolutions in Boundary-Layer Flow Adjacent to a Stretching Wall," IMA J. Appl. Math., **36**, pp. 263–273.
[7] Arafune, K., and Hirata, A., 1999, "Thermal and Solutal Marangoni Convection in In-Ga-Sb System," J. Cryst. Growth, **197**, pp. 811–817.
[8] Schwabe, D., and Metzger, J., 1989, "Coupling and Separation of Buoyant and Thermocapillary Convection," J. Cryst. Growth, **97**, pp. 23–33.

Journal of Heat Transfer

Technical Notes

This section contains shorter technical papers. These shorter papers will be subjected to the same review process as that for full papers.

Numerical Investigation of Forced Convection in a Horizontal Channel With a Built-In Triangular Prism

H. Abbassi, S. Turki, and S. Ben Nasrallah
Heat and Mass Transfer Laboratory, National Engineering High School of Monastir (Tunisia)

Keywords: Channel Flow, Computational, Forced Convection, Heat Transfer, Periodic

Introduction

Flow past bluff bodies between two parallel walls has been investigated by many researchers both numerically and experimentally. This flow situation is popular not only because of its academic attractiveness but also owing to its related technical problems associated with energy conservation and structural design. This type of flow is of relevance for many practical applications, such as electronic cooling and heat exchanger systems.

The incompressible flow around a circular cylinder represents one of the most investigated prototypes of bluff body wakes. The flow around a rectangular cylinder has received far less attention than the flow around a circular cylinder, but no references have been found which simulate the laminar flow around a triangular prism placed in a channel. Furthermore the effect of presence of bluff body in the heat transfer in a flow with heat source has not yet been investigated. This has motivated the present work that is concerned with structure of laminar flow and heat transfer in a two dimensional channel differentially heated with a built-in triangular prism. This specifically shaped cylinder is specially used in systems of vortex flowmeters and flame stabilizer in combustion chambers. The investigation is carried out from the numerical solutions of complete Navier-Stokes and energy equations by Control Volume Finite Element Method. The effects of presence of triangular prism on the flow structure and heat transfer are the subject of the present work.

Results and Discussion

The system of interest is a horizontal plane channel, a triangular prism is symmetrically placed in the channel axis as indicated in Fig. 1. Boundary conditions expressed in dimensionless form are as follows:

$$\text{at } 0 \leqslant x \leqslant L/B; y=0: u=v=0, \theta=1$$

$$\text{at } 0 \leqslant x \leqslant L/B; y=4: u=v=0, \theta=0$$

$$\text{at } x=0; 0 \leqslant y \leqslant 4: u=y(4-y)/4, v=0, \theta=0$$

$$\text{at } x=L/B; 0 \leqslant y \leqslant 4: \frac{\partial u}{\partial x}=\frac{\partial v}{\partial x}=\frac{\partial \theta}{\partial x}=0; \quad \int_0^4 u\,dy=8/3$$

The thermal heat flux transferred from the hot bottom wall to the flow is characterized by the space-averaged Nusselt number evaluated as follows:

$$\overline{\mathrm{Nu}}=\frac{1}{L/B}\int_0^{L/B}\mathrm{Nu}\,dx,$$

where Nu is the local Nusselt number defined as

$$\mathrm{Nu}=-\frac{\partial \theta}{\partial y}.$$

The space- and time-averaged Nusselt number is defined as

$$\langle\overline{\mathrm{Nu}}\rangle=\left(\frac{1}{\tau_2-\tau_1}\right)\int_{\tau_1}^{\tau_2}\overline{\mathrm{Nu}}\,d\tau,$$

where the time interval $(\tau_2-\tau_1)$ is the period of oscillation of the space-averaged Nusselt number Nu.

A modified version of Control Volume Finite-Element Method (CVFEM) of Saabas and Baliga [1] is adapted to the standard staggered grid for solving the dimensionless equations of continuity, momentum, and energy. The obtained numerical code was successfully validated with many standard test flows. We can quote the flow in a horizontal channel with a built-in square cylinder where results obtained are in good agreement with those reported by Davis et al. [2] as indicated in Table 1. The maximum error committed in the Strouhal numbers is less than 6.5 percent by report to numerical values and less than 9.3 percent in comparison with experimental measurements. We can also quote the Poiseuille-Benard channel flow at Re=10, Pe=20/3, and Ra $=10^4$ (see Table 2). Especially our results are close to that reported by Evans and Paolucci [3] where the errors in the period and in the space- and time-averaged Nusselt number are respectively 4.7 percent and 0.9 percent. These results demonstrate good accuracy and competence of our numerical code.

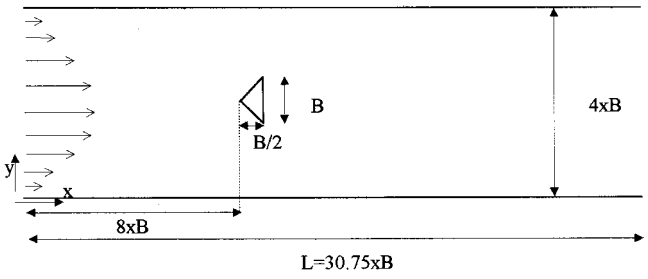

Fig. 1 Flow in a horizontal channel with built-in triangular prism

Contributed by the Heat Transfer Division for publication in the JOURNAL OF HEAT TRANSFER. Manuscript received by the Heat Transfer Division October 18, 1999; revision received November 13, 2000. Associate Editor: C. T. Avedisian.

Table 1 Flow in a horizontal channel with a built-in square cylinder: Variation of Strouhal numbers with Reynolds numbers.

Re	250	500	750
Present	0.188	0.200	0.190
Numerical values of Davis[2]	0.201	0.198	0.183
Experimental values of Davis[2]	-----	0.183	0.178

Table 2 Poiseuille-Benard channel flow at Re=10, Pe=20/3, and Ra=10^4

Reference	Present	Evans[3]	Comini[4]
Period Θ	1.395	1.332	1.273
$<\overline{Nu}>$	2.536	2.558	2.574

After verifying that the implemented numerical code gives accurate results for laminar two dimensional flows, a solution for the flow described in Fig. 1 is next sought. Grid refinement tests have been performed for the case Re=100 using three non uniform grids 72×13, 105×21, and 131×32. Results shows that when we pass from a grid of 105×21 to a grid of 131×32 the space and time-averaged Nusselt number $\langle\overline{Nu}\rangle$ and the Strouhal number St undergoes an increase of only 4.2 percent and 2.8 percent respectively, then, for reasons of calculation coast, the grid of 105×21 is retained.

Solutions are first obtained for Re=30. For this relatively low Reynolds number, the convergence of the numerical procedure is easily obtained. The velocity profiles at different axial locations in the channel are symmetrical about the channel axis. Two symmetrical vortices appear behind the triangular prism on each side of the wake turning in place in opposite sense. The flow is steady state.

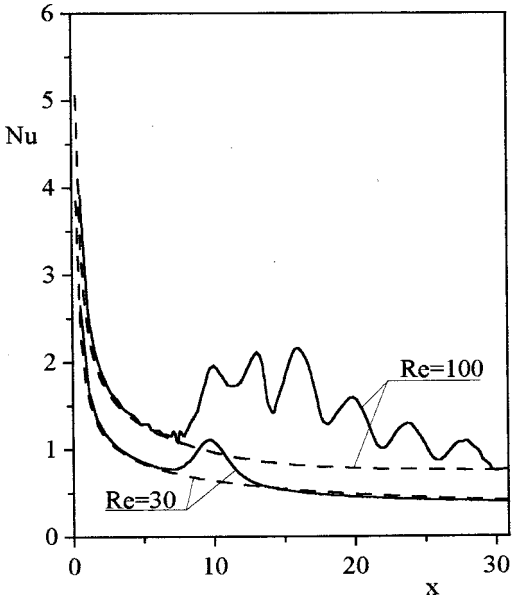

Fig. 2 Local Nusselt number distribution along the lower wall: Solid line: flow with triangular prism; dashed: flow without triangular prism

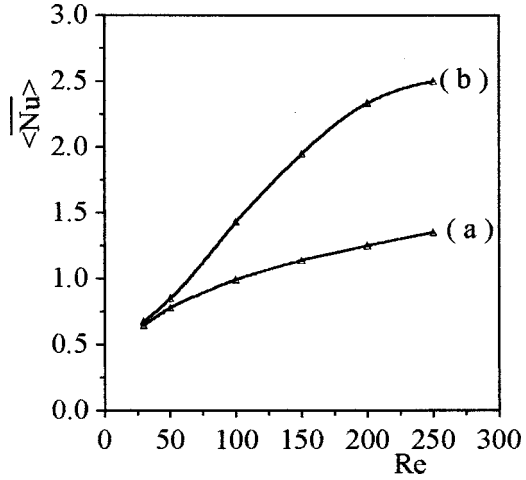

Fig. 3 Variation of the space and time-averaged Nusselt numbers with Reynolds numbers: (a) flow without; and (b) flow with triangular prism

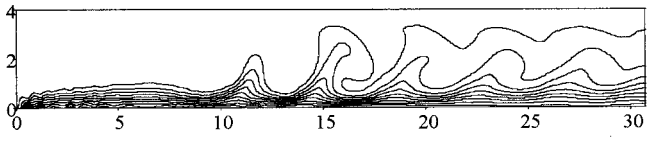

Fig. 4 Isotherms at Re=100 for the flow with triangular prism from 1 (at the bottom wall) to 0 (at the top wall) by interval 0.1

A series of computations were carried out, by increasing slowly the Reynolds number to determine the critical Reynolds number separating the symmetric and periodic flows. At Re=45 the wake loses its original symmetry. Oscillations in the wake grow in magnitude, and it begins to shed vortices into the stream. The flow in the wake becomes periodic. As in references [2,5], the destabilization of the flow happens without any need of imposing external perturbations, the action of small truncation errors and computer's round-off errors were sufficient to initiate vortex shedding. Jackson [6] report a critical Reynolds number of 31 from numerical investigation of flow around a triangular prism of the same geometry as ours but placed in an infinite medium (0 percent blockage). We estimate that this difference in Re_c is due to the presence of an important blockage (25 percent) in our configuration. As mentioned by Sohankar et al. [7], it may be conjectured that the critical Reynolds number characterizing the onset of vortex shedding increases with increasing blockage.

Recently, Fey et al. [8], based on their experiments, propose a new law for the vortex shedding from a circular cylinder which describes the Strouhal-Reynolds number dependency as: $St=a+b/\sqrt{Re}$. They have shown that such a formula seems to fit the data to some extent. In fact, this law, represents the first two terms of a series expansion in 1/root(Re) [$St=a+b/\sqrt{Re}+c/Re+\ldots$]. In the range $47<Re<180$, coefficients are $a=0.2684$ and $b=-1.0356$. For the triangular prism, this law is also in good agreement with numerical results, but coefficients are different and takes the values $a=0.2294$ and $b=-0.4736$. Comparing the coefficients b we deduce that the Strouhal number varies more quickly with Reynolds number for the circular cylinder placed in an infinite media than for triangular prism placed between two parallel plates.

In the following study our attention will be focused on the effect of the presence of the triangular prism on the heat transferred from the hot wall to the flow. Figure 2 is a plot of the local Nusselt number along the hot plate. At Re=30, the presence of triangular prism has just a little local effect by increasing slowly the local Nusselt number. In contrast, at Re=100 the effect of the presence of the triangular prism is more important, the solid line is well disturbed, but appears floating above the dashed line. An immediate conclusion can be made: the periodic flow leads to favor the heat transfer from the hot plate to the near flow, this heat is immediately transported by the Von Karmen street to the medium flow.

Figure 3 summarizes the variation of the space and time-averaged Nusselt numbers with Reynolds numbers. At relatively low Reynolds numbers corresponding to the symmetric and the beginning of periodic flows (Re$\leqslant$50) the presence of the triangular prism has no significant effect in the space and time-averaged Nusselt number $\langle\overline{\mathrm{Nu}}\rangle$. Increasing Reynolds number, curves start to separate, the presence of the triangular prism leads to an important increase of the space and time-averaged Nusselt number compared with that obtained without prism. At Re=250 this augmentation is about 85 percent. Indeed, in presence of the triangular prism, and for the fully periodic flow, the thermal boundary layer is well disturbed by the Von Karman street leading enhance heat transfer from the bottom wall to the flow (Fig. 4).

Conclusion

For the studied configuration shown in Fig. 1, results are summarized as follows: (1) the transition from symmetric flow to periodic flow is observed at Reynolds number in the vicinity of 45; (2) the Strouhal number of the periodic flow behaves as $\mathrm{St}=0.2294-0.4736/\sqrt{\mathrm{Re}}$; and (3) for the symmetric flow (Re$<$45) the presence of the triangular prism has only a local weak effects on the heat transfer and on the flow pattern, while, in periodic flow (Re$\geqslant$45), heat transfer is seen to increase strongly with Reynolds number in presence of the triangular prism. This result can be of interest in engineering.

References

[1] Saabas, H. J., and Baliga, B. R., 1994, ''Co-Located Equal-Order Control-Volume Finite-Element Method for Multidimensional, Incompressible, Fluid Flow Part I: Formulation,'' Numer. Heat Transfer, Part B, **26**, pp. 381–407.

[2] Davis, R. W., Moore, E. F., and Purtell, L. P., 1984, ''A Numerical-Experimental Study of Confined Flow Around Rectangular Cylinders,'' Phys. Fluids, **27**, No. 1, pp. 46–59.

[3] Evans, G., and Paolucci, S., 1990, ''The Thermoconvective Instability of Plane Poiseuille Flow Heated From Below: A Benchmark Solution for Open Boundary Flow,'' Int. J. Numer. Methods Fluids, **11**, pp. 1001–1013.

[4] Comini, G., Manzan, M., and Cortella, G., 1997, ''Open Boundary Conditions for the Streamfunction of Unsteady Laminar Convection,'' Numer. Heat Transfer, Part B, **31**, pp. 217–234.

[5] Persillon, H., and Braza, M., 1998, ''Physical Analysis of the Transition to Turbulence in the Wake of a Circular Cylinder by Three-Dimensional Navier-Stokes Simulation,'' J. Fluid Mech., **365**, pp. 23–88.

[6] Jackson, C. P., 1987, ''A Finite-Element Study of the Onset of Vortex Shedding in Flow Past Variously Shaped Bodies,'' J. Fluid Mech., **182**, pp. 23–45.

[7] Sohankar, A., Norberg, C., and Davidson, L., 1998, ''Low-Reynolds-Number Flow Around a Square Cylinder at Incidence: Study of Blockage, Onset of Vortex Shedding and Outlet Boundary Condition,'' Int. J. Numer. Methods Fluids, **26**, pp. 39–56.

[8] Fey, U., Konig, M., and Eckelmann, H., 1998, ''A new Strouhal-Reynolds-Number Relationship for the Circular Cylinder in the Range $47<\mathrm{Re}<2\times10^5$,'' Phys. Fluids, **10**, No. 7, pp. 1547–1549.

Combined Free and Forced Convection Film Condensation on a Finite-Size Horizontal Wavy Plate

Chi-Chang Wang
Postgraduate Student

Cha'o-Kuang Chen
e-mail: ckchen@mail.ncku.edu.tw
Professor

Department of Mechanical Engineering, National Cheng Kung University, Tainan,
Taiwan 701, Republic of China

Mixed-convection film condensation with downward flowing vapors onto a finite-size horizontal wavy plate is studied by a simple mathematical model and the spline alternating-direction implicit method. Effects of the wavy geometry, the interfacial vapor shear and the pressure gradient on the local condensate film thickness and the heat transfer characteristics have been studied independently. Results show that the pressure gradient tends to increase the heat transfer rate and to decrease the influence of the wavy amplitude. The appropriate wave number which can enhance the maximum condensation heat transfer rate is found in the neighborhood of lunder all circumstances. [DOI: 10.1115/1.1458019]

Keywords: Condensation, Film Cooling, Heat Transfer, Two-Phase, Wavy

Introduction

The problem of laminar film condensation of pure vapor on surfaces of various forms has been studied since Nusselt [1] obtained simple and explicit solutions for varied parameters. Following this, geometries such as plates and tubes have been studied under various conditions by many investigators. The free convection film condensation on the horizontal flat plate has been studied by Leppert and Nimmo [2] and Shigechi et al. [3]. Moreover, Shigechi proposed the following equation:

$$\mathrm{Nu}_m=0.82(\mathrm{Ra/Ja})^{0.2}. \tag{1}$$

In previous studies, the film condensation thickness at the plate edge (a necessary boundary condition) is either arbitrarily assumed or established by means of ''trial and error''. In fact, the above problem can be dealt with the concept of minimum mechanical energy in open-channel flow [4].

The prediction of heat transfer from irregular surface is a topic of fundamental importance. Irregularities frequently occur in the process of manufacture. Moreover, surfaces are sometimes intentionally roughened to enhance heat transfer since the presence of rough surfaces disturbs the flow and alter the heat transfer rate [5,6]. Another method to enhance heat transfer rate is about the velocity of the oncoming vapor. When the vapor surrounding a horizontal plate is moving with velocity, the problem becomes a type of mixed-convection film condensation and the analysis must consider the gravity, interfacial vapor shear force and the pressure gradient force. The objective of this study is to analyze the mixed-convection film condensation on a finite-size horizontal wavy plate, which is based on Nusselt's assumptions, together with

Contributed by the Heat Transfer Division for publication in the JOURNAL OF HEAT TRANSFER. Manuscript received by the Heat Transfer Division January 8, 2001; revision received July 31, 2001. Associate Editor: K. S. Ball.

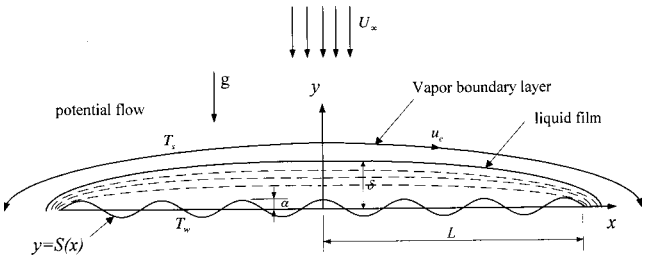

Fig. 1 Physic model and coordinate system

adopting the vapor shear model of Shekriladze and Gomelauri. Moreover, the film thickness at the plate edge will be determined by the concept of minimum mechanical energy.

Mathematical Formulation

The physical model and the coordinate system used are shown in Fig. 1. A wavy horizontal plate described by $S(x)=\alpha\cos(n\pi x/L)$ is immersed in downward flowing pure vapor which is at its saturation temperature T_s and moves at uniform velocity U_∞. This horizontal wavy plate is cooled internally thus the wall temperature T_w is uniform and lower than the vapor saturation temperature T_s. Therefore, a continuous condensate film will occur on the wall and run outward from the plate center to the plate edge under the combined effect of gravity, pressure gradient force, and interfacial vapor shear force. Based on these assumptions of Nusselt [1], the mass equation, momentum equations and the energy balance equation for the liquid laminar flow are described by the following equations:

$$\dot{m}=\int_{S(x)}^{\delta(x)}\rho u\,dy \tag{2}$$

$$0=-\frac{\partial p}{\partial x}+\mu\frac{\partial^2 u}{\partial y^2} \tag{3}$$

$$0=-\frac{\partial p}{\partial y}-\rho g \tag{4}$$

$$h'_{fg}\dot{m}'=k\left.\frac{\partial T}{\partial y}\right|_{y=S}\approx k\frac{T_s-T_w}{\delta-S}=k\frac{\Delta T}{\delta-S} \tag{5}$$

with the boundary and interface conditions

$$\text{(a)}\quad \text{at the wavy-wall (i.e., } y=S):u=0 \tag{6}$$

$$\text{(b)}\quad \text{at the interface (i.e., } y=\delta):\mu\frac{\partial u}{\partial y}\approx\dot{m}'u_e, \tag{7}$$

where $h'_{fg}=h_{fg}+3Cp\Delta T/8$ is the modified latent heat of condensate proposed by Rohsenow [7] to account for the effects of heat convection in the film. And at the liquid-vapor interface, the shear stress is equal to the loss of momentum flux of condensing vapor which is similar to that of Shekriladze and Gomelauri's [8].

Solve u in Eq. (3) and use Eqs. (4), (6) and (7), the following equation can be obtained:

$$u=\frac{1}{\mu}(\rho g\,\delta'-\rho_v u_e u'_e)\left(\frac{y^2+S^2}{2}-y\,\delta+\delta S\right)+\frac{\dot{m}'}{\mu}u_e(y-S), \tag{8}$$

where u_e is the tangential vapor velocity at the edge of the boundary layer. It can be obtained by potential flow theory.

Substitute Eqs. (2) and (8) into Eq. (5) and use the following dimensionless variables

Table 1 A comparison of δ and $\mathrm{Re}^{-1/2}\,\mathrm{Nu}_m$ for different grid numbers ($F=20$, $P=1$, $\alpha=0.05$, $n=5.5$)

Grid number	δ		$\mathrm{Re}^{-1/2}Nu_m$	
	x=0	x=1	x=0	x=4
100	0.696986	0.003280	1.545628	1.738114
300	0.684907	0.003291	1.575033	1.789175
500	0.684962	0.003324	1.574898	1.787904
300*	0.685141	0.003266	1.574454	1.765389

*:Uniform grid

$$\bar{x}=\frac{x}{L},\quad \bar{\delta}=\frac{\delta}{L}\sqrt{\mathrm{Re}},\quad \bar{\alpha}=\frac{\alpha}{L}\sqrt{\mathrm{Re}},\quad \bar{u}_e=\frac{u_e}{U_\infty},\quad \mathrm{Ja}=\frac{C_p\Delta T}{h'_{fg}}$$
$$\mathrm{Ra}=\frac{\rho^2 g\,\mathrm{Pr}\,L^3}{\mu},\quad \mathrm{Re}=\frac{\rho U_\infty L}{\mu},\quad \mathrm{Pr}=\frac{\mu C_p}{k},\quad F=\frac{\mathrm{Ra}}{\mathrm{Ja}\,\mathrm{Re}^{5/2}}, \tag{9}$$
$$P=\frac{\mathrm{Pr}}{\mathrm{Ja}}\frac{\rho_v}{\rho}.$$

The dimensionless governing equation may then become

$$(\bar{\delta}-\bar{S})\frac{d}{d\bar{x}}\left\{(F\bar{\delta}'-P\bar{u}_e\bar{u}'_e)\frac{(\bar{S}-\bar{\delta})^3}{3}+\bar{u}_e\frac{\bar{\delta}-\bar{S}}{2}\right\}=1 \tag{10}$$

with the following boundary conditions:

$$\text{(a)}\quad \text{at } \bar{x}=0:\frac{d\bar{\delta}}{d\bar{x}}=0 \tag{11}$$

$$\text{(b)}\quad \text{at } \bar{x}=1:3456\dot{\bar{m}}^3+180\dot{\bar{m}}^2\bar{u}_e-\left(2240\frac{\mathrm{Pr}}{\mathrm{Ja}}F\dot{\bar{m}}(\bar{\delta}-\bar{S})+\bar{u}_e^3\right)=0, \tag{12}$$

where

$$\dot{\bar{m}}=\frac{\bar{u}_e}{2}+\frac{1}{3}(P\bar{u}_e\bar{u}'_e-F\bar{\delta}')(\bar{\delta}-\bar{S})^2. \tag{13}$$

In Eq. (12), the film thickness at the plate edge is established by the application of minimum mechanical energy principle, i.e.,

$$\left[\frac{\partial}{\partial\delta}\int_S^\delta\left(\frac{u^2}{2}+gy+\frac{p}{\rho}\right)\rho u\,dy\right]\Bigg|_{\dot{m}_c}=0. \tag{14}$$

The mean Nusselt number is defined as

$$\mathrm{Nu}_m=\frac{h_m L}{k}\frac{\sigma(x)}{x}=\frac{\sqrt{\mathrm{Re}}}{\bar{x}}\int_0^{\bar{x}}\frac{1}{\bar{\delta}-\bar{S}}d\bar{x}, \tag{15}$$

where

$$h_m=\frac{-k}{\sigma(T_w-T_\infty)}\int_0^\sigma\sqrt{(\partial T/\partial x)^2+(\partial T/\partial y)^2}\,d\sigma \tag{16}$$

$$\sigma=\int_0^x(1+S'^2)^{1/2}dx. \tag{17}$$

Table 2 A comparison of mean Nusselt numbers, Nu_m, for natural film condensation on a horizontal flat plate ($F=20$, $P=1$, $\alpha=0.05$, $n=5.5$, grid number=300)

Ra/Ja	Present method			Shigechi(1990)
	Pr/Ja=1	Pr/Ja=10	Pr/Ja=100	
1×10^2	1.86924	2.03384	2.05738	2.0597
1×10^4	4.69501	5.10805	5.16716	5.1739
1×10^6	11.79302	12.83157	12.98005	12.996
1×10^8	29.62201	32.23073	32.60368	32.644

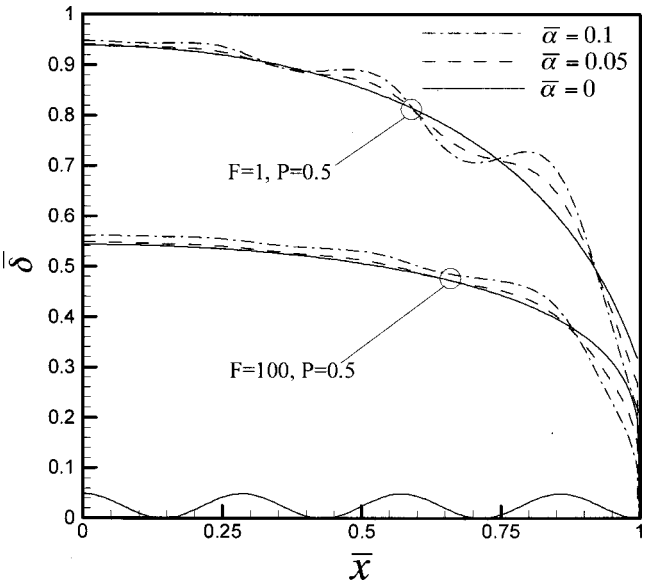

Fig. 2 Normalized film thickness along wavy plates for $P = 0.5$, $n = 7$, and Pr/Ja=50

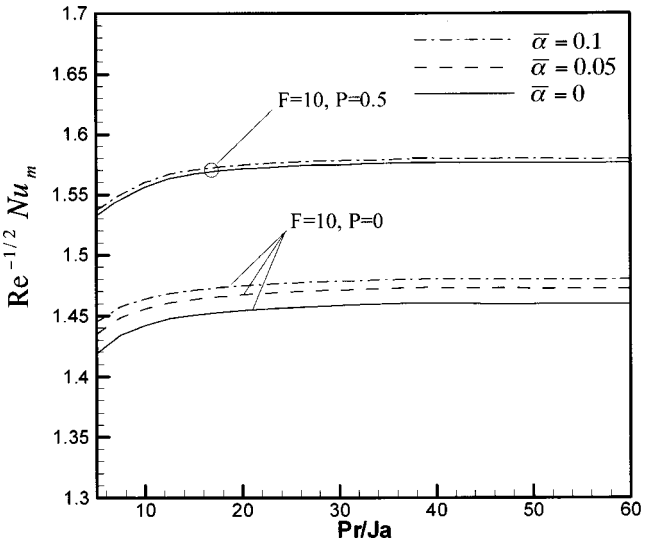

Fig. 4 A comparison of mean Nusselt numbers for a flat plate and wavy plates ($F = 10$, $n = 7$)

It should be noted that the mean Nusselt number is obtained by averaging the heat transfer flux over the surface from the plate center to $\sigma(x)$.

Results and Discussion

Equation (22) is solved numerically by using the cubic spline approximation [9]. This method can evaluate the spatial derivative terms directly without any finite difference discretization and the requirement of a uniform mesh is not necessary. As shown in Table 1, the test of grid independence, which shows that the difference between results of grids of 300 and 500 is less than 0.1 percent in both condensate film thickness and mean Nusselt number. Therefore, the nonuniform grid of 300 with smaller spacing mesh near the plate edge is employed in this study. To verify the accuracy of the present method, comparing with Shigechi [3] has also been shown in Table 2 and finds to agree favorably.

Figure 2 shows the variation of the film thickness along the wavy plate, the film thickness at the middle plate increases with the dimensionless wavy amplitude. Next, the dimensionless film thickness of the wavy plate tends to decrease rapidly near the plate edge as the fluid moves downstream, which is different from the behavior of the flat plate. It is also found that the amplitude of the dimensionless film thickness tends to increase with the axial coordinate $\overline{x}$ and the wavy amplitude.

Figure 3 shows the variation of $\mathrm{Re}^{-1/2}\,\mathrm{Nu}_m$ with $\overline{x}$. As the axial coordinate increases or the dimensionless wavy amplitude decreases, the amplitude of the mean Nusselt number will decrease. Therefore, we can observe that the variation of the mean Nusselt number only occurs near the plate center when larger wavy amplitudes are used. Also, a lower F results in a lower $\mathrm{Re}^{-1/2}\,\mathrm{Nu}_m$ for all wavy surfaces.

Figure 4 shows the variation of the mean Nusselt number with Pr/Ja. The parameter Pr/Ja is only found in Eq. (12) that can determine the film thickness $\overline{\delta}_{\min}$ at the plate edge. In cases of the

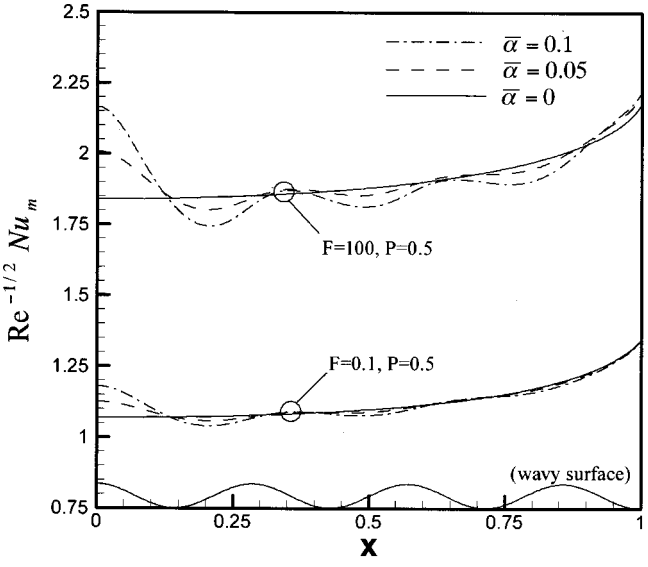

Fig. 3 Distribution of mean Nusselt number for $P = 0.5$, $n = 7$, and Pr/Ja=50

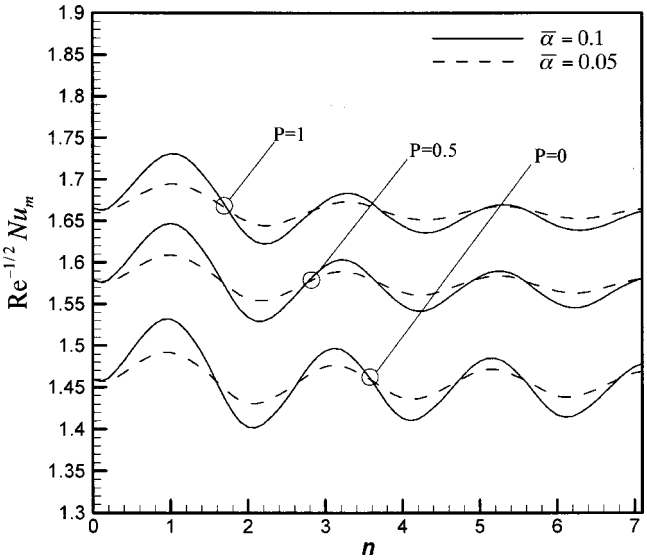

Fig. 5 Dependence of mean Nusselt number on wave number for $F = 10$ and Pr/Ja=100

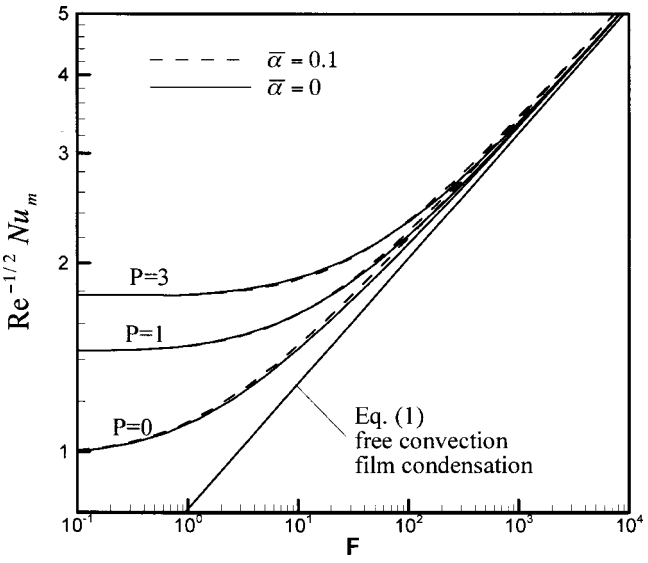

Fig. 6 Dependence of mean Nusselt number on *F* for combined forced and natural convection condensation (*n*=7, Pr/Ja =100)

flat surface and the wavy surface, both mean Nusselt numbers increase with parameter Pr/Ja and approach constant values. Moreover, the mean Nusselt number of wavy surface is higher than that of the flat plate, especially if the pressure gradient parameter is small.

Figure 5 show the dependence of the mean Nusselt number on the wave number. It is found that, for increasing the wave number the mean Nusselt numbers of the wavy surface show the sinusoidal curves, whose amplitudes decrease with the pressure gradient and increase with the wave amplitude. Peaks of the mean Nusselt number curres will occur under the wave number approaches to be odd (i.e., 1,3,5 . . .). As the wave number is quite large (i.e., the case of a rough surface), the mean Nusselt number tends to be a constant value, which equals that of the flat plate (i.e., $n=0$). This outcome is due to that although the wavy surface has a larger heat transfer area, the thermal resistance will also increase for the condensate accumulates between the trough and crest.

Figure 6 shows the dependence of the mean Nusselt number on *F*. It is seen that as *F* is greater than 100, all solutions in Eq. (10) tend to blend with the free convection (quiescent vapor) film condensation solution. For the other extreme, when *F* decreases to be zero (e.g., vapor velocity increases and the effect of gravity decreases), the mean heat transfer will change from the free-convection region into the forced-convection region through a transition zone. Moreover, increasing the pressure gradient makes the mean heat transfer coefficient increase, especially in the forced-condensation region.

Conclusions Remarks

1. The harmonic curves of the film thickness and mean Nusselt numbers have the same frequency as that of the wavy surface.
2. A larger pressure gradient will increase the total heat transfer rate but decrease the influence of wavy amplitude.
3. The maximum enhancement in heat transfer rate is found as only one wavy surface exists in the plate. It is due to that the special case has the smallest thermal resistance and the best angle to accelerate the flow outward at the plate edge.

Nomenclature

C_p = specific heat of the fluid at constant pressure
F = dimensionless parameter
g = acceleration of gravity
h_{fg} = latent heat of condensate
Ja = Jacob number
k = thermal conductivity of condensate
L = plate half length
$\dot{m}$ = condensate mass flow rate
n = wavy number
Nu_x, Nu_m = local and mean Nusselt number
p = pressure
P = dimensionless pressure gradient parameter
Pr = Prandtl number
Ra = Rayleigh number
Re = generalized Reynolds number
u_e = vapor velocity at the edge of the boundary layer
T = temperature
u,v = velocity components

Greek Symbols

α = amplitude of wavy surface
δ = condensate film thickness
μ = dynamic viscosity
ρ, ρ_v = density of condensate and vapor, respectively

Superscripts

$\bar{}$ = dimensionless variables
$'$ = derivative with respect to x, i.e., d/dx

References

[1] Nusselt, W., 1916, "Oberflachen Condensation Des Wasserdampfes," Zeitschrift des Vereines Deutscher Ininuere, **60**, pp. 541–569.
[2] Leppert, G., and Nimmo, B., 1968, "Laminar Film Condensation on Surfaces Normal to Body of Inertial Forces," ASME J. Heat Transfer, **80**, pp. 178–179.
[3] Shigechi, T., Kawa, N., Tokita, Y., and Yamada, T., 1990, "Film Condensation Heat Transfer on a Finite-Size Horizontal Plate Facing Upward," Trans. Jpn. Soc. Mech. Eng., Ser. B, **56**, pp. 205–210.
[4] Yang, S. A., and Chen, C. K., 1992, "Laminar Film Condensation on a Finite-Size Horizontal Plate with Suction at the Wall," Appl. Math. Model., **16**, pp. 325–329.
[5] Webb, R. L., Rudy, T. M., and Kedzierski, M. A., 1985, "Prediction of the Condensation Coefficient on Horizontal Integral-Fin Tubes," ASME J. Heat Transfer, **107**, pp. 369–376.
[6] Honda, H., Takamatsu, H., and Takata, N., 1999, "Experimental Measurements for Condensation of Downward-Flowing R123/R134a in a Staggered Bundle of Horizontal Low-Finned Tubes with Four Fin Geometries," Int. J. Refrig., **22**, 615–624.
[7] Rohsenow, W. M., 1956, "Heat Transfer and Temperature Distribution in Laminar Film Condensation on a Horizontal Tube," Int. J. Heat Mass Transf., **27**, pp. 39–47.
[8] Shekriladze, I. G., and Gomelauri, V. I., 1966, "The Theoretical Study of Laminar Film Condensation of a Flowing Vapor," Int. J. Heat Mass Transf., **9**, pp. 581–591.
[9] Rubin, S. G., and Graves, R. A., 1975, "Viscous Flow Solution with a Cubic Spline Approximation," Comput. Fluids, **1**, No. 5, pp. 1–36.

Enclosed Buoyant Convection With Internal Heat Generation Under Oscillating Sidewall Temperature

Gi Bin Kim

Jae Min Hyun
e-mail: jmhyun@cais.kaist.ac.kr

Department of Mechanical Engineering,
Korea Advanced Institute of Science & Technology,
373-1 Kusong-dong, Yusong-gu,
Taejon 305-701, South Korea

Ho Sang Kwak
School of Mechanical Engineering,
Kumoh National University of Technology,
188 Shinpyung-dong, Kumi,
Kyongbuk 730-701, South Korea

Keywords: Unsteady Buoyant Convection, Internal Heat Generation, Resonance

1 Introduction

Buoyant convection in an enclosure induced by uniform internal heat generation has been extensively studied (Acharya and Goldstein [1], Bergholz [3], Fusegi et al. [4], Kulacki and Goldstein [6], May [10]). One canonical layout is a rectangular cavity with two vertical sidewalls at constant temperatures and two insulated horizontal endwalls, with large Rayleigh number Ra ($>10^5$), Prandtl number O(1) and cavity aspect ratio O(1). In particular, when both vertical sidewalls are maintained at the same temperature T_0, the overall flow is expectedly symmetric about the vertical centerline. In each half-cavity, the fluid rises (sinks) near the centerline (near the vertical sidewall) region, which forms a single circulation cell.

Recently, buoyant flows induced by time-periodic boundary conditions, with no internal heat generation, emerge to be a subject of considerable interest (Antohe and Lage [2], Kwak and Hyun [7], Kwak et al. [8], Lage and Bejan [9]). The overriding concern here is the existence of resonance, which was first observed in the numerical studies of Lage and Bejan [9] and was corroborated later by Antohe and Lage [2]. It was illustrated that, when the frequency of the time-periodic boundary condition matches the proper resonance frequency, convective activities in the cavity are invigorated. This gives rise to a substantial increase in the amplitude of the fluctuating heat transfer coefficient in the cavity interior. The analytical endeavor of Lage and Bejan [9], based on the concept of a fluid wheel inside the cavity, suggested ways to make an order-of-magnitude estimate of the resonance frequency. In a related effort, Kwak and Hyun [7] and Kwak et al. [8] asserted that resonance is anticipated when the basic mode of the system eigenfrequencies is excited. They further argued that the system eigenfrequencies are characterized by the internal gravity oscillations in the interior, which are supported by the prevailing stratification.

This paper describes the time-dependent buoyant convection in an enclosure, with the presence of internal heat generation, under a time-periodic thermal boundary condition. Estimations of the resonance frequencies will be made, and physical explanations will be offered. This configuration simulates simplified models of post-accident heat removal in nuclear reactors and geophysical problems. Also, natural convection is important in fluids undergoing electrolytic processes or exothermic chemical reactions. As emphasized earlier, utilization of time-periodic thermal boundary conditions is explored as a possible means to control these processes or reactions. Convection in an air-conditioned room, subject to the daily-varying environmental temperature, provides an easy example of technological applications of the flow configuration under present study.

2 Formulation

Consider a square cavity, filled with an incompressible Newtonian fluid with spatially-uniform internal heat generation of constant strength q_0''', as sketched in Fig. 1. The left vertical sidewall is maintained at constant temperature T_0. The temperature T_r at the right vertical sidewall varies about T_0 sinusoidally with time, $T_r = T_0 + \Delta T' \sin(ft)$, in which $\Delta T'$ and f denote, respectively, the amplitude and frequency of oscillation.

Flow is governed by the time-dependent Navier-Stokes equations, with the invocation of the Boussinesq-fluid relationship $\rho = \rho_0[1-\beta(T-T_0)]$, which, after non-dimensionalization, read

$$\frac{\partial U}{\partial X} + \frac{\partial V}{\partial Y} = 0, \tag{1}$$

$$\frac{\partial U}{\partial t} + U\frac{\partial U}{\partial X} + V\frac{\partial U}{\partial Y} = -\frac{\partial P}{\partial X} + \left(\frac{\mathrm{Pr}}{\mathrm{Ra}_I}\right)^{1/2}\left(\frac{\partial^2 U}{\partial X^2} + \frac{\partial^2 U}{\partial Y^2}\right), \tag{2}$$

$$\frac{\partial V}{\partial t} + U\frac{\partial V}{\partial X} + V\frac{\partial V}{\partial Y} = -\frac{\partial P}{\partial Y} + \left(\frac{\mathrm{Pr}}{\mathrm{Ra}_I}\right)^{1/2}\left(\frac{\partial^2 V}{\partial X^2} + \frac{\partial^2 V}{\partial Y^2}\right) + \theta, \tag{3}$$

$$\frac{\partial \theta}{\partial t} + U\frac{\partial \theta}{\partial X} + V\frac{\partial \theta}{\partial Y} = \left(\frac{1}{\mathrm{Ra}_I\mathrm{Pr}}\right)^{1/2}\left(\frac{\partial^2 \theta}{\partial X^2} + \frac{\partial^2 \theta}{\partial Y^2}\right) + \left(\frac{1}{\mathrm{Ra}_I\mathrm{Pr}}\right)^{1/2}. \tag{4}$$

The associated boundary conditions can be expressed as

$$U = V = \frac{\partial \theta}{\partial Y} = 0, \quad \text{at } Y = 0,1; \tag{5}$$

$$U = V = \theta = 0, \quad \text{at } X = 0; \tag{6}$$

$$U = V = 0, \quad \theta = \varepsilon \sin(\omega\tau), \quad \text{at } X = 1. \tag{7}$$

In the above, dimensionless quantities are defined as

$$\tau = t(\mathrm{Ra}_I\mathrm{Pr})^{1/2}\frac{\kappa}{H^2}; \quad (X,Y) = \frac{(x,y)}{H};$$

$$(U,V) = (u,v)(\mathrm{Ra}_I\mathrm{Pr})^{-1/2}\frac{H}{\kappa};$$

$$\theta = \frac{k(T-T_0)}{H^2 q_0'''}; \quad P = \frac{(p+\rho_0 g y)H^2}{\rho_0 \kappa^2 \mathrm{Ra}_I\mathrm{Pr}}; \quad \mathrm{Pr} = \nu/\kappa; \tag{8}$$

$$\mathrm{Ra}_I = \frac{g\beta q_0''' H^5}{\kappa\nu k},$$

where (u,v) indicate dimensional velocity components in the horizontal (x) and vertical (y) directions, and ρ_0 the reference density evaluated at the cold-wall temperature (T_0), and ν and κ denote the kinematic viscosity and thermal diffusivity, respectively, and β the isobaric coefficient of volumetric thermal expansion. The strength of internal heat generation is represented by the internal Rayleigh number, Ra_I. All fluid properties are assumed to be constant.

Contributed by the Heat Transfer Division for publication in the JOURNAL OF HEAT TRANSFER. Manuscript received by the Heat Transfer Division April 3, 2001; revision received September 6, 2001. Associate Editor: M. Faghri.

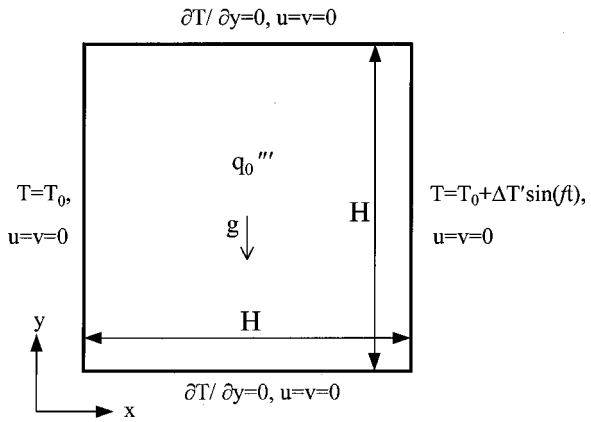

Fig. 1 Flow configuration

Time is nondimensionalized by using the system Brunt-Väisäla frequency N, i.e.,

$$N \equiv \left[\frac{g\beta(q_0'''H^2/k)}{H}\right]^{1/2} = (\mathrm{Ra}_I \mathrm{Pr})^{1/2}\frac{\kappa}{H^2}. \tag{9}$$

The nondimensional amplitude and frequency of the right-sidewall temperature fluctuation are

$$\varepsilon \equiv \frac{k\Delta T'}{q_0'''H^2}; \quad \omega \equiv \frac{f}{N}. \tag{10a,b}$$

In the above development, the system-wide temperature scale is derived from the internal heat generation, i.e., $q_0'''H^2/k$, and this scale is employed consistently, e.g., in Eqs. (8), (9), and (10*a*).

Numerical solutions are acquired by using the well-documented finite-volume computational procedure (e.g., Hayase et al. [5], Patankar [12]).

3 Results and Discussion

For all the computations, the Prandtl number was set Pr=7.0 to simulate water.

In the computations, the value of ε was set $\varepsilon/\theta_m = 0.3$. This choice of ε was based on the considerations explained below. First, ε should be small enough not to seriously distort the prevailing steady-state flow. In a series of detailed calculations, Kwak et al. [8] demonstrated that, when ε is small, i.e., $\varepsilon \leqslant 0.5$, the amplitude of fluctuating Nusselt number in the interior is approximately proportional to ε. Secondly, the presence of multiple resonance was observed by Antohe and Lage [2] when the nondimensional amplitude of wall heat flux oscillation was larger than 0.1. The value of $\varepsilon/\theta_m = 0.3$ was selected to meet the aforementioned two dynamical issues. The nondimensional frequency of oscillation ω encompasses a wide range, $0.005 \leqslant \omega \leqslant \mathrm{O}(1)$.

In the analysis of the computed results, it is advantageous to introduce the following notations, i.e.,

$$\mathrm{Nu}_X^*(\tau) \equiv \frac{\mathrm{Nu}_X(\tau) - \mathrm{Nu}_X^B}{\mathrm{Nu}_{X=1}^B}, \tag{11a}$$

$$A(\mathrm{Nu}_X^*) \equiv \frac{\mathrm{Max}\{\mathrm{Nu}_X^*(\tau)\} - \mathrm{Min}\{\mathrm{Nu}_X^*(\tau)\}}{2}, \quad \tau_0 \leqslant \tau \leqslant \tau_0 + \frac{2\pi}{\omega}. \tag{11b}$$

In the above, $\mathrm{Nu}_X^*(\tau)$ indicates the difference between the instantaneous Nu value (at $X=X$ and $\tau=\tau$) and the corresponding value Nu_X^B of the case of non-oscillating sidewall temperature ($\varepsilon=0$). The amplitude of Nu-value fluctuations is expressed by $A(\mathrm{Nu}_X^*)$.

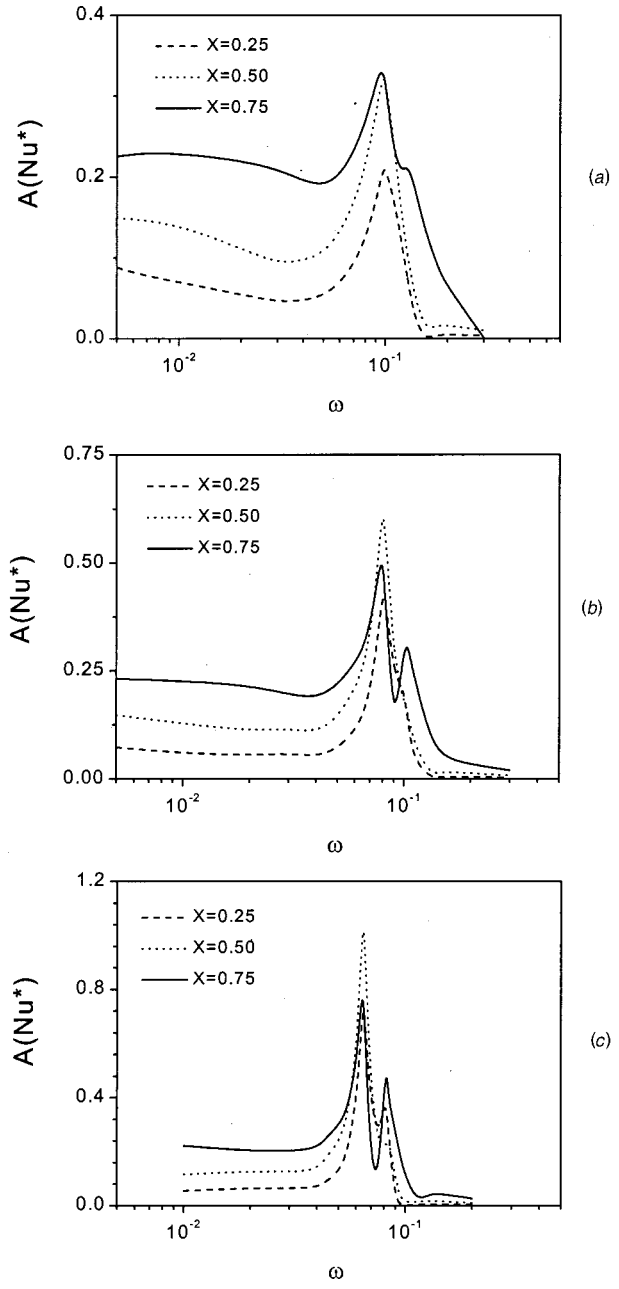

Fig. 2 *A*(Nu*) versus ω plots: (*a*) $\mathrm{Ra}_I = 10^8$; (*b*) $\mathrm{Ra}_I = 10^9$; and (*c*) $\mathrm{Ra}_I = 10^{10}$.

As stressed by Lage and Bejan [9], the amplitude of Nu-fluctuation, $A(\mathrm{Nu}^*)$, at the centerline ($X=0.5$) is of particular interest. This is representative of the intensity of time-dependent heat transfer activities in the interior core. Figure 2 displays the collection of numerical data of $A(\mathrm{Nu}_X^*)$ in the interior region versus ω for varying Ra_I. It is clear that the amplitude of Nu-fluctuation, $A(\mathrm{Nu}_X^*)$, peaks at certain particular frequencies; this was interpreted to manifest the existence of resonance in the context of enclosed buoyant convection (Lage and Bejan [9]). Frames (*a*), (*b*), and (*c*) of Fig. 2 show that the frequency at which the primary peak occurs, ω_{r1}, is largely unaffected by Ra_I. Furthermore, the secondary peak at ω_{r2} is visible for very high values of Ra_I, i.e., $\mathrm{Ra}_I \geqslant 10^9$.

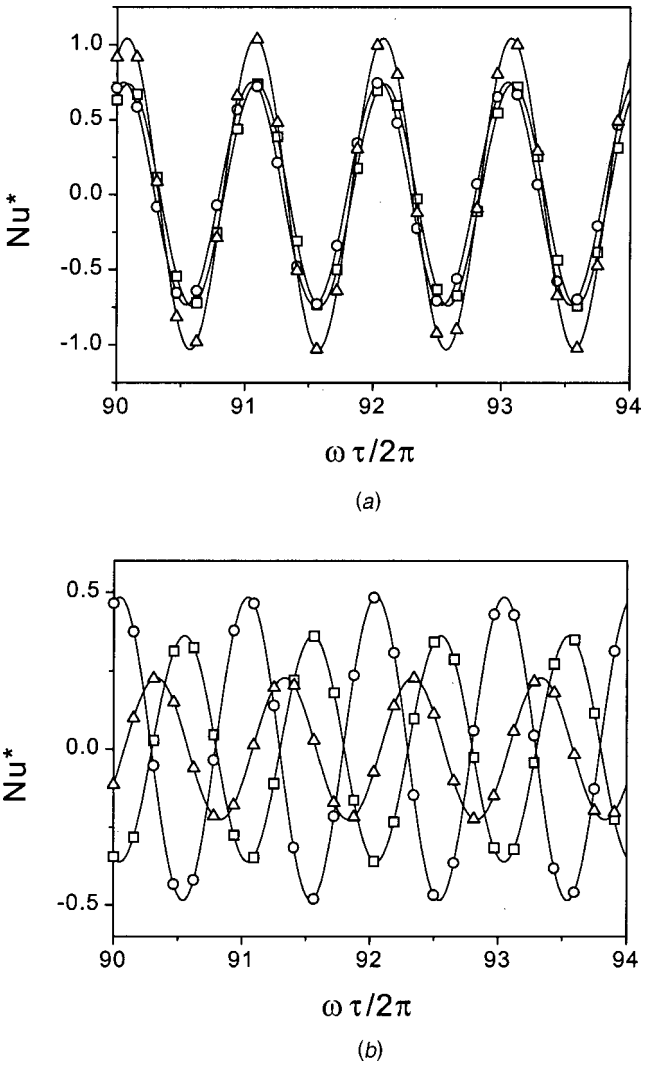

Fig. 3 Time history of Nu* at resonance frequencies. $Ra_I = 10^{10}$. Symbols □, △, and ○ denote the positions, $X = 0.25$, 0.5, and 0.75, respectively: (*a*) $\omega = 0.065(\approx \omega_{r1})$; and (*b*) $\omega = 0.082(\approx \omega_{r2})$.

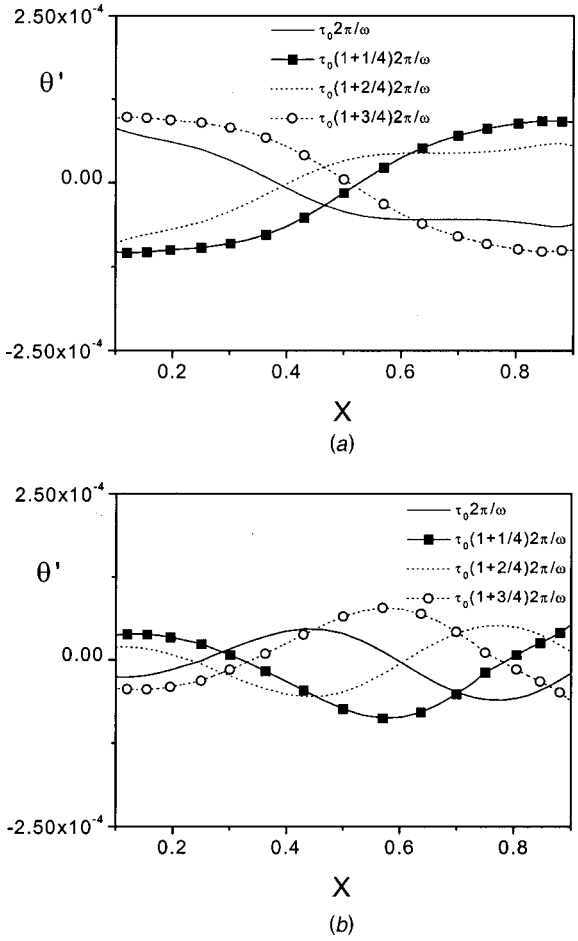

Fig. 4 Temperature fluctuations relative to the basic state. $Y = 0.5$, $Ra_I = 10^{10}$: (*a*) $\omega = 0.065(\approx \omega_{r1})$; and (*b*) $\omega = 0.082(\approx \omega_{r2})$.

The prior expositions by Kwak et al. [7–8] ascertained that resonance is anticipated when the eigenfrequencies of the system are excited. Furthermore, these intrinsic eigenfrequencies are characterized by the internal gravity oscillations in the stably stratified interior core. Paolucci and Chenoweth [11] calculated the modes of these oscillations, which, for a square cavity, can be expressed, in the present nondimensional form, as

$$\omega_n \equiv \frac{f_n}{N} = \frac{(\partial\theta/\partial Y)^{1/2}}{(1+1/n^2)^{1/2}}. \tag{12}$$

In the above, $\partial\theta/\partial Y$ denotes the average strength of stratification in the interior. In the practical calculation of $\partial\theta/\partial Y$, a linear curve-fitting was applied to the interior vertical temperature profile at a given location X. Here, n is the mode index, which is the ratio of the wave numbers in the horizontal and vertical directions. The primary mode is identified to be $n=1$, i.e., the scale of the whole cavity. The theoretical values of ω_1 obtainable from Eq. (12) are 0.098, 0.079, and 0.062 for $Ra_I = 10^8$, 10^9, and 10^{10}, respectively. The computed primary resonance frequencies ω_{r1}, as illustrated in Fig. 2, are respectively 0.098, 0.080, and 0.065, which are in close agreement with the results of Eq. (12). This comparison gives credence to the assertion that the resonance frequencies are determined by the modes of internal gravity oscillations. The secondary peak in Fig. 2 is identified to be the consequence of the excitation of ω_2 mode of Eq. (12). In this case, fluid motions based on $n=2$, which have the size of half-cavity, are under focus. Again, ω_2, calculated by Eq. (12), are 0.124, 0.100, and 0.078, while the present computed data for ω_{r2} are 0.123, 0.103, and 0.082, respectively, for $Ra_I = 10^8$, 10^9 and 10^{10}. As before, this favorable agreement reinforces the finding that the modes of internal gravity oscillations are the principal eigenfrequencies of the system.

The time histories of Nu_X^* are revealing. For the primary resonance mode ($\omega \cong \omega_{r1}$), as demonstrated in Fig. 3(*a*), convective fluid motions are intensified throughout the entire interior region of the cavity. Because of the dominant convective activities, the amplitudes of Nu-oscillation are substantial. The invigorated convective flows are propagated to the bulk of the interior from the sidewall of oscillating temperature; much of Nu in the cavity interior core does not show appreciable phase lags. When the sidewall temperature oscillates at the secondary resonance frequency ($\omega \cong \omega_{r2}$), as depicted in Fig. 3(*b*), considerable phase lags are discernible in the interior. The phase lag is π radian between $X = 0.25$ and $X = 0.75$. This implies that the convective motions at ω_{r2} take place with opposite phases between these two locations.

At higher values of ω, the effect of sidewall temperature oscillation is confined to the region close to the wall, and the influence of sidewall temperature oscillation is meager at far-away locations. As a result, the amplitude of Nu_X^* oscillation at $X=0.75$ is larger than at other locations.

The behavior of temperature fluctuation in the interior at resonance is plotted in Fig. 4. The horizontal profiles of interior temperature oscillation at mid-height ($Y=0.5$) clearly exhibit [see Fig. 4(a)] the periodic tilting with ω_{r1}, which points to the source of internal gravity oscillations. This pattern is qualitatively similar to the observations of Kwak and Hyun [7] for a differentially-heated cavity with $q_0'''=0$. The spatial behavior of thermal field fluctuations at the secondary resonance frequency (ω_{r2}) is slightly more complex. A closer inspection of Fig. 4(b) discloses that there exist two branches of tilting, with a phase difference of approximately π radian, in the left and right regions of the cavity. This points to the fact that the gradients of fluctuating temperature in both regions have opposite signs at each time instant.

4 Concluding Remarks

The primary-peak resonance at ω_{r1} is distinct. The secondary-peak resonance at ω_{r2} is detected for higher Ra_I. The instantaneous Nusselt number fluctuation at ω_{r1} indicates the presence of cavity—scale motions, which are qualitatively similar to those of a differentially—heated cavity. For the secondary resonance frequency ω_{r2}, the tilting of the interior isotherms is of a concave/convex shape. The theoretical predictions of the resonance frequencies, based on the modes of internal gravity oscillations, are in accord with the present numerical data.

Acknowledgment

This work was supported by the grants from NRL, South Korea.

References

[1] Acharya, S., and Goldstein, R. G., 1985, "Natural Convection in An Externally Heated Vertical or Inclined Square Box Containing Internal Energy Sources," ASME J. Heat Transfer, **107**, pp. 855–866.

[2] Antohe, B. V., and Lage, J. L., 1996, "Amplitude Effect on Convection Induced by Time-Periodic Horizontal Heating," Int. J. Heat Mass Transf., **39**, No. 6, pp. 1121–1133.

[3] Bergholz, R. F., 1980, "Natural Convection of a Heat Generating Fluid in a Closed Cavity," ASME J. Heat Transfer, **102**, pp. 242–247.

[4] Fusegi, T., Hyun, J. M., and Kuwahara, K., 1992, "Natural Convection in a Differentially Heated Square Cavity With Internal Heat Generation," Numer. Heat Transfer, **21**, pp. 215–229.

[5] Hayase, T., Humphery, J. A. C., and Grief, R., 1992, "A Consistently Formulated QUICK Scheme for Fast and Stable Convergence Using Finite-Volume Iterative Calculation Procedures," J. Comput. Phys., **98**, pp. 108–118.

[6] Kulacki, F. A., and Goldstein, R. J., 1972, "Thermal Convection in a Horizontal Fluid Layer With Uniform Volumetric Energy Sources," J. Fluid Mech., **55**, pp. 271–287.

[7] Kwak, H. S., and Hyun, J. M., 1996, "Natural Convection in an Enclosure Having a Vertical Sidewall With Time-Varying Temperature," J. Fluid Mech., **329**, pp. 65–88.

[8] Kwak, H. S., Kuwahara, K., and Hyun, J. M., 1998, "Resonant Enhancement of Natural Convection Heat Transfer in a Square Enclosure," Int. J. Heat Mass Transf., **41**, pp. 2837–2846.

[9] Lage, J. L., and Bejan, A., 1993, "The Resonance of Natural Convection in an Enclosure Heated Periodically From the Side," Int. J. Heat Mass Transf., **36**, pp. 2027–2038.

[10] May, H. O., 1991, "A Numerical Study on Natural Convection in an Inclined Square Enclosure Containing Internal Heat Sources," Int. J. Heat Mass Transf., **34**, No. 4, pp. 919–928.

[11] Paolucci, S., and Chenoweth, D. R., 1989, "Transition to Chaos in a Differentially Heated Vertical Cavity," J. Fluid Mech., **210**, pp. 379–410.

[12] Patankar, S. V., 1980, *Numerical Heat Transfer and Fluid Flow*, McGraw-Hill.

A Method to Accelerate Convergence and to Preserve Radiative Energy Balance in Solving the P_1 Equation by Iterative Methods

Genong Li and Michael F. Modest

Department of Mechanical Engineering, The Pennsylvania State University, University Park, PA 16802

An acceleration method is proposed particularly for the P_1 equation. The radiative energy balance is used as a constraint to correct iterative solutions. The method not only accelerates convergence but also preserves the radiative energy balance, the latter being of great importance when radiation calculations are coupled with flow calculations. This acceleration method can be applied to other elliptical problems with boundary conditions of the second and/or the third kind. [DOI: 10.1115/1.1423318]

Keywords: Computational, Numerical Methods, Radiation, Acceleration, Iterative Method

Introduction

The P_1 approximation reduces the equation of transfer from a very complicated integro-differential equation to a relatively simple partial differential equation (the P_1 equation). Yet, the P_1 approximation is powerful, allowing non-black surfaces, non-constant properties, anisotropic scattering, etc. For the vast majority of important engineering problems (i.e., in the absence of extreme anisotropy in the intensity field), the method provides high accuracy at very reasonable computational cost. Furthermore, the P_1 approximation can easily be combined with sophisticated spectral models such as the Weighted-Sum-of-Gray-Gases method (WSGG) [1]. Currently, many commercial CFD codes such as FLUENT [2] have the P_1 approximation as an optional solution technique for radiation calculations.

The P_1 equation is a Helmholtz equation and it is conceptually simple to solve numerically. The only problem is that the boundary condition for this equation is of the third kind, which causes the convergence of the solution, by even the most sophisticated iterative methods, to be quite slow, especially when the absorption coefficient of the medium is small. A parallel problem is that unconverged, intermediate solutions of the P_1 equation during the iterative process do not satisfy the basic energy balance–computed total radiative heat source within the medium is not equal to computed total radiative heat flux through boundaries. When such a radiation calculation, without a fully-converged solution, is coupled with a flow calculation, the total energy balance is destroyed during the iterative process and may not converge.

Many approaches have been devised to speed up convergence of iterative methods such as block correction [3] and multigrid acceleration techniques [4]. While these approaches are effective in general and are already widely used in commercial CFD codes, they are not efficient enough, in particular, for equations with boundary conditions of the second and/or the third kind only, e.g., the P_1 approximation. This is because boundary conditions of the second and third kind prescribe only the gradient of an unknown, or a relation between the gradient of an unknown and the unknown itself. A large number of iterations are required for interior nodes as well as boundary nodes to adjust themselves to satisfy

Contributed by the Heat Transfer Division for publication in the JOURNAL OF HEAT TRANSFER. Manuscript received by the Heat Transfer Division February 22, 2001; revision received August 30, 2001. Associate Editor: R. Skocypec.

their governing equations and boundary conditions. Traditional acceleration techniques such as block correction and multigrid acceleration speed up convergence by adding some corrections to drive the solution toward global conservation. Such techniques may not be effective for elliptic equations with boundary conditions of the second and/or third kind. Another acceleration approach is the mesh rebalance method, which was developed by Wachspress [5] and Reed [6] in the context of neutron transport. The characteristic of the mesh rebalance method is that it corrects base iterative results by multiplying with correction factors to speed up convergence. This method has been applied to the discrete ordinated method (DOM) to solve the radiative transfer equation (RTE) [7].

A reduced mesh rebalance acceleration method, which corrects intermediate iterations by a uniform multiplication factor to satisfy the total radiative energy balance, is proposed in this note specifically for the P_1 approximation (a Helmholtz equation with boundary conditions of the second and/or third kind). The method can be used in conjunction with any existing iterative method to achieve faster convergence when solving the P_1 equation.

The Correction Procedure

In the P_1 approximation, the incident radiation, G, is governed by the Helmholtz equation [1]

$$\nabla\cdot\left(\frac{1}{\kappa+\sigma}\nabla G\right)=-3\kappa(4\pi I_b-G) \tag{1}$$

subject to the boundary condition,

$$-\frac{2-\epsilon}{\epsilon}\frac{2}{3}\hat{n}\cdot\nabla G=(\kappa+\sigma)(4\pi I_{bw}-G), \tag{2}$$

where κ and σ are the absorption and scattering coefficients of the radiating gas, respectively, I_b is the Planck function, ϵ is the surface emissivity, and $\hat{n}$ is the surface normal. In practice, the discretized P_1 equation is solved by iterative methods. Due to the nature of the boundary condition of the third kind, convergence of the solution tends to be very slow.

Conservation of radiative energy states that total radiative heat source in a radiating medium is always equal to total radiative heat flux through its boundaries, i.e.,

$$\int\int\int_{\mathcal{V}}\nabla\cdot\underline{q}^R dV=-\int\int_{\mathcal{S}}\hat{n}\cdot\underline{q}^R dS, \tag{3}$$

where q^R is the radiative heat flux vector, which also follows from the divergence theorem. In the P_1 approximation, the divergence of the radiative heat flux vector and the radiative heat flux at the boundaries are calculated as [1]

$$\nabla\cdot\underline{q}^R=\kappa(4\pi I_b-G),\quad -\hat{n}\cdot\underline{q}^R=\frac{\epsilon}{2(2-\epsilon)}(G-4\pi I_{bw}). \tag{4}$$

In iterative methods the converged solution of the P_1 equation satisfies the above energy balance; intermediate solutions during iterative process, however, often do not. In any realistic fire/combustion simulation, the solution to radiative transfer equation is coupled with the solution to the overall energy equation. Since $\nabla\cdot\underline{q}^R$ enters the energy equation as a source, while $-\hat{n}\cdot\underline{q}^R$ appears in the boundary conditions of the energy equation, it is apparent that the total energy balance will also be destroyed during the iterative process, if a partially converged radiative solution is employed. This, in turn, may slow down convergence of the overall energy equation as well.

To speed up convergence and to preserve radiative energy balance, Eq. (3) can be used as a constraint to correct the computed incident radiation field. The computed incident radiation at any node i after the n^{th} iteration, $G_i^{(n)}$, is multiplied uniformly by a factor $f^{(n)}$ to satisfy the discretized form of the energy balance. That is,

$$\sum_{i=1}^{N}\kappa_i(4\pi I_{b,i}-f^{(n)}G_i^{(n)})V_i=\sum_{j=1}^{M}\frac{\epsilon_j}{2(2-\epsilon_j)}(f^{(n)}G_j^{(n)}-4\pi I_{bw,j})A_j, \tag{5}$$

where N is the total number of nodes throughout the whole computational domain and M is the total number of boundary nodes; and V_i and A_j are the nodal volume of the i^{th} node and the boundary surface area of the j^{th} node, respectively.

The correction factor for the n^{th} iteration, $f^{(n)}$, is determined from the above equation as

$$f^{(n)}=\frac{\sum_{i=1}^{N}4\pi\kappa_i I_{b,i}V_i+\sum_{j=1}^{M}\frac{\epsilon_j}{2-\epsilon_j}2\pi I_{bw,j}A_j}{\sum_{i=1}^{N}\kappa_i G_i^{(n)}V_i+\sum_{j=1}^{M}\frac{\epsilon_j}{2(2-\epsilon_j)}G_i^{(n)}A_j}. \tag{6}$$

To implement this method, after each iteration the correction factor is calculated based on Eq. (6). The whole incident radiation field is then corrected by multiplication with the correction factor, $f^{(n)}$, guaranteeing that Eq. (3) is satisfied. As the solution converges, the correction factor gradually moves toward unity. Therefore, the correction procedure does not change the converged incident radiation field.

This correction method not only preserves the total radiative energy balance for partially converged solutions, but also accelerates convergence of the P_1 equation. This is because the correction procedure connects the incident radiation at boundary nodes directly to those of interior nodes, allowing the boundary condition to propagate much more quickly to the inner points, which usually means that the solution converges faster.

Test Problem

A simple two-dimensional problem has been chosen to test the convergence rate of the method, namely a cylindrical combustion chamber, which is 4 m long and 1 m in radius. The temperature field is given by $T(x,r)=8000(x/L)(1-x/L)(1-r/R)$ (K), where x,r, are axial and radial coordinates, respectively. The incident radiation field is to be calculated for different constant absorption coefficients. The problem is axisymmetric and an equally-spaced nodal system with 20×20 nodes is used. The P_1 equation is discretized at these nodes and different iterative methods are used to solve the discretized linear equations. The initial field of incident radiation is set to zero and the convergence criterion is set to $|f-1|\leqslant 1.0\times10^{-5}$. The Gauss-Seidel and the alternating direction line-by-line TDMA iterative methods (supplemented with block correction [3]) will be used with and without our new acceleration scheme. The latter iterative method is widely used and is the main iterative method adopted by many commercial CFD codes. In this method one complete iteration consists of block corrections and line-by-line TDMA sweeps in the row direction and in the column direction. The computed radiative heat sources and the number of iterations to reach the converged solu-

Table 1 Summary of numerical results from test problem

κ	Gauss-Seidel iteration				Line-by-line TDMA iteration			
	$\iiint \nabla \cdot \underline{q}^R dV$ (W)		number of iterations		$\iiint \nabla \cdot \underline{q}^R dV$ (W)		number of iterations	
(1/m)	w/o corr.	with corr.	w/o corr.	with corr.	w/o corr.	with corr.	w/o corr.	with corr.
10	2726	2699	20	9	2716	2698	6	5
1	421869	421491	987	210	421868	421786	165	44
0.1	113773	113756	14474	771	113773	113768	2449	192
0.01	12292	12292	149537	934	12292	12292	25927	236

tion are summarized in Table 1. From the table it is seen that the correction procedure is very effective, especially for optically thin media. For an absorption coefficient of $\kappa = 0.01\ \mathrm{m}^{-1}$ the required number of iterations, or, essentially, the cpu time (since the overhead of cpu time spent in the correction procedure is small—only about five percent of that used in the original base iteration) is reduced to less than 1 percent, regardless of whether the Gauss-Seidel or the line-by-line TDMA iterative methods are employed. Although the line-by-line TDMA iterative method converges after fewer iterations than the Gauss-Seidel method, the correction procedure is equally effective with either one, especially for optically thin media. To further evaluate the performance gains from the correction method, a relative error, defined as $1/N\Sigma_{i=1}^{N}|G_i - G_{\mathrm{conv},i}|/G_{\mathrm{conv},i}$, where $G_{\mathrm{conv},i}$ denotes the converged solution at node i, is plotted versus the number of iterations in Fig. 1 for the case of $\kappa = 1\ \mathrm{m}^{-1}$. It is clear that the solution converges after fewer iterations to the exact solution if the correction procedure is applied. The evolution of the computed total radiative heat source and the total radiative heat flux along the iterative process is shown in Fig. 2. Although an energy balance is ultimately reached when the solution has converged, the total radiative heat source is not equal to the total radiative heat flux through the boundaries during the iterative process if the conventional method is used. In contrast, the method with correction procedure always maintains equilibrium between radiative heat source and the radiative wall flux throughout the iterative process.

While the P_1 approximation with its Helmholtz equation was of particular interest here, its applicability is not limited to this type of problem. The method should perform equally well for all elliptic problems with boundary conditions of the second (specified gradient) and/or third (mixed) kind. For example, applying the method to steady-state conduction of a two-dimensional cylinder with convective boundary conditions leads to very similar results and conclusions (i.e., best acceleration for small heat transfer coefficients, corresponding to small absorption coefficients in the P_1 approximation, and preservation of the conductive energy balance during iterative process).

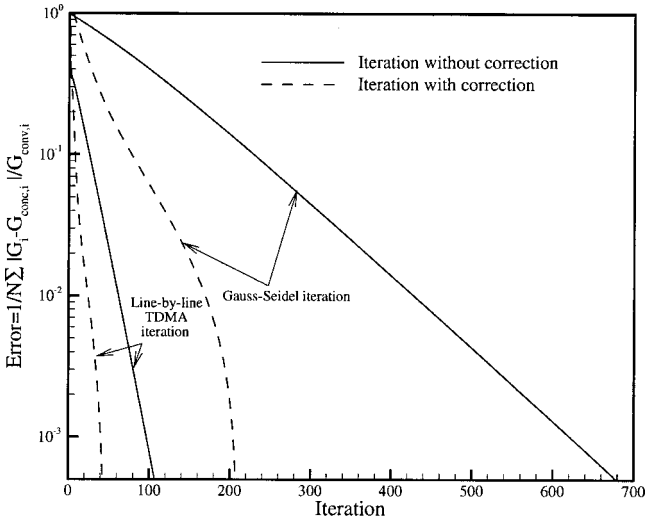

Fig. 1 Relative error change versus number of iterations

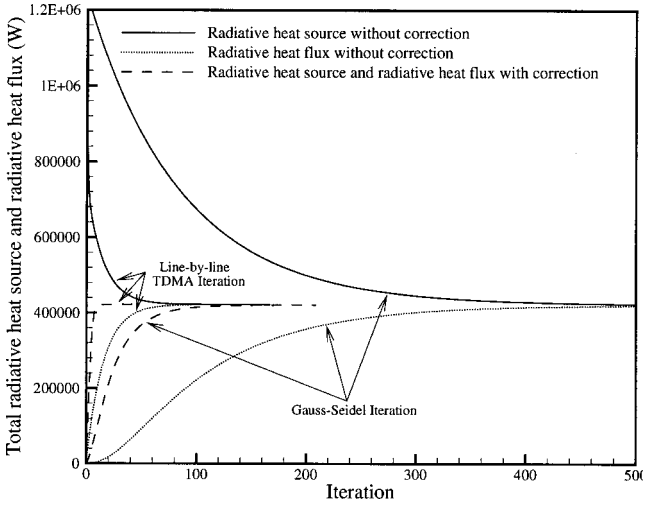

Fig. 2 Computed radiative heat source and radiative heat flux versus number of iterations

Conclusions

A corrective acceleration procedure is proposed for the iterative solution of the discretized P_1 equation (or any other elliptical partial differential equations subject to boundary conditions of the second or third kind), which can be used in conjunction with any iterative method. The procedure not only accelerates the convergence rate of the solution, but also preserves the radiative energy balance during the iterative process, which is desirable when radiation calculations are coupled with flow field calculations. A test problem demonstrated that accelerated iteration is achieved for all optical regimes, with speed-up of more than 100 times for optically thin situations.

Acknowledgment

This research is funded by the National Science Foundation through grant number CTS-9732223.

References

[1] Modest, M. F., 1993, *Radiative Heat Transfer*, McGraw-Hill, New York.
[2] FLUENT, 1995, "Computational Fluid Dynamics Software," Version 4.
[3] Patankar, S. V., 1981, "A Calculation Procedure for Two-Dimensional Elliptic Situations," Numer. Heat Transfer, **4**, pp. 409–425.
[4] Ferziger, J. H., 1998, *Numerical Methods for Engineering Application*, John Wiley & Sons, New York.
[5] Wachspress, E. L., 1966, *Iterative Solution of Elliptic Systems and Applications to the Neutron Diffusion Equations of Reactor Physics*, Prentice-Hall, Englewood Cliffs, NJ.
[6] Reed, W. H., 1971, "The Effectiveness of Acceleration Techniques for Iterative Methods in Transport Theory," Nucl. Sci. Eng., **45**, No. 3, pp. 245–254.
[7] Fiveland, W. A. and Jessee, J. P., 1996, "Acceleration Schemes for the Discrete Ordinates Method," J. Thermophys. Heat Transfer, **10**, No. 3, pp. 445–451.

Stagnation Line Heat Transfer Augmentation Due to Freestream Vortical Structures and Vorticity

Aung N. Oo
Graduate Student
e-mail: aung@engr.mun.ca
Faculty of Engineering and Applied Science,
Memorial University of Newfoundland,
St. John's, Newfoundland, A1B 3X5, Canada

Chan Y. Ching
Associate Professor
Department of Mechanical Engineering, McMaster University, Hamilton, Ontario, L8S 4L7, Canada

An experimental study has been performed to investigate the effect of freestream vortical structures and vorticity on stagnation region heat transfer. A heat transfer model with a cylindrical leading edge was tested in a wind tunnel at Reynolds numbers ranging from 67,750 to 142,250 based on leading edge diameter of the model. Grids of parallel rods were placed at several locations upstream of the heat transfer model in orientations where the rods were perpendicular and parallel to the stagnation line to generate freestream turbulence with distinct vortical structures. All three components of turbulence intensity, integral length scale and the spanwise and transverse vorticity were measured to characterize the freestream turbulence. The measured heat transfer data and freestream turbulence characteristics were compared with existing empirical models for the stagnation line heat transfer. A new correlation for the stagnation line heat transfer has been developed that includes the spanwise fluctuating vorticity components.
[DOI: 10.1115/1.1471526]

Keywords: Convection, Enhancement, Heat Transfer, Turbulence, Vortex

Introduction

Heat transfer augmentation in the stagnation region due to freestream turbulence has been studied extensively [1–7]. Several studies [1–3,6,7] have been performed to understand the physics of the turbulent heat transport mechanism in the stagnation region and to develop empirical models of the heat transfer augmentation due to freestream turbulence. In most studies, the freestream turbulence is nearly isotropic generated using square-meshed grids. However, isotropic turbulence is more the exception in real life engineering applications. It is well established that the coherent vortical structures in a turbulent flow play an important role in momentum and heat transfer. However, attempts to examine the relationship between freestream vortical structures and stagnation region heat transfer are very limited. Oo and Ching [8] performed an experiment where grids of parallel rods were used to generate freestream turbulence with different orientations of vortical structures. They determined that heat transfer in the stagnation region due to freestream turbulence with different coherent structures had distinct characteristics.

A knowledge of the interaction of freestream vortical structures with the stagnation region boundary layer should lead to improved models of stagnation region heat transfer. The vorticity field is closely related with the turbulence structure and dissipation rate [9]. Analyzing the correlation between the vorticity field and the heat transfer augmentation should, therefore, provide further insight to the turbulent heat transfer mechanism in the stagnation region. There are several empirical models [1–3,6,7] that relate stagnation line heat transfer with the characteristics of the freestream turbulence, namely Reynolds number, streamwise turbulence intensity and the integral length scale. These empirical models, however, fail to reveal the influence of vorticity and vortical structures of the freestream turbulence.

Characterizing freestream turbulence with Tu, Re_D, and λ_x does not provide a complete picture of the turbulence, especially when the turbulence is anisotropic. Freestream turbulence can be better described if information pertaining to the vorticity field and the coherent vortical structures are included. The objective of this technical note is to present a relationship between the characteristics of the freestream turbulence, including the vorticity field, and stagnation region heat transfer presented in a previous paper [8]. The freestream vorticity was measured and an empirical model for the heat transfer augmentation that includes the freestream vorticity field developed.

Experimental Details

Heat transfer in the stagnation region was measured using a model with a cylindrical leading edge in a low-speed wind tunnel. Freestream turbulence with different orientations of primary vortices was generated using grids of 2.86 cm, 1.59 cm, and 0.95 cm diameter parallel rods. The grids were arranged in two different orientations, perpendicular and parallel to the stagnation line (Fig. 1). Heat transfer measurements were made with the grids 25d to 125d upstream of the model at three different Re_D of 67,750, 108,350, and 142,250. The experimental details and data reduction for the turbulence intensity and integral length scale are given in Oo and Ching [8]. The spanwise fluctuating vorticity components, ω_z and ω_y, were measured using a vorticity probe similar to the design of Foss and Haw [10]. The vorticity probe consists of a pair of parallel wires and an X-wire. The two spanwise fluctuating vorticity components were obtained separately by rotating the vorticity probe 90 deg. The hot wires were operated using DANTEC 55M01 constant temperature bridges, and the output voltages of the anemometers were digitized using a 16 channel 12 bit Keithley 570 System A/D converter, interfaced to a personal computer. The frequency response of each circuit was determined by standard square-wave test, and found to be about 30 kHz. The sampling frequency of the study ranged from 20 to 30 kHz.

The spanwise vorticity components were measured using the vorticity probe and approximated by:

$$\Omega_z = \frac{\Delta V}{\Delta x} - \frac{\Delta U}{\Delta y} = -\frac{1}{U}\frac{\Delta V}{\Delta t} - \frac{\Delta U}{\Delta y} \tag{1.a}$$

$$\Omega_y = \frac{\Delta U}{\Delta z} - \frac{\Delta W}{\Delta x} = \frac{\Delta U}{\Delta z} + \frac{1}{U}\frac{\Delta W}{\Delta t} \tag{1.b}$$

where ΔU is the difference between the instantaneous streamwise velocity measured by a pair of parallel wires separated in spanwise directions, Δy and Δz. The spanwise velocity derivatives, $\Delta V/\Delta x$ and $\Delta W/\Delta x$, were estimated using Taylor's hypothesis, i.e., $\Delta/\Delta x = -U^{-1}\,\Delta/\Delta t$. The performance of the vorticity probe was tested in the wake of a circular cylinder and the results are in agreement with those of Antonia et al. [11]. Experimental uncertainties in fluctuating vorticity components based on the uncertainty analysis of hot wire data by Yavuzkurt [12], was estimated to be 9.43 percent. The details of the uncertainty analysis are provided in a later section and the results presented in Tables 1 and 2.

Contributed by the Heat Transfer Division for publication in the JOURNAL OF HEAT TRANSFER. Manuscript received by the Heat Transfer Division September 1, 2001; revision received February 1, 2002. Associate Editor: H. S. Lee.

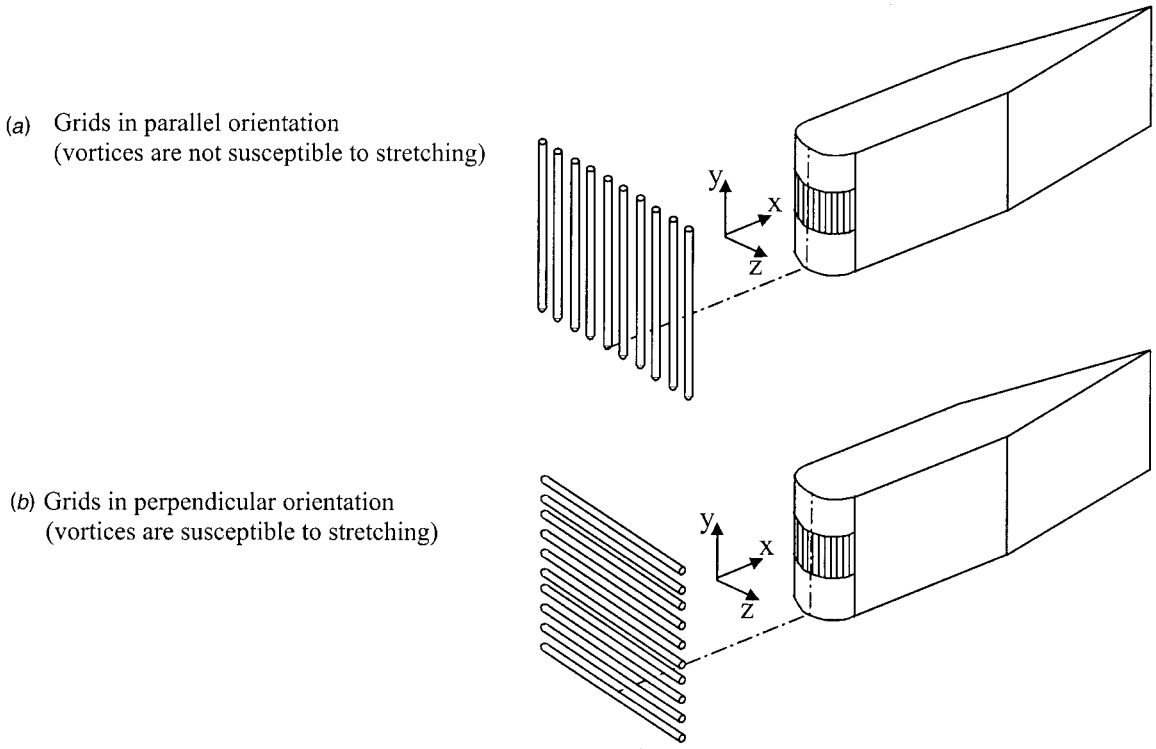

Fig. 1 Arrangements of grids

Table 1 Experimental uncertainty in Fr (percent)

Variable	Bias Error		Precision Error	
	Experimental Reynolds Number Range			
	Max.	Min.	Max.	Min.
Current I	0.18	0.26	0.53	0.51
Voltage Vo	0.06	0.08	0.20	0.21
Temperature difference ΔT	3.20	3.20	0.53	0.53
Conduction heat Q_{cond}	4.60	4.60	0.75	0.75
Radiation heat Q_{rad}	12.80	12.80	2.12	2.12
Convection heat Q_{cov}	1.61	2.10	0.55	0.60
Reynolds number Re_D	0.05	0.10	0.32	0.37
Frossling number *Fr*	3.58	3.83	0.79	0.82

Table 2 Experimental uncertainty in Tu, λx, and ω (percent)

	Experimental Reynolds Number Range	
	Maximum	Minimum
Velocity Calibration (Tu, λ_x)	0.07	0.14
Velocity Curve Fitting (Tu, λ_x)	2.18	2.18
Autocorrelation Curve Fitting (λ_x)	10.50	10.50
Turbulence Intensity *Tu*	3.09	3.09
Integral Length Scale λ_x	10.95	10.95
Fluctuating vorticity ω_z and ω_y	9.43	9.43

Results and Discussion

The turbulence intensity, integral length scale and spanwise velocity fluctuations downstream of the turbulence generating grids were presented in a previous paper [8]. The streamwise distribution of spanwise vorticity, normalized with the mean freestream velocity and diameter of the leading edge, are presented in Fig. 2 for Re_D=108,350. Since greater vorticity is usually associated with the smaller eddies in turbulence [9], the fluctuating vorticity component increases with smaller grid-rod for a given mean freestream velocity. For instance, at $x/d=25$, $\omega U/D$ ranges from about 20 to 25 for the 2.86 cm grid while it varies from about 32 to 39 for the 0.95 cm grid. An attempt to examine the isotropy of the rod-grid turbulence was made by estimating the degree of isotropy of the turbulence from the measurements taken with the single wire and the vorticity probe. For isotropic turbulence, $5\overline{(\partial u/\partial x)^2}$ is equal to $\overline{\omega_z^2}$ and $\overline{\omega_y^2}$ [13]. Therefore, the degree of isotropy is defined as:

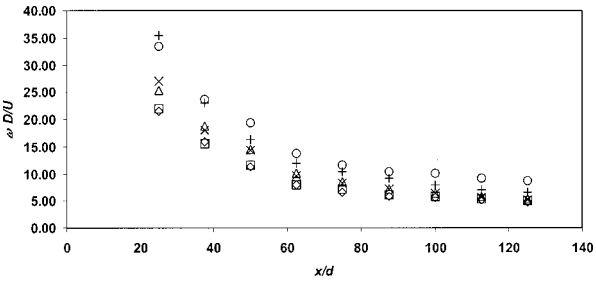

Fig. 2 RMS fluctuating vorticity components of grids in perpendicular orientation for Re_D=108,350 (2.86 cm rod-grid: ◇, ω_z; □, ω_y; 1.59 cm rod-grid: △, ω_z; ×, ω_y; 0.95 cm rod-grid: ○, ω_z; +, ω_y)

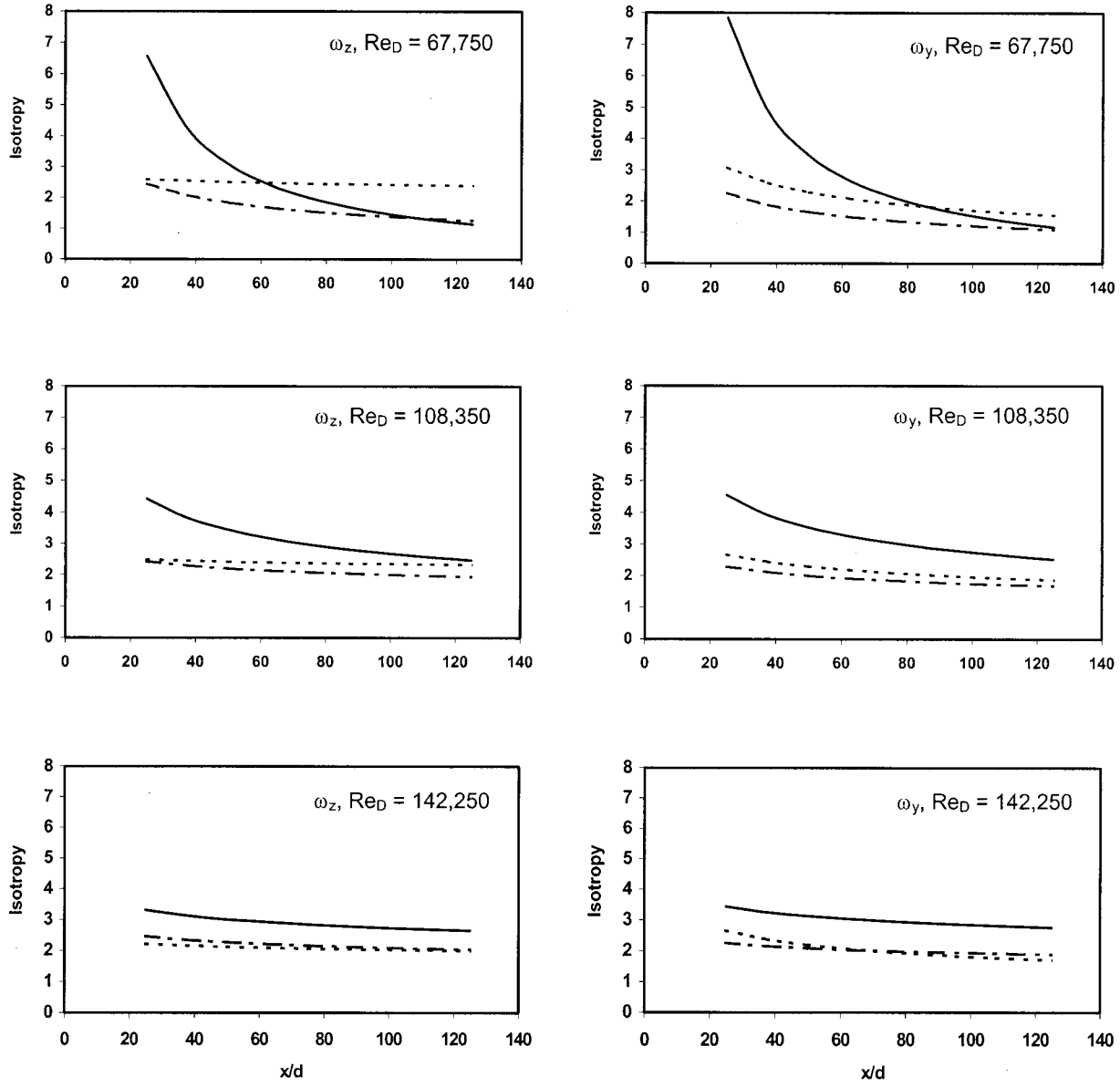

Fig. 3 Streamwise trends of the degree of isotropy (rod-grids of: —, 2.86 cm; - — -, 1.59 cm; - - -, 0.95 cm)

$$\mathrm{Iso} = \frac{\overline{\omega^2}}{5\left(\overline{\frac{\partial u}{\partial x}}\right)^2} \tag{2}$$

where $\overline{\omega^2}$ is the mean square value of fluctuating vorticity components and $\partial u/\partial x$ is estimated from single wire measurements. The streamwise distributions of the estimated degree of isotropy, which is calculated from the best-fit curves of vorticity components and $\partial u/\partial x$, are shown in Fig. 3. For the 2.86 cm rod-grid, deviation from isotropy is highest (Iso of an order of 7 at $x/d = 25$) at the lowest Reynolds number. At freestream Re_D of 67,750, the grid turbulence approaches isotropy with downstream distance for all grids (Iso$\sim$1 at $x/d = 125$). Deviation from isotropy is higher for the higher Reynolds numbers (Iso$\sim$2 at $x/d = 125$ for Re_D of 108,350 and 142,250). The general trend is that turbulence approaches isotropy as downstream distance increases, and the degree of anisotropy is highest with the biggest rod-grid.

The stagnation line heat transfer data from the three grids are compared with the correlation of VanFossen et al. [7] in Fig. 4.

$$\mathrm{Fr} = 0.008\sqrt{\mathrm{Tu}\ \mathrm{Re}_D^{0.8}\left(\frac{\lambda_x}{D}\right)^{-0.574}} + 0.939 \tag{3}$$

There is a significant discrepancy between the present experimental data and Eq. (3) for the 2.86 cm rod-grid, but the agreement improves with decreasing size of rod. For the 0.95 cm rod-grid, 87 percent of data falls within ± 4 percent of Eq. (3). It is clear from Fig. 4 that correlations developed for isotropic turbulence generated by square mesh grids should be corrected to predict the heat transfer due to turbulence with distinct coherent vortical structures. The errors are larger for the 2.86 cm rod-grid, where the freestream turbulence has a greater distinction between the primary and secondary vortices. It is unlikely that correlations developed for isotropic turbulence can be used to estimate heat transfer to gas turbine blades, where the turbulence from the combustor and wakes from the upstream blades is highly anisotropic and laced with well-defined vortical structures.

The freestream turbulence needs to be characterized more comprehensively to obtain more accurate empirical models. It seems plausible that incorporating the vorticity field and spanwise veloc-

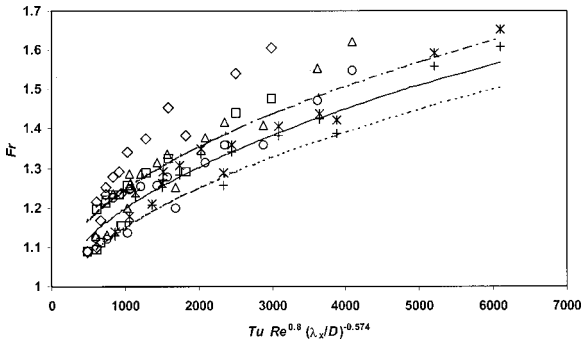

Fig. 4 Stagnation line Fr versus correlation parameter proposed by VanFossen et al. [7] (perpendicular Rod-grids: ◇, 2.86 cm; △, 1.59 cm; *, 0.95 cm; parallel rod-grids: □, 2.86 cm; ○, 1.59 cm; +, 0.95 cm; correlation lines: —, VanFossen et al. [7]; – – –, +4%; - - -, −4%)

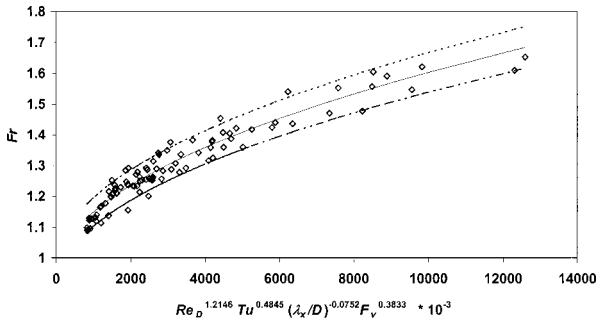

Fig. 5 Stagnation line Fr versus correlation parameter with spanwise vorticity and velocity fluctuations for both grid orientations (◇, data, correlation lines: —, Eq. (5); - - -, +4%; - · - ·, −4%)

ity fluctuations would improve the correlation, since they highlight the distinct structure of turbulence. Since vorticity amplification due to vortex stretching is hypothesized to influence the stagnation region heat transfer, the fluctuating vorticity component of primary vortices, i.e., ω_z and ω_y for turbulence generated by the rod-grids in perpendicular and parallel orientations, respectively, were considered to form a new turbulence parameter. The products of spanwise vorticity and velocity fluctuating components, $v\omega_z$ and $w\omega_y$, are taken as additional parameters to be included in the correlation. The products, $v\omega_z$ and $w\omega_y$, can be interpreted to represent the vortex forces in turbulence, which are analogous to the Coriolis forces [9]. The additional turbulence parameter used to develop a new correlation for the stagnation line heat transfer is defined as:

$$F_\nu = \frac{\nu\omega_z D}{U^2} \quad \text{for grid-rods in perpendicular orientation} \tag{4.a}$$

$$F_\nu = \frac{w\omega_y D}{U^2} \quad \text{for grid-rods in parallel orientation} \tag{4.b}$$

Therefore, the additional parameter is the vortex force due to primary vortices of freestream normalized by the diameter of the leading edge and the mean freestream velocity. The new correlation is obtained by a regression analysis and is presented in Fig. 5. It can be seen that 95 percent of experimental data fall within the ±4 percent of the new correlation given by:

$$\mathrm{Fr} = 0.00021\sqrt{\mathrm{Re}_D{}^{1.2146}\mathrm{Tu}^{0.4845}\left(\frac{\lambda_x}{D}\right)^{-0.0752} F_\nu^{0.3833}} + 0.939 \tag{5}$$

The improved correlation suggests that the inclusion of the vorticity field and spanwise velocity components takes into account the vortical structures of the freestream to a certain extent. It is clear that freestream turbulence with different orientations of coherent vortical structures have different influences over the heat transfer in the stagnation region, and the consideration of vortical structures of turbulence would improve the empirical models for prediction of gas turbine heat transfer.

Conclusions

Heat transfer enhancement in the stagnation region by freestream turbulence with distinct coherent vortical structures is different to that by turbulence generated using square-mesh grids. The present heat transfer data, obtained using an array of parallel rods in different orientations, are poorly predicted by existing correlation models. A new correlation model was developed by including the lateral fluctuating velocity and vorticity components of the freestream. The new correlation model predicts the heat transfer data of this study within ±4 percent. Any empirical model should take into account the distinct nature of the coherent vortical structures of the turbulence to improve its predictive capability.

Acknowledgments

The support of the Natural Sciences and Engineering Research Council (NSERC) of Canada is gratefully acknowledged.

Appendix

Analysis of Experimental Uncertainties. Following the uncertainty analysis methods of Moffat [14] the uncertainty in Fr can be expressed as:

$$(Un_{\mathrm{Fr}})^2 = (Un_{\mathrm{Nu}})^2 + 0.25(Un_{\mathrm{Re}D})^2$$

where Un_{Fr} = Uncertainty in Fr (%)
Un_{Nu} = Uncertainty in Nu (%)
$Un_{\mathrm{Re}\,D}$ = Uncertainty in Re_D (%)

The uncertainty in Fr and the influencing variables with 95 percent confidence levels are given in Table 1 for both maximum and minimum freestream velocities. Uncertainties in temperature were considered in estimating conduction heat loss, radiation heat losses and convection heat transfer. Uncertainties associated with leading edge diameter (D), thermal conductivity (k), and area (A) are assumed to be negligible since these values are based on the data specified by manufacturers.

The techniques proposed by Yavuzkurt [12] were used to estimate the uncertainties in Tu and λ_x and ω. The uncertainties are given in Table 2.

Nomenclature

d = diameter of a grid-rod (m)
D = diameter of cylindrical leading edge (m)
Fr = Frossling number ($\mathrm{Nu}/\sqrt{\mathrm{Re}_D}$)
F_ν = dimensionless vortex force
Iso = degree of isotropy
Re_D = Reynolds number based on D
t = time (s)
Tu = streamwise turbulence intensity
u = rms of fluctuating velocity component in streamwise direction (m/s)
U = mean freestream velocity (m/s)
v = rms of fluctuating velocity component in spanwise Y-direction (parallel to stagnation line) (m/s)
w = rms of fluctuating velocity component in spanwise Z-direction (m/s)
x = distance downstream of the grid (m)

Ω_y = instantaneous vorticity in spanwise *Y*-direction (l/s)
Ω_z = instantaneous vorticity in spanwise *Z*-direction (l/s)
λ_x = streamwise integral length scale of turbulence (m)
ω_y = rms of fluctuating vorticity component in spanwise *Y*-direction (l/s)
ω_z = rms of fluctuating vorticity component in spanwise *Z*-direction (l/s)

References

[1] Smith, M. C., and Kuethe, A. M., 1966, "Effects of Turbulence on Laminar Skin Friction and Heat Transfer," Phys. Fluids, **9**(12), pp. 2337–2344.
[2] Kestin, J., and Wood, R. T., 1971, "The Influence of Turbulence on Mass Transfer from Cylinders," ASME J. Heat Transfer, **93C**, pp. 321–327.
[3] Lowery, G. W., and Vachon, R. I., 1975, "Effect of Turbulence on Heat Transfer from Heated Cylinders," Int. J. Heat Mass Transf., **18**(11), pp. 1229–1242.
[4] O'Brien, J. E., and VanFossen, G. J., 1985, "The Influence of Jet-Grid Turbulence on Heat Transfer from the Stagnation Region of a Cylinder in Crossflow," ASME Paper 85-HT-58.
[5] Mehendale, A. B., Han, J. C., and Ou, S., 1991, "Influence of High Mainstream Turbulence on Leading Edge Heat Transfer," ASME J. Heat Transfer, **113**, pp. 843–850.
[6] Yeh, F. C., Hippensteele, S. A., VanFossen, G. J., Poinsatte, P. E., and Ameri, A. 1993, "High Reynolds Number and Turbulence Effects on Aerodynamics and Heat Transfer in a Turbine Cascade," Paper No. AIAA-93-2252.
[7] VanFossen, G. J., Simoneau, R. J., and Ching, C. Y., 1995, "Influence of Turbulence Parameters, Reynolds Number and Body Shape on Stagnation Region Heat Transfer," ASME J. Heat Transfer, **117**, pp. 597–603.
[8] Oo, A. N., and Ching, C. Y., 2001, "Effect of Turbulence with Different Vortical Structures on Stagnation Region Heat Transfer," ASME J. Heat Transfer, **123**, pp. 665–674.
[9] Tennekes, H., and Lumley, J. L., 1972, *A First Course in Turbulence*, The MIT Press, The Massachusetts Institute of Technology.
[10] Foss, J. F., and Haw, R. C., 1990, "Transverse Vorticity Measurements Using a Compact Array of Four Sensors," *The Heuristics of Thermal Anemometry*, D. E. Stock, S. A. Sherif, and A. J. Smits, eds., ASME-FED 97, pp. 71–76.
[11] Antonia, R. A., Browne, L. W. B., and Shah, D. A., 1988, "Characteristics of Vorticity Fluctuation in a Turbulent Wake," J. Fluid Mech., **189**, pp. 349–365.
[12] Yavuzkurt, S., 1984, "A Guide to Uncertainty Analysis of Hot-Wire Data," ASME J. Fluids Eng., **106**, pp. 181–186.
[13] Zhou, T., and Antonia, R. A., 2000, "Reynolds Number Dependence of the Small-Scale Structure of Grid Turbulence," J. Fluid Mech., **406**, pp. 81–107.
[14] Moffat, R. J., 1988, "Describing the Uncertainties in Experimental Results," Exp. Therm. Fluid Sci., **1**, pp. 3–17.

Similarity Solution for Marangoni Convection Over a Flat Surface

David M. Christopher
Associate Professor
Mem. ASME
e-mail: dmc@tsinghua.edu.cn

Buxuan Wang
Professor

Thermal Engineering Department, Tsinghua University, Beijing, 100084, China

A similarity solution is presented for Marangoni flow over a flat surface for both the velocity and temperature profiles assuming developing boundary layer flow along the surface with various imposed temperature profiles. Marangoni flow results from variations of the surface tension along a liquid-vapor interface and is especially noticeable in microgravity. Solutions are presented for the surface velocity, the total flow rate and the heat transfer for various temperature profiles and various Prandtl numbers. [DOI: 10.1115/1.1473143]

Keywords: Boiling, Convection, Heat Transfer, Thermocapillary

Introduction

Marangoni flow due to surface tension variations is of importance in various processes including the flow in crystal growth melts in both microgravity and normal earth gravity conditions where the Marangoni flow can affect crystal quality and in boiling where the Marangoni flow may significantly affect the heat transfer as shown by boiling tests in microgravity [1,2].

The numerous investigations of Marangoni flow have been reviewed in the literature (e.g., [3,4]) so only the studies most closely related to this paper are reviewed here. Okano et al. [5] presented an order-of-magnitude analysis of Marangoni flow that showed the general trends for the Grashof number, Marangoni number, and Prandtl number dependence on the Reynolds number. Banks and Zaturska [6] and Arafune and Hirata [7] presented a similarity solution for the momentum boundary layer equations with the flat surface velocity specified as a function of the distance along the surface. Arafune and Hirata [7] also presented experimental results for Marangoni flow along a flat surface. Schwabe and Metzger [8] experimentally investigated Marangoni flow on a flat surface combined with natural convection in a unique geometry where the Marangoni and buoyancy effects could be varied independently.

This paper presents a similarity solution for both the momentum and energy boundary layer equations for Marangoni flow over a flat surface with an imposed surface temperature gradient that is a power-law function of the location. The resulting family of solutions can also be applied qualitatively to other flows that have surface temperature variations that can be related to the assumed temperature variation as has been done with the Falkner-Skan family of flows [6]. The momentum and energy boundary layer equations are transformed to ordinary differential equations which are then solved using the Runge-Kutta method. The present results extend previous solutions by including the solution of the energy equation so that the velocity distribution is related to the specified temperature distribution through the Marangoni boundary condition rather than just specifying the surface velocity distribution as done previously.

Theoretical Analysis

The continuity equation and the momentum and energy equations are solved for laminar boundary layer flow of a Newtonian fluid in the half plane $0<y<\infty$ having a flat surface in the x direction starting at $x=0$. The boundary conditions at the surface are:

$$\mu \left.\frac{\partial u}{\partial y}\right|_{y=0} = -\frac{d\sigma}{dT}\left.\frac{\partial T}{\partial x}\right|_{y=0}$$
$$\nu(x,0)=0 \tag{1}$$
$$T(x,0)=T(0,0)+Ax^{k+1}$$

Far from the surface, the boundary conditions are:

$$u(x,\infty)=0$$
$$T(x,\infty)=T_\infty=T(0,0) \tag{2}$$

Using the standard definition of the stream function, similarity variables are introduced as:

$$\eta=C_1x^dy$$
$$f(\eta)=C_2x^a\psi(x,y) \tag{3}$$
$$\varphi(\eta)=(T(x,y)-T(0,0))x^h/A$$

so the governing equations can be written as:

Contributed by the Heat Transfer Division for publication in the JOURNAL OF HEAT TRANSFER. Manuscript received by the Heat Transfer Division April 11, 2000; revision received February 25, 2002. Associate Editor: S. S. Sadhal.

$$f^m = f'^2(d-a) + aff''$$
$$\varphi'' = \Pr(af\varphi' - hf'\varphi) \tag{4}$$

The coefficients are defined as:

$$C_1 = \sqrt[3]{\frac{\frac{d\sigma}{dT}A\rho}{\mu^2}}; \quad C_2 = \sqrt[3]{\frac{\rho^2}{\frac{d\sigma}{dT}A\mu}} \tag{5}$$

For similarity, the exponents are related to k in Eq. (1) by:

$$d = \frac{k-1}{3}; \quad a = \frac{-2-k}{3}; \quad h = -1-k \tag{6}$$

The boundary conditions are:

$$f(0) = 0; \quad f''(0) = -1; \quad f'(\infty) = 0 \tag{7}$$

$$\varphi(0) = 1; \quad \varphi(\infty) = 0 \tag{8}$$

The surface velocity given by the similarity solution is:

$$u(x,0) = \sqrt[3]{\frac{\left(\frac{d\sigma}{dT}A\right)^2}{\rho\mu}} f'(0)x^{(2k+1)/3} \tag{9}$$

The temperature gradient coefficient can be defined in terms of the total temperature difference along a surface of length L as $A = \Delta T/L^{k+1}$ so that the Marangoni number can then be defined for a general temperature profile as:

$$\mathrm{Ma}_L = \frac{\frac{d\sigma}{dT}\frac{\Delta T}{L^{k+1}}L^{k+2}}{\mu\alpha} = \frac{\frac{d\sigma}{dT}\Delta TL}{\mu\alpha} \tag{10}$$

The Reynolds number defined in terms of the surface velocity is then related to the Marangoni number as:

$$\mathrm{Re}_L = \frac{u(x,0)L}{\nu} = f'(0)\mathrm{Ma}_L^{2/3}\mathrm{Pr}^{-2/3} \tag{11}$$

The total mass flow in the boundary layer per unit width can be written as:

$$\dot{m} = \int_0^\infty \rho u dy = \sqrt[3]{\frac{d\sigma}{dT}A\rho\mu}x^{(k+2)/3} f(\infty) \tag{12}$$

The problem statement in this analysis differs in several ways from that used by Arafune and Hirata [7], Banks and Zaturska [6] and others. While the definitions of the similarity variables are only slightly different, the surface boundary condition for the momentum equation in this analysis is based on the Marangoni boundary condition rather than the specified velocity variation as in previous works. In addition, the current derivation is extended to include the energy equation so that the velocity distribution throughout the liquid region is a function of the temperature distribution. The surface velocity distribution given in Eq. (9), while similar to the form of the velocity distribution used by others, is a result of the derivation that clarifies the relationship between the velocity and temperature distributions.

Discussion of Similarity Results

The governing equations, Eq. (4), were solved numerically using the fourth-order Runge-Kutta method with at least 20,000 steps. The shooting method was used to determine the unknown boundary conditions at $\eta = 0$, $f'(0)$ for the momentum equation and $\phi'(0)$ for the energy equation. The maximum value for the independent variable, η, which was a function of the Prandtl number, was always chosen to be at least 4 times the maximum momentum or thermal boundary layer thickness. The results presented in the following section were all independent of the number of steps and the maximum value of η.

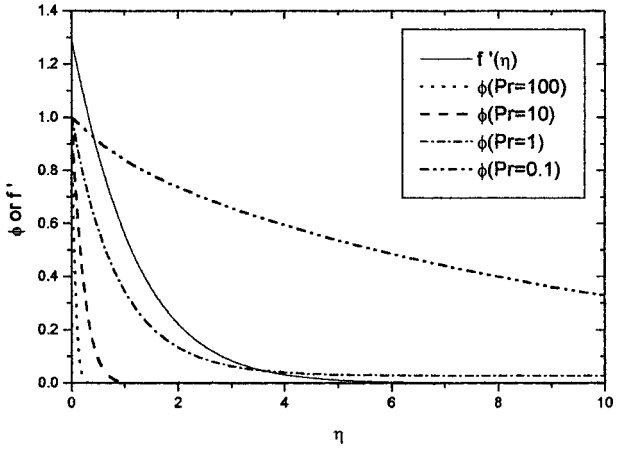

Fig. 1 Velocity and temperature profiles for $k=0$

The similarity stream function, f, is a function of the exponent, k, while the temperature function, ϕ, is a function of both k and the Prandtl number. The governing equations were solved subject to the boundary conditions in Eqs. (7) and (8) for various values of k and Pr. Typical velocity and temperature profiles are given in Fig. 1 for several representative values of the Prandtl number and for $k=0$ which is a linear surface temperature profile.

The variations of the surface velocity, the boundary layer thickness and the total flow rate in the boundary layer are given as functions of k in Fig. 2, of which $k=0$ refers to a linear profile and $k=1$ is quadratic, while $k=-0.5$ would be a temperature variation relative to the square root of x. The minimum value of k is -1, which results in no temperature variation on the surface and thus no Marangoni flow. The momentum boundary layer thickness is defined as the point where the velocity function, f, is 1 percent of the value at the surface. The surface velocity for small values of k is greater because for a fixed total temperature difference across the surface (i.e., fixed A), the profile for a small value of k is steeper near the leading edge which provides more flow. For larger values of k, the slope of the temperature profile is larger near the trailing edge where the boundary layer is thicker and the additional acceleration of the flow has less effect. The mass flow rate follows the same trend. The boundary layer thickness is greatest for the uniformly increasing temperature profile, $k=0$. For k greater than or less than 0, the temperature profile over part of the surface is relatively flat, so the flow does not accelerate much in that region and the boundary layer does not grow.

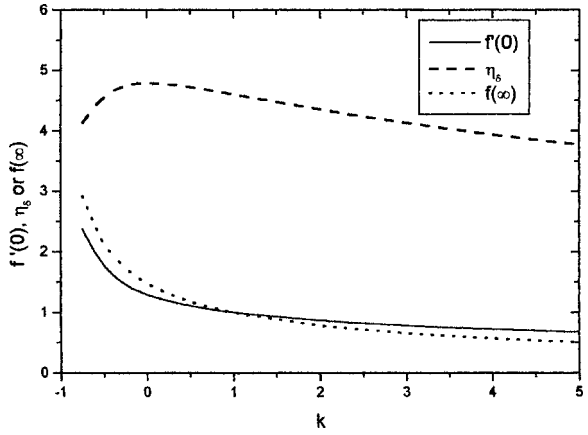

Fig. 2 Variations of surface velocity, boundary layer thickness, and flow rate for various temperature gradient exponents

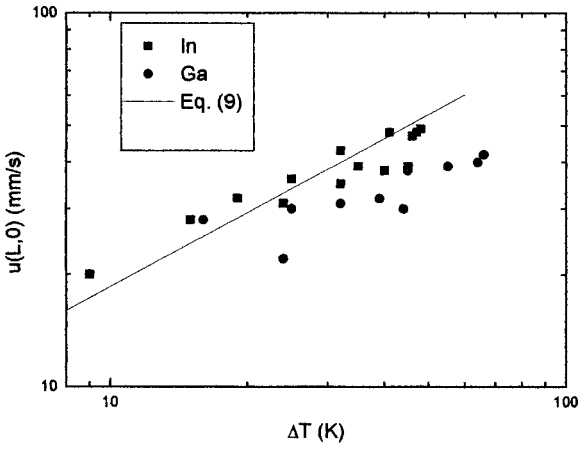

Fig. 3 Comparison of experimental results from Arafune and Hirata [7] with the predicted surface velocities for $k=0$

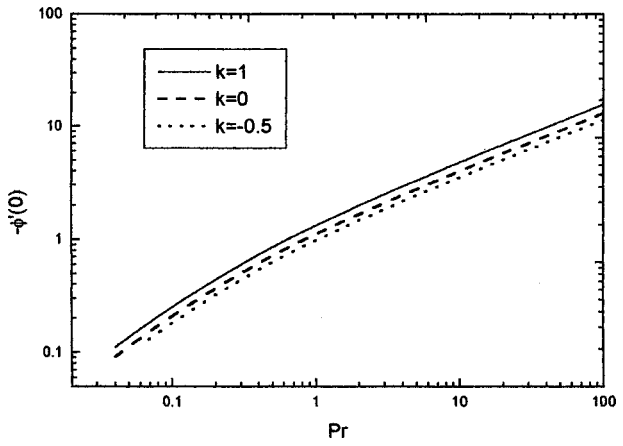

Fig. 4 Variation of the surface heat flux

The predicted surface velocities for $k=0$ agree well with the surface velocities measured by Arafune and Hirata [7] for Marangoni driven flow of gallium and indium in a shallow pool shown in Fig. 3. The slopes of the similarity and experimental results also agree with the analysis of Okano et al. [5] which showed that the Reynolds number should vary as the two-thirds root of the Marangoni number for large Reynolds numbers.

The variation of the surface heat flux as a function of the Prandtl number and the temperature gradient exponent is shown in Fig. 4. The local Nusselt number is:

$$\mathrm{Nu}_x=\frac{q''(x)x}{\lambda(T(x,0)-T(x,\infty))}=-\mathrm{Ma}_x^{1/3}\mathrm{Pr}^{-1/3}\left(\frac{x}{L}\right)^{(k+2)/3}\phi'(0) \tag{13}$$

The similarity analysis is based on the boundary layer equations which assume that the transverse derivatives of the velocity and temperature are much larger than their axial derivatives. Analysis of the similarity transformation shows that both are true if:

$$C_1L^{(k+2)/3}=\sqrt[3]{\frac{d\sigma}{dT}\frac{A\rho L^{k+2}}{\mu^2}}=\mathrm{Ma}_L^{1/3}\mathrm{Pr}^{-1/3}\gg 1 \tag{14}$$

Conclusions

A similarity solution was given for Marangoni boundary layer flow over a flat surface with an imposed temperature gradient. The predicted surface velocities agree well with measured values for shallow pools of liquid indium and gallium [7].

The analysis gives the variations of the velocity and temperature distributions in the boundary layer for power-law variations of the surface temperature gradient. Equations are then given for the surface velocity, the total mass flow rate and the heat flux at the interface as functions of the Marangoni, Prandtl and Reynolds numbers, the exponent k and the location. For $k=0$, the analysis agrees with previous results using a specified surface velocity distribution [5] that the Reynolds number based on the surface velocity varies as the two-thirds power of the Marangoni number.

Acknowledgment

The project was financially supported by the National Natural Science Foundation of China with grant number 59995550-3.

Nomenclature

a, d, h = exponents in similarity transformation
A = temperature gradient coefficient (K/m^{k+1})
C_1 = similarity transformation coefficient (m^a)
C_2 = similarity transformation coefficient ($s\ m^{(k-4)/3}$)
$f(\eta)$ = stream function similarity variable
k = temperature gradient exponent
$\dot{m}$ = mass flow rate per unit width (kg/m s)
Ma = Marangoni number, Eq. (10)
Nu = Nusselt number, Eq. (13)
Pr = Prandtl number
q'' = heat flux (W/m^2)
Re = Reynolds number, Eq. (11)
T = temperature (K)
u, v = velocities (m/s)
x, y = coordinates (m)

Greek

α = thermal diffusivity (m^2/s)
ϕ = dimensionless similarity temperature
η = location similarity variable
η_δ = dimensionless momentum boundary layer thickness
λ = thermal conductivity (W/mK)
μ = dynamic viscosity (Ns/m^2)
ν = kinematic viscosity (m^2/s)
ρ = density (kg/m^3)
σ = surface tension (N/m)
ψ = stream function (m^2/s)

Subscripts

L = average over surface length
x = local value

References

[1] Straub, J., 1994, "The Role of Surface Tension for Two-Phase Heat and Mass Transfer in the Absence of Gravity," Exp. Therm. Fluid Sci., **9**, pp. 253–273.
[2] Christopher, D., and Wang, B., 1998, "Marangoni Convection around a Bubble in Microgravity," *Heat Transfer, 1998, Proceedings 11th International Heat Transfer Conference*, J. S. Lee, ed., Taylor and Francis, Inc., Levittown, PA, **3**, pp. 489–494.
[3] Arafune, K., and Hirata, A., 1998, "Interactive Solutal and Thermal Marangoni Convection in a Rectangular Open Boat," Numer. Heat Transfer, Part A, **34**, pp. 421–429.
[4] Croll, A., Muller-Sebert, W., and Nitsche, R., 1989, "The Critical Marangoni Number for the Onset of Time-dependent Convection in Silicon," Mater. Res. Bull., **24**, pp. 995–1004.
[5] Okano, Y., Itoh, M., and Hirata, A., 1989, "Natural and Marangoni Convections in a Two-Dimensional Rectangular Open Boat," J. Chem. Eng. Jpn., **22**, pp. 275–281.
[6] Banks, W. H. H., and Zaturska, M. B., 1986, "Eigensolutions in Boundary-Layer Flow Adjacent to a Stretching Wall," IMA J. Appl. Math., **36**, pp. 263–273.
[7] Arafune, K., and Hirata, A., 1999, "Thermal and Solutal Marangoni Convection in In-Ga-Sb System," J. Cryst. Growth, **197**, pp. 811–817.
[8] Schwabe, D., and Metzger, J., 1989, "Coupling and Separation of Buoyant and Thermocapillary Convection," J. Cryst. Growth, **97**, pp. 23–33.

Journal of Heat Transfer

Technical Notes

This section contains shorter technical papers. These shorter papers will be subjected to the same review process as that for full papers.

Numerical Investigation of Forced Convection in a Horizontal Channel With a Built-In Triangular Prism

H. Abbassi, S. Turki, and S. Ben Nasrallah
Heat and Mass Transfer Laboratory, National Engineering High School of Monastir (Tunisia)

Keywords: Channel Flow, Computational, Forced Convection, Heat Transfer, Periodic

Introduction

Flow past bluff bodies between two parallel walls has been investigated by many researchers both numerically and experimentally. This flow situation is popular not only because of its academic attractiveness but also owing to its related technical problems associated with energy conservation and structural design. This type of flow is of relevance for many practical applications, such as electronic cooling and heat exchanger systems.

The incompressible flow around a circular cylinder represents one of the most investigated prototypes of bluff body wakes. The flow around a rectangular cylinder has received far less attention than the flow around a circular cylinder, but no references have been found which simulate the laminar flow around a triangular prism placed in a channel. Furthermore the effect of presence of bluff body in the heat transfer in a flow with heat source has not yet been investigated. This has motivated the present work that is concerned with structure of laminar flow and heat transfer in a two dimensional channel differentially heated with a built-in triangular prism. This specifically shaped cylinder is specially used in systems of vortex flowmeters and flame stabilizer in combustion chambers. The investigation is carried out from the numerical solutions of complete Navier-Stokes and energy equations by Control Volume Finite Element Method. The effects of presence of triangular prism on the flow structure and heat transfer are the subject of the present work.

Results and Discussion

The system of interest is a horizontal plane channel, a triangular prism is symmetrically placed in the channel axis as indicated in Fig. 1. Boundary conditions expressed in dimensionless form are as follows:

$$\text{at } 0 \leqslant x \leqslant L/B; y=0: u=v=0, \theta=1$$

$$\text{at } 0 \leqslant x \leqslant L/B; y=4: u=v=0, \theta=0$$

$$\text{at } x=0; 0 \leqslant y \leqslant 4: u=y(4-y)/4, v=0, \theta=0$$

$$\text{at } x=L/B; 0 \leqslant y \leqslant 4: \frac{\partial u}{\partial x}=\frac{\partial v}{\partial x}=\frac{\partial \theta}{\partial x}=0; \quad \int_0^4 u\,dy=8/3$$

The thermal heat flux transferred from the hot bottom wall to the flow is characterized by the space-averaged Nusselt number evaluated as follows:

$$\overline{\mathrm{Nu}}=\frac{1}{L/B}\int_0^{L/B}\mathrm{Nu}\,dx,$$

where Nu is the local Nusselt number defined as

$$\mathrm{Nu}=-\frac{\partial \theta}{\partial y}.$$

The space- and time-averaged Nusselt number is defined as

$$\langle\overline{\mathrm{Nu}}\rangle=\left(\frac{1}{\tau_2-\tau_1}\right)\int_{\tau_1}^{\tau_2}\overline{\mathrm{Nu}}\,d\tau,$$

where the time interval $(\tau_2-\tau_1)$ is the period of oscillation of the space-averaged Nusselt number Nu.

A modified version of Control Volume Finite-Element Method (CVFEM) of Saabas and Baliga [1] is adapted to the standard staggered grid for solving the dimensionless equations of continuity, momentum, and energy. The obtained numerical code was successfully validated with many standard test flows. We can quote the flow in a horizontal channel with a built-in square cylinder where results obtained are in good agreement with those reported by Davis et al. [2] as indicated in Table 1. The maximum error committed in the Strouhal numbers is less than 6.5 percent by report to numerical values and less than 9.3 percent in comparison with experimental measurements. We can also quote the Poiseuille-Benard channel flow at Re=10, Pe=20/3, and Ra $=10^4$ (see Table 2). Especially our results are close to that reported by Evans and Paolucci [3] where the errors in the period and in the space- and time-averaged Nusselt number are respectively 4.7 percent and 0.9 percent. These results demonstrate good accuracy and competence of our numerical code.

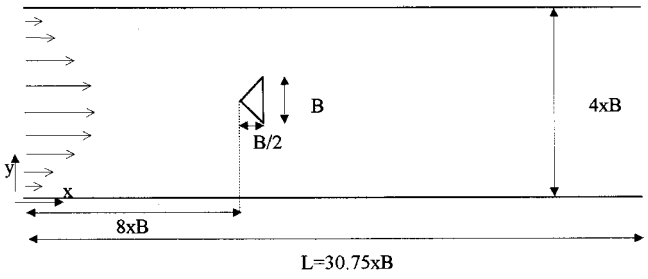

Fig. 1 Flow in a horizontal channel with built-in triangular prism

Contributed by the Heat Transfer Division for publication in the JOURNAL OF HEAT TRANSFER. Manuscript received by the Heat Transfer Division October 18, 1999; revision received November 13, 2000. Associate Editor: C. T. Avedisian.

Table 1 Flow in a horizontal channel with a built-in square cylinder: Variation of Strouhal numbers with Reynolds numbers.

Re	250	500	750
Present	0.188	0.200	0.190
Numerical values of Davis[2]	0.201	0.198	0.183
Experimental values of Davis[2]	-----	0.183	0.178

Table 2 Poiseuille-Benard channel flow at Re=10, Pe=20/3, and Ra=10^4

Reference	Present	Evans[3]	Comini[4]
Period Θ	1.395	1.332	1.273
$<\overline{Nu}>$	2.536	2.558	2.574

After verifying that the implemented numerical code gives accurate results for laminar two dimensional flows, a solution for the flow described in Fig. 1 is next sought. Grid refinement tests have been performed for the case Re=100 using three non uniform grids 72×13, 105×21, and 131×32. Results shows that when we pass from a grid of 105×21 to a grid of 131×32 the space and time-averaged Nusselt number $\langle\overline{Nu}\rangle$ and the Strouhal number St undergoes an increase of only 4.2 percent and 2.8 percent respectively, then, for reasons of calculation coast, the grid of 105×21 is retained.

Solutions are first obtained for Re=30. For this relatively low Reynolds number, the convergence of the numerical procedure is easily obtained. The velocity profiles at different axial locations in the channel are symmetrical about the channel axis. Two symmetrical vortices appear behind the triangular prism on each side of the wake turning in place in opposite sense. The flow is steady state.

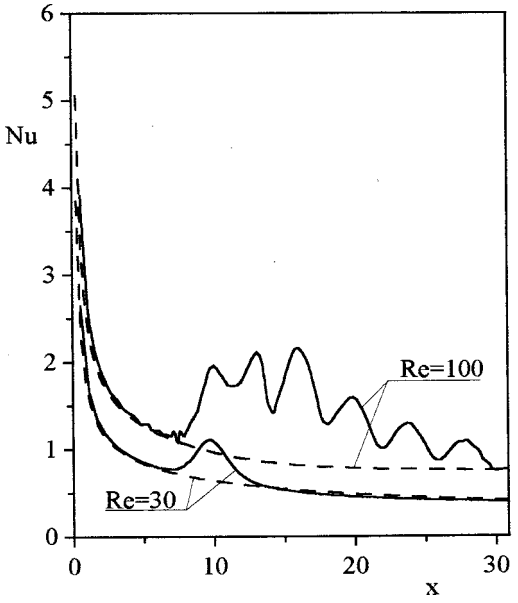

Fig. 2 Local Nusselt number distribution along the lower wall: Solid line: flow with triangular prism; dashed: flow without triangular prism

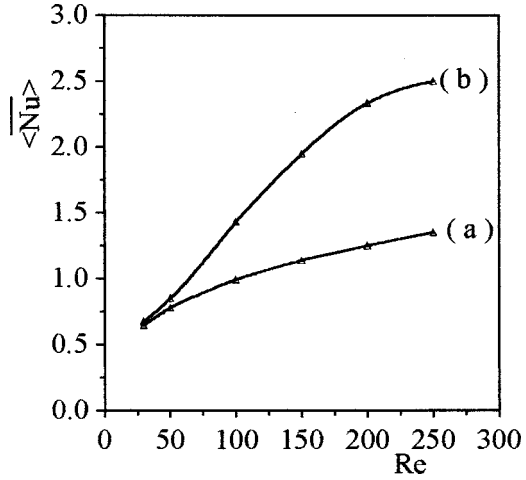

Fig. 3 Variation of the space and time-averaged Nusselt numbers with Reynolds numbers: (a) flow without; and (b) flow with triangular prism

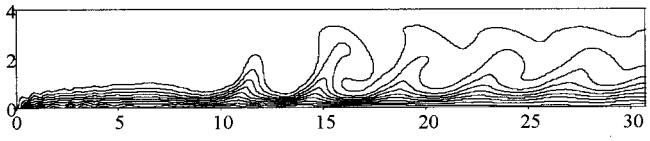

Fig. 4 Isotherms at Re=100 for the flow with triangular prism from 1 (at the bottom wall) to 0 (at the top wall) by interval 0.1

A series of computations were carried out, by increasing slowly the Reynolds number to determine the critical Reynolds number separating the symmetric and periodic flows. At Re=45 the wake loses its original symmetry. Oscillations in the wake grow in magnitude, and it begins to shed vortices into the stream. The flow in the wake becomes periodic. As in references [2,5], the destabilization of the flow happens without any need of imposing external perturbations, the action of small truncation errors and computer's round-off errors were sufficient to initiate vortex shedding. Jackson [6] report a critical Reynolds number of 31 from numerical investigation of flow around a triangular prism of the same geometry as ours but placed in an infinite medium (0 percent blockage). We estimate that this difference in Re_c is due to the presence of an important blockage (25 percent) in our configuration. As mentioned by Sohankar et al. [7], it may be conjectured that the critical Reynolds number characterizing the onset of vortex shedding increases with increasing blockage.

Recently, Fey et al. [8], based on their experiments, propose a new law for the vortex shedding from a circular cylinder which describes the Strouhal-Reynolds number dependency as: $St=a+b/\sqrt{Re}$. They have shown that such a formula seems to fit the data to some extent. In fact, this law, represents the first two terms of a series expansion in 1/root(Re) [$St=a+b/\sqrt{Re}+c/Re+\ldots$]. In the range $47<Re<180$, coefficients are $a=0.2684$ and $b=-1.0356$. For the triangular prism, this law is also in good agreement with numerical results, but coefficients are different and takes the values $a=0.2294$ and $b=-0.4736$. Comparing the coefficients b we deduce that the Strouhal number varies more quickly with Reynolds number for the circular cylinder placed in an infinite media than for triangular prism placed between two parallel plates.

In the following study our attention will be focused on the effect of the presence of the triangular prism on the heat transferred from the hot wall to the flow. Figure 2 is a plot of the local Nusselt number along the hot plate. At Re=30, the presence of triangular prism has just a little local effect by increasing slowly the local Nusselt number. In contrast, at Re=100 the effect of the presence of the triangular prism is more important, the solid line is well disturbed, but appears floating above the dashed line. An immediate conclusion can be made: the periodic flow leads to favor the heat transfer from the hot plate to the near flow, this heat is immediately transported by the Von Karmen street to the medium flow.

Figure 3 summarizes the variation of the space and time-averaged Nusselt numbers with Reynolds numbers. At relatively low Reynolds numbers corresponding to the symmetric and the beginning of periodic flows (Re$\leqslant$50) the presence of the triangular prism has no significant effect in the space and time-averaged Nusselt number $\langle\overline{\mathrm{Nu}}\rangle$. Increasing Reynolds number, curves start to separate, the presence of the triangular prism leads to an important increase of the space and time-averaged Nusselt number compared with that obtained without prism. At Re=250 this augmentation is about 85 percent. Indeed, in presence of the triangular prism, and for the fully periodic flow, the thermal boundary layer is well disturbed by the Von Karman street leading enhance heat transfer from the bottom wall to the flow (Fig. 4).

Conclusion

For the studied configuration shown in Fig. 1, results are summarized as follows: (1) the transition from symmetric flow to periodic flow is observed at Reynolds number in the vicinity of 45; (2) the Strouhal number of the periodic flow behaves as $\mathrm{St}=0.2294-0.4736/\sqrt{\mathrm{Re}}$; and (3) for the symmetric flow (Re$<$45) the presence of the triangular prism has only a local weak effects on the heat transfer and on the flow pattern, while, in periodic flow (Re$\geqslant$45), heat transfer is seen to increase strongly with Reynolds number in presence of the triangular prism. This result can be of interest in engineering.

References

[1] Saabas, H. J., and Baliga, B. R., 1994, ''Co-Located Equal-Order Control-Volume Finite-Element Method for Multidimensional, Incompressible, Fluid Flow Part I: Formulation,'' Numer. Heat Transfer, Part B, **26**, pp. 381–407.

[2] Davis, R. W., Moore, E. F., and Purtell, L. P., 1984, ''A Numerical-Experimental Study of Confined Flow Around Rectangular Cylinders,'' Phys. Fluids, **27**, No. 1, pp. 46–59.

[3] Evans, G., and Paolucci, S., 1990, ''The Thermoconvective Instability of Plane Poiseuille Flow Heated From Below: A Benchmark Solution for Open Boundary Flow,'' Int. J. Numer. Methods Fluids, **11**, pp. 1001–1013.

[4] Comini, G., Manzan, M., and Cortella, G., 1997, ''Open Boundary Conditions for the Streamfunction of Unsteady Laminar Convection,'' Numer. Heat Transfer, Part B, **31**, pp. 217–234.

[5] Persillon, H., and Braza, M., 1998, ''Physical Analysis of the Transition to Turbulence in the Wake of a Circular Cylinder by Three-Dimensional Navier-Stokes Simulation,'' J. Fluid Mech., **365**, pp. 23–88.

[6] Jackson, C. P., 1987, ''A Finite-Element Study of the Onset of Vortex Shedding in Flow Past Variously Shaped Bodies,'' J. Fluid Mech., **182**, pp. 23–45.

[7] Sohankar, A., Norberg, C., and Davidson, L., 1998, ''Low-Reynolds-Number Flow Around a Square Cylinder at Incidence: Study of Blockage, Onset of Vortex Shedding and Outlet Boundary Condition,'' Int. J. Numer. Methods Fluids, **26**, pp. 39–56.

[8] Fey, U., Konig, M., and Eckelmann, H., 1998, ''A new Strouhal-Reynolds-Number Relationship for the Circular Cylinder in the Range $47<\mathrm{Re}<2\times10^5$,'' Phys. Fluids, **10**, No. 7, pp. 1547–1549.

Combined Free and Forced Convection Film Condensation on a Finite-Size Horizontal Wavy Plate

Chi-Chang Wang
Postgraduate Student

Cha'o-Kuang Chen
e-mail: ckchen@mail.ncku.edu.tw
Professor

Department of Mechanical Engineering, National Cheng Kung University, Tainan,
Taiwan 701, Republic of China

Mixed-convection film condensation with downward flowing vapors onto a finite-size horizontal wavy plate is studied by a simple mathematical model and the spline alternating-direction implicit method. Effects of the wavy geometry, the interfacial vapor shear and the pressure gradient on the local condensate film thickness and the heat transfer characteristics have been studied independently. Results show that the pressure gradient tends to increase the heat transfer rate and to decrease the influence of the wavy amplitude. The appropriate wave number which can enhance the maximum condensation heat transfer rate is found in the neighborhood of lunder all circumstances. [DOI: 10.1115/1.1458019]

Keywords: Condensation, Film Cooling, Heat Transfer, Two-Phase, Wavy

Introduction

The problem of laminar film condensation of pure vapor on surfaces of various forms has been studied since Nusselt [1] obtained simple and explicit solutions for varied parameters. Following this, geometries such as plates and tubes have been studied under various conditions by many investigators. The free convection film condensation on the horizontal flat plate has been studied by Leppert and Nimmo [2] and Shigechi et al. [3]. Moreover, Shigechi proposed the following equation:

$$\mathrm{Nu}_m=0.82(\mathrm{Ra/Ja})^{0.2}. \tag{1}$$

In previous studies, the film condensation thickness at the plate edge (a necessary boundary condition) is either arbitrarily assumed or established by means of ''trial and error''. In fact, the above problem can be dealt with the concept of minimum mechanical energy in open-channel flow [4].

The prediction of heat transfer from irregular surface is a topic of fundamental importance. Irregularities frequently occur in the process of manufacture. Moreover, surfaces are sometimes intentionally roughened to enhance heat transfer since the presence of rough surfaces disturbs the flow and alter the heat transfer rate [5,6]. Another method to enhance heat transfer rate is about the velocity of the oncoming vapor. When the vapor surrounding a horizontal plate is moving with velocity, the problem becomes a type of mixed-convection film condensation and the analysis must consider the gravity, interfacial vapor shear force and the pressure gradient force. The objective of this study is to analyze the mixed-convection film condensation on a finite-size horizontal wavy plate, which is based on Nusselt's assumptions, together with

Contributed by the Heat Transfer Division for publication in the JOURNAL OF HEAT TRANSFER. Manuscript received by the Heat Transfer Division January 8, 2001; revision received July 31, 2001. Associate Editor: K. S. Ball.

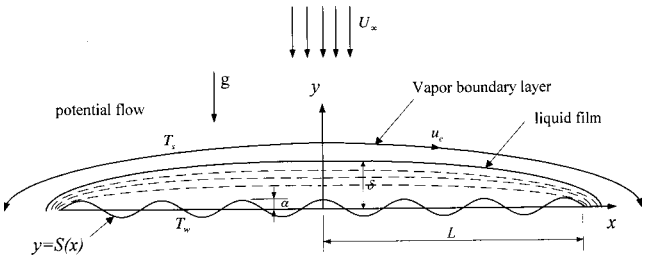

Fig. 1 Physic model and coordinate system

adopting the vapor shear model of Shekriladze and Gomelauri. Moreover, the film thickness at the plate edge will be determined by the concept of minimum mechanical energy.

Mathematical Formulation

The physical model and the coordinate system used are shown in Fig. 1. A wavy horizontal plate described by $S(x)=\alpha\cos(n\pi x/L)$ is immersed in downward flowing pure vapor which is at its saturation temperature T_s and moves at uniform velocity U_∞. This horizontal wavy plate is cooled internally thus the wall temperature T_w is uniform and lower than the vapor saturation temperature T_s. Therefore, a continuous condensate film will occur on the wall and run outward from the plate center to the plate edge under the combined effect of gravity, pressure gradient force, and interfacial vapor shear force. Based on these assumptions of Nusselt [1], the mass equation, momentum equations and the energy balance equation for the liquid laminar flow are described by the following equations:

$$\dot{m}=\int_{S(x)}^{\delta(x)}\rho u\,dy \tag{2}$$

$$0=-\frac{\partial p}{\partial x}+\mu\frac{\partial^2 u}{\partial y^2} \tag{3}$$

$$0=-\frac{\partial p}{\partial y}-\rho g \tag{4}$$

$$h'_{fg}\dot{m}'=k\left.\frac{\partial T}{\partial y}\right|_{y=S}\approx k\frac{T_s-T_w}{\delta-S}=k\frac{\Delta T}{\delta-S} \tag{5}$$

with the boundary and interface conditions

$$\text{(a)}\quad \text{at the wavy-wall (i.e., } y=S):u=0 \tag{6}$$

$$\text{(b)}\quad \text{at the interface (i.e., } y=\delta):\mu\frac{\partial u}{\partial y}\approx\dot{m}'u_e, \tag{7}$$

where $h'_{fg}=h_{fg}+3Cp\Delta T/8$ is the modified latent heat of condensate proposed by Rohsenow [7] to account for the effects of heat convection in the film. And at the liquid-vapor interface, the shear stress is equal to the loss of momentum flux of condensing vapor which is similar to that of Shekriladze and Gomelauri's [8].

Solve u in Eq. (3) and use Eqs. (4), (6) and (7), the following equation can be obtained:

$$u=\frac{1}{\mu}(\rho g\,\delta'-\rho_v u_e u'_e)\left(\frac{y^2+S^2}{2}-y\,\delta+\delta S\right)+\frac{\dot{m}'}{\mu}u_e(y-S), \tag{8}$$

where u_e is the tangential vapor velocity at the edge of the boundary layer. It can be obtained by potential flow theory.

Substitute Eqs. (2) and (8) into Eq. (5) and use the following dimensionless variables

Table 1 A comparison of δ and $\mathrm{Re}^{-1/2}\,\mathrm{Nu}_m$ for different grid numbers ($F=20$, $P=1$, $\alpha=0.05$, $n=5.5$)

Grid number	δ		$\mathrm{Re}^{-1/2}Nu_m$	
	x=0	x=1	x=0	x=4
100	0.696986	0.003280	1.545628	1.738114
300	0.684907	0.003291	1.575033	1.789175
500	0.684962	0.003324	1.574898	1.787904
300*	0.685141	0.003266	1.574454	1.765389

*:Uniform grid

$$\bar{x}=\frac{x}{L},\quad \bar{\delta}=\frac{\delta}{L}\sqrt{\mathrm{Re}},\quad \bar{\alpha}=\frac{\alpha}{L}\sqrt{\mathrm{Re}},\quad \bar{u}_e=\frac{u_e}{U_\infty},\quad \mathrm{Ja}=\frac{C_p\Delta T}{h'_{fg}}$$
$$\mathrm{Ra}=\frac{\rho^2 g\,\mathrm{Pr}\,L^3}{\mu},\quad \mathrm{Re}=\frac{\rho U_\infty L}{\mu},\quad \mathrm{Pr}=\frac{\mu C_p}{k},\quad F=\frac{\mathrm{Ra}}{\mathrm{Ja}\,\mathrm{Re}^{5/2}}, \tag{9}$$
$$P=\frac{\mathrm{Pr}}{\mathrm{Ja}}\frac{\rho_v}{\rho}.$$

The dimensionless governing equation may then become

$$(\bar{\delta}-\bar{S})\frac{d}{d\bar{x}}\left\{(F\bar{\delta}'-P\bar{u}_e\bar{u}'_e)\frac{(\bar{S}-\bar{\delta})^3}{3}+\bar{u}_e\frac{\bar{\delta}-\bar{S}}{2}\right\}=1 \tag{10}$$

with the following boundary conditions:

$$\text{(a)}\quad \text{at } \bar{x}=0:\frac{d\bar{\delta}}{d\bar{x}}=0 \tag{11}$$

$$\text{(b)}\quad \text{at } \bar{x}=1:3456\dot{\bar{m}}^3+180\dot{\bar{m}}^2\bar{u}_e-\left(2240\frac{\mathrm{Pr}}{\mathrm{Ja}}F\dot{\bar{m}}(\bar{\delta}-\bar{S})+\bar{u}_e^3\right)=0, \tag{12}$$

where

$$\dot{\bar{m}}=\frac{\bar{u}_e}{2}+\frac{1}{3}(P\bar{u}_e\bar{u}'_e-F\bar{\delta}')(\bar{\delta}-\bar{S})^2. \tag{13}$$

In Eq. (12), the film thickness at the plate edge is established by the application of minimum mechanical energy principle, i.e.,

$$\left[\frac{\partial}{\partial\delta}\int_S^\delta\left(\frac{u^2}{2}+gy+\frac{p}{\rho}\right)\rho u\,dy\right]\Bigg|_{\dot{m}_c}=0. \tag{14}$$

The mean Nusselt number is defined as

$$\mathrm{Nu}_m=\frac{h_m L}{k}\frac{\sigma(x)}{x}=\frac{\sqrt{\mathrm{Re}}}{\bar{x}}\int_0^{\bar{x}}\frac{1}{\bar{\delta}-\bar{S}}d\bar{x}, \tag{15}$$

where

$$h_m=\frac{-k}{\sigma(T_w-T_\infty)}\int_0^\sigma\sqrt{(\partial T/\partial x)^2+(\partial T/\partial y)^2}\,d\sigma \tag{16}$$

$$\sigma=\int_0^x(1+S'^2)^{1/2}dx. \tag{17}$$

Table 2 A comparison of mean Nusselt numbers, Nu_m, for natural film condensation on a horizontal flat plate ($F=20$, $P=1$, $\alpha=0.05$, $n=5.5$, grid number=300)

Ra/Ja	Present method			Shigechi(1990)
	Pr/Ja=1	Pr/Ja=10	Pr/Ja=100	
1×10^2	1.86924	2.03384	2.05738	2.0597
1×10^4	4.69501	5.10805	5.16716	5.1739
1×10^6	11.79302	12.83157	12.98005	12.996
1×10^8	29.62201	32.23073	32.60368	32.644

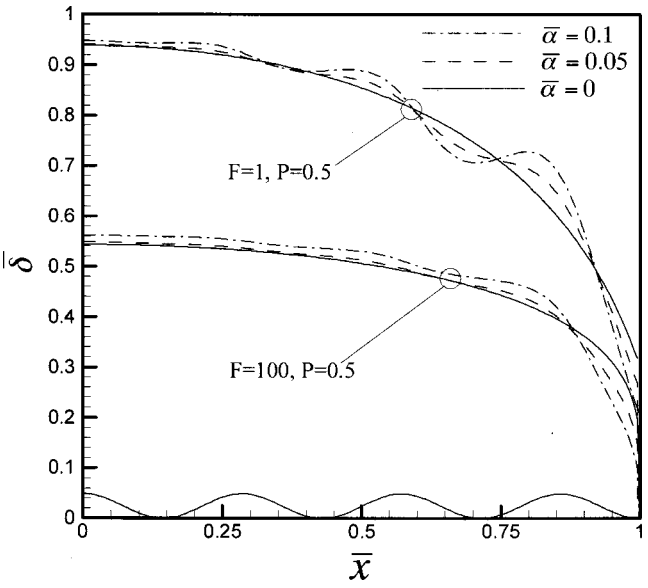

Fig. 2 Normalized film thickness along wavy plates for $P = 0.5$, $n = 7$, and Pr/Ja=50

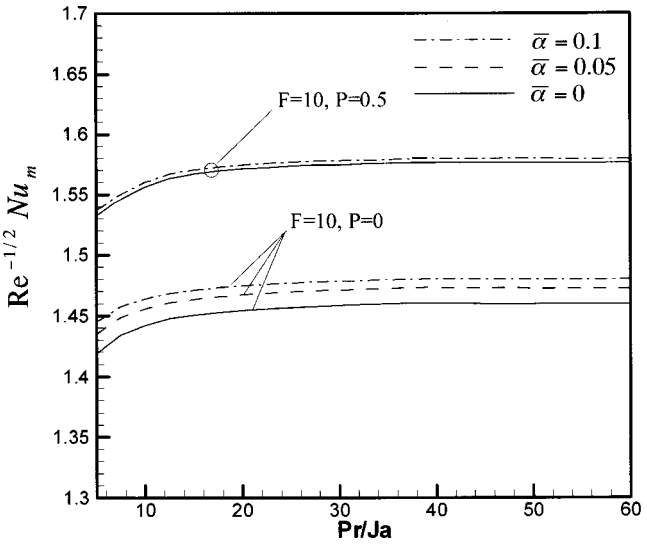

Fig. 4 A comparison of mean Nusselt numbers for a flat plate and wavy plates ($F = 10$, $n = 7$)

It should be noted that the mean Nusselt number is obtained by averaging the heat transfer flux over the surface from the plate center to $\sigma(x)$.

Results and Discussion

Equation (22) is solved numerically by using the cubic spline approximation [9]. This method can evaluate the spatial derivative terms directly without any finite difference discretization and the requirement of a uniform mesh is not necessary. As shown in Table 1, the test of grid independence, which shows that the difference between results of grids of 300 and 500 is less than 0.1 percent in both condensate film thickness and mean Nusselt number. Therefore, the nonuniform grid of 300 with smaller spacing mesh near the plate edge is employed in this study. To verify the accuracy of the present method, comparing with Shigechi [3] has also been shown in Table 2 and finds to agree favorably.

Figure 2 shows the variation of the film thickness along the wavy plate, the film thickness at the middle plate increases with the dimensionless wavy amplitude. Next, the dimensionless film thickness of the wavy plate tends to decrease rapidly near the plate edge as the fluid moves downstream, which is different from the behavior of the flat plate. It is also found that the amplitude of the dimensionless film thickness tends to increase with the axial coordinate $\overline{x}$ and the wavy amplitude.

Figure 3 shows the variation of $\mathrm{Re}^{-1/2}\,\mathrm{Nu}_m$ with $\overline{x}$. As the axial coordinate increases or the dimensionless wavy amplitude decreases, the amplitude of the mean Nusselt number will decrease. Therefore, we can observe that the variation of the mean Nusselt number only occurs near the plate center when larger wavy amplitudes are used. Also, a lower F results in a lower $\mathrm{Re}^{-1/2}\,\mathrm{Nu}_m$ for all wavy surfaces.

Figure 4 shows the variation of the mean Nusselt number with Pr/Ja. The parameter Pr/Ja is only found in Eq. (12) that can determine the film thickness $\overline{\delta}_{\min}$ at the plate edge. In cases of the

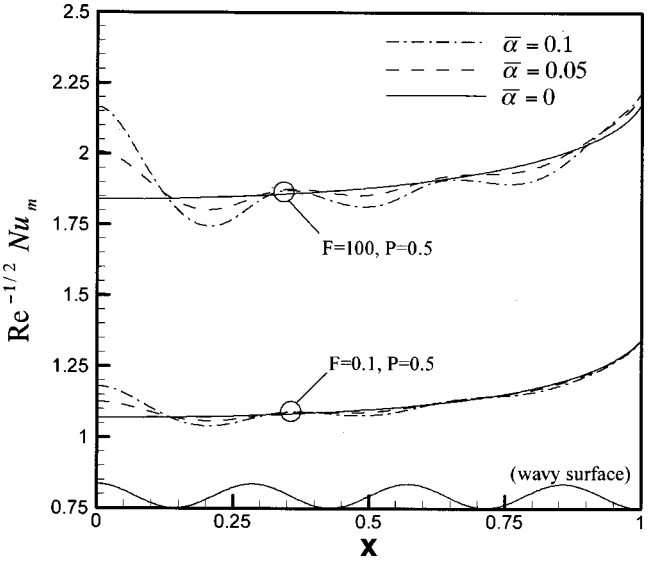

Fig. 3 Distribution of mean Nusselt number for $P = 0.5$, $n = 7$, and Pr/Ja=50

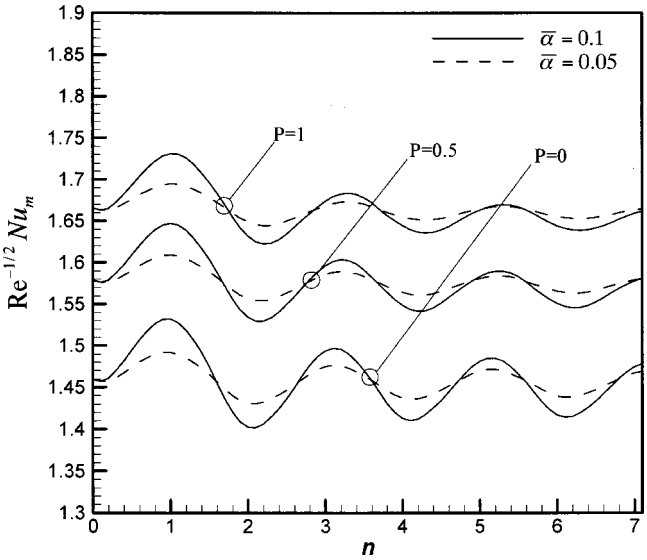

Fig. 5 Dependence of mean Nusselt number on wave number for $F = 10$ and Pr/Ja=100

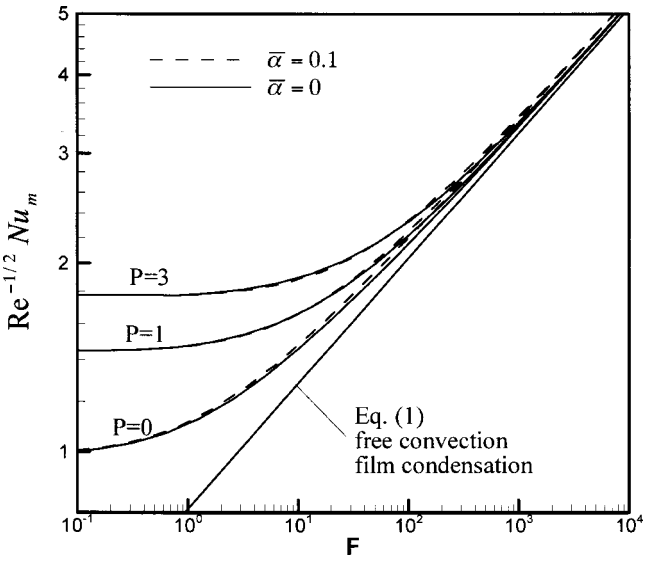

Fig. 6 Dependence of mean Nusselt number on *F* for combined forced and natural convection condensation (*n*=7, Pr/Ja =100)

flat surface and the wavy surface, both mean Nusselt numbers increase with parameter Pr/Ja and approach constant values. Moreover, the mean Nusselt number of wavy surface is higher than that of the flat plate, especially if the pressure gradient parameter is small.

Figure 5 show the dependence of the mean Nusselt number on the wave number. It is found that, for increasing the wave number the mean Nusselt numbers of the wavy surface show the sinusoidal curves, whose amplitudes decrease with the pressure gradient and increase with the wave amplitude. Peaks of the mean Nusselt number curres will occur under the wave number approaches to be odd (i.e., 1,3,5 . . .). As the wave number is quite large (i.e., the case of a rough surface), the mean Nusselt number tends to be a constant value, which equals that of the flat plate (i.e., $n=0$). This outcome is due to that although the wavy surface has a larger heat transfer area, the thermal resistance will also increase for the condensate accumulates between the trough and crest.

Figure 6 shows the dependence of the mean Nusselt number on *F*. It is seen that as *F* is greater than 100, all solutions in Eq. (10) tend to blend with the free convection (quiescent vapor) film condensation solution. For the other extreme, when *F* decreases to be zero (e.g., vapor velocity increases and the effect of gravity decreases), the mean heat transfer will change from the free-convection region into the forced-convection region through a transition zone. Moreover, increasing the pressure gradient makes the mean heat transfer coefficient increase, especially in the forced-condensation region.

Conclusions Remarks

1. The harmonic curves of the film thickness and mean Nusselt numbers have the same frequency as that of the wavy surface.
2. A larger pressure gradient will increase the total heat transfer rate but decrease the influence of wavy amplitude.
3. The maximum enhancement in heat transfer rate is found as only one wavy surface exists in the plate. It is due to that the special case has the smallest thermal resistance and the best angle to accelerate the flow outward at the plate edge.

Nomenclature

C_p = specific heat of the fluid at constant pressure
F = dimensionless parameter
g = acceleration of gravity
h_{fg} = latent heat of condensate
Ja = Jacob number
k = thermal conductivity of condensate
L = plate half length
$\dot{m}$ = condensate mass flow rate
n = wavy number
Nu_x, Nu_m = local and mean Nusselt number
p = pressure
P = dimensionless pressure gradient parameter
Pr = Prandtl number
Ra = Rayleigh number
Re = generalized Reynolds number
u_e = vapor velocity at the edge of the boundary layer
T = temperature
u,v = velocity components

Greek Symbols

α = amplitude of wavy surface
δ = condensate film thickness
μ = dynamic viscosity
ρ, ρ_v = density of condensate and vapor, respectively

Superscripts

$\bar{}$ = dimensionless variables
$'$ = derivative with respect to x, i.e., d/dx

References

[1] Nusselt, W., 1916, "Oberflachen Condensation Des Wasserdampfes," Zeitschrift des Vereines Deutscher Ininuere, **60**, pp. 541–569.
[2] Leppert, G., and Nimmo, B., 1968, "Laminar Film Condensation on Surfaces Normal to Body of Inertial Forces," ASME J. Heat Transfer, **80**, pp. 178–179.
[3] Shigechi, T., Kawa, N., Tokita, Y., and Yamada, T., 1990, "Film Condensation Heat Transfer on a Finite-Size Horizontal Plate Facing Upward," Trans. Jpn. Soc. Mech. Eng., Ser. B, **56**, pp. 205–210.
[4] Yang, S. A., and Chen, C. K., 1992, "Laminar Film Condensation on a Finite-Size Horizontal Plate with Suction at the Wall," Appl. Math. Model., **16**, pp. 325–329.
[5] Webb, R. L., Rudy, T. M., and Kedzierski, M. A., 1985, "Prediction of the Condensation Coefficient on Horizontal Integral-Fin Tubes," ASME J. Heat Transfer, **107**, pp. 369–376.
[6] Honda, H., Takamatsu, H., and Takata, N., 1999, "Experimental Measurements for Condensation of Downward-Flowing R123/R134a in a Staggered Bundle of Horizontal Low-Finned Tubes with Four Fin Geometries," Int. J. Refrig., **22**, 615–624.
[7] Rohsenow, W. M., 1956, "Heat Transfer and Temperature Distribution in Laminar Film Condensation on a Horizontal Tube," Int. J. Heat Mass Transf., **27**, pp. 39–47.
[8] Shekriladze, I. G., and Gomelauri, V. I., 1966, "The Theoretical Study of Laminar Film Condensation of a Flowing Vapor," Int. J. Heat Mass Transf., **9**, pp. 581–591.
[9] Rubin, S. G., and Graves, R. A., 1975, "Viscous Flow Solution with a Cubic Spline Approximation," Comput. Fluids, **1**, No. 5, pp. 1–36.

Enclosed Buoyant Convection With Internal Heat Generation Under Oscillating Sidewall Temperature

Gi Bin Kim

Jae Min Hyun
e-mail: jmhyun@cais.kaist.ac.kr

Department of Mechanical Engineering,
Korea Advanced Institute of Science & Technology,
373-1 Kusong-dong, Yusong-gu,
Taejon 305-701, South Korea

Ho Sang Kwak
School of Mechanical Engineering,
Kumoh National University of Technology,
188 Shinpyung-dong, Kumi,
Kyongbuk 730-701, South Korea

Keywords: Unsteady Buoyant Convection, Internal Heat Generation, Resonance

1 Introduction

Buoyant convection in an enclosure induced by uniform internal heat generation has been extensively studied (Acharya and Goldstein [1], Bergholz [3], Fusegi et al. [4], Kulacki and Goldstein [6], May [10]). One canonical layout is a rectangular cavity with two vertical sidewalls at constant temperatures and two insulated horizontal endwalls, with large Rayleigh number Ra ($>10^5$), Prandtl number O(1) and cavity aspect ratio O(1). In particular, when both vertical sidewalls are maintained at the same temperature T_0, the overall flow is expectedly symmetric about the vertical centerline. In each half-cavity, the fluid rises (sinks) near the centerline (near the vertical sidewall) region, which forms a single circulation cell.

Recently, buoyant flows induced by time-periodic boundary conditions, with no internal heat generation, emerge to be a subject of considerable interest (Antohe and Lage [2], Kwak and Hyun [7], Kwak et al. [8], Lage and Bejan [9]). The overriding concern here is the existence of resonance, which was first observed in the numerical studies of Lage and Bejan [9] and was corroborated later by Antohe and Lage [2]. It was illustrated that, when the frequency of the time-periodic boundary condition matches the proper resonance frequency, convective activities in the cavity are invigorated. This gives rise to a substantial increase in the amplitude of the fluctuating heat transfer coefficient in the cavity interior. The analytical endeavor of Lage and Bejan [9], based on the concept of a fluid wheel inside the cavity, suggested ways to make an order-of-magnitude estimate of the resonance frequency. In a related effort, Kwak and Hyun [7] and Kwak et al. [8] asserted that resonance is anticipated when the basic mode of the system eigenfrequencies is excited. They further argued that the system eigenfrequencies are characterized by the internal gravity oscillations in the interior, which are supported by the prevailing stratification.

This paper describes the time-dependent buoyant convection in an enclosure, with the presence of internal heat generation, under a time-periodic thermal boundary condition. Estimations of the resonance frequencies will be made, and physical explanations will be offered. This configuration simulates simplified models of post-accident heat removal in nuclear reactors and geophysical problems. Also, natural convection is important in fluids undergoing electrolytic processes or exothermic chemical reactions. As emphasized earlier, utilization of time-periodic thermal boundary conditions is explored as a possible means to control these processes or reactions. Convection in an air-conditioned room, subject to the daily-varying environmental temperature, provides an easy example of technological applications of the flow configuration under present study.

2 Formulation

Consider a square cavity, filled with an incompressible Newtonian fluid with spatially-uniform internal heat generation of constant strength q_0''', as sketched in Fig. 1. The left vertical sidewall is maintained at constant temperature T_0. The temperature T_r at the right vertical sidewall varies about T_0 sinusoidally with time, $T_r = T_0 + \Delta T' \sin(ft)$, in which $\Delta T'$ and f denote, respectively, the amplitude and frequency of oscillation.

Flow is governed by the time-dependent Navier-Stokes equations, with the invocation of the Boussinesq-fluid relationship $\rho = \rho_0[1-\beta(T-T_0)]$, which, after non-dimensionalization, read

$$\frac{\partial U}{\partial X} + \frac{\partial V}{\partial Y} = 0, \tag{1}$$

$$\frac{\partial U}{\partial t} + U\frac{\partial U}{\partial X} + V\frac{\partial U}{\partial Y} = -\frac{\partial P}{\partial X} + \left(\frac{\mathrm{Pr}}{\mathrm{Ra}_I}\right)^{1/2}\left(\frac{\partial^2 U}{\partial X^2} + \frac{\partial^2 U}{\partial Y^2}\right), \tag{2}$$

$$\frac{\partial V}{\partial t} + U\frac{\partial V}{\partial X} + V\frac{\partial V}{\partial Y} = -\frac{\partial P}{\partial Y} + \left(\frac{\mathrm{Pr}}{\mathrm{Ra}_I}\right)^{1/2}\left(\frac{\partial^2 V}{\partial X^2} + \frac{\partial^2 V}{\partial Y^2}\right) + \theta, \tag{3}$$

$$\frac{\partial \theta}{\partial t} + U\frac{\partial \theta}{\partial X} + V\frac{\partial \theta}{\partial Y} = \left(\frac{1}{\mathrm{Ra}_I\mathrm{Pr}}\right)^{1/2}\left(\frac{\partial^2 \theta}{\partial X^2} + \frac{\partial^2 \theta}{\partial Y^2}\right) + \left(\frac{1}{\mathrm{Ra}_I\mathrm{Pr}}\right)^{1/2}. \tag{4}$$

The associated boundary conditions can be expressed as

$$U = V = \frac{\partial \theta}{\partial Y} = 0, \quad \text{at } Y = 0,1; \tag{5}$$

$$U = V = \theta = 0, \quad \text{at } X = 0; \tag{6}$$

$$U = V = 0, \quad \theta = \varepsilon \sin(\omega\tau), \quad \text{at } X = 1. \tag{7}$$

In the above, dimensionless quantities are defined as

$$\tau = t(\mathrm{Ra}_I\mathrm{Pr})^{1/2}\frac{\kappa}{H^2}; \quad (X,Y) = \frac{(x,y)}{H};$$

$$(U,V) = (u,v)(\mathrm{Ra}_I\mathrm{Pr})^{-1/2}\frac{H}{\kappa};$$

$$\theta = \frac{k(T-T_0)}{H^2 q_0'''}; \quad P = \frac{(p+\rho_0 g y)H^2}{\rho_0 \kappa^2 \mathrm{Ra}_I\mathrm{Pr}}; \quad \mathrm{Pr} = \nu/\kappa; \tag{8}$$

$$\mathrm{Ra}_I = \frac{g\beta q_0''' H^5}{\kappa\nu k},$$

where (u,v) indicate dimensional velocity components in the horizontal (x) and vertical (y) directions, and ρ_0 the reference density evaluated at the cold-wall temperature (T_0), and ν and κ denote the kinematic viscosity and thermal diffusivity, respectively, and β the isobaric coefficient of volumetric thermal expansion. The strength of internal heat generation is represented by the internal Rayleigh number, Ra_I. All fluid properties are assumed to be constant.

Contributed by the Heat Transfer Division for publication in the JOURNAL OF HEAT TRANSFER. Manuscript received by the Heat Transfer Division April 3, 2001; revision received September 6, 2001. Associate Editor: M. Faghri.

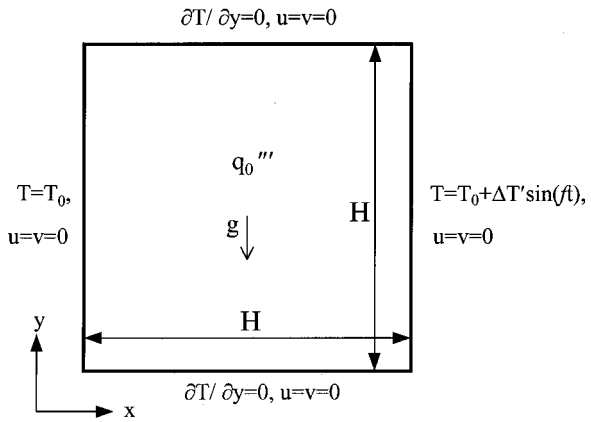

Fig. 1 Flow configuration

Time is nondimensionalized by using the system Brunt-Väisäla frequency N, i.e.,

$$N \equiv \left[\frac{g\beta(q_0'''H^2/k)}{H}\right]^{1/2} = (\mathrm{Ra}_I \mathrm{Pr})^{1/2}\frac{\kappa}{H^2}. \tag{9}$$

The nondimensional amplitude and frequency of the right-sidewall temperature fluctuation are

$$\varepsilon \equiv \frac{k\Delta T'}{q_0'''H^2}; \quad \omega \equiv \frac{f}{N}. \tag{10a,b}$$

In the above development, the system-wide temperature scale is derived from the internal heat generation, i.e., $q_0'''H^2/k$, and this scale is employed consistently, e.g., in Eqs. (8), (9), and (10*a*).

Numerical solutions are acquired by using the well-documented finite-volume computational procedure (e.g., Hayase et al. [5], Patankar [12]).

3 Results and Discussion

For all the computations, the Prandtl number was set Pr=7.0 to simulate water.

In the computations, the value of ε was set $\varepsilon/\theta_m = 0.3$. This choice of ε was based on the considerations explained below. First, ε should be small enough not to seriously distort the prevailing steady-state flow. In a series of detailed calculations, Kwak et al. [8] demonstrated that, when ε is small, i.e., $\varepsilon \leqslant 0.5$, the amplitude of fluctuating Nusselt number in the interior is approximately proportional to ε. Secondly, the presence of multiple resonance was observed by Antohe and Lage [2] when the nondimensional amplitude of wall heat flux oscillation was larger than 0.1. The value of $\varepsilon/\theta_m = 0.3$ was selected to meet the aforementioned two dynamical issues. The nondimensional frequency of oscillation ω encompasses a wide range, $0.005 \leqslant \omega \leqslant \mathrm{O}(1)$.

In the analysis of the computed results, it is advantageous to introduce the following notations, i.e.,

$$\mathrm{Nu}_X^*(\tau) \equiv \frac{\mathrm{Nu}_X(\tau) - \mathrm{Nu}_X^B}{\mathrm{Nu}_{X=1}^B}, \tag{11a}$$

$$A(\mathrm{Nu}_X^*) \equiv \frac{\mathrm{Max}\{\mathrm{Nu}_X^*(\tau)\} - \mathrm{Min}\{\mathrm{Nu}_X^*(\tau)\}}{2}, \quad \tau_0 \leqslant \tau \leqslant \tau_0 + \frac{2\pi}{\omega}. \tag{11b}$$

In the above, $\mathrm{Nu}_X^*(\tau)$ indicates the difference between the instantaneous Nu value (at $X=X$ and $\tau=\tau$) and the corresponding value Nu_X^B of the case of non-oscillating sidewall temperature ($\varepsilon=0$). The amplitude of Nu-value fluctuations is expressed by $A(\mathrm{Nu}_X^*)$.

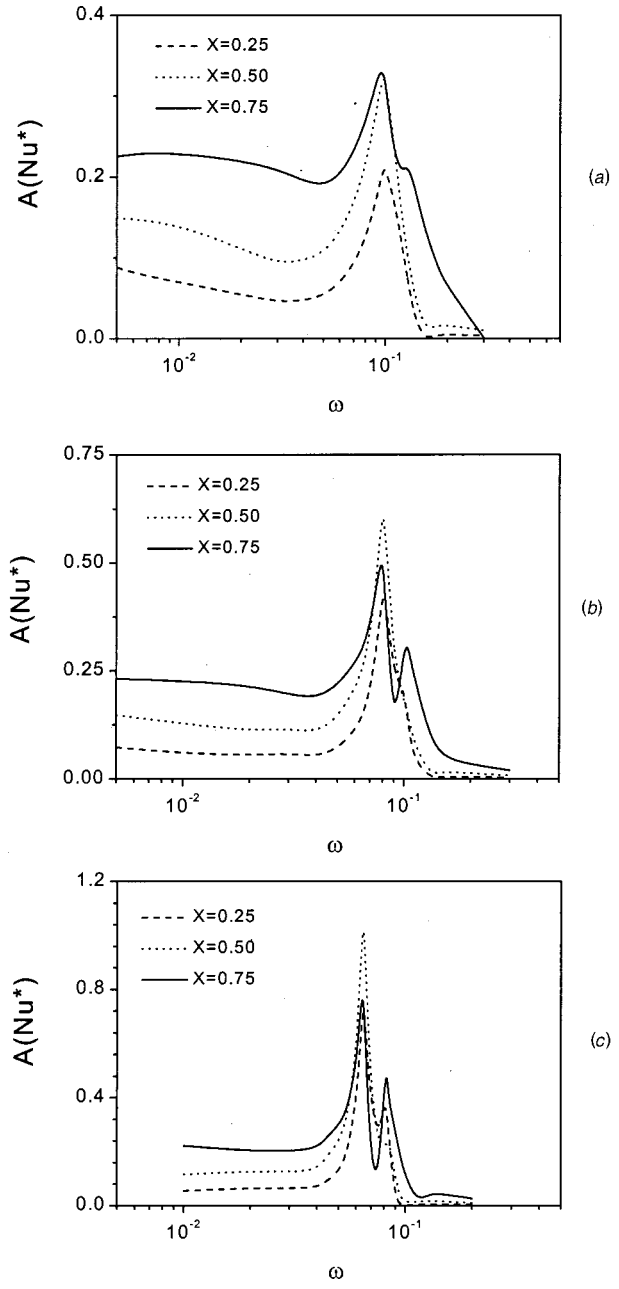

Fig. 2 *A*(Nu*) versus ω plots: (*a*) $\mathrm{Ra}_I = 10^8$; (*b*) $\mathrm{Ra}_I = 10^9$; and (*c*) $\mathrm{Ra}_I = 10^{10}$.

As stressed by Lage and Bejan [9], the amplitude of Nu-fluctuation, $A(\mathrm{Nu}^*)$, at the centerline ($X=0.5$) is of particular interest. This is representative of the intensity of time-dependent heat transfer activities in the interior core. Figure 2 displays the collection of numerical data of $A(\mathrm{Nu}_X^*)$ in the interior region versus ω for varying Ra_I. It is clear that the amplitude of Nu-fluctuation, $A(\mathrm{Nu}_X^*)$, peaks at certain particular frequencies; this was interpreted to manifest the existence of resonance in the context of enclosed buoyant convection (Lage and Bejan [9]). Frames (*a*), (*b*), and (*c*) of Fig. 2 show that the frequency at which the primary peak occurs, ω_{r1}, is largely unaffected by Ra_I. Furthermore, the secondary peak at ω_{r2} is visible for very high values of Ra_I, i.e., $\mathrm{Ra}_I \geqslant 10^9$.

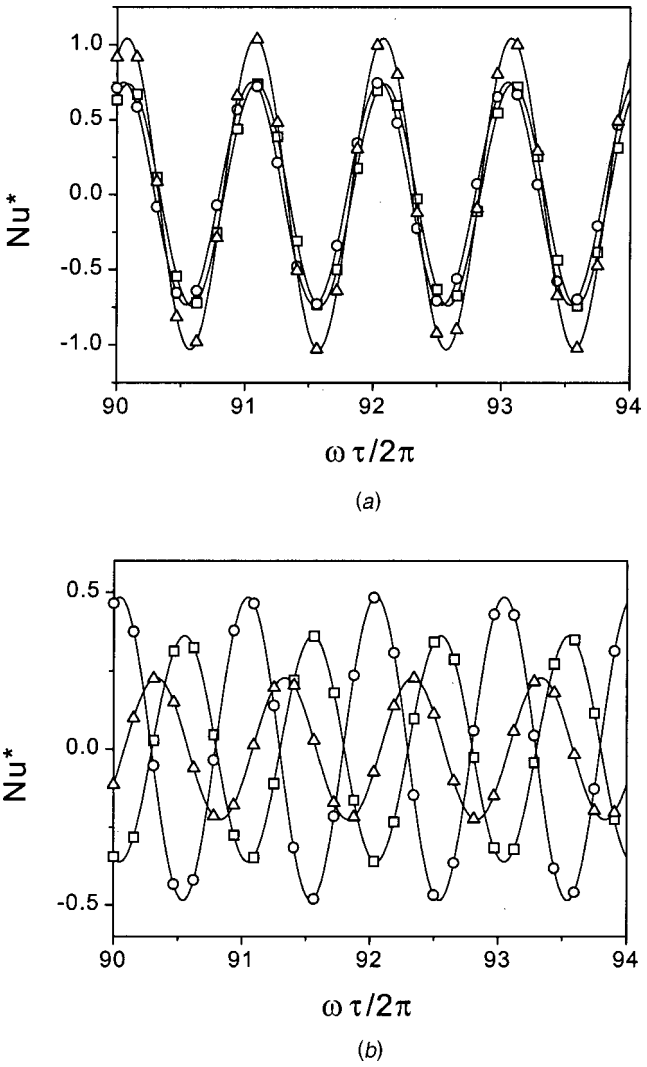

Fig. 3 Time history of Nu* at resonance frequencies. $Ra_I = 10^{10}$. Symbols □, △, and ○ denote the positions, $X = 0.25$, 0.5, and 0.75, respectively: (*a*) $\omega = 0.065(\approx \omega_{r1})$; and (*b*) $\omega = 0.082(\approx \omega_{r2})$.

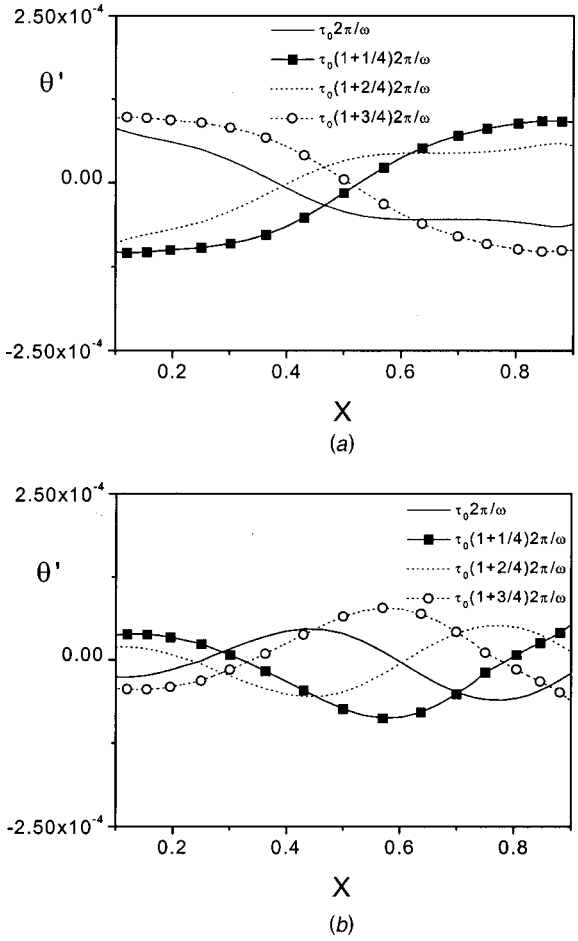

Fig. 4 Temperature fluctuations relative to the basic state. $Y = 0.5$, $Ra_I = 10^{10}$: (*a*) $\omega = 0.065(\approx \omega_{r1})$; and (*b*) $\omega = 0.082(\approx \omega_{r2})$.

The prior expositions by Kwak et al. [7–8] ascertained that resonance is anticipated when the eigenfrequencies of the system are excited. Furthermore, these intrinsic eigenfrequencies are characterized by the internal gravity oscillations in the stably stratified interior core. Paolucci and Chenoweth [11] calculated the modes of these oscillations, which, for a square cavity, can be expressed, in the present nondimensional form, as

$$\omega_n \equiv \frac{f_n}{N} = \frac{(\partial\theta/\partial Y)^{1/2}}{(1+1/n^2)^{1/2}}. \tag{12}$$

In the above, $\partial\theta/\partial Y$ denotes the average strength of stratification in the interior. In the practical calculation of $\partial\theta/\partial Y$, a linear curve-fitting was applied to the interior vertical temperature profile at a given location X. Here, n is the mode index, which is the ratio of the wave numbers in the horizontal and vertical directions. The primary mode is identified to be $n=1$, i.e., the scale of the whole cavity. The theoretical values of ω_1 obtainable from Eq. (12) are 0.098, 0.079, and 0.062 for $Ra_I = 10^8$, 10^9, and 10^{10}, respectively. The computed primary resonance frequencies ω_{r1}, as illustrated in Fig. 2, are respectively 0.098, 0.080, and 0.065, which are in close agreement with the results of Eq. (12). This comparison gives credence to the assertion that the resonance frequencies are determined by the modes of internal gravity oscillations. The secondary peak in Fig. 2 is identified to be the consequence of the excitation of ω_2 mode of Eq. (12). In this case, fluid motions based on $n=2$, which have the size of half-cavity, are under focus. Again, ω_2, calculated by Eq. (12), are 0.124, 0.100, and 0.078, while the present computed data for ω_{r2} are 0.123, 0.103, and 0.082, respectively, for $Ra_I = 10^8$, 10^9 and 10^{10}. As before, this favorable agreement reinforces the finding that the modes of internal gravity oscillations are the principal eigenfrequencies of the system.

The time histories of Nu_X^* are revealing. For the primary resonance mode ($\omega \cong \omega_{r1}$), as demonstrated in Fig. 3(*a*), convective fluid motions are intensified throughout the entire interior region of the cavity. Because of the dominant convective activities, the amplitudes of Nu-oscillation are substantial. The invigorated convective flows are propagated to the bulk of the interior from the sidewall of oscillating temperature; much of Nu in the cavity interior core does not show appreciable phase lags. When the sidewall temperature oscillates at the secondary resonance frequency ($\omega \cong \omega_{r2}$), as depicted in Fig. 3(*b*), considerable phase lags are discernible in the interior. The phase lag is π radian between $X = 0.25$ and $X = 0.75$. This implies that the convective motions at ω_{r2} take place with opposite phases between these two locations.

At higher values of ω, the effect of sidewall temperature oscillation is confined to the region close to the wall, and the influence of sidewall temperature oscillation is meager at far-away locations. As a result, the amplitude of Nu_X^* oscillation at $X=0.75$ is larger than at other locations.

The behavior of temperature fluctuation in the interior at resonance is plotted in Fig. 4. The horizontal profiles of interior temperature oscillation at mid-height ($Y=0.5$) clearly exhibit [see Fig. 4(a)] the periodic tilting with ω_{r1}, which points to the source of internal gravity oscillations. This pattern is qualitatively similar to the observations of Kwak and Hyun [7] for a differentially-heated cavity with $q_0'''=0$. The spatial behavior of thermal field fluctuations at the secondary resonance frequency (ω_{r2}) is slightly more complex. A closer inspection of Fig. 4(b) discloses that there exist two branches of tilting, with a phase difference of approximately π radian, in the left and right regions of the cavity. This points to the fact that the gradients of fluctuating temperature in both regions have opposite signs at each time instant.

4 Concluding Remarks

The primary-peak resonance at ω_{r1} is distinct. The secondary-peak resonance at ω_{r2} is detected for higher Ra_I. The instantaneous Nusselt number fluctuation at ω_{r1} indicates the presence of cavity—scale motions, which are qualitatively similar to those of a differentially—heated cavity. For the secondary resonance frequency ω_{r2}, the tilting of the interior isotherms is of a concave/convex shape. The theoretical predictions of the resonance frequencies, based on the modes of internal gravity oscillations, are in accord with the present numerical data.

Acknowledgment

This work was supported by the grants from NRL, South Korea.

References

[1] Acharya, S., and Goldstein, R. G., 1985, "Natural Convection in An Externally Heated Vertical or Inclined Square Box Containing Internal Energy Sources," ASME J. Heat Transfer, **107**, pp. 855–866.

[2] Antohe, B. V., and Lage, J. L., 1996, "Amplitude Effect on Convection Induced by Time-Periodic Horizontal Heating," Int. J. Heat Mass Transf., **39**, No. 6, pp. 1121–1133.

[3] Bergholz, R. F., 1980, "Natural Convection of a Heat Generating Fluid in a Closed Cavity," ASME J. Heat Transfer, **102**, pp. 242–247.

[4] Fusegi, T., Hyun, J. M., and Kuwahara, K., 1992, "Natural Convection in a Differentially Heated Square Cavity With Internal Heat Generation," Numer. Heat Transfer, **21**, pp. 215–229.

[5] Hayase, T., Humphery, J. A. C., and Grief, R., 1992, "A Consistently Formulated QUICK Scheme for Fast and Stable Convergence Using Finite-Volume Iterative Calculation Procedures," J. Comput. Phys., **98**, pp. 108–118.

[6] Kulacki, F. A., and Goldstein, R. J., 1972, "Thermal Convection in a Horizontal Fluid Layer With Uniform Volumetric Energy Sources," J. Fluid Mech., **55**, pp. 271–287.

[7] Kwak, H. S., and Hyun, J. M., 1996, "Natural Convection in an Enclosure Having a Vertical Sidewall With Time-Varying Temperature," J. Fluid Mech., **329**, pp. 65–88.

[8] Kwak, H. S., Kuwahara, K., and Hyun, J. M., 1998, "Resonant Enhancement of Natural Convection Heat Transfer in a Square Enclosure," Int. J. Heat Mass Transf., **41**, pp. 2837–2846.

[9] Lage, J. L., and Bejan, A., 1993, "The Resonance of Natural Convection in an Enclosure Heated Periodically From the Side," Int. J. Heat Mass Transf., **36**, pp. 2027–2038.

[10] May, H. O., 1991, "A Numerical Study on Natural Convection in an Inclined Square Enclosure Containing Internal Heat Sources," Int. J. Heat Mass Transf., **34**, No. 4, pp. 919–928.

[11] Paolucci, S., and Chenoweth, D. R., 1989, "Transition to Chaos in a Differentially Heated Vertical Cavity," J. Fluid Mech., **210**, pp. 379–410.

[12] Patankar, S. V., 1980, *Numerical Heat Transfer and Fluid Flow*, McGraw-Hill.

A Method to Accelerate Convergence and to Preserve Radiative Energy Balance in Solving the P_1 Equation by Iterative Methods

Genong Li and Michael F. Modest

Department of Mechanical Engineering, The Pennsylvania State University, University Park, PA 16802

An acceleration method is proposed particularly for the P_1 equation. The radiative energy balance is used as a constraint to correct iterative solutions. The method not only accelerates convergence but also preserves the radiative energy balance, the latter being of great importance when radiation calculations are coupled with flow calculations. This acceleration method can be applied to other elliptical problems with boundary conditions of the second and/or the third kind. [DOI: 10.1115/1.1423318]

Keywords: Computational, Numerical Methods, Radiation, Acceleration, Iterative Method

Introduction

The P_1 approximation reduces the equation of transfer from a very complicated integro-differential equation to a relatively simple partial differential equation (the P_1 equation). Yet, the P_1 approximation is powerful, allowing non-black surfaces, non-constant properties, anisotropic scattering, etc. For the vast majority of important engineering problems (i.e., in the absence of extreme anisotropy in the intensity field), the method provides high accuracy at very reasonable computational cost. Furthermore, the P_1 approximation can easily be combined with sophisticated spectral models such as the Weighted-Sum-of-Gray-Gases method (WSGG) [1]. Currently, many commercial CFD codes such as FLUENT [2] have the P_1 approximation as an optional solution technique for radiation calculations.

The P_1 equation is a Helmholtz equation and it is conceptually simple to solve numerically. The only problem is that the boundary condition for this equation is of the third kind, which causes the convergence of the solution, by even the most sophisticated iterative methods, to be quite slow, especially when the absorption coefficient of the medium is small. A parallel problem is that unconverged, intermediate solutions of the P_1 equation during the iterative process do not satisfy the basic energy balance–computed total radiative heat source within the medium is not equal to computed total radiative heat flux through boundaries. When such a radiation calculation, without a fully-converged solution, is coupled with a flow calculation, the total energy balance is destroyed during the iterative process and may not converge.

Many approaches have been devised to speed up convergence of iterative methods such as block correction [3] and multigrid acceleration techniques [4]. While these approaches are effective in general and are already widely used in commercial CFD codes, they are not efficient enough, in particular, for equations with boundary conditions of the second and/or the third kind only, e.g., the P_1 approximation. This is because boundary conditions of the second and third kind prescribe only the gradient of an unknown, or a relation between the gradient of an unknown and the unknown itself. A large number of iterations are required for interior nodes as well as boundary nodes to adjust themselves to satisfy

Contributed by the Heat Transfer Division for publication in the JOURNAL OF HEAT TRANSFER. Manuscript received by the Heat Transfer Division February 22, 2001; revision received August 30, 2001. Associate Editor: R. Skocypec.

their governing equations and boundary conditions. Traditional acceleration techniques such as block correction and multigrid acceleration speed up convergence by adding some corrections to drive the solution toward global conservation. Such techniques may not be effective for elliptic equations with boundary conditions of the second and/or third kind. Another acceleration approach is the mesh rebalance method, which was developed by Wachspress [5] and Reed [6] in the context of neutron transport. The characteristic of the mesh rebalance method is that it corrects base iterative results by multiplying with correction factors to speed up convergence. This method has been applied to the discrete ordinated method (DOM) to solve the radiative transfer equation (RTE) [7].

A reduced mesh rebalance acceleration method, which corrects intermediate iterations by a uniform multiplication factor to satisfy the total radiative energy balance, is proposed in this note specifically for the P_1 approximation (a Helmholtz equation with boundary conditions of the second and/or third kind). The method can be used in conjunction with any existing iterative method to achieve faster convergence when solving the P_1 equation.

The Correction Procedure

In the P_1 approximation, the incident radiation, G, is governed by the Helmholtz equation [1]

$$\nabla\cdot\left(\frac{1}{\kappa+\sigma}\nabla G\right)=-3\kappa(4\pi I_b-G) \tag{1}$$

subject to the boundary condition,

$$-\frac{2-\epsilon}{\epsilon}\frac{2}{3}\hat{n}\cdot\nabla G=(\kappa+\sigma)(4\pi I_{bw}-G), \tag{2}$$

where κ and σ are the absorption and scattering coefficients of the radiating gas, respectively, I_b is the Planck function, ϵ is the surface emissivity, and $\hat{n}$ is the surface normal. In practice, the discretized P_1 equation is solved by iterative methods. Due to the nature of the boundary condition of the third kind, convergence of the solution tends to be very slow.

Conservation of radiative energy states that total radiative heat source in a radiating medium is always equal to total radiative heat flux through its boundaries, i.e.,

$$\int\int\int_{\mathcal{V}}\nabla\cdot\underline{q}^R dV=-\int\int_{\mathcal{S}}\hat{n}\cdot\underline{q}^R dS, \tag{3}$$

where q^R is the radiative heat flux vector, which also follows from the divergence theorem. In the P_1 approximation, the divergence of the radiative heat flux vector and the radiative heat flux at the boundaries are calculated as [1]

$$\nabla\cdot\underline{q}^R=\kappa(4\pi I_b-G),\quad -\hat{n}\cdot\underline{q}^R=\frac{\epsilon}{2(2-\epsilon)}(G-4\pi I_{bw}). \tag{4}$$

In iterative methods the converged solution of the P_1 equation satisfies the above energy balance; intermediate solutions during iterative process, however, often do not. In any realistic fire/combustion simulation, the solution to radiative transfer equation is coupled with the solution to the overall energy equation. Since $\nabla\cdot\underline{q}^R$ enters the energy equation as a source, while $-\hat{n}\cdot\underline{q}^R$ appears in the boundary conditions of the energy equation, it is apparent that the total energy balance will also be destroyed during the iterative process, if a partially converged radiative solution is employed. This, in turn, may slow down convergence of the overall energy equation as well.

To speed up convergence and to preserve radiative energy balance, Eq. (3) can be used as a constraint to correct the computed incident radiation field. The computed incident radiation at any node i after the n^{th} iteration, $G_i^{(n)}$, is multiplied uniformly by a factor $f^{(n)}$ to satisfy the discretized form of the energy balance. That is,

$$\sum_{i=1}^{N}\kappa_i(4\pi I_{b,i}-f^{(n)}G_i^{(n)})V_i=\sum_{j=1}^{M}\frac{\epsilon_j}{2(2-\epsilon_j)}(f^{(n)}G_j^{(n)}-4\pi I_{bw,j})A_j, \tag{5}$$

where N is the total number of nodes throughout the whole computational domain and M is the total number of boundary nodes; and V_i and A_j are the nodal volume of the i^{th} node and the boundary surface area of the j^{th} node, respectively.

The correction factor for the n^{th} iteration, $f^{(n)}$, is determined from the above equation as

$$f^{(n)}=\frac{\sum_{i=1}^{N}4\pi\kappa_i I_{b,i}V_i+\sum_{j=1}^{M}\frac{\epsilon_j}{2-\epsilon_j}2\pi I_{bw,j}A_j}{\sum_{i=1}^{N}\kappa_i G_i^{(n)}V_i+\sum_{j=1}^{M}\frac{\epsilon_j}{2(2-\epsilon_j)}G_i^{(n)}A_j}. \tag{6}$$

To implement this method, after each iteration the correction factor is calculated based on Eq. (6). The whole incident radiation field is then corrected by multiplication with the correction factor, $f^{(n)}$, guaranteeing that Eq. (3) is satisfied. As the solution converges, the correction factor gradually moves toward unity. Therefore, the correction procedure does not change the converged incident radiation field.

This correction method not only preserves the total radiative energy balance for partially converged solutions, but also accelerates convergence of the P_1 equation. This is because the correction procedure connects the incident radiation at boundary nodes directly to those of interior nodes, allowing the boundary condition to propagate much more quickly to the inner points, which usually means that the solution converges faster.

Test Problem

A simple two-dimensional problem has been chosen to test the convergence rate of the method, namely a cylindrical combustion chamber, which is 4 m long and 1 m in radius. The temperature field is given by $T(x,r)=8000(x/L)(1-x/L)(1-r/R)$ (K), where x,r, are axial and radial coordinates, respectively. The incident radiation field is to be calculated for different constant absorption coefficients. The problem is axisymmetric and an equally-spaced nodal system with 20×20 nodes is used. The P_1 equation is discretized at these nodes and different iterative methods are used to solve the discretized linear equations. The initial field of incident radiation is set to zero and the convergence criterion is set to $|f-1|\leqslant 1.0\times10^{-5}$. The Gauss-Seidel and the alternating direction line-by-line TDMA iterative methods (supplemented with block correction [3]) will be used with and without our new acceleration scheme. The latter iterative method is widely used and is the main iterative method adopted by many commercial CFD codes. In this method one complete iteration consists of block corrections and line-by-line TDMA sweeps in the row direction and in the column direction. The computed radiative heat sources and the number of iterations to reach the converged solu-

Table 1 Summary of numerical results from test problem

κ	Gauss-Seidel iteration				Line-by-line TDMA iteration			
	$\iiint \nabla \cdot \underline{q}^R dV$ (W)		number of iterations		$\iiint \nabla \cdot \underline{q}^R dV$ (W)		number of iterations	
(1/m)	w/o corr.	with corr.	w/o corr.	with corr.	w/o corr.	with corr.	w/o corr.	with corr.
10	2726	2699	20	9	2716	2698	6	5
1	421869	421491	987	210	421868	421786	165	44
0.1	113773	113756	14474	771	113773	113768	2449	192
0.01	12292	12292	149537	934	12292	12292	25927	236

tion are summarized in Table 1. From the table it is seen that the correction procedure is very effective, especially for optically thin media. For an absorption coefficient of $\kappa = 0.01\ \mathrm{m}^{-1}$ the required number of iterations, or, essentially, the cpu time (since the overhead of cpu time spent in the correction procedure is small—only about five percent of that used in the original base iteration) is reduced to less than 1 percent, regardless of whether the Gauss-Seidel or the line-by-line TDMA iterative methods are employed. Although the line-by-line TDMA iterative method converges after fewer iterations than the Gauss-Seidel method, the correction procedure is equally effective with either one, especially for optically thin media. To further evaluate the performance gains from the correction method, a relative error, defined as $1/N\Sigma_{i=1}^{N}|G_i - G_{\mathrm{conv},i}|/G_{\mathrm{conv},i}$, where $G_{\mathrm{conv},i}$ denotes the converged solution at node i, is plotted versus the number of iterations in Fig. 1 for the case of $\kappa = 1\ \mathrm{m}^{-1}$. It is clear that the solution converges after fewer iterations to the exact solution if the correction procedure is applied. The evolution of the computed total radiative heat source and the total radiative heat flux along the iterative process is shown in Fig. 2. Although an energy balance is ultimately reached when the solution has converged, the total radiative heat source is not equal to the total radiative heat flux through the boundaries during the iterative process if the conventional method is used. In contrast, the method with correction procedure always maintains equilibrium between radiative heat source and the radiative wall flux throughout the iterative process.

While the P_1 approximation with its Helmholtz equation was of particular interest here, its applicability is not limited to this type of problem. The method should perform equally well for all elliptic problems with boundary conditions of the second (specified gradient) and/or third (mixed) kind. For example, applying the method to steady-state conduction of a two-dimensional cylinder with convective boundary conditions leads to very similar results and conclusions (i.e., best acceleration for small heat transfer coefficients, corresponding to small absorption coefficients in the P_1 approximation, and preservation of the conductive energy balance during iterative process).

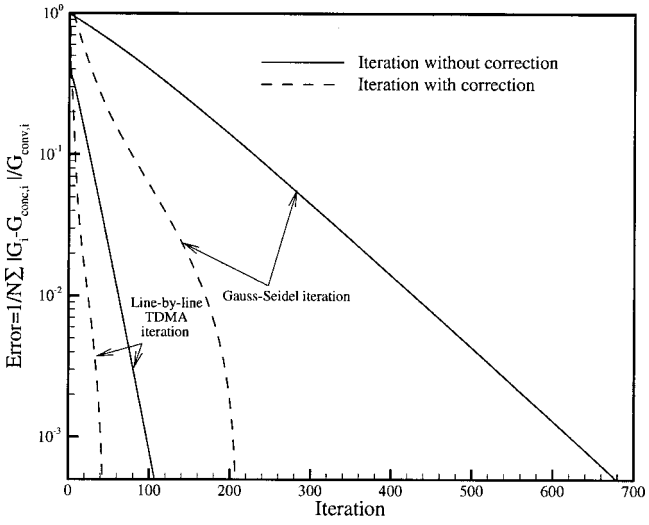

Fig. 1 Relative error change versus number of iterations

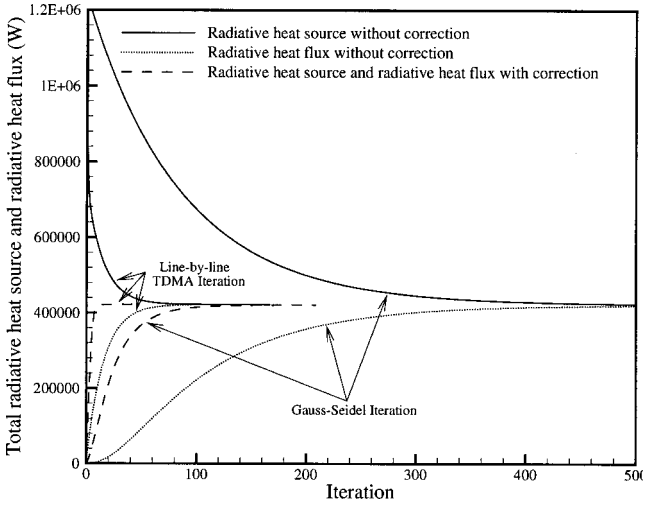

Fig. 2 Computed radiative heat source and radiative heat flux versus number of iterations

Conclusions

A corrective acceleration procedure is proposed for the iterative solution of the discretized P_1 equation (or any other elliptical partial differential equations subject to boundary conditions of the second or third kind), which can be used in conjunction with any iterative method. The procedure not only accelerates the convergence rate of the solution, but also preserves the radiative energy balance during the iterative process, which is desirable when radiation calculations are coupled with flow field calculations. A test problem demonstrated that accelerated iteration is achieved for all optical regimes, with speed-up of more than 100 times for optically thin situations.

Acknowledgment

This research is funded by the National Science Foundation through grant number CTS-9732223.

References

[1] Modest, M. F., 1993, *Radiative Heat Transfer*, McGraw-Hill, New York.
[2] FLUENT, 1995, "Computational Fluid Dynamics Software," Version 4.
[3] Patankar, S. V., 1981, "A Calculation Procedure for Two-Dimensional Elliptic Situations," Numer. Heat Transfer, **4**, pp. 409–425.
[4] Ferziger, J. H., 1998, *Numerical Methods for Engineering Application*, John Wiley & Sons, New York.
[5] Wachspress, E. L., 1966, *Iterative Solution of Elliptic Systems and Applications to the Neutron Diffusion Equations of Reactor Physics*, Prentice-Hall, Englewood Cliffs, NJ.
[6] Reed, W. H., 1971, "The Effectiveness of Acceleration Techniques for Iterative Methods in Transport Theory," Nucl. Sci. Eng., **45**, No. 3, pp. 245–254.
[7] Fiveland, W. A. and Jessee, J. P., 1996, "Acceleration Schemes for the Discrete Ordinates Method," J. Thermophys. Heat Transfer, **10**, No. 3, pp. 445–451.

Stagnation Line Heat Transfer Augmentation Due to Freestream Vortical Structures and Vorticity

Aung N. Oo
Graduate Student
e-mail: aung@engr.mun.ca
Faculty of Engineering and Applied Science,
Memorial University of Newfoundland,
St. John's, Newfoundland, A1B 3X5, Canada

Chan Y. Ching
Associate Professor
Department of Mechanical Engineering, McMaster University, Hamilton, Ontario, L8S 4L7, Canada

An experimental study has been performed to investigate the effect of freestream vortical structures and vorticity on stagnation region heat transfer. A heat transfer model with a cylindrical leading edge was tested in a wind tunnel at Reynolds numbers ranging from 67,750 to 142,250 based on leading edge diameter of the model. Grids of parallel rods were placed at several locations upstream of the heat transfer model in orientations where the rods were perpendicular and parallel to the stagnation line to generate freestream turbulence with distinct vortical structures. All three components of turbulence intensity, integral length scale and the spanwise and transverse vorticity were measured to characterize the freestream turbulence. The measured heat transfer data and freestream turbulence characteristics were compared with existing empirical models for the stagnation line heat transfer. A new correlation for the stagnation line heat transfer has been developed that includes the spanwise fluctuating vorticity components.
[DOI: 10.1115/1.1471526]

Keywords: Convection, Enhancement, Heat Transfer, Turbulence, Vortex

Introduction

Heat transfer augmentation in the stagnation region due to freestream turbulence has been studied extensively [1–7]. Several studies [1–3,6,7] have been performed to understand the physics of the turbulent heat transport mechanism in the stagnation region and to develop empirical models of the heat transfer augmentation due to freestream turbulence. In most studies, the freestream turbulence is nearly isotropic generated using square-meshed grids. However, isotropic turbulence is more the exception in real life engineering applications. It is well established that the coherent vortical structures in a turbulent flow play an important role in momentum and heat transfer. However, attempts to examine the relationship between freestream vortical structures and stagnation region heat transfer are very limited. Oo and Ching [8] performed an experiment where grids of parallel rods were used to generate freestream turbulence with different orientations of vortical structures. They determined that heat transfer in the stagnation region due to freestream turbulence with different coherent structures had distinct characteristics.

A knowledge of the interaction of freestream vortical structures with the stagnation region boundary layer should lead to improved models of stagnation region heat transfer. The vorticity field is closely related with the turbulence structure and dissipation rate [9]. Analyzing the correlation between the vorticity field and the heat transfer augmentation should, therefore, provide further insight to the turbulent heat transfer mechanism in the stagnation region. There are several empirical models [1–3,6,7] that relate stagnation line heat transfer with the characteristics of the freestream turbulence, namely Reynolds number, streamwise turbulence intensity and the integral length scale. These empirical models, however, fail to reveal the influence of vorticity and vortical structures of the freestream turbulence.

Characterizing freestream turbulence with Tu, Re_D, and λ_x does not provide a complete picture of the turbulence, especially when the turbulence is anisotropic. Freestream turbulence can be better described if information pertaining to the vorticity field and the coherent vortical structures are included. The objective of this technical note is to present a relationship between the characteristics of the freestream turbulence, including the vorticity field, and stagnation region heat transfer presented in a previous paper [8]. The freestream vorticity was measured and an empirical model for the heat transfer augmentation that includes the freestream vorticity field developed.

Experimental Details

Heat transfer in the stagnation region was measured using a model with a cylindrical leading edge in a low-speed wind tunnel. Freestream turbulence with different orientations of primary vortices was generated using grids of 2.86 cm, 1.59 cm, and 0.95 cm diameter parallel rods. The grids were arranged in two different orientations, perpendicular and parallel to the stagnation line (Fig. 1). Heat transfer measurements were made with the grids 25d to 125d upstream of the model at three different Re_D of 67,750, 108,350, and 142,250. The experimental details and data reduction for the turbulence intensity and integral length scale are given in Oo and Ching [8]. The spanwise fluctuating vorticity components, ω_z and ω_y, were measured using a vorticity probe similar to the design of Foss and Haw [10]. The vorticity probe consists of a pair of parallel wires and an X-wire. The two spanwise fluctuating vorticity components were obtained separately by rotating the vorticity probe 90 deg. The hot wires were operated using DANTEC 55M01 constant temperature bridges, and the output voltages of the anemometers were digitized using a 16 channel 12 bit Keithley 570 System A/D converter, interfaced to a personal computer. The frequency response of each circuit was determined by standard square-wave test, and found to be about 30 kHz. The sampling frequency of the study ranged from 20 to 30 kHz.

The spanwise vorticity components were measured using the vorticity probe and approximated by:

$$\Omega_z = \frac{\Delta V}{\Delta x} - \frac{\Delta U}{\Delta y} = -\frac{1}{U}\frac{\Delta V}{\Delta t} - \frac{\Delta U}{\Delta y} \tag{1.a}$$

$$\Omega_y = \frac{\Delta U}{\Delta z} - \frac{\Delta W}{\Delta x} = \frac{\Delta U}{\Delta z} + \frac{1}{U}\frac{\Delta W}{\Delta t} \tag{1.b}$$

where ΔU is the difference between the instantaneous streamwise velocity measured by a pair of parallel wires separated in spanwise directions, Δy and Δz. The spanwise velocity derivatives, $\Delta V/\Delta x$ and $\Delta W/\Delta x$, were estimated using Taylor's hypothesis, i.e., $\Delta/\Delta x = -U^{-1}\,\Delta/\Delta t$. The performance of the vorticity probe was tested in the wake of a circular cylinder and the results are in agreement with those of Antonia et al. [11]. Experimental uncertainties in fluctuating vorticity components based on the uncertainty analysis of hot wire data by Yavuzkurt [12], was estimated to be 9.43 percent. The details of the uncertainty analysis are provided in a later section and the results presented in Tables 1 and 2.

Contributed by the Heat Transfer Division for publication in the JOURNAL OF HEAT TRANSFER. Manuscript received by the Heat Transfer Division September 1, 2001; revision received February 1, 2002. Associate Editor: H. S. Lee.

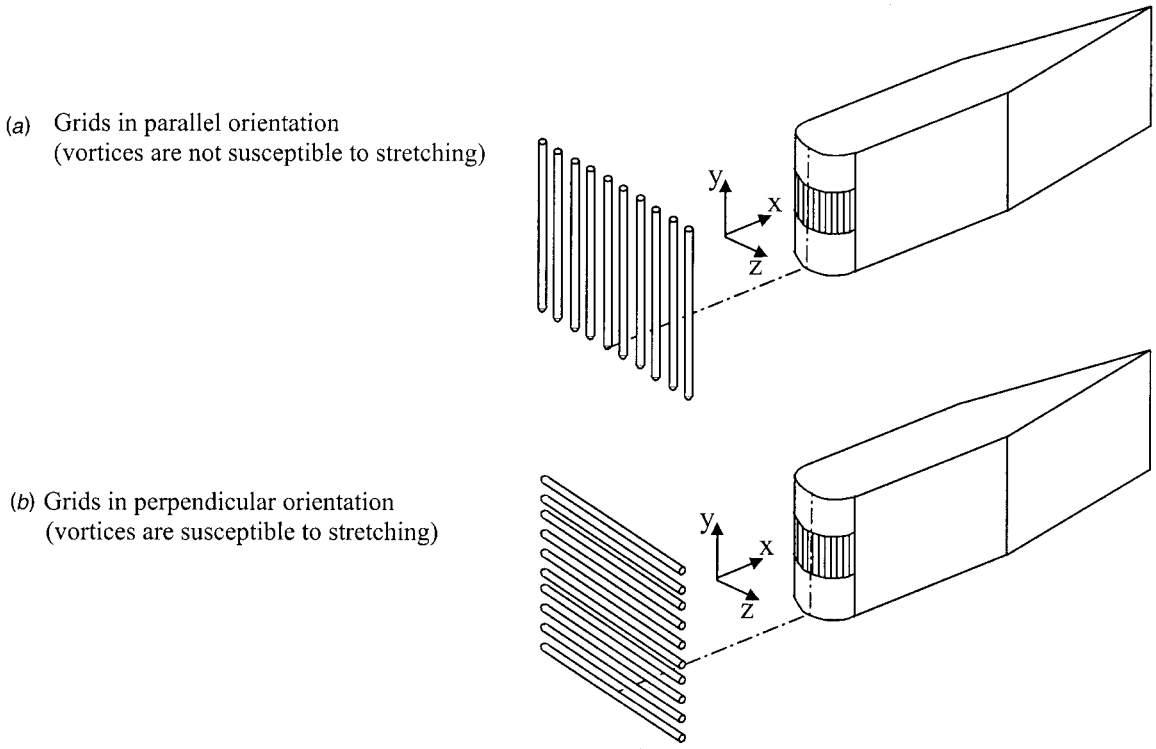

Fig. 1 Arrangements of grids

Table 1 Experimental uncertainty in Fr (percent)

Variable	Bias Error		Precision Error	
	Experimental Reynolds Number Range			
	Max.	Min.	Max.	Min.
Current I	0.18	0.26	0.53	0.51
Voltage Vo	0.06	0.08	0.20	0.21
Temperature difference ΔT	3.20	3.20	0.53	0.53
Conduction heat Q_{cond}	4.60	4.60	0.75	0.75
Radiation heat Q_{rad}	12.80	12.80	2.12	2.12
Convection heat Q_{cov}	1.61	2.10	0.55	0.60
Reynolds number Re_D	0.05	0.10	0.32	0.37
Frossling number *Fr*	3.58	3.83	0.79	0.82

Table 2 Experimental uncertainty in Tu, λx, and ω (percent)

	Experimental Reynolds Number Range	
	Maximum	Minimum
Velocity Calibration (Tu, λ_x)	0.07	0.14
Velocity Curve Fitting (Tu, λ_x)	2.18	2.18
Autocorrelation Curve Fitting (λ_x)	10.50	10.50
Turbulence Intensity *Tu*	3.09	3.09
Integral Length Scale λ_x	10.95	10.95
Fluctuating vorticity ω_z and ω_y	9.43	9.43

Results and Discussion

The turbulence intensity, integral length scale and spanwise velocity fluctuations downstream of the turbulence generating grids were presented in a previous paper [8]. The streamwise distribution of spanwise vorticity, normalized with the mean freestream velocity and diameter of the leading edge, are presented in Fig. 2 for Re_D=108,350. Since greater vorticity is usually associated with the smaller eddies in turbulence [9], the fluctuating vorticity component increases with smaller grid-rod for a given mean freestream velocity. For instance, at $x/d=25$, $\omega U/D$ ranges from about 20 to 25 for the 2.86 cm grid while it varies from about 32 to 39 for the 0.95 cm grid. An attempt to examine the isotropy of the rod-grid turbulence was made by estimating the degree of isotropy of the turbulence from the measurements taken with the single wire and the vorticity probe. For isotropic turbulence, $5\overline{(\partial u/\partial x)^2}$ is equal to $\overline{\omega_z^2}$ and $\overline{\omega_y^2}$ [13]. Therefore, the degree of isotropy is defined as:

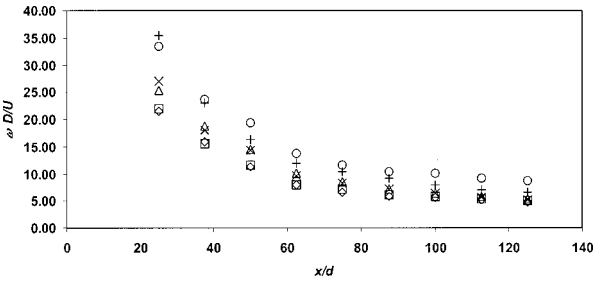

Fig. 2 RMS fluctuating vorticity components of grids in perpendicular orientation for Re_D=108,350 (2.86 cm rod-grid: ◇, ω_z; □, ω_y; 1.59 cm rod-grid: △, ω_z; ×, ω_y; 0.95 cm rod-grid: ○, ω_z; +, ω_y)

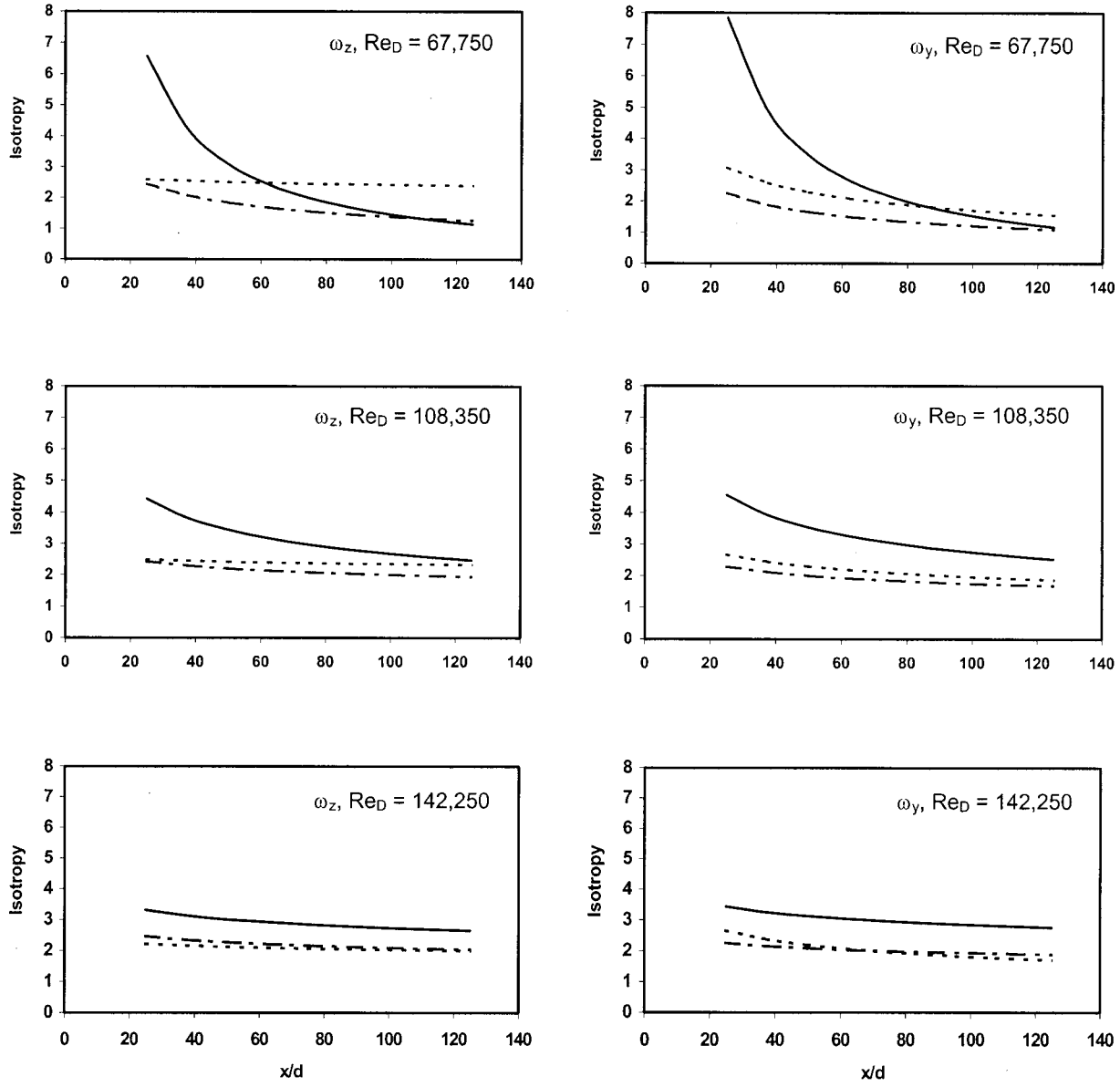

Fig. 3 Streamwise trends of the degree of isotropy (rod-grids of: —, 2.86 cm; - — -, 1.59 cm; - - -, 0.95 cm)

$$\mathrm{Iso} = \frac{\overline{\omega^2}}{5\left(\overline{\frac{\partial u}{\partial x}}\right)^2} \tag{2}$$

where $\overline{\omega^2}$ is the mean square value of fluctuating vorticity components and $\partial u/\partial x$ is estimated from single wire measurements. The streamwise distributions of the estimated degree of isotropy, which is calculated from the best-fit curves of vorticity components and $\partial u/\partial x$, are shown in Fig. 3. For the 2.86 cm rod-grid, deviation from isotropy is highest (Iso of an order of 7 at $x/d = 25$) at the lowest Reynolds number. At freestream Re_D of 67,750, the grid turbulence approaches isotropy with downstream distance for all grids (Iso$\sim$1 at $x/d = 125$). Deviation from isotropy is higher for the higher Reynolds numbers (Iso$\sim$2 at $x/d = 125$ for Re_D of 108,350 and 142,250). The general trend is that turbulence approaches isotropy as downstream distance increases, and the degree of anisotropy is highest with the biggest rod-grid.

The stagnation line heat transfer data from the three grids are compared with the correlation of VanFossen et al. [7] in Fig. 4.

$$\mathrm{Fr} = 0.008\sqrt{\mathrm{Tu}\ \mathrm{Re}_D^{0.8}\left(\frac{\lambda_x}{D}\right)^{-0.574}} + 0.939 \tag{3}$$

There is a significant discrepancy between the present experimental data and Eq. (3) for the 2.86 cm rod-grid, but the agreement improves with decreasing size of rod. For the 0.95 cm rod-grid, 87 percent of data falls within ± 4 percent of Eq. (3). It is clear from Fig. 4 that correlations developed for isotropic turbulence generated by square mesh grids should be corrected to predict the heat transfer due to turbulence with distinct coherent vortical structures. The errors are larger for the 2.86 cm rod-grid, where the freestream turbulence has a greater distinction between the primary and secondary vortices. It is unlikely that correlations developed for isotropic turbulence can be used to estimate heat transfer to gas turbine blades, where the turbulence from the combustor and wakes from the upstream blades is highly anisotropic and laced with well-defined vortical structures.

The freestream turbulence needs to be characterized more comprehensively to obtain more accurate empirical models. It seems plausible that incorporating the vorticity field and spanwise veloc-

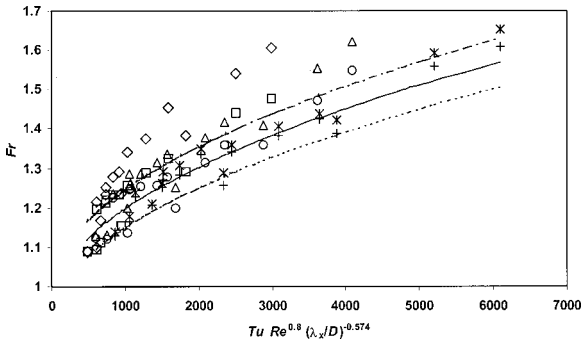

Fig. 4 Stagnation line Fr versus correlation parameter proposed by VanFossen et al. [7] (perpendicular Rod-grids: ◇, 2.86 cm; △, 1.59 cm; *, 0.95 cm; parallel rod-grids: □, 2.86 cm; ○, 1.59 cm; +, 0.95 cm; correlation lines: —, VanFossen et al. [7]; – – –, +4%; - - -, −4%)

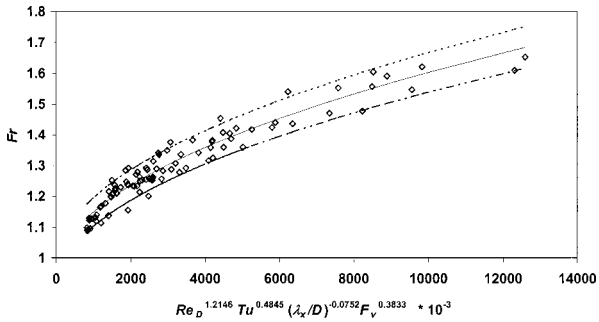

Fig. 5 Stagnation line Fr versus correlation parameter with spanwise vorticity and velocity fluctuations for both grid orientations (◇, data, correlation lines: —, Eq. (5); - - -, +4%; - · - ·, −4%)

ity fluctuations would improve the correlation, since they highlight the distinct structure of turbulence. Since vorticity amplification due to vortex stretching is hypothesized to influence the stagnation region heat transfer, the fluctuating vorticity component of primary vortices, i.e., ω_z and ω_y for turbulence generated by the rod-grids in perpendicular and parallel orientations, respectively, were considered to form a new turbulence parameter. The products of spanwise vorticity and velocity fluctuating components, $v\omega_z$ and $w\omega_y$, are taken as additional parameters to be included in the correlation. The products, $v\omega_z$ and $w\omega_y$, can be interpreted to represent the vortex forces in turbulence, which are analogous to the Coriolis forces [9]. The additional turbulence parameter used to develop a new correlation for the stagnation line heat transfer is defined as:

$$F_\nu = \frac{\nu\omega_z D}{U^2} \quad \text{for grid-rods in perpendicular orientation} \tag{4.a}$$

$$F_\nu = \frac{w\omega_y D}{U^2} \quad \text{for grid-rods in parallel orientation} \tag{4.b}$$

Therefore, the additional parameter is the vortex force due to primary vortices of freestream normalized by the diameter of the leading edge and the mean freestream velocity. The new correlation is obtained by a regression analysis and is presented in Fig. 5. It can be seen that 95 percent of experimental data fall within the ±4 percent of the new correlation given by:

$$\mathrm{Fr} = 0.00021\sqrt{\mathrm{Re}_D{}^{1.2146}\mathrm{Tu}^{0.4845}\left(\frac{\lambda_x}{D}\right)^{-0.0752} F_\nu^{0.3833}} + 0.939 \tag{5}$$

The improved correlation suggests that the inclusion of the vorticity field and spanwise velocity components takes into account the vortical structures of the freestream to a certain extent. It is clear that freestream turbulence with different orientations of coherent vortical structures have different influences over the heat transfer in the stagnation region, and the consideration of vortical structures of turbulence would improve the empirical models for prediction of gas turbine heat transfer.

Conclusions

Heat transfer enhancement in the stagnation region by freestream turbulence with distinct coherent vortical structures is different to that by turbulence generated using square-mesh grids. The present heat transfer data, obtained using an array of parallel rods in different orientations, are poorly predicted by existing correlation models. A new correlation model was developed by including the lateral fluctuating velocity and vorticity components of the freestream. The new correlation model predicts the heat transfer data of this study within ±4 percent. Any empirical model should take into account the distinct nature of the coherent vortical structures of the turbulence to improve its predictive capability.

Acknowledgments

The support of the Natural Sciences and Engineering Research Council (NSERC) of Canada is gratefully acknowledged.

Appendix

Analysis of Experimental Uncertainties. Following the uncertainty analysis methods of Moffat [14] the uncertainty in Fr can be expressed as:

$$(Un_{\mathrm{Fr}})^2 = (Un_{\mathrm{Nu}})^2 + 0.25(Un_{\mathrm{Re}D})^2$$

where Un_{Fr} = Uncertainty in Fr (%)
Un_{Nu} = Uncertainty in Nu (%)
$Un_{\mathrm{Re}\,D}$ = Uncertainty in Re_D (%)

The uncertainty in Fr and the influencing variables with 95 percent confidence levels are given in Table 1 for both maximum and minimum freestream velocities. Uncertainties in temperature were considered in estimating conduction heat loss, radiation heat losses and convection heat transfer. Uncertainties associated with leading edge diameter (D), thermal conductivity (k), and area (A) are assumed to be negligible since these values are based on the data specified by manufacturers.

The techniques proposed by Yavuzkurt [12] were used to estimate the uncertainties in Tu and λ_x and ω. The uncertainties are given in Table 2.

Nomenclature

d = diameter of a grid-rod (m)
D = diameter of cylindrical leading edge (m)
Fr = Frossling number ($\mathrm{Nu}/\sqrt{\mathrm{Re}_D}$)
F_ν = dimensionless vortex force
Iso = degree of isotropy
Re_D = Reynolds number based on D
t = time (s)
Tu = streamwise turbulence intensity
u = rms of fluctuating velocity component in streamwise direction (m/s)
U = mean freestream velocity (m/s)
v = rms of fluctuating velocity component in spanwise Y-direction (parallel to stagnation line) (m/s)
w = rms of fluctuating velocity component in spanwise Z-direction (m/s)
x = distance downstream of the grid (m)

Ω_y = instantaneous vorticity in spanwise *Y*-direction (l/s)
Ω_z = instantaneous vorticity in spanwise *Z*-direction (l/s)
λ_x = streamwise integral length scale of turbulence (m)
ω_y = rms of fluctuating vorticity component in spanwise *Y*-direction (l/s)
ω_z = rms of fluctuating vorticity component in spanwise *Z*-direction (l/s)

References

[1] Smith, M. C., and Kuethe, A. M., 1966, "Effects of Turbulence on Laminar Skin Friction and Heat Transfer," Phys. Fluids, **9**(12), pp. 2337–2344.
[2] Kestin, J., and Wood, R. T., 1971, "The Influence of Turbulence on Mass Transfer from Cylinders," ASME J. Heat Transfer, **93C**, pp. 321–327.
[3] Lowery, G. W., and Vachon, R. I., 1975, "Effect of Turbulence on Heat Transfer from Heated Cylinders," Int. J. Heat Mass Transf., **18**(11), pp. 1229–1242.
[4] O'Brien, J. E., and VanFossen, G. J., 1985, "The Influence of Jet-Grid Turbulence on Heat Transfer from the Stagnation Region of a Cylinder in Crossflow," ASME Paper 85-HT-58.
[5] Mehendale, A. B., Han, J. C., and Ou, S., 1991, "Influence of High Mainstream Turbulence on Leading Edge Heat Transfer," ASME J. Heat Transfer, **113**, pp. 843–850.
[6] Yeh, F. C., Hippensteele, S. A., VanFossen, G. J., Poinsatte, P. E., and Ameri, A. 1993, "High Reynolds Number and Turbulence Effects on Aerodynamics and Heat Transfer in a Turbine Cascade," Paper No. AIAA-93-2252.
[7] VanFossen, G. J., Simoneau, R. J., and Ching, C. Y., 1995, "Influence of Turbulence Parameters, Reynolds Number and Body Shape on Stagnation Region Heat Transfer," ASME J. Heat Transfer, **117**, pp. 597–603.
[8] Oo, A. N., and Ching, C. Y., 2001, "Effect of Turbulence with Different Vortical Structures on Stagnation Region Heat Transfer," ASME J. Heat Transfer, **123**, pp. 665–674.
[9] Tennekes, H., and Lumley, J. L., 1972, *A First Course in Turbulence*, The MIT Press, The Massachusetts Institute of Technology.
[10] Foss, J. F., and Haw, R. C., 1990, "Transverse Vorticity Measurements Using a Compact Array of Four Sensors," *The Heuristics of Thermal Anemometry*, D. E. Stock, S. A. Sherif, and A. J. Smits, eds., ASME-FED 97, pp. 71–76.
[11] Antonia, R. A., Browne, L. W. B., and Shah, D. A., 1988, "Characteristics of Vorticity Fluctuation in a Turbulent Wake," J. Fluid Mech., **189**, pp. 349–365.
[12] Yavuzkurt, S., 1984, "A Guide to Uncertainty Analysis of Hot-Wire Data," ASME J. Fluids Eng., **106**, pp. 181–186.
[13] Zhou, T., and Antonia, R. A., 2000, "Reynolds Number Dependence of the Small-Scale Structure of Grid Turbulence," J. Fluid Mech., **406**, pp. 81–107.
[14] Moffat, R. J., 1988, "Describing the Uncertainties in Experimental Results," Exp. Therm. Fluid Sci., **1**, pp. 3–17.

Similarity Solution for Marangoni Convection Over a Flat Surface

David M. Christopher
Associate Professor
Mem. ASME
e-mail: dmc@tsinghua.edu.cn

Buxuan Wang
Professor

Thermal Engineering Department, Tsinghua University, Beijing, 100084, China

A similarity solution is presented for Marangoni flow over a flat surface for both the velocity and temperature profiles assuming developing boundary layer flow along the surface with various imposed temperature profiles. Marangoni flow results from variations of the surface tension along a liquid-vapor interface and is especially noticeable in microgravity. Solutions are presented for the surface velocity, the total flow rate and the heat transfer for various temperature profiles and various Prandtl numbers. [DOI: 10.1115/1.1473143]

Keywords: Boiling, Convection, Heat Transfer, Thermocapillary

Introduction

Marangoni flow due to surface tension variations is of importance in various processes including the flow in crystal growth melts in both microgravity and normal earth gravity conditions where the Marangoni flow can affect crystal quality and in boiling where the Marangoni flow may significantly affect the heat transfer as shown by boiling tests in microgravity [1,2].

The numerous investigations of Marangoni flow have been reviewed in the literature (e.g., [3,4]) so only the studies most closely related to this paper are reviewed here. Okano et al. [5] presented an order-of-magnitude analysis of Marangoni flow that showed the general trends for the Grashof number, Marangoni number, and Prandtl number dependence on the Reynolds number. Banks and Zaturska [6] and Arafune and Hirata [7] presented a similarity solution for the momentum boundary layer equations with the flat surface velocity specified as a function of the distance along the surface. Arafune and Hirata [7] also presented experimental results for Marangoni flow along a flat surface. Schwabe and Metzger [8] experimentally investigated Marangoni flow on a flat surface combined with natural convection in a unique geometry where the Marangoni and buoyancy effects could be varied independently.

This paper presents a similarity solution for both the momentum and energy boundary layer equations for Marangoni flow over a flat surface with an imposed surface temperature gradient that is a power-law function of the location. The resulting family of solutions can also be applied qualitatively to other flows that have surface temperature variations that can be related to the assumed temperature variation as has been done with the Falkner-Skan family of flows [6]. The momentum and energy boundary layer equations are transformed to ordinary differential equations which are then solved using the Runge-Kutta method. The present results extend previous solutions by including the solution of the energy equation so that the velocity distribution is related to the specified temperature distribution through the Marangoni boundary condition rather than just specifying the surface velocity distribution as done previously.

Theoretical Analysis

The continuity equation and the momentum and energy equations are solved for laminar boundary layer flow of a Newtonian fluid in the half plane $0<y<\infty$ having a flat surface in the x direction starting at $x=0$. The boundary conditions at the surface are:

$$\mu \left.\frac{\partial u}{\partial y}\right|_{y=0} = -\frac{d\sigma}{dT}\left.\frac{\partial T}{\partial x}\right|_{y=0}$$
$$\nu(x,0)=0 \tag{1}$$
$$T(x,0)=T(0,0)+Ax^{k+1}$$

Far from the surface, the boundary conditions are:

$$u(x,\infty)=0$$
$$T(x,\infty)=T_\infty=T(0,0) \tag{2}$$

Using the standard definition of the stream function, similarity variables are introduced as:

$$\eta=C_1x^dy$$
$$f(\eta)=C_2x^a\psi(x,y) \tag{3}$$
$$\varphi(\eta)=(T(x,y)-T(0,0))x^h/A$$

so the governing equations can be written as:

Contributed by the Heat Transfer Division for publication in the JOURNAL OF HEAT TRANSFER. Manuscript received by the Heat Transfer Division April 11, 2000; revision received February 25, 2002. Associate Editor: S. S. Sadhal.

$$f^m = f'^2(d-a) + aff''$$
$$\varphi'' = \Pr(af\varphi' - hf'\varphi) \tag{4}$$

The coefficients are defined as:

$$C_1 = \sqrt[3]{\frac{\frac{d\sigma}{dT}A\rho}{\mu^2}}; \quad C_2 = \sqrt[3]{\frac{\rho^2}{\frac{d\sigma}{dT}A\mu}} \tag{5}$$

For similarity, the exponents are related to k in Eq. (1) by:

$$d = \frac{k-1}{3}; \quad a = \frac{-2-k}{3}; \quad h = -1-k \tag{6}$$

The boundary conditions are:

$$f(0) = 0; \quad f''(0) = -1; \quad f'(\infty) = 0 \tag{7}$$

$$\varphi(0) = 1; \quad \varphi(\infty) = 0 \tag{8}$$

The surface velocity given by the similarity solution is:

$$u(x,0) = \sqrt[3]{\frac{\left(\frac{d\sigma}{dT}A\right)^2}{\rho\mu}} f'(0)x^{(2k+1)/3} \tag{9}$$

The temperature gradient coefficient can be defined in terms of the total temperature difference along a surface of length L as $A = \Delta T/L^{k+1}$ so that the Marangoni number can then be defined for a general temperature profile as:

$$\mathrm{Ma}_L = \frac{\frac{d\sigma}{dT}\frac{\Delta T}{L^{k+1}}L^{k+2}}{\mu\alpha} = \frac{\frac{d\sigma}{dT}\Delta TL}{\mu\alpha} \tag{10}$$

The Reynolds number defined in terms of the surface velocity is then related to the Marangoni number as:

$$\mathrm{Re}_L = \frac{u(x,0)L}{\nu} = f'(0)\mathrm{Ma}_L^{2/3}\mathrm{Pr}^{-2/3} \tag{11}$$

The total mass flow in the boundary layer per unit width can be written as:

$$\dot{m} = \int_0^\infty \rho u dy = \sqrt[3]{\frac{d\sigma}{dT}A\rho\mu}x^{(k+2)/3} f(\infty) \tag{12}$$

The problem statement in this analysis differs in several ways from that used by Arafune and Hirata [7], Banks and Zaturska [6] and others. While the definitions of the similarity variables are only slightly different, the surface boundary condition for the momentum equation in this analysis is based on the Marangoni boundary condition rather than the specified velocity variation as in previous works. In addition, the current derivation is extended to include the energy equation so that the velocity distribution throughout the liquid region is a function of the temperature distribution. The surface velocity distribution given in Eq. (9), while similar to the form of the velocity distribution used by others, is a result of the derivation that clarifies the relationship between the velocity and temperature distributions.

Discussion of Similarity Results

The governing equations, Eq. (4), were solved numerically using the fourth-order Runge-Kutta method with at least 20,000 steps. The shooting method was used to determine the unknown boundary conditions at $\eta = 0$, $f'(0)$ for the momentum equation and $\phi'(0)$ for the energy equation. The maximum value for the independent variable, η, which was a function of the Prandtl number, was always chosen to be at least 4 times the maximum momentum or thermal boundary layer thickness. The results presented in the following section were all independent of the number of steps and the maximum value of η.

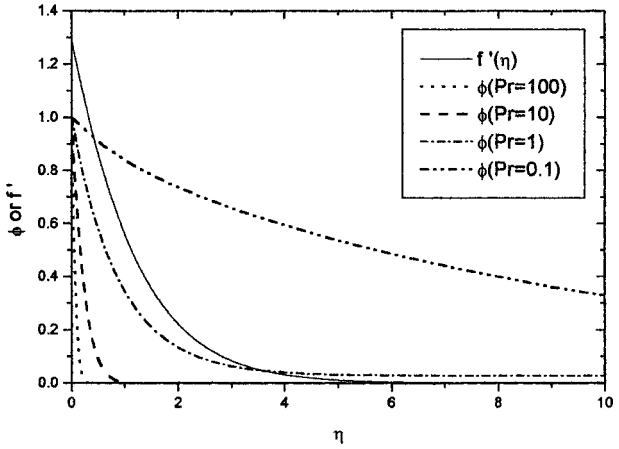

Fig. 1 Velocity and temperature profiles for $k=0$

The similarity stream function, f, is a function of the exponent, k, while the temperature function, ϕ, is a function of both k and the Prandtl number. The governing equations were solved subject to the boundary conditions in Eqs. (7) and (8) for various values of k and Pr. Typical velocity and temperature profiles are given in Fig. 1 for several representative values of the Prandtl number and for $k=0$ which is a linear surface temperature profile.

The variations of the surface velocity, the boundary layer thickness and the total flow rate in the boundary layer are given as functions of k in Fig. 2, of which $k=0$ refers to a linear profile and $k=1$ is quadratic, while $k=-0.5$ would be a temperature variation relative to the square root of x. The minimum value of k is -1, which results in no temperature variation on the surface and thus no Marangoni flow. The momentum boundary layer thickness is defined as the point where the velocity function, f, is 1 percent of the value at the surface. The surface velocity for small values of k is greater because for a fixed total temperature difference across the surface (i.e., fixed A), the profile for a small value of k is steeper near the leading edge which provides more flow. For larger values of k, the slope of the temperature profile is larger near the trailing edge where the boundary layer is thicker and the additional acceleration of the flow has less effect. The mass flow rate follows the same trend. The boundary layer thickness is greatest for the uniformly increasing temperature profile, $k=0$. For k greater than or less than 0, the temperature profile over part of the surface is relatively flat, so the flow does not accelerate much in that region and the boundary layer does not grow.

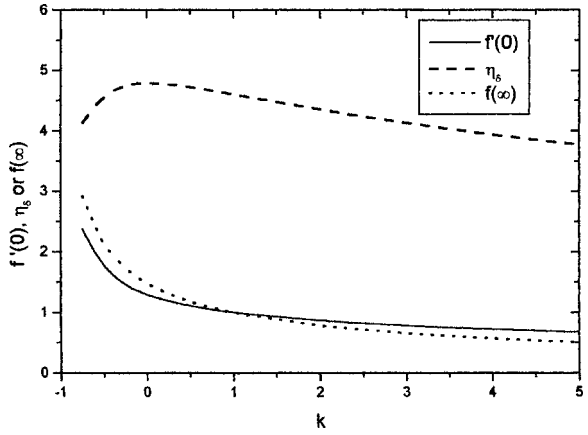

Fig. 2 Variations of surface velocity, boundary layer thickness, and flow rate for various temperature gradient exponents

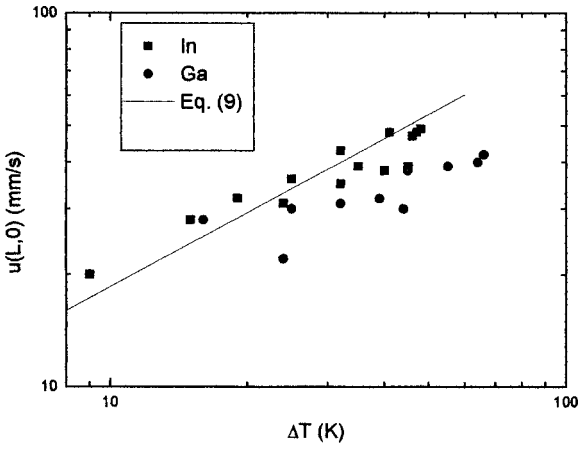

Fig. 3 Comparison of experimental results from Arafune and Hirata [7] with the predicted surface velocities for $k=0$

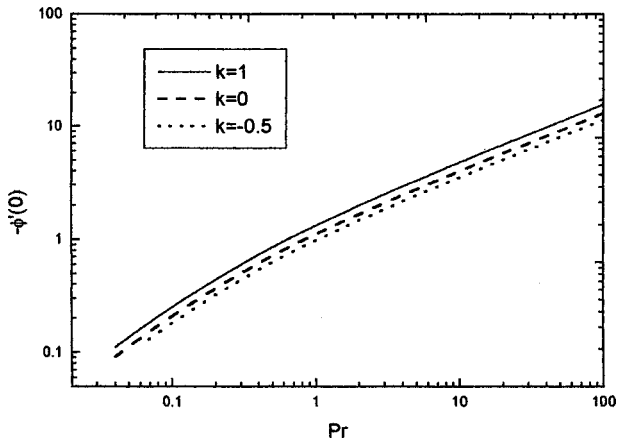

Fig. 4 Variation of the surface heat flux

The predicted surface velocities for $k=0$ agree well with the surface velocities measured by Arafune and Hirata [7] for Marangoni driven flow of gallium and indium in a shallow pool shown in Fig. 3. The slopes of the similarity and experimental results also agree with the analysis of Okano et al. [5] which showed that the Reynolds number should vary as the two-thirds root of the Marangoni number for large Reynolds numbers.

The variation of the surface heat flux as a function of the Prandtl number and the temperature gradient exponent is shown in Fig. 4. The local Nusselt number is:

$$\mathrm{Nu}_x=\frac{q''(x)x}{\lambda(T(x,0)-T(x,\infty))}=-\mathrm{Ma}_x^{1/3}\mathrm{Pr}^{-1/3}\left(\frac{x}{L}\right)^{(k+2)/3}\phi'(0) \tag{13}$$

The similarity analysis is based on the boundary layer equations which assume that the transverse derivatives of the velocity and temperature are much larger than their axial derivatives. Analysis of the similarity transformation shows that both are true if:

$$C_1L^{(k+2)/3}=\sqrt[3]{\frac{d\sigma}{dT}\frac{A\rho L^{k+2}}{\mu^2}}=\mathrm{Ma}_L^{1/3}\mathrm{Pr}^{-1/3}\gg 1 \tag{14}$$

Conclusions

A similarity solution was given for Marangoni boundary layer flow over a flat surface with an imposed temperature gradient. The predicted surface velocities agree well with measured values for shallow pools of liquid indium and gallium [7].

The analysis gives the variations of the velocity and temperature distributions in the boundary layer for power-law variations of the surface temperature gradient. Equations are then given for the surface velocity, the total mass flow rate and the heat flux at the interface as functions of the Marangoni, Prandtl and Reynolds numbers, the exponent k and the location. For $k=0$, the analysis agrees with previous results using a specified surface velocity distribution [5] that the Reynolds number based on the surface velocity varies as the two-thirds power of the Marangoni number.

Acknowledgment

The project was financially supported by the National Natural Science Foundation of China with grant number 59995550-3.

Nomenclature

a, d, h = exponents in similarity transformation
A = temperature gradient coefficient (K/m^{k+1})
C_1 = similarity transformation coefficient (m^a)
C_2 = similarity transformation coefficient ($s\ m^{(k-4)/3}$)
$f(\eta)$ = stream function similarity variable
k = temperature gradient exponent
$\dot{m}$ = mass flow rate per unit width (kg/m s)
Ma = Marangoni number, Eq. (10)
Nu = Nusselt number, Eq. (13)
Pr = Prandtl number
q'' = heat flux (W/m^2)
Re = Reynolds number, Eq. (11)
T = temperature (K)
u, v = velocities (m/s)
x, y = coordinates (m)

Greek

α = thermal diffusivity (m^2/s)
ϕ = dimensionless similarity temperature
η = location similarity variable
η_δ = dimensionless momentum boundary layer thickness
λ = thermal conductivity (W/mK)
μ = dynamic viscosity (Ns/m^2)
ν = kinematic viscosity (m^2/s)
ρ = density (kg/m^3)
σ = surface tension (N/m)
ψ = stream function (m^2/s)

Subscripts

L = average over surface length
x = local value

References

[1] Straub, J., 1994, "The Role of Surface Tension for Two-Phase Heat and Mass Transfer in the Absence of Gravity," Exp. Therm. Fluid Sci., **9**, pp. 253–273.
[2] Christopher, D., and Wang, B., 1998, "Marangoni Convection around a Bubble in Microgravity," *Heat Transfer, 1998, Proceedings 11th International Heat Transfer Conference*, J. S. Lee, ed., Taylor and Francis, Inc., Levittown, PA, **3**, pp. 489–494.
[3] Arafune, K., and Hirata, A., 1998, "Interactive Solutal and Thermal Marangoni Convection in a Rectangular Open Boat," Numer. Heat Transfer, Part A, **34**, pp. 421–429.
[4] Croll, A., Muller-Sebert, W., and Nitsche, R., 1989, "The Critical Marangoni Number for the Onset of Time-dependent Convection in Silicon," Mater. Res. Bull., **24**, pp. 995–1004.
[5] Okano, Y., Itoh, M., and Hirata, A., 1989, "Natural and Marangoni Convections in a Two-Dimensional Rectangular Open Boat," J. Chem. Eng. Jpn., **22**, pp. 275–281.
[6] Banks, W. H. H., and Zaturska, M. B., 1986, "Eigensolutions in Boundary-Layer Flow Adjacent to a Stretching Wall," IMA J. Appl. Math., **36**, pp. 263–273.
[7] Arafune, K., and Hirata, A., 1999, "Thermal and Solutal Marangoni Convection in In-Ga-Sb System," J. Cryst. Growth, **197**, pp. 811–817.
[8] Schwabe, D., and Metzger, J., 1989, "Coupling and Separation of Buoyant and Thermocapillary Convection," J. Cryst. Growth, **97**, pp. 23–33.

Discussion: "Sensitivity Analysis for Nonlinear Heat Condition," (Dowding, K. J., and Blackwell, B. F., 2001, ASME J. of Heat Transfer, 123(1), pp. 1–10)

Michael Shusser[1]

Dowding and Blackwell [1] derived sensitivity equations for general nonlinear heat conduction. What is surprising is that they chose to write these equations in dimensional form. One would expect that such a study must begin with writing the equations in nondimensional form and using Pi Theorem [2], p. 93 to find dimensionless groups of parameters on which the solution really depends. By failing to do this, the authors left undetected the fact that some of their sensitivity coefficients are linear dependent. In a practical calculation, this would unnecessarily increase the number of equations to solve.

The simple problem of steady one-dimensional heat conduction with temperature-dependent thermal conductivity used in [1] as a verification problem provides a good example to illustrate this point. Defining

$$\theta=\frac{T-T_L}{T_R-T_L},\quad z=\frac{x}{L},\quad r=\frac{k}{k_3} \tag{1}$$

one can re-write Eqs. (28)–(30) of [1] as

$$\frac{d}{dz}\left(r\frac{d\theta}{dz}\right)=0 \tag{2}$$

$$\theta\big|_{z=0}=0,\quad \theta\big|_{z=1}=1 \tag{3}$$

$$r(\theta)=\begin{cases} r_1+(r_2-r_1)\left(\dfrac{\theta-\theta_1}{\theta_2-\theta_1}\right), & \theta_1\leqslant\theta\leqslant\theta_2 \\ r_2+(1-r_2)\left(\dfrac{\theta-\theta_2}{\theta_3-\theta_2}\right), & \theta_2\leqslant\theta\leqslant\theta_3 \end{cases} \tag{4}$$

Here

$$r_1=\frac{k_1}{k_3},\quad r_2=\frac{k_2}{k_3} \tag{5}$$

We see that the dependence of the solution on thermal conductivity changes is determined not by three parameters k_1, k_2, k_3, as in [1], but by only *two* parameters r_1, r_2. Following [1], the corresponding sensitivity coefficients θ_{r_1}, θ_{r_2} can be defined:

$$\theta_{r_1}=r_1\frac{\partial\theta}{\partial r_1},\quad \theta_{r_2}=r_2\frac{\partial\theta}{\partial r_2} \tag{6}$$

Applying the chain rule, one can relate θ_{r_1}, θ_{r_2} to the dimensional sensitivities T_{k_1}, T_{k_2}, T_{k_3} defined in [1]:

$$T_{k_1}=k_1(T_R-T_L)\frac{\partial\theta}{\partial r_1}\frac{\partial r_1}{\partial k_1}=(T_R-T_L)\theta_{r_1} \tag{7}$$

$$T_{k_2}=k_2(T_R-T_L)\frac{\partial\theta}{\partial r_2}\frac{\partial r_2}{\partial k_2}=(T_R-T_L)\theta_{r_2} \tag{8}$$

$$T_{k_3}=k_3(T_R-T_L)\left(\frac{\partial\theta}{\partial r_1}\frac{\partial r_1}{\partial k_3}+\frac{\partial\theta}{\partial r_2}\frac{\partial r_2}{\partial k_3}\right)=-(T_R-T_L)(\theta_{r_1}+\theta_{r_2}) \tag{9}$$

We can conclude that the sensitivities T_{k_1}, T_{k_2}, T_{k_3} are not independent but satisfy

$$T_{k_1}+T_{k_2}+T_{k_3}=0 \tag{10}$$

It is seen from Fig. 2 of [1] that Eq. (10) is indeed satisfied.

[1]Department of Mechanical Engineering, California Institute of Technology, MC 104-44, Pasadena, CA 91125

References

[1] Dowding, K. J., and Blackwell, B. F., 2001. "Sensitivity Analysis for Nonlinear Heat Conduction," ASME J. Heat Transfer, **123(1)**, pp. 1–10.
[2] Birkhoff, G., 1960, *Hydrodynamics. A Study in Logic, Fact and Similitude*, 2nd ed., Princeton University Press, Princeton.

Closure to "Discussion: 'Sensitivity Analysis for Nonlinear Heat Condition,' (2001, ASME J. of Heat Transfer, 123(1), pp. 1–10)"

K. J. Dowding and B. F. Blackwell
Sandia National Laboratories, Validation and Uncertainty Quantification Process, P.O. Box 5800 M/S 0828, Albuquerque, NM 87185-0828

We agree completely with the analysis of Professor Shusser that the sensitivity coefficients for our verification problem are correlated. From our considerable experience in parameter estimation, this is something we are very familiar with. Perhaps in our article we failed to make it clear that we are attempting to address parameter sensitivity for multidimensional transient heat conduction problems in complex geometries. These problems may have tens to hundreds of parameters and it will be difficult to ascertain which parameters are correlated or pertinent dimensionless groups. By their nature, these problems require large computer codes and putting the equations in dimensionless form is not a realistic option. Our interest in the rather simple one-dimensional steady state problem with two linear conductivity segments was purely as a verification problem for our software implementation and the correlation of the sensitivity coefficients was not thought to be a significant issue in our work.

